



University of HUDDERSFIELD

University of Huddersfield Repository

Boulbrima, Alexandre

Structural and Functional characterization of the Arabidopsis thaliana Voltage Dependent Anion Channel 1 and the Kinesin-like mKlp2 proteins

Original Citation

Boulbrima, Alexandre (2019) Structural and Functional characterization of the Arabidopsis thaliana Voltage Dependent Anion Channel 1 and the Kinesin-like mKlp2 proteins. Doctoral thesis, University of Huddersfield.

This version is available at <http://eprints.hud.ac.uk/id/eprint/35129/>

The University Repository is a digital collection of the research output of the University, available on Open Access. Copyright and Moral Rights for the items on this site are retained by the individual author and/or other copyright owners. Users may access full items free of charge; copies of full text items generally can be reproduced, displayed or performed and given to third parties in any format or medium for personal research or study, educational or not-for-profit purposes without prior permission or charge, provided:

- The authors, title and full bibliographic details is credited in any copy;
- A hyperlink and/or URL is included for the original metadata page; and
- The content is not changed in any way.

For more information, including our policy and submission procedure, please contact the Repository Team at: E.mailbox@hud.ac.uk.

<http://eprints.hud.ac.uk/>

**Structural and Functional characterization of the *Arabidopsis thaliana*
Voltage Dependent Anion Channel 1 and the Kinesin-like mKlp2
proteins**

Alexandre Boulbrima

A thesis submitted to the University of Huddersfield

In partial fulfilment of the requirements for

The degree of Doctor of Philosophy

April 2019

Copyright declaration

1. The author of this thesis (including any appendices and/or schedules to this thesis) owns any copyright in it (the “Copyright”) and he has given The University of Huddersfield the right to use such Copyright for any administrative, promotional, educational and/or teaching purposes.
2. Copies of this thesis, either in full or in extracts, may be made only in accordance with the regulations of the University Library. Details of these regulations may be obtained from the Librarian. This page must form part of any such copies made.
3. The ownership of any patents, designs, trademarks and any and all other intellectual property rights except for the Copyright (the “Intellectual Property Rights”) and any reproductions of copyright works, for example graphs and tables (“Reproductions”), which may be described in this thesis, may not be owned by the author and may be owned by third parties. Such Intellectual Property Rights and Reproductions cannot and must not be made available for use without the prior written permission of the owner(s) of the relevant Intellectual Property Rights and/or Reproductions.

Abstract

The Voltage Dependent Anion Channel (VDAC) is a well characterized mitochondrial porin, known to participate in multiple cellular processes, ensuring the transport of ions, ATP, ADP and proteins of the respiratory chain between intermembrane space (IMS) and the cytosol. Hence, their abundance and strategic localization in the Outer Mitochondrial Membrane (OMM) cast them as a gatekeeper for the transit of ions and metabolites between the mitochondria and the cytosol. These channels were shown to exhibit a strong response to a variation of current, with frequent opening and closure of the channel, and the conservation in their three-dimensional structure attest to their essential role. The study of plant VDACs could offer interesting insights into the cellular and sub-cellular functions of the channel, as the importance of VDACs in plant development, fertility and physiology, was only recently been uncovered. Filling this knowledge gap on plant VDAC could greatly enrich our understanding of VDAC physiology in all eukaryotes.

Here, we report the successful purification of native and mutant *Arabidopsis thaliana* VDAC1 proteins. We highlight micelle-embedded AtVDAC structures by Small Angle X-Ray Scattering in 0.1 % (v/v) LDAO and show that *in vitro* refolded AtVDAC1 is mostly composed of beta sheets with a small helicity in circular dichroism experiments, in harmony with previous observations on eukaryotic VDACs. We demonstrate that the AtVDAC1 channel can exhibit voltage mediated gating activity when incorporated into a lipid bilayer, with an open state S0 conductance of 0.54 nS and at least two closed states, S1 and S2, with conductances of 0.43 nS and 0.31 nS, respectively, close to those reported for other VDACs in similar salt concentrations. We also attempt to understand its sensing ability and denote a current-mediated preference for S1 state at -20 mV. Finally, we introduce a new parameter for the electrophysiological characterisation of the channel, the “power of charge” and report similar transfer of charges at -20 mV and -40 mV despite the lower gating activity associated with the S2 state.

In parallel, a potential AtVDAC1-binding partner, mKlp2C-Ter (a truncated version of a mitochondria-restricted kinesin-like protein from *A. thaliana*), was also heterologously expressed, purified and characterised. We report its behaviour in solution using SAXS, and preliminary functional characterization by Isothermal-Titration Calorimetry (ITC), highlighting an ability to bind zinc ions. These first steps constitute the groundwork for future binding studies focusing on AtVDAC1 interaction with cytosolic partners, and the molecular and electro-physiological consequences of these interactions.

Total word count 77577

Table of contents

1. Chapter 1: Introduction	20
1.1. The mitochondrion	20
1.2. The programmed cell death (PCD)	23
1.3. Mitochondria and apoptosis	25
1.4. Mitochondria and pathology	26
1.4.1. Mitochondria and the theory of aging	27
1.5. The Voltage-Dependent Anion Channel (VDAC)	28
1.5.1. VDAC gene family	28
1.5.2. Expression and location	29
1.5.3. The VDACs from <i>Arabidopsis thaliana</i>	31
1.6. Structural organization of VDAC proteins	33
1.6.1. Plant VDACs	40
1.7. Roles and Functions of VDACs	43
1.7.1. Transport of ions	43
1.7.1.1. BLM: the example of mVDAC1	46
1.7.2. VDAC1 and the transport of metabolites	48
1.7.3. VDAC1 as a gateway for Reactive Oxygen Species (ROS)	48
1.7.4. VDAC1 as a cholesterol transporter	50
1.7.5. VDAC1 as a lipid transporter	50
1.7.6. VDAC1 and the regulation of Calcium transport	51
1.8. VDAC1 as a mediator of apoptosis	53
1.8.1. VDAC oligomerization as a potential gateway for cytochrome C release from the mitochondria	54
1.9. The Permeability Transition Pore (PTP)	57
1.10. Summary	59
1.10.1. AtVDAC partners	59
1.11. Kinesins	62
1.11.1. General structural organization of kinesins	62
1.11.2. Motor domain of kinesins	63
1.11.3. Tail domain of kinesins	65
1.12. Aims and objectives of this study	67
2. Chapter 2: Materials and Methods	69
2.1. Buffers and media	69
2.2. Plasmids and gene sequences	71
2.3. Microbiology	75
2.3.1. Bacterial strain genotypes	75

2.3.2.	Preparation of chemically competent cells	75
2.3.3.	Bacterial cell transformation	76
2.3.4.	Heterologous gene expression in <i>E. coli</i>	76
2.3.4.1.	IPTG induction	76
2.3.4.2.	Auto-induction	77
2.4.	Molecular Biology methods	78
2.4.1.	PCR amplification	78
2.4.1.1.	Colony PCR	79
2.4.2.	Restriction endonuclease digests	79
2.4.3.	Agarose Gel purification of digested pET-20b(+) and <i>AtVDAC genes</i>	81
2.4.4.	Ligation	81
2.4.5.	PCR based site directed mutagenesis	82
2.4.6.	Agarose gel electrophoresis	83
2.5.	Biochemical Methods	84
2.5.1.	Bacterial lysis by sonication	84
2.5.2.	Washing of inclusion bodies (VDACs only)	84
2.5.3.	<i>In vitro</i> refolding (VDACs only)	86
2.5.3.1.	Small scale refolding screen	86
2.5.4.	Ion exchange chromatography	88
2.5.4.1.	<i>AtVDAC</i> proteins	88
2.5.4.2.	mKlp2 C-terminal tail (mKlp2C-Ter)	88
2.5.5.	Desalting and protein concentrating	89
2.5.6.	Size exclusion chromatography	89
2.5.6.1.	Size exclusion column calibration on Superdex 75	89
2.5.6.2.	Size exclusion column calibration on Superose 6	90
2.5.7.	Determination of protein concentration	93
2.5.7.1.	BCA assay	93
2.5.8.	Acetone precipitation	93
2.5.9.	Lipid reconstitution	94
2.5.10.	SDS PAGE electrophoresis	95
2.5.10.1.	SDS-PAGE gel casting	95
2.5.10.2.	SDS-PAGE gel electrophoresis	96
2.5.11.	Western Blotting	98
2.5.12.	Thin Layer Chromatography	101
2.6.	Biophysical methods	102
2.6.1.	SAXS	102
2.6.1.1.	Data collection	103

2.6.1.2. Data analysis	104
2.6.2. Electrophysiology	104
2.6.3. Iso-thermal titration calorimetry (ITC)	108
2.6.4. Circular Dichroism (CD)	110
2.7. Bioinformatics	112
3. Chapter 3: AtVDAC1	113
3.1. Heterologous production of AtVDAC proteins in <i>Escherichia coli</i>	113
3.2. Preparation of Inclusion bodies for AtVDAC1	114
3.3. Optimization of native AtVDAC1 refolding and purification process	115
3.3.1. Optimisation of the first AtVDAC1 refolding step (RF1)	115
3.3.2. Chromatography Stage	118
3.4. Purification of Native-like AtVDAC1 protein by Ion (cation) Exchange Chromatography (IEX) using an HiTrap solid support	122
3.5. Size exclusion chromatography of native AtVDAC1 on Superose6 Increase®	124
3.6. Structural characterisation of AtVDAC1 by Circular Dichroism (CD)	126
3.7. Functional characterization of AtVDAC1 by Planar Lipid Bilayer: Electrophysiology	130
3.7.1. Introduction to Planar lipid bilayer assay	131
3.7.2. Electrophysiological characterization of AtVDAC1	131
3.7.3. Determination of dwell times between AtVDAC1 conducting states	142
3.8. Discussion	147
3.8.1. Heterologous production and purification of AtVDAC1 protein in <i>E.coli</i>	147
3.8.2. Structural characterisation of AtVDAC1 by Circular Dichroism (CD)	150
3.8.3. Functional characterisation of AtVDAC1 by Black Lipid Membrane (BLM)	152
3.8.3.1. Comparison of the “power” of charge between -40 mV and -20 mV	156
3.8.3.2. Troubleshooting of BLM experiments on AtVDAC1 channel	157
4. Chapter 4: AtVDAC1 mutants D177N, T156C and D258N	161
4.1. Identification of AtVDAC1 residues for mediation of contacts with hexokinase III	161
4.2. Amplification and screening of mutant constructs	164
4.3. Optimization of the purification process of AtVDAC1 mutants	167
4.4. Purification of AtVDAC1-D177N mutant protein by Cation Exchange Chromatography (CEX) using an HiTrap solid support	169
4.4.1. Size exclusion chromatography of purified AtVDAC1-D177N using a Superose6 Increase®	171
4.5. Purification of AtVDAC1-D258N mutant protein by Cation Exchange Chromatography (CEX) using an HiTrap solid support	173
4.5.1. Size exclusion chromatography of AtVDAC1-D258N protein using a Superose6 Increase®	175
4.6. Purification of AtVDAC1-T156C mutant protein by Cation Exchange Chromatography (CEX) using an HiTrap solid support	177

4.6.1.	Size exclusion chromatography of AtVDAC-T156C using a Superose6 Increase®	179
4.7.	Identification of AtVDAC purified proteins by Western Blotting	181
4.8.	Discussion	183
5.	Chapter 5: Small Angle Scattering of AtVDAC proteins	185
5.1.	Introduction to Small Angle X-Ray scattering (SAXS)	185
5.2.	Important parameters in SAXS	185
5.3.	Analysis of scattering data and generation of preliminary protein envelopes	187
5.4.	Generation of the Bovine Serum Albumin (BSA) Envelope	191
5.4.1.	Data Collection on BSA at 5 mg/mL	191
5.4.2.	Primary analysis of the BSA (5 mg/mL) scattering data	192
5.4.3.	Quality analysis on BSA (5 mg/mL) scattering data	195
5.4.4.	Evaluation of the P(r) distribution function of the 5 mg/mL BSA scattering data	198
5.4.5.	Generation of molecular envelopes for BSA at 5 mg/mL	200
5.4.6.	Evaluation of the generated envelopes for BSA	201
5.4.7.	Final envelope refinement for BSA at 5 mg/mL	203
5.5.	Structural characterization of AtVDAC1 protein by Small Angle X-ray Scattering (SAXS)	205
5.5.1.	Data collection for AtVDAC1	205
5.5.2.	Calculation of the radius of gyration for AtVDAC1	207
5.5.3.	Kratky and Porod analysis of the analysed AtVDAC1 samples	209
5.5.4.	Evaluation of the P(r) distribution of AtDAC1 scattering curves at 4 and 2 mg/mL	210
5.5.5.	Generation and refinement of calculated molecular envelopes for AtVDAC1	211
5.6.	Structural characterization of AtVDAC1 D177N mutant by Small Angle X-ray Scattering (SAXS)	215
5.6.1.	Data collection for AtVDAC1 D177N	215
5.6.2.	Calculation of the radius of gyration for the AtVDAC1 D177N	217
5.6.3.	Kratky and Porod analysis of AtVDAC1 D177N at 2, 1, 0.5 and 0.25 mg/mL	219
5.6.4.	Evaluation of the P(r) distribution of D177N scattering curves at 2 and 1 mg/mL	221
5.6.5.	Generation and refinement of calculated molecular envelopes for D177N	223
5.7.	Structural characterization of D258N mutant by Small Angle X-ray Scattering (SAXS)	226
5.7.1.	Data collection for D258N	226
5.7.2.	Calculation of the radius of gyration for D258N	228
5.7.3.	Kratky and Porod analysis of D258N at 2, 1, 0.5 and 0.25 mg/mL	230
5.7.4.	Evaluation of the P(r) distribution of D258N scattering curves for at 2 and 1 mg/mL	231
5.7.5.	Generation and refinement of calculated molecular envelopes for D258N	233
5.8.	SAXS simulations with AtVDAC hypothetical 3D structures	236
5.9.	Summary of molecular envelopes dimensions for AtVDAC proteins	238
5.10.	Structural characterization of LDAO by Small Angle X-ray Scattering (SAXS)	239

5.10.1.	Data collection for LDAO	239
5.10.2.	Calculation of the radius of gyration for LDAO	240
5.10.3.	Kratky and Porod analysis of LDAO at 0.01, 0.0575, 0.115 and 0.23 % (v/v)	242
5.10.4.	Evaluation of the P(r) distribution for LDAO at 0.23 and 0.115 % (v/v)	244
5.10.5.	Generation and refinement of calculated molecular envelopes for LDAO	246
5.11.	Discussion	249
6.	Chapter 6: The Kinesin-like mKlp2C-Ter	252
6.1.	Cloning of <i>mKlp2C-Ter</i>	254
6.2.	Heterologous expression of mKlp2C-Ter in <i>E.coli</i>	254
6.3.	Purification of mKlp2-Ter by affinity chromatography using a Protino Ni-Nta solid support	254
6.3.1.	Resin reuse analysis of the Protino Ni-Nta solid support for the purification of mKlp2-Ter by affinity chromatography	258
6.4.	Size exclusion chromatography of purified mKlp2C-Ter using a Superose6 Increase®	259
6.5.	Stability studies on mKlp2C-Ter	262
6.5.1.	Dialysis	262
6.5.2.	Stability of mKlp2C-Ter in 10 mM Zinc	263
6.6.	Removal of the N-Terminal 6xHis-Tag domain of mKlp2C-Ter	266
6.6.1.	Small scale optimization of His-Tag removal with thrombin cleavage	266
6.6.2.	Large scale of mKlp2C-Ter with thrombin cleavage	269
6.7.	Functional characterization of mKlp2C-Ter by Isothermal Titration Calorimetry (ITC)	271
6.7.1.	Introduction to Isothermal Titration Calorimetry (ITC)	271
6.7.2.	Titration of mKlp2C-Ter with ZnCl ₂	272
6.8.	Structural characterization of mKlp2C-Ter by Small Angle X-ray Scattering (SAXS)	281
6.8.1.	Data collection for mKlp2C-Ter	281
6.8.2.	Calculation of the radius of gyration for mKlp2C-Ter	283
6.8.3.	Kratky and Porod analysis of mKlp2C-Ter at 4, 2 and 1 mg/mL	285
6.8.4.	Evaluation of the P(r) distribution for mKlp2C-Ter scattering curve at 4 mg/mL	286
6.8.5.	Generation and refinement of molecular envelopes for mKlp2C-Ter at 4 mg/mL	287
6.9.	Discussion	290
6.9.1.	Heterologous production of mKlp2C-Ter in <i>E.coli</i> and purification by affinity chromatography	290
6.9.2.	Removal of the 6xHis-Tag from mKlp2C-Ter	291
6.9.3.	SAXS experiments on mKlp2C-Ter protein	293
6.9.4.	Titration of mKlp2C-Ter with zinc ions (ITC)	295
7.	Conclusion and Future directions	298
8.	References	301
9.	Chapter 8 Appendixes	318

9.1.	Sanger DNA sequencing of AtVDAC constructs	318
9.2.	Example of calculations for the lipid reconstitution of AtVDAC1 protein in DMPC	323
9.3.	Identification of amino acids involved the docking of Hexokinase 1 to AtVDACs	324
9.4.	Protein sequence alignment of VDACS	325
9.5.	TLC experiment on AtVDAC1 oligomer and monomer fractions	328
9.6.	Secondary structure prediction of mKlp2C-Ter	328
9.7.	High Tension (HT) Voltage of AtVDAC1 monomer and oligomer	329
9.8.	Conversion between Theta (mDeg) and delta epsilon ($M^{-1}.cm^{-1}$)	329
9.9.	Calculation the mean residue molar ellipticity $[\theta]$	330
9.10.	Circular Dichroism analysis (raw data)	330

List of Figures

Figure 1.1 Schematic representation of a mitochondrion with its essential features.	21
Figure 1.2 Schematic representation of the extrinsic and intrinsic pathway of the PGD..	24
Figure 1.3 Typical symptom in Kearns-Sayre syndrome.	26
Figure 1.4 N-Terminal tail sequence alignment of AtVDACs.	32
Figure 1.5 Core structure of Voltage-dependant anion channels (VDACs).	33
Figure 1.6 Three-dimensional structure of mouse mVDAC1.	34
Figure 1.7 Three-dimensional structures of VDACs.	35
Figure 1.8 Organisation of secondary structure elements in the solved VDAC structures..	37
Figure 1.9 Charge distribution of mVDAC1.	38
Figure 1.10 Predicted 3D-model comparisons of AtVDAC1 and AtVDAC2.	41
Figure 1.11 Predicted 3D-models of AtVDAC1-4 by homology modelling.	42
Figure 1.12 Typical current recording of mVDAC1.	46
Figure 1.13 VDAC oligomerization as a gateway for CytC release from the mitochondria.	55
Figure 1.14 Simplified model for the Permeability Transition Pore (PTP).	58
Figure 1.15 <i>In vivo</i> interaction between AtVDAC3 and Kp1.	61
Figure 1.16 Schematic representation of conventional Kinesins structure.	63
Figure 1.17 Three-dimensional structure of the human ubiquitous kinesin motor domain.	64
Figure 1.18 Kinesin moving alongside a microtubule.	65
Figure 2.1 pET-20b(+) Plasmid map and cloning region	72
Figure 2.2 PCR parameters.	79
Figure 2.3 Example of cohesive joining of fragments with sticky ends.	81
Figure 2.4 PCR site directed mutagenesis basic principle.	82
Figure 2.5 Washing of inclusions bodies.	85
Figure 2.6 Refolding screen (RF1).	87
Figure 2.7 Comparison of commercial strong cation exchangers.	88
Figure 2.8 Superdex75 calibration.	90

Figure 2.9 Superose 6 calibration.	92
Figure 2.11 Western Blot sandwich Assembly.	99
Figure 2.12 Representation of Small Angle X-Ray scattering experiment.	102
Figure 2.13 The black lipid membrane set-up.	105
Figure 2.14 Schematic representation of the Teflon-cross section (I) between compartments.	106
Figure 2.15 Schematic representation of a gating event.	107
Figure 2.16 Iso-Thermal Calorimetry (ITC): basic principle.	109
Figure 2.17 Representative examples of CD spectra of main secondary structural elements.	111
Figure 3.1 Heterologous production of AtVDAC proteins in <i>E.coli</i> by auto-induction.	113
Figure 3.2 Production, washing and concentrating of AtVDAC1 inclusion bodies (IB).	114
Figure 3.3 Refolding screen of AtVDAC1 in RF1 and in the presence of different additives.	117
Figure 3.4 Initial cation exchange chromatography of AtVDAC1 protein using an increasing gradient of NaCl.	118
Figure 3.5 Size exclusion chromatography (SEC) of AtVDAC1 using Superdex75 and Superose6 solid supports.	119
Figure 3.6 SDS-PAGE analysis of SEC-AtVDAC1 fractions.	121
Figure 3.7 Cation exchange chromatography of AtVDAC1 protein using a Hitrap SP XL® with an increasing gradient of NaCl.	123
Figure 3.8 Size exclusion chromatography of AtVDAC1 using a Superose6 Increase®.	125
Figure 3.9 Circular Dichroism spectra of AtVDAC1.	127
Figure 3.10 Heat denaturation profile of AtVDAC1 samples.	130
Figure 3.11 Voltage ramp experiment of a single AtVDAC1 channel reconstituted on a POPE/POPS planar bilayer.	133
Figure 3.12 Representative recordings of single AtVDAC1 channels reconstituted on a POPE/POPS planar bilayer at 40 mV.	134
Figure 3.13 Typical BLM recordings of single AtVDAC1 channels reconstituted on a POPE/POPS planar bilayer.	135
Figure 3.14 Intermediate open states of AtVDAC1 channel.	136

Figure 3.15 I/V (Ohm) plots used for the determination of the conducting AtVDAC1 states.	138
Figure 3.16 Overall conductance profile of AtVDAC1 channel.	139
Figure 3.17 Conductance profile for the closed states of AtVDAC1 channel.	140
Figure 3.18 Analysis of S1 dwell times at -40 mV and -20 mV.	143
Figure 3.19 Example of AtVDAC1 channels in opposite directions.	158
Figure 3.20 Repetitive issue in event detection of S2 state.	159
Figure 3.21 Representative recordings of single AtVDAC1 channels reconstituted on a POPE/POPS planar bilayer at -40 mV.	159
Figure 4.1 Example of docking experiment of the <i>Nicotiana benthamiana</i> Hexokinase 1 on AtVDAC1 (based on 3EMN1).	161
Figure 4.2 Screening of D258N, D177N, E256Q and D180S AtVDAC1 mutant constructs by restriction endonuclease digests.	165
Figure 4.3 SDS-PAGE analysis of preliminary SEC purifications of AtVDAC1 T156C, D258N and D177N mutants.	167
Figure 4.4 Hitrap SP XL anion exchange chromatography of D177N mutant protein with an increasing gradient of NaCl.	170
Figure 4.5 Size exclusion chromatography of AtVDAC1D177N mutant protein.	172
Figure 4.6 Hitrap anion exchange chromatography of D258N mutant protein with an increasing gradient of NaCl.	174
Figure 4.7 Size exclusion chromatography of AtVDAC1-D258N mutant protein using a Superose6 Increase®.	176
Figure 4.8 Anion exchange chromatography of AtVDAC1-T156C mutant protein using a HiTrap SP XL 5 mL ® with an increasing gradient of NaCl.	178
Figure 4.9 Size exclusion chromatography of AtVDAC1-T156C mutant protein using a Superose 6 Increase®.	180
Figure 4.10 Confirmation of identity of AtVDAC1 Native-like and mutant proteins by Western Blotting.	181
Figure 5.1 Raw Scattering Intensity plots of BSA at 5 mg/mL and its buffer.	192

Figure 5.2 Initial Guinier analysis of the 5 mg/mL BSA scattering curve.	193
Figure 5.3 Kratky Analysis of the 5 mg/mL BSA scattering data.	195
Figure 5.4 Porod plot analysis the 5 mg/mL BSA scattering data.	196
Figure 5.5 P(r) distribution of BSA at 5 mg/mL.	199
Figure 5.6 Molecular envelopes of BSA at 5 mg/mL.	201
Figure 5.7 Predicted molecular envelopes for BSA at 5 mg/mL.	204
Figure 5.8 Raw Scattering Intensity plots of AtVDAC1 at 4, 2, 1, 0.5 and 0.25 mg/mL.	206
Figure 5.9 Guinier analysis of AtVDAC1 at 4, 2, 1 and 0.5 mg/mL.	208
Figure 5.10 Quality assessment of collected AtVDAC1 scattering curves at different protein concentrations.	210
Figure 5.11 P(r) distribution plots of AtVDAC1 scattering data.	211
Figure 5.12 SAXS derived 3D molecular envelopes for AtVDAC1.	214
Figure 5.13 Raw Scattering Intensity plots of mutant D177N at 2, 1, 0.5 and 0.25 mg/mL.	216
Figure 5.14 Guinier analysis of D177N at 2, 1, 0.5 and 0.25 mg/mL.	218
Figure 5.15 Quality assessment of D177N scattering curves at different protein concentrations.	220
Figure 5.16 P(r) distribution plots of D177N scattering data.	222
Figure 5.17 Generated molecular envelopes for D177N at 2 and 1 mg/mL.	225
Figure 5.18 Raw Scattering Intensity plots of mutant D258N at 2, 1, 0.5 and 0.25 mg/mL.	227
Figure 5.19 Guinier analysis of D258N at 2, 1, 0.5 and 0.25 mg/mL.	229
Figure 5. 20 Quality assessment of D258N scattering curves at different protein concentrations.	231
Figure 5. 21 P(r) distribution plots of D258N scattering data.	232
Figure 5.22 Generated molecular envelopes for D258N at 2 and 1 mg/mL.	235
Figure 5.23 Computed SAXS profiles based on AtVDAC predicted 3D-models.	237
Figure 5.24 Scattering Intensity plots of LDAO at 0.01, 0.0575, 0.115 and 0.23 % (v/v).	240
Figure 5.25 Initial Guinier analysis of LDAO at 0.0575, 0.115 and 0.23 % (v/v).	241
Figure 5.26 Quality assessment of LDAO scattering curves at different protein concentrations.	243
Figure 5.27 P(r) distribution plots of LDAO scattering data.	245
Figure 5.28 Generated molecular envelopes for LDAO at 0.23 and 0.115 % (v/v).	248

Figure 5.29 P(r) distribution plots of AtVDACs scattering data.	250
Figure 6.1 Identification of a zinc finger in the C-Terminal domain of mKlp2.	252
Figure 6.2 Ni-NTA affinity chromatography for mKlp2-Cter with an increasing gradient of [Imidazole] using a Protino 5 mL HisTrap.	255
Figure 6.3 Ni-NTA affinity chromatography of mKlp2-Cter with a step-gradient of [Imidazole] using a Protino 5 mL HisTrap.	257
Figure 6.4 Ni-NTA affinity chromatography of mKlp2-Cter with a step-gradient of [Imidazole] using a Protino 5 mL HisTrap after 20 cycles.	258
Figure 6.5 Size exclusion chromatography of 8 mg/mL (undiluted) mKlp2-Cter using a Superose6 Increase®.	260
Figure 6.6 Size exclusion chromatography of 4 mg/mL (diluted) mKlp2-Cter using a Superose6 Increase®.	261
Figure 6.7 Stability study of dialyzed mKlp2C-Ter.	263
Figure 6.8 Stability study on mKlp2C-Ter in the presence of 10 mM zinc.	265
Figure 6.9 N-Terminal domain of mKlp2C-Ter.	266
Figure 6.10 Optimisation of His-tag digestion from mKlp2C-Ter with thrombin cleavage.	268
Figure 6.11 Large scale digestion of mKlp2C-Ter-His6 with thrombin.	270
Figure 6.12 Single titration of 31 μ M mKlp2C-Ter with 40 mM ZnCl ₂ .	273
Figure 6.13 Prolonged titration of 31 μ M mKlp2C-Ter with 40 mM ZnCl ₂ .	275
Figure 6.14 Corrected prolonged titration of 31 μ M mKlp2C-Ter with 40 mM ZnCl ₂ .	277
Figure 6.15 Single titration of 6 μ M mKlp2C-Ter with 50 mM ZnCl ₂ .	278
Figure 6.16 Raw Scattering Intensity plots of mKlp2C-Ter at 4, 2 and 1 mg/mL.	282
Figure 6.17 Guinier analysis of mKlp2C-Ter at 4, 2 and 1 mg/mL.	284
Figure 6.18 Quality assessment of mKlp2C-Ter.	286
Figure 6. 19 P(r) distribution plot of mKlp2C-Ter scattering data at 4 mg/mL.	287
Figure 6.20 Final molecular envelopes for mKlp2C-Ter at 4 mg/mL.	289

List of Tables

Table 1.1 AtVDACs phylogeny.	31
Table 2.1. Buffers and media.	69
Table 2.2 DNA sequences of AtVDACs and mKlp2C-Ter genes.	73
Table 2.3 Primers used for the amplification of <i>AtVDACs</i> .	74
Table 2.4 <i>Escherichia coli</i> strains and associated genotypes.	75
Table 2.5 PCR components.	78
Table 2.6 AtVDAC restriction digest components.	80
Table 2.7 Restriction endonucleases and their application.	80
Table 2.8 Mutagenic primers and enzymes used to control nucleotide replacements.	83
Table 2.9 Lower gel (10%, resolving) recipe.	95
Table 2.10 Upper gel (4%, stacking) recipe. Components (left) and their corresponding volumes when making two stacking gels (middle) or one (right).	96
Table 2.11 SDS PAGE buffer recipes.	97
Table 2.12 Antibodies.	99
Table 3.1 Selected parameters for AtVDAC1 Circular Dichroism experiments.	126
Table 3.2 Secondary structure content from three CD-analysed AtVDAC samples.	128
Table 3.3 Statistical analysis of ATVDAC1 closed states.	141
Table 3.4 Probabilities of AtVDAC1 opening and closure channel at -40 and -20 mV.	144
Table 3.5 Total variation of charge for the AtVDAC1 channel.	145
Table 3.6 Famous VDACs Gating conductance.	153
Table 4.1 Redundant amino acids involved in the docking of <i>N.benthamiana</i> Hexokinase 1 to AtVDAC isoforms 1, 2 and 4.	162
Table 4.2 Mutant screening patterns.	164
Table 5.1 Table 5.1. Important SAXS <i>ab initio</i> Programs.	188
Table 5.2 Summary Table of R _g and I(0) values for BSA at 5 mg/mL.	194
Table 5.3 Summary of DAMSEL and DAMSUP results for BSA at 5 mg/mL.	202

Table 5.4 Derived R_g values for AtVDAC1 samples at different concentrations.	209
Table 5.5 Summary of DAMSEL and DAMSUP results for AtVDAC1 at 4 mg/mL and 2 mg/mL.	212
Table 5.6 Summary Table of R_g values for D177N.	219
Table 5.7 Summary of DAMSEL and DAMSUP results for D177N at 2 mg/mL and 1 mg/mL.	223
Table 5. 8 Summary Table of R_g values for D258N.	230
Table 5.9 Summary of DAMSEL and DAMSUP results for D258N at 2 mg/mL and 1 mg/mL.	233
Table 5. 10. Summary of parameters for the SAXS envelopes and predicted 3D models of AtVDAC proteins.	238
Table 5.11 Summary Table of R_g values for LDAO.	242
Table 5.12 Summary of DAMSEL and DAMSUP results for LDAO at 0.23 and 0.115 % (v/v).	246
Table 6.1 Binding parameters of zinc (40 mM) to mKlp2C-Ter (31 μ M).	274
Table 6.2 Binding parameters of zinc (40 mM) to mKlp2C-Ter (6 μ M).	279
Table 6.3 Summary Table of R_g values for mKlp2C-Ter.	285
Table 6.4 Summary of DAMSEL and DAMSUP results for mKlp2C-Ter at 4 mg/mL.	288
Table 7.1 Famous VDACS Gating conductance.	277

List of equations

Equation 2.1 Equation 2.1 Calculation of the amount of insert.	81
Equation 2.2 Thermodynamic laws defining the Gibbs free energy.	108
Equation 3.1 Ohm's Law.	136
Equation 3.2 Definition of a coulomb.	144
Equation 5.1 Scattering Intensity $I(q)$ as a function of the momentum transfer q (scattering vector).	186
Equation 5.2 Calculation of the Radius of gyration (R_g) by Guinier analysis.	193
Equation 6.1 Gibbs free energy main formula.	271
Equation 6.2 Definition of the binding affinity constant K for a single independent site.	272
Equation 6.3 Definition of the binding affinity constant K_i in sequential binding.	274

List of abbreviation

ADP	Adenosine di-phosphate
ATP	Adenosine tri-phosphate
Bax	Bcl-2-associated X
BLAST	Basic Local Alignment Search Tool
BLM/PLB	Black lipid membrane/Planar lipid bilayer
CD	Circular Dichroism
Cu/ZnSOD	Copper/zinc superoxide dismutase
DISC	Death-inducing signalling complex
FAS	Apoptosis antigen-1
FASL	Apoptosis antigen-1 ligand
HK	Hexokinase
hVDAC	Human Voltage dependent anion channel
IEX	Ion exchange chromatography
KIFC3	Kinesin family member C3
LDAO	N,N-Dimethyldodecylamine N-oxide
MnSOD	Manganese superoxide dismutase
mVDAC	Murine Voltage dependent anion channel
NADH	Nicotinamide adenine dinucleotide
OG	n-octyl- β -D-glucoside
OMP	Outer membrane protein
PCD	Programmed cell death
POPS	Phosphatidylserine
POPE	Phosphatidylethanolamine
R _g	Radius of Gyration
SAXS	Small-Angle X-ray Scattering
SDS	Sodium dodecyl sulphate

SDS-PAGE	Sodium dodecyl sulphate - polyacrylamide gel electrophoresis
SEC	Size Exclusion Chromatography
StAR	Steroidogenic acute regulatory protein
TNF	Tumour necrosis factor
TNFR1	Tumour necrosis factor receptor 1
TRAIL	Tumour necrosis factor-related apoptosis-inducing ligand
TSPO	Translocator protein
USP47	Ubiquitin-specific protease
VDAC	Voltage dependent anion channel
zfVDAC	Zebrafish Voltage dependent anion channel

Acknowledgements

First and foremost I want to thank my supervisor, Dr Georgios Psakis for providing me the opportunity to pursue this work. I am also grateful for its continuous support, patience and dedication throughout my PhD.

I thank the University of Huddersfield for providing a fee waiver and scholarship, as well as a place to undertake this research. I also thank the biological sciences technical staffs for their tremendous help over the past few years.

I thank Dr Marcus Allen (University of Brighton) for providing me the opportunity to train in Planar lipid bilayer assays, the University of Leeds for providing the resources for the Circular Dichroism experiments and the Diamond Light Source for funding and supporting SAXS experiments (Session ID: SM16748-1 at the Beamline B21 on Wed 27 Sep 2017).

Finally, I would like to thank my partner, Dr Ophelie Torres, for her priceless support over the past few years, contagious motivation and delicious meals.

1. Chapter 1: Introduction

1.1. The mitochondrion

Originally discovered in the late 19th century and called bioblast by Richard Altmann (Ernster and Schatz 1981), the mitochondrion is one of the main organelles in eukaryotic cells. Early observations lead to believe it was composed of protein and lipids. Sometimes called “grana”, it was soon named “mitochondrion” by Carl Benda in 1890. It became apparent early that the organelle was associated with respiration in cells.

The process of respiration was demonstrated first in 1939 by using minced muscle cells (Belitser and Tsybakova 1939). Two years later, Alfred Lipmann elaborated the concept that energy was being associated with Adenosine phosphate molecules (ADP and ATP) (Lipmann 1941). Further investigation and theories were elaborated during the next decade, but the involvement of the mitochondrion in this cellular process was still unknown (Ernster and Schatz 1981).

The introduction of newer methods of tissue fractionation by Albert Claude allowed mitochondria to be isolated (Claude and Fullam 1945). This helped greatly in the biochemical characterization of mitochondria alone. Consequently, many enzymes such as the cytochrome oxidase were proven to be restricted exclusively to mitochondria (Ernster and Schatz 1981). In 1948, discoveries highlighted the mitochondrion as the site of oxidative phosphorylation in eukaryotes (Kennedy and Lehninger 1948).

Over the past 50 years, great progress has been in the description, composition and characterization of mitochondria. In summary (Figure 1.1), the outer mitochondrial membrane surrounding the organelle was measured at 60 to 75 angstroms (Å) thick and has a protein-to-phospholipid ratio like that of the cell plasma membrane (1:1 weight). It comprises two bilayers, probably resulting from the endosymbiosis of a proteobacterium into another bacterium (Thrash, Boyd et al. 2011).

As the “energy factories” of the cell, mitochondria are involved in the production of energy in the form of ATP, via the citric acid cycle (Krebs cycle) and the oxidative phosphorylation. In cell development, the mitochondrion is essential, providing the necessary energy for cellular growth (Teixeira, Sanchez et

al. 2015). Furthermore, mitochondria are involved in numerous pathways in the cell such as those of the fatty acid metabolism, as well as those of calcium storage, programmed cell death (apoptosis) and the defence against pathogens (Greenberg 1996).

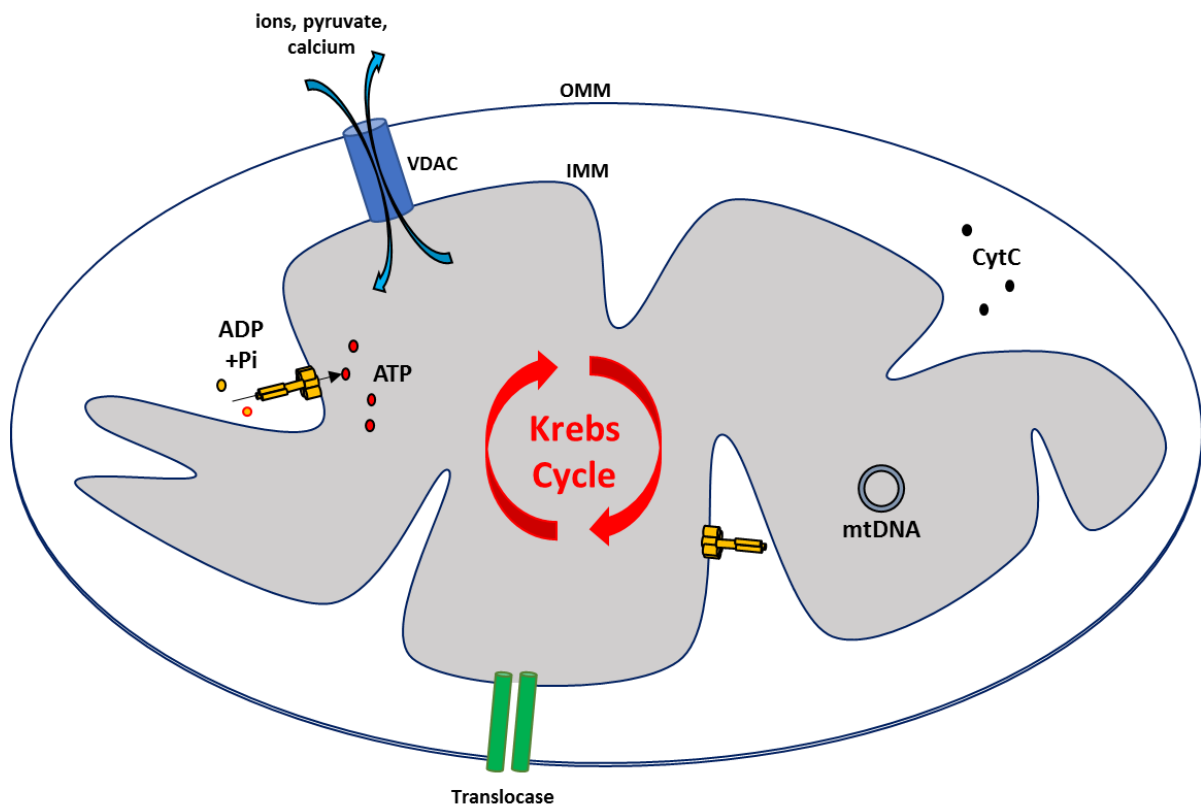


Figure 1.1 Schematic representation of a mitochondrion with its essential features. Composed of two bilayers, the outer mitochondrial membrane (OMM) and inner mitochondrial membrane (IMM), the mitochondrion serves as the energy factory of the cell. ATP (red dots) is produced via the oxidative phosphorylation of ADP and Pi (yellow dots) catalysed by the ATP synthase (yellow). The different elements necessary for this reaction are produced via the Krebs Cycle (red), and series of complexes in the IMM such as the Cytochrome C (black). The transport across the membrane is achieved through specific channels (VDAC, in blue) for small reagents, or translocases (green) in the case of bigger proteins, pro-proteins and complexes. Most of its mitochondrial DNA (mtDNA) has been transferred to the nucleus, except for few genes.

Structurally, the mitochondrion contains large numbers of membrane proteins called porins, amongst which the most abundant and major trafficking protein is the voltage-dependent anion channel (VDAC) (Colombini, Blachly-Dyson et al. 1996). Additional proteins such as translocases (Figure 1.1) can also be found but in a much lower concentration. The VDAC is the primary transporter of nucleotides, ions and metabolites between the cytosol and the intermembrane space (Blachly-Dyson and Forte, Hoogenboom, Suda et al. 2007). Larger proteins generally enter the mitochondrion with the help of a

N-terminus signal sequence, often binding to specific protein complexes called translocases (the complex TIM/TOM being the most famous), which will facilitate their transport across the membrane (Herrmann and Neupert 2000).

1.2. The programmed cell death (PCD)

The programmed cell death (PCD) or apoptosis is a process involving multiple cascades with fundamental cellular consequences such as DNA degradation (Bortner, Oldenburg et al. 1995), proteolysis (Solary, Eymin et al. 1998) and membrane permeabilization (Henry-Mowatt, Dive et al. 2004). It can be initiated by two signalling pathways, extrinsically or intrinsically (Elmore 2007) (Figure 1.2).

On one hand, the extrinsic pathway is characterized by the binding of extracellular signals, such as the tumour necrosis factor (TNF), the tumour necrosis factor-related apoptosis-inducing ligand (TRAIL) and the apoptosis antigen-1 ligand (FASL), to specific receptors (death receptors), like the tumour necrosis factor receptor 1 (TNFR1) and the apoptosis antigen-1 FAS (Iqbal, Aatur Rahman et al. 2015). The binding of the ligand to its receptor will induce the recruitment of an adaptor protein as well as the initiating procaspase 8 to the cytoplasmic domain of the death receptor. Upon formation of this complex named the death-inducing signalling complex (DISC), the procaspase 8 will be activated (by auto-proteolysis), converting it into a mature caspase 8 (Kantari and Walczak 2011). The latter will then activate additional caspases (namely 3, 7 and 6) (Slee, Adrain et al. 2001), triggering apoptosis, which will result in a proteolysis and DNA degradation in the cell, ultimately leading to cell death.

On the other hand, the intrinsic pathway can be triggered by intracellular stress signals, most notably by oxidative stress or DNA damage (Ott, Gogvadze et al. 2007). Then, the mitochondrial stress will lead to mitochondrial permeabilization and the subsequent release of inter-membrane apoptogenic proteins such as the Cytochrome C (CytC), the Second Mitochondria-derived Activator of Caspases/direct IAP binding protein with low pI complex (Smac/DIABLO) and the apoptosis inducing factor (AIF) (Li, Nijhawan et al. 1997, Verhagen, Ekert et al. 2000, Li, Srinivasula et al. 2002, Suen, Norris et al. 2008). As a result, the CytC will then interact with the apoptotic protease-activating factor 1 (Apaf-1) in the cytosol, to enhance oligomerization and formation of an apoptosome (Wang 2001). The apoptosome is formed with pro-caspase 9, which will then activate caspases 3 and 7, inducing cell death (Kroemer, Galluzzi et al. 2007).

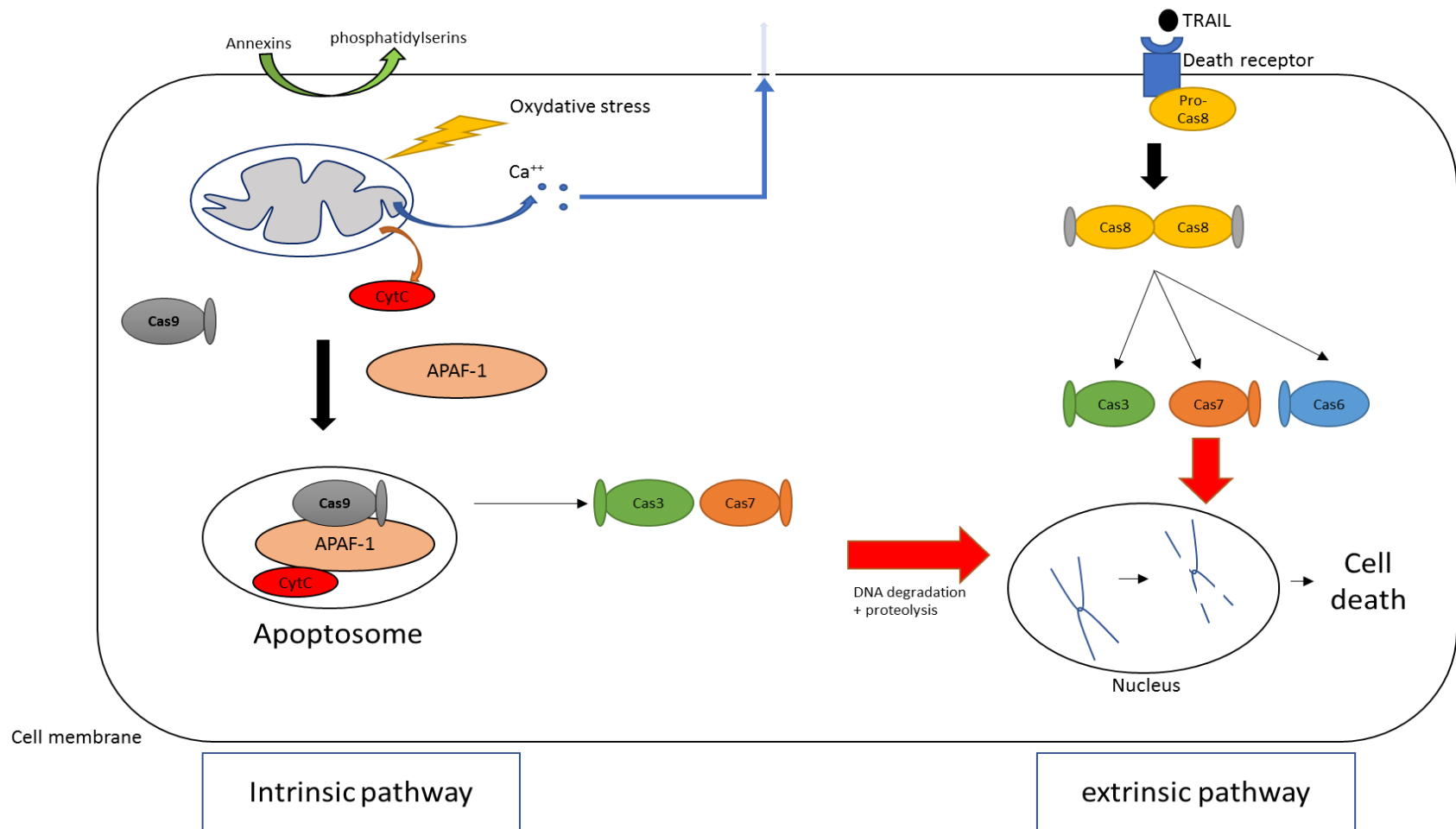


Figure 1.2 Schematic representation of the extrinsic and intrinsic pathway of the PCD. The extrinsic pathway is characterized by the binding of extracellular signals, such as the tumour necrosis factor-related apoptosis-inducing ligand (TRAIL) to specific receptors (death receptors). The binding of the ligand to its receptor will induce the recruitment of the initiating procaspase 8 to the cytoplasmic domain of the death receptor, and its activation into mature caspase 8. The latter will convert then activate additional caspases (namely 3, 7 and 6), triggering apoptosis, which will result in a proteolysis and DNA degradation in the cell. On the opposite, the intrinsic pathway can be triggered by intracellular stress signals, most notably by oxidative stress or DNA damage, that will lead to the mitochondria permeabilization and the subsequent release of intermembrane apoptogenic proteins such as the Cytochrome c (CytC). As a result, the CytC will then interact with the apoptotic protease-activating factor 1 (Apaf-1) in the cytosol, to enhance oligomerization and formation of an apoptosome. The apoptosome is formed with pro-caspase 9, which will then activate caspases 3 and 7, inducing cell death.

1.3. Mitochondria and apoptosis

The mitochondrion indirectly plays a key role in the regulation of the intrinsic pathway which is modulated at different levels (Wang 2001). For example, the release of CytC and caspases from the mitochondria can be enhanced by members of the B cell lymphoma 2 (Bcl-2) family of proteins (Cory and Adams 2002) and by the Inhibitor of Apoptosis (IAP) family of proteins (Altieri 2010) respectively. Furthermore it has been proposed that the release of CytC from mitochondria could be regulated via the phosphorylation of its Tyr48 *in vivo* (Yu, Lee et al. 2008). Indeed, a mutant of a phospho-mimetic CytC homolog (which lost its mimetism) failed to induce downstream caspase activation (Pecina, Borisenko et al. 2010).

Additionally, the Apoptosis Inducing Factor (AIF) released from the mitochondria also acts as an effector of the programmed cell death (Susin, Lorenzo et al. 1999). Upon release and cleavage of AIF by calpains and cathepsins, AIF is then translocated to the nucleus, where it will induce chromatin condensation (Yuste, Moubarak et al. 2005) and the fragmentation of the nuclear DNA (Susin, Lorenzo et al. 1999).

Interestingly, the caspase 8-mediated cleavage of BH3 interacting-domain death agonist (Bid) into tBid (truncated Bid), and the subsequent translocation of its C-terminal fragment will cause (either directly or indirectly) the release of CytC, inducing apoptosome formation, caspase activation and cell death (Wei, Lindsten et al. 2000). Consequently, the extrinsic pathway can be linked to the intrinsic pathway through apoptotic signals initiated by death receptors.

In summary, the cell death is an essential process for the development and growth of many organisms, involving multiple interactions and cascades, thus multiple protagonists. For example, PCD mainly allows the formation of a mechanical support for the plant to develop (Greenberg 1996, Vanyushin, Bakeeva et al. 2004). Without this support, the plant could not sustain its own weight and would not be able to reach light, thus its development would be greatly affected (Greenberg 1996, Vanyushin, Bakeeva et al. 2004).

1.4. Mitochondria and pathology

Any damage or dysfunction of mitochondria can compromise their integrity. These alterations of the mitochondria play an important role in many human diseases, because of the strong participation of the organelle on the overall cell metabolism.

As a result, mitochondrial disorders often induce neurological disorders (Griffiths and Levy 2017), myopathy, diabetes, multiple endocrinopathy, and a wide range of systemic disorders (Zeviani and Di Donato 2004). One of the causes for the loss of mitochondrial integrity can arise from mutations in the mtDNA, and is a known factor in several diseases such as the Leber's hereditary optic neuropathy, the MELAS syndrome and the Kearns-Sayre syndrome (Taylor and Turnbull 2005) (example in Figure 1.3). Since the mitochondrial DNA in the zygote is coming from the maternal ovum, a lot of deficiencies are maternally inherited. Typically, mitochondrial DNA integrity is compromised by some large mtDNA rearrangements in the case of Kearns-Sayre syndrome, or point mutations in the case of the MELAS and the Kearns-Sayre syndromes (Zeviani and Di Donato 2004, Taylor and Turnbull 2005).



Figure 1.3 Typical symptom in Kearns-Sayre syndrome. People with Kearns-Sayre syndrome have progressive external ophthalmoplegia, a weakness or paralysis of the eye muscles that impairs eye movement and causes drooping eyelids (ptosis).

Similarly, defects in nuclear genes can also lead to the malfunction of mitochondrial proteins, and these are associated with several diseases such as Friedreich's ataxia (McCormack, Guttman et al. 2000) or Wilson's disease (Chinnery and Schon 2003). Fortunately, these diseases are generally recessive as they can affect vital proteins such the enzymes of the oxidative phosphorylation, like the coenzyme Q10 deficiency (Zeviani and Di Donato 2004). Overall, the list of diseases is remarkably broad and includes

devastating pathologies such as the Parkinson's disease, epilepsy, stroke, cardiovascular disease, schizophrenia, dementia, Alzheimer's disease and diabetes (Pieczenik and Neustadt 2007, Lim, Rhein et al. 2010).

1.4.1. Mitochondria and the theory of aging

Considering the central role of the mitochondrion in the production of energy necessary for cell survival, development and growth, its involvement in cellular aging process has been hinted for decades. A number of changes can occur to mitochondria during the aging process (Harman 1972).

The main hypothesis, commonly referred as the mitochondrial free radical theory of aging, involves possible leakage of the high-energy electrons in the respiratory chain to form reactive oxygen species (see section 1.7.6), resulting in significant oxidative stress in the mitochondria (Harman 1956, Harman 1972). This will lead to a high mutation rates in the mitochondrial DNA (mtDNA), ultimately causing its degradation (Bugger and Abel 2010). As a result, mutated mtDNA can only be found in about 0.2% of very old cells (Boffoli, Scacco et al. 1994). In addition, large deletions in the mitochondrial genome have also been strongly linked to neuro-degenerative diseases such Parkinson's disease (De Grey 2004).

1.5. The Voltage-Dependent Anion Channel (VDAC)

Originally discovered in the mid-70s (Colombini and Mannella 2012), the VDAC drew attention from the start. Indeed, they are most abundant proteins in the outer mitochondrial membrane (OMM) (Burdman, De Mot R Fau - Vanderleyden et al.).

The abundance and strategic location of VDACs in the OMM, casts them in the role of safe keeper of mitochondrial function, as their opening and closure define the route that mitochondria should follow: normal respiration or suppression of mitochondrial metabolism leading to apoptosis and cell death (Madesh and Hajnóczky 2001).

1.5.1. VDAC gene family

VDACs are ubiquitous among eukaryotes and have been characterized in several eukaryotic species, across all kingdoms. Interestingly, the number of isoforms is variable, ranging from one to six, but remains consistent in certain clades such as mammals (Blachly-Dyson and Forte 2001). For example, *Saccharomyces cerevisiae* has two isoforms (POR1/YVDAC1 and POR2/YVDAC2) (Cherry, Hong et al. 2012), but most plant species have 4 to 5 (Sayers, Barrett et al. 2009). In *S. cerevisiae*, the two known isoforms (POR1 and POR2) have been characterized so far, with POR1 being the essential porin and POR2 function still to be explained.

Conversely, mammalian VDACs comprise three different isoforms (VDAC1, VDAC2 and VDAC3). These isoforms already display structural difference in their mRNAs due to exons counts (9 exons for VDAC1 and VDAC3 as opposed to 10 exons for VDAC2). However, they all have their start codon in the second exon, the first one being part of the 5' UTR of corresponding mRNA (Sayers, Barrett et al. 2009).

Overall VDACs are part of a highly conserved family, with above 90 % nucleotide sequence identity between mice and human variants for example (Sampson, Lovell et al. 1997, Blachly-Dyson and Forte 2001). Consequently, VDACs often share highly conserved features, such as their core structure (section

1.8) with some minor differences. In terms of evolution, DNA sequences suggest the different isoforms arose by gene duplication and evolved later to suit their functions (Young, Bay et al. 2007). To this day, some of the main differences remain to be explained or attributed to a specific function, like the N-terminal extension (around 10 to 12 amino acids) at the end of hVDAC2 protein, likely required for NADH permeability (Bauer, Gieschler et al. 2011). Interestingly, hVDAC2 well-structured N-terminus and its enrichment in thiols confer to this isoform additional regulatory functions, anti-apoptotic features and contribution to gametogenesis (Maurya and Mahalakshmi 2013, Maurya and Mahalakshmi 2016). Nevertheless, it was proven that all VDACs share conserved ancestral features, and could mostly be inter-changeable, as highlighted by rescue experiments in yeast. In fact, POR2 was actually discovered by suppression of POR1 in *S. cerevisiae* (Blachly-Dyson, Song et al. 1997). It was further demonstrated that POR2 did not confer additional activity but rather a possible involvement in additional cellular process (Blachly-Dyson, Song et al. 1997). Overall, it seems that the number of isoforms correlates with the complexity of the cells and hence the complexity of the organism (Homblé, Krammer et al. 2012).

1.5.2. Expression and location

So far, numerous experiments have demonstrated the presence of all isoforms is not always essential for cell survival. For example, mice lacking the VDAC2 gene (VDAC2^{-/-}) would die in the embryonic stage, as opposed to those lacking VDAC1, and could not be rescued by over-expression of VDAC1 (Shoshan-Barmatz, De Pinto et al. 2010, Shoshan-Barmatz and Mizrachi 2012, Reddy 2013). Furthermore, there are several examples showing a differential location of the various isoform within one organism (Tateda, Watanabe et al. 2011).

In mice, VDAC1 is the most highly expressed and displays a homogenous and high expression pattern compared to the other two isoforms, namely VDAC2 and VDAC3 (Sampson, Lovell et al. 1997). This is a clear example of differential expression and it suggests a potential variation in the role and importance of the different isoforms. Associated with the different expression pattern is the variable

localization of these isoforms. Indeed, VDACs are not only be restricted to the OMM, but can be exported to different compartments (Sampson, Lovell et al. 1997).

This hypothesis was later confirmed when hVDAC1, thought to be located exclusively in the OMM, was reported to be localized in other cell compartments via immunofluorescence, flow cytometry and EM immunogold labelling (De Pinto, Messina et al. 2010). Similarly, hVDAC3 was shown to be located in the centriole of certain cells (De Pinto, Guarino et al. 2010). Moreover, these alternate compartments would differ depending on the cell type i.e.the plasma membrane of various cells (De Pinto, Messina et al. 2010), the sarcoplasmic reticulum of skeletal muscles (Shoshan-Barmatz, Hadad et al. 1996), the endoplasmic reticulum (ER) of rat cerebellum (Shoshan-Barmatz, Zalk et al. 2004), were all identified as VDAC locations. Following this discovery, the plasma membrane localized VDAC was named plasmalemmal VDAC1 ((pl)-VDAC1). Besides, the targeting of the channel to the plasma membrane is thought to be induced by a N-terminal signal peptide on the (pl)-VDAC1 (Buettner, Papoutsoglou et al. 2000). Even though this isoform has clearly been identified in other vicinities than the OMM, its function and relevance are still questioned (Akanda, Tofighi et al. 2008). Its proposed roles include the rectification of the depolarization-induced chloride channel complex (Reymann, Florke et al. 1995), being involved in brain tissue volume regulation (Dermietzel, Hwang et al. 1994), and contributing to ATP release and the regulation of the cell volume (Okada, Neal et al. 2004).

1.5.3. The VDACs from *Arabidopsis thaliana*

Plant VDACs have been understudied for many years due to their limited impact in the pharmaceutical industry. However, they have been described to act in plant mediation of development, growth or defence against pathogens (Greenberg 1996). In consequence, they could potentially be used as tools for the modulation of the growth or the defence against pathogens, or an alternative to pesticides.

When the protein sequences of the four *Arabidopsis thaliana* VDAC isoforms (AtVDACs) are compared to each other, the degree of homology between sequences is variable (from 62% to 83%, see Table 1.1). AtVDAC1 is a house-keeping protein and its deletion prevents plant growth; whereas the other three seem to display variable sub-cellular location and function (Tateda, Watanabe et al. 2011). An additional pseudo-gene called AtVDAC5 has been identified but lacked essential structural elements of the channel (a number of beta-strands are missing), hence its relevance remained to be explained.

Table 1.1 AtVDACs phylogeny. Similarity percentages between the protein sequences of *Arabidopsis thaliana* VDAC isoforms AtVDAC1, AtVDAC2, AtVDAC3 and AtVDAC4.

	AtVDAC1	AtVDAC2	AtVDAC3	AtVDAC4
AtVDAC1		69%	83%	63%
AtVDAC2	69%		65%	64%
AtVDAC3	83%	65%		62%
AtVDAC4	63%	64%	62%	

The N-Terminal sequences of the AtVDACs are remarkably well conserved (Figure 1.4) suggesting a conservation of their primary function or structure. It has been demonstrated that the N-Terminal part of the sequence could be either located within or outside of the pore (see section 1.6) and that the alpha helical tail is known to be essential for ion trafficking in other organisms (Mertins, Psakis et al. 2012). Therefore, the high sequence homology could arise from a conservation of either the interactions with cytosolic partners, or their ion gating properties.

```

AtVDAC1  1  MVKGPGLYTEIGKKARDLLYKDHNSDQKFSITTFSPAGVAITSTGTTKGDLLLGDVAFQSRRNITTDLKVCTDSTFLIT  80
AtVDAC3  1  MVKGPGLYTEIGKKARDLLYRDYQGDQKFSVTTYSTGVAITTTGTNKGSLFLGDVATQVKNNMFTADVKVSTDSLLTT  80
AtVDAC2  1  MSKGPGLFTDIGKKAKDLLTRDYNSDQKFSISTYSASGVALTSTALKKGGVHAADVATQYKYKNALFDVKIDTDSVLT  80
AtVDAC4  1  MGSSPAPFADIGKKAKDLLNKDYIFDHKFTLMLSATGTEFVATGLKKDDFFFGDSTLYKGNITIVDLKIDSHSSVSTK  80

```

Figure 1.4 N-Terminal tail sequence alignment of AtVDACs. Protein sequence alignment of the first 80 amino acids of the *Arabidopsis thaliana* VDAC isoforms 1 to 4. Amino acids shared by all AtVDACs are shown in red. Isoforms are sorted out by the degree of similarity they share. Hence AtVDAC1 and AtVDAC3 are highly similar in their N-terminal sequence, and share a common feature known as the mitochondrial porin signal (MPS) later in the sequence (not shown).

In plants, e.g. *A. thaliana*, some of its isoforms are restricted strictly to the mitochondrion (AtVDAC1 and AtVDAC3) whereas AtVDAC2 and 4 can also be exported in other compartments, showing a uniform cellular expression (Tateda, Watanabe et al. 2011). Moreover, AtVDAC3 is weakly expressed and only found in leaf tips of seedlings, shoot meristems, and anthers, whereas the other three isoforms are expressed more ubiquitously (Tateda, Watanabe et al. 2011). Although AtVDAC1 and AtVDAC3 share a common mitochondrial porin signal (MPS) in their C-Terminal region, which allows their restriction to the mitochondrial compartment (Tateda, Watanabe et al. 2011), only AtVDAC1 is essential for plant growth. This suggest AtVDAC3 might play a different role in plant metabolism, whereas AtVDAC1, AtVDAC2 and AtVDAC4 are already known to also play important roles in the reproductive stage (Tateda, Watanabe et al. 2011).

In summary, plant VDAC isoforms must be exported to the right compartment (by the inclusion of targeting signals) so that they can interact with their cytoplasmic partners. these protein-protein interactions may differ from one compartment to another. Therefore, the VDACs from *A. thaliana* (AtVDAC1, AtVDAC2, AtVDAC3 and AtVDAC4) could provide interesting insights into Voltage dependent Channels' panel of functions in the cell and the molecular interactions that drive the binding of different partners.

1.6. Structural organization of VDAC proteins

In the past 35 years, numerous experiments have been conducted to probe the structure of VDACs. Noticeably, the predicted structure of VDACs (in all kingdoms) always consists of a core of 19- to 20- beta strands and an N-terminal tail (Figure 1.5, yellow and blue respectively). This great degree of structural conservation is reflected in all kingdoms, as illustrated by the comparison of the predicted secondary structures of *S. cerevisiae*, *Homo sapiens* and *A. thaliana* (Figure 1.5).

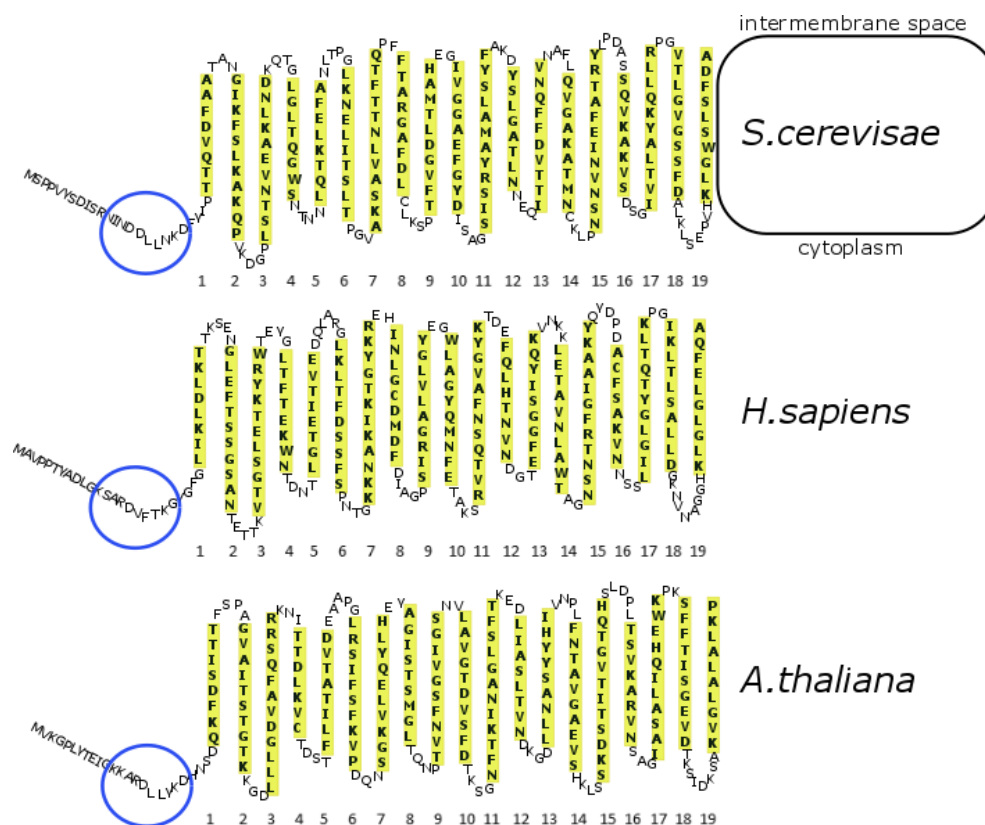


Figure 1.5 Core structure of Voltage-dependant anion channels (VDACs). 2D representation of VDACs structure in different organisms: *S. cerevisiae*, *H. sapiens* and *A. thaliana*. This structure are based on structural simulations from Jpred (Drozdetskiy, Cole et al. 2015) and Forte webserver (Tomii and Akiyama 2004). Intermembrane segments (beta-barrels) are shown in yellow, whereas the N-terminal tail is circled in blue.

Different structural experiments have been conducted over the years. In 2008, the three-dimensional structure of VDAC isoform 1 was characterized at the atomic resolution by three different experimental methods (Bayrhuber, Meins et al. 2008, Hiller, Garces et al. 2008, Ujwal, Cascio et al. 2008). More precisely, the structure of the human VDAC1 (hVDAC1) was solved by nuclear magnetic resonance

spectroscopy (NMR) (Hiller, Garces et al. 2008), as well as a combined approach using nuclear magnetic resonance spectroscopy and X-ray crystallography (Bayrhuber, Meins et al. 2008).

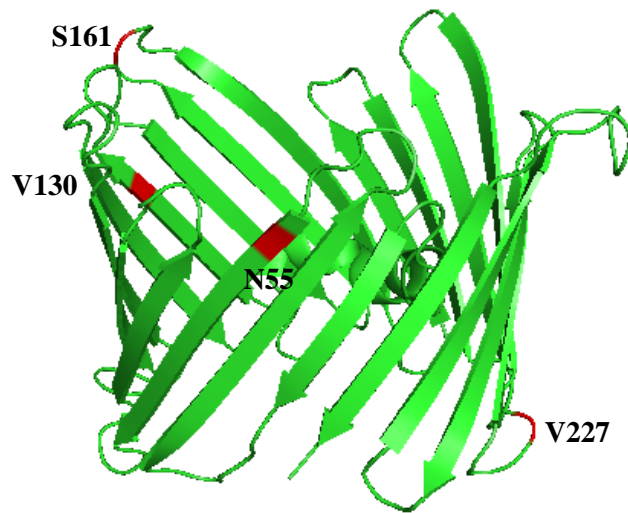


Figure 1.6 Three-dimensional structure of mouse mVDAC1. Crystal structure of the mouse VDAC1 3EMN at 2.3 Å resolution. Residues N55, V130, S161 and V227, different from the human hVDAC1, are represented in red (displayed using Pymol (L DeLano 2002)).

Recently, another mammalian VDAC, the mouse VDAC1 (mVDAC1), had its structure solved by X-ray crystallography (Ujwal, Cascio et al. 2008). The mouse mVDAC1 is highly similar to hVDAC1, with the exception of four amino acids (T55N, M130V, A161S and I227V), all located within or in close proximity of the loops (Figure 1.6, red).

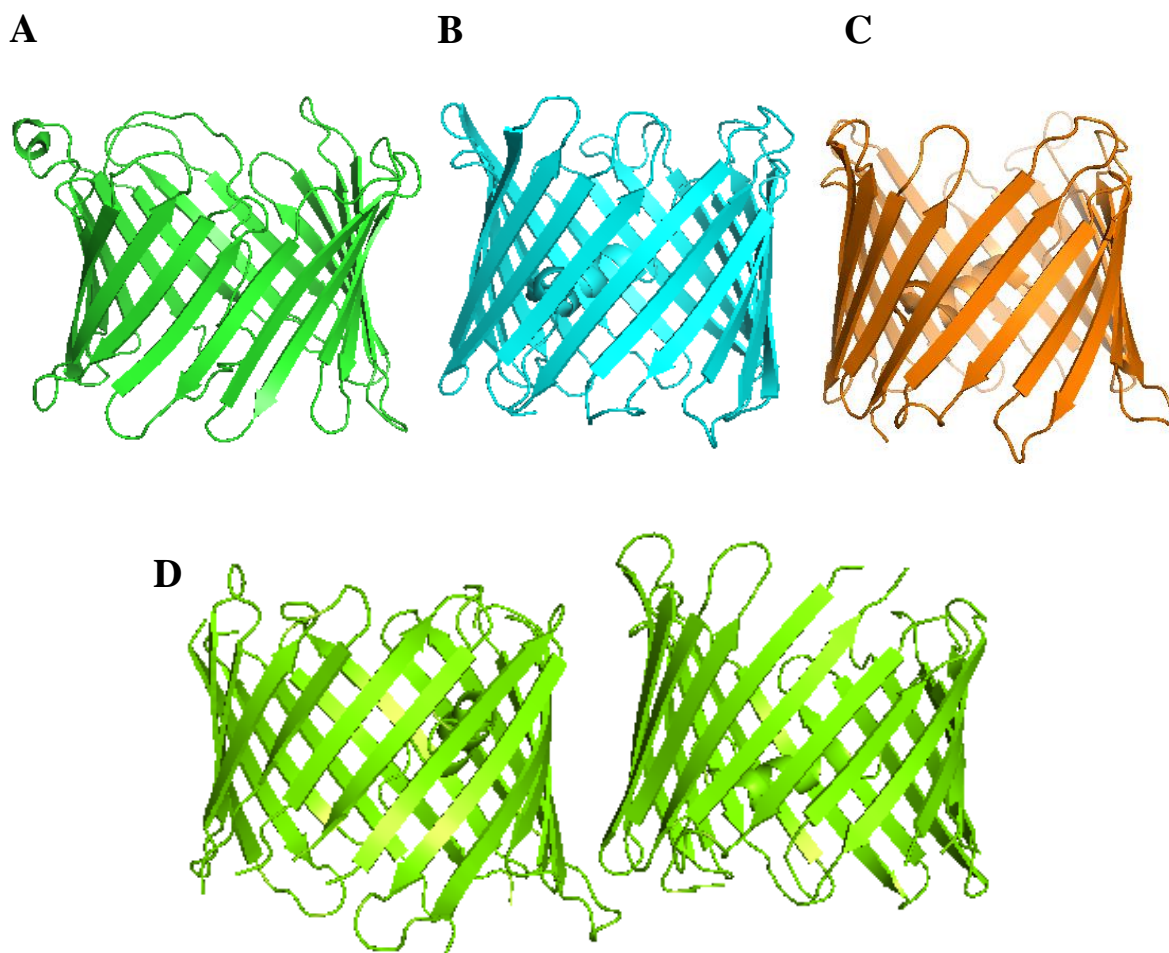


Figure 1.7 Three-dimensional structures of VDACs. Known three-dimensional structures of VDAC proteins from multiple species (displayed using Pymol (L DeLano 2002)). (A) Solution NMR structure of hVDAC1 in green. (B) Crystal structure of the mouse VDAC1 3EMN at 2.3 Å resolution, in blue. (C) Crystal structure of the zebrafish VDAC2 zfVDAC2 at 2.8 Å resolution, in orange. (D) Dimer structure of hVDAC1 5XDO (in C222 space group) at 3.1 Å resolution in light green.

The VDAC crystal structures are fairly identical and feature the expected 19-stranded beta-barrel and the N-terminal alpha-helix, positioned horizontally midway within the pore (Ujwal, Cascio et al. 2008). This odd number of strands is characteristic of VDAC proteins, unlike other known transmembrane beta-barrels (Omp channels for example). Hence the barrel closure is dependent on parallel hydrogen bonding between strands 1 and 19, which constitute a weak point in the barrel structure (Bayrhuber, Meins et al. 2008, Hiller, Abramson et al. 2010). Additionally, the N-terminal helix is necessary for the preservation of a cylindrical barrel structure in hVDAC1, as well as fundamental functions such as ion

gating (Geula, Ben-Hail et al. 2012). Later studies further improved our understanding of the VDAC1 structure and allowed the identification of structurally or functionally important amino acid residues (Shanmugavadivu, Apell et al. 2007, Aram, Geula et al. 2010, Deniaud, Liguori et al. 2010, Reina, Palermo et al. 2010). For example, replacing glycine residues in the N-terminal domain provides the flexibility needed for N-terminal translocation from the internal pore to the channel face, to allow interaction with anti-apoptotic partners such as Bcl-2 (Geula, Ben-Hail et al. 2012). On the opposite, two cysteines residues were investigated in rat VDAC1, but were shown to be required neither for apoptosis nor for VDAC1 oligomerization (Aram, Geula et al. 2010).

In contrast to VDAC1, the three-dimensional structure of VDAC2 and 3 have not been yet fully determined in human or mouse. Recently, the structure of zebrafish VDAC2 was resolved at 2.8 Å resolution in solution, using double electron–electron resonance spectroscopy and cross-linking experiments. A surprising outcome of this study was the concrete evidence that VDAC2 could be found as a dimer (Schredelseker, Paz et al. 2014), although the nature of the experiment (crystallography) might enhance this phenomenon.

The crystal or NMR structures of VDACs (Figure 1.7) confirmed the great identity and the associated high degree of conservation of the structural motifs. Beyond the conservation of their core structure, the local content displayed a similar degree of homology (Figure 1.8) . Beta-sheets form the main core of the channel, while multiple loops are responsible for linking the various transmembrane strands. Located in the lumen of the pore, the N-terminal domain forms a relatively short alpha helix, whose flexibility is highly enhanced in solution (compared to its structure in crystals), as shown by hVDAC1 solution NMR structure (Figure 1.8A).

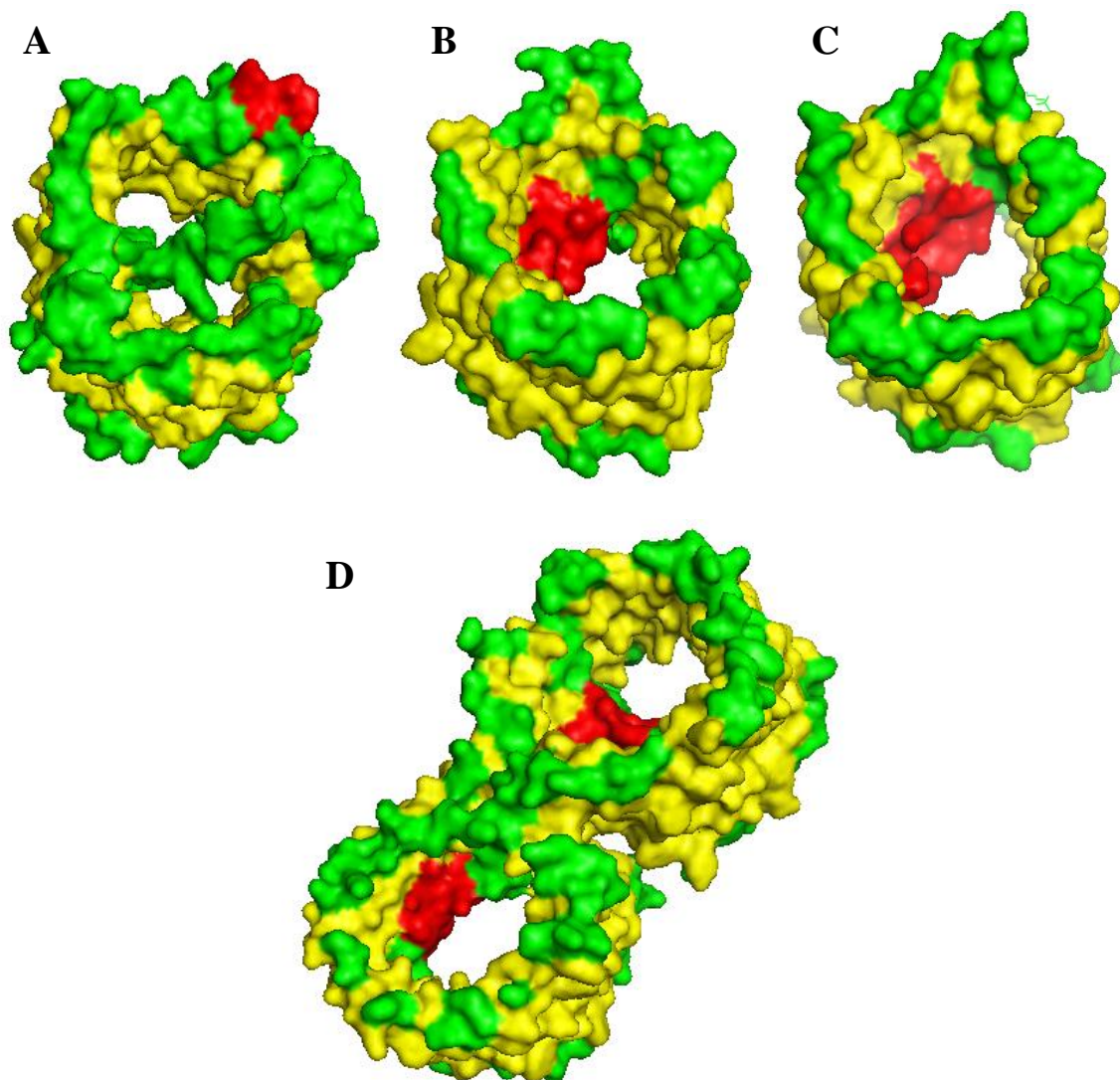


Figure 1.8 Organisation of secondary structure elements in the solved VDAC structures. Known three-dimensional structures of VDAC proteins from multiple species and displayed using Pymol (L DeLano 2002), and coloured depending on the secondary structure composition; beta-sheets (yellow), loops (green) and alpha helix (red). (A) Solution NMR structure of hVDAC1. (B) Crystal structure of the mouse VDAC1 3EMN at 2.3 Å resolution. (C) Crystal structure of the zebrafish VDAC2 zfVDAC2 at 2.8 Å resolution. (D) Crystallographic dimer structure of hVDAC1 5XDO (in C222 space group) at 3.1 Å resolution.

The mouse mVDAC1 3EMN was used to illustrate the overall charge distribution within the protein (based on amino acid composition; Figure 1.9). In fact, a great concentration of charges (positive and negative) can be found within the pore of mVDAC1, on the inner layer of the beta-barrel as well as on the alpha helical N-terminal domain. As expected, the external side of the pore is exposed to the lipidic environment of the OMM and does display a much greater concentration of hydrophobic chains. Non-

surprisingly, the loops exhibit a relatively high concentration of charges, potentially helping directing ions through the pore or serving as binding platform for potential binding partners.

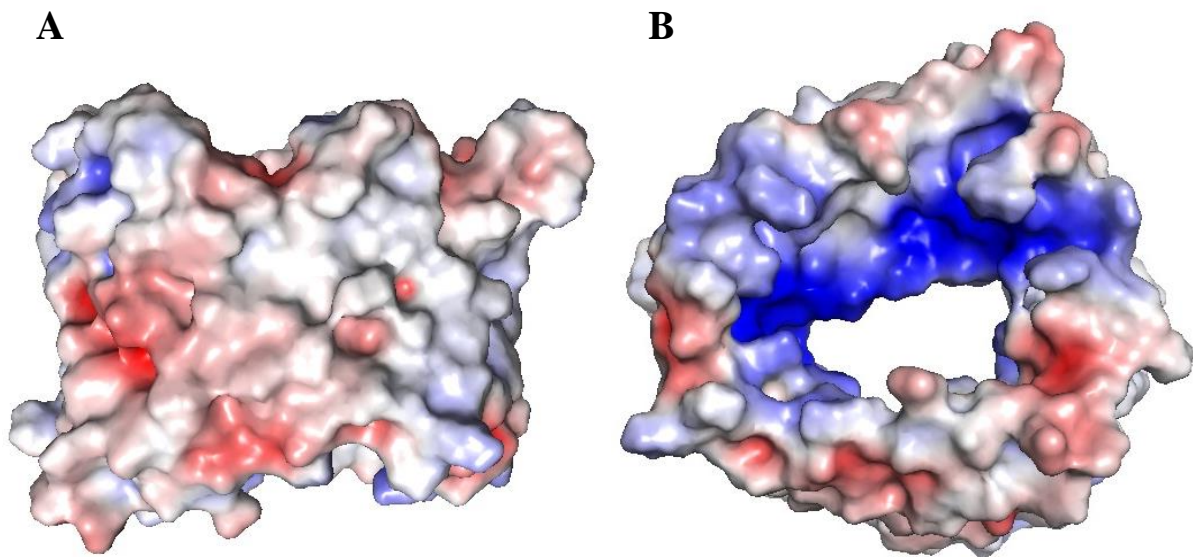


Figure 1.9 Charge distribution of mVDAC1. Known three-dimensional structure of Mouse mVDAC1 (3EMN) displayed using Pymol (L DeLano 2002), and coloured depending electrostatic charge. Positive (in red), negative (in blue) and neutral (in white). (A) Side view and Top view (B) of the crystal structure of the mouse VDAC1 3EMN at 2.3 Å resolution coloured as described above.

Considering the residues after the N-terminal region are mostly involved in the formation of the core channel (with the exception of the loops), focus has been greatly directed toward the N-terminal 25 residues of VDAC1, to understand the functional implications of this domain. So far studies suggested this domain can position itself in various manners, such as being exposed to the cytoplasm (De Pinto, Messina et al. 2003), crossing the membrane (Colombini 2004) or lying on the membrane surface (Reymann, Florke et al. 1995).

The great flexibility of the N-terminal domain contrasts with the crystal structures obtained to this date. In fact, all three-dimensional structures of VDAC1 confirmed that the N-terminal region is mostly alpha helical and located inside the pore. It is thought to be only weakly bound to the channel wall, thus retaining a high flexibility even within the channel pore (Bayrhuber, Meins et al. 2008, Hiller, Garces et al. 2008, Ujwal, Cascio et al. 2008). This is achieved mainly through several hydrogen bonds between the N-terminal domain and the beta-barrels (Ujwal, Cascio et al. 2008). Noticeably, the stable alpha

helical region of this domain is relatively short (around 10 to 15 amino acids) and is positioned within the barrel, approximately halfway through the channel pore (Bayrhuber, Meins et al. 2008).

The position and organisation of the helix was similar in crystal structure of mouse VDAC1, with the helical region (amino acids 6 to 20) formed by two segments. Residues 11-20 were difficult to observe by NMR, confirming the expected flexibility of this segment (Hiller, Garces et al. 2008).

Another important feature of the N-terminal helix of VDAC1 is the presence of a great number of glycine residues (²¹GlyTyrGlyPheGly²⁵) (Colombini and Mannella 2012, Shoshan-Barmatz and Mizrachi 2012), which is thought to provide the flexibility required for N-terminal domain translocation out of the internal pore of the channel (Geula, Ben-Hail et al. 2012). Furthermore, the portion that connects the N-terminal domain to the first beta-strand of the barrel is highly conserved among mammals (Summers and Court 2010). However, despite the “GlyTyrGlyPheGly” motif being conserved in mammalian VDAC1s (Ujwal, Cascio et al. 2008) (as well as in *Caenorhabditis elegans*), it is not present in yeast, indicating an evolutionary divergence (Summers and Court 2010).

Further investigations suggested that the N-terminal region of VDAC1 exhibits a dynamic equilibrium, being either located within the pore or outside of the channel, on the cytoplasmic side of the OMM (Geula, Ben-Hail et al. 2012). For example, the use of anti-VDAC1 antibodies targeting the N-terminal region highlighted an interaction with membrane-bound VDAC1, indicating this portion can also be accessible, thus possibly located outside the pore (Gincel, Silberberg Sd Fau - Shoshan-Barmatz et al. , Junankar, Dulhunty et al. 1995, Abu-Hamad, Sivan et al. 2006).

Moreover, the mobility and location of the N-terminal domain has been proven to be essential in multiple processes such as interacting with the anti-apoptotic and pro-survival factors, hexokinase Bcl2, (HK)-I and HK-II (Abu-Hamad, Arbel et al. 2009, Geula, Ben-Hail et al. 2012) or voltage gating (Popp, Court et al. 1996, Mannella 1997, Koppel, Kinnally et al. 1998) and. For example, N-terminal-truncated murine VDAC1 exhibited no voltage dependence but still displayed high conductance at different membrane potentials (Popp, Court et al. 1996, Koppel, Kinnally et al. 1998, Abu-Hamad, Arbel et al. 2009). Supporting evidence was also offered from mutagenesis experiments, where mutations in the

alpha-helix of the Yeast VDAC led to a modulation the voltage-sensing mechanism of the channel (Thomas, Blachly-Dyson et al. 1993).

In summary, Voltage-dependent anion channels generally comprise 19 beta-strands forming transmembrane domains and an alpha-helix at the beginning of the sequence, inserting itself into the lumen of the barrel protein (Figure 1.8). When predicting the structure of a VDAC using bioinformatics, the number of transmembrane domains can vary from 18 to 19 depending on the software flexibility (Figure 1.5). Typically, NMR experiments and/or X-ray crystallography experiments are conducted to finally uncover the structural features of a specific VDAC, thus leading to changes in the structural paradigm of these proteins.

1.6.1. Plant VDACs

To this date, no crystal structure has yet been published for any plant VDACs. In the case of *A.thaliana*, the comparison of the predicted structures demonstrates the high degree of sequence and structural homology. It is defined mainly by the pore, consisting of 19 beta-strands, whereas most differences are concentrated on the loops (or the edges of the beta-strands), which are expected to form potential binding sites for interactions with cytosolic partners. An example is given in Figure 1.10, with predicted structure of AtVDAC1, generated by homology modelling using SWISS-Model workspace (Artimo, Jonnalagedda et al. 2012)) with 3EMN (mouse VDAC) as template. The amino acids differing in AtVDAC2 were highlighted (Figure 1.10, green) on the AtVDAC1 model, and proved to be mostly on the loops between the intermembrane domains or in their vicinity.

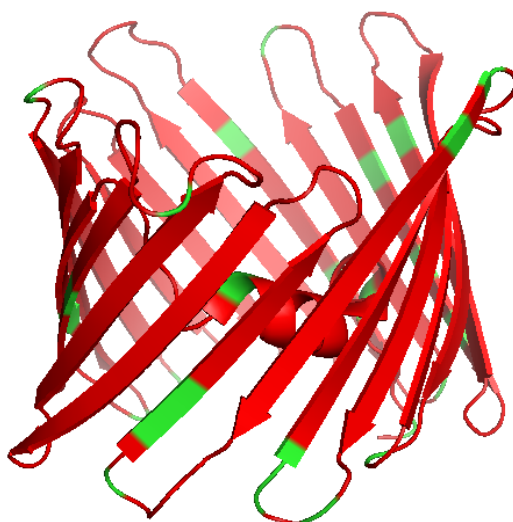


Figure 1.10 Predicted 3D-model comparisons of AtVDAC1 and AtVDAC2. Structure of AtVDAC1 obtained using the ExPasy server for structural modelling by homology (SWISS-Model workspace (Artimo, Jonnalagedda et al. 2012)) with 3EMN (mouse VDAC) as template, and shown using Pymol (L DeLano 2002). Common amino acids between AtVDAC1&2 are shown in red. Different amino acids are in green.

In parallel, all four AtVDAC structures were obtained as above, by homology modelling using mVDAC1 3EMN as a template, and compared (Figure 1.11). No dramatic changes could be observed when superposing the structures. Minor conformational changes, mostly in the loops linking the transmembrane domains, can be distinguished, but again not to a dramatic extent. These minor differences may facilitate interactions with different protein partners.



Figure 1.11 Predicted 3D-models of AtVDAC1-4 by homology modelling. Structures of the four AtVDACs were obtained using the Expasy server for structural modelling by homology (SWISS-Model workspace (Artimo, Jonnalagedda et al. 2012)) with 3EMN (mouse VDAC) as template, and shown using Pymol (L DeLano 2002). AtVDAC1, AtVDAC2, AtVDAC3 and AtVDAC4 are shown in green, blue, red and yellow respectively.

1.7. Roles and Functions of VDACs

1.7.1. Transport of ions

The main role of the Voltage dependent anion channel is the regulation of mitochondrial osmosis by ensuring the transport of ions across the membrane (Colombini 1989). The characterization of VDACs conductance has been in progress for over 30 years, with numerous examples. In humans, the three isoforms share structural and functional similarities despite different expression and location patterns (see section 1.5.2) (Engelhardt, Meins et al. 2007, De Pinto, Guarino et al. 2010, Yu, Raschle et al. 2012, Maurya and Mahalakshmi 2013). The Planar Lipid Bilayer assay (PLB), or Black Lipid membrane (BLM), is a powerful method used to probe the electrophysiological behaviour of VDAC channels.

Such experiments were undertaken for hVDAC1 and hVDAC2 and demonstrated channel activity upon reconstitution into lipid bilayers (Xu, Decker et al. 1999). More recently, the third isoform (hVDAC3) was also characterized by BLM but exhibited only slightly voltage-dependent conductance (Checchetto, Reina et al. 2014). Additional assays were performed on other organisms, such as the mouse mVDAC1 (Mertins, Psakis et al. 2012), to improve our understanding of the channel gating behaviour.

Overall, VDAC channels are highly dependent on the voltage across the membrane, as the latter modulates the ion-selectivity of the channel (Hodge and Colombini 1997). This phenomenon is known as voltage dependence and is defined by a response of the channel to the application of a membrane potential. Typically, the channel will open and close upon application of a voltage, allowing the passage of ions in the directions of the current or in the opposite direction. This last parameter is dependent on the ability of the channel to either conduct cations, anions or both (Hodge and Colombini 1997).

In the main open conductance state, VDAC1 selectivity shift towards anions as opposed to cations, whereas the close state can exhibit a preference for cations and a diminished selectivity for anions (Colombini, Blachly-Dyson et al. 1996). The closed VDAC1 is mostly permeable to small ions (e.g. Cl^- , K^+ , Na^+) but to large anions as well, such as glutamate (Gincel, Silberberg et al. 2000), ADP and ATP (Rostovtseva and Colombini 1997). Large cations, such as acetylcholine, dopamine (Gincel,

Silberberg et al. 2000) and Tris (Benz, Kottke et al. 1990) have also been shown to be transported in some cases.

Overall, VDACs are known to exhibit a linear response to the application of a voltage (Figure 1.12., instantaneous VDAC), with an increase in absolute current recorded upon increase of the absolute voltage. Nevertheless, a decrease in the observed current can sometimes be observed at high voltages applied, ultimately corresponding to the closure of the channel under these conditions (Figure 1.12., Steady-state VDAC). Structural elements as well as modification to the channel (phosphorylation for example) can also influence the channel's response to the voltage.

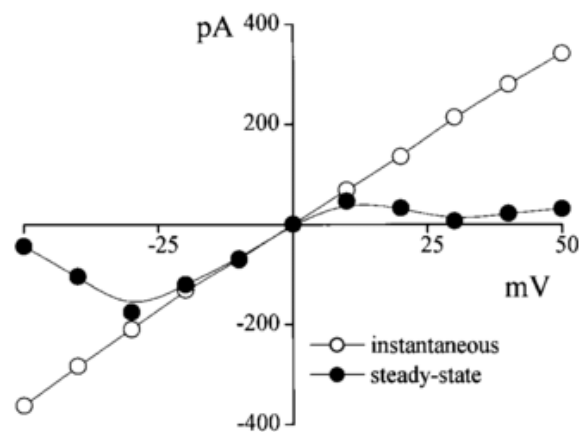


Figure 1.12 Typical current recording of VDAC. I/V (Ohm) plot for VDAC, under instantaneous (short pulse, empty dots) or whole cell current (steady-state, black dots). The decreasing trend at higher voltages is a result from a complete closure from the channel (Sabirov et al. 2001).

The N-terminal region of VDAC1, considered a 25 residue-long sequence containing at least an alpha-helical structure, seems to have an obvious role in the voltage gating of the channel. Over time, this hypothesis has been demonstrated in several studies (Peng, Blachly-Dyson et al. 1992, Thomas, Blachly-Dyson et al. 1993, Popp, Court et al. 1996, Koppel, Kinnally et al. 1998, Abu-Hamad, Arbel et al. 2009, Geula, Ben-Hail et al. 2012).

In *S. cerevisiae*, VDAC1 (scVDAC) mutants were also tested. It was shown that mutations in the alpha-helix (Asp16 and Lys20, both highly conserved residues) and in beta-strands β 1 to β 5 (Lys46, Lys61,

Lys65 and Lys84) all affected the voltage-sensing mechanism of the channel (Thomas, Blachly-Dyson et al. 1993). A wide range of suggestions have already been proposed to explain the flexibility of the domain. Possibly, the N-terminal domain could be part (to some extent) of the channel wall but act as well as a voltage sensor. Finally, its ideal location within the centre of the pore can either allow or prevent the passage of ions and other metabolites through the VDAC channel (Colombini, Blachly-Dyson et al. 1996, Koppel, Kinnally et al. 1998).

For example, the voltage dependence of the channel was abolished in N-terminal-truncated mutant of the mouse VDAC1 ($\Delta(26)$ mVDAC1) at any voltages (De Pinto, Reina et al. 2008, Abu-Hamad, Arbel et al. 2009).

1.7.1.1. BLM: the example of mVDAC1

An example of a typical BLM recording is given in Figure 1.12 for the mVDAC1 (Mertins, Psakis et al. 2012). Briefly, the protein is inserted into a lipid bilayer between two compartments filled with either symmetric or asymmetric solutions of salt. A voltage is then applied, creating membrane potential, resulting in gating activity for the channel. In this instance, two chambers (CP2A and a bilayer chamber BCH-22A from Warner Instruments) were both filled with 10 mM Tris/HCl (pH 7.4), 1 M KCl and 5 mM CaCl₂. Protein (7.5–15 µg, resuspended in DMPC) was added to one of the compartments beside the planar lipid layer and a membrane potential was created. Current was recorded using a Multi-patch 700B patch-clamp amplifier connected to a Digidata 1440A A/D converter and traces were visualized through the pClamp 10.2 software (Axon Instruments). Data were collected at 5 kHz and sampled at 200 Hz for analysis.

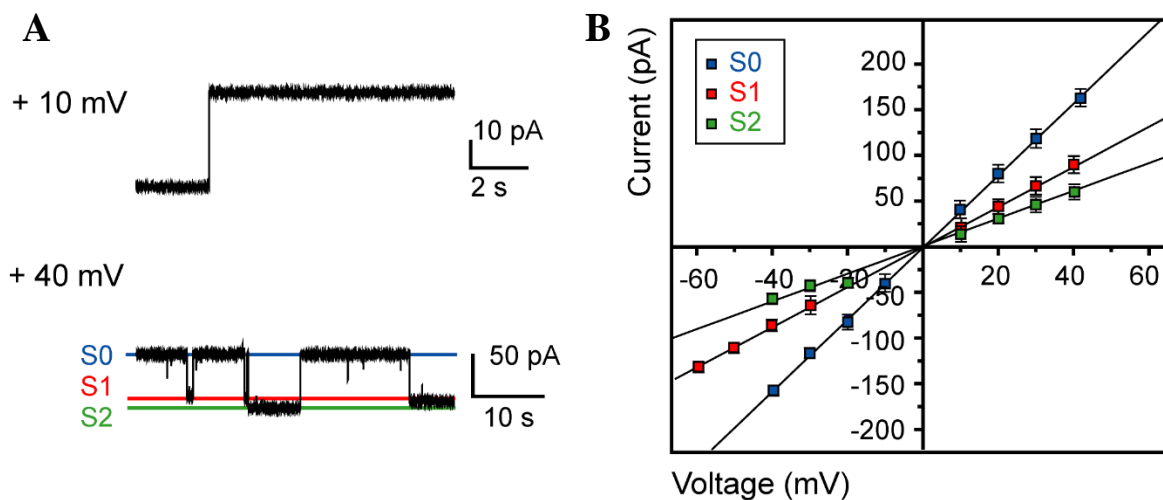


Figure 1.13 Typical current recording of mVDAC1. A. Representative traces of the recorded current during a BLM assay on mVDAC1 (Mertins, Psakis, 2012). Different gating activities could be observed at +10 mV and +40 mV, and three states could be identified, namely the open state S0 (conductance = 3.94 nS, in blue), and two closed states S1 (conductance = 2.61 nS, in red) and S2 (conductance = 1.90 nS, in green). B. Corresponding I/V (Ohm) plot for mVDAC1. Colour for the different states (S0, S1 and S2) are as above.

The native channel mVDAC1 exhibited an expected gating behaviour, corresponding to a linear response to the application of both positive and negative potentials (Figure 1.12B). Noticeably, the porin sequentially alternated between its open state, denoted S0 and at least two closed states of various

conductances, denoted S1 and S2. This type of behaviour is typical of VDAC, and perfectly illustrates the variety of responses the channel can exhibit when voltage is applied. For reference, the conductance calculated of the open state, called S0, was characterized at 3.94 nS, whereas the two closed states S1 and S2 were reported to be 2.61 nS and 1.90 nS respectively (Mertins, Psakis et al. 2012). These values were in close proximity to the previously published VDAC conductance of various organisms (see chapter 7, Table 7.1), usually around 4 nS for the open state, and a two-fold lower conductance (around 2 nS) for the closed states (Blachly-Dyson, Peng et al. 1990, Colombini 2016).

1.7.2. **VDAC1 and the transport of metabolites**

As mentioned previously, the voltage-dependent anion channel is responsible not only for the traffic of ions across the OMM, but also other metabolites. In fact, VDAC1 has been shown to mediate the influx of metabolites such as NADH, pyruvate, succinate and malate into mitochondria and the efflux of newly formed molecules stemming from mitochondrial processes such as hemes (Shoshan-Barmatz, De Pinto et al. 2010). In the open state, ATP and ADP molecules can transit through VDAC1, allowing the exchange of newly produced ATP against ADP from the cytosol (Rostovtseva and Colombini 1997). The latter will then be converted to ATP via the oxidative phosphorylation, whereas the former will be utilized as energy supply in multiple cell reactions (Bonora, Patergnani et al. 2012, Lu, Huang et al. 2014). Furthermore, the role of VDAC1 in the cell homeostasis has been demonstrated by down-regulation of VDAC1 expression, resulting in reduced metabolite exchange between the mitochondrion and the cytosol. This greatly inhibited cell growth, and confirmed the previous findings and hypothesis (Abu-Hamad, Sivan et al. 2006). An additional layer of regulation comes from the VDAC itself as it is capable of limiting the flux of metabolites from and to the mitochondria (Vander Heiden, Chandel et al. 2000, Holmuhamedov and Lemasters 2009).

In addition to channelling ATP and ADP, VDAC1 supposedly acts as a binding platform for kinases from the cytoplasm. By allowing a close proximity between the enzymes and their substrates, the VDAC enhances the use of the metabolites by the Hexokinase 1 (HK1) and the creatine kinase (CrK) to produce glucose-6-phosphate and creatine phosphate in brain and muscle, respectively (Dolder, Wendt et al. 2001). This hypothesis involves the formation of a complex between VDAC1, the creatine kinase and a phospho-nucleotide carrier, the adenine nucleotide translocase (ANT) (Dolder, Wendt et al. 2001). In parallel, the interaction of VDAC1 with HK1 allows for a cross-talk between glycolysis and oxidative phosphorylation (Dolder, Wendt et al. 2001, Sun, Shukair et al. 2008). Recently, dimeric $\alpha\beta$ -tubulin was shown to block VDAC1 conductance, regulating its permeability to ATP (Gurnev, Rostovtseva et al. 2011), adding an additional level of regulation to the cell osmosis via VDAC1.

1.7.3. **VDAC1 as a gateway for Reactive Oxygen Species (ROS)**

Reactive oxygen species (ROS) such as hydrogen peroxide H_2O_2 , superoxide anions O_2^- and hydroxyls are known to be produced during the respiratory chain reactions, taking place in the mitochondria. In human mitochondria, ROS represent up to 2 % of the consumed oxygen converted (Murphy 2009). When released to the cytosol, ROS are highly reactive molecules that will attack everything from lipid to protein and DNA (Ott, Gogvadze et al. 2007). Typically, around 99 percent of the ROS is contained and processed by mitochondrial enzymes such as the Manganese superoxide dismutase (MnSOD) and Copper/zinc superoxide dismutase (Cu/ZnSOD) (Valko, Rhodes et al. 2006, Mailloux, McBride et al. 2013), but the remaining percent still represent a threat to the cell survival, especially when enhanced by a sudden release of ROS from the mitochondria.

However, the mechanism of transport of ROS from the mitochondria is yet to be unveiled, although a hypothesis involving VDAC1 has been formulated, where the latter would mediate the release of ROS from the Inter-membrane space (IMS) to the cytosol (Han, Antunes et al. 2002). Furthermore, the closure of VDAC1 seemed to cause oxidative stress in the mitochondria, thus reinforcing this theory (Tikunov, Johnson et al. 2010).

ROS are a well-known contributor to cell proliferation and cell death (Buttke and Sandstrom 1994, Patel, Day et al. 1996, Fiskum 2000, Yuan and Yankner 2000). ROS have been linked to the release of CytC from the mitochondria (Petrosillo, Ruggiero et al. 2001, Petrosillo, Ruggiero et al. 2003). Interestingly, the apoptosis induced by superoxide anions O_2^- was greatly affected when using antibodies targeted at VDAC1 or channel inhibitors (Shoshan-Barmatz, Hadad et al. 1996, Madesh and Hajnóczky 2001, Simamura, Hirai et al. 2006).

Finally, the interaction between kinases and VDAC1 was shown to have an effect on the release of ROS from the mitochondria (Sun, Shukair et al. 2008). More precisely, over-expressed hexokinase HK-I and HK-II bound to VDAC1 induced a decrease in ROS release in HEK cells (Ahmad, Ahmad et al. 2002, Bryson, Coy et al. 2002, da-Silva, Gómez-Puyou et al. 2004), as well as protection against cell death (Bryson, Coy et al. 2002). Hence, the interaction between hexokinases and VDAC1 might act as a mediator and regulator of ROS release from the mitochondria, and ultimately cell death or apoptosis.

1.7.4. **VDAC1 as a cholesterol transporter**

VDAC1 is a necessary component of a protein complex ensuring the cholesterol distribution and transport to mitochondria (Rone, Fan et al. 2009). Therefore, it plays an important role in the altered level of cholesterol in Morris hepatoma cells (Campbell and Chan 2008). Indeed, the cholesterol import into the mitochondrion is mediated by a complex called the “transduceosome” (Rone, Midzak et al. 2012). This multi-protein complex is composed by a combination of proteins from the cytosolic and from the Outer mitochondrial membrane, namely the steroidogenic acute regulatory protein (StAR), translocator protein (TSPO), and VDAC1 (Papadopoulos, Liu et al. 2007, Aghazadeh, Rone et al. 2012, Rone, Midzak et al. 2012).

Moreover, high concentration of cholesterol has been shown to reduce the overall activity of membrane-associated proteins. Indirectly, this attribute is responsible for the inhibition of a decent number of metabolic functions of VDAC1 (Campbell and Chan 2008). In addition, it was suggested that higher concentration of cholesterol found in the mitochondria of cancer cells affected the binding of hexokinase HK to VDAC1 (Baggetto, Clottes et al. 1992, Pastorino and Hoek 2008). Finally, it was suggested that the glycine rich region the N-terminal region of VDAC1 could contain the binding site for cholesterol (position 22 to 24) (Thinnes and Burckhardt 2012).

1.7.5. **VDAC1 as a lipid transporter**

It was recently shown that VDAC1 might act as a lipid sensor and associate with additional proteins to form a complex allowing the transport of fatty acids through the OMM in rat liver mitochondria (Lee, Kerner et al. 2011, Martel, Allouche et al. 2013). In this theory, VDAC could be described as an anchor between the outer surface of the OMM and the intermembrane space. Proteins such as the acyl-CoA synthetase (ACSL) and the carnitine palmitoyl-transferase 1a (CPT1a) are thought to be part of the complex and work closely to convert acyl-CoenzymeA into acylcarnitine (Lee, Kerner et al. 2011).

Finally, the biological synthesis of cholesterol, called cholesterologenesis, displayed elevated level in various cancer cells (Mares-Perlman and Shrago 1988). Noticeably, cancer cells usually display a two to ten-fold increase in mitochondrial cholesterol content, mainly in the OMM, in comparison to liver mitochondria (Pedersen 1978, Baggetto, Clottes et al. 1992, Yu, Gong et al. 2005).

1.7.6. **VDAC1 and the regulation of Calcium transport**

Calcium is a known cellular co-factor implicated in many cellular processes, such as the modulation of cytosolic calcium signals (Gunter, Buntinas et al. 2000), the secretion (Maechler, Kennedy et al. 1997, Lee, Miles et al. 2003), the control of oxidative phosphorylation (Cox and Matlib 1993, Maack, Cortassa et al. 2006), the indirect modulation of the glycolysis and the Krebs cycle (Nichols and Denton 1995, Martinovich, Golubeva et al. 2012) and the cell death (Giacomello, Drago et al. 2007).

The transport of calcium into the mitochondria can also be linked to the apoptotic cell death. The high level of calcium will enhance the release of the CytC, leading to apoptosis. In cancer cells, calcium can also be associated with the high content of reactive oxygen species (ROS) (Martinovich, Golubeva et al. 2012).

However, all known mitochondrial calcium transporters are located within the inner mitochondrial membrane (Gincel, Zaid et al. 2001). These transporters are only accessible through the participation of VDAC1 in the OMM (Gincel, Zaid et al. 2001, Rapizzi, Pinton et al. 2002, Tan and Colombini 2007). Besides, VDAC1 has been shown to exert an actual control of the permeability of OMM to calcium (Rapizzi, Pinton et al. 2002, Báthori, Csordás et al. 2006). Interestingly, both open and closed states of VDAC1 exhibited different permeability to calcium, with the closed showing a preference for the divalent cation (Gincel, Vardi et al. 2002, Tan and Colombini 2007).

More recently, an additional mechanism involving protein/protein interactions between Bcl-xL and VDAC isoforms 1 and 3 was discovered. This interaction can modulate the transfer of calcium into the mitochondrion by increasing calcium transfer across the OMM, and is one of many pieces of evidence

for the involvement of VDAC1 in the cross-talk between mitochondria and the endoplasmic reticulum (ER) (Huang, Hu et al. 2013).

1.8. VDAC1 as a mediator of apoptosis

Early experiments such as the over-expression of VDAC1 were key in demonstrating the ability of the channel to induce apoptotic cell death (regardless of cell type) (Godbole, Varghese et al. 2003, Zaid, Abu-Hamad et al. 2005, Ghosh, Pandey et al. 2007, Lü, Dong et al. 2007, Abu-Hamad, Zaid et al. 2008). More precisely, it has been shown that VDAC1 over-expression in endothelial cells enhanced the activation of caspase 9 leading the overproduction of ROS, thus resulting in an increase of the endostatin-induced apoptosis (Yuan, Fu et al. 2008).

Conversely, several functions of the VDAC confer this channel a central role as a gateway to the mitochondria, as well as from the mitochondria to the cytosol. Indeed, the release of apoptosis-inducing proteins from mitochondria to the cytosol seems to always involve the VDAC channel directly or indirectly (Tsujiimoto and Shimizu 2002, De Pinto, Messina et al. 2003, Shoshan-Barmatz and Gincel 2003, Shoshan-Barmatz, Israelson et al. 2006, Shoshan-Barmatz, De Pinto et al. 2010, Golan 2012, Shoshan-Barmatz and Ben-Hail 2012).

Mainly, the involvement of VDAC1 in the multiple processes regulating the release from CytC or its maintenance in the mitochondria are a testament to the VDAC1 function as a regulator of apoptosis via the mediation of cytochrome C release. Not only was VDAC1 shown to be responsible for the transit and release of CytC from proteoliposomes *in vitro* (Shimizu, Narita et al. 1999, Madesh and Hajnóczky 2001, Zalk, Israelson et al. 2005), but the use of specific anti-VDAC1 antibodies resulted in the inhibition of CytC release, the interaction between Bax (Bcl-2-associated X) and VDAC1 and ultimately cell death. (Madesh and Hajnóczky 2001, Shimizu, Matsuoka et al. 2001, Zheng, Shi et al. 2003). Similarly, in mutant yeast, VDAC1-deficient mitochondria also displayed a lack of CytC release (Shimizu, Narita et al. 1999, Shimizu, Shinohara et al. 2000), thus confirming the central role of VDAC in mitochondrial CytC osmosis.

Ultimately, the restriction of CytC into the mitochondria has been further characterized to include additional mediators, such as the Hexokinases or Bcl proteins, and highlighted again the central role of VDAC1 in providing a platform for apoptosis inducers or repressors. For example, the interaction

between mVDAC1 and Hexokinase HK1 was prevented in mVDAC1 mutants E72Q, E65Q and E188Q overexpressing both recombinant proteins in HEK cells (Zaid, Abu-Hamad et al. 2005, Abu-Hamad, Zaid et al. 2008). This abolition of the interaction between the VDAC channel and HK1 led to a decrease of CytC release and cell death (Abu-Hamad, Zaid et al. 2008). In other cases, the overexpression of HK1 would indeed protect against apoptosis (Zaid, Abu-Hamad et al. 2005, Abu-Hamad, Zaid et al. 2008). Similarly, recombinant Bcl-xL was shown to maintain VDAC in its open configuration, thus promoting its permeability to ADP and beta-NADH and preventing CytC release (Vander Heiden, Li et al. 2001). In addition, the interaction between Bcl-xL and mVDAC1 and mVDAC3 was also shown to promote matrix Calcium accumulation by increasing the transit of calcium across the outer mitochondrial membrane (Huang, Hu et al. 2013).

1.8.1. VDAC oligomerization as a potential gateway for cytochrome C release from the mitochondria

Although the diameter of the VDAC1 pore in its open state is about 2.5 nm (Hiller, Garces et al. 2008, Colombini 2016), which is sufficient to allow the passage of small molecules such as ions, ATP or other nucleotides in or out of the mitochondria, proteins such as CytC are likely to require an additional transport mechanism (Colombini 2016).

The oligomerization of VDAC1, leading to the formation of a large flexible pore (see Figure 1.13), has been proposed to explain the ability of CytC to transit between the cytoplasm and the OMM (Zalk, Israelson et al. 2005, Abu-Hamad, Arbel et al. 2009, Keinan, Tyomkin et al. 2010, Shoshan-Barmatz, De Pinto et al. 2010, Keinan, Pahima et al. 2013, Shoshan-Barmatz, Mizrachi et al. 2013). Interestingly, apoptosis induction in human cells lead to VDAC oligomerization (Keinan, Tyomkin et al. 2010). It was shown that VDAC1 can shift in from the monomeric toward the oligomeric form in response to various apoptosis inducers, regardless of the cell type or apoptosis inducer, including arsenic trioxide, staurosporine, etoposide, curcumin, cisplatin, selenite, H₂O₂, tumour-necrosis factor α , or simply UV

light. In that instance, oligomerization was enhanced up to 20-fold, confirming the preference for an oligomeric state during apoptosis (Colombini 2016).

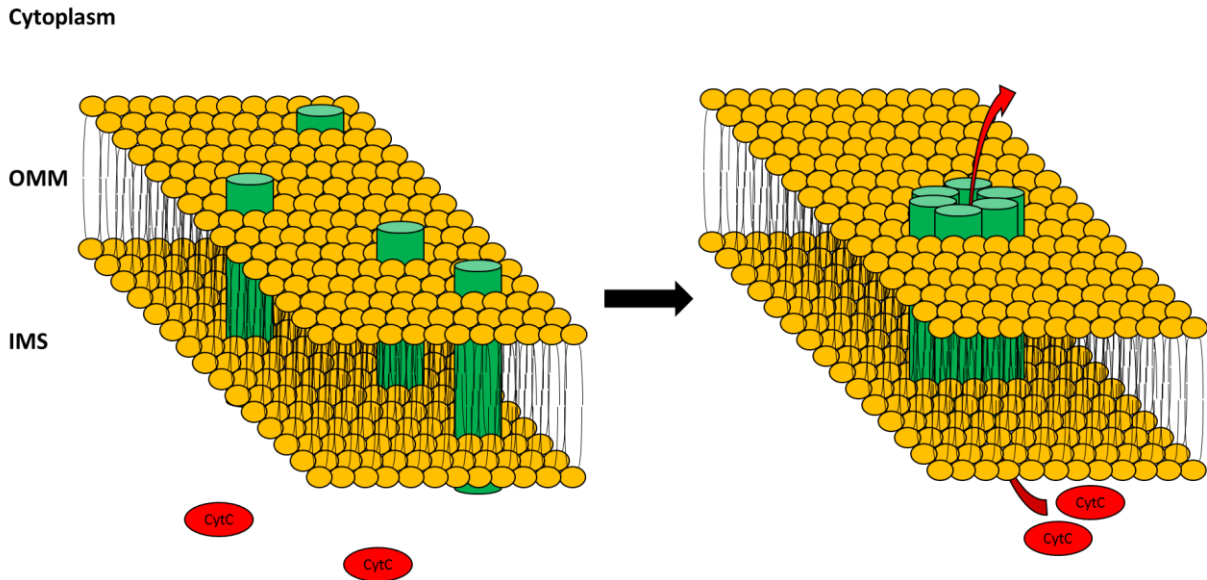


Figure 1.14 VDAC oligomerization as a gateway for CytC release from the mitochondria. The monomeric VDAC (left, in green) will oligomerize to form a supra-molecular assembly allowing the transit of cytochrome (CytC) from the IMS to the cytoplasm.

So far, VDAC1 has been demonstrated to be able to exist as higher-order oligomers, such as dimers, trimers, tetramers, and hexamers (Shi, Chen et al. 2003, Zalk, Israelson et al. 2005, Gonçalves, Buzhynskyy et al. 2007, Hoogenboom, Suda et al. 2007, Malia and Wagner 2007, Keinan, Tyomkin et al. 2010, Shoshan-Barmatz, De Pinto et al. 2010). FRET experiments highlighted the dynamicity of the oligomerization process, defined by an equilibrium between monomeric and oligomeric forms (Zalk, Israelson et al. 2005), whereas atomic force microscopy (AFM) experiments on native VDAC1 and chemical cross-linking experiments using both purified and membrane-embedded VDAC1 confirmed the assembly of dimers, trimers, tetramers and higher VDAC1 oligomers (Zalk, Israelson et al. 2005, Gonçalves, Buzhynskyy et al. 2007, Hoogenboom, Suda et al. 2007). Finally, electron microscopy-based analysis of crystallized OMM highlighted the propensity of VDAC1 channels to be organized into ordered arrays of hexamers with inter-channel contacts (Guo, Smith et al. 1995). Recently it was

suggested that the particular lipid composition of the OMM, significantly enhances VDAC1 oligomerization (Betaneli, Petrov et al. 2012).

In addition to the oligomerization of VDAC channels, an additional theory involving the oligomerization of Bax and Bak, and the subsequent formation of a selective large channel, sufficient for CytC release across the OMM, has been proposed (Antonsson, Montessuit et al. 2000, Eskes, Desagher et al. 2000, Antonsson, Montessuit et al. 2001, Reed 2006). Briefly, Bax is normally found as a monomer in the cytosol of cells and its oligomerization is prevented by another regulator named Bcl-2. Upon apoptosis induction and activation by tBid (Lovell, Billen et al. 2008), Bax will form large complexes (between 96 kDa and 260 kDa) that will associate with the mitochondria, and insert into the mitochondrial membrane (Bleicken, Classen et al. 2010, Zhang, Zhu et al. 2010), allowing the transit of CytC from the mitochondria to the cytosol. Again, its association with VDAC1 to form hetero-oligomers allowing CytC release was also suggested (Banerjee and Ghosh 2004). Although multiple pathways and mechanisms of CytC release has been proposed, the possibility of them co-existing within a single model of cell death is reasonable, and their activation might depend on the cell type and the nature of the stimulus (Gogvadze, Orrenius et al. 2006, Galluzzi and Kroemer 2007).

1.9. The Permeability Transition Pore (PTP)

In normal cells, a number of pro-apoptotic factors such as CytC, Smac/DIABLO and AIF resides in the mitochondria, most notably in inter-membrane space (IMS) (Shoshan-Barmatz, Israelson et al. 2006, Shoshan-Barmatz, De Pinto et al. 2010, Shoshan-Barmatz and Mizrachi 2012). The mechanism allowing the release of these factors during mitochondria-mediated apoptosis still remains unclear, especially concerning their transition through the OMM.

Different models have been proposed, either involving a disruption of OMM integrity by osmotic matrix swelling or an increase in OMM permeability due to the formation of a large supramolecular assembly allow for the release of proteins, such as CytC (see section 1.8.1).

The osmotic matrix swelling involves closure of VDAC1 channel which will cause a defect in mitochondrial ATP/ADP exchange in the mitochondrial, which will in turn lead to the disruption of the OMM and the subsequent release of inter-membrane proteins into the cytosol (Vander Heiden, Chandel et al. 2000, Vander Heiden, Li et al. 2001).

Nevertheless, the main hypothesis involves the formation of a large multi-protein complex called the Permeability Transition Pore or PTP. This supramolecular assembly has been demonstrated to participate in many cell death scenarios and to serve as a calcium release channel, regulating the matrixial level of calcium via its transient or persistent opening, the latter leading to an uncontrolled release of calcium (Rasola and Bernardi 2011). High concentration of calcium will in turn depolarizes the mitochondria by opening the PTP. The opening this “megapore” will allow the release of IMS proteins such as CytC (Crompton 1999, Baumgartner, Gerasimenko et al. 2009), inducing apoptosis and possibly necrotic cell death as well (Rasola and Bernardi 2011).

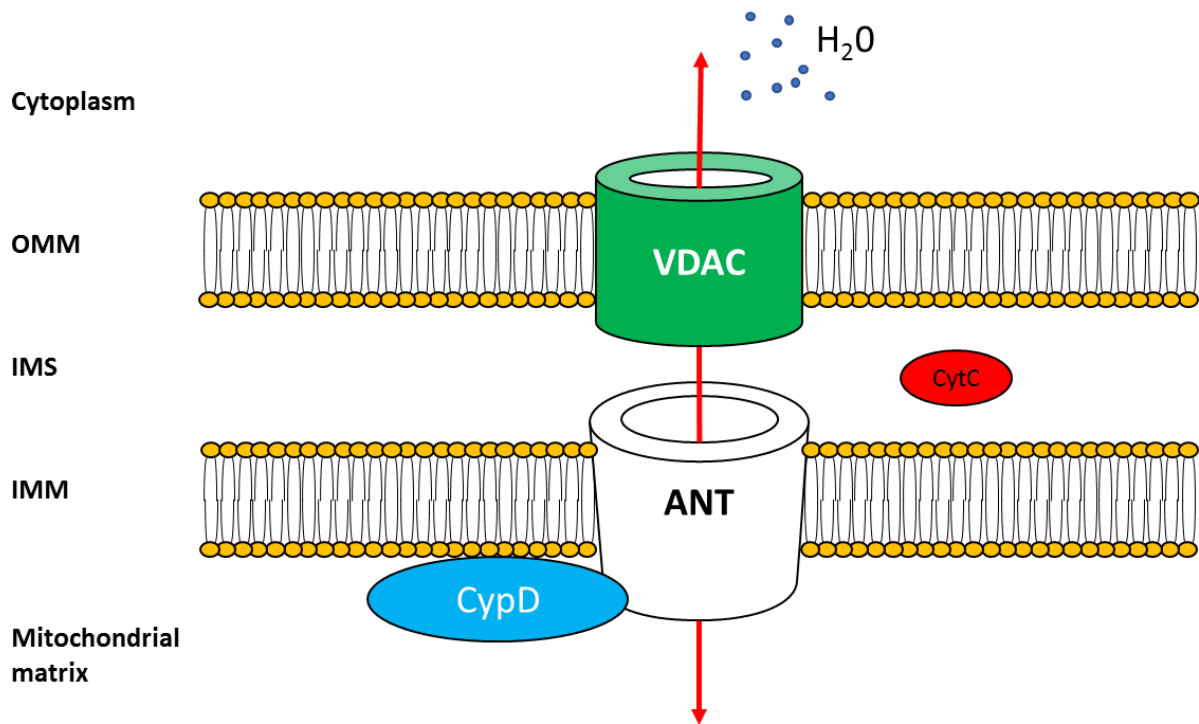


Figure 1.15 Simplified model for the Permeability Transition Pore (PTP). Schematic representation of the core complex called the PTP, which allows the free exchange of small and large metabolites, pro-apoptotic factors (CytC) or water between the cytoplasm, the intermembrane space (IMS) and the mitochondrial matrix. The different contributor to this supra-molecular complex are VDAC1 at the OMM, adenine nucleotide translocase (ANT) in the IMM, and cyclophilin D (CypD) in the mitochondrial matrix.

The proposed PTP complex is likely composed of VDAC1 at the OMM, adenine nucleotide translocase (ANT) in the IMM, and cyclophilin D (CypD), which is present in the mitochondrial matrix (Shoshan-Barmatz and Gincel 2003, Tsujimoto and Shimizu 2007). The PTP is thought to form a high-conductance non-specific pore linking the inner and outer mitochondrial membranes (Figure 1.14). Its opening is likely to occur in response to over-production of ROS or calcium in the cytosol and will allow free transit of water and low-molecular weight metabolites into the mitochondrial matrix. This influx of substrates will ultimately provoke mitochondria swelling and the release of pro-apoptotic factors into the cytosol (Halestrap, Doran et al. 2000, Shoshan-Barmatz and Gincel 2003, Tsujimoto and Shimizu 2007).

1.10. Summary

Voltage dependent anion channels (VDACs) are the eukaryotic equivalent of bacterial outer-membrane porins (Zeth 2010). Located in the outer-mitochondrial membrane (OMM) (Shoshan-Barmatz and Gincel 2003), VDACs allow the exchange of different metabolites, such as ions, ATP, for ADP, Pi and other respiratory substrates (e.g. pyruvate, malate) into the mitochondrion (Vanyushin, Bakeeva et al. 2004, Tan and Colombini 2007).

Moreover, VDACs are capable of mediating the flux of Ca^{2+} (Tan and Colombini 2007) or superoxide anions (Han, Antunes et al. 2002), and influence the uptake of cholesterol (Shoshan-Barmatz and Gincel 2003), essential for multiple signalling cascades in young, normal, aged and diseased cells. This exchange is dependent on the ability of the channel to switch between open and closed states with the later state being impermeable to substrates like ADP and ATP (Shoshan-Barmatz and Gincel 2003, Colombini 2016). The open state of the channel confers predominately anion selectivity and the partially or fully closed forms of VDACs conduct cations (Madesh and Hajnóczky 2001). It is believed that transient potentials across the OMM (metabolically or inner mitochondrial membrane driven) are sufficient to support the channel's gating *in vivo* (Mertins, Psakis et al. 2012).

The abundance and strategic location of VDACs in the OMM, casts them in the role of a safekeeper of mitochondrial function, as their opening and closure define the route that mitochondria should follow: normal respiration or suppression of mitochondrial metabolism leading to apoptosis and cell death (Madesh and Hajnóczky 2001).

1.10.1. AtVDAC partners

The strategic location of VDACs in the OMM implies that there might act as binding partners for cytosolic proteins. Mammalian hexokinases have long been described to interact with VDACs, resulting in a shift in the susceptibility of mitochondria to pro-apoptotic signals (John 2003, Pastorino and Hoek

2008). This can lead to suppression of apoptosis, a mechanism particularly interesting in the study of tumours (John 2003).

In plants, studies using virus-induced gene silencing (VIGS) of a hexokinase-encoding *Hxk1* caused necrotic lesions on leaves, abnormal leaf morphology, and retarded plant growth in *Nicotiana benthamiana*. It was further demonstrated that the Hexokinase 1 Hxk1 was associated with the mitochondria, and this association required the N-terminal membrane anchor (Kim, Lim et al. 2006).

An interesting discovery concerned the interaction between VDACs and tubulin, the latter acting as an inhibitor of VDACs (Rostovtseva and Bezrukov 2012). These findings showed that not only does the mitochondria bind to the cytoskeleton (for movement across the cell), but there are other interactions involved in the process, leading to a different cascade of reactions. Indeed, VDAC interaction with tubulin at the mitochondria–cytosol interface enhances a mechanism of regulation of mitochondrial energetics, limiting the uptake of ATP and other metabolites (Rostovtseva and Bezrukov 2012).

Another member of the cytoskeleton, the kinesins, has been described to interact with VDACs in plants. Indeed, the *A. thaliana* kinesin KP1 specifically interacts with AtVDAC3, regulating the respiration during seed germination at low temperatures (Yang, Chen et al. 2011). An example of this interaction is given in Figure 1.15 with the colocalization of AtVDAC3 and KP1 using YFP-tagged recombinant proteins expressed in *A.thaliana*. Both proteins colocalised in the mitochondria of the protoplasts, confirming the interaction between the channel and the kinesin. This feature casts as well both VDACs and associated kinesins as potential regulators of energy supply within the plant cells.

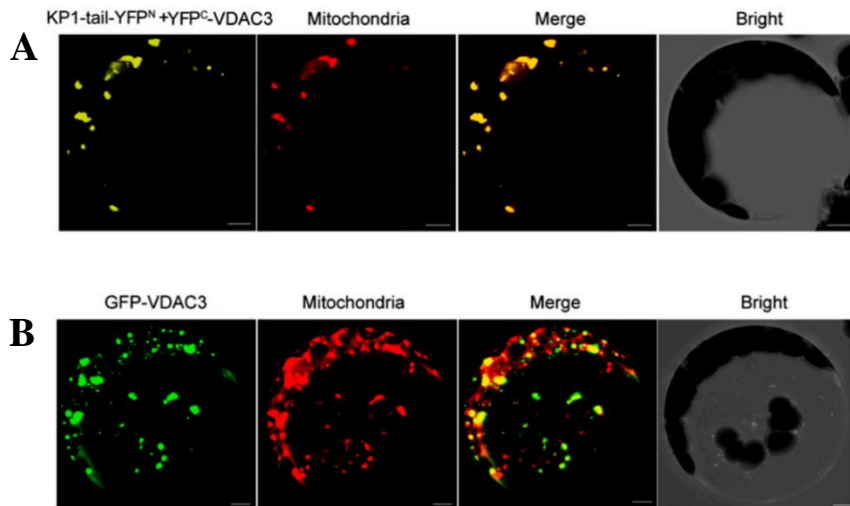


Figure 1.16 In vivo interaction between AtVDAC3 and Kp1. Taken from Yang et al. (2011)(Yang, Chen et al. 2011) **(A)** Co-localisation of the KP1 and VDAC3 complex with mitochondria in *Arabidopsis thaliana* mesophyll protoplasts transformed with the constructs KP1-tail-YFPN and YFPC-VDAC3. The mitochondria were stained by MitoTracker. And the scale is given by grey bars (5 μ m). **(B)** Co-localisation of VDAC3 with mitochondria. *Arabidopsis* mesophyll protoplasts transiently overexpressing GFP-VDAC3 were stained as above.

Finally, some of the VDACs features, including specific interactions, are conserved amongst species. For example, recent studies showed that members of the apoptosis regulator Bcl (*B-cell lymphoma*) family, which are not present in plants, can interact with plant VDACs (Vander Heiden, Li et al. 2001, Godbole, Varghese et al. 2003).

In summary, members of the hexokinase family, Bcl family and kinesin family all displayed a direct or indirect (via the mitochondria) interaction with the VDAC channel from *A.thaliana*. These families of protein can constitute a great foundation for the characterization of potential AtVDAC binding partners, and their molecular interactions with the channel. More specifically, the kinesin family of protein will be a subject of interest in this study in parallel to the VDAC channel.

1.11. Kinesins

Kinesins represent a superfamily of microtubule-based motor proteins that are essential in the cell. They perform various functions, the most common being the transport of organelles or different “cargos”, such as vesicles, super-complexes of proteins, and even chromosomes during the mitosis across the cell (Lawrence, Dawe et al. 2004, Hirokawa, Noda et al. 2009). They can contribute to the regulation of microtubules (important for mitosis) (Hirokawa, Noda et al. 2009), transcription factor (example of Kif7/Gli transcription factor (Cheung, Zhang et al. 2009)) or other proteins such as VDAC (Yang, Chen et al. 2011) but the mechanism of action is still unclear (Hirokawa, Noda et al. 2009). In plants, a Kinesin-like protein, called KIN-7D, MKRP2 or mKlp2 (accession number; Q8W5R5), contains an extended region in its N-Terminal motor domain that has been proven to act as an MTS (mitochondrial targeting signal) (Itoh, Fujiwara et al. 2001), thus implying the possibility of AtVDAC protein acting as a binding platform for this kinesin.

1.11.1. General structural organization of kinesins

Kinesins conventionally comprise a heavy chain dimer and two light chains. The heavy chains are responsible for the overall structure of the complex; a conventional kinesin can be described as an elongated protein, with the head comprising the motor domains that bind to microtubules and allowing the movement of the protein, and the tail domains (Hirokawa, Noda et al. 2009). The tail domains, in association with the light chains, are responsible for the cargo recognition and binding (Hirokawa, Noda et al. 2009). The region linking both main domains (head and tail) is called the stalk domain and allows the dimerization of the two heavy chains (Figure 1.16).

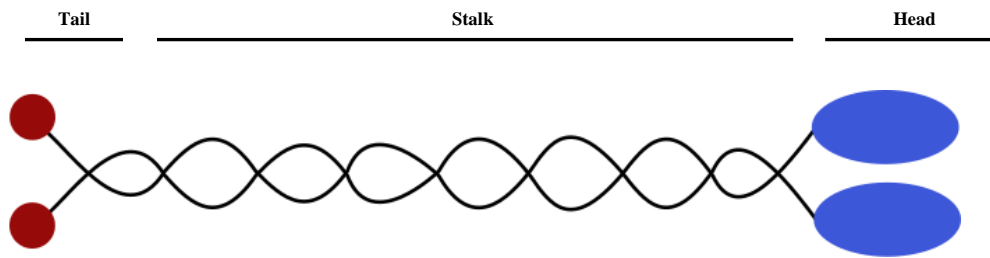


Figure 1.17 Schematic representation of conventional Kinesins structure. The motor domains (blue) are contained within the head, whereas the cargo binding sites (red) reside in the tail domain. The stalk is shown as a coiled structure (black) formed by the two heavy chains. Light chains are not shown here but are part of the tail, enabling substrate specific recognition and binding.

1.11.2. Motor domain of kinesins

In kinesins, the motor domain is responsible for the movement along the microtubules, harbouring both the ATP- and microtubule-binding activities (Cross 2004). Several crystal structures have been obtained of the motor domain alone and revealed strong structural similarities to the catalytic domain of the actin-based motor-myosin (Kull, Sablin et al. 1996). Briefly, the motor domain consists primarily of a single alpha/beta arrowhead-shaped domain, with a relatively wide nucleotide-binding cleft (Marx, Thormählen et al. 1998). It contains four motifs that are common to P-loop containing proteins with a Walker fold (Walker, Saraste et al. 1982) such as myosin and G-proteins. The Walker motif can be described as GxxxxGKT/S, which forms a phosphate binding loop (P-loop) between the third beta-strand and the second alpha helix, allowing nucleotide binding via the phosphate chain (Walker, Saraste et al. 1982). An example is given in Figure 1.17, with the bound to ADP (Figure 1.17, blue).

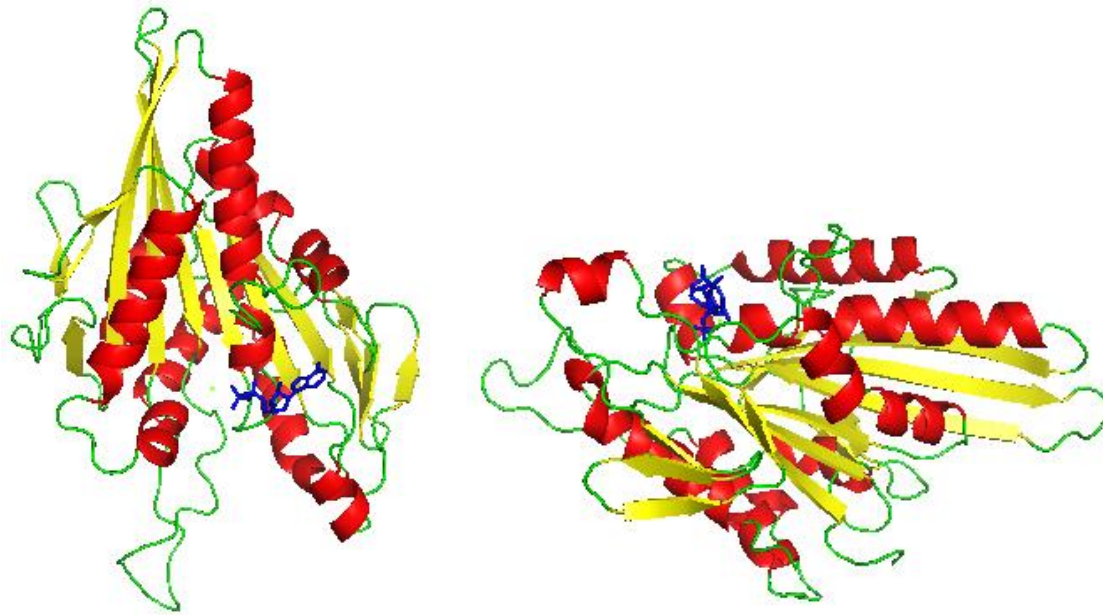


Figure 1. 18 Three-dimensional structure of the human ubiquitous kinesin motor domain. Crystal structure of the human ubiquitous kinesin motor domain 1BG2 at 1.8 Å resolution, shown from the front (**A**) or the side (**B**) of the molecule. A bound ADP molecule is shown in blue (displayed using Pymol (L DeLano 2002)).

The molecular movement, called motility, has been described previously. In summary, kinesin takes eight nanometres steps, each time alternating between its two heads (Asbury, Fehr et al. 2003), to move along microtubule protofilaments (Svoboda, Schmidt et al. 1993). The presence of ADP or ATP in the active site will dictate the conformation adopted by the kinesin motor domain on the microtubules (Cross 2004). Indeed, kinesin are strongly attached to the protofilaments in the presence of ATP or absence of nucleotides, and weakly bound when ADP is present in the catalytic site (Cross 2004).

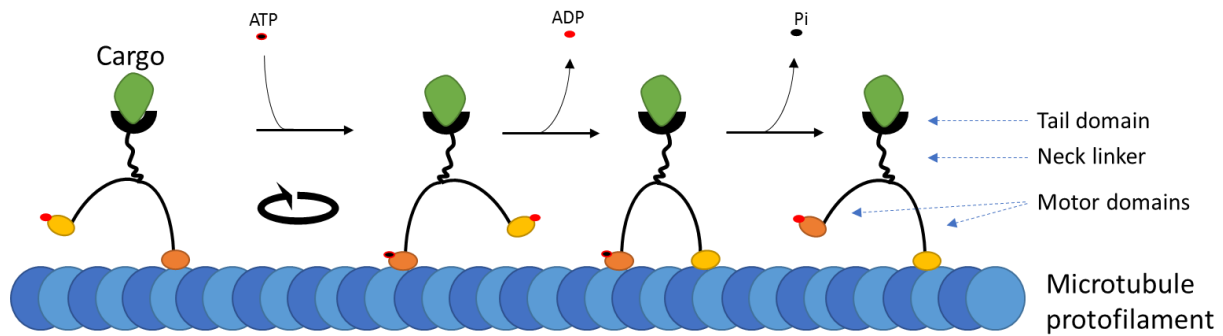


Figure 1.19 Kinesin moving alongside a microtubule. Schematic representation of kinesins moving along a microtubule protofilament (in blue). The binding of ATP (in red and black circle) on the first motor domain will induce a rotation of the neck linker, displacing the second motor domains upfront. The release of ADP (red dot) from the latter will allow this motor domain to strongly bind the microtubule. Finally, the hydrolysis from ATP to ADP and the release of pyrophosphate (Pi, black dot) will enhance the detachment of the first motor domain from the protofilament, creating movement of the cargo (green) alongside the microtubule.

The catalytic movement of kinesins alongside microtubules protofilaments is also associated the conformational changes of the neck linker, a 15 amino acid peptide at the C-terminal end of the motor domains (Rice, Lin et al. 1999). This peptide will adopts a well-defined structure as it docks onto the motor domain core, and will switch its orientation from the (-)end toward the microtubule (+)end (Asenjo, Krohn et al. 2003).

1.11.3. Tail domain of kinesins

Whereas the head domain is well defined as the microtubule binding and interacting region, the tail domain is intrinsically disordered (Seeger and Rice 2012).

This tail domain is really variable due to the different type of cargos the kinesins have to transport (Hirokawa, Noda et al. 2009). For example, the Kinesin-1 has been demonstrated to be involved on the intracellular transport of proteins (Xia, Roberts et al. 2003), ribonuclear protein complexes (Kanai, Dohmae et al. 2004) and cellular compartment such as Golgi (Echard, Jollivet et al. 1998), Endoplasmic Reticulum vesicles (Stauber, Simpson et al. 2006), endosomes (Imamura, Huang et al. 2003) or the mitochondria (Nangaku, Sato-Yoshitake et al. 1994, Wozniak, Melzer et al. 2005).

The variety of cargo the kinesins can recognize is mainly achieved through the kinesin light chains (Hammond, Griffin et al. 2008). Specific motifs known as tetratricopeptide repeat domains (D'Andrea and Regan 2003), a versatile protein interaction platform, have been identified to explain this great range of adaptative interactions.

Thus, alternative binding partners (aside from conventional cargos mentioned previously) can be identified. The example of KIFC3 (kinesin family member C3 from *Mus musculus*) highlight this feature; this kinesin can interact with the ubiquitin-specific protease USP47, a protease that removes ubiquitin chains from substrates and inhibits proteasome-mediated proteolysis (Sako-Kubota, Tanaka et al. 2014). The interaction of KIFC3 with USP47 will prevent the latter to remove ubiquitin chains from the E-cadherin and recruit it to the adherens junction of the cells. The depletion of either KIFC3 or USP47 will both result in cleavage of the E-cadherin, suggesting this interaction plays an important role in forming stable cell to cell adhesion in epithelial tissues (Sako-Kubota, Tanaka et al. 2014).

1.12. Aims and objectives of this study

Plant VDACs have been so far understudied in terms of structural and functional characterization. However, recent studies (Tateda, Watanabe et al. 2011) highlighted specific expression patterns of the four isoforms of *Arabidopsis thaliana*. Considering AtVDAC1 has been shown to be essential for cell development and growth, this isoform is the primary target for characterization studies focusing on its structure and its electrophysiological behaviour. Primary work has already begun with the successful cloning of *AtVDAC1* gene into an expression vector by Msc Felix Brademann, for the heterologous production of AtVDAC1 protein in *Escherichia coli* cells.

In addition to its essential function as an ion transporter, VDAC has been shown to interact with multiple partners such as Bcl protein, Hexokinases or kinesins. Thus, this study aims at providing the groundwork for future binding studies, focusing on the interaction of AtVDAC1 with chosen partners.

On one hand, AtVDAC1 mutants have to be designed to further explore the hypothesis that the channel might act as a platform for the aforementioned partners. On the other hand, several hypothetical AtVDAC1 partner proteins must be produced to be used in interaction studies with the native channel protein and/or its mutants.

Two specific partners have been identified, namely the *Nicotiana Benthamiana* Hexokinase 1 and the Kinesin-like mKlp2. The former has been shown to relocate to the mitochondria in *A.thaliana*, caused by the presence of an MTS. Due to the history of VDAC interaction with hexokinases, it is highly possible the Hexokinase 1 binding to the mitochondria is mediated through interaction with the VDAC channel. In a similar fashion, the *A.thaliana* Kinesin-like mKlp2 and mKlp1 has also been shown to relocate to the mitochondria via a possible MTS. Recently, the interaction between AtVDAC3 and the mKlp1 isoform was demonstrated, thus leaving the possibility for mKlp2 to use a similar platform to bind the mitochondrial surface.

In summary, the study will consist in the following steps:

- 1.Design of AtVDAC1 mutants and production of constructs by PCR-directed mutagenesis
- 2.Cloning of the *mKlp2* gene into a suitable expression vector
- 3.Subsequent heterologous expression of the different proteins in *E.coli* BL21 (mKlp2C-Ter) or Omp9 (AtVDACs) cells
- 4.Purification of the protein by a combination of either Ion exchange chromatography or affinity chromatography and Size exclusion chromatography.
- 5.Structural characterization of all proteins by Small Angle X-ray Scattering and/or Circular Dichroism
- 6.Functional characterization of AtVDAC1 protein by Black lipid membrane (BLM) assay
- 7.Functional characterization of mKlp2 by Iso-thermal titration calorimetry (ITC)

2. Chapter 2: Materials and Methods

2.1. Buffers and media

Buffers and media for this study were prepared according to the composition listed in Table 2.1.

Table 2.1. Buffers and media.

Buffer/media	Composition
Resuspension buffer (RE)	50 mM Tris-HCl (pH 8.0), 100 mM NaCl, 0.2 mM PMSF
TN buffer	50 mM Tris-HCl (pH 8.0), 100 mM NaCl
TEN-triton buffer	50 mM Tris-HCl (pH 8.0), 100 mM NaCl, 10 mM EDTA, 2 % (v/v) Triton X-100
Denaturation buffer	25 mM NaH ₂ PO ₄ / Na ₂ HPO ₄ (pH 7.0), 100 mM NaCl, 1 mM EDTA, 10 mM DTT, 6 M Guanidinium chloride
Refolding buffer 1	25 mM NaH ₂ PO ₄ / Na ₂ HPO ₄ (pH 7.0), 100 mM NaCl, 1 mM EDTA, 10 % (v/v) Glycerol, 2.29 % (v/v) LDAO
Refolding buffer 2	25 mM NaH ₂ PO ₄ / Na ₂ HPO ₄ (pH 7.0), 100 mM NaCl, 1 mM EDTA, 1 mM DTT, 10 % (v/v) Glycerol, 0.12 % (v/v) LDAO
Elution buffer for ion exchange chromatography (VDACs)	25 mM NaH ₂ PO ₄ / Na ₂ HPO ₄ (pH 7.0), 1 M NaCl, 1 mM EDTA, 1 mM DTT, 10 % (w/v) Glycerol, 0.12 % (v/v) LDAO
Elution buffer for size exclusion chromatography (VDACs)	25 mM NaH ₂ PO ₄ / Na ₂ HPO ₄ (pH 7.0), 100 mM NaCl, 1 mM EDTA, 1 mM DTT, 10 % (w/v) Glycerol, 0.12 % (v/v) LDAO
Elution buffer for affinity chromatography Ni-Nta (mKlp2C-Ter)	25 mM Tris-HCl (pH 7.0), 100 mM NaCl, 3 % (w/v) Glycerol, 500 mM Imidazole
Elution buffer for size exclusion chromatography (mKlp2C-Ter)	25 mM Tris-HCl (pH 7.0), 100 mM NaCl, 3 % (w/v) Glycerol
Dialysis Buffer	25 mM NaH ₂ PO ₄ /Na ₂ HPO ₄ (pH 7.0), 50 mM NaCl, 1 mM EDTA, 1 mM DTT, 10 % (w/v) Glycerol

LB media	Tryptone 10 g/L, Yeast extract 5 g/L, NaCl 10 g/L. Add 1.5% Agar if solid (Plates)
LB Auto-Induction	Tryptone 20 g/L, Yeast extract 5 g/L, NaCl 5 g/L
SOB media	Tryptone 20 g/L, Yeast extract 50 g/L, NaCl 0.5 g/L
Transformation buffer (TB)	10 mM PIPES, 55 mM MnCl ₂ , 15 mM CaCl ₂ , 250 mM KCl
TBE Buffer	900 mM Tris base, 900 mM Boric acid, 20 mM EDTA, 12.5 mM NaOH
SDS Sample Buffer (Laemmli)	0.25 M Tris-HCl (pH 6.8), 0.5 M DTT, 10 % (w/v) SDS, 50 % (v/v) Glycerol, 0.5 % (w/v) Bromophenol blue
10x SDS Run Buffer (Laemmli)	250 mM Tris, 2 M Glycine, 1% (w/v) SDS
SDS-PAGE Coomassie Staining Solution	50 % (v/v) Methanol, 10 % (v/v) Glacial Acetic Acid, 0.25 % (w/v) Coomassie R-250
SDS-PAGE Destaining Solution	50 % (v/v) Methanol, 10 % (v/v) Glacial Acetic Acid
Silver Nitrate Solution	0.1 % (w/v) AgNO ₃ in dH ₂ O
Developing Solution	3 % (w/v) Na ₂ CO ₃ , 0.05 % (v/v) Formaldehyde
Silver destaining Solution A	633 mM NaCl, 231 mM Cupric Sulphate
Silver destaining Solution B	1.75 M Sodium Thiosulfate
TBS buffer	10 mM Tris-HCl (pH 7.5), 150 mM NaCl
TBS-Tween buffer	10 mM Tris-HCl (pH 7.5), 150 mM NaCl, 0.05 % (v/v) Tween
TBS-Tween/Triton buffer	10 mM Tris-HCl (pH 7.5), 150 mM NaCl, 0.05 % (v/v) Tween, 0.2 % (v/v) Triton X-100
Blocking buffer	0.5 % (w/v) Western blot Blocking reagent from Novex® in TBS-tween
Western Blot transfer buffer	1X blotting buffer from Novex® in 20 % (v/v) methanol
Thin layer chromatography solvent	63: 35: 5, v/v/v chloroform: methanol: ammonium hydroxide
Black lipid membrane BLM buffer	10 mM Tris-HCl (pH 7.4), 150 mM KCl, 50 mM Ca ²⁺

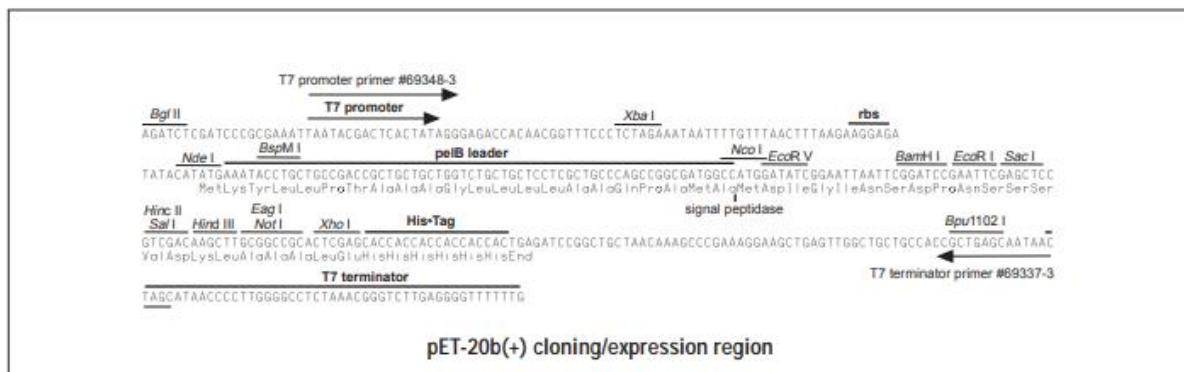
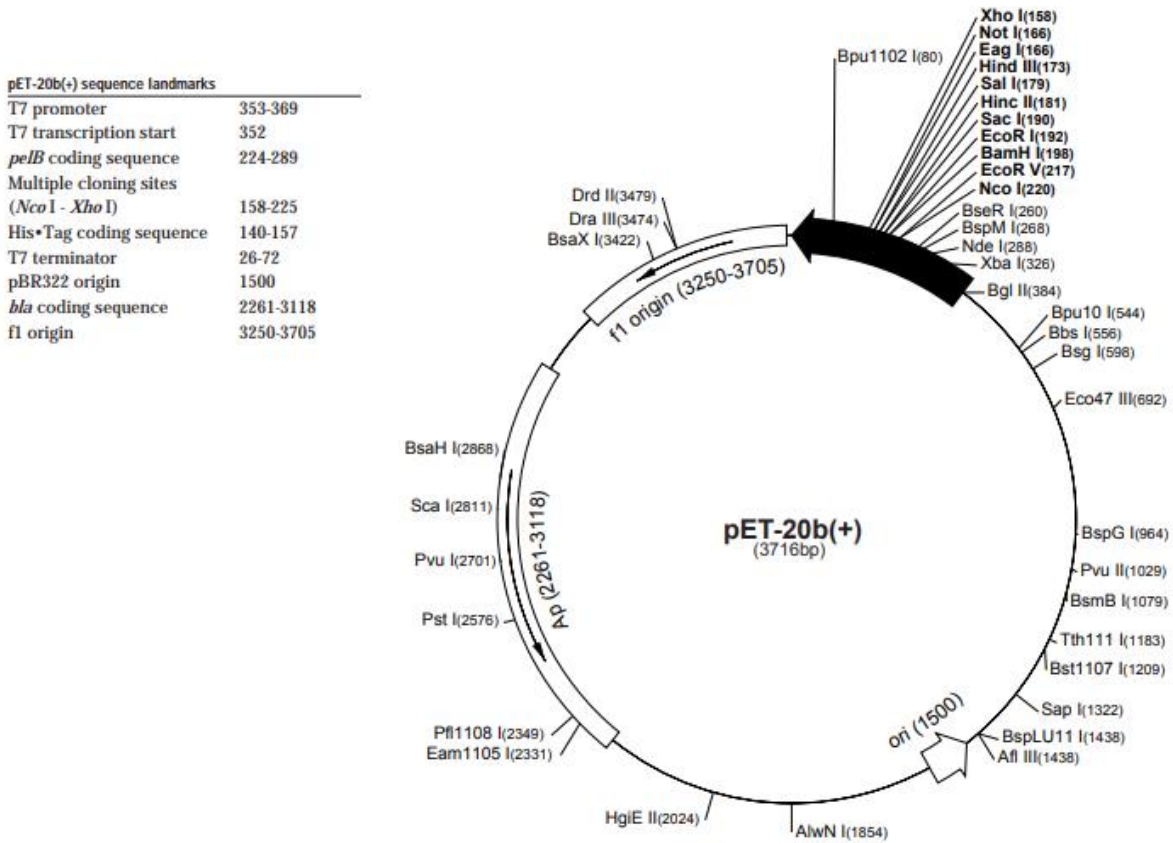


Figure 2.1 pET-20b(+) Plasmid map and cloning region – Overview of the pET-20b(+) vector map and the nucleotide sequence of the cloning/expression region, with the associated restriction sites. (Taken from Novagen®)

Gene sequences of the Voltage Dependent Anion Channels (AtVDAC1, AtVDAC2 and AtVDAC4) and the Kinesin-like mKlp2C-Ter from *Arabidopsis thaliana* are provided in Table 2.3. The corresponding Gene IDs and locus numbers are provided as well.

Table 2.2 DNA sequences of AtVDACs and mKlp2C-Ter genes. DNA sequences of the genes used in this study, provided in FASTA format, as well as their accession number on

Gene	DNA sequence
(Gene ID)	
(locus number)	
AtVDAC1 (820914) (AT3G01280)	<p>ATGGTGAAAGGTCCCGGTCTCTACACCGAAATCGGC AAAAAGGCCAGAGATCTTCTGTAC AAAGACCACAACAGTGACCAGAAATTCAGTATCACCACCTTTCTCTCCTGCCGGTGTGGCC ATCACCTCAACCGGAACATAAGAAAGGTGACTTATTGTTGGGAGATGTCGCTTTTCAGTCG AGGCGAAAGAACATTACTACTGATTTGAAAGTTTGCAGTACTTACTTTCTGATCACC GCTACCGTTGATGAGGCTGCACCCGGACTGAGGTCAATCTTCAGCTTCAAGGTTCCCTGAC CAAAATTCTGGCAAGGTTGAGCTGCAATACTTGCATGAGTACGCCGGTATCAGCACAAAGC ATGGGATTGACTCAGAACCAACTGTCAACTTCTCTGGTGTGATTGGCTCCAATGTCTTG GCTGTTGGTACTGATGTTTCATTTGACACCAAGTCTGGAAATTTACCAAGATCAATGCT GGTTTAAGCTTCACCAAGGAGGACTTAATTGCCTCCCTTACTGTGAACGACAAGGGCGAT CTATTGAATGCATCTTACTATCACATTGTGAACCCGCTGTTCAACACTGCGGTTGGAGCC GAAGTGAGCCACAAGTTATCTAGCAAGGACAGCACCATAACTGTTGGAACACAGCAGCTCG CTTGACCCCTTGACCTCTGTGAAGGCTCGTGTCAATAGTGCAGGATTGCAAGTCTCTC ATTCAACACGAGTGAAACCCAAAGTCATTCTTCACAATCTCTGGAGAAGTCGACACAAAG TCAATTGACAAGAGTGCTAAAGTTGGATTGGCTCTCGCACTCAAGCCTTGA</p>
AtVDAC2 (836886) (AT5G67500)	<p>ATGAGCAAAGGTCCAGGACTCTTACCAGATATCGGC AAGAAAGCCAAAGATCTGTTGACG AGAGACTACAATTCGATCAGAAGTTCAGTATCTCCACTTACAGTGCCTCCGGCGTGGGA ACTGAGAGAGAGAACGAGTATCAGGATGATATTTACTTCTGTTTAAAGAACTAGATGTTTG ATAATGAGTGAAAATGAGGCCCTTACGTCTACTGCTCTGAAGAAAGGAGGAGTTCATGCT GCTGATGTTGCCACCAATACAAGTACAAGAATGCTTTGTTTGTATGTTAAAATCGACACT GATTCTAGTGTGTTTGCACAACAGTCACACTTACCGAGATCCTCCCATCAACAAAAGCCATT GCCTCCTTCAAAGTCCCTGATTATAATTCGCCAAGCTCGAGGTGCAATACTTCCACGAC CACGCAACAGTTACCGCTGCTGCAGCTTTGAAACAAAACCCACTAATTGACATAACAGCT ACTCTTGGTTCGCCAGTCATCTCATTTGGTGTGAAAGCTGGATATGACACAACCTCCAAA ACTTTACCAAGTACAATGCCGGGATCAGTGTGACAAAACCCAGATGCTTGCCCTCTCCATA ATATTGGGAGACAAAGGAGACTCACTCAAAGCATCATACCTTCATCACTTTGATGAATTT AAGAGAACCGCAGCAGTTGGTGAGGTTTACAGGAAGTCTCGACAAAATGAAAACACGATA ACGGTGGTGGATTGTATGCGATTGATCATTGACTGCAGTGAAGCTAAGCTCAACAAC CATGGCACACTTGGTGTCTTCTGTCAGCACGAGGTCCTGCCAGATCACTAGTACTGTT TCCAGTGAGATTGACACTAAGGCTTTAGAAAAGCATCCAAGGTTTGGTCTCTCTCTTGCT CTCAAACCTTGAGAACACACTCACATCAGACCTGCTTGAGTCTTCTACTTTTCTCGT ATGCTCTCATTGTTGA</p>
AtVDAC4 (835853) (AT5G57490)	<p>ATGGGAAGCAGTCCAGCTCCGTTTGCCGATATTGGCAAGAAAGCCAAAGATCTCCTAAAC AAGGATTACATTTTTGACCACAAGTTTACTCTCACAAATGCTGAGTGCTACAGGAACGGAA TTTGTGGCTACTGGTTTGAAGAAGGATGATTTCTTTTTTTGGCGATATAAGCACACTATAT AAAGGTCAAAAACACCATTGTTGATCTGAAAATCGACAGCCACTCTAGTGTGTCGACGAAA GTA ACTCTCAAAAATCTCTTGCCATCCGCTAAAGCTGTAATTAGTTTCAAAAATACCTGAT CACAAGTCTGGCAAGCTGGATGTGCAATATGTTTCATCCTCATGCTACGCTCAATTCCAGC ATTGGCCTCAACCAACTCCTCTGTTAGATCTATCAGCAACTATCGGAAGCCAGAATGTT TGCCTTGGTGGTGAAGTCAGTTTCGACACAGCTTCATCATCACTAACAAAGTACAATGCA GGGATTGGTTTCAACAACCAAGGCGTCTCTGCTGCAGTACTACTGGAGGATAAAGGGGAG AGTCTGAGAGCTACTTACGTCCACACAGTGAACCCAAACCACATCCTTTGGTGCAGAACTG ATCCGTCGCTTCTCCAATTATAACAACAGCTTCACCGTCGGAAGCTCTCACTCTGTGGAT CAATTCACAGTGGTTAAGACCAGATTTTCTAACAGTGGGAAAGCAGGGATGGTGGTCCAG</p>

	AGAGAATGGAGACCGAAGTCGCACATCACTTTCTCAGCTGAGTATGACTCAAAGGCTGTG ACCTCTTCACCAAAGCTTGGTCTCGCCCTCGCCCTCAAACCATAA
mKlp2C-Ter (Kin-7D/ NM_120065) (AT4G39050)	CATATGGGTAGCAGCCATCATCATCACCATCATAGCAGCGGTCTGGTTCGCGGTGGTAGC CATGCAGTTAGCGGTGAATATGCAGATGAGCTGAAAAAAAAAATCCAGAGCCAAGAAATC GAGAACGAGGAAGTAAACTGGAACATGTGCAGATTGTTGAAGAAAATAGCGGTCTGCGT GTTTCAAGATCAGAACTGGCCGAAGAGGCAAGCTATGCAAAAAGAACTGGCAAGCGCAGCA GCAGTTGAACTGAAAAATCTGGCCAGCGAAGTTACCAAAGTGGAGCTGCAGAATACAAAA CTGGAAAAAGAACTGGCTGCAGCACGTGATCTGGCACAGACCCGTAATCCGATGAATGGT GTTAATCGCAAATATAACGATGGTGCACGTAGCGGTTCGTAAAGGTCGTATTAGCAGCAGC CGTAGCAGTGGTGTGATGAATTTGATGCATGGAATCTGGATCCGGAAGATCTGAAAATGGAA CTGCAGGTTTCGTAACAGCGTGAAGTTGCACTGGAAAGCGCACTGGCAGAAAAAGAATTC ATCGAAGATGAGTATCGCAAAAAAGCGGAAGAAGCAAAAACGTCGCGAAGAAGCCCTGGAA AACGATCTGGCAAATATGTGGGTTCTGGTTGCCAAACTGAAAAAAGATAATGGTGCAGTGC CCGGAACCGAATGGCACCGATCCGGGTCGTGAGCTGGAAAAATCACAGAGTCATGCAGTT CTGAAAGAACGTCAGGTTAGCAGCGCACCGCGTCAGCCGGAAGTTGTTGTTGTGGCAAAA ACCGAAGAAACCCCGAAAGAAGAACCCTGGTTGCACGTCTGAAAGCACGTATGCAAGAA ATGAAAGAAAAAGAGATGAAAAGCCAGGCAAATGGTGTGCAATAGCCATATTTGCAAAA GTGTGTTTTGAAAGCCCGACCGCAGCAATTCTGCTGCCGTGTCGTCATTTTTGTCTGTGT AAAAGCTGTAGCCTGGCATGTAGCGAATGTCCGATTTGTCGTACCAAAATTAGCGATCGT CTGTTTGCATTTCCGAGCTAACTCGAG

The *AtVDACs* genes were amplified by PCR from plasmid templates harbouring GFP-tagged *AtVDACs* (kindly provided by Prof. T.Kusano from Tohoku University, Japan). The primers used for this DNA amplification are reported in Table 2.3.

Table 2.3 Primers used for the amplification of *AtVDACs*. Expected sizes of PCR products pre- and post-double digests with *EcoRI* and *NdeI*, are indicated. The nucleotides responsible for binding *EcoRI* and *NdeI* are highlighted with a black and red line, respectively.

Gene	Primers	Sequence	PCR product size (bp)	Size after digestion* (bp)
AtVDAC1	Forward	GCGCC <u>CATATGGT</u> GAAAGGTCCCGGTCTCT	851	833
	Reverse	TAGCGGAATTC <u>T</u> TAAGGCTTGAGTGCAGAGCCA		
AtVDAC2	Forward	GCGCC <u>CATATG</u> AGCAAAGGTCCAGGACTCT	932	914
	Reverse	TAGCGGAATTC <u>T</u> TAAGGTTGAGAGCAAGAGAGA		
AtVDAC4	Forward	GCGCC <u>CATATGG</u> GAAAGCAGTCCAGCTCCGT	843	827
	Reverse	TAGCGGAATTC <u>T</u> TATGGTTGAGGGCGAGGGCGA		

*Standard overnight digest with restriction endonucleases *EcoRI* and *NdeI* from NEB® (see section 2.4.2).

2.3. Microbiology

2.3.1. Bacterial strain genotypes

Bacterial strains used in this study and their respective genotype are listed in Table 2.2. The cloning stages were performed using *Escherichia coli* DH5 α cells, whereas the expression of the recombinant proteins AtVDACs and mKlp2C-Ter was performed in Omp9 and BL21 DE3 cells, respectively.

Table 2.4 *Escherichia coli* strains and associated genotypes. *E. coli* strains used for the production and expression of proteins and their respective genotype. DH5 α cells were used to propagate and maintain plasmids, Omp9 and BL21 DE3 cells were used for the production and expression of AtVDAC proteins mKlp2C-ter protein, respectively.

<i>E.coli</i> strains	Genotype
DH5α	F- ϕ 80lacZ Δ M15 Δ (lacZYA-argF) U169 recA1 endA1 hsdR17 (rk-, mk+) phoA supE44 λ - thi- 1 gyrA96 relA1
Omp9	F- ompT hsdSB (rB- mB -) gal dcm (DE3), Δ lamB ompF: :Tn5 Δ ompA Δ ompC Δ ompN
BL21 DE3	<i>fhuA2 [lon] ompT gal (λ DE3) [dcm] ΔhsdS</i> <i>λ DE3 = λ sBamHIo ΔEcoRI-B int::(lacI::PlacUV5::T7 gene1) i21 Δnin5</i>

2.3.2. Preparation of chemically competent cells

Chemically competent cells were prepared based on a previous methodology (Inoue *et al.*,1990) (Inoue, Nojima et al. 1990), known to yield great amounts of competent cells.

Frozen cells were streaked onto a LB plate and incubated overnight at 37°C. The next morning, 10-12 large colonies were transferred to 250 mL SOB medium (Table 2.1) in a 2 L flask and incubated at 18 °C (200 rpm) until an OD₆₀₀ of 0.6 was reached. Then, the flask was immediately put on ice for at least 10 minutes, then moved to a sterile 500 mL Sorval bottle and centrifuged at 6,000g for 10 min (at 4 °C). Supernatant was discarded, and cells were re-suspended in 80 mL ice-cold transformation buffer (TB, Table 2.1) and incubated on ice for 10 minutes. Then, the cells were centrifuged again at 6,000g for 10 min (at 4 °C). Supernatant was discarded, and the final pellet was re-suspended in 20 mL of ice-cold TB buffer and DMSO (SIGMA®) was added at 7 % (v/v). Following a 10 minute incubation, cells

were aliquoted into 1 mL eppendorfs and immediately frozen in liquid nitrogen for long term storage at -80 °C.

2.3.3. Bacterial cell transformation

Storage, expression plasmids and/or plasmids harbouring synthetic genes were routinely used to transform *E. coli* DH5 α chemical competent cells. For IPTG inducible expressions, *E. coli* Omp9 chemical competent cells were transformed with pET-20b(+)-based expression plasmids. Omp9 cells' advantage is the absence of bacterial porins that could be co-produced, co-refolded and co-purified with AtVDACs (Mertins, Psakis et al. 2012). In the case of mKlp2C-Ter, *E. coli* BL21 (DE3) cells were used for overproduction.

50 μ L *E. coli* DH5 α or 200 μ L chemically competent (see section 2.3.2) *E. coli* Omp9 or BL21 (DE3) cells were thawed on ice. Following the addition of 1 to 5 μ L of desired plasmid (50 ng), cells were incubated for 30 minutes on ice. Then, they were heat shocked at 42 °C for 45 seconds and placed back immediately on ice for 2 minutes. After adding 800 to 950 μ L of LB-medium the solution was incubated for 1 hour at 37 °C with shaking at 180 rpm. Cells were subsequently centrifuged for 3 minutes at 3000 rpm. 800 μ L of the supernatant were discarded and cell pellet was resuspended in the remaining volume. Cells were then plated onto prepared LB-agar plates containing ampicillin (concentration = 200 μ g/mL) and incubated overnight at 37 °C.

2.3.4. Heterologous gene expression in *E. coli*

2.3.4.1. IPTG induction

40 mL of LB containing ampicillin (200 μ g/ mL) were inoculated with cells harbouring the gene of interest and left overnight at 37 °C shaking at 180 rpm. The following day, 2% (v/v) of the overnight cultures were used to inoculate 5 flasks of 400 mL LB, supplemented with ampicillin (200 μ g/ mL). When OD_{600nm} was between 0.4 and 0.6, IPTG was added to a final concentration of 1 mM and cells were incubated for 4 hours at 37 °C with shaking (180 rpm). Cultures were then centrifuged 10 minutes at 6,500 rpm (7,800g) (Avanti J-26 XPI from Beckmann Coulter®). Supernatant was either collected

(in the case of mKlp2C-Ter), or discarded, and pellets (in the case of AtVDACs only) were resuspended in a total of 20 to 45 mL of resuspension buffer RE (50 mM Tris-HCl (pH 8.0), 100 mM NaCl, 0.2 mM PMSF) and kept overnight at 4 °C.

2.3.4.2. **Auto-induction**

40 mL of LB containing ampicillin (200 µg/ mL) were inoculated with cells harbouring the gene of interest and left overnight at 37 °C shaking at 180 rpm. The following day, 2 % (v/v) of the overnight cultures were used to inoculate 5 flasks of 400 mL LB (Auto-Induction), supplemented with ampicillin (200 µg/ mL), 4 mL 60 % (v/v) Glycerol, 2 mL 10 % (w/v) Glucose and 10 mL 8% (w/v) Lactose. Cells were then incubated for 5 to 6 hours at 37°C with shaking (180 rpm), or overnight at 30°C. Cultures were then centrifuged 10 minutes at 6500 rpm (7800g) (Avanti J-26 XPI from Beckmann Coulter®). Supernatant was discarded, and pellets were resuspended in a total of 20 to 45 mL of resuspension buffer RE (50 mM Tris-HCl (pH 8.0), 100 mM NaCl, 0.2 mM PMSF) and kept overnight at 4°C.

2.4. Molecular Biology methods

2.4.1. PCR amplification

The different AtVDAC genes were amplified by PCR from plasmid templates harbouring GFP-tagged AtVDACs (kindly provided by Prof. T.Kusano from Tohoku University, Japan). The genes were amplified with primers designed to add EcoRI/NdeI restriction sites to facilitate sub-cloning into plasmid pET-20b(+). Primers used are detailed in Table 2.3 (section 2.2) and the components are listed in Table 2.5 (below).

Table 2.5 PCR components. Volumes and concentrations are indicated.

Components	Volumes	Final concentration
Polymerase buffer 5X	10 μ L	1X
dNTPs	1 μ L	200 μ M
DNA template	1 μ L	<250 ng*
Forward primer	2.5 μ L	0.5 μ M
Reverse primer	2.5 μ L	0.5 μ M
Polymerase (Phu®)	0.5 μ L	1U/50 μ L
Deionized water	Adjust to 50 μ L	0.25 μ L

*Typically, 1/10, 1/100 and 1/1000 dilutions of the DNA sample are tested

Components were mixed together according to the recipe in Table 2.5, and the mixture was left in a thermomixer. The parameters used for the amplification by PCR are shown in Figure 2.

Initial step	98°C for 30 seconds	
Denaturation step	98°C for 10 seconds	← 35X
Annealing step	65°C for 30 seconds	
Elongation step	72°C for 30 seconds	
Final extension	72°C for 10 minutes	
Final step	4° forever	

Figure 2.2 PCR parameters. Scheme representing the parameters used for the amplification of the *AtVDAC* genes by PCR.

The correct amplification of the different fragments was analysed by Agarose gel electrophoresis (see 2.4.6). Once amplified, each fragment was digested with EcoRI/NdeI (Table 2.3).

2.4.1.1. Colony PCR

Colony PCR were used to monitor the production of pET-20b(+)*AtVDAC1* plasmid from colonies picked up from an LB(+amp) plate. This test would serve as a pre-screen for the expression of *AtVDAC1* gene from *E.coli* Omp9 cells.

Typically, a single colony would be picked up from an LB plate (+ampicillin at 200 µg/mL) and resuspended in 10 µL of dH₂O. This would serve as the DNA template for the PCR reaction, as 1 µL would be used in the PCR mixture (see Table 2.5), and the remaining volume would be used as a primary inoculum for the cell cultures.

2.4.2. Restriction endonuclease digests

Prior to insert and vector ligations, DNA fragments (PCR amplified *AtVDAC* genes (section 2.4.1) and pET-20b(+)) were digested with EcoRI and NdeI (Table 2.6). Reactions were incubated at 37 °C overnight or for 2 to 4 hours according to the manufacturer's instructions.

Table 2.6 AtVDAC restriction digest components. Volumes and concentrations are indicated.

Components	Standard overnight digest	Quick control digest
Buffer 10X Cutsmart®	5 µL	1 µL
DNA	20 to 40 µL	4 µL
Restriction endonuclease 1	1.25 µL	0.25 µL
Restriction endonuclease 2	1.25 µL	0.25 µL
Deionized water	Adjust to 50 µL	Adjust to 10 µL

Additionally, restriction endonuclease digests were used for the identification of colonies transformed with the desired plasmid construct are listed in table 2.5 (for more information on the mutants, see section 2.4.5).

Table 2.7 Restriction endonucleases and their application.

Enzyme	Application	Supplier
XmnI	E256Q mutant	New England Biolabs ®
Hpy99I	E256L and K260S mutant	ThermoFisher ®
HpaI	D258N mutant	New England Biolabs ®
BanII	D180S mutant	New England Biolabs ®
HindII	D177N mutant	New England Biolabs ®
EcoRI	Cloning of AtVDACs	New England Biolabs ®
NdeI	Cloning of AtVDACs	New England Biolabs ®

2.4.3. Agarose Gel purification of digested pET-20b(+) and *AtVDAC* genes

Digested fragments (vector pET-20b(+) and insert *AtVDAC* genes) were analysed on 1.5% (w/v) agarose gel (in 900 mM Tris base, 900 mM Boric acid, 20 mM EDTA, 12.5 mM NaOH). They were then excised from the gel and purified using the QIAGEN gel purification Kit®, according to the manufacturer's instructions.

2.4.4. Ligation

The ligation is the process of covalent linking between two DNA fragments, catalysed by the T4 DNA ligase, using cohesive binding. An example is given in Figure 2.2, where the palindromic regions of the enzyme *EcoRI* can be seen close to each other. This specific pattern is typical of restriction endonucleases and can allow (when using two different enzymes) a directed insertion of an insert into its respective vector.

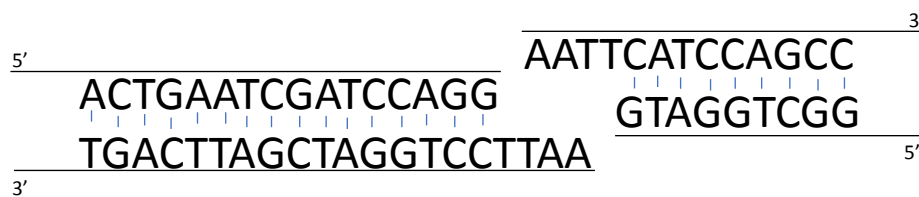


Figure 2.3 Example of cohesive joining of fragments with sticky ends. Two fragments of double stranded DNA harbouring cohesive nucleotides. The palindromic site is typical of the restriction enzyme *EcoRI*.

The reaction is performed with various Insert/vector molar ratios ranging from 1:1 to 9:1 depending on the reagent concentration, with a minimum of 50ng of vector pET-20b(+). In the case of *AtVDACs* (on average), for a 1:1 molar ratio, the N amount of insert needed (for 50 ng of vector) using a size ratio R is given in equation 2.1.

$$N = \frac{\text{amount of vector}}{\text{size ratio}} = \frac{50}{4.1} = 12.5 \text{ ng} \text{ with size ratio } R = \frac{\text{vector size (bp)}}{\text{insert size (bp)}} = \frac{3.7}{0.9} = 4.1$$

Equation 2.1 Calculation of the amount of insert. The N amount of insert is calculated using the amount of vector and size ratio R, defined the by ratio between the sizes (in bp or kbp) of the vector and insert.

Depending on the molar ratio and the concentration of the different DNA preparations, volumes of insert and vector are mixed together with a T4 ligase buffer (to a 1X concentration), 1 Unit of T4 DNA ligase, and water to a total of (10-20 μ L). The ligation mix is then incubated for 16 hrs at 16°C and then used to transform competent *E. coli* DH5a cells.

2.4.5. PCR based site directed mutagenesis

Mutagenesis was carried out using the Q5® Site-Directed Mutagenesis Kit from New England Biolabs (NEB®), according to the manufacturer's instructions. Briefly, pET-20b(+) harbouring the *AtVDAC1* gene was used as a PCR template. The *AtVDAC1* gene was amplified with back to back primers (Figure 2.4) containing single to triple point mutations in their sequences (Table 2.6). Successful mutations allowed the desired codon alteration and the incorporation of unique restriction endonuclease sites, facilitating screening of positive clones. After re-ligation, the newly amplified plasmid would contain the mutation of interest.

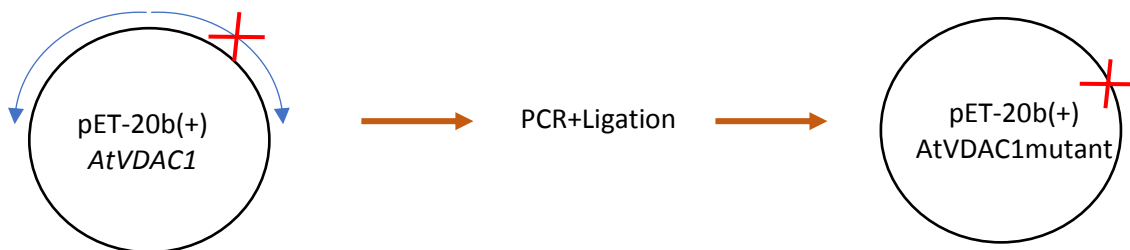


Figure 2.4 PCR site directed mutagenesis basic principle. Schematic representation of the methodology used in the PCR driven mutagenesis. The native plasmid pET-20b(+) *AtVDAC1* (left) is amplified by PCR using back to back primers (in blue). After ligation the newly amplified plasmid (right) contains the mutation of interest (red cross).

In the case of T156C mutant primers, no appropriate unique restriction enzyme binding site could be engineered into the *AtVDAC1* gene. Consequently, its identity was confirmed by automated DNA sequencing performed on a few colonies. For all other mutants, only the positive colonies identified by restriction digests would be sent for DNA sequencing (Eurofins®). Results of the DNA sequencing are provided in Appendix 9.1.

Table 2.8 Mutagenic primers and enzymes used to control nucleotide replacements. Mutated nucleotides inserted via the primer are highlighted in red.

Mutation	Forward primer	Reverse primer	Enzyme
E256Q	CAATCTGGACAAGTTGACACAAG	TGAAGAATGACTTCGGTTTCCACTC	XmnI
E256L	CAATCTCTGGACTCGTCGACACAAAG	TGAAGAATGACTTGGGTTTCCACTC	Hpy99I
D258N	CTGGAAGTTAACACAAAGTCAA	AGATTGTGAAGAATGACTTGGGTT	HpaI
K260S	AAGTCGACACATCGTCGATTGACAAGA	TCCAGAGATTGTGAAGAATGACTTGGG	Hpy99I
T156C	CTGGAAATTTCTGCAAGATCAATGC	ACTTGGTGTCAAATGAAACATCAGTAC	none
D180S	CGACAAGGGCTCTCTATTGAATGCA	TTCACAGTAAGGGAGGCAATTAAGTCC	HgiIII
D177N	TCCCTTACTGTCAACAACAAGGGCGAT CTA	GGCAATTAAGTCCTCCTTGGTGAAGC	HincII

2.4.6. Agarose gel electrophoresis

Agarose gels were prepared in TBE buffer (see section 2.1). Typically, 0.4g of agarose would be mixed into 40mL of TBE buffer and warmed in the microwave. Once completely dissolved the agarose solution was allowed to cool down briefly before adding SybRsafe reagent (Invitrogen ®) at 1/10000 ratio. Once mixed properly, the solution was poured into a gel casting device and left to set for 30 to 40 minutes. Once set, the gel was moved into an electrophoresis chamber filled with TBE buffer. Samples and a 1 kb DNA size ladder from NEB ® would then be loaded into predefined wells and run at 200V for 30min.

2.5. Biochemical Methods

2.5.1. Bacterial lysis by sonication

Resuspended cell pellets (in 50 mM Tris-HCl (pH 8.0), 100 mM NaCl, 0.2 mM PMSF) were sonicated with a Vibra Cell™ sonicator. The sonicator will mechanically disrupt cell membranes and release cellular components. The parameters were as follows: 5 seconds of pulse followed by 10 seconds pause to dissipate heat generated by the sonication process, for 10 minutes. The procedure was repeated twice.

2.5.2. Washing of inclusion bodies (VDACs only)

Sonicated samples were then washed with different buffers to reduce contaminant levels, prior to IB solubilisation and subsequently concentrate the desired protein in those fractions (Figure 2.5). Samples were first resuspended in TEN-triton buffer (50 mM Tris-HCl (pH 8), 100 mM NaCl, 10 mM EDTA, 2% (v/v) Triton X-100) and centrifuged at 33500g for 20min. The process was repeated 4 times before 3 washes with TN buffer (50 mM Tris-HCl (pH 8), 100 mM NaCl) followed. Finally, samples were resuspended in 10-20 mL 50 mM Tris-HCl (pH 8), 100 mM NaCl and aliquoted in Eppendorf cups. The aliquots were directly frozen in liquid nitrogen and stored at -20 °C until further use.

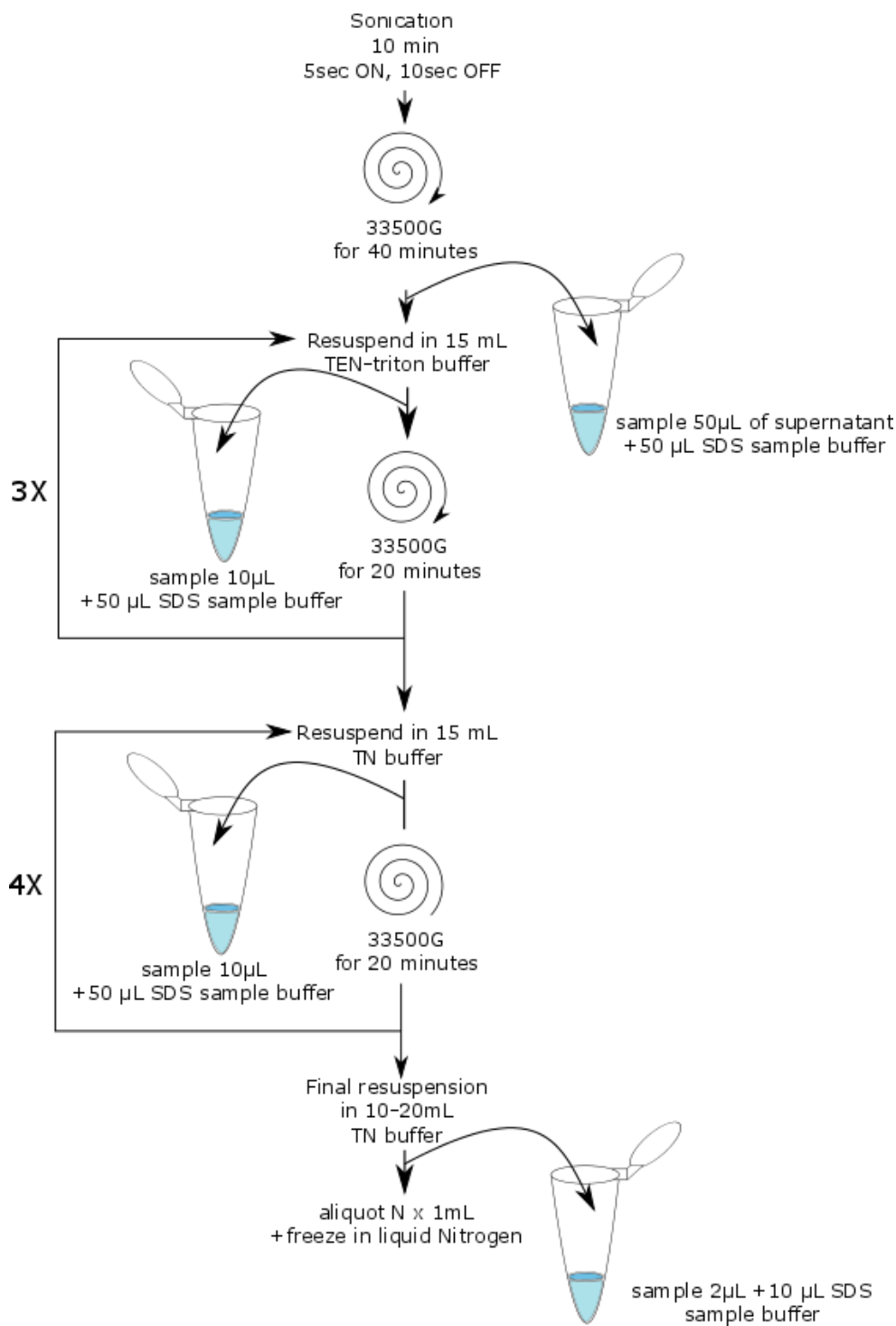


Figure 2.5 Washing of inclusions bodies. Flow diagram illustrating the experimental procedures used for the washes of AtVDAC-containing inclusion bodies. Steps in which samples were taken for further analyses are indicated.

2.5.3. *In vitro* refolding (VDACs only)

The *in vitro* refolding step was carried out based on an approved method (Yamaguchi and Miyazaki 2014). Inclusion bodies produced in the previous steps were mixed with denaturation buffer (25mM $\text{NaH}_2\text{PO}_4/\text{Na}_2\text{HPO}_4$ (pH 7.0), 100 mM NaCl, 1 mM EDTA, 10 mM DTT, 6 M Guanidinium chloride) to a final concentration of 10 mg/mL in a total volume of 5 mL (50 mg total). Samples were then heated for 10 minutes at 60 °C and subsequently centrifuged for 10 minutes at 14000 rpm. The supernatant was then added drop wise to 45 mL of refolding buffer 1 (RF1; 25mM $\text{NaH}_2\text{PO}_4/\text{Na}_2\text{HPO}_4$ (pH 7.0), 100 mM NaCl, 1 mM EDTA, 10% (v/v) Glycerol, 2.29% (v/v) LDAO) and left stirring overnight at 4 °C. The following day the solution was centrifuged at 5,700 rpm (6,400g) for 10 minutes and the supernatant was added again drop wise to 450 mL of refolding buffer 2 (RF2; 25 mM $\text{NaH}_2\text{PO}_4/\text{Na}_2\text{HPO}_4$ (pH 7.0), 100 mM NaCl, 1 mM EDTA, 10 % (v/v) Glycerol, 0.12 % (v/v) LDAO) and left stirring overnight at 4 °C. The next day the solution was filter-sterilized using Corning® bottle-top vacuum filters and subjected to Ion Exchange Chromatography (IEC).

2.5.3.1. Small scale refolding screen

Since AtVDAC1 proteins can putatively exhibit different biochemistry and stability regarding the additives used, their refolding efficiency may vary. A refolding screen was carried out to test different types of salts and sugars known to contribute to the refolding of proteins (Alibolandi and Mirzahoseini 2011). Solubility was expressed by the percentage of successfully refolded AtVDAC relative to the unfolded protein (Figure 2.6) in the refolding buffer tested. Different samples are collected during the dilution process and analysed on SDS PAGE 10 % (v/v). The amount of AtVDAC protein is then estimated for each lane using ImageJ ® software and a ratio is calculated between the supernatant fractions and their corresponding resuspended pellets. Additional samples are collected beforehand to assess the initial amounts and monitor potential issues during the process. Thus, they can be used to normalize data.

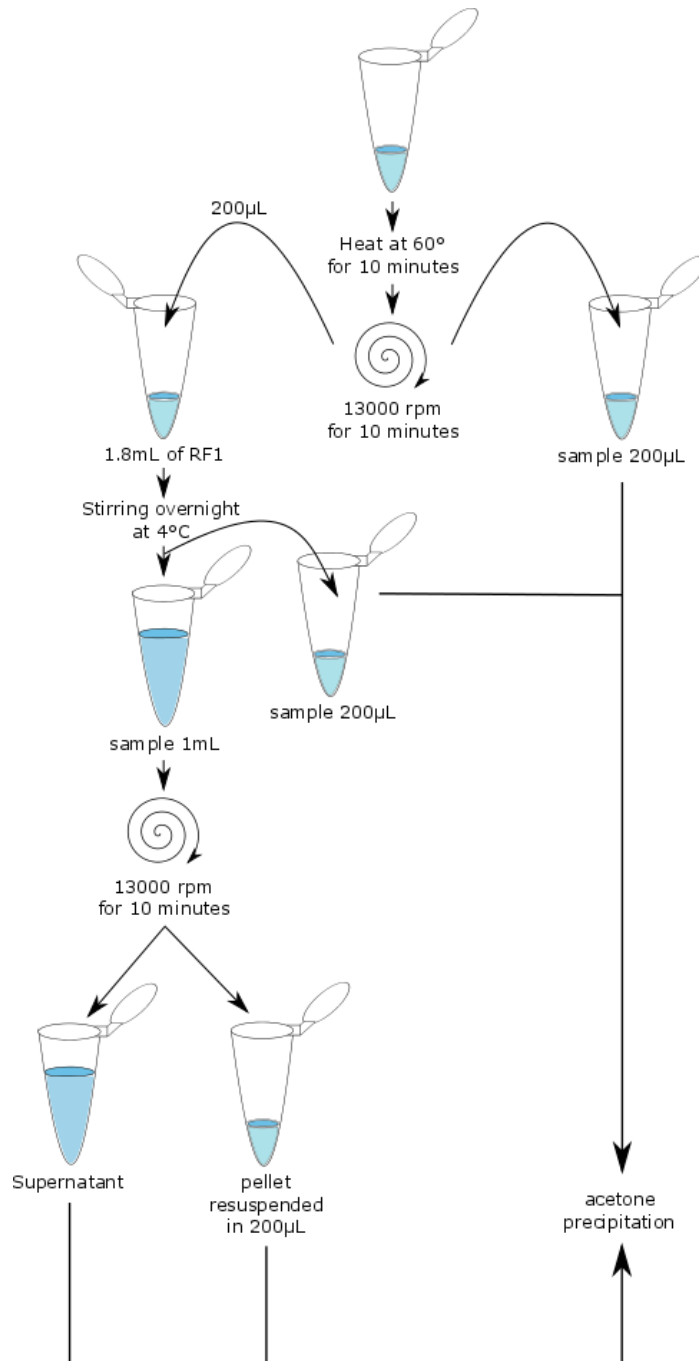


Figure 2.6 Refolding screen (RF1). Flow diagram illustrating the experimental procedure used in a small-scale refolding by sequential dilution of the AtVDAC protein. Sample is first heated at 60 °C for 10 minutes, centrifuged and resuspended in refolding buffer 1 (RF1) with a 1 to 10 dilution. After stirring overnight at 4 °C, the process is repeated with the refolding buffer 2 (RF2). The refolded protein is now solubilized in the supernatant. Samples were taken at each step to assess the impact of use or refolding aids on the protein integrity and refolding yield.

2.5.4. Ion exchange chromatography

2.5.4.1. AtVDAC proteins

Filtered refolded protein was applied overnight at 4 °C to a strong cation exchanger (Fractogel® EMD SO_3^- (M) from Merck Millipore®, or HiTrap SP XL 1 mL and 5 mL from Life Sciences®), using a peristaltic pump. The following day the protein of interest was eluted with an increasing concentration of NaCl (from 1 mM to 1 M, see Table 2.1), using the AKTA Prime® device. The solid supports used, possess different structural and chemical properties. More precisely, the Fractogel® EMD SO_3^- (M) contains a matrix of long methacrylate chains carrying the functional ligand, offering a greater surface of binding and an increased binding capacity (Figure 2.7).

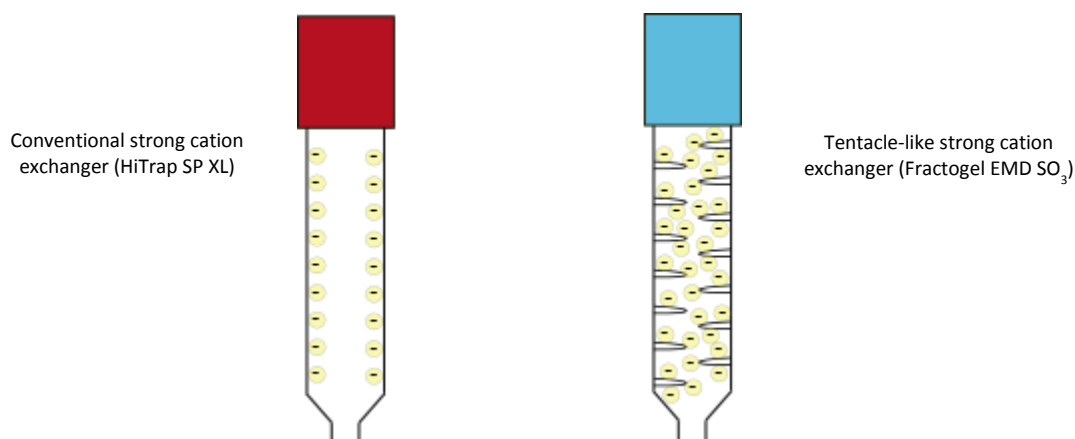


Figure 2.7 Comparison of commercial strong cation exchangers. Schematic representation of a conventional cation exchanger (HiTrap SP XL from Life Sciences®, left) vs a “tentacle-like” cation exchanger (Fractogel® EMD SO_3^- (M) from Merck Millipore®, with its increased binding hence binding capacity.

2.5.4.2. mKlp2 C-terminal tail (mKlp2C-Ter)

Protein was applied overnight at 4 °C to a strong Ni-Nta matrix (Protino 5 mL HisTrap from Merck Millipore®) via a peristaltic pump. The following day the protein of interest was eluted with 500 mM Imidazole (25 mM Tris-HCl (pH 7.0), 100 mM NaCl, 3 % (w/v) Glycerol, 500 mM Imidazole), using the AKTA Prime® device.

2.5.5. Desalting and protein concentrating

Fractions containing the protein of interest were pooled together and applied to a PD-10 desalting column (Life Sciences) to remove excess NaCl, EDTA, or imidazole. Samples were eluted in 3.5 mL of an elution buffer suitable for size exclusion chromatography (25 mM NaH₂PO₄/Na₂HPO₄ (pH 7.0), 100 mM NaCl, 1 mM EDTA, 1 mM DTT, 10% (w/v) Glycerol, 0.115% (v/v) LDAO for VDACs, or 25 mM Tris-HCl (pH 7.0), 100 mM NaCl, 3% (w/v) Glycerol for mKlp2C-Ter). Finally, the sample was concentrated to final volume of 500 µL using 30K cut-off AMICON Ultra-15 Centrifugal Filter Units®.

2.5.6. Size exclusion chromatography

Purified and concentrated samples (maximum 500 µl) were applied to a prepacked Superdex 75 10/300 GL (Life Sciences®) or Superose 6 10/300 GL (Life Sciences®) at the top of the column. Sample was then pushed through the column by the elution buffer (25 mM NaH₂PO₄/Na₂HPO₄ (pH 7.0), 100 mM NaCl, 1 mM EDTA, 1 mM DTT, 10% (w/v) Glycerol, 0.12% (v/v) LDAO for VDACs, or 25 mM Tris-HCl (pH 7.0), 100 mM NaCl, 3% (w/v) Glycerol for mKlp2C-Ter), using the AKTA Prime® device. Proteins in the sample were then separated depending on their size, bigger proteins coming first and lower molecular weight proteins coming last.

2.5.6.1. Size exclusion column calibration on Superdex 75

A mixture of purified proteins of known molecular weight (IgG, BSA, Alpha-amylase, Lysozyme and Ribonuclease A, 0.5 mg each) was applied to the Superdex 75 10/300 GL (Life Sciences®). The corresponding elution profile (Figure 2.8A) was used to build a standard curve (Figure 2.8B), allowing the extrapolation of the molecular weight of a protein depending on the volume at which the aforementioned protein is eluted. Separation of standards was attempted in both size exclusion buffers (25 mM NaH₂PO₄/ Na₂HPO₄ (pH 7.0), 100 mM NaCl, 1 mM EDTA, 1 mM DTT, 10 % (w/v) Glycerol, 0.12 % (v/v) LDAO for AtVDACs and 25 mM Tris-HCl (pH 7.0), 100 mM NaCl, 3 % (w/v) Glycerol for mKlp2C-Ter). As no noticeable difference in the separation profiles of the standards was observed when using different buffers, only the AtVDAC buffer profile is shown for clarity (Figure 2.8).

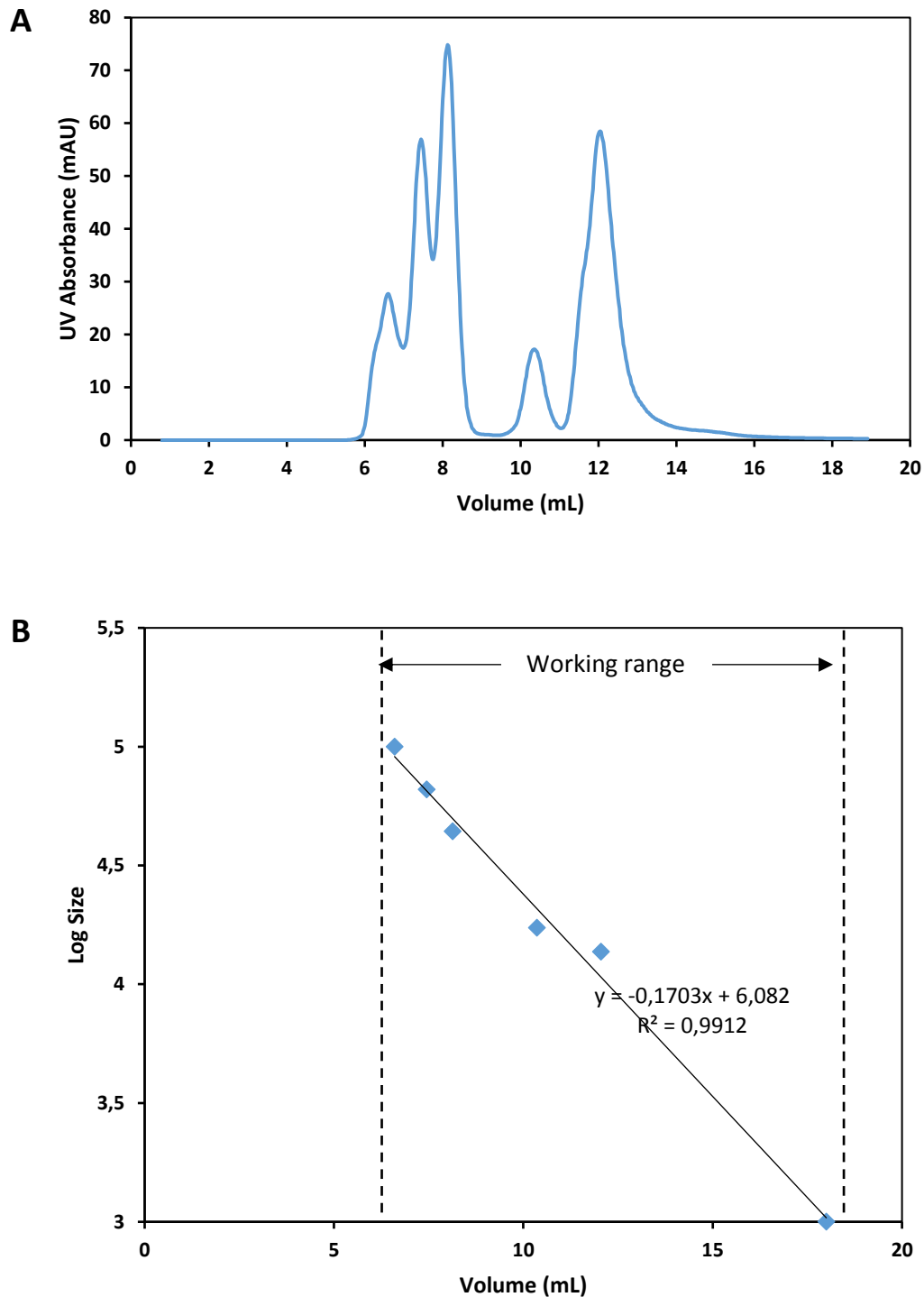


Figure 2.8 Superdex75 calibration. (A). Elution profile showing the absorbance (in mAU) at 280 nm wavelength versus the volume (mL) of the samples collected. A mixture of purified proteins of known molecular weight (IgG, BSA, Alpha-amylase, Lysozyme and Ribonuclease A, 0.5 mg each) was applied. (B). Their respective molecular weights were plotted against their peak elution volume (blue line). A trend line (black) was then established and the corresponding formula was used to calculate unknown molecular weights.

2.5.6.2. Size exclusion column calibration on Superose 6

A mixture of purified proteins of known molecular weight (IgG, BSA, Alpha-amylase, Lysozyme and Ribonuclease A, 0.5 mg each) was applied to the Superose 6 10/300 GL (Life Sciences®). The corresponding elution profile (Figure 2.9A) was used to build a standard curve (Figure 2.9B), allowing the extrapolation of the molecular weight of a protein depending on the volume at which the aforementioned protein is eluted. Again, both size exclusion buffer for VDACS (NaH₂PO₄/ Na₂HPO₄ (pH 7.0) 25 mM, NaCl 1 M, EDTA 1 mM, DTT 1 mM, Glycerol 10 % (w/v), LDAO (Stock:30 %) 0.12 % (v/v)) and mKlp2C-Ter (TrisHCl (pH 7.0) 25 mM, NaCl 100 M, Glycerol 3 % (w/v)) were used but did not lead to different pattern. Only one profile is shown in Figure 2.9, with the VDACS buffer.

The column maintenance was performed on a run to run basis, and a cleaning in place (CIP) was performed on a regular basis, depending on the purification yields obtained. Calibration was reassessed over time using the same procedure as described above. No noticeable difference was found after two years.

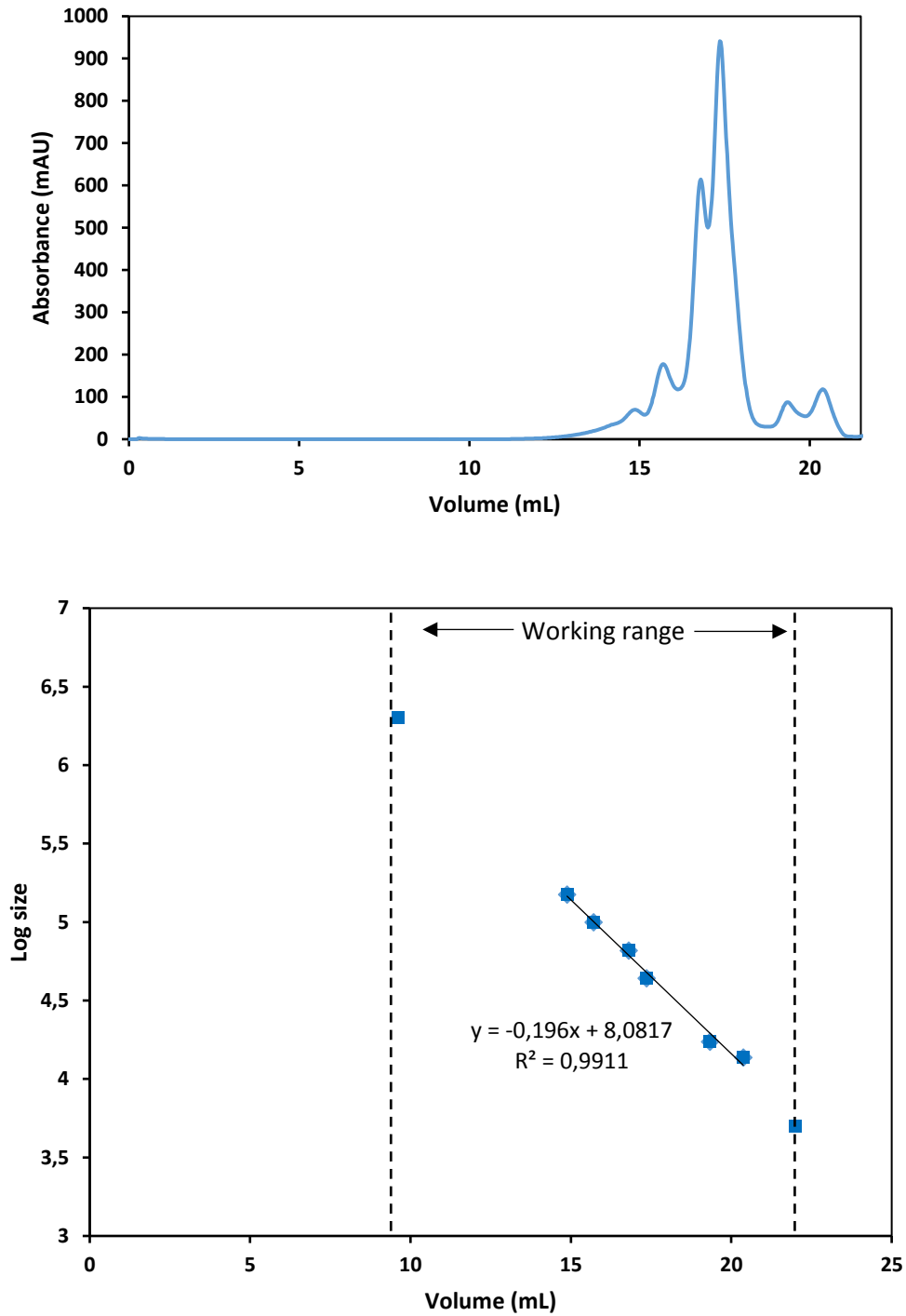


Figure 2.9 Superose 6 calibration. (A). Elution profile showing the absorbance (mAU) at 280nm wavelength depending on the Volume (mL). A mixture of purified proteins of known molecular weight (IgG, BSA, Alpha-amylase, Lysozyme and Ribonuclease A, 0.5 mg each) was applied. (B). Their respective molecular weights were plotted against their peak elution volume (blue line). A trend line (black) was then established and the corresponding formula was used to calculate unknown molecular weight.

2.5.7. Determination of protein concentration

2.5.7.1. BCA assay

The BCA assay is a colorimetric assay for the determination of protein concentrations using the capacity of reduced Copper to form tetradentate complexes with peptide bonds. The bicinchonic acid will form a complex with reduced copper, and further interact with aromatic amino acids, cysteines and cystines, exhibiting a maximal absorption wavelength at 562 nm. The absorbance recorded is proportional to the amount of protein present in the sample.

50 μ L of each sample were tested using the BCA assay Kit from Merck Millipore® following the manufacturer's instructions. Some components such as reducing agent DTT (dithiothreitol) EDTA (Ethylenediaminetetraacetic acid) or Guanidinium can interfere with the process. In this case samples were acetone precipitated (section 2.5.8) and resuspended in TN buffer (50 mM Tris-HCl (pH 8.0), 100 mM NaCl) prior to the assay.

2.5.8. Acetone precipitation

Acetone precipitation allowed the selective precipitation of proteins and the removal of buffer components that could potentially interfere with downstream applications.

200 μ L of each protein sample were mixed with 1 mL acetone and incubated for 1 hour at -20 °C. Samples were then centrifuged for 3 minutes at 13000 rpm and 4 °C. Supernatants were discarded and protein pellets were washed with 50 μ L ice cold dH₂O and then centrifuged for 3 minutes at 13,000 rpm and 4 °C. Supernatants were discarded and protein pellets were washed with 50 μ L of ice cold ethanol (100%). Washed samples were then centrifuged for 3 minutes at 13000 rpm and 4 °C, supernatants were discarded, and protein pellets were air-dried. Protein pellets were finally resuspended in 50 μ L TN buffer (50 mM Tris-HCl (pH 8.0), 100 mM NaCl). Samples were subsequently analysed by 10% (v/v) SDS-PAGE.

2.5.9. Lipid reconstitution

E. coli lipids (50 mg/mL in chloroform) were added in a molar ratio of 2000:1 (lipid to Membrane Protein) to the solubilized membrane protein (AtVDACs) and incubated at 30 °C for an hour (STEP A). In parallel (STEP B), 750 mg biobeads from Biorad® were washed in 10 mL of 100 % (v/v) methanol. After letting the biobeads settle down, the supernatant was discarded. This washing step was repeated three times with 10 mL of distilled water. Finally, the biobeads were washed twice in the buffer used for the detergent solution (SEC buffer without detergent; 50 mM NaH₂PO₄/ Na₂HPO₄ (pH 7.0), 100 mM NaCl, 10 % (v/v) Glycerol). Biobeads were then pre-saturated with lipids: 100 µl of the lipid suspension were added to 1 mL of washed biobeads in 10 mL of detergent buffer (SEC buffer without detergent, 50 mM NaH₂PO₄/ Na₂HPO₄ (pH 7.0), 100 mM NaCl, 10 % (v/v) Glycerol) and incubated for 30 min at room temperature.

Once both prepared (STEP C), lipid-presaturated biobeads (step B) were added in a ratio biobeads:detergent of 100:1 (w/w) to a vial containing the lipids and the refolded protein solution (step A). The detergent was let to adsorb to the biobeads by incubation overnight on a shaker at 30°C.

Next morning, the vial was removed from the shaker and biobeads were left to settle down. The supernatant was then transferred into a new vial. Then a new incubation step was initiated with a second aliquot of lipid-presaturated biobeads for 6 h at 30°C on a shaker. Following incubation, the supernatant containing the proteoliposomes was harvested. Pellet was resuspended in dialysis Buffer without detergent (25 mM NaH₂PO₄/Na₂HPO₄ (pH 7.0), 50 mM NaCl, 1 mM EDTA, 1 mM DTT, 10% (w/v) Glycerol), the proteoliposomes can be stored at 4°C until or frozen in liquid nitrogen until further analysis. An example is given in Appendix 9.2 for AtVDAC1, with calculations.

2.5.10. SDS PAGE electrophoresis

2.5.10.1. SDS-PAGE gel casting

SDS PAGE gels were either purchased from Invitrogen® or made in house. Precast gels were treated according to manufacturer's instruction. Home-made gels recipe is detailed in Table 2.9.

Table 2.9 Lower gel (10%, resolving) recipe. Components (left) and their corresponding volumes when making two resolving gels (middle) or one (right) based on Laemmli buffer gel composition (He 2011).

Solution	2 Gels (mL)	1 Gel (mL)
H ₂ O	2.250	1.125
Acrylamide/Bisacrylamide 40% (29:1) (v/v)	3.125	1.560
Tris-HCl 1.5M (pH 8.5)	4.700	2.350
SDS 10% (w/v)	0.125	0.063
Sucrose 50% (w/v)	2.000	1.000
Ammonium Persulfate (APS) 10% (w/v)	0.156	0.078
TEMED	0.004	0.002

Ammonium Persulfate and TEMED were added last since they are responsible for the catalysis of the acrylamide polymerization. Immediately after adding TEMED, the solution was pipetted between glass plates in a caster-device, filling at least two third of the container. Then pure ethanol or pure isopropanol was layered (1 to 2 mL) on top of the resolving gel to insulate the gel from air, even the surface of the resolving gel and remove any bubbles.

After an hour, ethanol was poured away, and the top of the gel was gently dried with Whattman paper. The stacking part or stacking part of the gel was then prepared as described in Table 2.10.

Table 2.10 Upper gel (4%, stacking) recipe. Components (left) and their corresponding volumes when making two stacking gels (middle) or one (right).

Solution	2 Gels (mL)	1 Gel (mL)
H ₂ O	3.000	1.500
Acrylamide/Bisacrylamide 40% (29:1) (v/v)	0.625	0.312
Tris-HCl 1M (pH 6.8)	2.100	1.050
SDS 10% (w/v)	0.063	0.031
Ammonium Persulfate (APS) 10% (w/v)	0.250	0.125
TEMED	0.0025	0.00125

“Homemade” gels were stored for up to one week in the fridge (2 to 8°C), wrapped in paper towels soaked in 1x SDS-PAGE running buffer (recipe) and sealed in cling film.

2.5.10.2. SDS-PAGE gel electrophoresis

Protein samples were prepared for loading with SDS sample buffer (0.25 M Tris-HCl (pH 6.8), 0.5 M DTT, 10 % (w/v) SDS, 50 % (v/v) Glycerol, 0.5 % (w/v) Bromophenol blue) with the corresponding dilution and heated between 60-80°C for 10 minutes. In parallel, gel assembly was put into tank, and filled with 1xSDS run buffer (25 mM Tris, 200 mM Glycine, 0.1 % (w/v) SDS), ensuring wells were covered adequately. Combs were removed, and samples were loaded into the wells (each could accommodate a maximum volume of 25 µL). Run was performed at 200 V (around 110 mA) for 60-85 minutes.

Once the run finished, gels were gently removed from their cassettes and placed in Coomassie Blue staining solution (50 % (v/v) Methanol, 10 % (v/v) Glacial Acetic Acid, 0.25 % (w/v) Coomassie R-

250), shaking for one hour. Gel was then rinsed with water three times to remove high excess of staining solution, and finally placed in destaining solution (50 % (v/v) Methanol, 10 % (v/v) Glacial Acetic Acid) for 30 minutes. Finally, gels were photographed and left in deionised water overnight. Gels were photographed the next day.

Solutions and Reagents were routinely prepared in the laboratory, ensuring a constant availability of gels ready-to-use. For preparation of SDS-PAGE gel and buffer components, the following recipes were used (Table 2.11):

Table 2.11 SDS PAGE buffer recipes. Typical day-to-day recipes of main solutions used in SDS PAGE.

Solution	Component	Final Weight/Volume
10x SDS Run Buffer	SDS	10g
	Tris Base	30g
	Glycine	144g
	H ₂ O	1L
SDS-PAGE Coomassie Staining Solution	Coomassie R-250	1.25g
	Methanol	225ml
	H ₂ O	225ml
	Glacial Acetic Acid	50ml
SDS-PAGE	Methanol 100% (v/v)	500ml
Destaining Solution	Glacial Acetic Acid 100% (v/v)	100ml
	H ₂ O	400ml

2.5.11. Western Blotting

Western Blotting is multi-step process. Routinely, samples were loaded in duplicates on SDS-PAGE gels, allowing for one side of the gel to be stained with Coomassie Blue or by silver staining, and the other to be probed by Western Blotting. Following completion of electrophoresis, gels were removed from their casting plates, and soaked in Blot-transfer buffer (1X blotting buffer from Novex® in 20 % (v/v) Methanol) for 5 minutes.

In parallel, PVDF (Life sciences) membranes were soaked in 100% (v/v) Methanol for ten to thirty minutes to reduce its hydrophobicity and activate its protein binding capability. Whatman filter papers and blotting pads of the XCell SureLock Mini-Cell blot module, were placed in a tray containing Blot-transfer buffer for 30 minutes. Following the activation of the PVDF membrane by Methanol, the membrane was briefly soaked in Blot-transfer buffer for 2 minutes.

For assembling the blot sandwich (Figure 2.11), two to three pre-soaked blotting pads, as well as two filter papers, were placed onto the cathode (-) core of the module. Then, the Blot-transfer buffer-pre-soaked gel was gently placed on top, followed by the Blot-transfer buffer-pre-soaked PVDF membrane, ensuring no air bubbles were trapped between them. Then two more filter papers as well as two blotting pads were placed on top of the setup, enough to rise over 0.5cm rim of the cathode core. Finally, the anode core was placed on top of the pads, securely holding the two halves of the blot module (Figure 2.11). Once assembled, the system was transferred into a tank unit. Blot module was then filled with Blot-transfer buffer until the gel/membrane sandwich was fully covered in buffer. Any potentially remaining air bubbles were again removed, by firmly pressing the anode and cathode against each other. Outer chamber was then filled with cold deionized water, to help dissipating heat during the run. Lid was then placed on the tank and run was performed at 35 V, 200 mA for two hours.

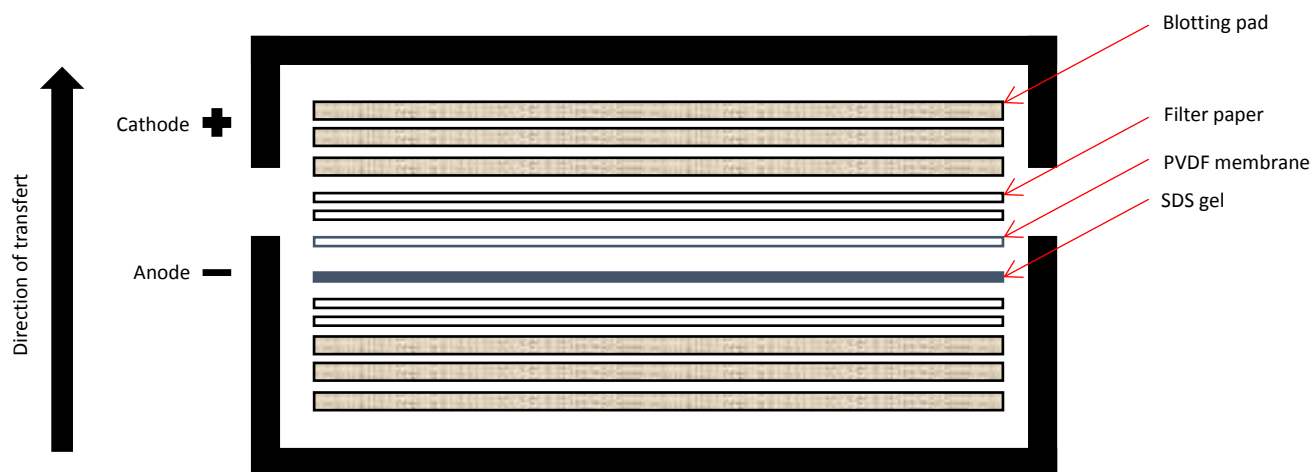


Figure 2.10 Western Blot sandwich Assembly. Gel (in blue) is sandwiched against a PVDF membrane (blue open rectangle), between two filters and three blotting pads on each side.

At the end of the run, the sandwich was disassembled and the PVDF membrane was placed in Blocking buffer (5 % (w/v) Western blot Blocking reagent from Novex® in 10 mM Tris-HCl (pH 7.5), 150 mM NaCl, 0.05 % (v/v) Tween 20) overnight at 4 °C.

The next morning, the membrane was washed twice for 10 minutes in TBS-Tween/Triton buffer at room temperature (15-25 °C). This step was then repeated with TBS buffer. Once washed the membrane was incubated with either rabbit anti-AtVDAC1 (Agrisera®), or penta-His-HRP (Qiagen®, for mKlp2C-Ter) antibodies in blocking buffer at room temperature (15-25 °C) for 1 hour at specific dilutions (Table 2.12).

Table 2.12 Antibodies. Antibodies used for Western Blotting and their respective dilution factor.

Solution	Final dilution	Supplier	Function	Protein
Rabbit polyclonal	1:1000	Agrisera Antibodies	Primary antibody	AtVDAC1
Anti-Rabbit IgG	1:1000	Agrisera Antibodies	Secondary antibody	AtVDAC1
Penta-His-HRP	1:5000	Qiagen	Conjugated antibody	mKlp2C-Ter

After incubation with a primary antibody, the membrane was again washed twice for 10 minutes in TBS-Tween/Triton buffer at room temperature (15-25 °C), followed by one additional wash in TBS buffer at room temperature (15-25 °C). The membrane was then either a) soaked in chemi-luminescence substrate (if using anti-His conjugated antibody) or b) incubated with a secondary antibody (if using the rabbit-AtVDAC1 antibody) as reported in Table 2.12.

The incubation with a secondary antibody (mouse anti-rabbit IgG-HRP) was then performed for one hour at room temperature (15-25 °C). Following incubation, the membrane was washed three to four times in TBS-Tween/Triton buffer, and one wash in TBS buffer, at room temperature (15-25 °C). Once washed, the membrane was soaked in chemi-luminescence substrate.

Preparation of the chemi-luminescence substrate was carried out according to Mruk and Cheng (2011)(Mruk and Cheng 2011). Briefly, 22 µl of p-coumaric acid (90 mM in DMSO), 50 µl of luminol (250 mM in DMSO) and 3 µl H₂O₂ were mixed in 10 mL of 0.1 M Tris-HCl (pH 8.6). Once prepared, single drops were applied to cover the entire membrane, then the rest of the reagent was poured in, and the membrane was incubated for 2 minutes at room temperature, without shaking. Excess reagent was then discarded, and the membrane gently wrapped in a thin layer of Clingfilm.

In a dark room, wrapped membrane was placed in an X-Ray proof cassette, and covered by an auto-radiographic film (Life sciences). Cassette was then closed firmly for 10 seconds to 2 minutes. The photographic film was then removed and placed in developing solution (Kodak) or 10 to 20 seconds, until bands of desired intensity started appearing. The film was then washed with water and immediately placed in a tray containing fixing solution (Kodak) to remove any background noise from the film.

2.5.12. Thin Layer Chromatography

A beaker was set-up with 10 to 20 mL of TLC solvent (63: 35: 5, v/v/v chloroform: methanol: ammonium hydroxide) and the level of solvent was checked with filter paper, ensuring origin point was not submerged into solvent (Eriks, Mayor et al. 2003).

In parallel, the origin points and loading positions for samples were gently marked on a TLC plate () using a pencil, leaving enough space for samples to run (0.5 to 1 cm). Samples were then “spotted” on the TLC plate drop-wise (1 μ L of each sample at the time), with 30 seconds waiting time, between additions, to ensure effective and uniform adsorption of the sample at the corresponding position. Once dried, the TLC plate was gently placed into the beaker, and covered with aluminium film (to avoid vapour coming out). Samples were then allowed to run until reaching the top of the TLC plate (1cm from the top of the plate).

Once samples reached the top, the TLC solvent was discarded, and the plate left to dry for two minutes. The TLC plate was then placed back in a beaker with one (or two) iodine crystals and covered with aluminium foil. The beaker was warmed up using a heating block (50-60°C), allowing the iodine vapour to stain the migrated samples on the plate, giving a brown tinge to the organic spots on the plates. Once the spots were revealed, the plate was removed from the beaker, dried, and pictures were taken at different intervals (important if samples were saturated, giving them a dark brown to black colour, that faded after a few minutes).

Conventionally, the R_f would be calculated and used for each sample (see formula below).

$$R_f = \frac{\text{distance travelled by component}}{\text{distance travelled by solvent}}$$

However, since only the concentration of LDAO in purified and refolded AtVDAC samples was investigated, the analysis was performed using surface calculation (area covered by the sample) on ImageJ®. Using a standard curve designed with samples of known concentrations, unknown samples' areas were compared to those of the standard curve, and the concentrations of the unknown samples were extrapolated.

2.6. Biophysical methods

2.6.1. SAXS

Developed in the late 30s by Guinier (Rice 1956), this technique allows nanoscale density differences in a sample to be measured. As a result, the nanoparticle size distribution can help modelling the surface or overall shape of a macro-molecule. The technique uses an X-ray monochromatic beam which is brought to the sample by a series of mirrors (Figure 2.12).

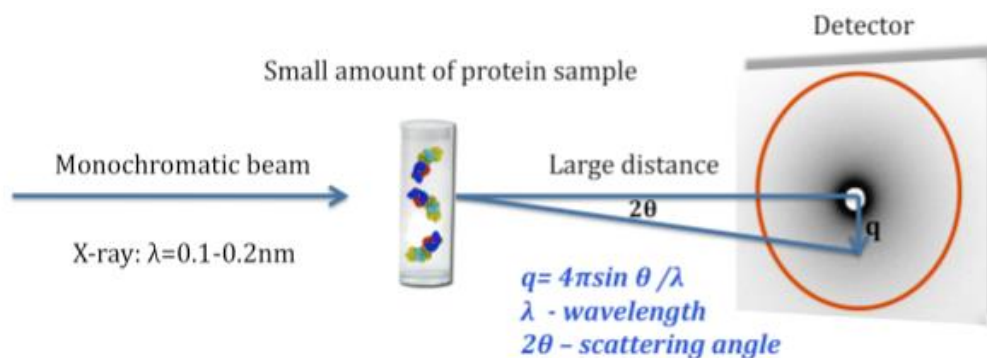


Figure 2.11 Representation of Small Angle X-Ray scattering experiment. Taken from (Tuukkanen, Spilotros et al. 2017) A monochromatic beam of X-rays is directed to a sample. Upon passing through the sample, some of the X-rays will scatter at specific angles (2θ). The scattered X-rays form a radially developed pattern of elastic scattering which is then acquired by a detector which is typically a 2-dimensional flat X-ray detector situated behind the sample perpendicular to the direction of the primary beam that initially hit the sample. The scattering pattern is a radially organised positioning of detected intensities. Those intensities are a function of scattering angles which feed information to the momentum transfer vector q .

The scattered X-rays form a radially developed pattern of elastic scattering which is then acquired by a detector which is typically a 2-dimensional flat X-ray detector situated behind the sample perpendicular to the direction of the primary beam that initially hit the sample (Figure 2.12). The scattering pattern is a radially organised positioning of detected intensities. Those intensities are a function of scattering angles which feed information to the momentum transfer vector q (Trewella, Duff et al. 2017).

2.6.1.1. Data collection

Samples were dialysed for three (mKlp2C-Ter) to seven days (AtVDAC proteins) and centrifuged briefly (6,000g for 10 minutes) to remove high molecular weight aggregates. SAXS data were first acquired in-house using a Bruker Nanostar ®, with 70 µL samples (concentration ranging from 1.2mg/mL to 4.0mg/mL for VDACs, and from 1.4 mg/mL to 6.0 mg/mL for mKlp2C-Ter) in their respective dialysis buffers (25 mM NaH₂PO₄/Na₂HPO₄ (pH 7.0), 100 mM NaCl, 1 mM EDTA, 1 mM DTT, 10% (w/v) Glycerol, 0.12% (v/v) LDAO for VDACs, or 25 mM Tris-HCl (pH 7.0), 100 mM NaCl, 3% (w/v) Glycerol for mKlp2C-Ter).

For in-house experiments, the distance of the sample from the detector was set to 106.850 cm. Samples were exposed to X-rays for 7,500 seconds, resulting in roughly 500,000 counts per image. A full data set consisted of 10 to 13 images of the sample at 7,500 seconds each (maximum of 97,500 seconds in total). Collection of excess frames would allow the discarding of some aberrant frames. SAXS experiments were conducted on protein solutions and buffers alone (blank) to enable subtraction of the solvent's component ambient scattering and to eventually reveal the density contributions of the solute molecules. This scattering data were then integrated using the circular integration method (rotation around Chi) to obtain a raw scattering curve. Primus software (ATSAS)(Petoukhov, Franke et al. 2012, Franke, Petoukhov et al. 2017) was then used to take the average of the 10 scattering curves from both sample and blank, and buffer effects were subtracted from the protein-buffer mixture.

Data generated, helped awarding time at the Beamline B21 in the Diamond Light Source in Oxford. Samples were treated as above, dialyzed prior to transport and brought to the site frozen at -20 °C. Again, different dilutions (50 µL samples with a concentration ranging from 1.2mg/mL to 4.0mg/mL for VDACs, and from 1.4 mg/mL to 6.0 mg/mL for mKlp2C-Ter) were subjected for 1 to 2 seconds in their respective dialysis buffer (25 mM NaH₂PO₄/Na₂HPO₄ (pH 7.0), 100 mM NaCl, 1 mM EDTA, 1 mM DTT, 10% (w/v) Glycerol, 0.12% (v/v) LDAO for VDACs, or 25 mM Tris-HCl (pH 7.0), 100 mM NaCl, 3% (w/v) Glycerol for mKlp2C-Ter). The strength of the beam allowed the capture of millions of

frames for each individual protein, which were collected and partially analysed on-site for integrity. Rest of the analysis was carried out in-house (see section 2.6.1.2 and 5.2.2).

2.6.1.2. **Data analysis**

Guinier and Kratky plots were generated in Primus software or Scatter Software (BioIsis) (Rambo and Tainer 2013). GNOM (ATSAS) (Petoukhov, Franke et al. 2012, Franke, Petoukhov et al. 2017) was used to generate the P(r) function (pair-distance distribution function). *Ab initio* shape determination using dummy atoms was performed using the online ATSAS package (Petoukhov, Franke et al. 2012, Franke, Petoukhov et al. 2017) with default settings. DAMMIF (Franke and Svergun 2009) automated analysis allowed the generation of 20 models through DAMMIN, which were then aligned and averaged by DAMAVER. Outliers were removed, and an average model was generated in DAMFILT. PDB envelopes (as dummy atoms) were generated in PyMOL (L DeLano 2002).

2.6.2. **Electrophysiology**

Electrophysiology experiments were conducted at the University of Brighton, under the supervision of Dr Marcus Allen. The activity of lipid-reconstituted porins was monitored via the planar lipid bilayer assay (or Black Lipid Membrane BLM). The protein was inserted in a lipid bilayer made of a 1:1 mixture of POPE (1-Palmitoyl-2-Oleoyl-sn-glycero-3-phosphoethanolamine, Avanti Polar Lipids®) and POPS (1-Palmitoyl-2-Oleoyl-sn-glycero-3-[phosphor-L-serine], Avanti Polar Lipids®) resuspended in N-Decane, using BLM buffer (10 mM Tris/HCl (pH 7.4), 150 mM KCl, 50 mM CaCl₂) on each side of the bilayer. Data were recorded using a Warner Instruments PC-501A amplifier, capable of bilayer recordings and single channel currents were digitised using an analogue to digital converter (CED micro1401 MkII).



Figure 2.12 The black lipid membrane set-up. Two chambers (or a lipid bilayer cups) for bilayer formation (Warner Instruments chamber BCH-13A and cup CP13A-250) were connected via potassium chloride (KCl) agar bridges and silver/silver chloride (Ag/AgCl) electrodes to the amplifier head stage. The amplifier used (Warner Instruments PC-501A) was capable of bilayer recordings and single channel currents were digitised using an analogue to digital converter (CED micro1401 MkII), controlled by single channel analysis software (WinEDR®, University of Strathclyde, UK). A Faraday cage was used to minimize external interferences.

Typically, this type of assay is carried out in two steps, firstly the membrane elevation and then the protein insertion (reconstitution).

The membrane elevation is the process by which the lipid bilayer (generally a mixture of Phosphatidylcholine and Phosphatidylethanolamine) is raised between a Teflon-lined hole (few microns) at the interface of two joined compartments, each filled with buffer (10 mM Tris-HCl (pH 7.4), 150 mM KCl, 50 mM CaCl₂). A small volume of lipid mixture would be applied (painting) on the small hole (aperture) between the upper and lower chamber of the setup, and buffer would be added on both sides (Figure 2.13 step I and II). Correct elevation of the membrane is monitored on screen, since its presence would prevent ion movement across compartments, with or without applied current. The optimal width of the bilayer would be monitored via its capacitance, as the most stable and thinnest possible membrane is erected (just before its breaking point).

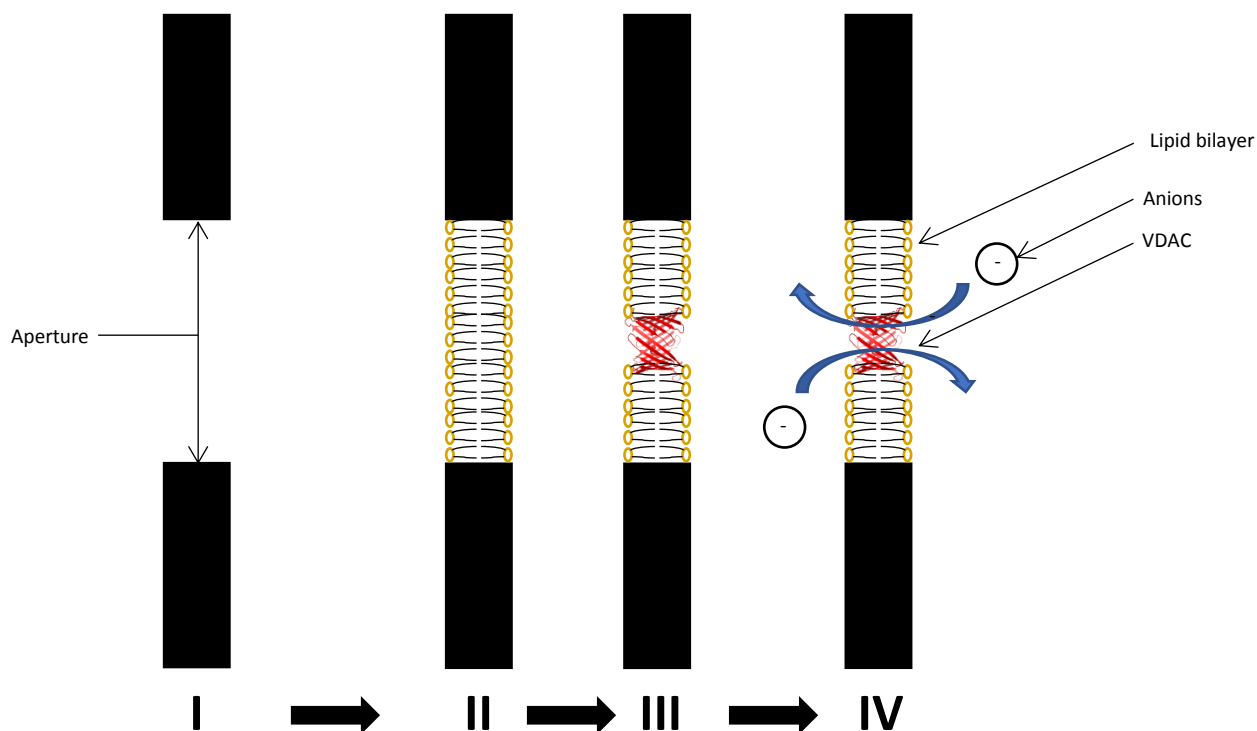


Figure 2.13 Schematic representation of the Teflon-cross section (I) between compartments. First, a stable lipid bilayer is set by “painting” lipids across the aperture, or by successively raising a lipid solution level, applied on either side of the aperture (step II); then the porin is introduced (step III). In the presence of an applied voltage, ions align in the direction of the applied field, and can cross the bilayer, through the reconstituted porin. In absence of a set current, ions are flowing on each side of the bilayer.

Once a thin and stable bilayer is set, a small volume (typically one or two microliters) of lipid-reconstituted membrane protein was added in the trans chamber. Ideally, one protein is inserted into the bilayer by vesicle fusion with the lipid bilayer. The protein insertion is monitored on screen when applying a current. Indeed, once inserted the porin will allow the flux of anions across the membrane (Figure 2.13 Step IV), leading to the recording of a specific current trace.

Data were recorded for as long as possible (generally few minutes to few hours depending on the stress applied to the membrane). Application of different voltages, ranging from -60V to +60V (can be stretched to $\pm 130\text{mV}$), were explored, for ten seconds to a minute per step (generally with a 10mV step increase). Data were recorded and gating events (Figure 2.14) were characterized.

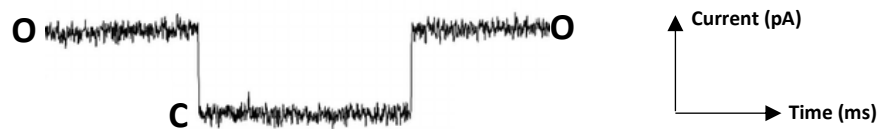


Figure 2.14 Schematic representation of a gating event. The channel is open (O) then closes (C) for a few moments (typically milliseconds) and re-opens again. The resulting current in pA from both open and closed states, as well as the time of opening/closing, the current applied can be recorded and further analysed.

Analysis was performed using a combination of tools. Win-EDR ® free software to detect the signal and map the main raw data, Excel ® was used for data storage as well as the main analysis and Magicplot® Software was used for the Gaussian fitting on the channel conductance profile and statistical analysis of the model relevance (see 3.2.3 for detailed analysis).

2.6.3. Iso-thermal titration calorimetry (ITC)

Iso-thermal titration calorimetry (ITC) is a method used to probe interactions between molecules, using thermodynamic parameters measured in solution. Experiments were performed at the University of Huddersfield, using a Malvern Microcal VP-iTC®. Typically, a sample of protein would be left mixing in a thermo-regulated chamber and small amount of titrant containing the binding partner would be injected at regular intervals (see Figure 2.15A). The difference in energy resulting from the addition of titrant would be reported and used to calculate different parameters such as dissociation/association constants, the stoichiometry or the enthalpy of the reaction (see Figure 2.15B). The main Thermodynamic law formula driving this experiment is presented in equation 2.2, where T is the absolute temperature in Kelvin and R is the gas constant.

$$\Delta G = -RT \ln Ka = \Delta H - T\Delta S$$

Equation 2.2 Thermodynamic laws defining the Gibbs free energy. T is the temperature, ΔG is the variation of free energy, ΔH is the variation of enthalpy and ΔS is the variation of entropy within the system.

Analysis of the raw data was performed using a combination of Originlab®, Excel and Magicplot®. The initial recordings were monitored using Originlab® and the resulting traces were transferred via Excel to Magicplot® for further analysis on the binding model.

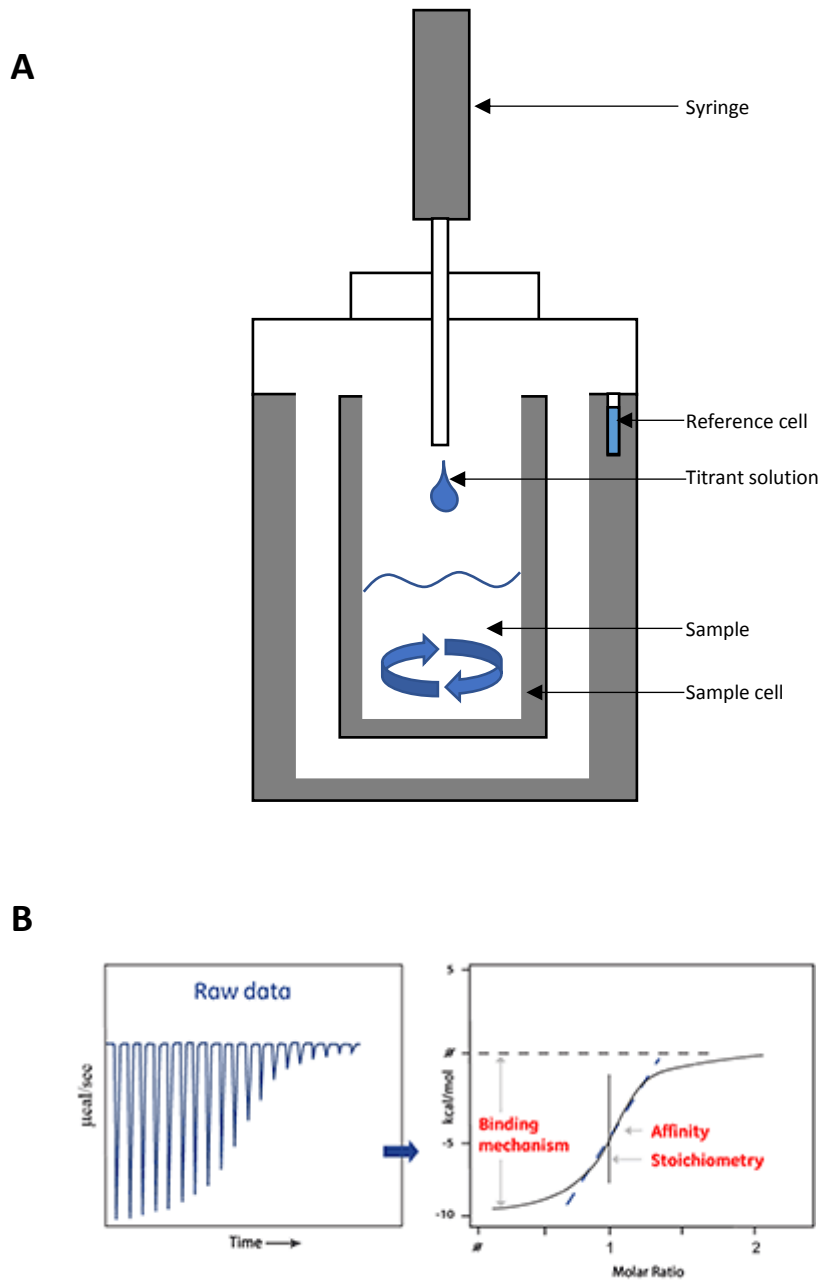


Figure 2.15 Iso-Thermal Calorimetry (ITC): basic principle. (A). Schematic representation of the instrument (Microcal VP-iTC from Malvern ®) used for the ITC study. The sample is mixing in the sample cell, and the titrant solution is delivered through a syringe via a specific volume at regular intervals. (B). Taken from *Malvern Panalytical*. Typical curve obtained in ITC (left) and the corresponding analysis (right). The binding mechanism (ΔH), the affinity (K_b) and the stoichiometry are shown in red.

2.6.4. Circular Dichroism (CD)

Circular Dichroism (CD) is a widely used technique to probe the secondary structure composition of macromolecules (proteins, DNAs, RNAs), as a consequence of the interaction of polarised light with their chiral nature.

A linearly polarised monochromatic light is defined by having its oscillations confined to a single plane. All polarised light states can be described as a sum of two linearly polarised states at defined angles to each other, usually referred as vertically and horizontally polarised light. In fact, a monochromatic linearly polarised light can be turned into either left- or right-circularly polarised light (LCP and RCP respectively) by passing it through a quarter-wave plate whose unique axis is at 45 degrees to the linear polarisation plane. A molecule that absorbs LCP and RCP differently is deemed optically active (or chiral). Hence, circular dichroism relies on the difference in light absorbance between left- (L-CPL) and right- circularly polarised light (R-CPL) by the molecule under investigation. It is generally described as the difference in absorption of ER (R-CPL absorption signal) and EL (L-CPL absorption signal), known as $\Delta\epsilon$ (Purdie 1996, Snyder 1996) :

$$\Delta\epsilon = \Delta A(\lambda) = A(\lambda)_{\text{LCPL}} - A(\lambda)_{\text{RCPL}}$$

Molecules containing chromophores will display singular patterns of differential absorption, in correlation with their structural composition. Therefore, proteins provide really good study-subjects using this technique. This is due to the fact that most of the amino acids (19 of the 20) that form proteins are themselves chiral. However, the CD spectrum of a protein is not merely a sum of the CD spectra of the individual residues or bases. Instead, the tertiary structure of the molecule can influence the signal obtained by CD (van Stokkum, Spoelder et al. 1990).

It has been shown that a specific CD-signature is attributed to a precise secondary structure. following consequence, structural conformational changes in the tested macromolecules can be followed, through changes in these signatures (Kelly, Jess et al. 2005). The most widely studied circular dichroism signatures of proteins are those corresponding to their secondary structural elements (see Figure 3.21).

Particularly, CD spectra in the far-UV (below 260nm) can be used to predict the percentages of each secondary structural element in the structure of a protein (Kelly, Jess et al. 2005).

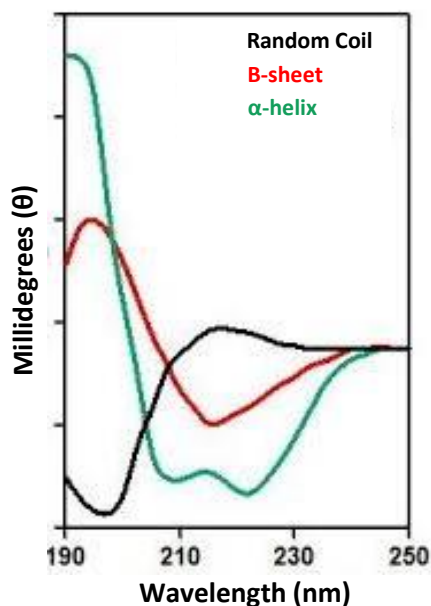


Figure 2.16 Representative examples of CD spectra of main secondary structural elements. Representative Circular Dichroism spectra of molecules with high beta-sheet content (red line), high alpha helical content (green line) and random coiled molecules (black line).

Experiments were conducted at the Astbury Centre for Molecular Biology at the University of Leeds and data were collected using a Jasco J715 spectropolarimeter. The difference of absorption between left- and right-polarized light are measured for air, buffer, and up to 5 samples. The process is repeated at wavelengths ranging from 180 nm to 260 nm with a 1 nm increment. The instrument can also perform temperature ramping, allowing measurements at increasing temperature and probe their structure recovery after heating up and cooling down for example. Additional parameters such as the temperature or the voltage are also recorded and can help monitoring the integrity of the sample throughout the experiment.

CD data outputs are generally given in millidegree (mDeg), or ellipticity θ . Using the molar concentration (in mole/L) and the path length (in cm), the Molar ellipticity $[\theta]$ can then be calculated and used for comparison with other proteins. In addition, using also the Mean Residual Weight of a given protein (Molecular weight/number of amino acids) can help convert θ to $\Delta\epsilon$.

Using dedicated software (Dichroweb) and algorithms (CONTINLL or CDSSTR for example)(Sreerama and Woody 2000), the structural content (in percentages of beta, alpha helix and random coil) can be calculated for a specific protein in a specific condition (temperature or buffer for example)(Kelly, Jess et al. 2005).

2.7. Bioinformatics

DNA sequences were retrieved from Pubmed® (Sayers, Barrett et al. 2009), either by direct search via the accession number or keywords, or by using BLAST alignment tool (McGinnis and Madden 2004) from NCBI® webserver. Multiple sequences alignments were also performed on the NCBI platform.

The basic properties of the proteins used in this study such as the molecular weight or the homology modelling were performed using the ExPASy platform (Artimo, Jonnalagedda et al. 2012) and SWISS modeller (Waterhouse, Rempfer et al. 2018) respectively (though the latter is also accessible through the same platform).

Most of the three-dimensional structural analysis of the SAXS envelopes, the crystal structures, the homology models were performed using Pymol®(L DeLano 2002) and Chimera® software (Pettersen, Goddard, Huang, Meng et al. 2014). The known crystal structures data-files (pdb files) were retrieved from the RCSB Protein Data Bank.

3. Chapter 3: AtVDAC1

3.1. Heterologous production of AtVDAC proteins in *Escherichia coli*

Cloning of *AtVDAC1* into the pET-20b(+) was performed by Felix Brademann at the University of Marburg, as part of his master thesis (see 2.2) under the supervision of Dr Georgios Psakis. The pET-20b(+)AtVDAC1 construct was kindly provided and would be used for the subsequent production of AtVDAC1 protein in OMP9 cells.

Test expression were carried out to confirm the correct overexpression of the *ATVDAC1* gene by auto-induction (see section 2.3.4.2). A 12 % (v/v) SDS-PAGE was performed to monitor the production of the translated protein AtVDAC1 (Figure 3.1) by Coomassie Blue staining. Indeed, an additional band around 30 to 40 kDa would appear on gel after 6 to 12 hours of incubation (Figure 3.1 lane 7 and 8).

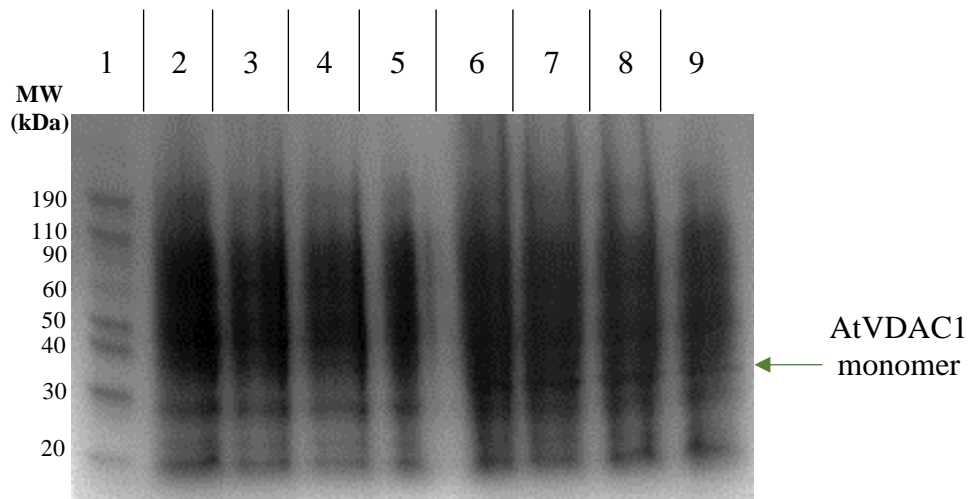


Figure 3.1 Heterologous production of AtVDAC proteins in *E.coli* by auto-induction. Whole cell extracts, taken during the over-production of AtVDAC1 in OMP9 cells were analysed on 10 % (v/v) SDS-PAGE in 1x Laemmli running buffer. Lane 1 contains the ladder from Novex®. 1 μ L of the pelleted fraction after 0.5, 1, 2, 3, 4, 6, 12 and 18 hours (lane 2 to 9) of auto-induction were analysed. The position of the AtVDAC1 monomer is indicated by a green arrow.

3.2. Preparation of Inclusion bodies for AtVDAC1

Following auto-induction (see section 2.3.4.2) in Omp9 cells with the best possible clone, the production of AtVDAC1 in inclusion bodies and their subsequent washing were analysed by 12% (v/v) SDS-PAGE in 25 mM Tris, 200 mM Glycine, 0.1 % (w/v) SDS (Figure 3.2, see 2.5.2 for further details on the samples). Supernatants (Figure 3.2, lanes 2 to 3) after the first centrifugation were devoid of the protein of interest (~29.5 kDa as predicted with the ExPASy webserver (Artimo, Jonnalagedda et al. 2012)). Pellet fractions resuspended in TEN-Triton (50 mM Tris-HCl (pH 8.0), 100 mM NaCl, 10 mM EDTA, 2% (v/v) Triton X-100), show distinctively a protein band around 30 kDa (Figure 3.2, lanes 4 to 7), most likely AtVDAC1 monomer (green arrow). After washing in buffer TN (50 mM Tris-HCl (pH 8.0), 100 mM NaCl) the protein's band intensity increased (Figure 3.2, lanes 8 to 10), to reach saturation after the final resuspension in a smaller volume (Figure 3.2, lane 12). The identity of the protein was later confirmed by Western Blot (Figure 3.2, @AtVDAC1) using a polyclonal antibody targeted at AtVDAC1 at a dilution of 1/1000.

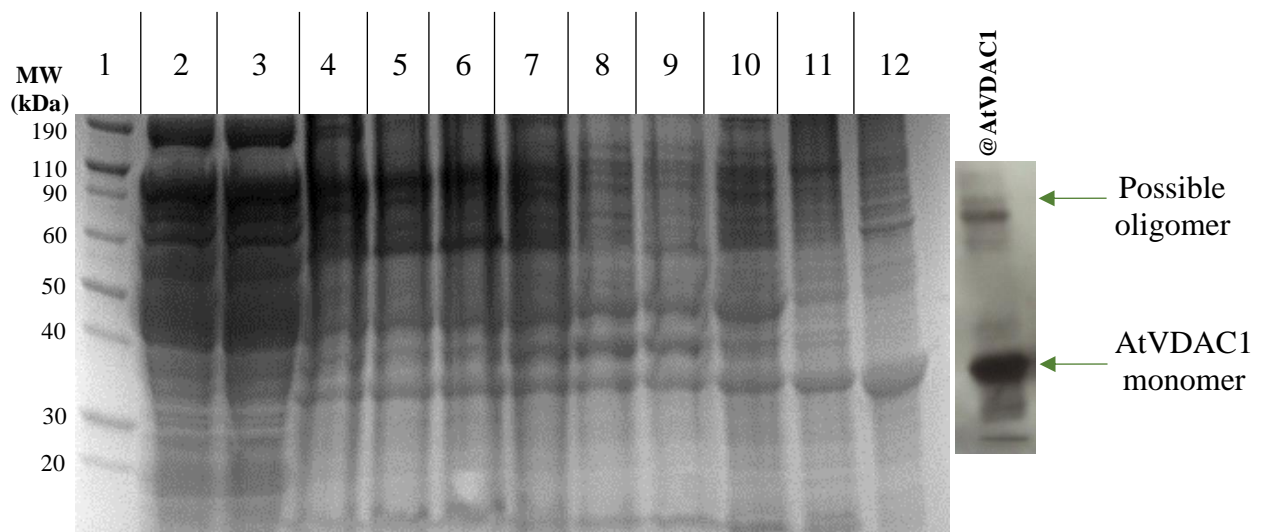


Figure 3.2 Production, washing and concentrating of AtVDAC1 inclusion bodies (IB). Samples taken during the production of AtVDAC1 were analysed on 12 % (v/v) SDS-PAGE in 1x Laemmli running buffer. 25 μ L of each of the supernatant fraction from the first wash in TEN Triton (lane 2 to 3), 5 μ L of each resuspended pellet in TEN Triton (lane 4 to 7) or TN buffer (lane 8 to 10), 5 μ L of the pooled pellets (lane 11) and 2 μ L of the finally resuspended and concentrated AtVDAC1 inclusion bodies (lane 12) were analysed. The identity of the protein was confirmed by Western Blotting (right) using an @AtVDAC1 polyclonal antibody (from Agrisera) at 1/1000 dilution. The position of the AtVDAC1 monomer as well as a possible oligomer are indicated by green arrows.

3.3. Optimization of native AtVDAC1 refolding and purification process

The relatively low yield of protein generated (10 to 30 %, or 5 to 15 mg of purified protein for 50 mg of inclusion bodies) may be limiting for downstream applications (De Bernardez Clark 1998, Lilie, Schwarz et al. 1998). Therefore, different steps of the refolding and purification processes were optimized, to enhance the yield of purified protein as well as the robustness of the method. Firstly, use of different additives was considered in improving the refolding yields (see section 2.5.3.1) and subsequently different chromatographic solid supports were used in improving purification yields (see section 2.5.4 and 2.5.6).

3.3.1. Optimisation of the first AtVDAC1 refolding step (RF1)

The refolding step is often regarded as the most limiting in membrane protein purification, leading generally to a dramatic loss of protein (generally 80 %)(De Bernardez Clark 1998, Lilie, Schwarz et al. 1998). Thus, appropriate additive selection for protein stabilisation and subsequent refolding is pivotal. As described in section 2.5.3.1, a screen was performed on the buffer used in the first dilution step of the *in vitro* refolding (25 mM NaH₂PO₄/ Na₂HPO₄ (pH 7.0), 100 mM NaCl, 1 mM EDTA, 10 % (v/v) Glycerol, 2.29 % (v/v) LDAO). Choice of additives tested was guided by investigations of Yamaguchi *et al.* (2014) (Yamaguchi and Miyazaki 2014) and the screening methodology was inspired from Bondos *et al.* (2003) (Bondos and Bicknell 2003).

Results of the refolding screens performed on two different batches of AtVDAC1 Inclusion bodies (labelled AtVDAC1 and AtVDAC1b) were regrouped in Figure 3.3. More precisely, they were represented as the percentage of refolded AtVDAC1 protein out of the total amount initially denatured. Out of the eleven conditions tested, the refolding buffer containing NaCl and glycerol appeared to be the best for the refolding of AtVDAC1 and AtVDAC1b. The only components providing high AtVDAC refolding efficiency (high ratio) for both replicates were NaCl and Glycerol, (NH₄)₂SO₄, Na₂SO₄, lactose and glucose. NaCl and Glycerol combination offered a ratio over 0.9 (or 90%) whereas the other four conditions provided slightly lower efficiencies (between 0.8 and 0.9 or 80% and 90%).

Interestingly, the different batches sometimes exhibited different behaviours in regard to specific components such as Magnesium sulphate (MgSO_4) and inositol. The latter is the most intriguing as the difference appeared significant (53 % for AtVDAC1 against 92 % for AtVDAC1b). This was explained by the variable behaviour of the preparations when using inositol, which tended to precipitate upon dilution. Hence, significant variation was obtained when triplicating the measurements.

Overall, the first refolding step appeared not to be as crucial as the second dilution step. Indeed, most of the protein is refolded and solubilized instead of aggregating in pellets and many of the conditions tested in Figure 3.3 worked with an efficiency of 80% to 90%. Unfortunately, a screen for the second dilution step of the *in vitro* refolding was not possible using this methodology, due to the higher dilution factor (over 100) and the increasing errors in the measurements.

Nevertheless, the high refolding efficiency achieved with the chosen buffer (25 mM NaH_2PO_4 / Na_2HPO_4 (pH 7.0), 100 mM NaCl, 1 mM EDTA, 10 % (v/v) Glycerol, 2.29 % (v/v) LDAO) gave us confidence it was the most suitable for use.

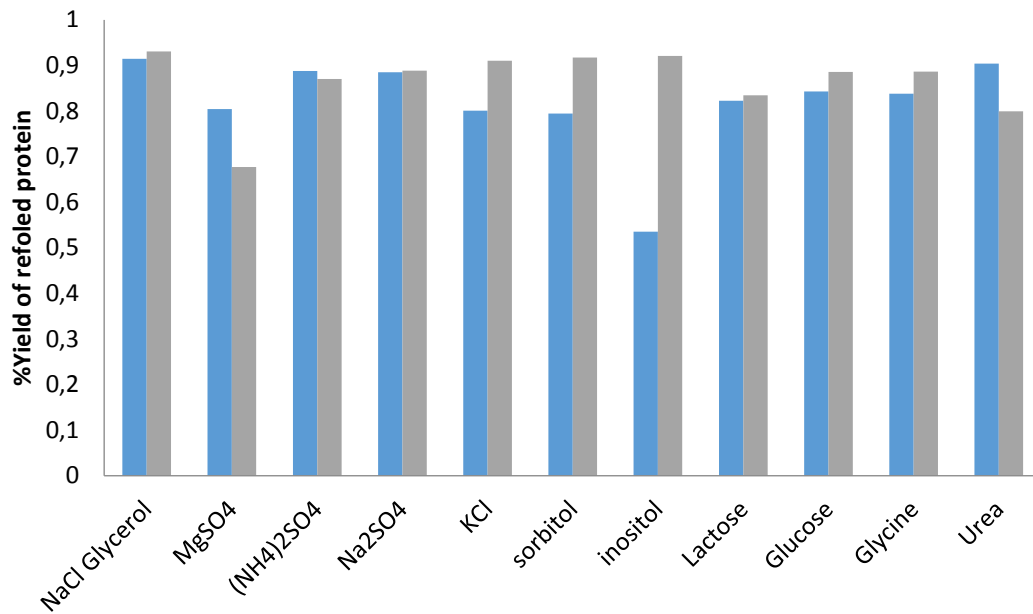


Figure 3.3 Refolding screen of AtVDAC1 in RF1 and in the presence of different additives. The relative solubility effectiveness is normalised to the AtVDAC1 protein that is soluble in the denaturing buffer (25 mM NaH₂PO₄/ Na₂HPO₄ (pH 7.0), 100 mM NaCl, 1 mM EDTA, 10 mM DTT, 6 M Guanidinium chloride) . If not refolded, the protein will aggregate, and following centrifugation the amount of soluble protein will decrease. Two different batches of Inclusion bodies were used for this experiment (AtVDAC1 and ATVDAC1b). Ratios for AtVDAC1 are in blue and in grey for AtVDAC1b.

3.3.2. Chromatography Stage

Originally, a combination of Fractogel® EMD SO₃⁻ (M) and with Superdex75 ® was used to capture the AtVDAC1 protein via ion exchange chromatography and control its monodispersity via gel filtration, respectively (see sections 2.5.4.1 and 2.5.6).

For cation exchange chromatography, using a 5 mL Fractogel® EMD SO₃⁻ (M), a NaCl gradient of 1 mM to 1 M (cation exchange chromatography elution buffer, Table 2.1) and the protocol described in section 2.5.4.1, the protein would elute within a single peak of approximately 2 column volumes (CVs)), and a maximum absorbance (280 nm) of 100 mAU at around 12 mL (Figure 3.4). The main collection peak was determined to be eluting between 10 and 14 mL, or 280 mM to 600 mM salt concentration (using a 1 mM to 1 M NaCl gradient), peaking at 500 mM NaCl.

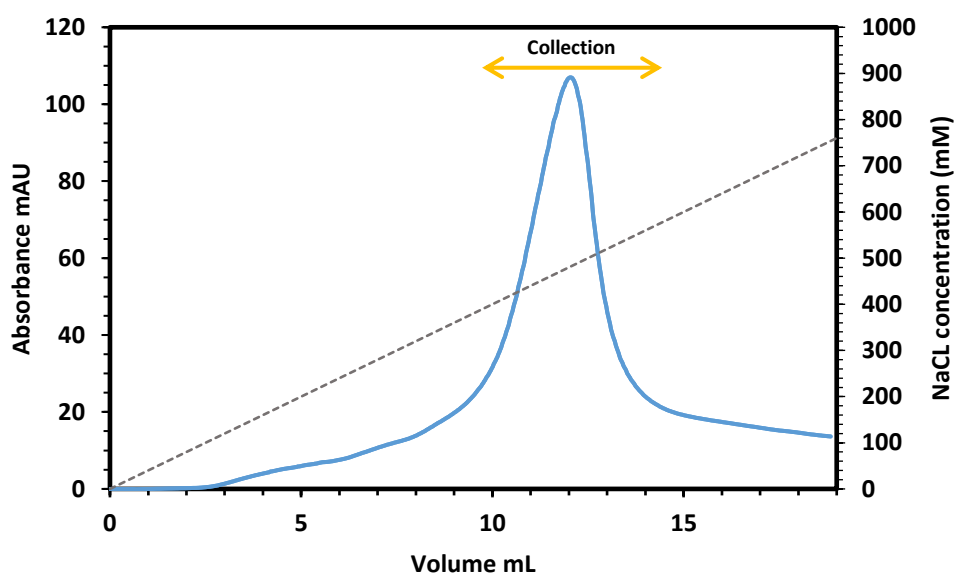


Figure 3.4 Initial cation exchange chromatography of AtVDAC1 protein using an increasing gradient of NaCl. Purification profile (in mAU, in blue) of AtVDAC1 protein using a Fractogel® EMD SO₃⁻ (M) and a linear gradient (grey) of NaCl (25 mM NaH₂PO₄/ Na₂HPO₄ (pH 7.0), 1 mM to 1 M NaCl, 1 mM EDTA, 1 mM DTT, 10 % (w/v) Glycerol, 0.12 % (v/v) LDAO). Absorbance (280 nm) was recorded against the collected fractions. Elution was carried out in an Akta Start ® device.

Fractions were pooled together (Figure 3.4; yellow arrow), buffer exchanged and concentrated using an Amicon ® concentrator with a 10 kDa cut off. Sample (500 µL of 0.84 µg/µL AtVDAC1 eluate from

the previous step) was injected onto a Superdex 75® (Figure 3.5A) gel filtration column and eluted in size exclusion chromatography buffer (SEC for VDACs, Table 2.1).

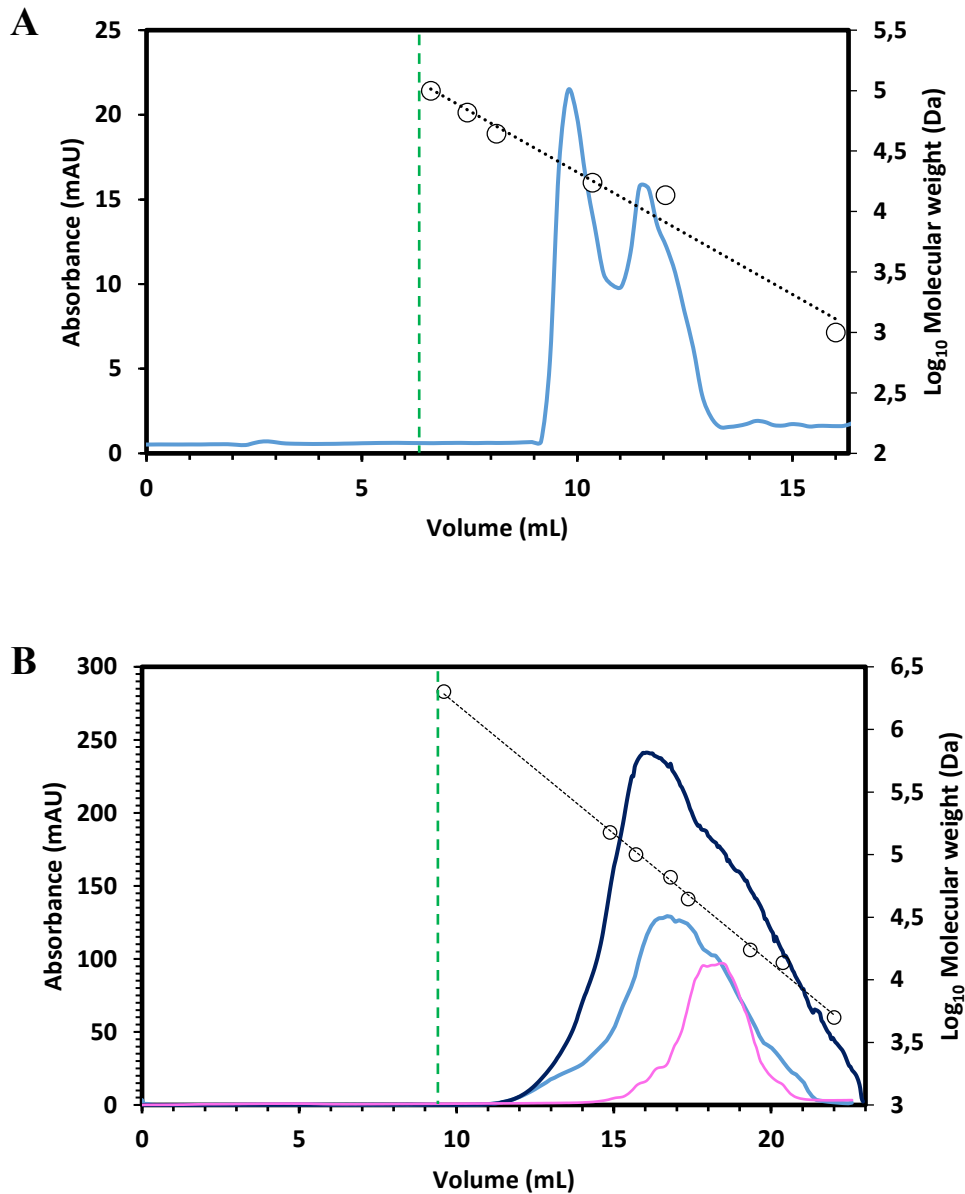


Figure 3.5 Size exclusion chromatography (SEC) of AtVDAC1 using Superdex75 and Superose6 solid supports. **(A)** 500 μL of 0.84 $\mu\text{g}/\mu\text{L}$ IEC purified and concentrated AtVDAC1 were injected onto a Superdex75 column attached to an Akta Prime® device. **(B)** 500 μL of 0.84 $\mu\text{g}/\mu\text{L}$ (dark blue line), 0.42 $\mu\text{g}/\mu\text{L}$ (light blue line) or 0.21 $\mu\text{g}/\mu\text{L}$ (pink line) of IEC purified and concentrated AtVDAC1 were injected onto a Superose6 Increase® column attached to an Akta Prime® device. Experiments were carried out in elution buffer (25 mM $\text{NaH}_2\text{PO}_4/\text{Na}_2\text{HPO}_4$ (pH 7.0), 100 M NaCl, 1 mM EDTA, 1 mM DTT, 10 % (w/v) Glycerol, 0.12 % (v/v) LDAO). In both cases, the minimum working range (void volume) is indicated by a green dashed line.

The chromatograph recorded (Figure 3.5A, blue curve) in mAU, indicated the presence of two main peaks. The first main peak eluted at its maximum at 9.6 mL after injection, corresponding to an approximate size of 28 kDa (based on the calibration curve, see section 2.5.6.1), in accordance with the expected size of 29 kDa (calculated from ExPASy webserver (Artimo, Jonnalagedda et al. 2012)). The remaining protein fully entering the column eluted within a second peak, around 12 mL and an approximate size of or 14 kDa. Surprisingly, when fractions from both peaks were analysed on a 10 % (v/v) SDS-PAGE (Figure 3.6, lane 2 to 4), only the AtVDAC1 monomer could be detected at high purity (above 95 %). However, higher column pressure as well as precipitation would be observed occasionally during the run when loading concentrated samples on the Superdex75 size exclusion column. The first peak would elute in the void volume (7 mL as estimated with Dextran Blue). The protein's purification yield, under these conditions was generally low (few hundred micrograms at best, Figure 3.6, lanes 2 to 4), despite looking relatively pure.

To ensure the sample would fully enter the size exclusion chromatography bed volume and increase purification yields, gel filtration was attempted using a Superose6 Increase® column (Figure 3.5B), under the same conditions in which the Superdex 75 experiment was conducted. The resulting chromatogram (Figure 3.5B, dark blue curve) showed a broad peak with a maximum absorbance recorded around 16.2 mL after injection (around 64 kDa), with an additional shoulder becoming prominent at 18 mL (around 32 kDa). Although exhibiting clear differences in size on size exclusion chromatography, no difference was detected between SDS-PAGE analysed fractions from the main elution peak (Figure 3.6 lane 5), and SDS-PAGE analysed fractions from the shoulder peak (Figure 3.6, lane 6). SDS-PAGE analysed fractions from both peaks revealed the presence of a putative AtVDAC1 monomer around 30 kDa (Figure 3.6 green arrow).

To further investigate possible protein and or detergent concentration effects on the quality of the collected profiles, two different protein dilutions (dilution factor of 2 and 4, in size exclusion buffer) of the same sample were also subjected to SEC. The resulting chromatograms (Figure 3.5B, light blue curve and pink curve for the dilution by 2 and 4, respectively) demonstrated a shift of the predominant peak towards the position of the shoulder peak of the concentrated sample (around 18 mL). This result

confirmed the concentration dependency of the purification profile as well as the potential oligomerization of AtVDAC1 monomer protein.

Typically, the combination Fractogel EMD SO3 (M)/ Superose6 yielded generally 2 mL purified protein at a concentration of 1 mg/mL from a batch of 50 mg of Inclusion bodies. This was deemed acceptable although limiting for a certain number of assays such as Black lipid membrane (BLM) assay or Far Western Blotting. However, a significant percentage of contaminating proteins (10 to 25 %), especially of high molecular weight (above 60 kDa, Figure 3.6 lane 5 and 7), was still present in the main elution peaks. Additionally, the later fractions (Figure 3.6 lane 6 and 8), although purer, did not yield enough monomer per run for a single Small Angle X-Ray Scattering (SAXS) experiment. Consequently, SEC would have to be repeated with individual diluted samples, making the process inefficient and tedious.

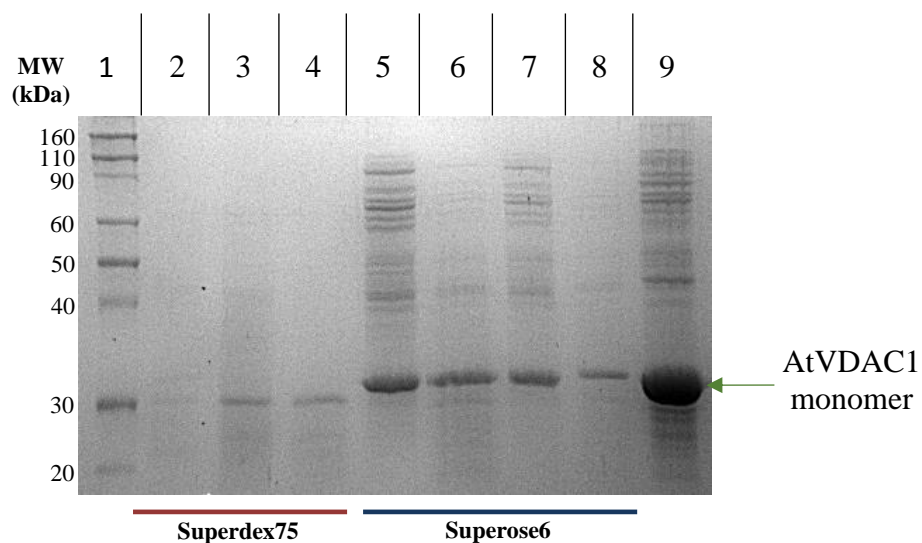


Figure 3.6 SDS-PAGE analysis of SEC-AtVDAC1 fractions. 10 μ L of each fraction were loaded on 10 % (v/v) SDS-PAGE in 1x Laemmli running buffer. Lane 1; ladder from Novex®. Lane 2 to 4; samples collected at 9, 10 and 12 mL respectively from the Superdex75 column, Lanes 5 to 6; samples collected at 16 and 18 mL respectively from 0.84 μ g/ μ L AtVDAC1 injected onto the Superose6 column, Lane 7; sample collected at 16 mL, from a 0.42 μ g/ μ L AtVDAC1 loaded onto Superose6. Lane 8; sample collected at 18 mL from a 0.21 μ g/ μ L AtVDAC1 loaded onto Superose6 and Lane 9; AtVDAC1 inclusion bodies used as sizing control monomers (green arrow).

3.4. Purification of Native-like AtVDAC1 protein by Ion (cation) Exchange Chromatography (IEX) using an HiTrap solid support

Refolded AtVDAC1 was treated as described in section 2.5.4.1. Using a linear gradient of NaCl (Table 2.1) for the protein elution from the support, the protein eluted as a relatively sharp peak with a tail at the end (Figure 3.7). Overall, the elution started around 300 mM NaCl, peaking at 400 mM salt and reaching completion around 600 mM salt. Fractions collected between 20 mAU (beginning of the peak) and 50 mAU (end of the peak) were pooled together, buffer-exchanged in SEC buffer (see Table 2.1) and concentrated using an Amicon® concentrator with a 10 kDa cut-off. Out of the 50 mg of Inclusion bodies used per batch of purification, 5 to 7 mL (1- 1.5 CV on 5 mL prepacked Hitrap SP XL®) of protein could be collected at a concentration of 1- 1.5 mg/mL. When the pooled and concentrated fractions were analysed on a 10 % (v/v) SDS PAGE (see 3.5.1.1, Figure 3.8A, lane 8), the AtVDAC1 monomer exhibited a strong signal, with a reasonable purity (above 80 % of the total signal, using ImageJ Software®). Compared to the previous purifications (see section 3.3.2), the number of contaminants and their concentration decreased greatly with this HiTrap resin. This was particularly true regarding the higher molecular weight contaminants observed in the analysis of previous samples (Figure 3.6, lane 5 to 8).

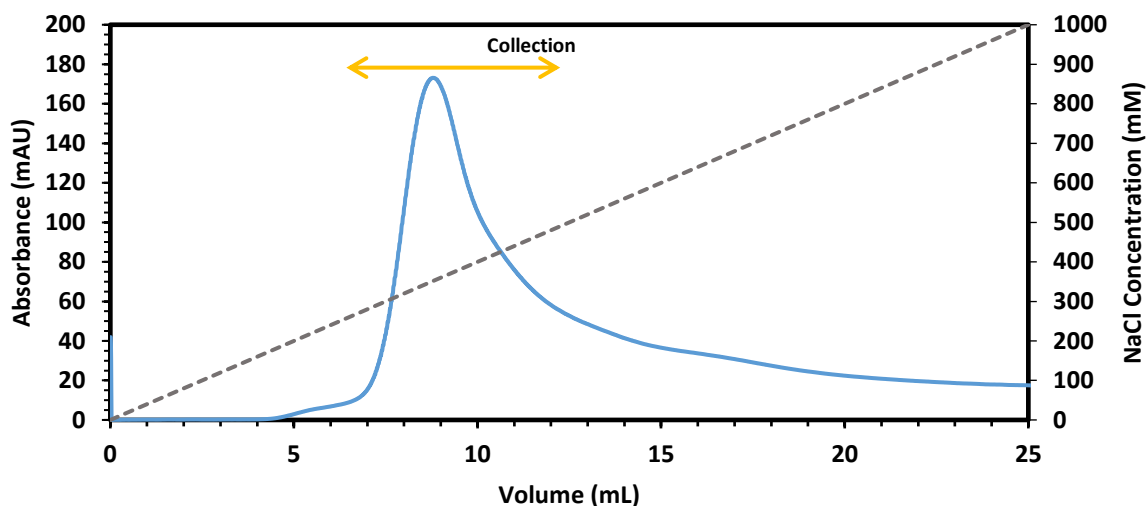


Figure 3.7 Cation exchange chromatography of AtVDAC1 protein using a Hitrap SP XL® with an increasing gradient of NaCl. UV absorbance profile (in mAU, in blue) recorded during the elution of AtVDAC1 protein using a linear gradient (grey) of NaCl (25 mM NaH_2PO_4 / Na_2HPO_4 (pH 7.0), 1 mM to 1 M NaCl, 1 mM EDTA, 1 mM DTT, 10 % (w/v) Glycerol, 0.12 % (v/v) LDAO). Elution was carried out in an Akta Start® device. The resin used was a HiTrap SP XL 5 mL®. Collection area is represented by an orange arrow.

HiTrap SP XL 5 mL® prepacked columns would be used for up to 50 cycles before exhibiting small decrease in binding capacity. However, this was easily countered by replacing the column with a fresh one. Binding capacity (total amount of protein eluted per mL of resin) would then be monitored at regular intervals and column would be replaced if a significant drop was observed.

3.5. Size exclusion chromatography of native AtVDAC1 on Superose6 Increase®

A sample (500 μ L of a 4 mg/mL eluate from IEC performed in section 3.4) was injected onto the column and the elution profile was recorded (Figure 3.8B), and recovered samples were analysed by 10 % (v/v) SDS PAGE in 1x Laemmli buffer (Figure 3.8A). AtVDAC1 eluted as a broad peak with a maximum absorbance recorded at 16.1 mL after injection (69 kDa), with an additional shoulder appearing around 17-18 mL (50 to 30 kDa) fractions collected separately.

The use of the HiTrap resin (as opposed the Fractogel resin) resulted in greater sharpness for the main peak (Figure 3.8B), resulting in a higher amount of AtVDAC1 monomer eluted, as well as a great reduction in the number and concentration of contaminants (higher molecular weight). Although exhibiting clear differences in size on analytical size exclusion chromatography, no difference could be found between a sample coming from the main elution peak (Figure 3.8A lanes 2 to 4), and a sample coming from the later shoulder of the peak (Figure 3.8A, lanes 5 to 7). Indeed, when loaded on SDS-PAGE (Figure 3.8), the main protein eluted would be the same protein of interest, i.e namely the AtVDAC1 monomer around 30 kDa on SDS PAGE (Figure 3.8, green arrow), thus confirming the oligomerization propensity of AtVDAC1 and its complete denaturation by the SDS.

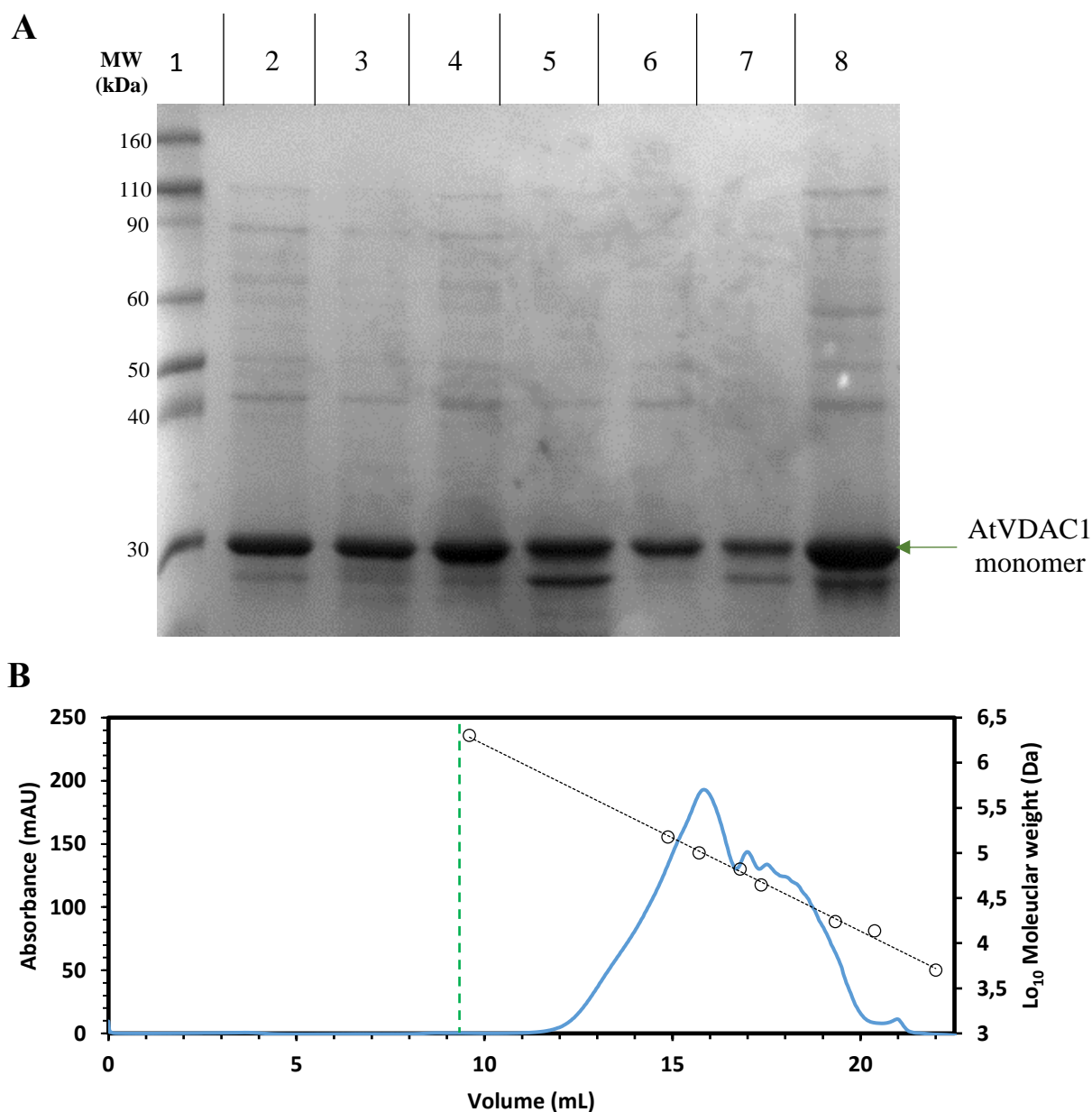


Figure 3.8 Size exclusion chromatography of AtVDAC1 using a Superose6 Increase®. SEC was carried out in an Akta Prime® device in SEC buffer (25 mM NaH₂PO₄/ Na₂HPO₄ (pH 7.0), 100 mM NaCl, 1 mM EDTA, 1 mM DTT, 10 % (w/v) Glycerol, 0.12 % (v/v) LDAO). (A). 10 µL of each purified AtVDAC1 fractions from SEC were analysed on a 10 % (v/v) SDS PAGE in 1 x Laemmli running buffer. Lane 1; ladder from Novex®. Lane 2 to 7; samples collected at 14, 15, 16, 17, 18 and 19 mL, from a 4 mg/mL AtVDAC1 loaded onto Superose6. Lane 8; 2 µL sample of the 4 mg/mL AtVDAC1 solution injected. The AtVDAC1 monomer is indicated by a green arrow. (B). Elution profile (UV absorbance in blue) of the size exclusion chromatography performed on AtVDAC1 after injection of partially purified sample (500 µL of a 4 mg/mL solution). The minimum working range (void volume) is indicated by a green dashed line.

3.6. Structural characterisation of AtVDAC1 by Circular Dichroism (CD)

Circular Dichroism (CD) experiments were performed at The University of Leeds, at the Astbury Centre for Molecular Biology on two different samples. Two sample from SEC (see section 3.5) were subjected to CD to monitor any conformational associated with the oligomerization of AtVDAC1. The first sample was collected 16 mL (labelled as AtVDAC1 oligomer) after injection and the second 18 mL after injection (referred as AtVDAC1 monomer). Protein concentration was determined by BCA assay (see section 2.5.7) and data were analysed using Dichroweb ® website (Lobley, Wallace et al. 2002, Whitmore and Wallace 2004) and algorithms CONTINLL (AtVDAC1 monomer) or CDSSTR (AtVDAC1 oligomer)(Sreerama and Woody 2000).

CD data were collected for both oligomer and monomer fractions as described above and repeated twice to ensure robustness of the data. Parameters are summarized in Table 3.1 and the corresponding CD spectra are presented in Figure 3.9.

Table 3.1 Selected parameters for AtVDAC1 Circular Dichroism experiments.

Parameter	AtVDAC1 oligomer	AtVDAC1 monomer
Temperature	20 °C	20 °C
Path length	1 cm	1 cm
Protein amount	15 µg	15 µg
Concentration	1.525 mg/mL	1.26 mg/mL
Wavelength range	180-260 nm	180-260 nm
Wavelength increment	1 nm	1 nm
Initial Wavelength	260 nm	260 nm
Final Wavelength	180 nm	180 nm
Analysis algorithm	CONTINLL	CONTINLL

Replicate CD spectra from AtVDAC1 oligomer (Figure 3.9A) and monomer (Figure 3.9B) were similar (1 and 2). In both cases, the profile remained extremely consistent across the experiments.

Oligomeric AtVDAC1 (Figure 3.9A), exhibited a typical CD spectrum of a beta-sheet rich protein (see Figure 2.16 in section 2.6.4), with its minimum reaching at 218 nm, consistent with previous findings

on β -barrel rich macromolecules (Greenfield and Fasman, 1969) (Greenfield and Fasman 1969). Data from 260 nm down to 190 nm were used to calculate the structural content of the protein (Table 3.2).

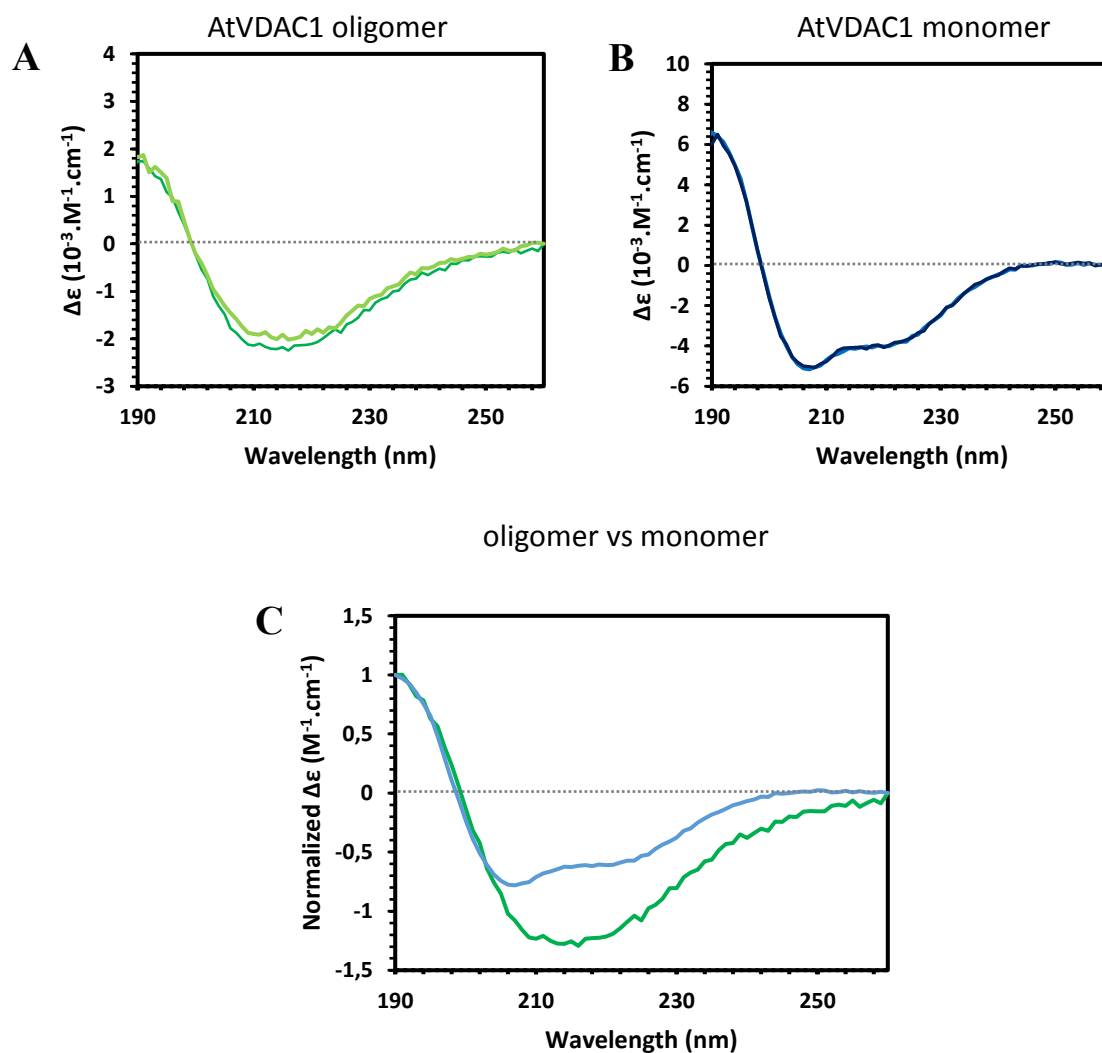


Figure 3.9 Circular Dichroism spectra of AtVDAC1. (A) CD spectra of AtVDAC1 oligomer (collected 16 mL after injection on SEC and buffer exchanged in 25 mM NaH_2PO_4/Na_2HPO_4 (pH 7.0), 0.12 % (v/v) LDAO). Repeat 1 and repeat 2 are represented in light and dark green respectively. (B) CD spectra of AtVDAC1 monomer (collected 18 mL after injection on SEC). Repeat 1 and repeat 2 are represented in light blue and dark blue respectively. (C). Comparison of normalized CD spectra from AtVDAC1 monomer (in green) and AtVDAC1 oligomer (in blue). The maximum value at 190 nm was used to normalize both spectra. All experiments were performed at 20 °C, at a scanning speed of 60 nm per minute.

On the other hand, the monomeric fraction (Figure 3.9B) displayed a composite CD spectrum. In fact, the beginning of the profile (from 190 to 214 nm wavelength) is similar to the one observed for the oligomeric fraction and resembled a beta barrel protein. However, from 214 to 260 nm the putative oligomer exhibited an increased helicity in the overall structural composition. When the data were analysed using Dichroweb website (Lobley, Wallace et al. 2002, Whitmore and Wallace 2004) and CONTINLL algorithm (Provencher and Gloeckner 1981, van Stokkum, Spoelder et al. 1990), the sum of the secondary structure was calculated to be 9.5 % alpha helical, 36.7 % beta barrel and 53.8 % random or unordered (Table 3.2). This confirmed the increased helicity observed on the raw data between AtVDAC1 oligomer and monomer (from 6.3 to 9.5 % alpha helix). It is likely that the signal of the beta barrel is overwhelming when considering an oligomer as opposed to the monomer. This could also be explained by a destabilization of the alpha helix (first 15 to 25 amino acids of AtVDAC1 protein), due to the oligomerization of AtVDAC1 monomers and the high dynamicity of the alpha helix (Hiller, Garces et al. 2008, Geula, Ben-Hail et al. 2012).

Table 3.2 Secondary structure content from three CD-analysed AtVDAC samples. CD data were analysed using algorithms CONTINLL (Provencher and Gloeckner 1981, van Stokkum, Spoelder et al. 1990) (AtVDAC1 monomer) or CDSSTR (Sreerama and Woody 2000) (AtVDAC1 oligomer). Secondary structure content of mouse VDAC1 (mVDAC1; based on 3EMN1) is indicated. Hypothetical structure content of VDACs based on their expected secondary structures is indicated as well (AtVDACs prediction).

Sample	Alpha helix	Beta barrel	Random
AtVDAC1 oligomer	6.3 %	42.4 %	51.7 %
AtVDAC1 mono	9.5 %	36.7 %	53.8 %
mVDAC1 3EMN1	3.7 %	62.7 %	33.6 %
AtVDACs predictions	4.3 %	50 %	45.7 %

In parallel, the secondary structure content of mouse VDAC1 (mVDAC1) was calculated based on its published crystal structure (3EMN1). Using a PDB to CD file converter (PDB2CD® (Mavridis and Janes 2016)), a hypothetical CD spectra was generated (based on SMP180 reference database for soluble and membrane proteins) and processed in Dichroweb (Lobley, Wallace et al. 2002, Whitmore and Wallace 2004) using CONTINLL algorithm (Provencher and Gloeckner 1981, van Stokkum, Spoelder et al. 1990). A similar approach was used to calculate an averaged structural content for AtVDACs (1

to 4), based this time on their expected secondary structure alone (no crystal structure available, see section 1.6.1).

The structural composition of the samples probed by CD seemed numerically close to those of the AtVDACs predictions, although the helical content was lower (4.3 %) and the beta barrel content was slightly higher (50 % against 36.7 to 42.4 % for the monomer and oligomer respectively) in the predictions. This could be explained by the averaged values of the prediction, taking into account all *Arabidopsis thaliana* VDAC proteins (AtVDAC1 to AtVDAC4).

Interestingly, the same trend could be observed for the structural content of mVDAC1, only on a smaller scale. Indeed, despite displaying a similar pattern (high beta barrel content with small helicity) to the AtVDAC1 proteins, the beta barrel percentage was significantly higher (from 36-42 % to 62.7 %) and the random structure lower (from 51-54 to 33.6%). This was attributed to the crystal form of the protein as opposed to its solubilized form, which is more dynamic due to interactions with the solvent. In contrast, within the crystal lattice, the structure is a more compact (hence the possibility to be crystallized) and the secondary structure content is dictated by the tertiary resolved structure of the protein.

To further investigate the compactness of the monomeric and oligomeric conformations of AtVDAC1 and whether the oligomerization conferred a decreased stability of the N-Terminal alpha helix of AtVDAC1, experiments were repeated, but with different temperatures. Samples would be denatured at high temperature, cooled down and CD spectra were recorded at each stage. In summary, the sample would be scanned at 20 °C, heated at 90 °C and re-scanned, then finally cooled down back to 20 °C to be re-scanned again.

The resulting spectra are presented in Figure 3.10 for both monomer (A) and oligomer (B). There is a very noticeable full denaturation of the AtVDAC1 oligomer after heating (Figure 3.10B, red line), and close to no refolding after cooling down (blue line). This complete loss of structure and difficulty to refold was expected, since the membrane protein needed an *in vitro* dilution for its refolding.

The monomer (Figure 3.10A) showed a more complex profile, with strong but incomplete denaturation after heating at 90 °C (Figure 3.10A, red line). Upon cooling, a small but noticeable amount of structure was recovered, although the refolding was far from achieved.

This result confirmed an increased stability of the AtVDAC1 monomer in comparison to its oligomer form, in regard to the temperature. Noticeably, the oligomer sample recovered a small amount of structure after cooling down (Figure 3.10B, blue line), partially resembling the profile of the monomer. Indeed, two invaginations could be observed, similar to the combined profile of the AtVDAC1 monomer, with the exception of the minima observed. This might be due to the difficulty of the multiple beta sheets to properly fold upon denaturation as opposed to a small alpha helix.

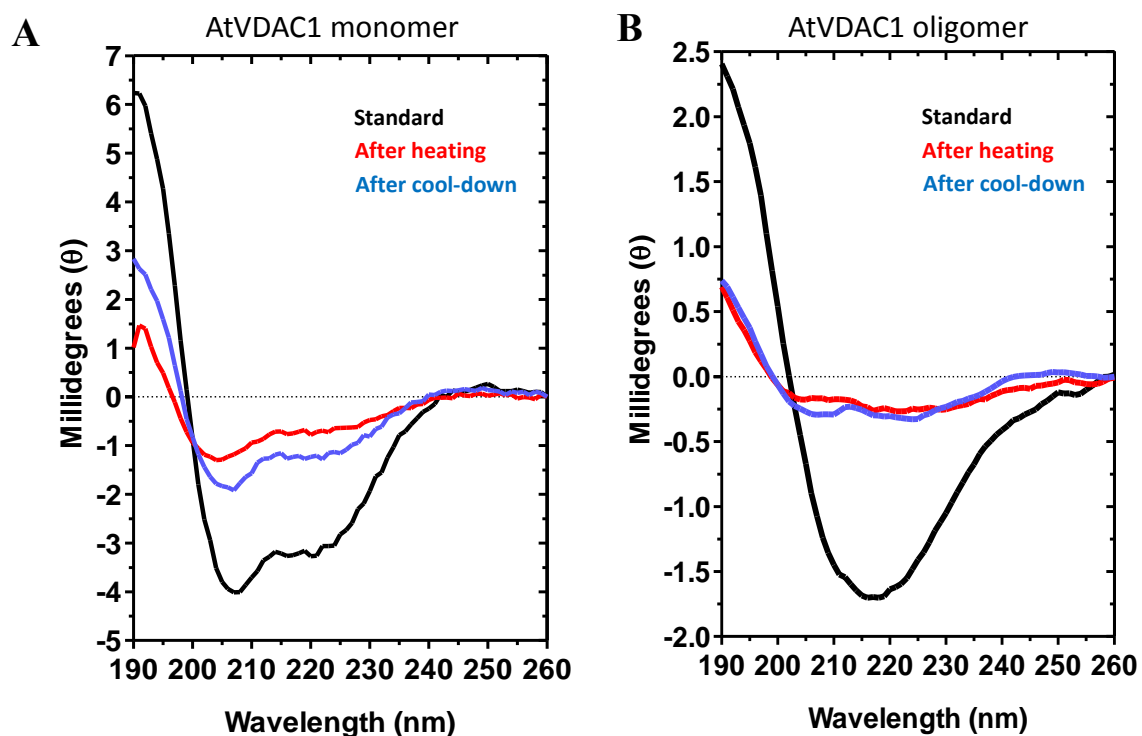


Figure 3.10 Heat denaturation profile of AtVDAC1 samples. (A) CD spectra of AtVDAC1 monomer (collected 18 mL after injection on SEC) at different temperature. Standard (20°C) measurement, denatured (90 °C) and measurement after cooling down to 20 °C are represented as a black, red and blue line respectively. (B) CD spectra of AtVDAC1 oligomer (collected 16 mL after injection on SEC) at different temperature. The same colouring scheme was used as in (A). All experiments were performed at a scanning speed of 40000 counts per seconds.

3.7. Functional characterization of AtVDAC1 by Planar Lipid Bilayer: Electrophysiology

3.7.1. Introduction to Planar lipid bilayer assay

Planar lipid bilayer assays or Black lipid membrane (BLM) assays, together with patch-clamping are electrophysiological techniques designed to evaluate physical properties and characteristics of ion transport/diffusion (Hanke and Miller 2008). All methods enable the characterisation of the gating behaviour of single channels. BLM, specifically, permits the study of gating properties of purified complexes in a well-controlled artificial lipid environment (Hanke and Miller 2008). Additionally, such techniques enable the investigation of direct effects of chemicals and enzymes on the channel's gating behaviour, while excluding possible indirect effects stemming from the presence of regulatory proteins under native/*in vivo* conditions. A description of a typical BLM setup has been described in section 2.6.2.

Typically, an electrophysiology experiment is performed by monitoring the transport rates of ions across membranes through ion channels. The rate of transport is measured as an ionic current (recorded in pA). Potentials/voltages, or membrane potentials (V_m ; in mV) can be generated across the membrane either electrically (e.g. by a battery with electrodes on either side of the membrane) or chemically by asymmetric distribution of ion concentration in solution. Recorded currents can then be analysed to characterise various parameters of the open and closed states of the ion channel under experimentation, such as their currents, their population distribution (one to multiple closed states), their conductance, and their dwell times (Maher and Allen 2018).

3.7.2. Electrophysiological characterization of AtVDAC1

Experiments were conducted at The University of Brighton, under the supervision of Dr Marcus Allen. Two chambers (or a lipid bilayer cups) for bilayer formation (Warner Instruments chamber BCH-13A and cup CP13A-250) were connected via potassium chloride (KCl) agar bridges and silver/silver chloride (Ag/AgCl) electrodes to the amplifier head stage. The amplifier used (Warner Instruments PC-501A) facilitated the detection of bilayer recordings and single channel currents were digitised using an analogue to digital converter (CED micro1401 MkII), controlled by single channel analysis software (WinEDR®, University of Strathclyde, UK).

The lipid bilayer was prepared using a 1:1 mixture of POPE (1-Palmitoyl-2-Oleoyl-sn-glycero-3-phosphoethanolamine, Avanti Polar Lipids®) and POPS (1-Palmitoyl-2-Oleoyl-sn-glycero-3-[phosphor-L-serine], Avanti Polar Lipids®) resuspended in N-Decane. A small volume (1 to 2 μL or 7.5 to 15 μg) was applied on the aperture (or pinhole, 200 μm wide) between the *cis* and *trans* chambers and the buffer (10 mM Tris-HCl (pH 7.4), 150 mM KCl, 50 mM CaCl_2) was added on each side of the bilayer. The correct elevation of the membrane was controlled through the absence of current across the chambers, and its limits were tested via mixing the solution while monitoring its capacitance. Because of mixing, the membrane size would decrease until reaching a breaking point (White and Thompson 1973). Experiments were carried out using the thinnest possible bilayer (just before that breaking point was reached).

A few microliters of AtVDAC1 protein (1.15 mg/mL) resuspended in DMPC (1,2-Dipalmitoylphosphatidylcholine) was applied to the *trans* chamber. The correct insertion of the porin into the bilayer was monitored on-screen by applying positive and negative potentials across the membrane (-40 and +40 mV). A current could be measured once the porin was properly incorporated, and its opening or closure was monitored at various membrane potentials.

Observations were made quickly to assess the stability of the porin inside the bilayer using membrane potentials ranging from -100 mV to +100 mV (Figure 3.11).

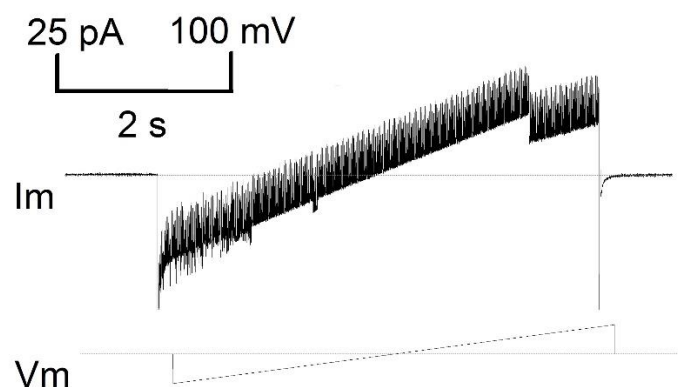


Figure 3.11 Voltage ramp experiment of a single AtVDAC1 channel reconstituted on a POPE/POPS planar bilayer. Increasing voltages (V_m) ranging from -100 to +100 mV were applied across the bilayer in 10 mM Tris/HCl (pH 7.4), 150 mM KCl, 50 mM Ca^{2+} . Currents (I_m) resulting from AtVDAC1 ion gating were recorded in pA.

Unfortunately, the current was highly unstable below -40 mV and above +40 mV, despite the porin displaying activity in all range of voltages applied. Consequently, experiments were generally performed between -40 and +40 mV membrane potentials. Mostly, the number of channels inserted into the bilayer needed to be kept to a minimum to prevent bilayer disruption. To further maintain the bilayer integrity, the DMPC-AtVDAC1 liposomes were filtered using two Hamilton gas tight 200 μ L syringes coupled together by a two R nut prior to the assay. Conventional methods such as mixing (with a vortex), sonication or freeze-thawing did not prove as efficient. Filtering improved the effectiveness of AtVDAC1 insertion into the bilayer and facilitated recording of measurements up to an hour.

Following the primary observation of the data collected on AtVDAC1 via BLM, gating events were detected using WinEDR® software analysis tool. In essence, the software can automatically detect events by setting a predefined threshold and defining an initial opening conductance (open state S_0). Following the detection, parameters such as the average current (in pA), the voltage applied (in mV), and the dwell time (in seconds) were extracted for each opening and closure event.

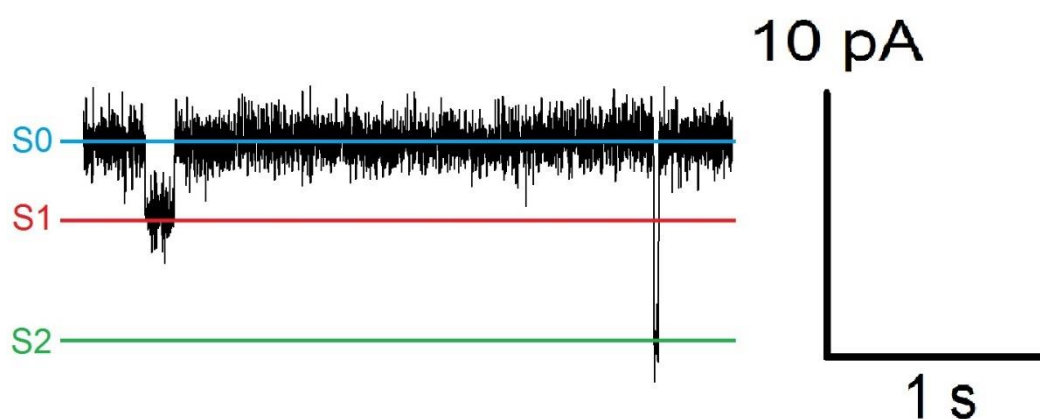


Figure 3.12 Representative recordings of single AtVDAC1 channels reconstituted on a POPE/POPS planar bilayer at 40 mV. Three different currents corresponding to three different states (1 open and two closed states) were observed for the inserted AtVDAC1 channel in the planar bilayer in 10 mM Tris/HCl (pH 7.4), 150 mM KCl, 50 mM CaCl₂) The open S0 and the closed states S1 and S2 are indicated by a blue, red and green line.

Interestingly, different closed states could be identified since they displayed obvious differences in these parameters (Figure 3.12). At least two different closed states could be identified (S1 and S2; Figure 3.12) shaping the gating of AtVDAC1. Each of these states exhibited unique current signatures with variable opening times. More specifically, the S1 and S2 states conducted currents of approximately 80 % and 50 %, respectively, with respect to the fully open state S0 (Figure 3.12, blue). This specific pattern of closure confirmed the identity of the channel, since this behaviour was already characterized in other VDACs such as the human hVDAC1 (Engelhardt, 2007) (Engelhardt, Meins et al. 2007) or more recently the mouse VDAC mVDAC1 (Mertins, Paskis, 2012) (Mertins, Psakis et al. 2012).

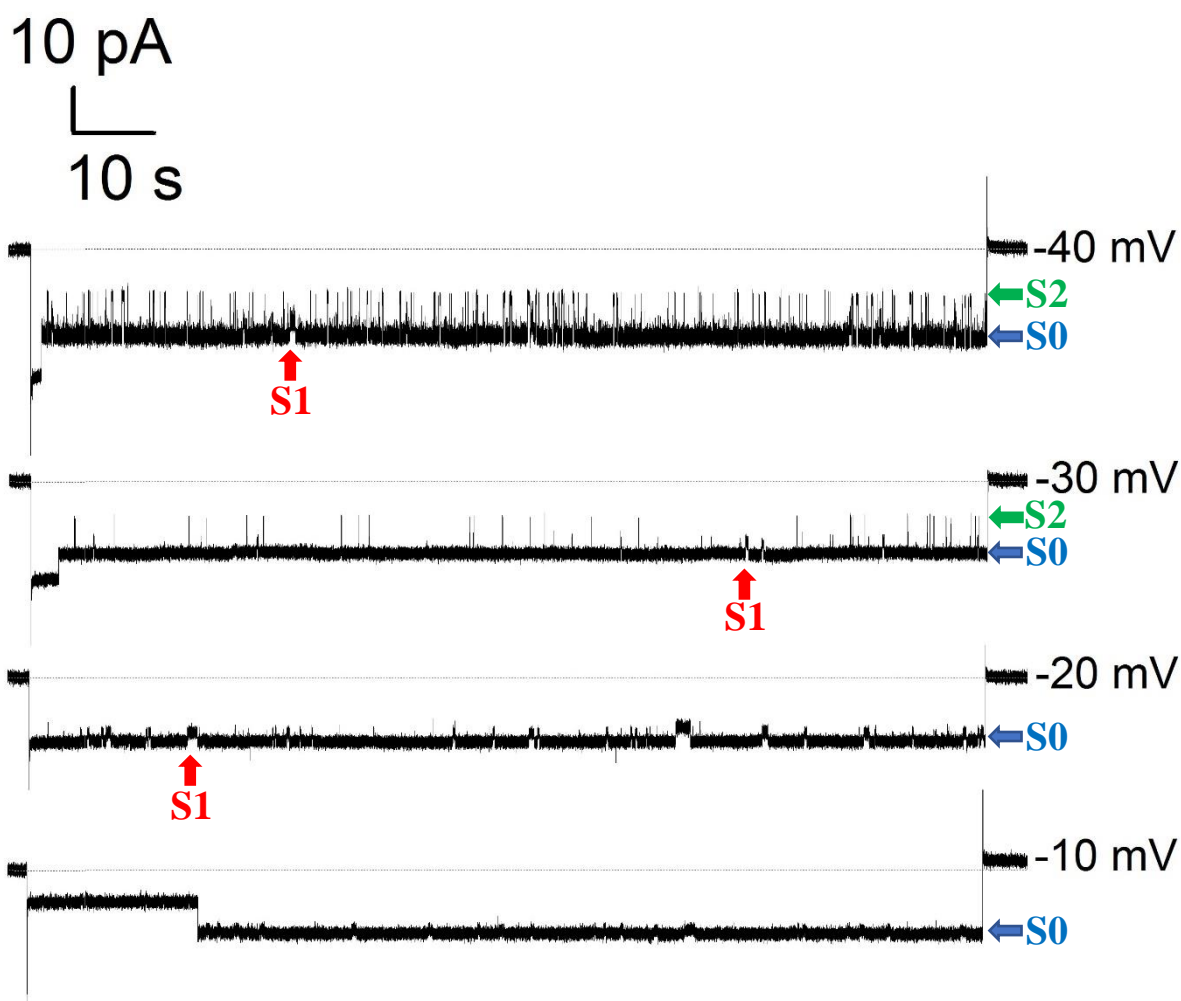


Figure 3.13 Typical BLM recordings of single AtVDAC1 channels reconstituted on a POPE/POPS planar bilayer. The protein (1.15 mg/mL) was inserted into the bilayer in 10 mM Tris/HCl (pH 7.4), 150 mM KCl, 50 mM Ca^{2+} . Currents measurements (in pA) were recorded for 100 seconds at four different voltages (-40, -30, -20 and -10 mV) in WinEDR® software. The open state S0 and the two closed states S1 and S2 are indicated blue, red and green arrows.

A typical BLM profile for the ATVDAC1 channel at different applied voltage (-40 to -10 mV) using the WinEDR® software is shown in Figure 3.13. Generally, the overall frequency of gating increased with the voltage applied across the membrane (Figure 3.13). This was reflected by an increasing number of channel opening and closing events at higher voltages (Figure 3.13, -40 mV) compared to lower voltages (Figure 3.13, -30 mV). A change in the duration and conductance of the closed states was noticeable, and evident when comparing traces at -20 and -30 mV (Figure 3.13, -30 and -20 mV, S1

state). Furthermore, occupancy of the closed states varied with applied voltage. For example, S2 states were mostly absent below ± 20 mV (Figure 3.13, -20 mV).

Finally, based upon previous observations on VDAC channels (Mertins et al. 2012), intermediate open states were identified most often at the beginning of the recording (Figure 3.14), and generally resulted from reverse potential application between the different voltage steps. These states can be described as transitional open states of higher conductance (black arrow), of generally few seconds (up to 20 seconds at lower voltages, below ± 20 mV).

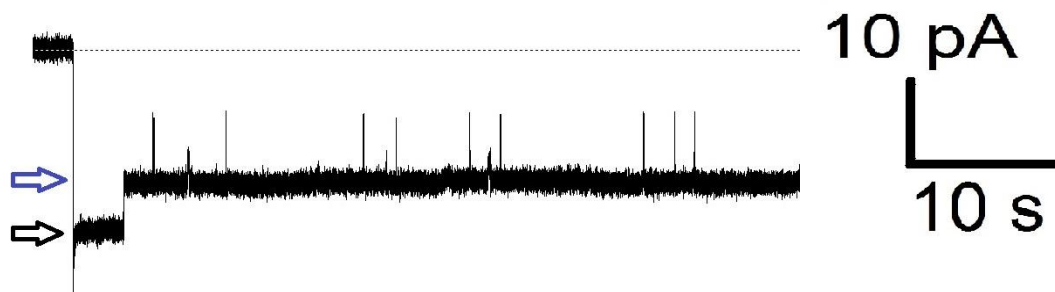


Figure 3.14 Intermediate open states of AtVDAC1 channel. First 40 seconds recordings of AtVDAC1 channel at -30 mV in a POPE/POPS lipid bilayer in 10 mM Tris/HCl (pH 7.4), 150 mM KCl, 50 mM Ca^{2+} . A transitional state (black arrow) can be observed at the beginning of the voltage pulse, preceding the “normal” opening state (blue arrow).

Using Ohm’s law (equation 3.1), the relationship between Voltage applied and current recorded can be examined to further understand the porin’s symmetric (or asymmetric) gating behaviour.

$$G = \frac{1}{R} = \frac{I}{V}$$

Equation 3.1 Ohm’s Law. The conductance G (in Siemens S) is the reverse of the resistance R (in Ohm Ω) and is defined by a relationship between current I (in Amperes A) and voltage V (in Volts V).

The different currents recorded were plotted against the applied voltage (Figure 3.15) for both closed states (S1 and S2) as well as the open state (S0). Over short periods of applied voltages (10 seconds per voltage), all three states displayed symmetric behaviour for their current recorded (Figure 3.15A). However, more asymmetric gating events were observed when exposing the porin for longer period of

time at specific membrane potentials (Figure 3.15B). This was mainly due to the appearance of intermediate states at longer exposure times as opposed to short bursts of 10 seconds. Therefore, the resulting graph (at longer voltage) resembled a kinetic curve, with linear behaviour at negative voltages, and logarithmic behaviour at positive voltages, indicating a probable outward rectification of the channel.

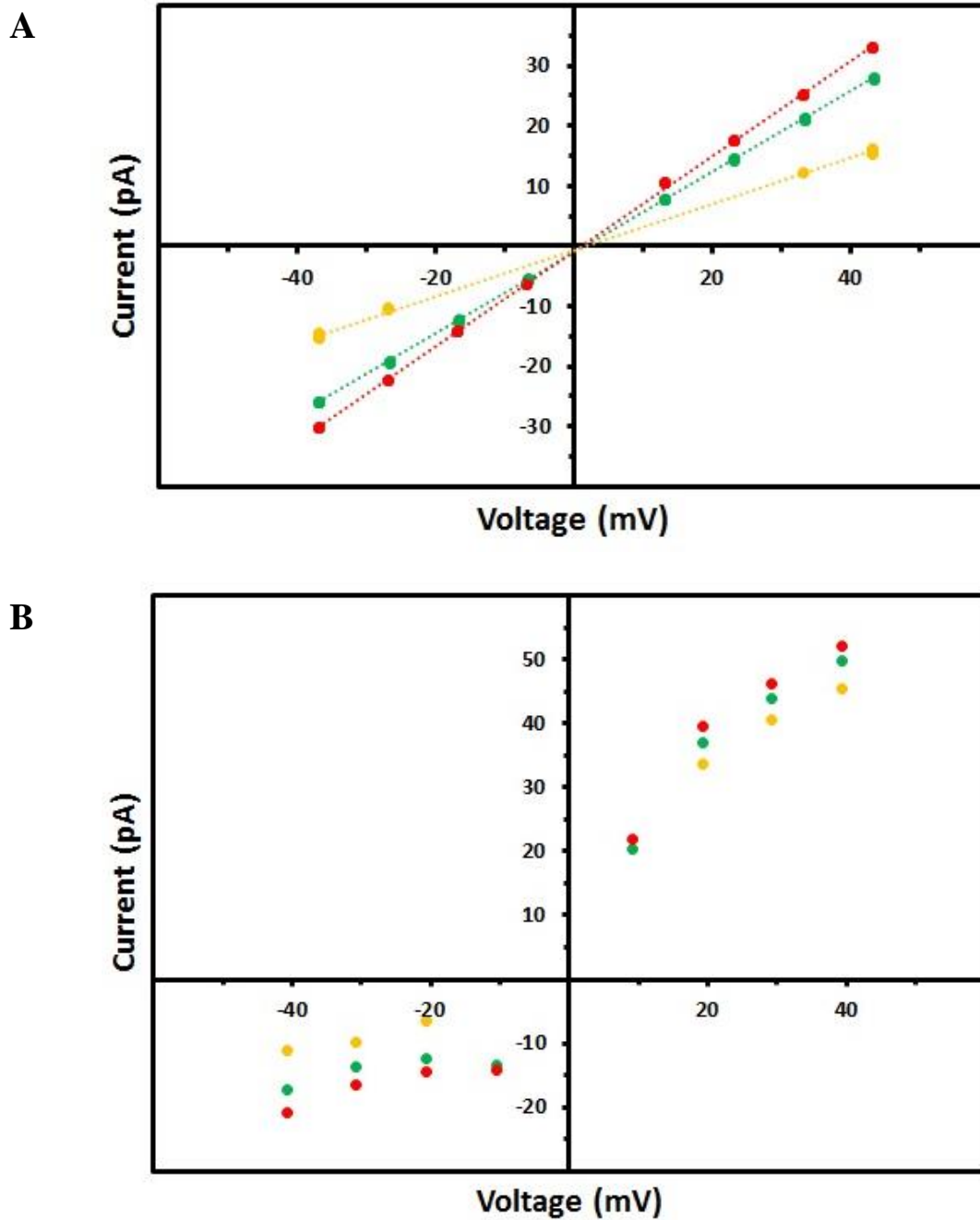


Figure 3.15 I/V (Ohm) plots used for the determination of the conducting AtVDAC1 states. Currents for the AtVDAC1 channel (in a POPE/POPS lipid bilayer in 10 mM Tris/HCl (pH 7.4), 150 mM KCl, 50 mM CaCl₂) were recorded for 10 seconds bursts (**A**) or 100 seconds (**B**) bursts at different voltages. The two observed closed states S2 (yellow) and S1 (green) as well as the open state (red) are represented. Recording and detection of gating events was performed using WinEDR® software.

Since apparent correlations between current and voltages were identified (Figure 3.15), conductance values were calculated for each opening and closure of the channel. The analysis of the occurrence of individual conducting states was performed in MagikPlot®, as WinEDR® package offered a limited panel of graph. Conductance values were sorted by how often they occurred during the gating events. The resulting histogram (Figure 3.16, in light blue) confirmed the previous observations made on the raw data. Indeed, at least two clear closed states, corresponding to the identified S2 state (yellow line) and S1 state (green line) of the channel, as well as the fully open state S0 (red line) could be fitted with gaussian curves. The combined curve (black dashed line) residual R^2 (or goodness of fit) was calculated to be 0.9243, thus explaining most of the variance associated with this model.

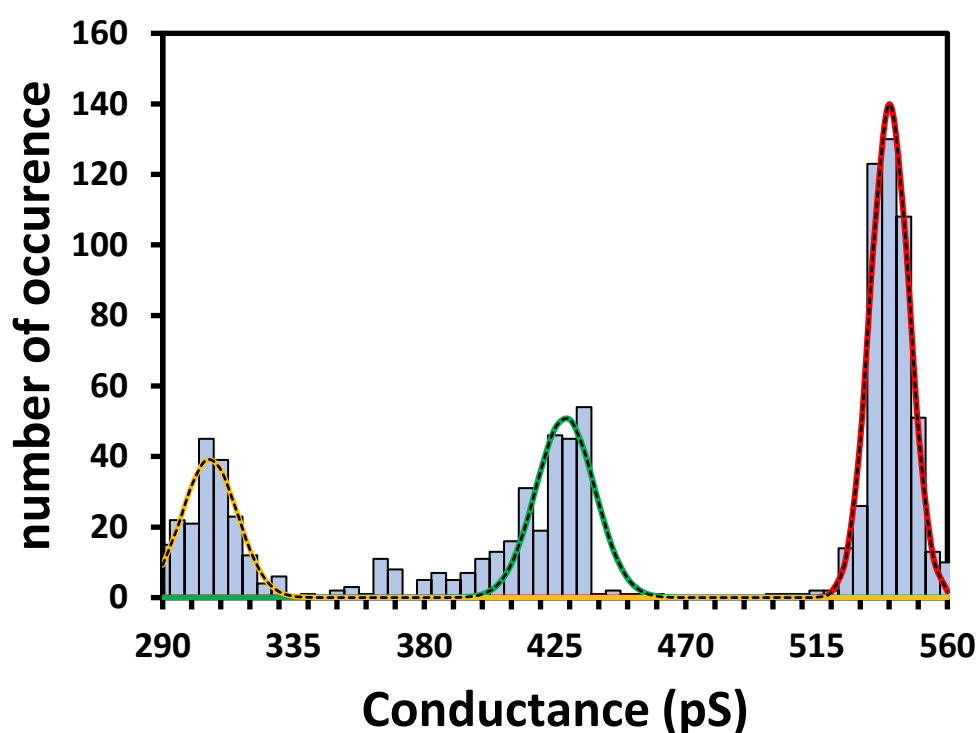


Figure 3.16 Overall conductance profile of AtVDAC1 channel. Combined graph of AtVDAC1 conductance measurements (light blue histogram) with the Gaussian fit for the closed states S2 (yellow line) and S1 (green line) as well the open state S0 (red line). The combined fitting model (black dashed line) residual R^2 was calculated to be 0.9243 ($N=960$), and the conductance for S2, S1 and S0 were established at 306,17 pS (± 1.49), 428.55 pS (± 1.3) and 540.16 pS (± 0.35) respectively.

Although this initial fitting model was deemed acceptable ($R^2 > 0.9$) when all states were considered, the total variance was not fully explained (ideally $R^2 > 0.99$). This was visually obvious for the S1 state as the single Gaussian fit lacked smoothness (Figure 3.16, green line), since the distribution potentially comprised additional sub-states. Further analysis was performed on the closed states only to further understand the distribution of possible sub-states under S1. When only the closed states were considered an initial single Gaussian fit analysis (Figure 3.16) covered 72 % of the data ($R^2 = 0.7231$). However, the fit with two additional Gaussians, resulted in a better fitting curve (Figure 3.17, black dashed line) with greater coverage ($R^2 = 0.9195$).

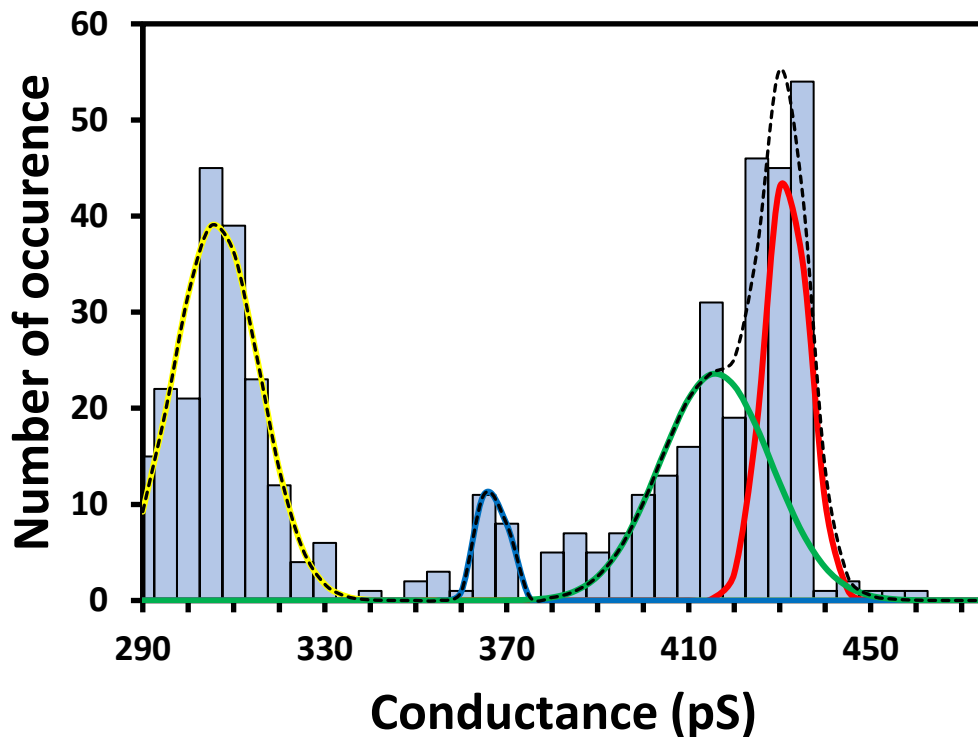


Figure 3.17 Conductance profile for the closed states of AtVDAC1 channel. Combined graph of AtVDAC1 conductance measurements (light blue histogram) with the gaussian fit for the closed states S2 (yellow line), S1a (red line), S1b (green line) and S1c (blue line). The combined fitting model (black dashed line) residual R^2 was calculated to be 0.9195, and the conductance for S2, S1a, S1b and S1c were established at 306.17 pS (± 1.13), 431.57 pS (± 0.81), 415.93 pS (± 7.1289) and 366.92 pS (± 1.92) respectively.

As advised, when considering multiple series, an ANOVA test was performed on the data series and confirmed ($p = 0.0087$, $N=960$) the significance of the model. Additionally, T-Tests were performed to ensure the statistical relevance of this model by comparing the sub-state variances. Results are regrouped in Table 3.3.

Table 3. 3 Statistical analysis of ATVDAC1 closed states.

State	Conductance (pS)	P value (T-test) for S1a	P value (T-test) for S1b	P value (T-test) for S1c
S2	306,17 (± 1.13)	>0.001	>0.001	>0.001
S1a	431.57 (± 0.81)		0.042	0.028
S1b	415.93 (± 7.1289)			0.039
S1c	366.92 (± 1.92)			

Conductance (in pS) was calculated for each state as well as their standard deviation. Series for each state were compared to each other using Student T-test. A p value > 0.05 is considered significant.

The S2 ($N=187$) state was not affected at all during this additional analysis, as reflected by the p values when compared to those of each sub-state. Sub-state S1c ($N=26$) and S1a ($N=151$) had the most significant difference amongst the S1 states, albeit their p values were overall relatively close. Unfortunately, the low number of events recorded for these sub-states greatly affected the statistical outcome. Further experiments are needed to strengthen the statistical relevance of the fit for the S1b ($N=114$) and S1c states.

3.7.3. Determination of dwell times between AtVDAC1 conducting states

Interestingly, S1 and S2 states had comparable occurrences (Figure 3.17) despite the primary observations made on the raw data (Figure 3.13, -40 and -20 mV), suggesting a bias possibly toward S2 state at higher voltage, and certainly towards S1 state (or sub-states) at lower voltages (below ± 20 mV). Consequently, dwell times were investigated for the S1 state at -40 and -20 mV (100 seconds pulse each), both of which had extremely different profiles. The S2 state, although present at -20 mV, was not identified often enough to guarantee a significant relevance for this comparative analysis. This confirmed the early suggestions of population bias toward S2 state at lower voltages, as opposed to the relatively similar distribution of S1 and S2 closure events at -40 mV (Figure 3.13).

Dwell times for the S1 AtVDAC1 states depended on the applied voltage and/or its duration. Noticeably, the S1 states were populated at short pulses of high voltages, e.g. -40 mV (Figure 3.18, orange dots; mostly below 1 ms). In contrast, long pulses (of half a second to one or two seconds) of lower voltages, e.g. -20 mV increased dwelling time at the S1 state (Figure 3.18, grey dots).

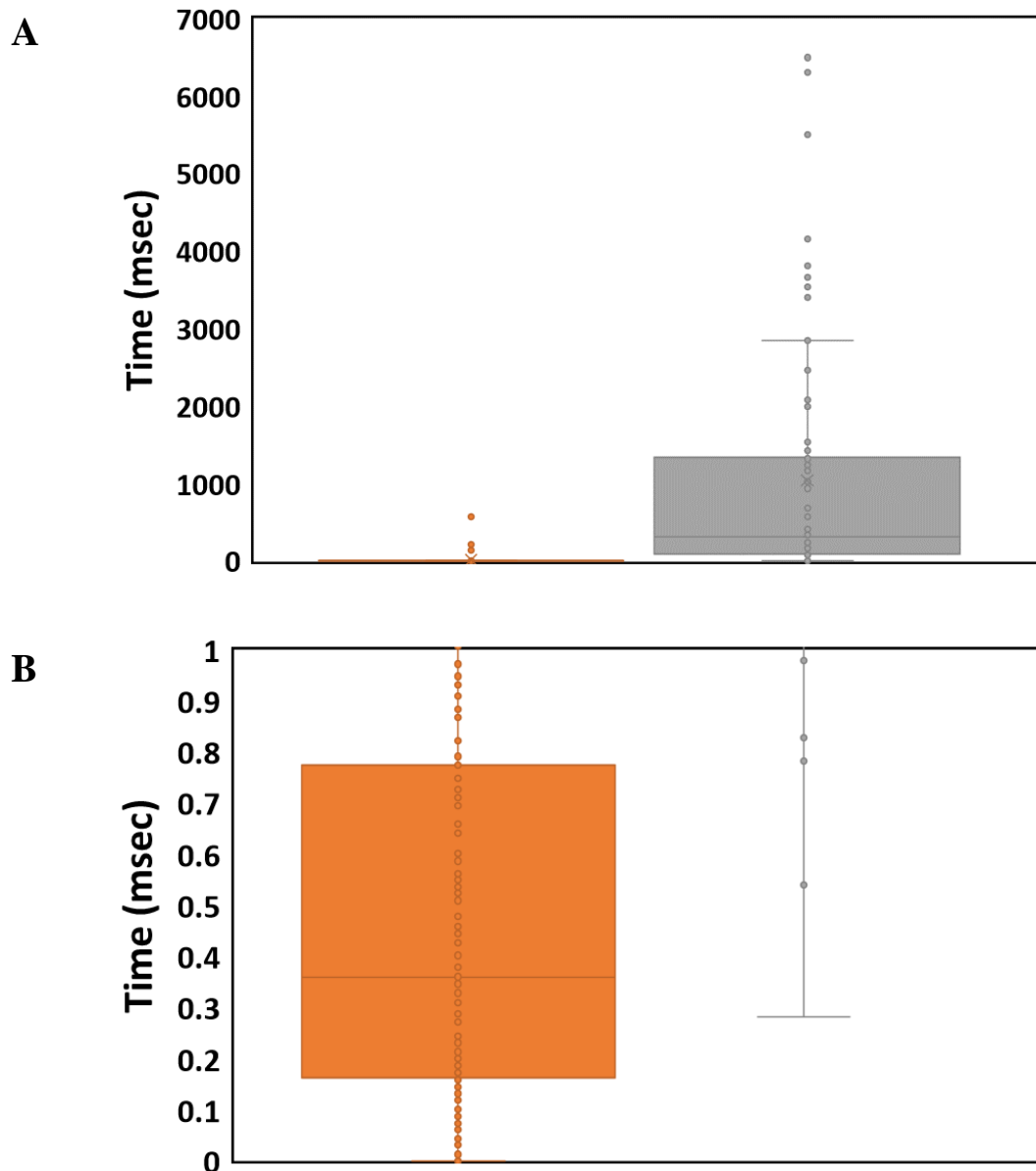


Figure 3.18 Analysis of S1 dwell times at -40 mV and -20 mV. Graph representing the distribution of the dwell times for the S1 state of the AtVDAC1 channel at -40 mV (orange) and -20 mV (grey). The median value was calculated to be 0.3 and 305 ms at -40 mV and -20 mV respectively. For convenience the same graph was shown at two different scales, from couple of seconds (**A**) to 1 millisecond (**B**).

Table 3.4 Probabilities of AtVDAC1 opening and closure channel at -40 and -20 mV. The sum of each dwell time was calculated for the open state S1 and the closed state (S1+S2). Results are presented as a percentage of the total recorded time.

State	-40 mV	-20 mV
Open	91.37 %	90.57 %
Close	8.63 %	9.43 %

To further examine possible voltage dependency of gating transitions, the open and closed probabilities for the channel's gating were determined (Table 3.4). Surprisingly, the channel was closed for a longer period at -20 mV. Although the difference in percentage of closure between -20 and -40 mV was only 0.80 %, the perspective of having a 110 % longer (9.43 % against 8.63 %) closure despite a twice lower voltage applied (-20 mV against -40 mV) greatly amplified the significance of this small variation.

Considering the activity of a channel is greatly dependent on the number of events, this last result unveiled a more complex gating behaviour for the AtVDAC1 channel (in a POPE/POPS lipid bilayer in 10 mM Tris-HCl (pH 7.4), 150 mM KCl, 50 mM CaCl₂). Indeed, the increase in number of events observed at higher voltages should theoretically involve a longer closure of the channel, unless additional mechanisms are involved. Further investigation was undertaken to fully understand this behaviour and characterize the channel's gating activity further. Since the activity is usually described as function of the current recorded and the dwell time, the total charge (in Coulomb) can be calculated using the relationship in equation 3.2.

$$Q = I \times t$$

Equation 3.2 Definition of a coulomb. A coulomb can be defined as the charge (Q) transported by a constant current (I) of one ampere in a time (t) of one second.

Moreover, VDACs are known to display a preference for cations (Colombini, Blachly-Dyson et al. 1996) (see section 1.7.1). Therefore, the variation of current between the closed and the open state was

calculated for each gating event at -20 and -40 mV. Values were then multiplied by their corresponding recorded dwell times following the relationship in Equation 3.2 and summed up together. The calculation of the area covered by the closure event would provide information on the total variation of charge (between the open and the closed states) and could be used as a measure of the “power of closure”. Theoretically, the number of ions passing through the channel could also be calculated using the elementary charge of an electron e^- (1.602×10^{-19}). However, the closure of the channel is characterized by a decrease in affinity for anions, an increased affinity for cations. Although largely in favour of cations in the closed state, this ratio between anions and cations should be included in the calculation of the number of ions. Hence, the use of the total charge or total number of charges Q can be useful in comparing similar states at different voltages.

Table 3.5 Total variation of charge for the AtVDAC1 channel. Variations of current were calculated between the open state and the closed states at -40 and -20 mV and multiplied by their corresponding dwell time.

Parameters	-40 mV	-20 mV
Total variation of charge (in pC)	67.21	168.57

The result was astounding as the total variation of charge was more than two-fold at -20 mV than -40 mV (Table 3.5). Despite the lower applied voltage, the lower number of events (Figure 3.13, -20 mV), the lower current recorded (Figure 3.15A), the displacement of charge generated by the closure event was greater at -20 mV. In other words, the surface covered by the closed states was greater at -20 mV than -40 mV, which was unexpected since the difference in activity (number of events) was overwhelming (see Figure 3.13).

In conclusion, the AtVDAC1 channel exhibited at least two closed states, namely S2 and S1, with conductances of 306.17 pS (± 1.49) and 428.55 pS (± 1.3) respectively. The channel exhibited its highest activity at -40 mV and was highly unstable at higher voltages. In addition, the channel exhibited a symmetric behaviour on Ohm plots over short voltage pulse (10 seconds) but became highly asymmetrical when exposed for 100 seconds, suggesting an outward rectification (Hedrich, Moran et al.

1995). Furthermore, a heterologous distribution of the closed states could be observed depending on the applied voltage, with a shift toward the S1 state at lower voltages. This led to a surprising finding as the S1 state (46:1 against the S2 state at -20 mV) was sufficiently present at low voltages to provide a comparable if not higher total power than all other closed states at -40 mV, despite greater number of closure events at higher voltages (6.5 fold).

3.8. Discussion

3.8.1. Heterologous production and purification of AtVDAC1 protein in *E.coli*

The first step required to facilitate the regular production of adequate amounts of protein for downstream applications was the optimization of the gene expression.

The successful cloning of AtVDAC1 gene into the expression plasmid pET-20b(+) as well the preliminary work on the expression of the AtVDAC1 protein was performed by Felix Brademann at The University of Marburg. This set the ground for the use of a robust and reproducible expression system, suitable for all the proteins produced in this work. Although initial over-expression attempts utilised IPTG, we quickly reverted into using auto-induction. This decision was not only based on practicality, but on efficiency, as well, since it increased the overall yield of protein by at least a factor of 5. Indeed, as the OMP9 *E. coli* cells lacked most porins required for their survival, their growth rate was slower than other experimental strains (40 minutes to 1 h per generation). Thus, overnight shaking in a highly rich media instead of a 4-hour induction was preferable, to ensure adequate cell densities.

The washing of inclusion bodies and their concentration yielded around 300 to 500 mg of partially folded protein per two litres of cell culture. Also, the washing of inclusion bodies served as a pre-purification step due to the removal of major contaminants from the overall mixture.

Protein refolding yields are generally low (Yamaguchi and Miyazaki 2014), often % less than 40 % (Zhi, Landry et al. 1992), leading to great losses of total protein material, particularly for membrane proteins. In consequence, detergent choice, as a refolding aid, is critical in ensuring adequate refolding yields. An initial screen was performed by Felix Brademann as well and helped to determine LDAO as the best detergent (results not shown). The additional additive screen described in this work (section 3.3.1), around the refolding buffer used in the first dilution step of the *in vitro* refolding, guaranteed the best condition for minimizing protein loss during the step. Time and resource constraints outweighed the usefulness of further additive screens. Nevertheless, alternative methods of high-throughput screening combined with Size exclusion-High Performance Liquid Chromatography (SEC-HPLC), may prove more useful in probing aggregate concentration (Hong, Koza et al. 2012).

The capture of the refolded AtVDAC1 protein via Ion Exchange Chromatography proved difficult and required further optimisation. Despite providing reasonable purification yields (overall around 10 %), the Fractogel® EMD SO3 and Superdex75® solid support combination did not provide a clear separation of the monomer from contaminants. It seemed that these contaminants interacted strongly with the Ion exchange chromatography matrix and were carried over in downstream experiments. The presence of LDAO in the mixture can explain their reluctance to be excluded as they might be embedded or encapsulated in micelles (Hayashi and Ikeda 1980, Thiyagarajan and Tiede 1994, Hiller, Garces et al. 2008, Hiller and Wagner 2009, Raschle, Hiller et al. 2009, Yu, Raschle et al. 2012). Luckily, most of these contaminants degraded faster than the AtVDAC monomeric protein over time, and the overall high concentration of the AtVDAC1 monomer ensured purer preparations.

Due to the propensity of VDAC to oligomerise and/or aggregate, large molecular weight species were completely excluded from the Superdex75®. In consequence, for successive gel-filtration experiments, Superose 6 Increase® was used as it was shown to successfully resolve membrane protein oligomers and/or aggregates (Hall and Huang 2012). Overall, the protein generally eluted as two relatively broad peaks around 16-17 mL to 18-19 mL, or 27-36 kDa to 62-70 kDa according to the calibration curve (section 3.5). The relatively large size of early-eluting-species suggested the protein could form oligomers. The confirmation by SDS-PAGE of the identity of the main protein eluting (AtVDAC1) within that volume supported that hypothesis. The presence of LDAO micelles, surrounding the protein species, would further impact on the total size of the complex. LDAO is known to form micelles of 17 to 21 kDa (Herrmann 1962, Strop and Brunger 2005). However, the larger size (above 60 kDa) compared to AtVDAC1 embedded in a LDAO micelle (29 + 17) suited more the oligomerization scenario (section 3.5). Besides, dilution of the protein led to a shift towards the second peak (believed to be associated with the monomer), suggesting equilibrium monomer-oligomer equilibrium (Josse, Ebel et al. 2002). This negated the possibility of a slightly larger micelle, as no variation in size was ever observed which does not fit the relatively dynamic behaviour of detergent micelles in general (Garavito and Ferguson-Miller 2001).

The major breakthrough came when a new set of solid support, known as the HiTrap 5 mL SP XL, was tested and did improve the yield of monomer purified, as well as allowing more concentrated samples to be subjected to size exclusion chromatography. Contrary to HiTrap SP XL, the increased binding capacity of the the Fractogel EMD SO3 (M), stems from the cross-linked poly-methacrylate, a long linear polymer chain where the ion exchanger groups are bonded, offering more binding sites (A. Sewell 2010). This was probably the reason additional contaminants were taken up, thus making the HiTrap a better choice for the purification of untagged proteins.

Obviously, the absence of a conventional purification tag such the His-tag required the protein to be purified using ion exchange chromatography rather than a conventional affinity-chromatography step. However, on occasion the presence of a purification tag was shown to interfere with both the affinity purification and the functionality of proteins studied (Carson, Johnson et al. 2007). Although optimisations around the solid support used for ion exchange chromatography where time consuming, it facilitated better purification and refolding yields, increasing from 10 % to 30 % overall.

3.8.2. Structural characterisation of AtVDAC1 by Circular Dichroism (CD)

The first structural experiment conducted on AtVDAC1 was the definition of its secondary structure content by Circular Dichroism, following its purification by size exclusion chromatography. For this assay, two different fractions, collected at 16 and 18 mL from a Superose6 Increase® purification (section 3.5) and subjected to CD experiment (section 3.6). These two different fractions eluted at specific volumes, that were in accordance with a size of a putative AtVDAC1 monomer (around 30 kDa) and an oligomer (around 60 kDa). Thus, it was possible to investigate the effect of oligomerization on the secondary structure of the AtVDAC1 channel.

Primary analysis of the CD spectra at 20 °C showed a typical beta barrel rich protein profile for the oligomer, whereas the monomer displayed a combination of beta barrels with a small alpha helical content. The subsequent analysis using Dichroweb website and algorithms CONTINLL and CDSSTR (Lobley, Wallace et al. 2002, Whitmore and Wallace 2004) confirmed the observations made on the raw profiles. Indeed, both samples would exhibit similar structural content, composed mainly of beta barrels (36 to 42 %) and random coils (around 50 %), with a small alpha helical content (6.3 % to 9.5%). Again, the difference between the monomer fraction and the oligomer fraction showed an increased helicity in the monomer, or a decreased helicity in the oligomer, depending on the approach. The decrease in helicity in the oligomer could be explained by the overwhelming signal of the beta-barrels in this configuration. More likely, the presence of detergent is known to affect the CD signal, creating what is referred as the solvent shift effect (Casio and Wallace 1995, Chen and Wallace 1997, Miles and Wallace 2016). To support this hypothesis, a comparative Thin layer Chromatography was performed on AtVDAC1 oligomer and monomer fractions (see Appendix 9.5). Although the concentrations were too low to accurately measure the detergent concentration, a noticeable difference could be observed between the oligomer and monomer samples, suggesting a higher concentration of LDAO in the oligomer fractions. This is in accordance with our previous hypothesis, indicating a shift effect due to the higher concentration of LDAO in the oligomer samples. Consequently, the calculation of the NRMSD (normalized-root-mean-square deviation) by the Dichroweb webserver (Lobley, Wallace

et al. 2002, Whitmore and Wallace 2004), which is a measure of the statistical relevance of the model, yielded values above 0.1 for this sample, considered not statistically relevant.

Nevertheless, the structural determination of AtVDAC1 monomer fraction confirmed the correct refolding of the protein using the *in vitro* dilution, since it displayed typical content of a VDAC channel (see section 1.6), and CD spectra is in agreement with previous reports on *S.cerevisiae* scVDAC in 1% LDAO (Koppel, Kinnally et al. 1998). Interestingly, it seems the type of detergent, the pH and temperature can also influence the CD spectra, as illustrated by the increased helicity of VDAC in the presence of LDAO and its decreased helicity in Octyl-glucoside (OG) (Shao, Kinnally et al. 1996).

The heating cooling process indicated a great degree of denaturation for the monomer. Upon cooling, a small amount of structure is recovered, and the profile remained highly comparable to the unheated protein spectra (section 3.6 Figure 3.10). On the opposite, the oligomer displayed an almost complete loss of structure following heating, and barely any recovery upon cooling (section 3.6, Figure 3.10). Furthermore, the profile for the latter seem to include an alpha helical content, similar to the one observed for the monomer. This result was expected since the alpha helix is shorter and easier to refold than beta sheets (Vijayakumar, Vishveshwara et al. 1993). Finally, a small increase in the HT spectrum indicated a probable aggregation in both cases (see Appendix 9.7).

3.8.3. Functional characterisation of AtVDAC1 by Black Lipid Membrane (BLM)

AtVDAC1 was successfully incorporated into a POPS/POPE lipid bilayer, and the channel exhibited gating activity in 10 mM Tris-HCl (pH 7.4), 150 mM KCl, 50 mM CaCl₂ (section 3.7).

Ramp experiments allowed the characterization of the optimum conditions for recording the activity of the channel. A clear instability was observed when a current above 40 mV was applied, often leading to bilayer disruption. This result was surprising since the VDAC channel has been reportedly capable of sustaining voltages up to 100 mV (Colombini 1989, Colombini 2004, Tan and Colombini 2007, Colombini 2016). However, the different composition in lipids (POPS/POPE instead of POPC)(Renne and de Kroon 2018) as well as the lower concentration of salt used in these experiments (Böckmann, Hac et al. 2003) might contribute to the instability of the bilayer.

Typically, the channel opened and closed rapidly, displaying at least three conductance states. The open state denoted S₀ was identified with a conductance of 540.16 pS (± 0.35). Two closed states, referred to as S₁ and S₂, exhibited conductances of 428.55 pS (± 1.3) and 306.17 pS (± 1.49), respectively. The S₂ state conductance was around 60 % of that of the open state S₀, in accordance with previous findings (Colombini 1989, Tan and Colombini 2007, Mertins, Psakis et al. 2012, Colombini 2016).

Surprisingly, the S₁ state exhibited a relatively high conductance, corresponding to 80 % of the open state S₀. Different sub-states were potentially identified (S_{1a}, S_{1b} and S_{1c}), but insufficient data prevented the generation of statistically relevant models. Additional experiments could provide the necessary amount of gating events to strengthen the model. The difference in the conductance of S₁ and S₂ could be explained by the fact that the channel can act as a sensor, alternatively switching preference to calcium or potassium cations in its closed state (Pavlov, Grigoriev et al. 2005, Tan and Colombini 2007).

Overall, the electrophysiology of the AtVDAC1 channel, fitted the gating behaviour of previously characterised orthologues, concerning the unique partial gating of the channel and the diversity of its closed states and/or the intermediate states (Figure 3.12). Hence, this experiment was very successful at characterizing the main conducting state (S₀, S₁ and S₂) of the channel AtVDAC1.

Table 3.6 Famous VDACs Gating conductance.

Protein	Open state (nS)	Closed state (nS)	Salt concentration	Reference
mVDAC1	3.70±0.40	1.70±0.20	1 M KCl	Ujwal <i>et al.</i> , 2008
mVDAC1	3.94±0.04	2.61±0.01 (S1), 1.90±0.06 (S2)	1 M KCl	Mertins, Psakis, <i>et al.</i> 2012
hVDAC1	4.50±0.50		1 M NaCl	Shanmugavadivu <i>et al.</i> , 2008
hVDAC1	3.90±1.50		1 M KCl	Hiller <i>et al.</i> , 2008
NcVDAC1	4.0	2.0	1 M KCl	Popp <i>et al.</i> , 1996
AtVDAC3	0.500	0.2 to 0.65	100 mM/300 mM KCl	Berrier <i>et al.</i> , 2015
rVDAC	4.50		1 M KCl	Colombini <i>et al.</i> , 1989
rVDAC	0.48		0.1 M KCl	Colombini <i>et al.</i> , 1989
ScVDAC	4.5		1 M KCl	Colombini <i>et al.</i> , 1989
ScVDAC	0.45		0.1 M KCl	Colombini <i>et al.</i> , 1989
AtVDAC1	0.54	0.31±0.0049 (S2), 0.43±0.0013 (S1)	150 mM KCl	

The lower conductance reported in this study, between 0.3 and 0.54 nS, can be correlated with the lower concentration of salt used in the BLM buffer (150 mM), compared to previously reported conductances of VDAC channels (see Table 7.1). Indeed, experiments conducted at concentrations lower or equal to 150 mM KCl generally revealed conductances 10-fold lower than those reported at higher

concentrations of salt, namely 1 M KCl. A perfect example is illustrated by the yeast VDAC (ScVDAC), which exhibits a conductance of 4.5 nS at 1 M KCl, and 0.45 nS at 0.1 M KCl (Colombini 1989). Therefore, it is very likely that the AtVDAC1 channel's conductance would be higher at 1 M KCl.

Most importantly, both AtVDAC1 and AtVDAC3 channels (Berrier, Peyronnet et al. 2015) exhibited highly similar conductance values for their open and closed states, potentially confirming the conservation of the ion gating function amongst AtVDAC isoforms. Considering these two isoforms are both residing largely in the mitochondrion (section 1.5.3), this similarity is to be expected, contrary to AtVDAC2 and AtVDAC4, whose expression and sub-cellular localization differs from the previous two isoforms (Tateda, Watanabe et al. 2011). The slight differences in the values reported (Table 7.1) might either arise from the different methodology used (symmetric versus asymmetric salt concentration) or small evolutionary divergence between the isoform 1 and 3 from *A.thaliana*. AtVDAC1 is known to be ubiquitous and essential for plant survival whereas AtVDAC3 is not essential and is restricted to leaf tips of seedlings, shoot meristems, and anthers (Tateda, Watanabe et al. 2011). It is possible that AtVDAC3 expression is only upregulated under specific conditions, where its gating activity might favour a certain biochemistry. Further research on the role of AtVDAC1 gating in plants could help unveiling more precisely the role of AtVDAC3 by designing chimeric constructs of AtVDAC1 and AtVDAC3. The chimeric channels would behave differentially to the application of a current depending on their relative composition in AtVDAC1 and AtVDAC3. This type of study can broaden our comprehension of the gating phenomenon and ultimately enlighten us on the structures responsible for the modulation of the conductance states. Finally, the study of AtVDAC3 offered an interesting insight into the cationic properties of the closed states at low voltages, which were highly similar to the S1 closed state trace patterns showed for AtVDAC1 in this work. As mentioned previously, the sensing ability of the channel might dictate which type of ions will pass through (Pavlov, Grigoriev et al. 2005, Tan and Colombini 2007). Various BLM experiments could be designed to confirm this ability, and potentially attribute a state to a specific ion for AtVDAC1. The use of different cations or asymmetric salt solutions, to replace the calcium or the potassium ions, would be useful tools for this type of investigations. Furthermore, considering new plant tissues such as the tips of the roots, and young leaves

can't properly form without a decent concentration of calcium (White and Broadley 2003), it would be interesting to test whether any of the AtVDAC isoforms has a strong preference for calcium ions. For example, since AtVDAC3 is highly restricted to the leaf tips of seedlings, shoot meristems, and anthers (Tateda, Watanabe et al. 2011), possible variation in the sensing ability could be expected with AtVDAC1, which is expressed ubiquitously.

3.8.3.1. Comparison of the “power” of charge between -40 mV and -20 mV

Additional investigations of the S1 state gating at “low” (-20 mV) and “high” applied voltages (-40 mV) allowed a deeper comprehension of the AtVDAC1 channel’s activity. Mostly under-looked, the gating at voltages above -20 mV and below 20 mV lacks characterization and the VDAC channel is often deemed “most active” at 40 mV (Colombini 1989, Tan and Colombini 2007, Mertins, Psakis et al. 2012, Colombini 2016). In the case of AtVDAC1, at low voltages, the distribution of the closed states was directed toward long closure events of relatively high conductance (or low variation from the open state), as exemplified by the acquisition of S1 state. Surprisingly, the channel was closed for a longer period of time (Table 3.3) at -20 mV, despite a higher number of closure events at -40 mV.

Finally, the use of the total variation of charge between the open and closed states allowed quantifying the “power” delivered during a 100 pulse at both -40 and -20 mV (or indirectly, the number of ions/charges concerned by the closure event). This confirmed the channel was still exhibiting a comparable processing of charges across the membrane at both voltages.

Furthermore, this preference for the S1 state at -20 mV could be further explored by modulating the concentration or the composition of ions present in the solution. As mentioned above, the sensing ability and preference for a specific ion at specific voltage could unveil mechanisms of calcium uptake from the mitochondria, well known to mediate cell fate (see section 1.7.3). Finally, it would also be interesting to investigate whether any other VDAC channel might be exhibiting similar pattern using this parameter.

In the end, the different issues encountered such as the rectification observed at long voltage exposure (100 s) prevented the collection of significant amounts of data for positive currents. The use of different concentration of salt could help explore and understand this rectification process, as demonstrated for the class 1 porin (PorA) from *Neisseria meningitidis* (Cervera, Komarov et al. 2008).

3.8.3.2. Troubleshooting of BLM experiments on AtVDAC1 channel

In summary, the Planar Lipid Bilayer assay was a powerful tool, rapidly generating a great amount of data for the AtVDAC1 channel, reconstituted in DMPC and inserted into a POPE/POPS lipid bilayer in 10 mM Tris-HCl (pH 7.4), 150 mM KCl, 50 mM CaCl₂. Nevertheless, a great number of challenges had to be overcome to enable the production of quality data.

First and foremost, the AtVDAC1 reconstitution in DMPC, albeit successful, enabled the generation of large GVO proteoliposomes which proved difficult to homogenize using conventional methods such as freeze/thawing, sonication and mixing (Scotto, Goodwyn et al. 1987, Winterstein, Kukovetz et al. 2018). Consequently, the early experiments were heavily affected by large micelles fusing with the bilayer. Thus, lots of channels were inserted at once, often causing the membrane to fall apart almost instantly. The determining factor in improving the proteoliposome homogenization came from using two Hamilton gas tight 200 µl syringes coupled together by a two R nut. In fact, this instrument improved immensely the quality of the data generated and is worth mentioning as it is typically used in crystallography.

Once the preparative work was optimized, experiments were conducted as described above, and early observations had to be made to distinguish specific behaviours that might affect data processing. In particular, the asymmetry observed at longer voltage exposure prevented the capture of multiple batches of 100 seconds. The logarithmic trend led to a great instability in the lipid bilayer as for bigger micelles, which generally resulted in the loss of the membrane. This behaviour is typical of outward rectifiers, who display a preference in their response to the orientation of the current (Molleman, Thuneberg et al. 1993, Hedrich, Moran et al. 1995), a feature VDACs are known to exhibit (Tan and Colombini 2007). Although the composition in lipids can affect the channel behaviour, the use of POPS and POPE minimized this phenomenon, as opposed to anionic lipids such as phosphoinositides (Tucker and Baukowitz 2008).

Sporadically, porins would be inserted in opposite directions (Figure 7.1, green and blue arrows). Although being an interesting feature to explore, it affected relatively the quality of the data, as the open

state S0 would be a combination of both *cis* and *trans* channels working together. Hence, data had to be treated separately or simply discarded.

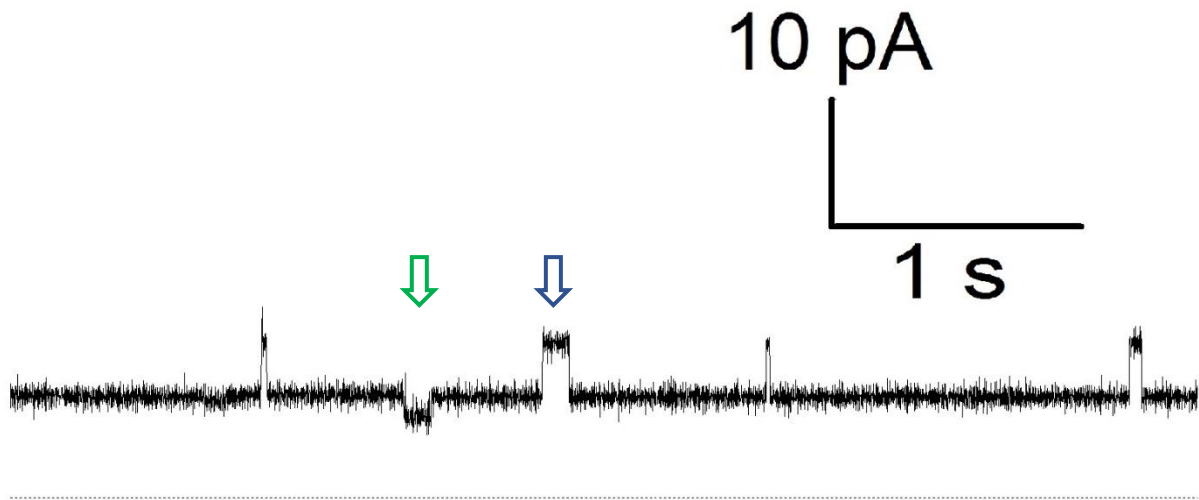


Figure 3.19 Example of AtVDAC1 channels in opposite directions. Two channels were inserted, in the direction of the current (green arrow) and in the opposite direction of the current (blue arrow). This is reflected by their closed states pointing in opposite directions. Fortunately, this phenomenon was relatively rare.

Another great challenge that needed to be resolved, was the correct detection of the gating events. The S1 state proved extremely difficult to correctly identify due to its close proximity to the open state conductance (around 80 % of the open state conductance). Data had to be scouted heavily and checked for the correct recording. Additional states had to be deleted manually to produce a final corrected signal (Figure 3.10, green line).

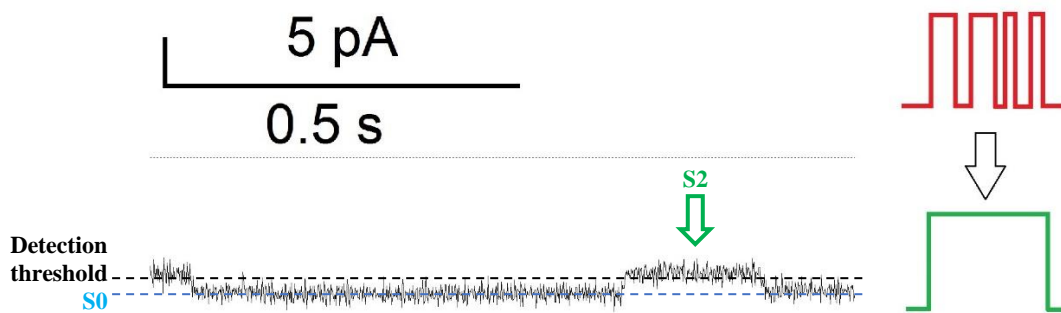


Figure 3.20 Repetitive issue in event detection of S2 state. Schematic representation of the refinement of the data obtained during the detection of gating events via WinEDR® software. As the S2 state was too close to the baseline and the detection threshold (dashed line), its initial profile looked odd (upper right, red line), and had to be readjusted by deleting the excess events (bottom right, green line).

The abrupt interruption of the recorded closure events above 440 pS (Figure 3.17 and 3.18) could be an additional consequence of the detection threshold being almost adjacent to the S1 state. Consequently, the lack of statistical relevance in the Gaussian models (section 3.7.2) is likely influenced by an incomplete Gaussian curve fit for the S1 state, due to the lack of closure events above 440 pS. Assuming the tail of the S1 Gaussian fit was absent, a broad Gaussian could be fitted and would potentially encompass both the S1a and S1b sub states.

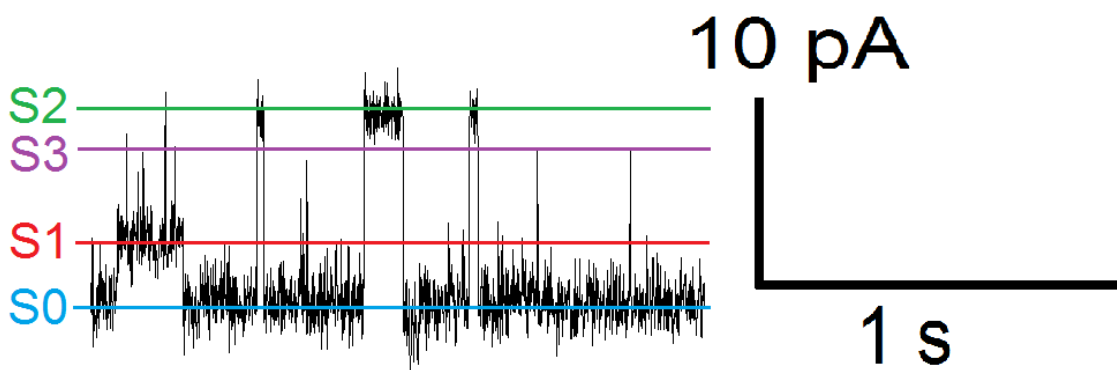


Figure 3.21 Representative recordings of single AtVDAC1 channels reconstituted on a POPE/POPS planar bilayer at -40 mV. Three different currents corresponding to three different states (1 open and two closed states) were observed for the inserted AtVDAC1 channel in the planar bilayer in 10 mM Tris/HCl (pH 7.4), 150 mM KCl, 50 mM Ca²⁺. The open S0 and the closed states S1 and S2 are indicated by a blue, red and green line. A potential third closed state named S3 is also represented.

The S1c states however, displayed strong statistical relevance despite the low number of counts compared to the other two states (section 3.7.2). an additional closed state of really short pulses (Figure 7.3; S3, in purple) can be found between S1 and S2 states, although rarely identified as previously mentioned. As a result, it will be called S2c (and not S3), until further data can strengthen the statistics.

Unfortunately, due to the limited time available for the electrophysiology work, effects of lipid composition as well as buffer concentration on the channel's gating were not fully explored. For example, AtVDAC1 proteins were reconstituted in DMPC and in Asolectine (a relatively crude mixture of plant lipids, potentially closer to the natural conditions of a plant bilayer). The Asolectine-AtVDAC1 mixture was originally tested but did not produce acceptable data as the insertion into the artificial bilayer was very difficult. Future experiments might focus on the use of these preparations, but they first require great optimization to ensure the channel can incorporate into the bilayer.

Similarly, use of high salt concentrations for BLM work was previously described to be effective (Colombini 1989, Blachly-Dyson, Peng et al. 1990, Blumenthal, Kahn et al. 1993, Hodge and Colombini 1997, Tan and Colombini 2007), but in this work appeared to compromise the stability of the bilayer. Consequently, it was deemed wise to use 150 mM KCl, to allow the formation of a stable lipid bilayer, and to maintain a salt environment closer to physiological conditions.

Incidentally, the use of such buffer might as well explain the low conductance observed for all states considered in comparison with previous findings on VDACs in similar experiments (Table 7.1). Indeed, the conductance values reported are around 5- to 10-fold lower on average in comparison with previous findings at 1 M KCl. Recent studies on VDAC from *Phaseolus coccineus* (soya seeds) highlighted a potential effect of the salt concentration on the overall conductance of the VDAC1 channel (Saidani, Grobys et al. 2016), and early studies (Colombini 1989) already reported similar values at 0.1 M KCl to those described in this work (see Table 7.1). However, testing higher concentrations of salt in BLM experiments with AtVDAC1 would allow direct comparisons with previous reports and characterize the channel response to the concentration of salt (Cervera, Komarov et al. 2008).

4. Chapter 4: AtVDAC1 mutants D177N, T156C and D258N

4.1. Identification of AtVDAC1 residues for mediation of contacts with hexokinase III

Considering previous data on the interaction of mammalian VDACs with hexokinase and/or glucokinase (Ahmad, Ahmad et al. 2002, Bryson, Coy et al. 2002, John 2003, da-Silva, Gómez-Puyou et al. 2004, Kim, Lim et al. 2006, Abu-Hamad, Zaid et al. 2008, Pastorino and Hoek 2008), hypothetical docking models were generated between the predicted AtVDAC1 structure (NP_186777) and that of *Nicotiana benthamiana* hexokinase 1 (AAP40021). Indeed, previous experiments (Kim et al., 2006) highlighted the role of this Mitochondria-associated Hexokinase in the control of Programmed cell death (PCD) in plants (see section 1.10) (Kim, Lim et al. 2006).

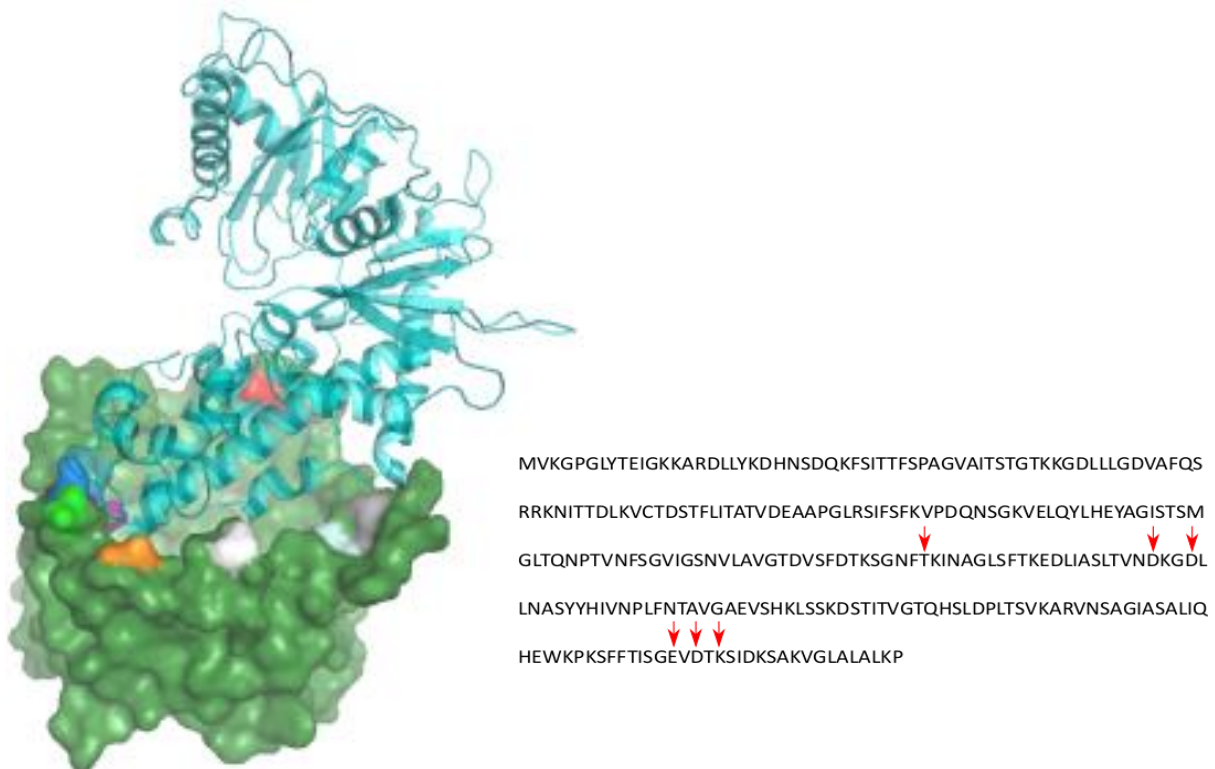


Figure 4.1 Example of docking experiment of the *Nicotiana benthamiana* Hexokinase 1 on AtVDAC1 (based on 3EMN1). Docking was carried out by Cluspro 2.0 software (Comeau, Gatchell et al. 2004, Kozakov, Beglov et al. 2013) between AtVDAC1 hypothetical structure (in green) and the Hexokinase 1 from *N.benthamiana* (in blue), both were generated using SWISS-MODELLER (Artimo, Jonnalagedda et al. 2012). Results were then analysed to putatively identify amino acids involved in hexokinase binding and provided the targets for further mutagenesis. Protein sequence of AtVDAC1 (NP_186777) with location of selected mutations showed by red arrows is indicated. Position 156T is shown in red, position 177D in white, position 180D in orange, position 256E in green, position 258D blue and position K260 in purple.

Multiple binding configurations were produced (an example is shown in Figure 4.1) and amino acids involved in protein-protein interaction were reported. The same approach was used for docking *N.benthamiana* Hexokinase 1 with isoforms AtVDAC2 and AtVDAC4, to highlight similarities and redundancies in the amino acid positions identified by this *in silico* study (see Appendix 9.3). In fact, AtVDACs are known to exhibit differential expression and cellular as well as sub-cellular localization patterns in *A.thaliana* (Tateda, Watanabe et al. 2011), thus potential differences in the interaction to the Hexokinase could be expected. Due to the relatively high sequence similarities between AtVDACs (from 62 to 80 %, see Table 1.1), amino acid substitution could be guided through this analysis.

Table 4.1 Redundant amino acid positions involved in the docking of *N.benthamiana* Hexokinase 1 to AtVDAC isoforms 1, 2 and 4. The amino acid identity corresponding to each isoform is also included.

	Amino acid		
	AtVDAC1	AtVDAC2	AtVDAC4
48	K	K	K
50	D	G	D
156	T	K	T
177	D	D	D
180	D	E	E
205	K	T	S
256	E	E	E
258	D	D	D

Docking was carried out by Cluspro 2.0 software (Comeau, Gatchell et al. 2004, Kozakov, Beglov et al. 2013) between AtVDAC1, 2 and 4 hypothetical structure and the Hexokinase 1 from *N.benthamiana*, both were generated using SWISS-MODELLER(Waterhouse, Rempfer et al. 2018) (Artimo, Jonnalagedda et al. 2012). Amino acid positions reported in at least on binding model (Appendix 9.3) for each isoform are indicated, as well as their corresponding identity.

Amino acids positions present in at least one binding configuration for AtVDAC1, AtVDAC2 and AtVDAC4 binding to Hexokinase 1 were identified and regrouped in Table 4.1. Amino acids at positions 48, 50, 156, 177, 180, 205, 256 and 258 were systematically predicted to be involved in the binding of Hexokinase 1 to AtVDACs. Furthermore, positions 48, 177, 256 and 258 harboured the same amino acid for all AtVDAC isoforms, namely a lysine (K48), an aspartic acid (D177), a glutamic acid (E256) and another aspartic acid (D258), indicating a conserved feature between AtVDAC1, AtVDAC2 and AtVDAC4. Finally, all amino acids involved in the binding of AtVDACs to Hexokinase 1 are positioned on the loops exposed to the external surface.

Interestingly, the binding of Hexokinase 1 to AtVDACs mostly involved the first 50 to 100 amino acids of the former. This observation is in accordance with previous data suggesting the involvement of the N-Terminal domain of the Hexokinase 1 as an anchor for its mitochondrial targeting (Kim, Lim et al. 2006, Abu-Hamad, Arbel et al. 2009, Arzoine, Zilberberg et al. 2009).

On the basis of the docking data (Figure 4.1, Appendix 9.3 and Table 4.1), eight putative AtVDAC1 amino acid residues were identified for mediation of protein-protein interactions. Additionally, sequence alignments were generated between AtVDAC1 and other orthologues (Appendix 9.4). Protein sequences of human, mouse, and zebrafish were chosen and aligned against AtVDAC1, AtVDAC2 and AtVDAC4. Human and mouse VDACs are the most studied eukaryotic porins to date, and the zebrafish VDAC offered a more evolutionary distant organism, as well as a known VDAC dimer structure (PDB ID: 4BUM)(Schredelseker, Paz et al. 2014). VDAC orthologues of distantly related organisms were also included in the alignment, to identify the most conserved amino acids, and variable amino acids which may be associated with organism-specific functions.

Overall, positions 177 and 258 on AtVDAC1 protein proved interesting since they were conserved in most of the analysed sequences. Interestingly, an Aspartic acid is present at both positions. This amino acid is not known for its propensity to be part of beta-sheets formation, thus leaving the possibility of being part of a binding platform for potential partners (see section 1.6).

The Aspartic acids of positions 177 and 258 (negatively charged) would be changed to Asparagine (polar and uncharged). In a similar fashion, E256 was changed to glutamine, whereas D180 was changed to serine, for its reduced steric hindrance. This last two positions (D180 and E256) were chosen based on their proximity to D177 and D258, respectively. Additionally, T156 was identified as being the ideal candidate for potential labelling experiments of cysteine with fluorophores (Puljung and Zagotta 2012), due to the reduced structural difference between the serine and cysteine residue (a sulphur atom replaces the oxygen on the lateral chain of the residue). Moreover, its close proximity to the N-Terminal alpha helix of AtVDAC1 could as well provide the basis for a cross linking-experiment for BLM assays, as highlighted in the mVDAC1 (Mertins, Psakis et al. 2012).

4.2. Amplification and screening of mutant constructs

After performing mini-preps on batches of 4 to 6 clones, purified mutant plasmids (section 2.4.5) were screened by restriction endonuclease analysis with their respective restriction enzymes (see Table 4.2) for the identification of putatively positive clones.

Table 4.2 Mutant screening patterns. Table containing mutations used in this study, the enzyme used for the screening of positive colonies, as well as the expected Wild-Type (WT) and Mutant DNA fragments size.

Mutation	Enzyme	WT pattern (bp)	Mutant pattern (bp)
D258N	HpaI/XmnI	2517+1934	1036+1482+1934
D177N	HincII	384+71+3996	144+240+71+3996
E256Q	XmnI	2517+1934	1041+1476+1934
D180S	BanII	4094+357	357+293+3801

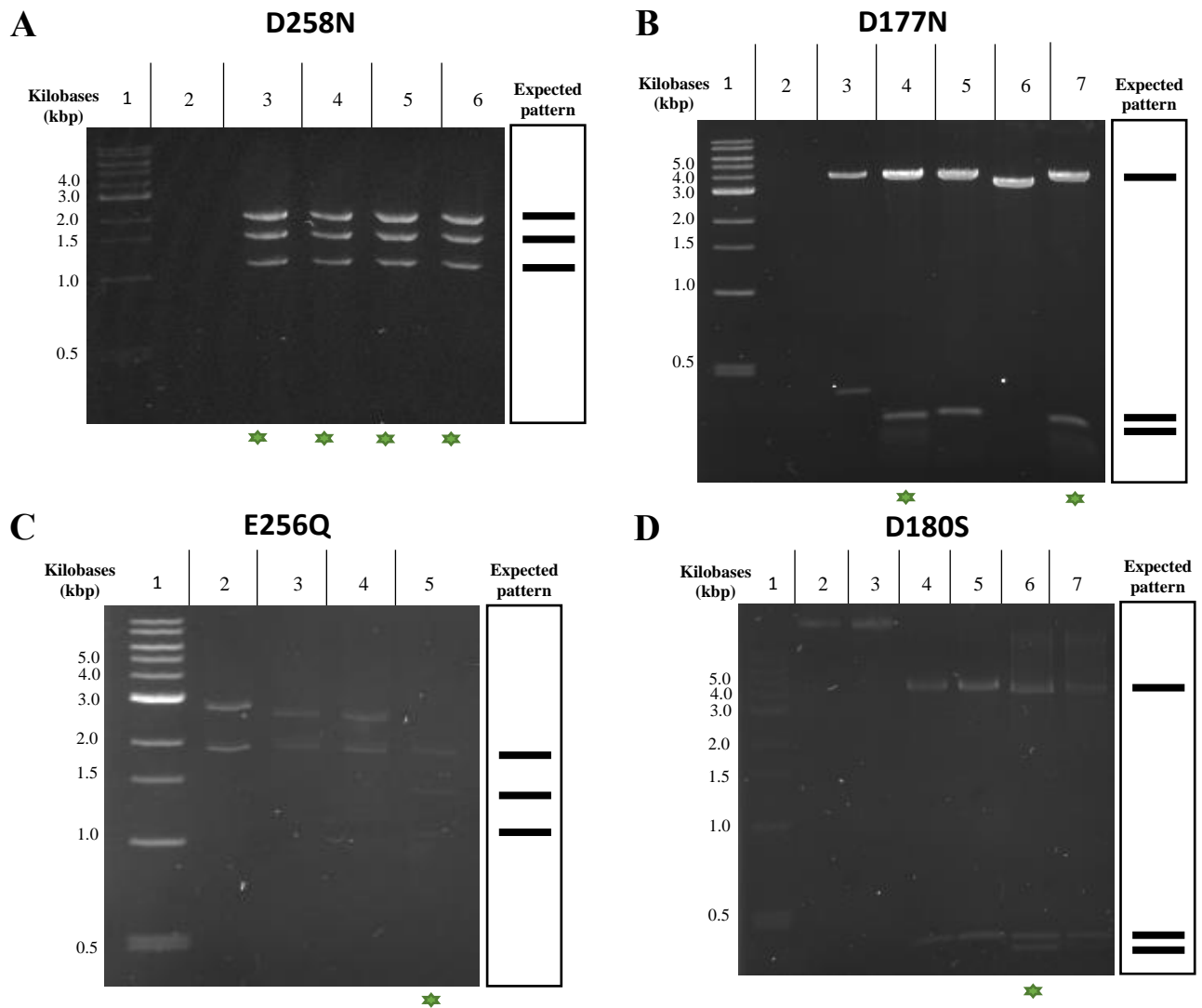


Figure 4.2 Screening of D258N, D177N, E256Q and D180S AtVDAC1 mutant constructs by restriction endonuclease digests. 5 μ L of digested pET-20b(+) plasmid, harbouring the corresponding AtVDAC mutant were analysed on a 1.5% (w/v) agarose gel in 1x TBE, with a 1 kb DNA ladder from NEB® loaded on lane 1. Expected digestion pattern is displayed by the right side of each gel. Plasmids sent for DNA sequencing are marked with a green star. (A) 4 potential AtVDAC1 D258N clones were analysed (lane 3 to 6). (B) Wild-type AtVDAC1 (lane 3) or AtVDAC1 D177N clones (lane 4 to 7) were analysed. (C) Wild-type AtVDAC1 (lane 2) or AtVDAC1 E256Q clones (lane 3 to 5) were analysed. (D) Wild-type AtVDAC1 (lane 4) and AtVDAC1 D180S clones (lane 5 to 8) were analysed. Green star indicates successful mutant construction.

Only one positive construct (green star) was generated during E256Q and D180S mutagenesis, and both were sent for DNA sequencing (Figure 4.2C and 4.2D). D258N mutagenesis yielded 4 positive constructs (Figure 4.2A lanes 3 to 6), whereas two D177N constructs were screened positives (Figure 4.2B lanes 4 and 7). Constructs were sent for DNA sequencing (See Appendix 9.1) alongside few T156C potential clones identified with the same method. Mutants D258N, D177N, T156C and D180S had their sequences confirmed by DNA sequencing. These constructs would be maintained (as described in section 2.3.3 and 2.3.4) and used to produce AtVDAC mutant proteins in Omp9 *E. coli* cells.

4.3. Optimization of the purification process of AtVDAC1 mutants

For analysis, D177N, D258N and T156C AtVDAC1 mutants were produced in inclusion bodies, completely denatured and refolded *in vitro* using the same conditions as for the native-like AtVDAC1 (see 3.4.1 for the refolding screen), prior to purification using the Fractogel® EMD SO3 (M) and the Superose 6 Increase®. Fractions containing the proteins of interest were pooled together and loaded on a 10 % (v/v) SDS PAGE 1x Laemmli running buffer (Figure 4.3).

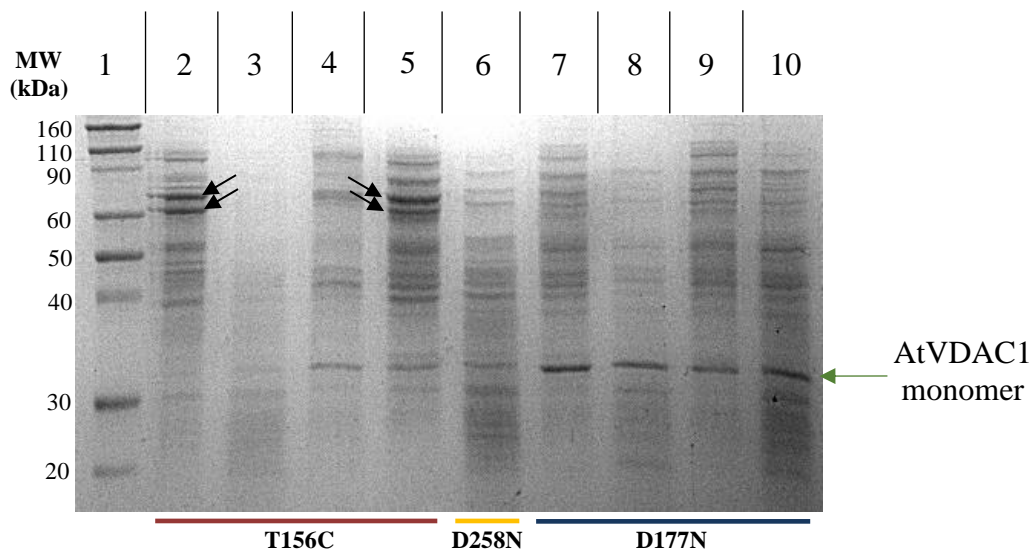


Figure 4.3 SDS-PAGE analysis of preliminary SEC purifications of AtVDAC1 T156C, D258N and D177N mutants. Fractions eluted from size exclusion chromatography using a Superose6 Increase® were pooled together and concentrated. 10 μ L of each purified AtVDAC1 mutant were analysed on a 10 % (v/v) SDS PAGE in 1 x Laemmli running. Lane 1; ladder from Novex®, Lane 2 to 4; samples from fractions 10, 11 and 12 mL respectively, on undiluted injection (0.5 mg/mL) of T156C. Lanes 5; additional sample collected at 10 mL during a second undiluted injection (0.5 mg/mL) of T156C. Lane 6; sample from a single purification of D258N mutant. Lane 7 to 8; samples collected at 10, and 12 mL respectively, on undiluted injection (0.5 mg/mL) of D177N. Lane 9 to 10; samples collected at 10, and 12 mL respectively, on diluted injection (0.25 mg/mL) of D177N. The monomeric AtVDAC is indicated by a green arrow. Possible oligomers (lane 2 and 5) are indicated by black arrows.

A similar electrophoresis profile to that of native AtVDAC1 was observed repeatedly for each mutant purified. However, it soon became apparent the mutants exhibited different behaviour to that of the Native-like AtVDAC1 (Figure 3.6). Whereas most of the mutant preparations do contain similar contaminants to those present in the native AtVDAC1, the yield of mutant monomers was variable and generally low in comparison to that of the native protein (Figure 3.6). Mutant D177N fractions (Figure

4.3, lanes 7 to 10) contained the highest amount of monomeric AtVDAC1 mutant compared to other contaminants in the same fractions (Figure 4.3, green arrow), amongst all mutants. Surprisingly, two proteins, both having an apparent molecular weight of 60-70 kDa (black arrows), were the major proteins present in mutant T156C fractions (Figure 4.3, lane 2 and lane 5). Finally, mutant D258N (Figure 4.3, lane 6) yielded the least monodisperse samples, with a barely detectable amount of monomer.

The diverse composition in terms of contaminants and the very low amount of monomer present in each mutant fraction, despite no issues detected at earlier stages (expression, Inclusions bodies preparation and refolding, results not shown); the amount and number of contaminants present in the AtVDAC1 mutant purified fractions, as well as the low yield, (Figure 4.3) deemed those preparations unsuitable for further works.

Finally, we attempted using the prepacked Hitrap SP XL ® 5 mL from Life Sciences® exchanger as it was successfully tested on the Native AtVDAC1 protein (see section 3.4). Fortunately, this solid support would guarantee a constant yield of AtVDAC mutant proteins for characterization studies (Black Lipid membrane or BLM and SAXS mainly) (sections 4.4 to 4.6).

4.4. Purification of AtVDAC1-D177N mutant protein by Cation Exchange Chromatography (CEX) using an HiTrap solid support

Using the previously optimized refolding methodology (see section 3.3.1), the mutant protein D177N was tested for its ability to bind to the new resin (Hitrap SP XL ® 5 mL from ThermoFisher ®). Using a linear gradient of NaCl (from 1 mM to 1 M), the protein would elute as a relatively sharp peak with tailing at the end of the run (Figure 4.4B). Overall, the elution started around 250 mM NaCl, peaking at 400 mM and reaching completion around 700 mM salt. Samples from collected fractions were analysed on a 10 % (v/v) SDS PAGE gel in 1x Laemmli running buffer (Figure 4.4A, lanes 2 to 10). The majority of the mutant protein appeared to have eluted between 300 mM and 600 mM sodium chloride (Figure 4.4, lanes 3 to 6) and contained mostly the protein of interest (around 30 kDa), with a purity around 75 to 80 % of the total signal (using ImageJ® Software (Schneider, Rasband et al. 2012, Schindelin, Rueden et al. 2015)). Some minor contaminants were detected (low and high molecular weight) in the main fractions, whereas the tail fractions collected between 600 and 750 mM NaCl largely contained lower molecular weight (below 30 kDa) contaminants (Figure 4.4A, lanes 7 to 10).

Use of Hitrap SP XL 5 mL greatly improved the purification yield of the AtVDAC1-D177N mutant, in comparison to previously used solid supports. Fractions between 7 and 12 mL (after the start of the gradient) were pooled together, buffer-exchanged and concentrated using an Amicon ® concentrator with a 10 kDa cut-off in SEC buffer. Out of the 50 mg of inclusion bodies used per batch of purification, 5 to 8 mL (1 to 1.6 CV on 5 mL prepacked Hitrap SP XL ®) of protein could be purified at a concentration of 1.5 mg/mL.

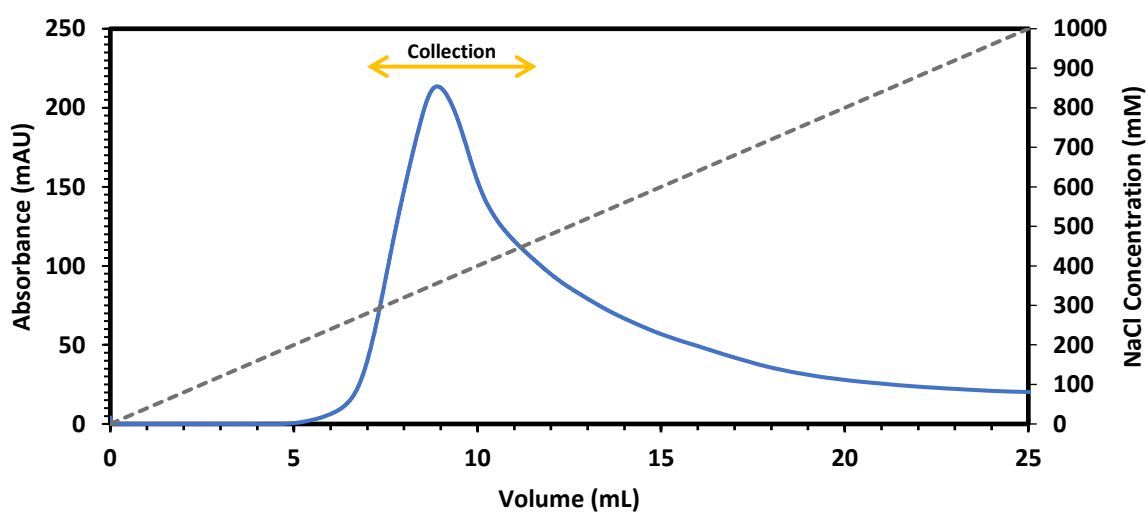
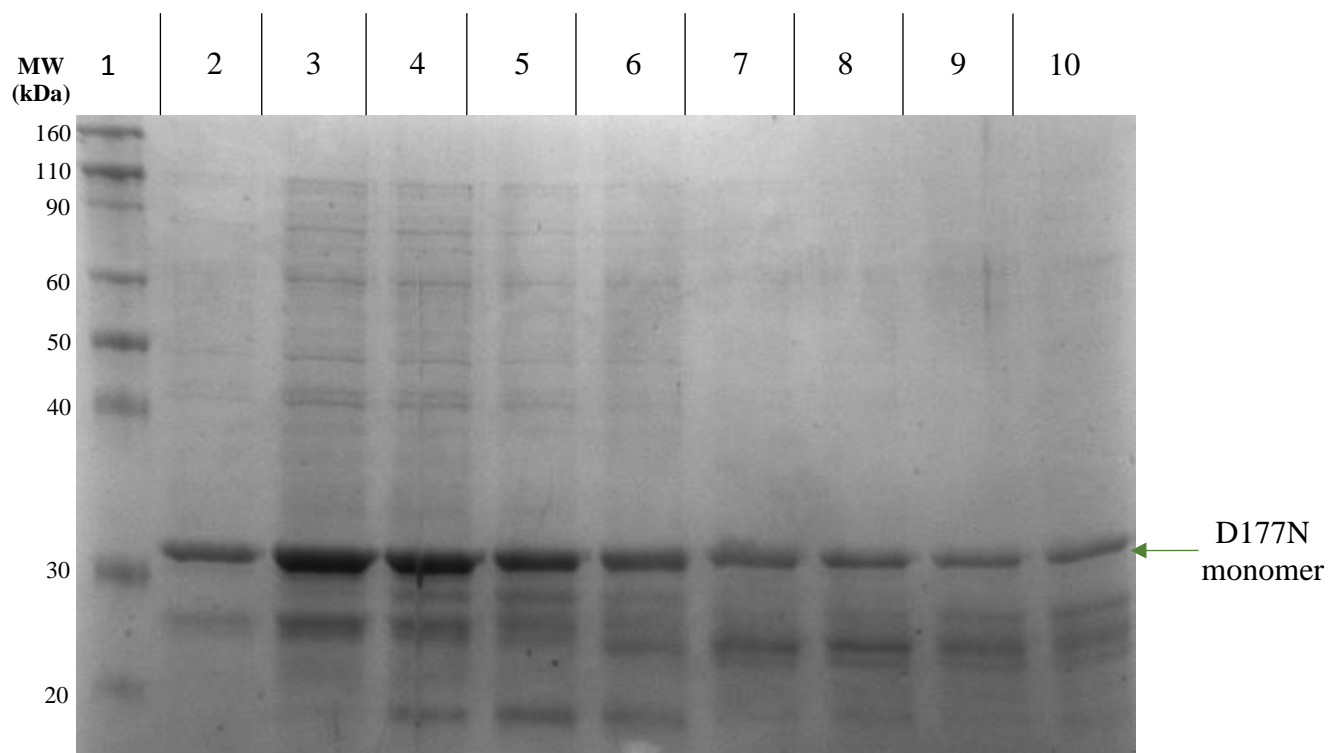


Figure 4.4 Hitrap SP XL cation exchange chromatography of D177N mutant protein with an increasing gradient of NaCl. Elution was carried out in an Akta Start® device using a gradient of NaCl (IEX Buffer). (A). 10 μ L of each purified D177N mutant fractions were loaded on 10 % (v/v) SDS PAGE in 1x Laemmli running buffer. First lane; Ladder from Novex®. Lanes 2 to 10; samples collected 8, 9, 10, 11, 12, 13, 14, 15 and 16 mL respectively after the start of the gradient (between 250 and 700 mM salt concentration). Monomer protein is indicated by a green arrow (B). Purification profile (in mAU, in blue) of D177N protein using a Hitrap SP XL and a linear gradient (grey) of NaCl (IEX Buffer). Absorbance (280 nm) was recorded against the collected fractions. Collection area is represented by an orange arrow.

4.4.1. Size exclusion chromatography of purified AtVDAC1-D177N using a Superose6

Increase®

500 µL of a 3.5 mg/mL AtVDAC1-D177N from IEX using an Hitrap solid support (See section 4.4) was injected onto the Superose6 Increase® column and the elution profile was recorded (Figure 4.5B). Recovered sec fractions were analysed by 10 % (v/v) SDS PAGE in 25 mM Tris, 200 mM Glycine, 0.1 % (w/v) SDS (Figure 4.5A). The mutant protein AtVDAC1-D177N eluted in a broad peak with a maximum absorbance recorded around 16.3 mL after injection (64 kDa), with a slight shoulder starting at 18 mL (28 kDa), which was collected separately.

For this mutant, no difference was detected between fractions of the main elution peak (Figure 4.5A lanes 3 to 6), and fractions belonging to the later shoulder (Figure 4.5A, lanes 7 to 8), upon SDS-PAGE analysis. Indeed, the main protein eluted was the D177N monomer around 30 kDa on SDS PAGE (Figure 4.5A, green arrow). However, an additional protein of approximately 28 kDa (on SDS PAGE) was present at decent concentration (5 to 10 % of the total signal). This pattern is similar to the one observed for the purification of Native AtVDAC1 protein (Figure 3.8, lane 5). Nevertheless, its presence in all the samples suggests a carry over or a degradation product. Further investigation by Western Blotting will be explored in section 4.7.

None the less, the SEC purification using a Superose6 Increase® resulted in substantially purer and more monodisperse fractions when using an Hitrap SP XL® for the IEX step in comparison to the use of the Fractogel EMD SO3® (M) (Figure 4.3, lanes 7 to 10).

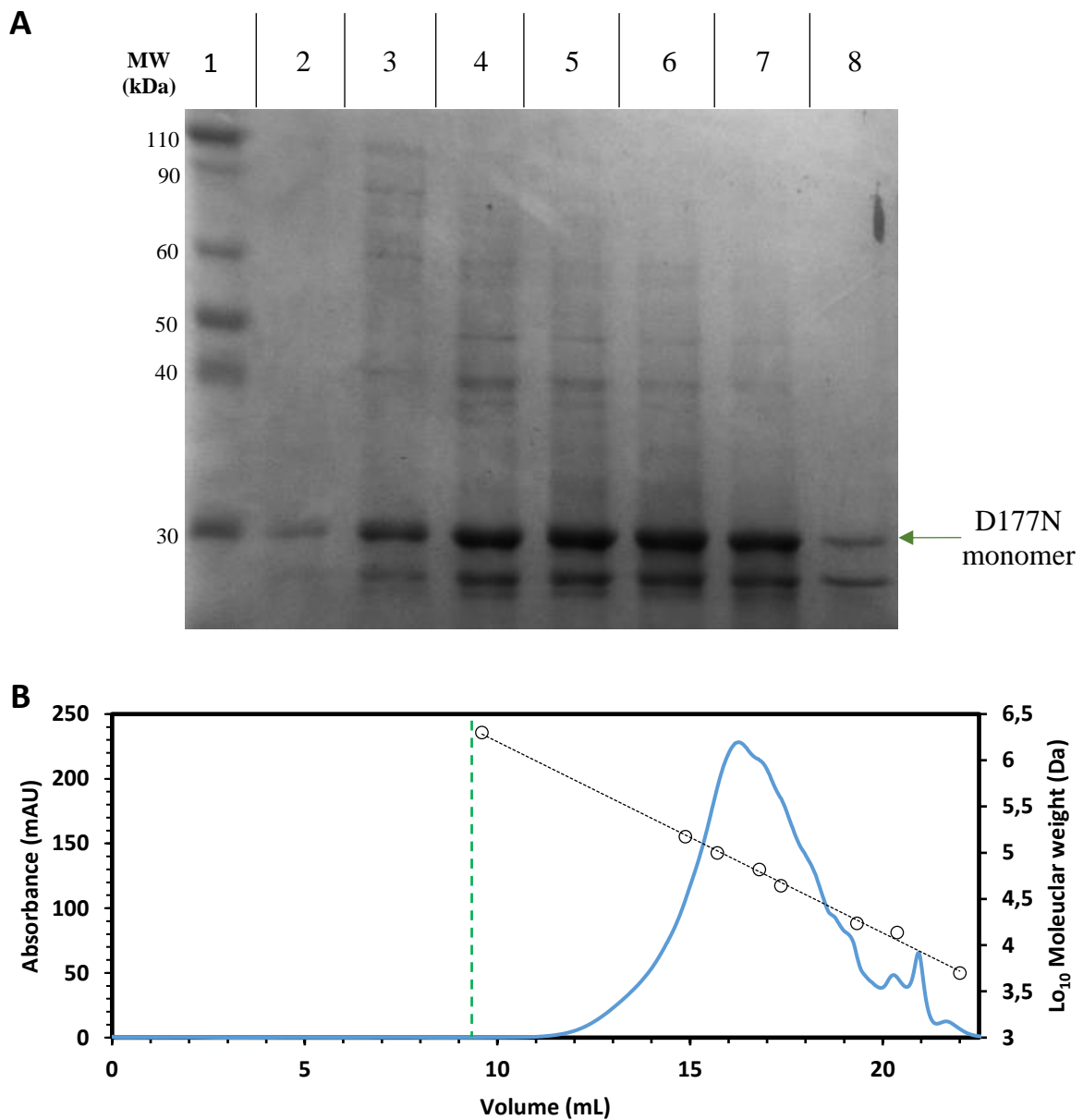


Figure 4.5 Size exclusion chromatography of AtVDAC1D177N mutant protein. SEC was carried out in an Akta Prime ® device using a Superose 6 Increase® in SEC buffer. (A). 10 µL of each fraction were loaded on a 10 % (v/v) SDS PAGE in 1x Laemmli running. First lane; ladder from Novex®. Lanes 2 to 8; samples collected at 13, 14, 15, 16, 17, 18 and 19 mL respectively from a 3.5 mg/mL AtVDAC1. The D177N mutant monomer is indicated by a green arrow. (B). Elution profile (UV absorbance in blue) of the size exclusion chromatography performed on D177N after injection of partially purified sample (500 µL of a 3.5 mg/mL solution). The minimum working range (void volume) is indicated by a green dashed line.

4.5. Purification of AtVDAC1-D258N mutant protein by Cation Exchange Chromatography (CEX) using an HiTrap solid support

AtVDAC1-D258N was refolded (section 2.5.3) and purified using a Hitrap SP XL 5 mL ® matrix (section 2.5.4). The protein eluted as a relatively sharp peak with tailing towards run completion (Figure 4.6B). Overall, the elution started around 300 mM NaCl, peaking at 400 mM and reaching completion around 550 mM salt. Samples were analysed on 10 % (v/v) SDS PAGE in 1x Laemmli running buffer (Figure 4.6A, lanes 2 to 10) to monitor purification efficiency. Fractions collected between 320 mM and 440 mM sodium chloride were rich in AtVDAC1-D258N (around 30 kDa) (Figure 4.6, lanes 3 to 5) and, with signal intensity suggesting a very good purity (90 to 95 % of the total signal, using ImageJ® Software (Schneider, Rasband et al. 2012, Schindelin, Rueden et al. 2015)). Some minor contaminants were detected (low and high molecular weight) in the main fractions, whereas tail fractions only contained lower molecular weight (below 30 kDa) contaminants (Figure 4.6A, lanes 6 to 10). Higher molecular weight contaminants detected in fractions 3 to 5 (Figure 4.6A) could be a potential oligomer due to their apparent molecular weight (around 60 kDa, or twice the size of AtVDAC monomer). Fractions collected from 7 to 11 mL (after the start of the gradient) were pooled together, buffer-exchanged in SEC buffer and concentrated using an Amicon® concentrator with a 10 kDa cut-off for size exclusion chromatography (section 4.5.1).

This experiment was a breakthrough towards purifying large amounts of AtVDAC1-D258N protein, as it allowed a massive increase of the overall capture and purity of the samples compared to previous experiments (Figure 4.3, lane 6). Out of the 50 mg of inclusion bodies used per batch of purification, a routine 4 to 6 mL (around 1 CV on 5 mL prepacked Hitrap SP XL ®) of protein could be purified at a concentration of 1.3 mg/mL.

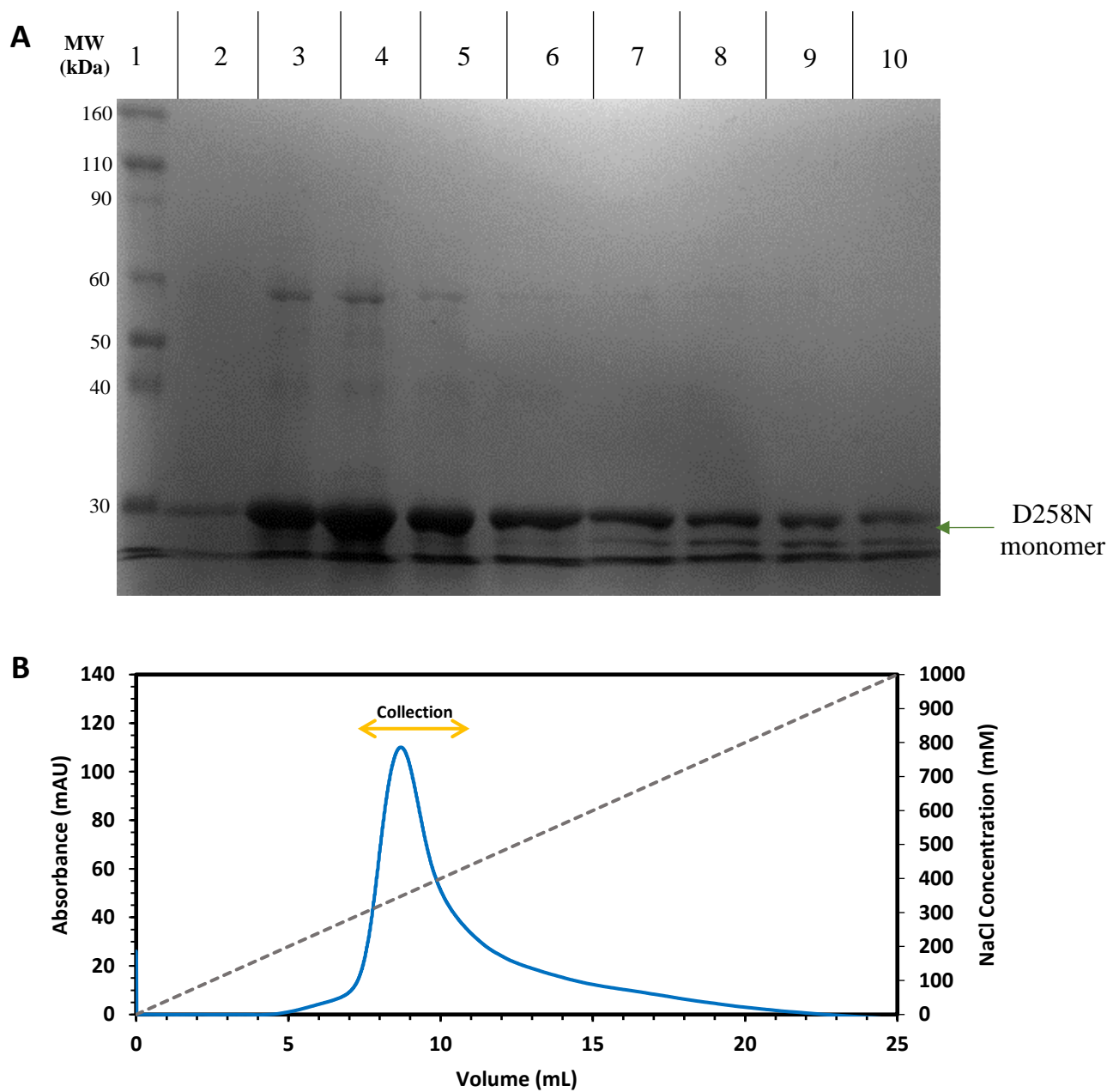


Figure 4.6 Hitrap cation exchange chromatography of D258N mutant protein with an increasing gradient of NaCl. Elution was carried out in an Akta Start® device using a gradient of NaCl (IEX buffer). The resin used was a HiTrap SP XL 5 mL®. (A). 10 µL of each fraction were analysed on a 10 % (v/v) SDS PAGE in 1x Laemmli running buffer (and Coomassie-stained). First lane; ladder from Novex®. Lanes 2 to 10; samples collected 7, 8, 9, 10, 11, 12, 13, 14 and 15 mL respectively after the start of the gradient (between 300 and 600 mM salt concentration). Monomer protein is indicated by a green arrow (B). Purification profile (in mAU, in blue) of D258N protein using a Hitrap SP XL and a linear gradient (grey) of NaCl (IEX Buffer). Absorbance (280 nm) was recorded against the collected fractions. Collection area is represented by an orange arrow.

4.5.1. Size exclusion chromatography of AtVDAC1-D258N protein using a Superose6

Increase®

500 μ L of a 2.5 mg/mL IEC purified AtVDAC1-D258N (section 4.5) was injected onto the Superose6 Increase® column and the elution profile was recorded (Figure 4.7B). Recovered fractions were analysed on a 10 % (v/v) SDS PAGE in 1x Laemmli running buffer (Figure 4.7A). AtVDAC1-D258N eluted within two sharp peaks with maximum absorbances recorded around 16.2 and 18 mL after injection (68 kDa and 28 kDa), respectively. A slight shoulder around 19 mL (22 kDa) following the second sharp peak was also observed.

When analysed on 10 % (v/v) SDS-PAGE (Figure 4.7A lanes 2 to 9), most of the protein would be denatured, as previously described for AtVDAC1 (section 3.5). However, the presence of a 60 kDa protein (lanes 3 to 5) suggested potential oligomerization of the AtVDAC1-D258N protein, that would partially resist the denaturation. Finally, fractions belonging to the tail of the second peak showed a distinctive pattern of two bands (Figure 4.7A, lanes 8 to 9), the first being likely AtVDAC1-D258N and the second a similarly sized contaminant to the one observed in previous purifications (see section 3.5 and 4.4.1), i.e a probable degradation product. As opposed to previous experiments, this contaminant was easily removed by size exclusion chromatography. As for D177N and T156C mutants, the hypothesis on the oligomer and the degradation will be investigated by Western Blot in section 4.7.

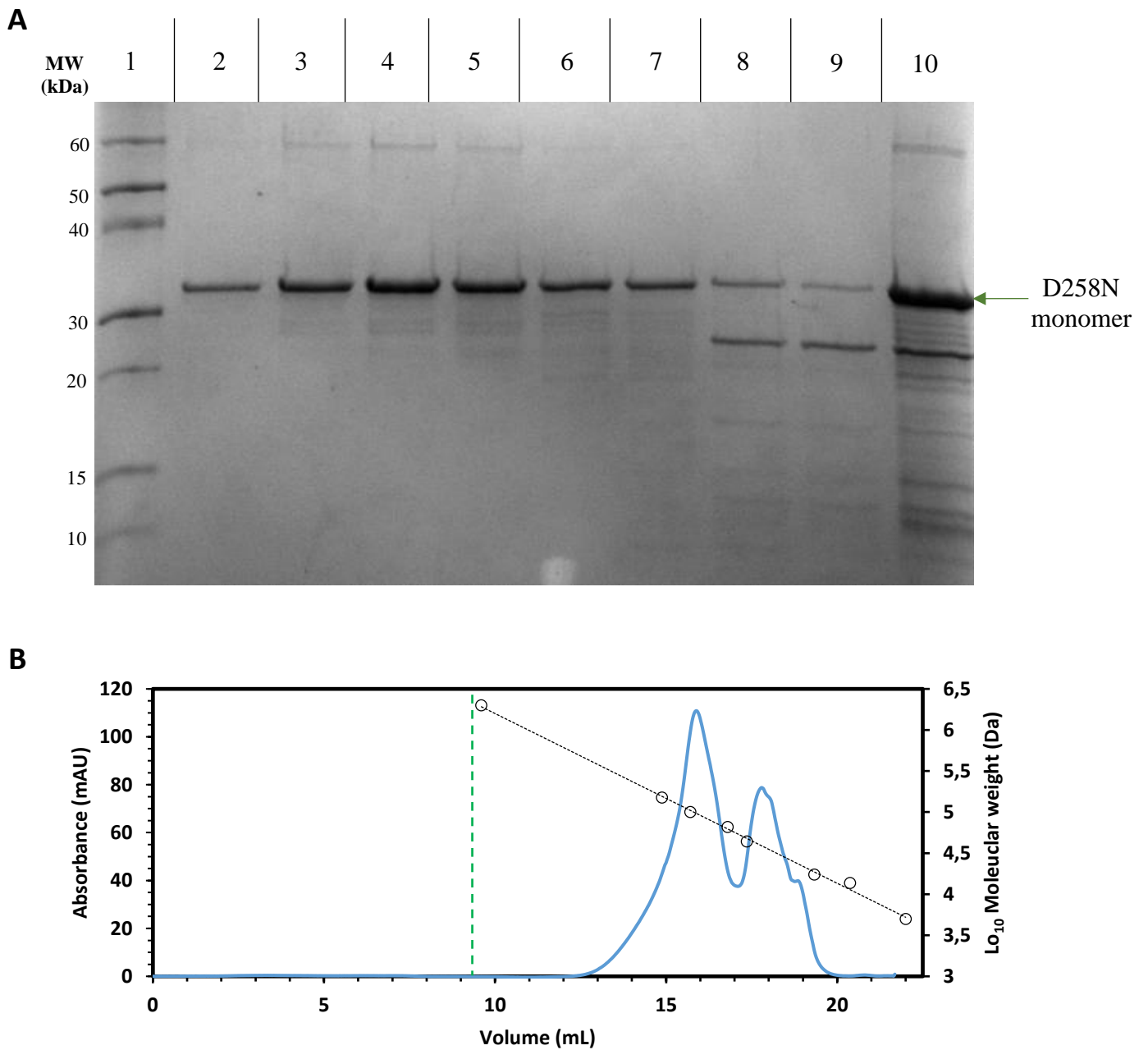


Figure 4.7 Size exclusion chromatography of AtVDAC1-D258N mutant protein using a Superose6 Increase®. SEC was carried out in an Akta Prime ® in SEC buffer. **(A)**. 10 µL of each fraction were loaded on SDS PAGE 10 % (v/v) in Laemmli buffer. First lane; Ladder from Novex®. Lanes 2 to 9; samples collected 14, 15, 16, 17, 18, 18.5, 19, and 20 mL respectively from a 2.5 mg/mL D258N. Lane 10; 2 µL sample of the 2.5 mg/mL D258N solution. The D258N mutant monomer is indicated by a green arrow **(B)**. Elution profile (UV absorbance in blue) of the size exclusion chromatography performed on 2.5 mg/mL D258N injection (500 µL). The minimum working range (void volume) is indicated by a green dashed line.

4.6. Purification of AtVDAC1-T156C mutant protein by Cation Exchange Chromatography (CEX) using an HiTrap solid support

AtVDAC1-T156C was treated as the other mutants (see previous sections). Using a linear gradient of NaCl (from 1 mM to 1 M), the protein eluted under two unresolved peaks, with a noisy tail towards the completion of the run (Figure 4.8B). Overall, the protein elution started around 240 mM NaCl, peaking at 300 and 400 mM, for the first and second peak respectively, and reaching completion around 550 mM salt. Collected fractions were analysed on a 10 % (v/v) SDS PAGE in 1x Laemmli running buffer (Figure 4.8A, lanes 2 to 10) to monitor purification yields. Fractions corresponding to the first peak (eluted between 240 mM and 350 mM NaCl) contained most of the protein (around 30 kDa), at a very good purity (around 80 to 85 % of the total signal, using ImageJ Software ®(Schneider, Rasband et al. 2012, Schindelin, Rueden et al. 2015)) (Figure 4.8A, lanes 3 to 5). Minor contaminants (low molecular weight) were detected in fractions eluting after 5 mL (Figure 4.8A, lane 6 and 7), whereas tail fractions only contained lower molecular weight (below 30 kDa) contaminants (Figure 4.8A, lanes 8 to 10), as well as the previously identified 28 kDa species (sections 4.4.1, 4.5.1). In contrast to previous purifications, no clear potential oligomer (usually around 60 kDa) could be detected on 10 % (v/v) SDS-PAGE.

Use of the Hitrap SP XL® solid support resulted in a 10-fold increase of the overall capture and particularly purity of the samples compared to previous experiments (Figure 4.3, lanes 2 to 5). Out of the 50 mg of inclusion bodies used per batch of purification, 3 to 5 mL (around 0.6 to 1 CV on 5 mL prepacked Hitrap SP XL ®) of protein could be purified at a concentration of 0.5 mg/mL).

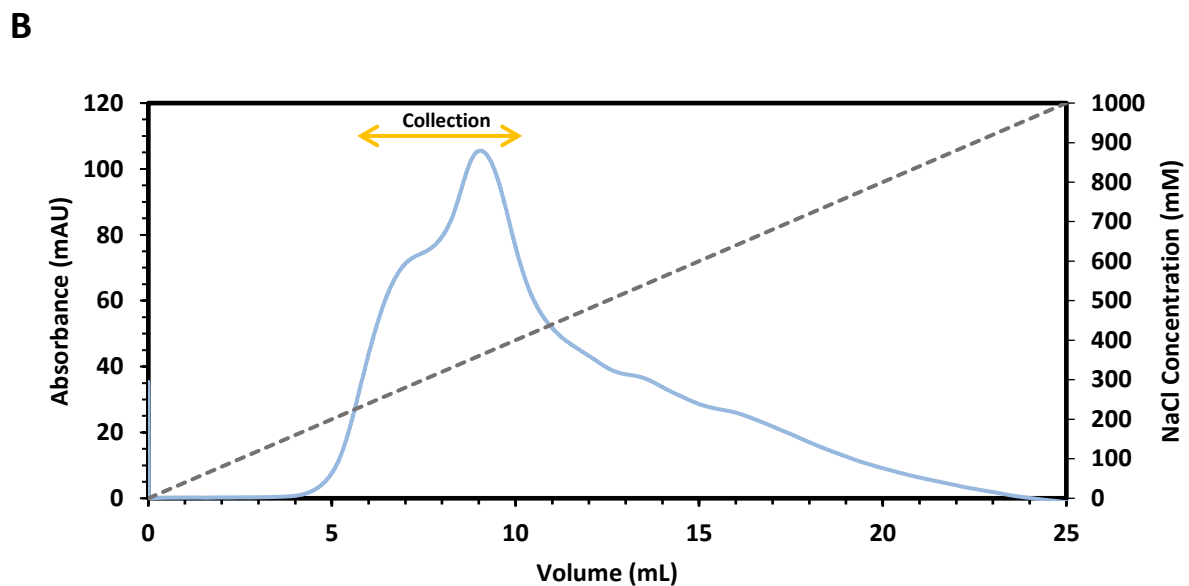
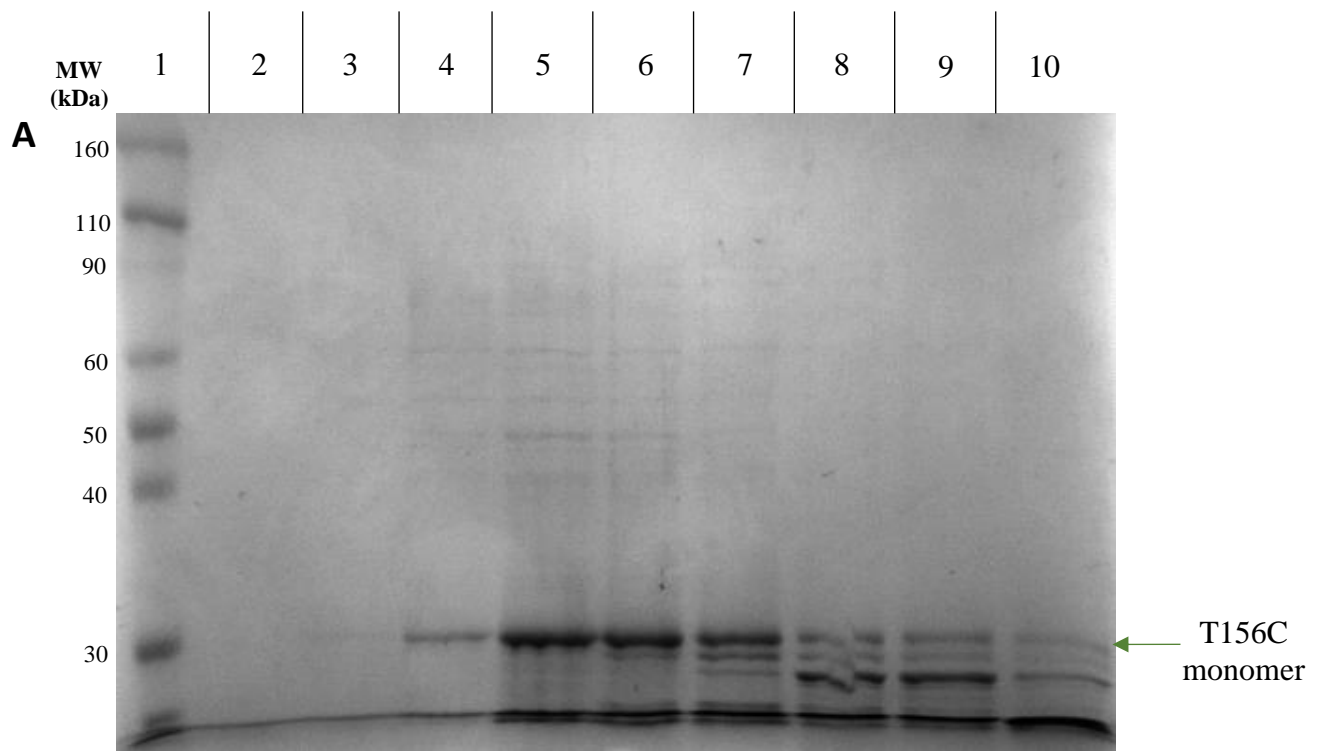


Figure 4.8 Cation exchange chromatography of AtVDAC1-T156C mutant protein using a HiTrap SP XL 5 mL[®] with an increasing gradient of NaCl. Elution was carried out in an Akta Start[®] device using a gradient of NaCl (IEX buffer). (A). 10 μ L of each fraction were analysed on a 10% (v/v) SDS PAGE in 1 x Laemmli Running buffer. First lane; ladder from Novex[®]. Lanes 2 to 10; samples collected 5, 6, 7, 8, 9, 10, 11, 12 and 13 mL respectively after the start of the gradient (between 200 and 500 mM salt concentration). Monomer protein is indicated by a green arrow (B). Purification profile (in mAU, in blue) of T156C protein using a Hitrap SP XL and a linear gradient (grey) of NaCl (IEX Buffer). Absorbance (280 nm) was recorded against the collected fractions. Collection area is represented by an orange arrow.

4.6.1. Size exclusion chromatography of AtVDAC-T156C using a Superose6 Increase®

500 μ L of a 1.5 mg/mL IEC purified AtVDAC-T156C (section 4.6) was injected onto the Superose6 Increase® column and its elution profile was recorded (Figure 4.9B). Collected samples were analysed by 10 % (v/v) SDS PAGE in 1x Laemmli running buffer (Figure 4.9A). AtVDAC1-T156C eluted under two peaks with maximum absorbances recorded around 18 and 21 mL after injection (28 kDa and 9 kDa respectively). A slight shoulder at the end of the first peak, around 18.5 mL (26 kDa), could be observed.

When analysed on 10 % (v/v) SDS-PAGE, fractions corresponding to the peak with the maximum absorbance contained most of the mutant protein (around 30 kDa) (Figure 4.9A lanes 2 to 9), at a very good purity (around 85 to 90 % of the total signal, using ImageJ Software ®). As the elution progressed (Figure 4.9A lanes 5 to 7), additional low molecular weight contaminants co-eluted with the monomeric T156C mutant protein, with possible degradation products showing a signal just below 30 kDa). The later peak eluted around 21 mL after injection but did not contain significant amounts of the target protein (Figure 4.9A, lane 8 and lane 9). Instead, the increased viscosity of the sample when handled suggested a high concentration of detergent present.

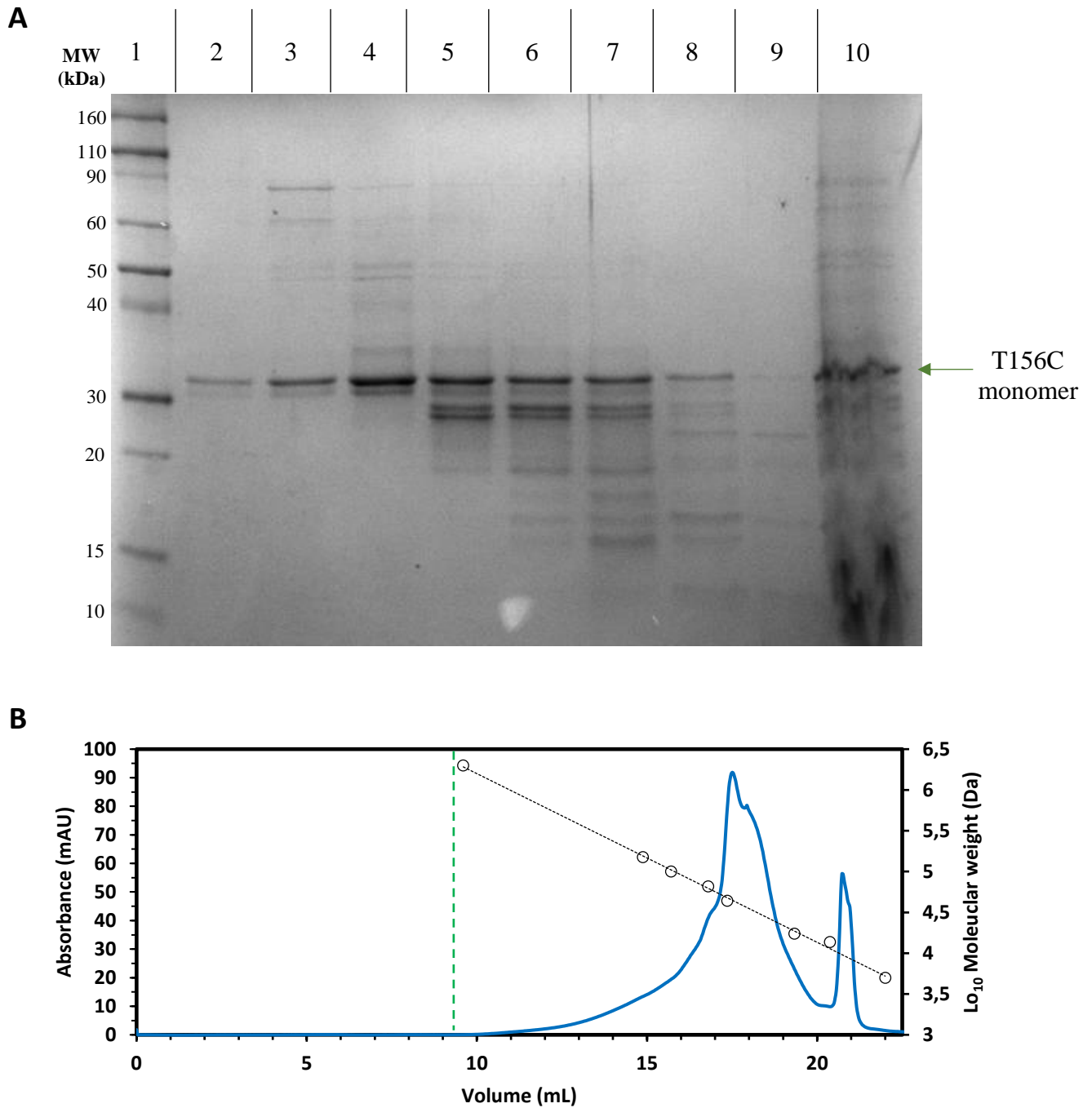


Figure 4.9 Size exclusion chromatography of AtVDAC1-T156C mutant protein using a Superose 6 Increase®. SEC was carried out in an Akta Prime® device in SEC buffer. (A). 10 µL of each fraction were loaded on SDS PAGE 10% (v/v) in 1x Laemmli buffer. First lane; ladder from novex®. Lanes 2 to 9; samples collected 15, 16, 17, 18, 19, 20, 21 and 22 mL respectively from a 1.5 mg/mL T156C. Lane 10; 2 µL sample of the 1.5 mg/mL T156C solution. The T156C mutant monomer is indicated by a green arrow (B). Elution profile (UV absorbance in blue) of the size exclusion chromatography performed on T156C after injection of partially purified sample (500 µL of a 1.5 mg/mL solution). The minimum working range (void volume) is indicated by a green dashed line.

4.7. Identification of AtVDAC purified proteins by Western Blotting

A Western Blot experiment was conducted to assess the purity of the samples and test the mutants for antibody recognition. Native-like and mutant proteins were analysed on 10% (v/v) SDS-PAGE in 1x Laemmli running buffer (Figure 4.10 left side) and probed by Western Blotting using a rabbit-polyclonal Anti-AtVDAC1 antibody at a 1/2500 dilution (Figure 4.10 right side).

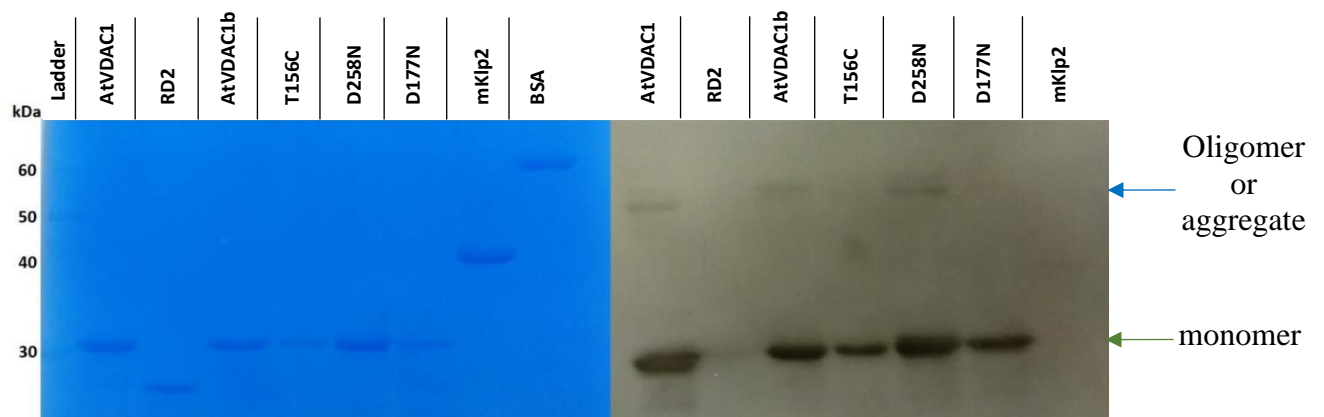


Figure 4.10 Confirmation of identity of AtVDAC1 Native-like and mutant proteins by Western Blotting. 10 μ L of each purified Native-like and mutant AtVDAC1 proteins were loaded on 10 % (v/v) SDS PAGE, (left side) in 1x Laemmli running buffer. First lane is the ladder. Lanes 2, 4, 5, 6 and 7 contains samples from Native AtVDAC1(batch 1 and 1b), T156C, D258N and D177N protein respectively. A random construct RD2 (lane 3) and mKlp2 purified protein (lane 8) were used as negative controls. Lane 9 contains a 1 μ L sample of a BSA solution at 5 mg/mL and served as a loading control. The samples were either stained by Coomassie Blue R250 (left) or probed by Western Blot with a polyclonal anti-AtVDAC1 antibody (from rabbit) at a 1/2500 dilution. The monomer protein as well as potential oligomers/aggregates are indicated by green and blue arrows.

A strong signal was detected on the photographic film for the native-like AtVDAC1 monomer and all of its mutants (Figure 4.10 right side). As expected, the intensity of the signal generated through Western Blotting correlated with the band intensity on Coomassie Blue stained SDS-PAGE gels (Figure 4.10 left). The mutations did not seem to affect (at least to a detectable threshold) the binding of the antibody to the protein. This result was expected since this antibody was supposed to bind the N-terminal segment of AtVDAC1 (according to manufacturer's instructions).

Native-like AtVDAC1 (AtVDAC1 and ATVDAC1b) and AtVDAC1-D258N samples, showed faint signals between 50 and 60 kDa on the photographic film, suggesting the presence of VDAC-oligomers (aggregates or specific dimers resisting SDS denaturation (Kumar, Gopalakrishna et al. 1993, Grigorian, Bustamante et al. 2005); Figure 4.10, blue arrow). This observation correlated with the SEC purification profiles of those proteins (section 3.5 and 4.5.1). Conversely, T156C mutant exhibited no higher molecular weight aggregate or oligomer which correlated with its SEC profile (single peak elution with a maximum absorbance at 18 mL or 28 kDa). However, no oligomer/aggregate was detected by WB in D177N fraction, despite its SEC profile suggesting a high tendency towards the higher molecular weight form.

Overall, the identity of the AtVDAC1 Native-like and its mutant proteins was confirmed using the same @AtVDAC1 antibody. This successful recognition gave confidence that the antibody could be used in downstream processes such as Far Western Blotting, to probe the interaction of AtVDAC proteins with potential binding partners.

4.8. Discussion

In parallel to the primary characterization of AtVDAC1, attention was given to prepare the groundwork for future experiments focusing on the interaction of the channel with potential binding partners. The Hexokinase-like 1 from *Nicotiana Benthamiana* (formerly known as Hexokinase 3) was an early candidate considered for the design of AtVDAC1 mutants. These mutants would harbour mainly mild mutations that would affect (instead of completely abolishing) a potential interaction. Mutants were designed not only with the aim of using them in binding assays with hexokinase, but also as general binding platforms with other cytosolic partners. By changing the overall charge in the cytoplasmically exposed part of the channel, the molecular basis for AtVDAC1-partner protein interactions could be unveiled. Additionally, the extent of conservation of these amino acids in other eukaryotic orthologues, suggested common features in the VDAC-partner protein recognition and interaction.

The PCR directed mutagenesis was overall successful and yielded multiple new constructs (pET-20b(+)-D258N, pET-20b(+)-D177N and pET-20b(+)-T156C). *E.coli* Omp9 cells were successfully transformed with the aforementioned constructs, and the corresponding mutant proteins were subsequently overproduced following the optimised protocols developed for the Native-like AtVDAC1 (section 3.3).

The AtVDAC1 mutants (T156C, D258N and D177N) were purified at least twice with the Fractogel solid support to ensure the process could be carried out reproducibly. Nevertheless, the yield of monomeric VDACS was low, overall, compared to the wild-type AtVDAC1 with the same setup (see section 4.3).

However, the use of the HiTrap SP XL® again proved very successful, with adequate amounts (around 5 to 10 mg of purified from a 50 mg inclusion bodies) produced for each protein, with relatively high purity (above 90-95 %) (section 3.3.1). The slight differences observed between the mutants and the wild-type concerning concentration and amounts could have simply arisen from their different refolding propensities. Indeed, these amino acids are well conserved across species (see Appendix 9.4), suggesting an importance in either the structural or functional properties of the VDAC.

Both mutants D258N and D177N were purified in reasonable amounts, suitable for downstream applications such as BLM or SAXS. However, mutant T156C concentration was deemed too low to produce robust data on SAXS. Nevertheless, this mutant could still be used in BLM assays or binding assays such as Far Western Blotting. The presence of a cysteine might explain its peculiar behaviour in comparison to the other two mutants. Indeed, the replacement of the aspartic acid by a cysteine residue might lead to greater structural and functional difference in comparison to substitutions where aspartate is exchanged for asparagine, e.g. in D258N and D177N mutants.

Interestingly, the behaviour of the mutant proteins on size exclusion chromatography often correlated with their ability to show SDS-resistant oligomeric forms on denaturing 10 % SDS-PAGE in 1x Laemmli buffer (section 2.1). For example, T156C SEC revealed a single peak and no oligomer/aggregate could be revealed by Western Blotting (section 2.5.11), whereas, D258N SEC showed two peaks corresponding to the oligomer (around 60 kDa) and monomer (30 kDa), with Western Blotting signals appearing at higher molecular weights than the monomer (between 60 and 65 kDa; section 4.7, Figure 4.10).

Surprisingly, D177N SEC was characterized by a single broad peak corresponding to the oligomer (around 16 mL after injection), but no higher molecular weight complexes could be identified on Western Blotting experiments (section 4.7).

This variation in the behaviour of the mutants on SEC and Western Blotting could stem from the impact of the different mutations on the formation and maintenance of the oligomeric form of AtVDAC1. Indeed, Additional mutants could be designed in these specific amino acid positions, to further explore this hypothesis.

5. Chapter 5: Small Angle Scattering of AtVDAC proteins

5.1. Introduction to Small Angle X-Ray scattering (SAXS)

Small angle X-ray scattering (SAXS) is a renowned method for the structural characterization of both ordered and disordered proteins in solution. It provides low resolution information about the sizes and shapes of proteins and complexes (Petoukhov and Svergun 2013, Kikhney and Svergun 2015, Trehella, Duff et al. 2017). Advances in SAXS instrumentation, especially using high intensity synchrotron sources, have been key in popularizing the technique (Mylonas and Svergun 2007). Possible to collect adequate amount of scattering data with short exposures, thus minimising the risk of radiation damage to the sample, as opposed to a conventional “in-house” instrument such as the Bruker Nanostar®. SAXS is often regarded as a secondary approach to structural characterization of proteins, compared to crystallography, due to its lower resolution (1-3 nm against few Angstroms). However, it has been predicted that more than 35% of human proteins have significant regions of disorder and about 25% are likely to be completely disordered (Kikhney and Svergun 2015). Hence, the absence of stable tertiary structure often leads to difficulties in obtaining protein crystals, thus compromising the possibility for X-ray crystallography experiments to be performed. Under physiological conditions, these partially disordered proteins constantly fluctuate between different structural states, resulting in a dynamic mixture of structural variants. SAXS can then prove to be the powerful tool to explore the “actual” shape of a protein in solution.

5.2. Important parameters in SAXS

Typically, a monochromatic beam of X-rays is directed to a sample by a series of mirrors. For structural experiments hard X-rays with wavelengths (λ) of 0.10-0.15 nm and energies of around 10keV are used. Upon passing through the sample, some of the X-rays will scatter. Specific detectors are positioned to collect the scattered photons, and a scattering intensity pattern will be obtained (Petoukhov and Svergun 2013, Kikhney and Svergun 2015, Trehella, Duff et al. 2017). The scattered X-rays form a radially developed pattern of elastic scattering which is collected by a 2-dimensional flat X-ray detector situated behind the sample perpendicular to the direction of the primary beam that initially hit the sample (see

section 2.6.1). The scattering pattern is a radially organised arrangement of detected intensities. Those intensities are a function of scattering angles which feed information to the momentum transfer vector q (as the molecule tumbles in solution with a certain speed). The major challenge that must be overcome in SAXS instrumentation is the separation of the weak scattered intensities from those of the powerful main beam (Petoukhov and Svergun 2013, Kikhney and Svergun 2015, Trewella, Duff et al. 2017). The smaller the forward scattering angle, the more difficult this separation becomes.

Since the macromolecules are in solution and not “frozen” and immobile as in tight crystalline lattice, their orientation is supposed to be homogenous in all directions. Thus, scattering is usually presented as a radially averaged one dimensional curve (Petoukhov and Svergun 2013, Kikhney and Svergun 2015, Trewella, Duff et al. 2017). The scattering curve is described by the intensity $I(q)$ as a function of the momentum transfer q (scattering vector), where s is defined as below:

$$q = \frac{4\pi s \sin\theta}{\lambda}$$

Equation 5.1 Scattering Intensity $I(q)$ as a function of the momentum transfer q (scattering vector). Where θ is the angle between the x-ray beam and the detector and λ is the wavelength of the x-rays.

Due to the high scattering intensity of a sample due its buffer composition and heterogeneity, a certain number of parameters are important to ensure background scattering noise can be minimized (Petoukhov and Svergun 2013, Kikhney and Svergun 2015, Trewella, Duff et al. 2017). First and foremost, the concentration of the macromolecules must be high enough so the contrast between the electron density of the molecule and those of the buffer can be distinguished from one another. If not, structural information will be lost during the subtraction of scattering profile of the buffer from the one of the analyte.

Another parameter that needs to be controlled is the monodispersity of a sample, which has to be maximised in order to avoid scattering interference by contaminants. Thus, the purer the sample the greater the chances of achieving a robust structural model, as in X-Ray crystallography. Typically,

filtering and high-speed centrifugation are performed to ensure removal of heavy aggregates and ensure monodispersity, following gel filtration chromatography.

Finally, it is of absolute importance that the buffer composition matches the one of the sample (Petoukhov and Svergun 2013, Kikhney and Svergun 2015, Trehwella, Duff et al. 2017). Indeed, a great deal in the generation of accurate data is the subtraction of the background intensities offered by the chosen buffer in which the desired molecule is solubilised. If buffers are not alike, troublesome variation will be obtained in the scattering profile, and the solvent might not be well excluded from the model. In the case of membrane proteins, dialysis is generally performed prior to the experiment, in the same buffer used for the background removal. It can be performed for an hour (soluble proteins) to days in the case of membrane proteins (due to the slower exchange kinetics of detergents) (Petoukhov and Svergun 2013, Kikhney and Svergun 2015, Trehwella, Duff et al. 2017).

5.3. Analysis of scattering data and generation of preliminary protein envelopes

Scattering profiles are generated for both the buffer and protein of interest. The removal of the buffer baseline is then obtained by subtraction of the buffer scattering intensity from the overall data (protein scattering intensity). A number of parameters can be directly or indirectly (via additional curves such as the $P(r)$ distribution function) identified from the resulting scattering intensity curve ($I(q)$) such as the radius of gyration (R_g), molecular mass (MM), the maximum diameter of the particle (D_{max}) and the intensity at zero scattering angle $I(0)$ (Trehwella, Duff et al. 2017). The software Primus® (Petoukhov, Franke et al. 2012, Franke, Petoukhov et al. 2017) is generally used to assess these parameters, but Scatter® software (Förster, Apostol et al. 2010) offers a more “all in one” approach, which makes it more user-friendly and more adapted for high-throughput methods.

The scattering intensity is then radially averaged to generate the pair distance function $P(r)$. $P(r)$ distribution relates the position of pairs of electrons within the scattering sample (Petoukhov and Svergun 2013, Kikhney and Svergun 2015, Trehwella, Duff et al. 2017). Electron distance is a one-dimension function, but the calculation of all the paired-electron distances enables a consequential reconstruction of 2D and 3D maps. The $P(r)$ distribution is a Fourier transformation of the scattering

profile $I(q)$ vs q plot commonly shown as $P(r)$ vs r (Petoukhov and Svergun 2013, Kikhney and Svergun 2015, Trewhella, Duff et al. 2017). This is achieved through the use of GNOM program or module (Table 5.1) (Petoukhov, Franke et al. 2012, Franke, Petoukhov et al. 2017).

The output file generated can be used to build a low-resolution model of the shape of the particles' density, using programs such as DAMMIN or DAMMIF (Table 5.1) (Franke and Svergun 2009). The latter, a more recent algorithm, uses a more automated approach, but its high-throughput processing can increase the statistical robustness of the generated models. In summary, the modelling program will generate a crude shape or volume filled with dummy atoms, often bigger than the protein (Franke and Svergun 2009); this is partly due to the bound solvent being accounted for. DAMMIN then produces a compact model by assigning the dummy atoms as part of either the solvent or as particles (from the core structure) and uses simulated annealing (Franke and Svergun 2009), in order to fit the experimental data. This process is repeated multiple times (>20), each time generating a slightly different model.

Statistical relevance is generally assessed through the χ^2 value, which can be defined as a measure of the goodness of fit character of the model (Franke, Petoukhov et al. 2017). For good relevance, the χ^2 must be at a minimum (below 0.5). DAMMIN generated volumes not fitting this criterion are not processed further.

DAMAVER module (Table 5.1) will superpose the models and produce an averaged model and a refined model (smaller since variable areas are not accounted for) (Petoukhov, Franke et al. 2012, Franke, Petoukhov et al. 2017).

Table 5.1 Table 5.1. Important SAXS *ab initio* Programs. List of Software used for SAXS envelope modelling and their corresponding function. Taken from Gemma Brown (PhD Thesis, 2016)(Brown 2016, Franke, Petoukhov et al. 2017).

Program	Function
SCATTER	An interface for performing manipulations of the scattering data including, subtraction, averaging, merging, extrapolation to zero concentration.

	Generation and evaluation of Guiner, Porod and Kratky plots.
	Build-in modules: GNOM, DAMMIN, DAMMIF, SUPCOMB, DAMSEL, DAMSUP, DAMAVER, DAMFILT
GNOM	An indirect transform program which takes one dimensional scattering curves and evaluates the P(r) and prepares .out files for modelling.
DAMMIN	A tool for ab-initio modelling of SAXS data based on bead modelling and simulated annealing.
DAMMIF	An improved ab-initio modelling program based upon the foundations of DAMMIN but implementing a new algorithm to speed up reconstruction by a factor of 25-40.
SUPCOMB	A program used to superimpose one 3D structure onto another and calculates a normal spatial discrepancy (NSD) which can be used to determine the best alignments between models.
DAMSEL	The program takes all generated models in PDB format and superimposes all possible pairs using SUPCOMB then generates an output table which determines which models are outliers and selects a reference model. Models are considered as outliers if the NSD exceeds two standard deviations away from the calculated mean.
DAMSUP	A program that aligns a set of models excluding the outliers to a selected reference model and calculates standard deviation from the NSD.
DAMAVER	The program averages models that have been aligned by DAMSUP and computes a probability map.

DAMFILT

Can take the DAMAVER file and filter the model by removal of low occupancy regions or loosely connected atoms, this model doesn't always reflect the true size of the experimental data.

5.4. Generation of the Bovine Serum Albumin (BSA) Envelope

Different parameters, such as the sample monodispersity or the buffer composition, are key to the success of a SAXS experiment on a macromolecule (Petoukhov and Svergun 2013). Nevertheless, the advance in technology and the use of powerful X-ray generators (synchrotrons) can minimize the impact of these parameters on the final scattering profile and still generate complete data sets. The electron beam strength will help generate enormous amount of data in few seconds and does not require multiple frames exposure as opposed to conventional “in-house” SAXS experiments. However, the strength of the beam can be deleterious to the protein integrity. Indeed, most samples decompose almost immediately (one to few seconds) during SAXS experiments. Hence, the first test performed when starting a SAXS experiment in the Diamond Light Source (Oxford, Oxfordshire) helps determine the “protective effect” of the buffer on the protein against radiation damage. A reference protein with known SAXS parameters as well as crystal structure must be used as a control to test the buffer protection against radiation damage and to relate radius of gyration to molecular weight and size of spherical envelopes. As a result, data were collected for 2 seconds at the Beamline B21 (see section 2.6.1) on buffer blank samples (dialysis buffer; 25 mM $\text{NaH}_2\text{PO}_4/\text{Na}_2\text{HPO}_4$ (pH 7.0), 50 mM NaCl, 1 mM EDTA, 1 mM DTT, 10 % (w/v) Glycerol, 0.12% (v/v) LDAO) and Bovine Serum Albumin at a concentration of 5 mg/mL in the same buffer.

5.4.1. Data Collection on BSA at 5 mg/mL

Raw scattering intensity data were obtained for both BSA (Figure 5.1; blue curve) and buffer (Figure 5.1; red curve). Data from the buffer were then subtracted from the sample to generate the new scattering curve (Figure 5.1, pink curve), that would be used for further processing. Theoretically, this curve only reflects the scattering data from the solvated protein (surrounded by solvent), as most of the buffer intrinsic noise had been removed (Petoukhov and Svergun 2013, Kikhney and Svergun 2015, Trewhella, Duff et al. 2017).

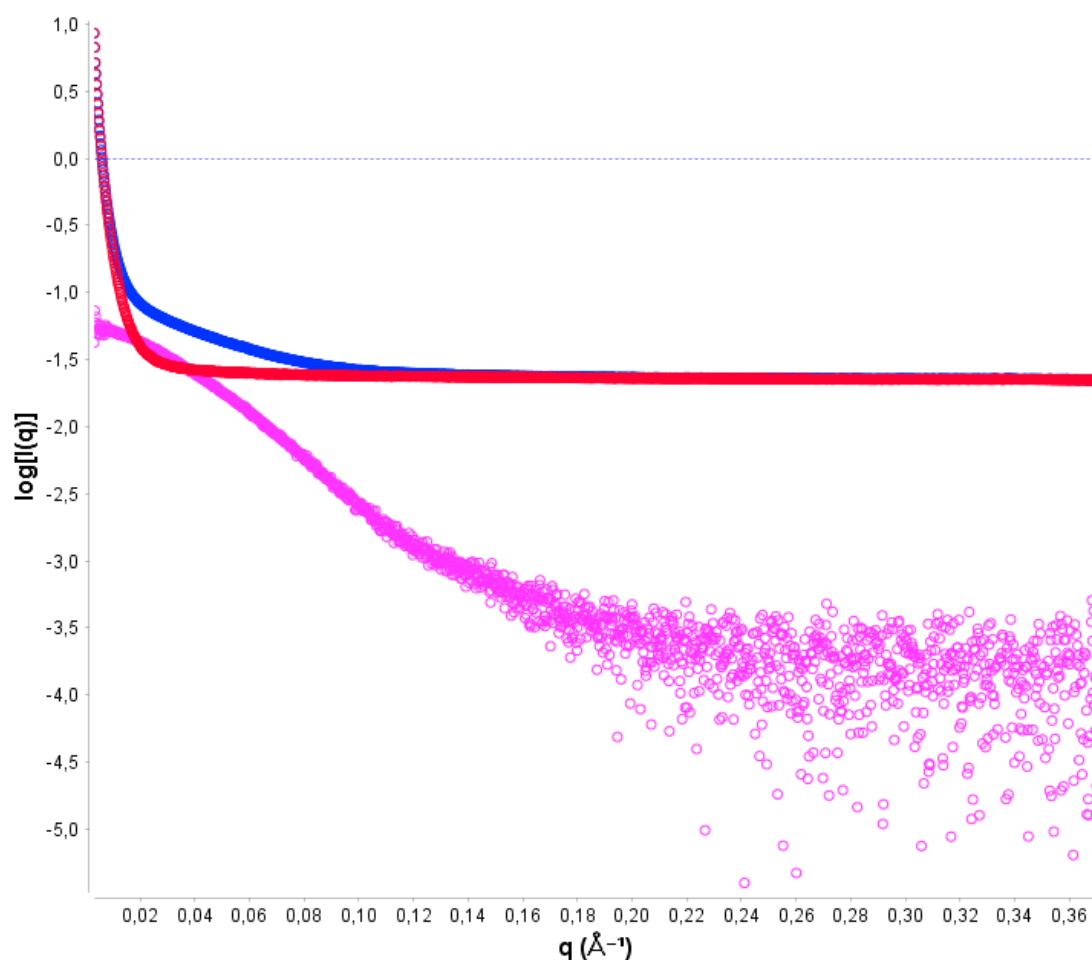


Figure 5.1 Raw Scattering Intensity plots of BSA at 5 mg/mL and its buffer. Scattering data recorded at the Beamline B21 and displayed as log of intensity over the scattering vector q (\AA^{-1}) and created using ScAtter Software® (Förster, Apostol et al. 2010). Blue line is the scattering intensity curve for the sample (BSA at 5 mg/mL in 25 mM $\text{NaH}_2\text{PO}_4/\text{Na}_2\text{HPO}_4$ (pH 7.0), 50 mM NaCl, 1 mM EDTA, 1 mM DTT, 10 % (w/v) Glycerol, 0.12% (v/v) LDAO). Red line is the scattering profile recorded for the blank sample (25 mM $\text{NaH}_2\text{PO}_4/\text{Na}_2\text{HPO}_4$ (pH 7.0), 50 mM NaCl, 1 mM EDTA, 1 mM DTT, 10 % (w/v) Glycerol, 0.12% (v/v) LDAO). The Pink line represents the adjusted scattering of BSA following buffer blank background subtraction.

5.4.2. Primary analysis of the BSA (5 mg/mL) scattering data

The initial approach when dealing with scattering data, is the primary evaluation of the radius of gyration (R_g) and the extrapolated intensity at zero scattering angle $I(0)$, using the Guinier approximation (Petoukhov and Svergun 2013, Kikhney and Svergun 2015, Trewthella, Duff et al. 2017). This approximation is made at low q values, as most spherical molecules display a relative consistency between hypothetical (calculated) and real (following ab initio modelling) parameters. R_g and intensity can be directly calculated by the Guinier plot using the equation below:

$$R_g = \sqrt{-3a}$$

Equation 5.2 Calculation of the Radius of gyration (R_g) by Guinier analysis. Where a is the slope of the scattering curve at low q values.

One of the main phenomena interfering with the quality of SAXS experiments and the generation of clean scattering data is protein aggregation (Petoukhov and Svergun 2013, Kikhney and Svergun 2015, Trehwella, Duff et al. 2017). Protein aggregation can be assessed directly on the scattering profile, as it will lead to a high upturn of $I(q)$ at low q values. In the case of BSA at 5 mg/mL (in 25 mM $\text{NaH}_2\text{PO}_4/\text{Na}_2\text{HPO}_4$ (pH 7.0), 50 mM NaCl, 1 mM EDTA, 1 mM DTT, 10 % (w/v) Glycerol, 0.12% (v/v) LDAO), more pronounced noise could be observed at low q values, but no high upturn of $I(q)$ was identified (Figure 5.1). Thus, there was no apparent aggregation of the samples and all scattering points could be used for the Guinier approximation.

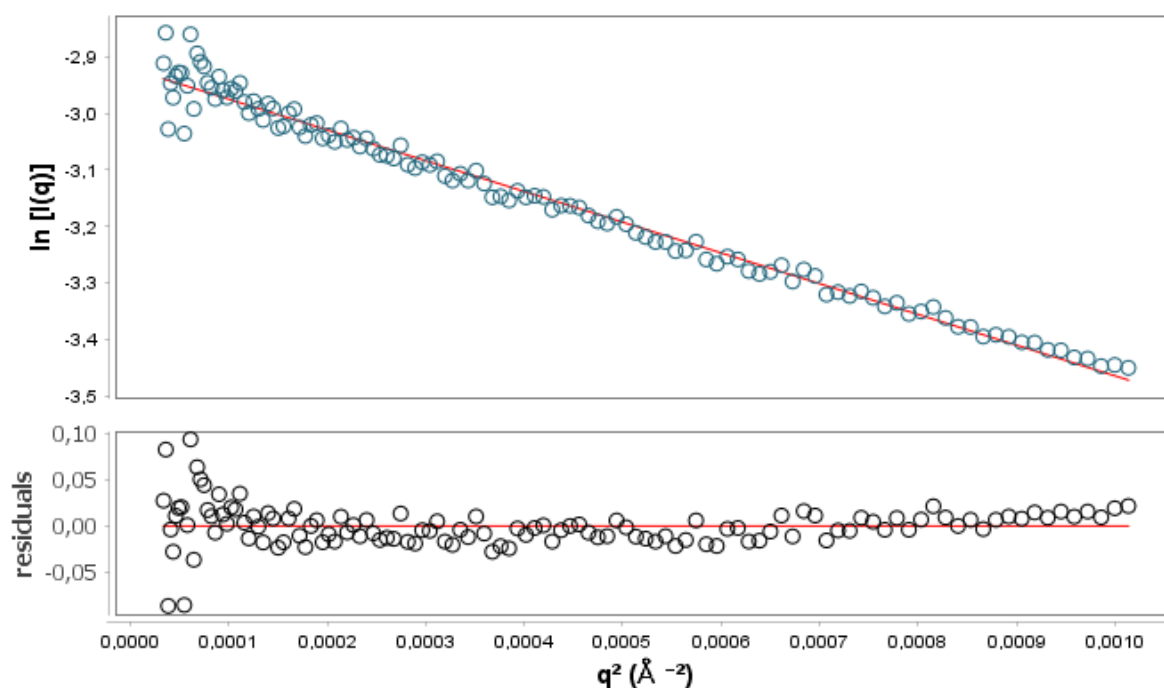


Figure 5.2 Initial Guinier analysis of the 5 mg/mL BSA scattering curve. (Top) First data points of the recorded scattering data displayed (in blue dots) as log of intensity over the scattering vector q (\AA) and created using ScAtter Software® (Förster, Apostol et al. 2010, Petoukhov and Svergun 2013, Kikhney and Svergun 2015, Trehwella, Duff et al. 2017). The first 130 data points were used to fit a linear curve (red) that would be used to calculate the hypothetical R_g . (Bottom) Residual analysis of the scattering data (black dots) from the tendency curve (red).

The Scatter® software, developed by Dr Rambo from the Diamond Light Source (Oxford, Oxfordshire), was used for the calculation of the hypothetical Rg and I(0) as well as their “real” parameters using GNOM (Franke, Petoukhov et al. 2017). Values for Rg and I(0) are reported in Table 5.2.

Table 5.2 Summary Table of Rg and I(0) values for BSA at 5 mg/mL.

Parameter	Value calculated by Scatter®
Rg (Reciprocal Space)	40.03
Rg (Real space)	41.00
I(0) (Reciprocal Space)	5.33×10^{-2}
I(0) (Real space)	5.36×10^{-2}

Rg and I(0) parameters were calculated by the Scatter Software® using the Guinier approximation (reciprocal space) and GNOM (Real Space).

For the reference protein BSA, all values were similar for both Rg and I(0) (Table 5.2), regardless of the methodology of calculation. Surprisingly, Rg values for the monomer BSA protein available on sasbdb® website (SAXS and SANS general data platform) were reported to be close to 27 Å (SASDBT4, <https://www.sasbdb.org/data/SASDBT4>). However, the higher Rg values reported here (around 40-41 Å) correlate with those of a BSA dimer, reported to be close to 39 Å (SASDBK3, <https://www.sasbdb.org/data/SASDBK3>) on SEC-SAXS (Size exclusion chromatography coupled with SAXS). This result is likely due to the detergent cooperative binding to BSA, leading to the formation of micelle-like aggregates (Santos, Zanette et al. 2003).

5.4.3. Quality analysis on BSA (5 mg/mL) scattering data

Additional parameters can be derived from the Raw scattering data using another type of analysis. The Kratky analysis or Kratky plot will provide information on the folding or “unfolded-ness” of macromolecules. It has been evidenced (Putnam et al., 2007) that a globular molecule displays a bell-shaped curve on this plot and the more unfolded the analyte is, the higher the $q^2 \times I(q)$ product at high q values (Figure 5.3A), and a more hyperbolic “structural signature” is evident as for completely unfolded proteins (Figure 5.3A, red curve).

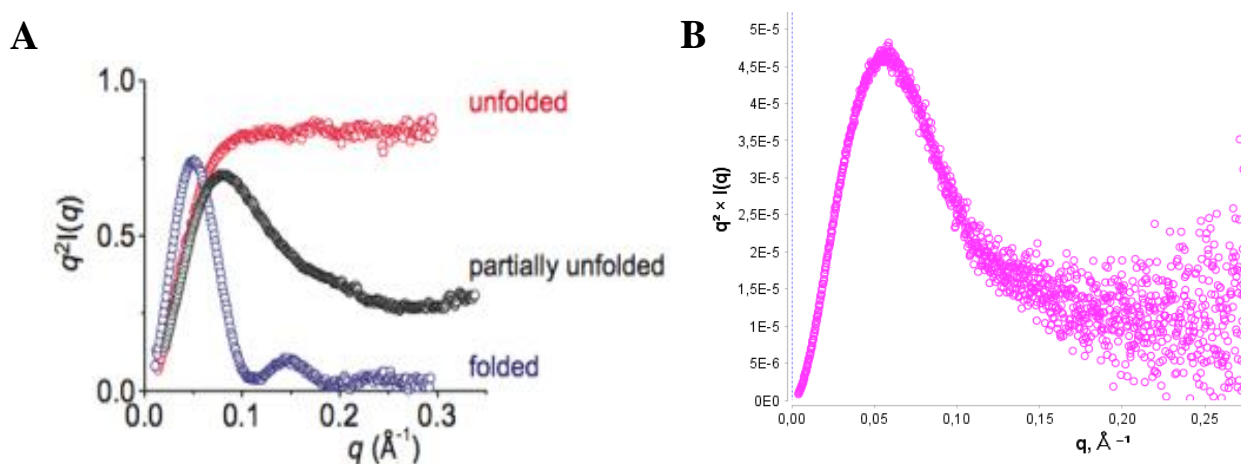


Figure 5.3 Kratky Analysis of the 5 mg/mL BSA scattering data. (A). Representative Kratky curves for a globular and folded (blue) molecule, partially unfolded (black) and completely unfolded (red). (B) Kratky plot (in pink) of the BSA protein at 5 mg/mL in 25 mM $\text{NaH}_2\text{PO}_4/\text{Na}_2\text{HPO}_4$ (pH 7.0), 50 mM NaCl, 1 mM EDTA, 1 mM DTT, 10 % (w/v) Glycerol, 0.12% (v/v) LDAO). The profile obtained corresponds to that of a relatively well folded protein with partial unfolding.

Analysis of the Kratky Plot from BSA at 5 mg/mL in 25 mM $\text{NaH}_2\text{PO}_4/\text{Na}_2\text{HPO}_4$ (pH 7.0), 50 mM NaCl, 1 mM EDTA, 1 mM DTT, 10 % (w/v) Glycerol, 0.12% (v/v) LDAO) revealed a bell-shaped curve (see example of blue curve in Figure 5.3A) with slight upturn at high q values similar to the one of a partially unfolded protein (Figure 5.3A, black curve). Altogether, these data indicated a substantial degree of folding with slight disorganization. The level of disorganisation is hardly influenced by the relative noise of the scattering data at high q values which could indicate imperfect buffer subtraction. Nevertheless, previous SAXS experiments on BSA displayed a similar level of noise above 0.20\AA^{-1}

(Trehwella, Duff et al. 2017), thus giving confidence there was no mismatch but rather a lack of robust scattering intensities for BSA above this scattering angle.

Porod plots (expressed in $q^4 \times I(q)$) follow a similar principle to Kratky plots, but instead of providing information on the “unfolded-ness”, they reveal information about the flexibility of the molecule (Petoukhov and Svergun 2013, Kikhney and Svergun 2015, Trehwella, Duff et al. 2017). In this case, a bell-shaped curve is indicative of a fairly compact protein, and its plateauing at high q values relate to a very flexible protein (which still display some level of folding).

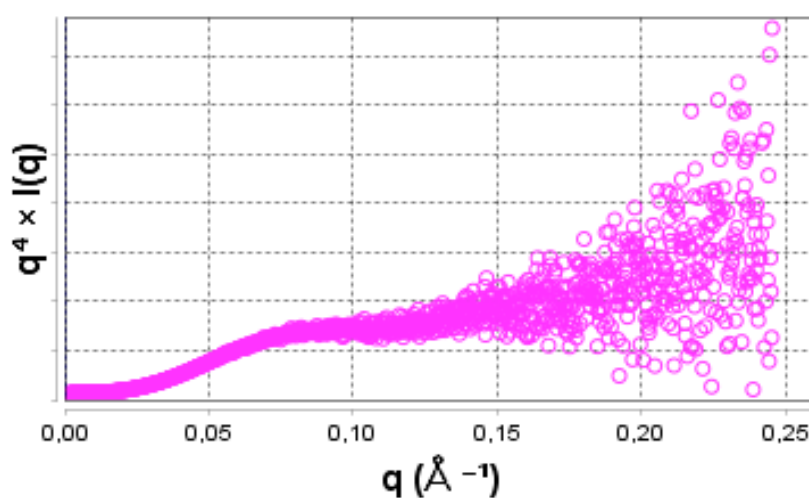


Figure 5.4 Porod plot analysis the 5 mg/mL BSA scattering data. Porod plot (in pink) of the BSA protein at 5 mg/mL (in 25 mM $\text{NaH}_2\text{PO}_4/\text{Na}_2\text{HPO}_4$ (pH 7.0), 50 mM NaCl, 1 mM EDTA, 1 mM DTT, 10 % (w/v) Glycerol, 0.12% (v/v) LDAO), generated through ScAtter Software © (REF). The profile obtained (expressed in $q^4 \times I(q)$) corresponds to that of a partially flexible protein.

In the case of BSA protein at 5 mg/mL in 25 mM $\text{NaH}_2\text{PO}_4/\text{Na}_2\text{HPO}_4$ (pH 7.0), 50 mM NaCl, 1 mM EDTA, 1 mM DTT, 10 % (w/v) Glycerol, 0.12% (v/v) LDAO), the Porod profile obtained resembled a bell-shaped curve at low q values, with decent upturn at high q values. This indicated the protein was relatively compact and lacked flexibility.

Overall, the quality assessment of the Scattering intensity of the 5 mg/mL BSA sample in the buffer of choice, revealed a well folded protein with a great degree of flexibility. The initial analysis did not reveal

parameters preventing the subsequent modelling using these data sets, such as high aggregation or a total absence of folding.

5.4.4. Evaluation of the P(r) distribution function of the 5 mg/mL BSA scattering data

Once the primary analysis on the data is performed (section 5.3), the P(r) distance distribution is calculated from the scattering curve and is processed through GNOM (Franke, Petoukhov et al. 2017). certain parameters need to be modulated, in order to obtain a representative P(r) function. For example, some scattering data points can be discarded at low and high q values (where the noise is at his highest), and the maximum distance between two pairs of electrons within the molecule (Dmax) can be adjusted to reflect the overall maximum distribution within the molecule. As with previous analyses, patterns can be identified and compared to those that had been generated from distinct and precise structural configurations (Figure 5.5A). Again, a bell-shaped curve corresponds to a spherical and globular molecular envelope, whereas, a multimodal curve will be potentially indicative of a multidomain protein.

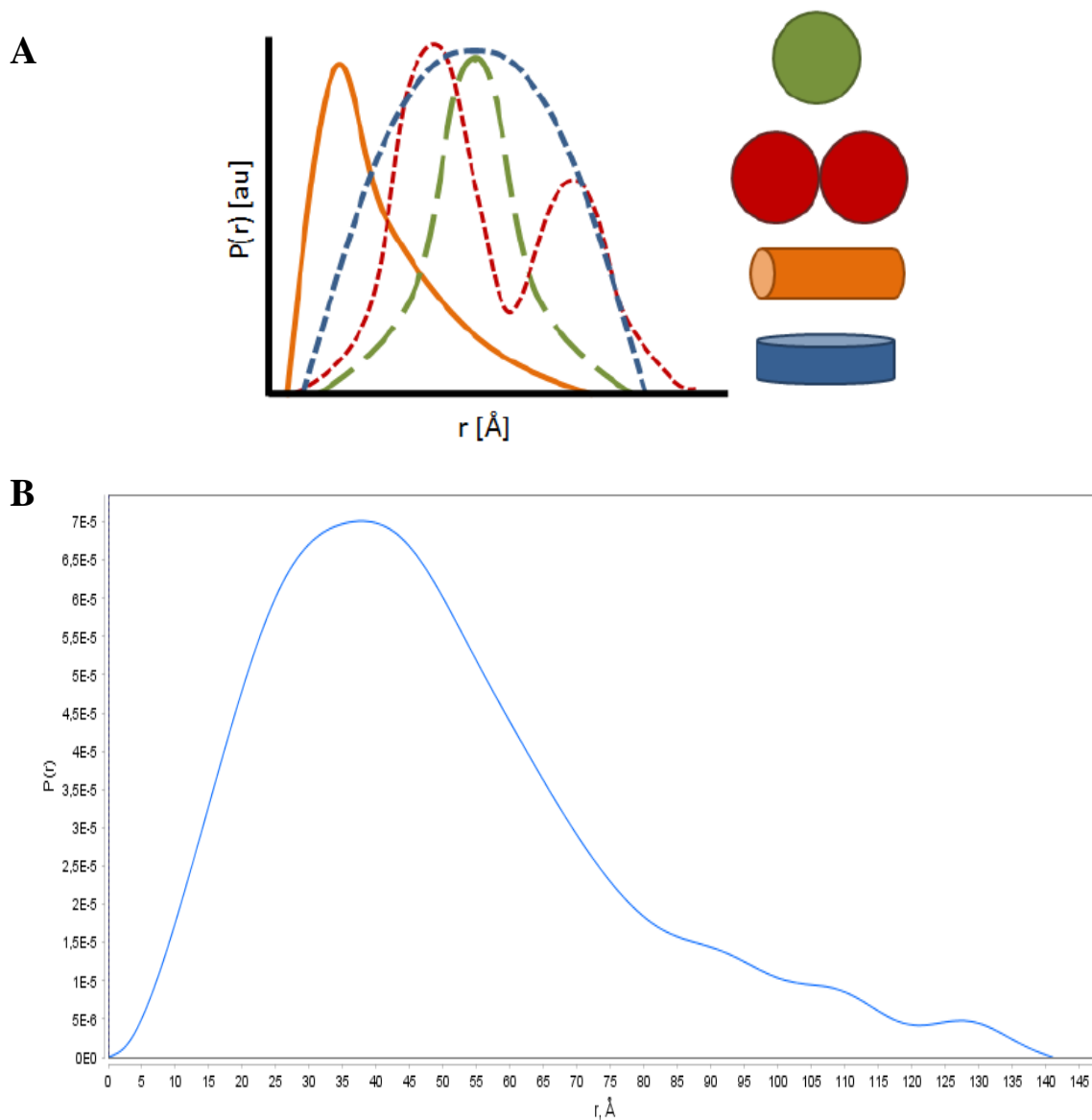


Figure 5.5 P(r) distribution of BSA at 5 mg/mL. (A) Representative P(r) distribution function for a globular and spherical (green), multi-domain (red), cylindrical (orange) and a disk (blue) shaped proteins. (B) P(r) distribution function of 5 mg/mL BSA in 25 mM $\text{NaH}_2\text{PO}_4/\text{Na}_2\text{HPO}_4$ (pH 7.0), 50 mM NaCl, 1 mM EDTA, 1 mM DTT, 10 % (w/v) Glycerol, 0.12% (v/v) LDAO.

The P(r) distribution function obtained for the 5 mg/mL BSA sample (in 25 mM $\text{NaH}_2\text{PO}_4/\text{Na}_2\text{HPO}_4$ (pH 7.0), 50 mM NaCl, 1 mM EDTA, 1 mM DTT, 10 % (w/v) Glycerol, 0.12% (v/v) LDAO) fitted a well-defined bell-shaped curve, suggesting the presence of a relatively globular and spherical core. However, the tailing in the profile indicated the presence of a more cylindrical component or at least an elongated protein. Altogether these results confirmed previous analysis performed on the raw scattering data (see 5.4.3).

5.4.5. Generation of molecular envelopes for BSA at 5 mg/mL

Using the $P(r)$ distribution function, output files are generated by Scatter® (through the GNOM module) and communicated to the DAMMIF *ab initio* modelling automated algorithm. As described in section 5.3, the program defines a search volume of dummy atoms and will either assign each dummy atom as part of the solvent or as part of the macromolecule (Franke and Svergun 2009). A compact model will be generated (by simulated annealing) from an arbitrary starting model, which should theoretically fit the experimental scattering data. The process was repeated 23 times, generating each time a different envelope (Figure 5.6).

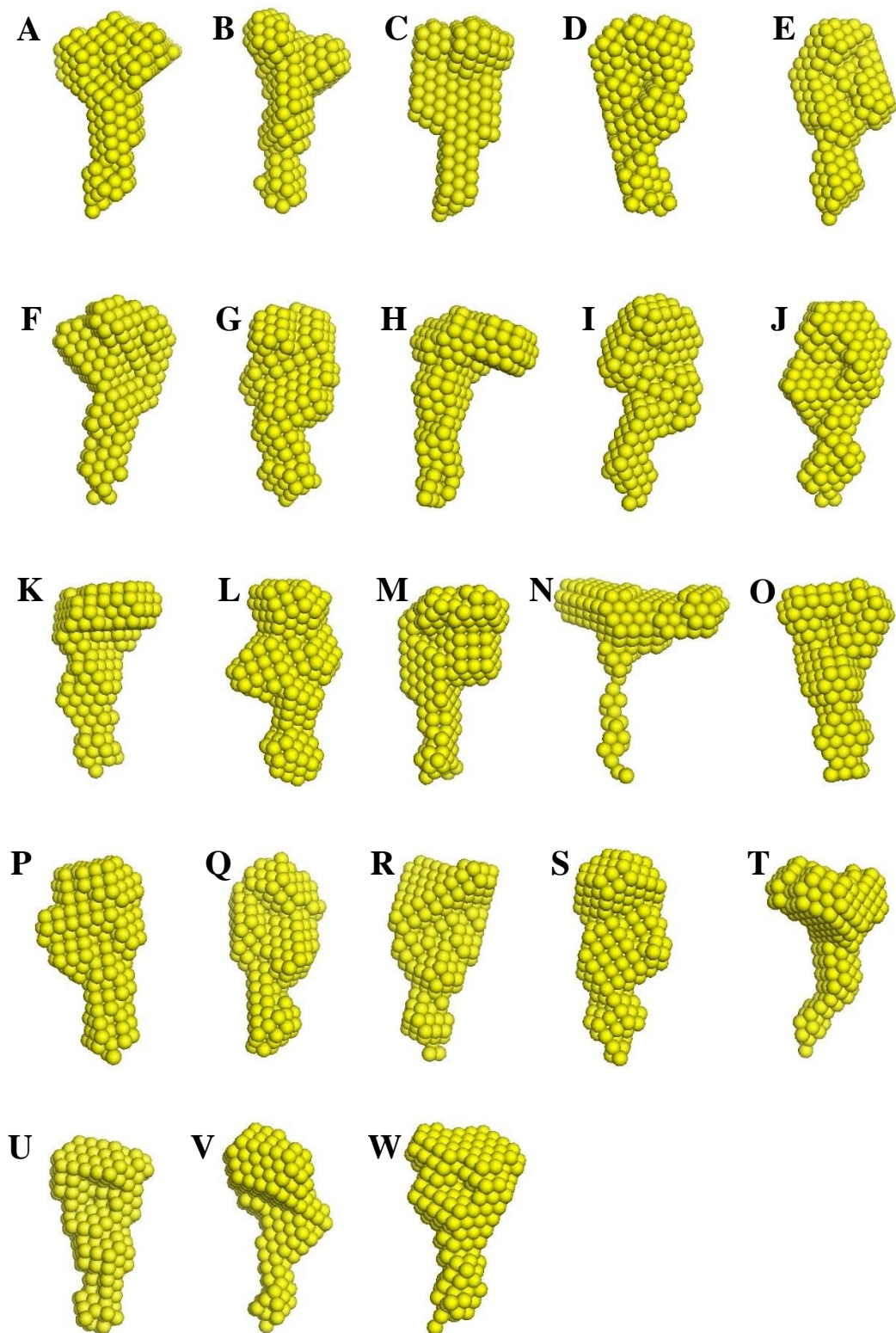


Figure 5.6 Molecular envelopes of BSA at 5 mg/mL. Twenty-three independent models (A to W) were generated using the DAMMIF algorithm (Franke and Svergun 2009) for the BSA protein in 25 mM $\text{NaH}_2\text{PO}_4/\text{Na}_2\text{HPO}_4$ (pH 7.0), 50 mM NaCl, 1 mM EDTA, 1 mM DTT, 10 % (w/v) Glycerol, 0.12% (v/v) LDAO.

5.4.6. Evaluation of the generated envelopes for BSA

The DAMSEL program (Franke and Svergun 2009) will calculate a parameter known as the normal spatial discrepancy (NSD) for each envelope and will discard any values with a NSD above two standard deviation from the mean NSD. DAMSUP will superpose the accepted models and calculate a standard deviation from the reference NSD (lowest amongst all remaining models). This procedure will help refining the model and discard any potential outliers prior to averaging the models (Franke and Svergun 2009).

Table 5.3 Summary of DAMSEL and DAMSUP results for BSA at 5 mg/mL.

Model	DAMSEL NSD	FATE	DAMSUP NSD
16	0.584	Reference	0.000
18	0.584	Include	0.536
3	0.585	Include	0.485
23	0.589	Include	0.555
21	0.592	Include	0.549
17	0.592	Include	0.538
13	0.594	Include	0.541
15	0.596	Include	0.541
4	0.599	Include	0.558
7	0.600	Include	0.507
10	0.601	Include	0.522
2	0.602	Include	0.591
6	0.604	Include	0.535
5	0.608	Include	0.544
9	0.609	Include	0.493
1	0.611	Include	0.565
19	0.613	Include	0.560
12	0.620	Include	0.541
11	0.621	Include	0.574
22	0.641	Include	0.634
8	0.671	Include	0.665
20	0.704	Include	0.668
14	1.102	Discard	N/A

The mean NSD value was calculated to be 0.631 with a standard deviation of 0.106. Models are sorted from the lowest to the highest NSD value. Model 16 had the best NSD at 0.584 and was taken as the reference for the superposition with DAMSUP. Model 14 had a NSD value of 1.102 and was subsequently discarded. DAMSUP superposes the accepted models and calculates deviation values from the reference NSD.

5.4.7. Final envelope refinement for BSA at 5 mg/mL

The accepted BSA envelope models were aligned and averaged by DAMAVER (Franke and Svergun 2009). The resulting volume (or probability map) was further filtered by DAMFILT using a predefined cut-off. Low occupancy regions were discarded and only the core (of high occupancy) was retained.

Both molecular envelopes (averaged and refined) can be visualized with software such as Pymol® or WMD® (Figure 5.7). A crystal structure of the reference protein is generally used to orient the envelope.

Although the molecular envelopes generated for the 5 mg/mL BSA in 25 mM NaH₂PO₄/Na₂HPO₄ (pH 7.0), 50 mM NaCl, 1 mM EDTA, 1 mM DTT, 10 % (w/v) Glycerol, 0.12% (v/v) LDAO) seemed adequate when compared the reference crystal structure of Bovine Serum Albumin (3V03), a certain portion of the latter is outside the volume defined by the SAXS analysis (Figure 5.7 blue ribbons). This might be due to the flexibility observed in the previous analyses (see 5.4.3) and the partial lack of folding, resulting in some part of the protein being considered as solvent and discarded in the earlier stages.

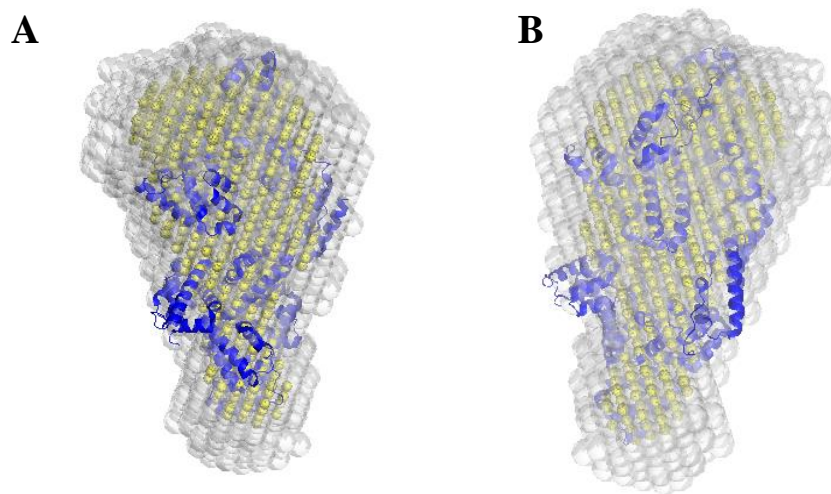


Figure 5.7 Predicted molecular envelopes for BSA at 5 mg/mL. Probability map (grey) and filtered (yellow) molecular envelope generated by DAMAVER on a BSA sample at 5 mg/mL in mL in 25 mM $\text{NaH}_2\text{PO}_4/\text{Na}_2\text{HPO}_4$ (pH 7.0), 50 mM NaCl, 1 mM EDTA, 1 mM DTT, 10 % (w/v) Glycerol, 0.12% (v/v) LDAO. The crystal structure of Bovine Serum Albumin 3V03 was added (in blue) and retrieved from the Protein Data Bank. The front (A) and back side (B) of the envelope are shown.

5.5. Structural characterization of AtVDAC1 protein by Small Angle X-ray Scattering (SAXS)

5.5.1. Data collection for AtVDAC1

SAXS data were collected at the Beamline B21 for AtVDAC1 at five different concentrations. Sample (4 mg/mL) was diluted in a 96-well plate four times, each time by a factor of 2. The resulting samples (4, 2, 1, 0.5 and 0.25 mg/mL) were all subjected to SAXS for 2 seconds, and triplicated. Series of triplicates were then averaged to produce a final scattering profile for each of the different concentrations (Figure 5.8A). The buffer blank (25 mM NaH₂PO₄/Na₂HPO₄ (pH 7.0), 50 mM NaCl, 1 mM EDTA, 1 mM DTT, 10 % (w/v) Glycerol, 0.12% (v/v) LDAO) was also subjected to SAXS measurements, and its scattering profile (Figure 5.8A blue line) was subtracted from the scattering data of the protein samples (Figure 5.8B). A high upturn of the scattering intensity at low q values could be observed for each sample, despite performing dilutions and centrifuging samples prior to the experiment. This indicates a degree of polydispersity in the samples, due to potential aggregation or oligomerization. The great level of noise observed on the scattering profile of the lowest dilution (0.25 mg/mL, Figure 5.8, grey line) indicated possible buffer mismatch (due to the low concentration) and was not analysed further.

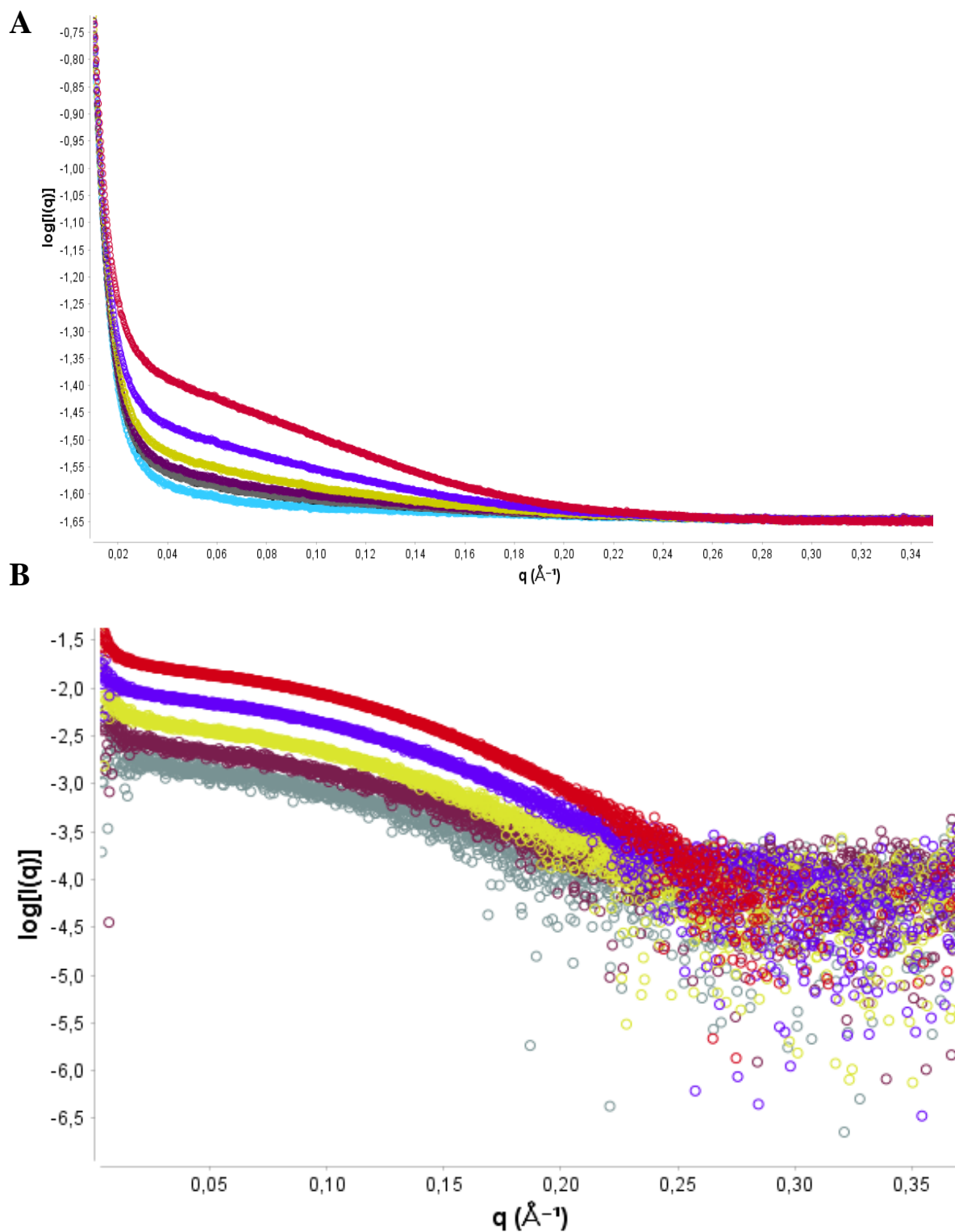


Figure 5.8 Raw Scattering Intensity plots of AtVDAC1 at 4, 2, 1, 0.5 and 0.25 mg/mL. Scattering data recorded at the Beamline B21 and displayed as log of intensity over the scattering vector q (\AA) and created using ScAtter Software® (Förster, Apostol et al. 2010). Samples were dialyzed for 5 days in 25 mM $\text{NaH}_2\text{PO}_4/\text{Na}_2\text{HPO}_4$ (pH 7.0), 50 mM NaCl, 1 mM EDTA, 1 mM DTT, 10 % (w/v) Glycerol, 0.12% (v/v) LDAO. (A) Raw Scattering data of AtVDAC1. The buffer blank (as above) is represented by a blue line. The scattering intensity curves for the AtVDAC1 samples at 4 (red), 2 (purple), 1 (yellow), 0.5 (burgundy) and 0.25 mg/mL (grey) are shown. (B) Subtracted scattering data for AtVDAC1 samples (colours are mentioned above).

5.5.2. Calculation of the radius of gyration for AtVDAC1

Data analysis for AtVDAC1 at 4, 2, 1, 0.5 mg/mL was carried out as previously described for the control protein BSA (section 5.4.2). The R_g was calculated using the Guinier approximation (Figure 5.9) and GNOM for all concentrations. Numerical R_g values are reported in Table 5.4.

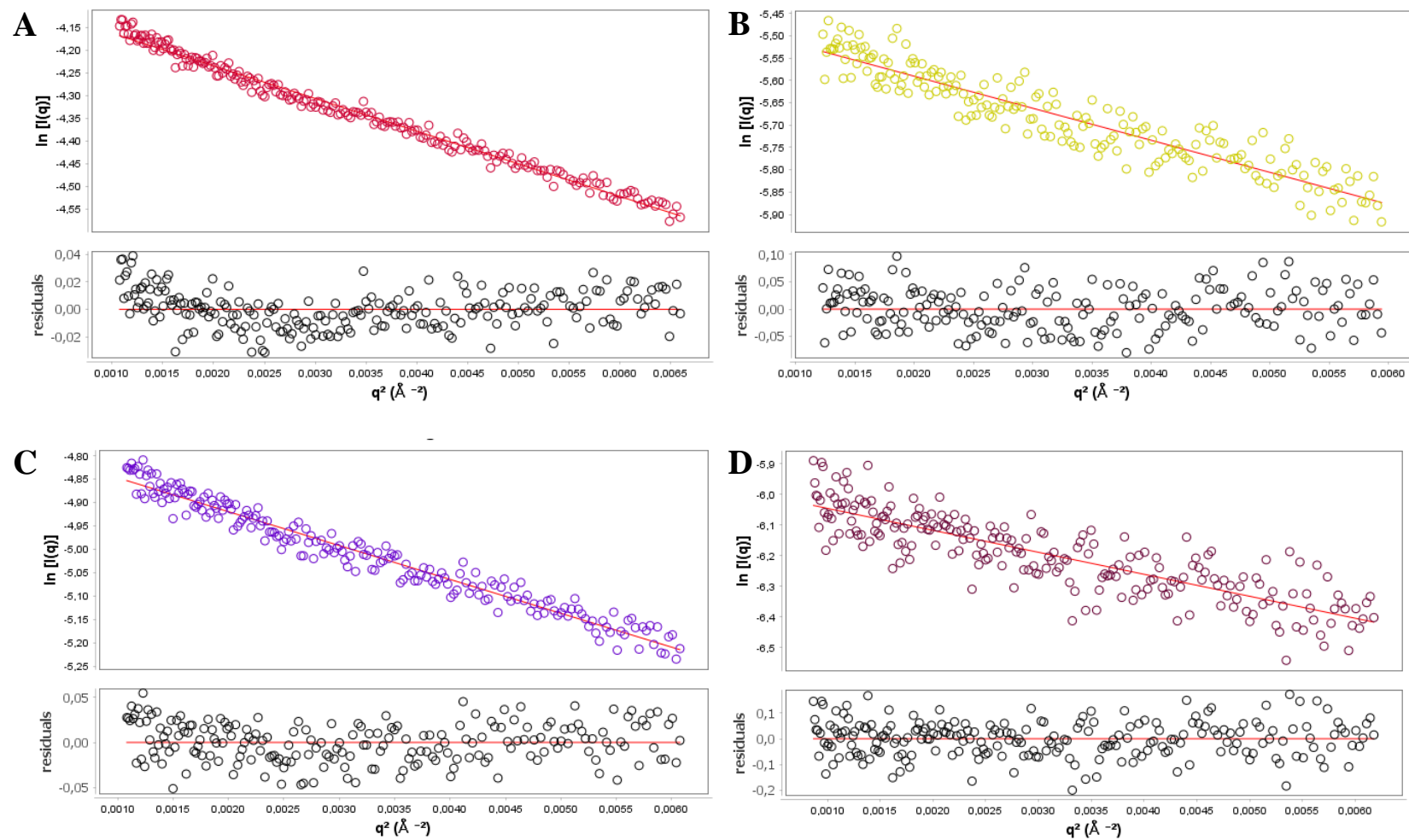


Figure 5.9 Guinier analysis of AtVDAC1 at 4, 2, 1 and 0.5 mg/mL. First data points of the recorded scattering data displayed (in coloured dots) as log of intensity over the scattering vector q (\AA^{-1}) and created using ScAtter Software® (Förster, Apostol et al. 2010). The first 200 points were used to fit a linear curve (red) that would be used to calculate the hypothetical R_g values. Residual analysis of the scattering data (black dots) from the tendency curve (red) is indicated at the bottom for each concentration. Guinier plots of AtVDAC1 at 4 (A), 2 (B), 1 (C) and 0.5 mg/mL (D) are represented by red, purple, yellow, burgundy and grey dots respectively.

Table 5.4 Derived Rg values for AtVDAC1 samples at different concentrations.

Sample	Rg (Reciprocal Space)	Rg (Real space)
AtVDAC1 at 4 mg/mL	14.56	13.88
AtVDAC1 at 2 mg/mL	14.64	14.05
AtVDAC1 at 1 mg/mL	14.59	14.04
AtVDAC1 at 0.5 mg/mL	14.57	13.74

Rg parameters were calculated by the Scatter Software® (Förster, Apostol et al. 2010) using the Guinier approximation (reciprocal space) and GNOM (Real Space).

All reciprocal Rg values were similar, and relatively close to their corresponding real values. A small decreasing trend in the GNOM derived Rg values was observed for the last dilution (0.5 mg/mL). However, the low concentration of the sample was not deemed suitable as possible buffer mismatch are likely to result in over-subtraction of the buffer scattering data from those of the sample, leading to a smaller Radius of gyration.

5.5.3. Kratky and Porod analysis of the analysed AtVDAC1 samples

Kratky and Porods plots (Figure 5.10) both showed bell-shaped curves for all concentrations of AtVDAC1 tested, indicating a great degree of folding compaction. However, only the scattering datasets from the 4 and 2 mg/mL AtVDAC1 samples were used for *ab initio* modelling since the other three dilutions (1, 0.5 and 0.25 mg/mL) did not produce envelope models of good quality, as their concentrations were too low to guarantee statistically relevant molecular envelopes ($\chi^2 > 0.5$).

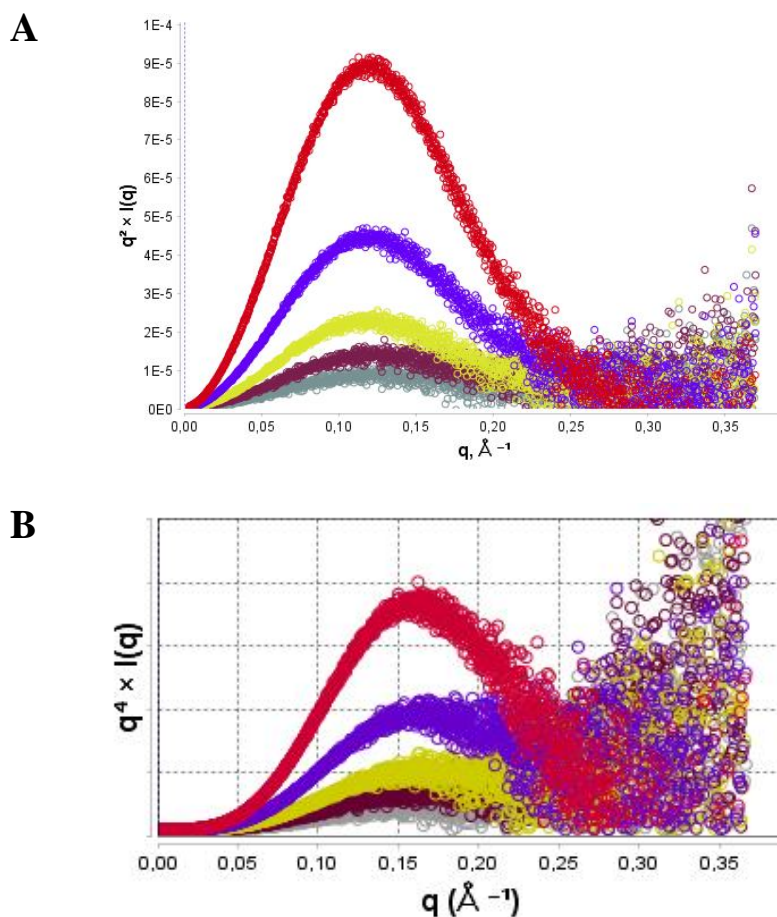


Figure 5.10 Quality assessment of collected AtVDAC1 scattering curves at different protein concentrations. (A) Kratky plot of AtVDAC1 samples at 4 (red), 2 (purple), 1 (yellow), 0.5 (burgundy) and 0.25 mg/mL (grey) are shown. (B) Corresponding Porod plots for the tested AtVDAC1 samples.

5.5.4. Evaluation of the $P(r)$ distribution of AtVDAC1 scattering curves at 4 and 2 mg/mL

Following the initial analysis of the scattering data from the tested AtVDAC1 concentrations, GNOM was used as an indirect transform program for the establishment of the $P(r)$ function for further *ab initio* modelling (Figure 5.11). For convenience, the fit between the scattering data and the tendency curve representing the $P(r)$ distribution is indicated. The two highest concentrations (4 and 2 mg/mL) revealed similar bell-shaped curves with a small extension at high r values, indicating relatively spherical conformations.

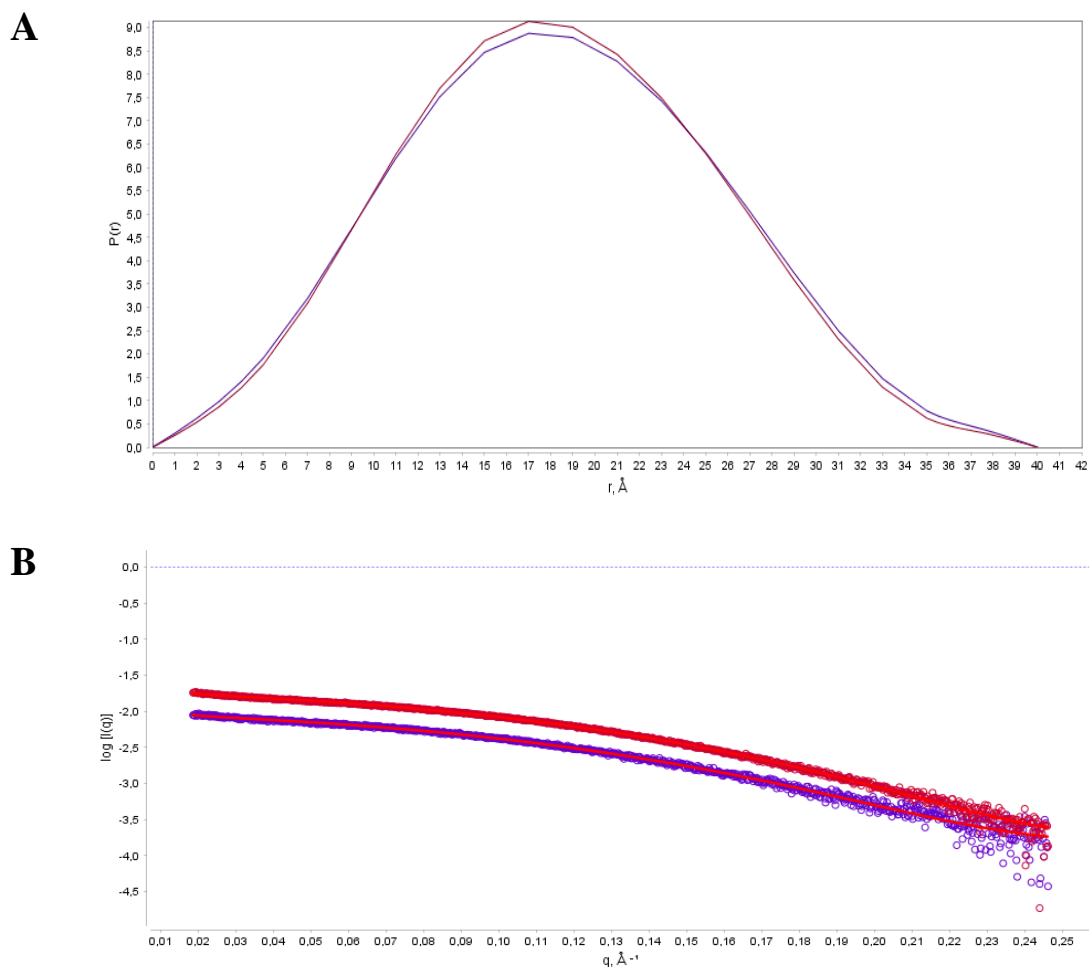


Figure 5.11 P(r) distribution plots of AtVDAC1 scattering data. (A) P(r) distribution function of the AtVDAC1 scattering data, collected from 4 mg/mL (red) and 2 mg/mL (purple) samples in 25 mM $\text{NaH}_2\text{PO}_4/\text{Na}_2\text{HPO}_4$ (pH 7.0), 50 mM NaCl, 1 mM EDTA, 1 mM DTT, 10 % (w/v) Glycerol, 0.12% (v/v) LDAO. (B) Scattering intensity of AtVDAC1 at 4 and 2 mg/mL. For each concentration, the tendency curve representing the P(r) distribution is indicated in red.

5.5.5. Generation and refinement of calculated molecular envelopes for AtVDAC1

Assessment of the quality of the generated envelopes was carried out by DAMSEL and DAMSUP (Table 5.5) as previously described for the BSA control protein (section 5.4.6). Outliers were identified using their NSD value (above two standard deviation from the calculated mean NSD) and removed from the superposition step. Envelopes 11 and 4 were chosen for AtVDAC1 at 4 mg/mL and 2 mg/mL respectively and used by DAMSEL as the reference envelopes for the superposition.

Table 5.5 Summary of DAMSEL and DAMSUP results for AtVDAC1 at 4 mg/mL and 2 mg/mL.

Model	DAMSEL NSD	FATE	DAMSUP NSD
AtVDAC1 at 4 mg/mL			
11	0.484	Reference	0.000
5	0.489	Include	0.376
12	0.490	Include	0.432
22	0.491	Include	0.486
17	0.492	Include	0.457
23	0.493	Include	0.478
13	0.493	Include	0.489
6	0.494	Include	0.440
15	0.495	Include	0.495
9	0.496	Include	0.481
1	0.496	Include	0.471
20	0.499	Include	0.507
10	0.499	Include	0.501
21	0.499	Include	0.487
2	0.500	Include	0.474
14	0.503	Include	0.497
16	0.503	Include	0.503
4	0.506	Include	0.498
3	0.508	Include	0.515
8	0.512	Include	0.514
19	0.519	Include	0.508
18	0.519	Include	0.495
7	0.533	Discard	N/A
AtVDAC1 at 2 mg/mL			
4	0.479	Reference	0.000
13	0.485	Include	0.484
12	0.487	Include	0.331
20	0.492	Include	0.481
11	0.494	Include	0.490
7	0.494	Include	0.483
1	0.495	Include	0.488
14	0.497	Include	0.502
8	0.498	Include	0.481
23	0.499	Include	0.463
2	0.503	Include	0.483
16	0.505	Include	0.487
3	0.506	Include	0.514
5	0.506	Include	0.374
6	0.507	Include	0.443
17	0.507	Include	0.501
10	0.507	Include	0.507
21	0.510	Include	0.504

18	0.513	Include	0.508
9	0.513	Include	0.509
19	0.515	Include	0.517
22	0.527	Discard	N/A
15	0.527	Discard	N/A

The mean NSD value was calculated to be 0.501 with a standard deviation of 0.012 (4 mg/mL), and 0.503 with a standard deviation of 0.012 (2 mg/mL). Models are sorted from the lowest to the highest NSD value. Models 11 and 4 had the best NSD at 0.484 and 0.479 (for 4 and 2 mg/mL respectively) and were taken as reference for the superposition with DAMSUP. On the opposite model 7 had an NSD value of 0.533 (AtVDAC1 at 4 mg/mL) and was subsequently discarded. In a similar manner, models 22 and 15 (NSD of 0.507 for both) were discarded for AtVDAC1 at 2 mg/mL. DAMSUP superposed the models and calculated a deviation from the reference NSD.

Following models' refinement by DAMAVER, the averaged probability map was generated, then filtered by DAMFILT which removed regions of low occupancy, to finally generate the final molecular envelopes for both AtVDAC1 tested concentrations (Figure 5.12).

Primary analysis of the molecular envelopes for AtVDAC1 using Pymol and the crystal structure of the mouse VDAC1 (3EMN1; reference) proved difficult. The generated model had a smaller density volume than expected, which lead to a significant number of residues being excluded from the envelope. Thus, the molecular structure of AtVDAC1 was generated by homology modelling using SWISS MODELLER (Waterhouse, Rempfer et al. 2018) and fitted into the SAXS molecular envelopes using UCSF-Chimera (Pettersen, Goddard Td Fau - Huang et al. , Huang, Meng et al. 2014). The average map values for AtVDAC1 at 4 mg/mL and 2 mg/mL calculated by UCSF-Chimera were reported to be 0.2782 (293 out of 2039 atoms outside contour) and 0.2798 (314 out of 2039 atoms outside contour) respectively.

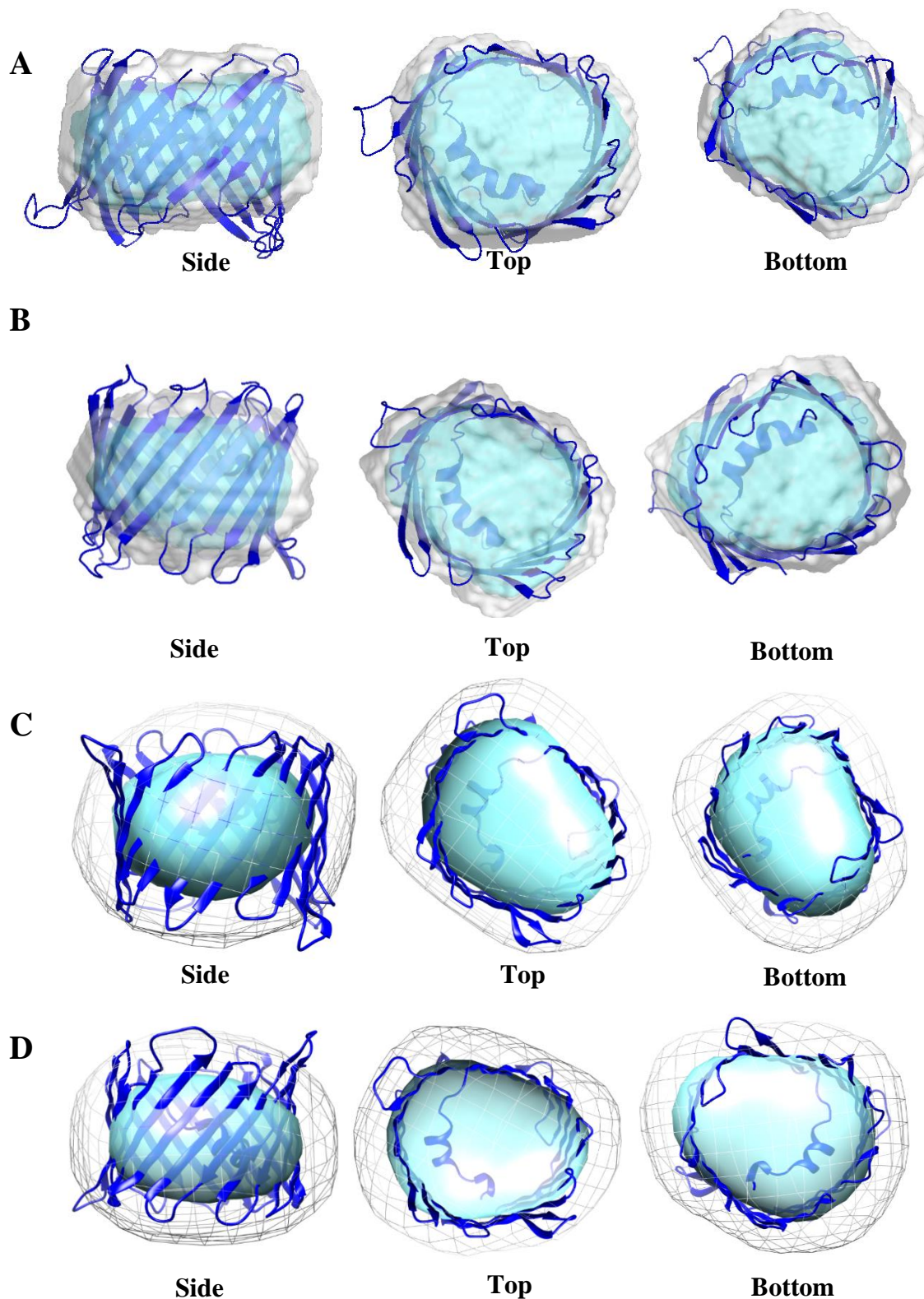


Figure 5.12 SAXS derived 3D molecular envelopes for AtVDAC1. AtVDAC1 probability maps (grey) and filtered (blue) molecular envelopes generated by DAMAVER from samples at 4 mg/mL (**A**) and 2 mg/mL (**B**) in 25 mM $\text{NaH}_2\text{PO}_4/\text{Na}_2\text{HPO}_4$ (pH 7.0), 50 mM NaCl, 1 mM EDTA, 1 mM DTT, 10 % (w/v) Glycerol, 0.12 % (v/v) LDAO. The crystal structure of mouse voltage-dependant anion channel (3EMN) (in dark blue) was fitted to the envelopes (**A**) and (**B**). Molecular structure of AtVDAC1 (in blue) generated using SWISS MODELLER (Waterhouse, Rempfer et al. 2018) and fitted into the AtVDAC1 SAXS molecular envelopes from at 4 mg/mL (**C**) and 2 mg/mL samples (**D**), using the Chimera software (Pettersen, Goddard Td Fau - Huang et al. , Huang, Meng et al. 2014).

5.6. Structural characterization of AtVDAC1 D177N mutant by Small Angle X-ray Scattering (SAXS)

5.6.1. Data collection for AtVDAC1 D177N

SAXS data were collected for AtVDAC1 D177N at four different concentrations. The protein sample (2 mg/mL) was diluted in a 96-well plate three times, each time by a factor of 2. The resulting samples (2, 1, 0.5 and 0.25 mg/mL) were all subjected to SAXS for 2 seconds, and triplicated. Triplicate measurements were then averaged to produce a final scattering profile for each of the different concentrations tested (Figure 5.13A). The buffer blank (25 mM NaH₂PO₄/Na₂HPO₄ (pH 7.0), 50 mM NaCl, 1 mM EDTA, 1 mM DTT, 10 % (w/v) Glycerol, 0.12% (v/v) LDAO) was subjected to SAXS measurements and its scattering profile (Figure 5.13A blue line) was subtracted from the scattering data of the protein samples (Figure 5.13B). A high upturn of the scattering intensity at low q values could be observed for each sample, despite performing dilutions and centrifuging samples prior to the experiment. This indicates a degree of polydispersity in the samples, due to potential aggregation or oligomerization.

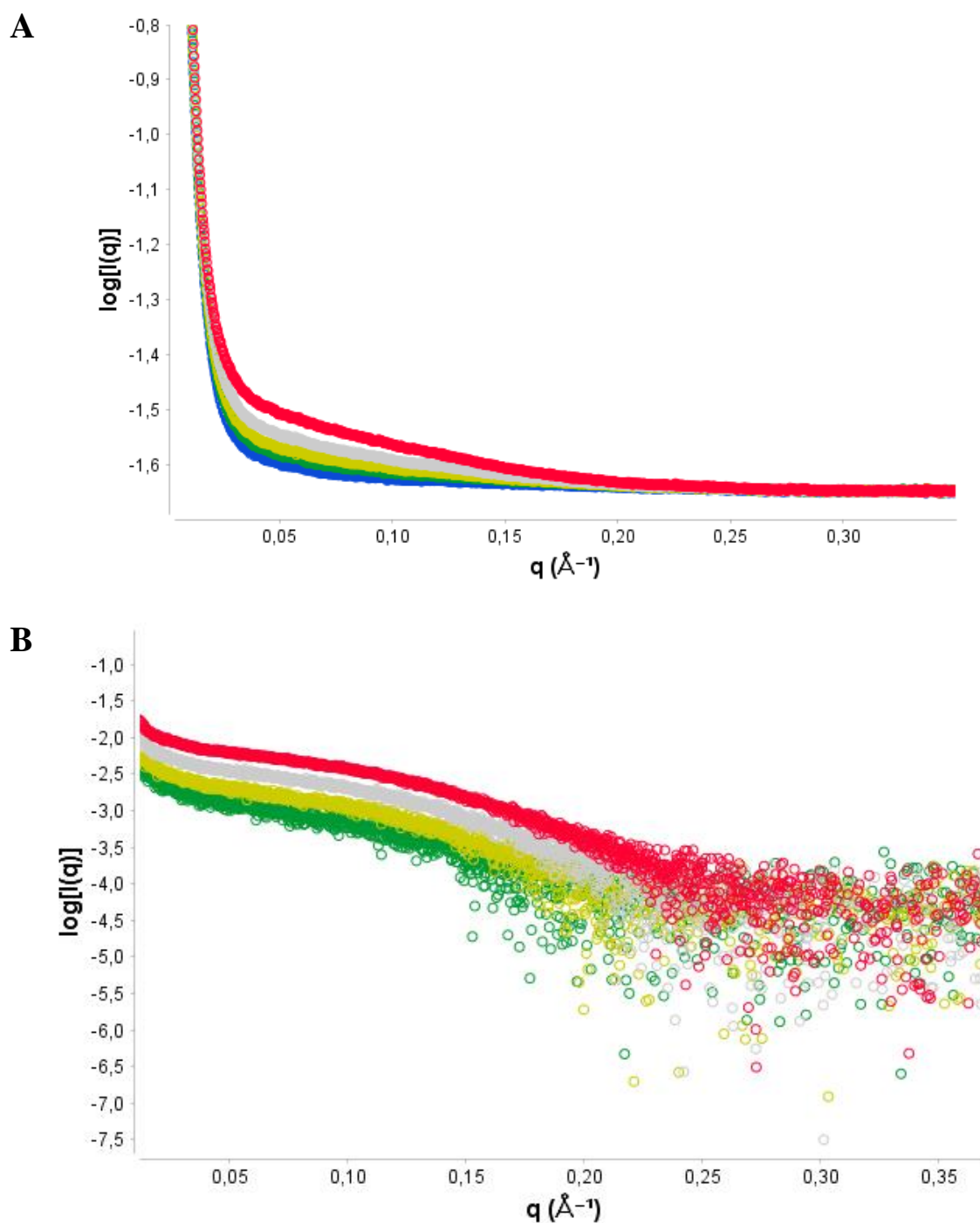


Figure 5.13 Raw Scattering Intensity plots of mutant D177N at 2, 1, 0.5 and 0.25 mg/mL. Scattering data recorded at the Beamline B21 and displayed as log of intensity over the scattering vector q (\AA) and created using ScAtter Software® (Förster, Apostol et al. 2010). Samples were dialyzed for 5 days in 25 mM $\text{NaH}_2\text{PO}_4/\text{Na}_2\text{HPO}_4$ (pH 7.0), 50 mM NaCl, 1 mM EDTA, 1 mM DTT, 10 % (w/v) Glycerol, 0.12% (v/v) LDAO. (A) Raw Scattering data of D177N. The buffer blank (as above) is represented by blue line. The scattering intensity curves for the D177N sample at 2, 1, 0.5 and 0.25 mg/mL are represented by a red, grey, yellow and green line respectively. (B) Subtracted scattering data for D177N samples (colours are mentioned above).

5.6.2. Calculation of the radius of gyration for the AtVDAC1 D177N

Data analysis for AtVDAC1 D177N at 2, 1, 0.5 and 0.25 mg/mL was carried out as previously described for the control protein BSA and AtVDAC1 (sections 5.4 and 5.5). The R_g was calculated using the Guinier approximation (Figure 5.14) and GNOM for all concentrations. Results are reported in Table 5.6.

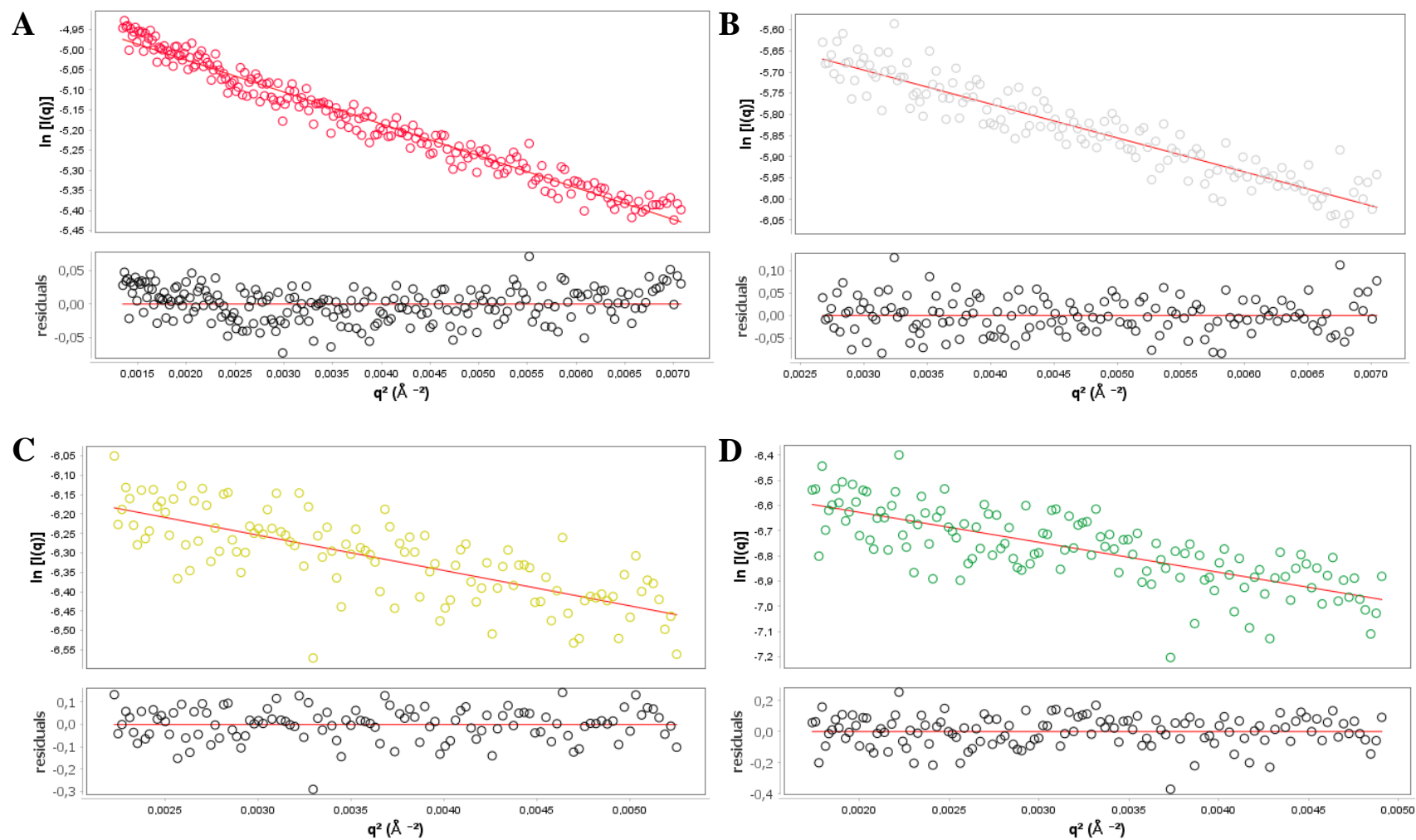


Figure 5.14 Guinier analysis of D177N at 2, 1, 0.5 and 0.25 mg/mL. First data points of the recorded scattering data displayed as log of intensity over the scattering vector q (\AA) and created using ScAtter Software® (Förster, Apostol et al. 2010). The first 200 points were used to fit a linear curve (red) that would be used to calculate the hypothetical R_g . Guinier plots of D177N at 2 (A), 1 (B), 0.5 (C), and 0.25 mg/mL (D) are represented by red, grey, yellow and green dots respectively. Residual analysis of the scattering data (black dots) from the tendency curve (red) is indicated at the bottom for each concentration.

Table 5.6 Summary Table of Rg values for D177N.

Sample	Rg (Reciprocal Space)	Rg (Real space)
D177N at 2 mg/mL	15.31	13.96
D177N at 1 mg/mL	15.40	14.25
D177N at 0.5 mg/mL	16.42	14.49
D177N at 0.25 mg/mL	18.78	14.53

Parameters Rg calculated by Scatter Software ® using approximation (reciprocal space) and GNOM (Real Space).

Reciprocal Space Rg values increased with the dilution factor and were relatively higher than their corresponding real values (overall more than 1 unit difference). A similar trend was observed for the Real Rg values, calculated by GNOM, indicating an effect of the dilution on the real Rg. The high upturn at low q values identified on scattering profile indicated a possible aggregation (for all of them), which was likely the cause of this trend.

5.6.3. Kratky and Porod analysis of AtVDAC1 D177N at 2, 1, 0.5 and 0.25 mg/mL

Kratky and Porods plots (Figure 5.15) both showed bell-shaped curves for all the tested AtVDAC1 D177N samples, indicating a great degree of folding and compaction. Nevertheless, only two datasets (2 mg/mL and 1 mg/mL samples) of D177N protein was used for ab initio modelling since the other two dilutions (0.5 and 0.25 mg/mL) did not produce envelope models of good quality, as their concentrations were too low to guarantee statistically relevant molecular envelopes ($\text{Chi}^2 > 0.5$).

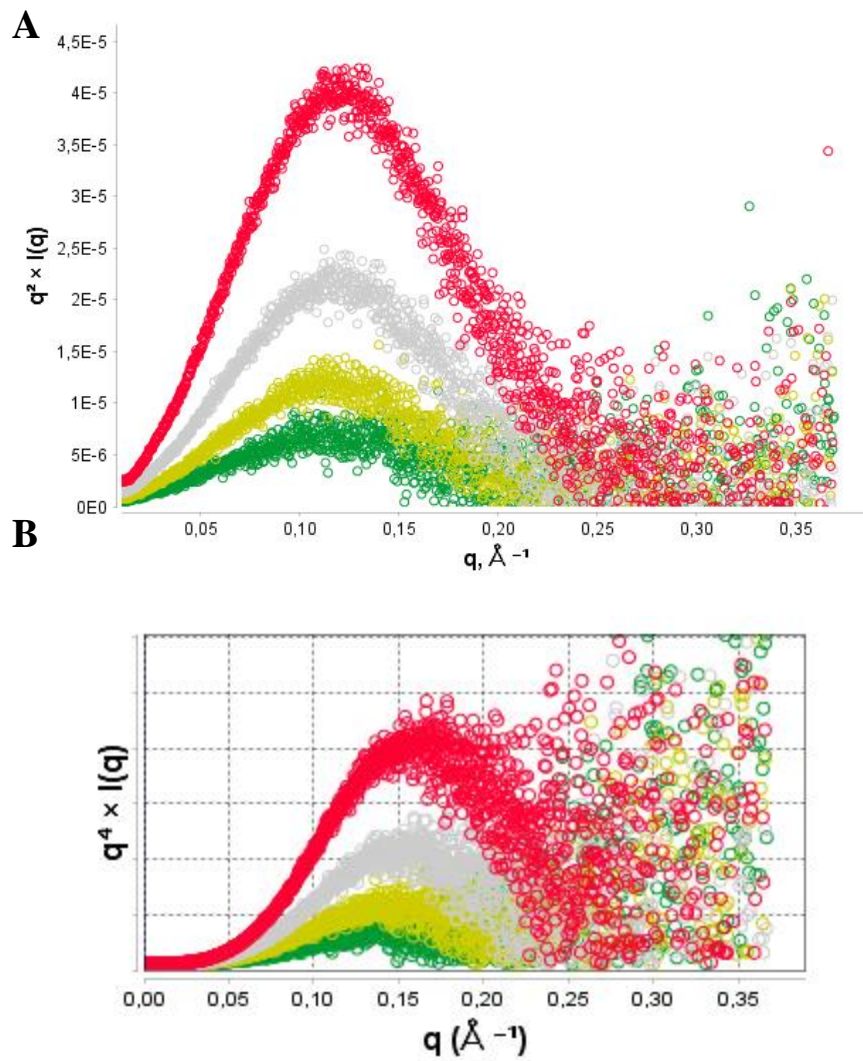


Figure 5.15 Quality assessment of D177N scattering curves at different protein concentrations. (A) Kratky plot of samples at 2, 1, 0.5 and 0.25 mg/mL are represented by a red, grey, yellow and green line respectively. (B) Corresponding Porod plots for D177N samples. Colours are as above.

5.6.4. Evaluation of the P(r) distribution of D177N scattering curves at 2 and 1 mg/mL

Following the initial analysis of the scattering data from D177N at various concentrations, GNOM was used as an indirect transform program for the establishment of the P(r) function for further *ab initio* modelling (Figure 5.16). For convenience, the fit between the scattering data and the tendency curve representing the P(r) distribution is indicated. Only two concentrations of D177N protein (2 mg/mL and 1 mg/mL) were used and revealed a similar bell-shaped curve with a small extension, indicating a relatively spherical shape, as for the native-like AtVDAC1 protein (see 5.5.4).

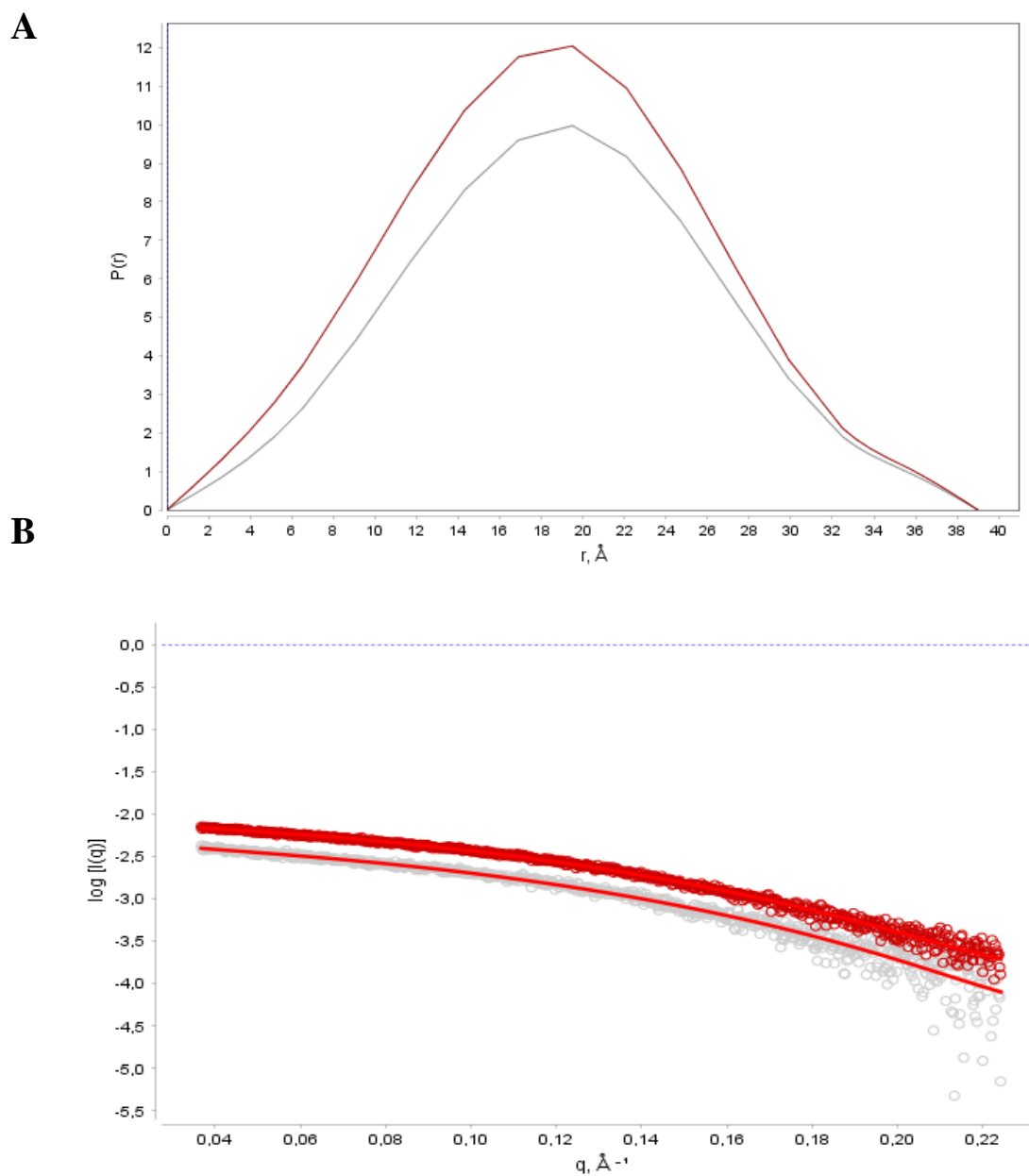


Figure 5.16 $P(r)$ distribution plots of D177N scattering data. (A) $P(r)$ distribution function of the D177N scattering data, collected from 2 mg/mL (red) and 1 mg/mL (purple) samples in 25 mM $\text{NaH}_2\text{PO}_4/\text{Na}_2\text{HPO}_4$ (pH 7.0), 50 mM NaCl, 1 mM EDTA, 1 mM DTT, 10 % (w/v) Glycerol, 0.12% (v/v) LDAO. (B) Scattering intensity of D177N at 2 and 1 mg/mL. For each concentration, the tendency curve representing the $P(r)$ distribution is indicated in red.

5.6.5. Generation and refinement of calculated molecular envelopes for D177N

Assessment of the generated envelopes (Table 5.7) was carried out by DAMSEL and DAMSUP as previously described for the BSA control protein and AtVDAC1 (see 5.4 and 5.5). Outliers were identified (model 4 and 2 for the 2 mg/mL and 1 mg/mL sample respectively) as two standard deviation units away from the calculated mean NSD, and excluded from the superposition step. Envelopes 17 in (both cases) were used by DAMSEL as the reference envelopes for D177N at 2 mg/mL and 1 mg/mL respectively.

Table 5.7 Summary of DAMSEL and DAMSUP results for D177N at 2 mg/mL and 1 mg/mL.

Model	DAMSEL NSD	FATE	DAMSUP NSD
D177N at 2 mg/mL			
17	0.461	Reference	0.000
12	0.465	Include	0.429
14	0.472	Include	0.477
3	0.473	Include	0.447
20	0.474	Include	0.486
6	0.474	Include	0.464
21	0.474	Include	0.439
5	0.477	Include	0.460
8	0.478	Include	0.305
10	0.480	Include	0.461
7	0.480	Include	0.451
11	0.480	Include	0.476
18	0.482	Include	0.463
16	0.489	Include	0.471
13	0.489	Include	0.445
1	0.489	Include	0.471
19	0.490	Include	0.476
22	0.490	Include	0.516
2	0.490	Include	0.504
9	0.493	Include	0.489
23	0.495	Include	0.455
15	0.506	Include	0.516
4	0.552	Discard	N/A
D177N at 1 mg/mL			
17	0.468	Reference	0.000
18	0.473	Include	0.259
14	0.477	Include	0.407
13	0.478	Include	0.439

1	0.483	Include	0.490
6	0.483	Include	0.477
22	0.473	Include	0.371
21	0.488	Include	0.498
19	0.489	Include	0.482
20	0.490	Include	0.465
9	0.490	Include	0.484
23	0.491	Include	0.471
4	0.491	Include	0.457
8	0.498	Include	0.519
3	0.499	Include	0.496
5	0.504	Include	0.496
12	0.505	Include	0.479
7	0.507	Include	0.498
15	0.509	Include	0.553
10	0.510	Include	0.523
11	0.511	Include	0.539
16	0.547	Include	0.503
2	0.583	Discard	N/A

The mean NSD value was calculated to be 0.485 with a standard deviation of 0.018 (2 mg/mL), and 0.498 with a standard deviation of 0.025 (2 mg/mL). Models are sorted from the lowest to the highest NSD value. Models 17 had the best NSD at 0.461 and 0.468 (for 2 and 1 mg/mL respectively) and were taken as reference for the superposition with DAMSUP. On the opposite model 4 had an NSD value of 0.552 (D177N at 2 mg/mL) and was subsequently discarded. In a similar manner, model 2 (NSD of 0.583) was discarded for D177N at 1 mg/mL. DAMSUP superposed the models and calculated a deviation from the reference NSD.

Following models' refinement by DAMAVER, the averaged probability map was created, then filtered by DAMFILT which removed regions of low occupancy to give a final molecular envelope for D177N at both 2 and 1 mg/mL (Figure 5.17).

Primary analysis of the molecular envelopes for D177N using Pymol® and the crystal structure of the mouse VDAC1 (3EMN1; reference) proved difficult. The generated model had a smaller density volume than expected, which lead to a significant number of residues being excluded from the envelope. Thus, the molecular structure of D177N was generated by homology modelling using SWISS MODELLER (Waterhouse, Rempfer et al. 2018) and fitted into the SAXS molecular envelopes using UCSF-Chimera (Pettersen, Goddard Td Fau - Huang et al. , Huang, Meng et al. 2014). The average map values for D177N at 2 mg/mL and 1 mg/mL calculated by UCSF-Chimera were reported to be 0.282 (307 out of 2066 atoms outside contour) and 0.2989 (248 out of 2066 atoms outside contour) respectively.

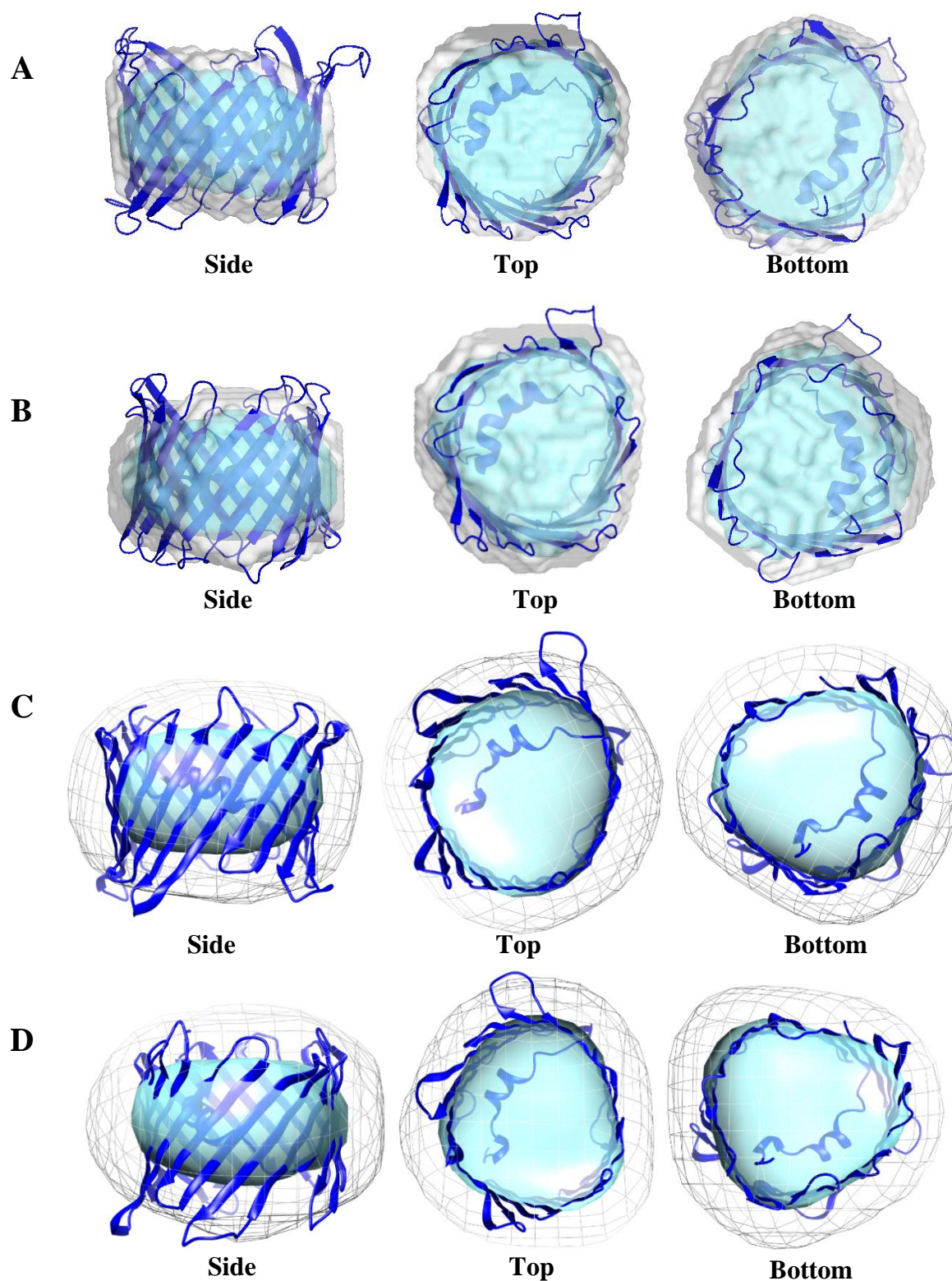


Figure 5.17 Generated molecular envelopes for D177N at 2 and 1 mg/mL. Probability map (grey) and filtered (blue) molecular envelope generated by DAMAVER on D177N samples at 2 mg/mL (**A**) and 1 mg/mL (**B**) in 25 mM $\text{NaH}_2\text{PO}_4/\text{Na}_2\text{HPO}_4$ (pH 7.0), 50 mM NaCl, 1 mM EDTA, 1 mM DTT, 10 % (w/v) Glycerol, 0.12% (v/v) LDAO. The crystal structure of Voltage-dependant Channel 1 from mouse 3EMN1 was added (in dark blue) and retrieved from the Protein Data Bank. (**C**) Molecular structure of D177N (in blue) generated using SWISS MODELLER (Waterhouse, Rempfer et al. 2018) and fitted into the SAXS molecular envelopes using Chimera software (Pettersen, Goddard Td Fau - Huang et al. , Huang, Meng et al. 2014) for AtVDAC1 at 2 mg/mL and 1 mg/mL (**D**).

5.7. Structural characterization of D258N mutant by Small Angle X-ray Scattering (SAXS)

5.7.1. Data collection for D258N

SAXS data were collected for D258N at four different concentrations. Sample (2 mg/mL) was diluted in a 96-well plate three times, each time by a factor of 2. The resulting samples (2, 1, 0.5 and 0.25 mg/mL) were all subjected to SAXS for 2 seconds, and triplicated. Series of triplicates were then averaged to produce a final scattering profile for each of the different concentrations (Figure 5.18A). The buffer blank (25 mM NaH₂PO₄/Na₂HPO₄ (pH 7.0), 50 mM NaCl, 1 mM EDTA, 1 mM DTT, 10 % (w/v) Glycerol, 0.12% (v/v) LDAO) was subjected to SAXS and its scattering profile (Figure 5.18A blue line) was removed from the samples data sets (Figure 5.18B). As for most previous AtVDAC proteins (section 5.5 and 5.6), a high upturn of the scattering intensity at low q values could be observed for each sample, despite performing dilutions and centrifuging samples prior to the experiment. This indicates a degree of polydispersity in the samples, due to potential aggregation or oligomerization.

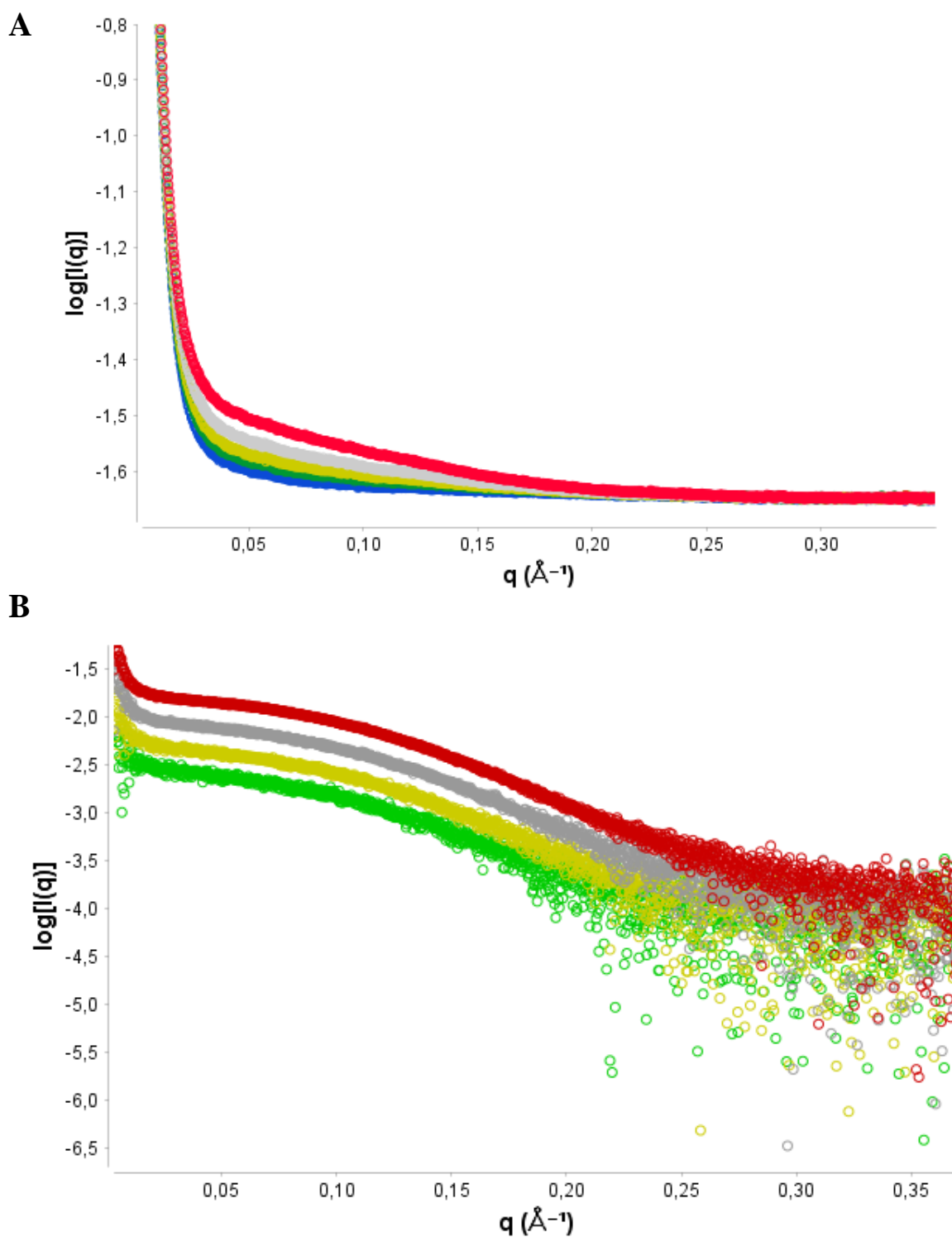


Figure 5.18 Raw Scattering Intensity plots of mutant D258N at 2, 1, 0.5 and 0.25 mg/mL. Scattering data recorded at the Beamline B21 and displayed as log of intensity over the scattering vector q (\AA) and created using ScAtter Software® (Förster, Apostol et al. 2010). Samples were dialyzed for 5 days in 25 mM $\text{NaH}_2\text{PO}_4/\text{Na}_2\text{HPO}_4$ (pH 7.0), 50 mM NaCl, 1 mM EDTA, 1 mM DTT, 10 % (w/v) Glycerol, 0.12% (v/v) LDAO. **(A)** Raw Scattering data of D258N. The buffer blank (as above) is represented by blue line. The scattering intensity curves for the D258N sample at 2, 1, 0.5 and 0.25 mg/mL are represented by a red, grey, yellow and green line respectively. **(B)** Subtracted scattering data for D258N samples (colours are as above).

5.7.2. Calculation of the radius of gyration for D258N

Data analysis for D258N at 2, 1, 0.5 and 0.25 mg/mL was carried out as previously described (sections 5.4 to 5.6). The R_g was calculated using the Guinier approximation (Figure 5.19) and GNOM for all concentrations. Results are reported in Table 5.8.

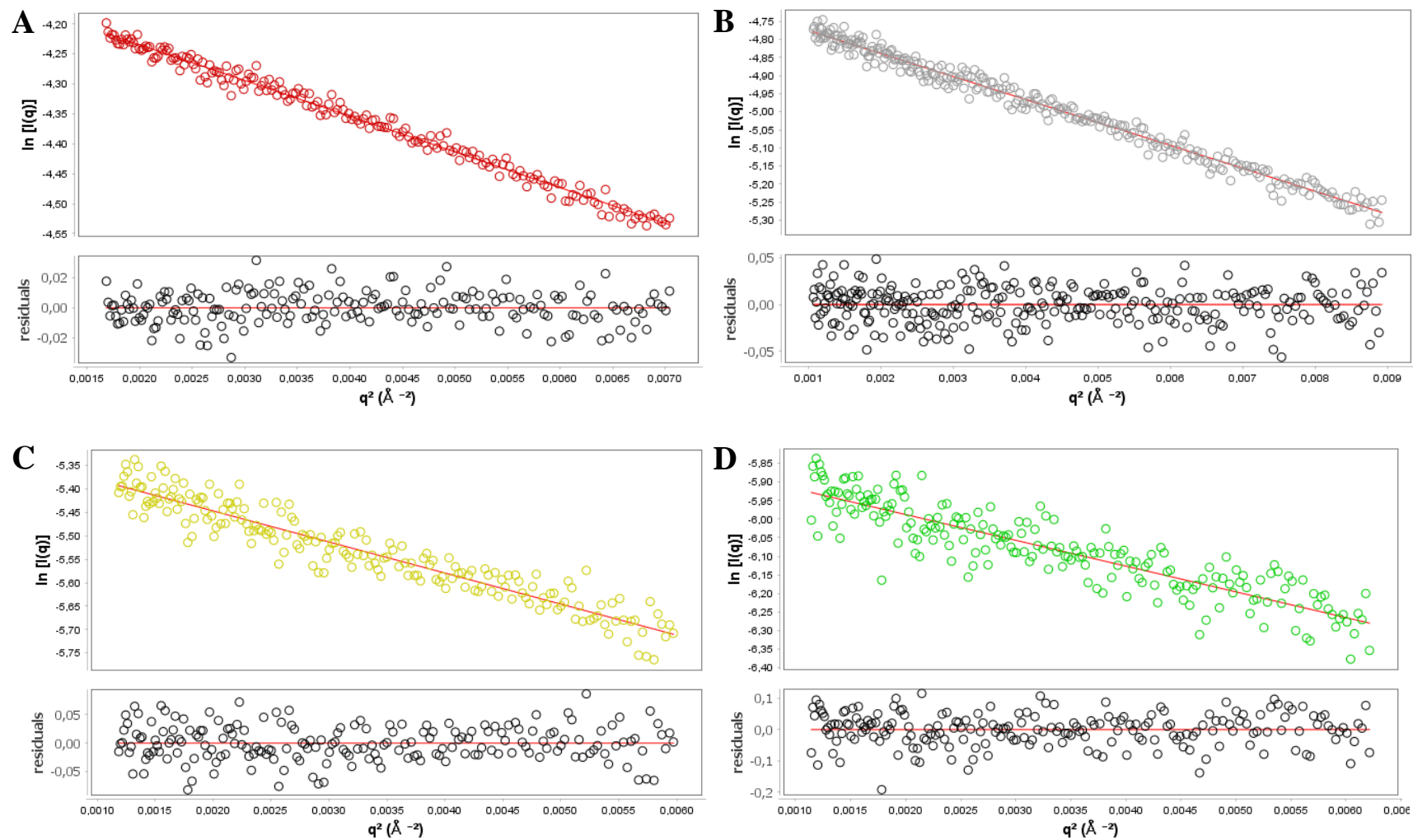


Figure 5.19 Guinier analysis of D258N at 2, 1, 0.5 and 0.25 mg/mL. First data points of the recorded scattering data displayed as log of intensity over the scattering vector q (\AA) and created using ScAtter Software® (Förster, Apostol et al. 2010). The first 200 points were used to fit a linear curve (red) that would be used to calculate the hypothetical R_g . Guinier plots of D258N at 2 (A), 1 (B), 0.5 (C), and 0.25 mg/mL (D) are represented by red, grey, yellow and green dots respectively. Residual analysis of the scattering data (black dots) from the tendency curve (red) is indicated at the bottom for each concentration.

Table 5. 8 Summary Table of Rg values for D258N.

Sample	Rg (Reciprocal Space)	Rg (Real space)
D258N at 2 mg/mL	13.29	13.70
D258N at 1 mg/mL	13.69	13.77
D258N at 0.5 mg/mL	14.00	13.96
D258N at 0.25 mg/mL	14.33	14.00

Parameters Rg calculated by Scatter Software ® using approximation (reciprocal space) and GNOM (Real Space).

Reciprocal Space Rg values increased with the dilution factor and were very close to their corresponding real values (overall less than 0.5 units difference). A similar trend can be observed for the Real Rg values, calculated by GNOM, indicating an effect of the dilution on the real Rg. As with previous SAXS analyses on AtVDACs (section 5.5 and 5.6), the high upturn at low q values identified on scattering profile indicated a possible aggregation (for all of them), which was the likely cause of this trend.

5.7.3. Kratky and Porod analysis of D258N at 2, 1, 0.5 and 0.25 mg/mL

Initial assessment of the data quality was performed on D258N samples at 2, 1, 0.5 and 0.25 mg/mL (Figure 5.20). Kratky and Porods plots both showed a bell-shaped curve for all D258N samples, indicating a great degree of folding and compaction. However, only two datasets (2 mg/mL and 1 mg/mL samples) of D258N protein was used for ab initio modelling since the concentrations and profile were reasonable. The other two dilutions (0.5 and 0.25 mg/mL) did not produce final models of good quality to guarantee statistically relevant molecular envelopes, as their concentrations were too low and their respective Rg values too much influenced by either buffer subtraction and/or aggregation.

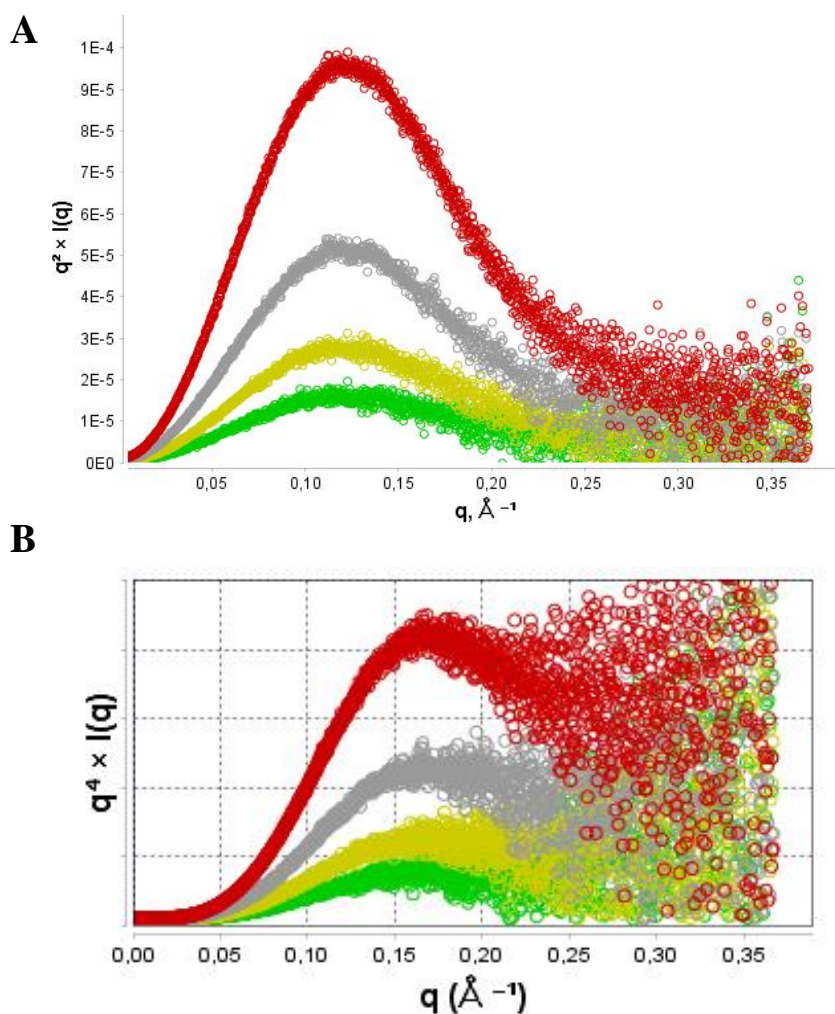


Figure 5. 20 Quality assessment of D258N scattering curves at different protein concentrations. (A) Kratky plot of samples at 2, 1, 0.5 and 0.25 mg/mL are represented by a red, grey, yellow and green line respectively. (B) Corresponding Porod plots for D258N samples. Colours are as above.

5.7.4. Evaluation of the $P(r)$ distribution of D258N scattering curves for at 2 and 1 mg/mL

Following the initial analysis of the scattering data from D258N at various concentrations, GNOM was used as an indirect transform program for the establishment of the $P(r)$ function for further *ab initio* modelling (Figure 5.21). For convenience, the fit between the scattering data and the tendency curve representing the $P(r)$ distribution is indicated. Only two concentrations of D258N protein (2 mg/mL and 1 mg/mL) were used and revealed a similar bell-shaped curve with a small extension, indicating a relatively spherical shape, as for AtVDAC1 and D177N protein (section 5.5.4 and 5.6.4).

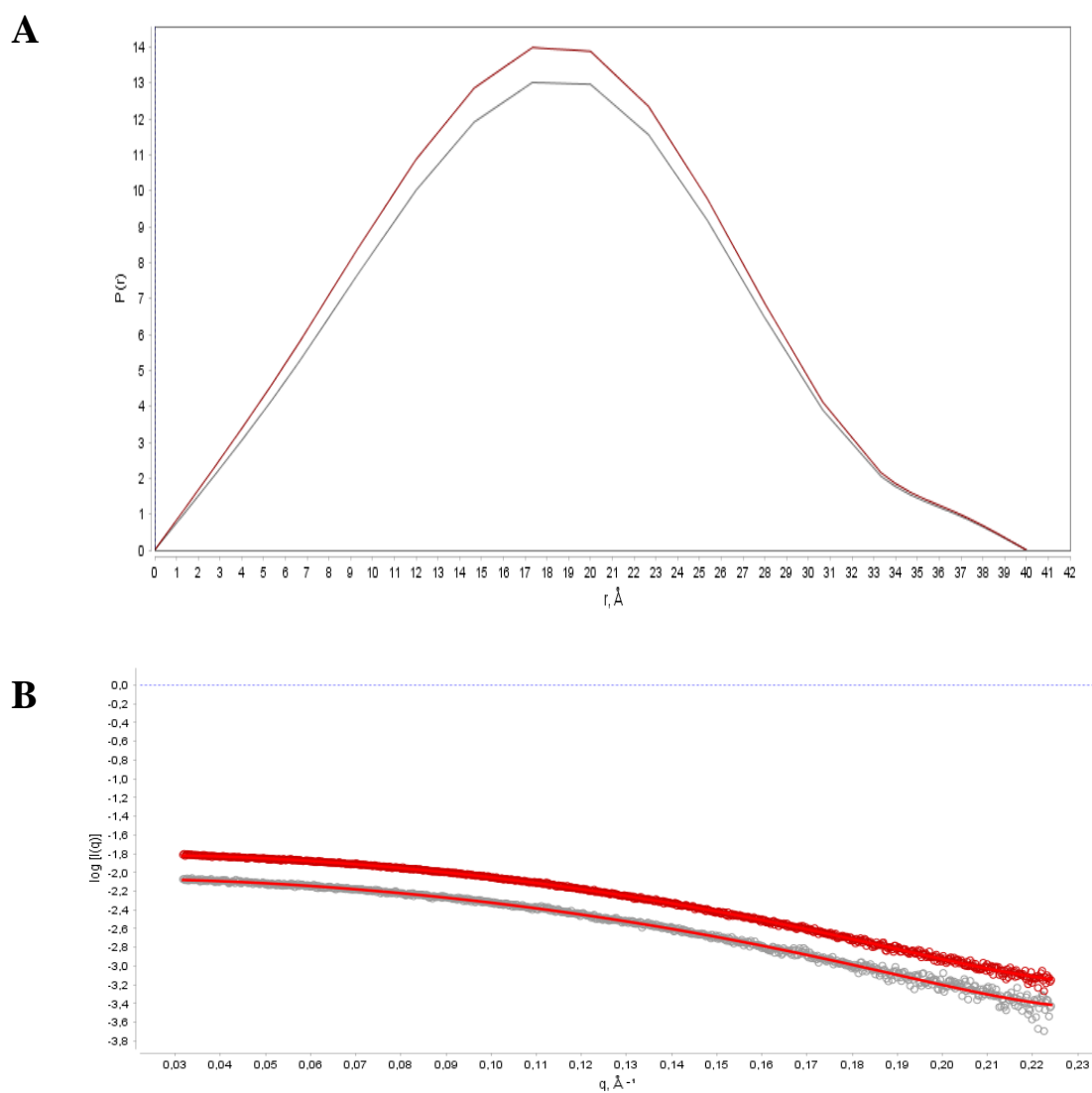


Figure 5. 21 P(r) distribution plots of D258N scattering data. (A) P(r) distribution function of the D258N scattering data, collected from the 2 mg/mL (red) and 1 mg/mL (purple) samples in 25 mM $\text{NaH}_2\text{PO}_4/\text{Na}_2\text{HPO}_4$ (pH 7.0), 50 mM NaCl, 1 mM EDTA, 1 mM DTT, 10 % (w/v) Glycerol, 0.12% (v/v) LDAO. (B) Scattering intensity of D258N at 2 and 1 mg/mL. For each concentration, the tendency curve representing the P(r) distribution is indicated in red.

5.7.5. Generation and refinement of calculated molecular envelopes for D258N

Assessment of the generated envelopes (Table 5.9) was carried out by DAMSEL and DAMSUP as previously described for the previous proteins (sections 5.4.5, 5.5.5 and 5.6.5). Outliers were identified (model 2 and 2 for the 2 mg/mL and 1 mg/mL sample respectively) as two standard deviations away from the calculated mean NSD and removed from the superposition step. Envelopes 17 in (both cases) were used by DAMSEL as the reference envelopes for D177N at 2 mg/mL and 1 mg/mL respectively.

Table 5.9 Summary of DAMSEL and DAMSUP results for D258N at 2 mg/mL and 1 mg/mL.

Model	DAMSEL NSD	FATE	DAMSUP NSD
D258N at 2 mg/mL			
5	0.446	Reference	0.000
6	0.448	Include	0.308
13	0.455	Include	0.386
12	0.461	Include	0.471
19	0.462	Include	0.489
8	0.462	Include	0.497
3	0.468	Include	0.474
4	0.470	Include	0.308
21	0.475	Include	0.499
22	0.477	Include	0.459
23	0.479	Include	0.494
9	0.480	Include	0.488
16	0.481	Include	0.464
17	0.481	Include	0.464
14	0.484	Include	0.494
20	0.485	Include	0.443
10	0.486	Include	0.493
15	0.486	Include	0.492
18	0.486	Include	0.491
7	0.491	Include	0.501
11	0.500	Include	0.485
1	0.500	Include	0.532
2	0.532	Discard	N/A
D258N at 1 mg/mL			
6	0.472	Reference	0.000
9	0.473	Include	0.259
7	0.475	Include	0.407
13	0.479	Include	0.439
22	0.481	Include	0.490
19	0.481	Include	0.477

14	0.482	Include	0.371
21	0.482	Include	0.498
18	0.485	Include	0.482
4	0.485	Include	0.465
20	0.487	Include	0.484
16	0.489	Include	0.471
17	0.490	Include	0.457
2	0.491	Include	0.519
23	0.492	Include	0.496
1	0.493	Include	0.496
3	0.493	Include	0.479
15	0.493	Include	0.498
10	0.494	Include	0.553
8	0.494	Include	0.523
12	0.494	Include	0.539
11	0.520	Include	0.503
5	0.600	Discard	N/A

The mean NSD value was calculated to be 0.478 with a standard deviation of 0.019 (2 mg/mL), and 0.492 with a standard deviation of 0.025 (1 mg/mL). Models are sorted from the lowest to the highest NSD value. Models 5 and 6 had the best NSD at 0.446 and 0.472 (for 2 and 1 mg/mL respectively) and were taken as reference for the superposition with DAMSUP. On the opposite model 2 had an NSD value of 0.532 (D258N at 2 mg/mL) and was subsequently discarded. In a similar fashion, model 5 (NSD of 0.600) was discarded for D258N at 1 mg/mL. DAMSUP superposed the models and calculated a deviation from the reference NSD.

Following models' refinement by DAMAVER, the averaged probability map was created, then filtered by DAMFILT which removed regions of low occupancy to give a final molecular envelope for D258N at both 2 and 1 mg/mL (Figure 5.22).

Primary analysis of the molecular envelopes for D258N using Pymol and the crystal structure of the mouse VDAC1 (3EMN1; reference) proved difficult. The generated model had a smaller density volume than expected, which lead to a significant number of residues being excluded from the envelope. Thus, the molecular structure of D258N was generated by homology modelling using SWISS MODELLER (Waterhouse, Rempfer et al. 2018) and fitted into the SAXS molecular envelopes using UCSF-Chimera (Pettersen, Goddard Td Fau - Huang et al. , Huang, Meng et al. 2014). The average map values for D258N at 2 mg/mL and 1 mg/mL calculated by UCSF-Chimera were reported to be 0.2666 (344 out of 2066 atoms outside contour) and 0.2453 (395 out of 2066 atoms outside contour) respectively.

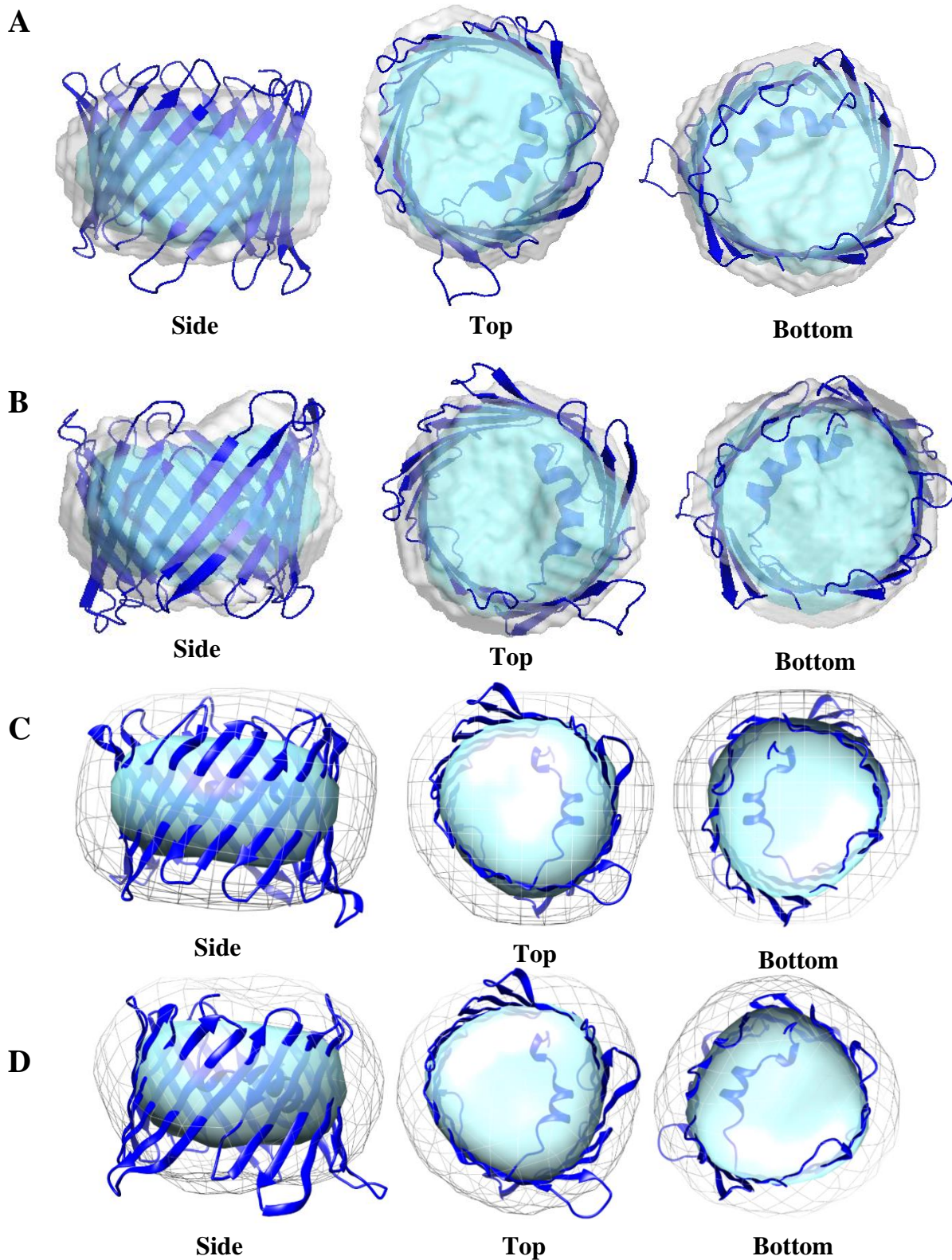


Figure 5.22 Generated molecular envelopes for D258N at 2 and 1 mg/mL. Probability map (grey) and filtered (blue) molecular envelope generated by DAMAVER on D258N samples at 2 mg/mL (**A**) and 1 mg/mL (**B**) in 25 mM $\text{NaH}_2\text{PO}_4/\text{Na}_2\text{HPO}_4$ (pH 7.0), 50 mM NaCl, 1 mM EDTA, 1 mM DTT, 10 % (w/v) Glycerol, 0.12% (v/v) LDAO. The crystal structure of Voltage-dependant Channel 1 from mouse 3EMN1 was added (in dark blue) and retrieved from the Protein Data Bank. (**C**) Molecular structure of D177N (in blue) generated using SWISS MODELLER (Waterhouse, Rempfer et al. 2018) and fitted into the SAXS molecular envelopes using Chimera software (Pettersen, Goddard Td Fau - Huang et al. , Huang, Meng et al. 2014) for AtVDAC1 at 2 mg/mL and 1 mg/mL (**D**).

5.8. SAXS simulations with AtVDAC hypothetical 3D structures

Primary analysis of the molecular envelopes for AtVDAC proteins using Pymol and the crystal structure of the mouse VDAC1 3EMN1 or their respective structures generated *in silico* revealed a smaller density volume than expected, with a substantial number of residues (15 % on average) left out of the envelope (section 5.5.5; 5.6.5 and 5.7.5.). Thus, the molecular structure of AtVDAC1 and its D258N and D177N mutants (created using homology modelling) were used to compute a theoretical SAXS profile using the Fox webserver (Schneidman-Duhovny, Hammel et al. 2010) (Figure 5.23, A to C). As expected, almost no difference was observed between the native-like AtVDAC1 and its mutant, although D258N showed a slight variation at very high q values (around 35 to 38 Å). However, a clear difference was evident between the calculated and the actual AtVDAC SAXS scattering profiles (Figure 5.23E). This difference can be accounted by the fact that the computational calculations were performed on a hypothetical 3D-model, as opposed to experimental data reflecting the structure of a protein in a detergent solution (LDAO) at five times its CMC (Herrmann 1962).

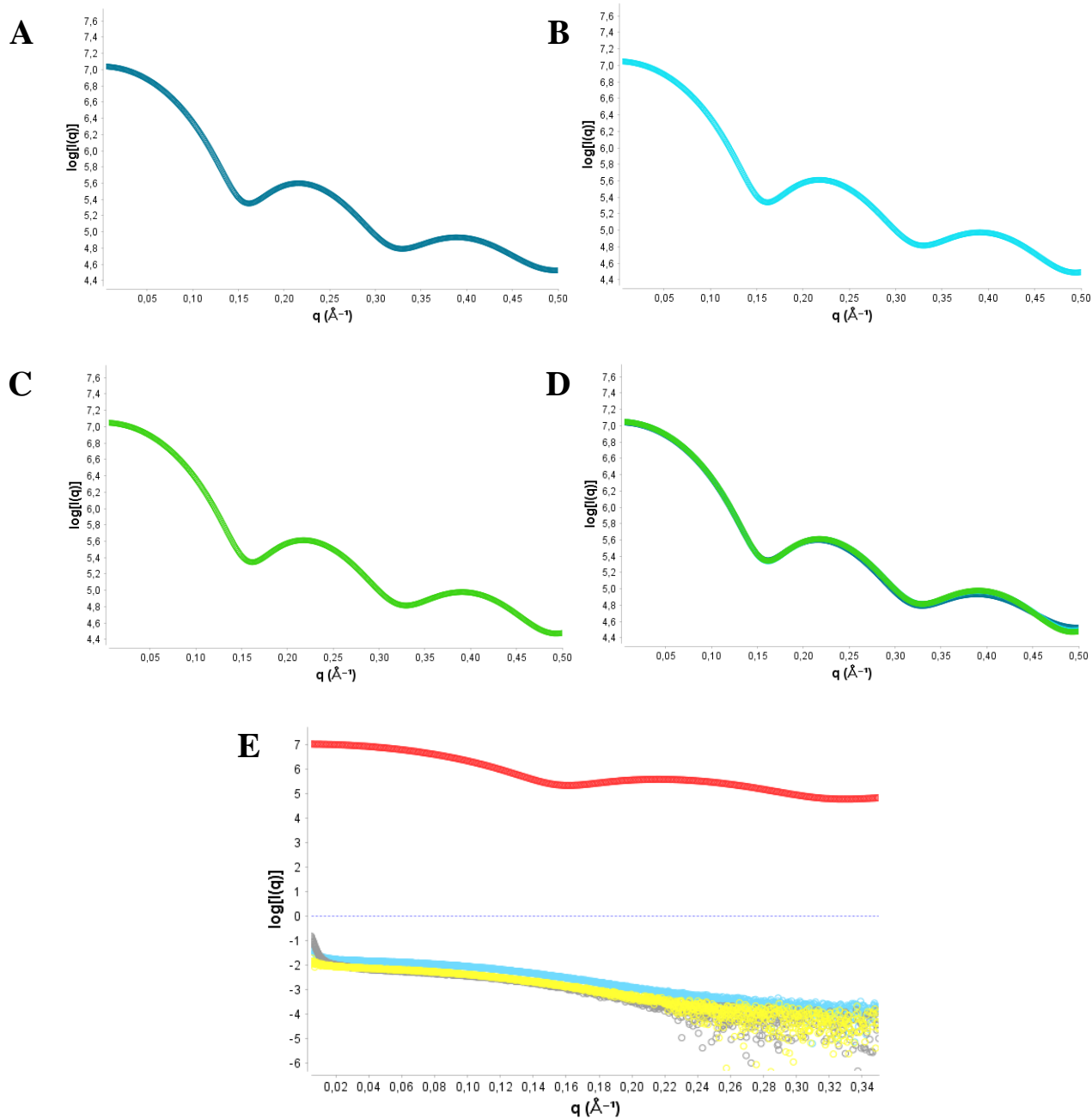


Figure 5.23 Computed SAXS profiles based on AtVDAC predicted 3D-models. Theoretical intensity curves using the constructed homology models of AtVDAC1 (A), D177N (B) and D258N (C) superposed (D) and generated by Chimera. (E) Theoretical intensity curve of AtVDAC1 (red) and actual SAXS scattering from AtVDAC1 (yellow), D177N (grey) and D258N (light blue), each at 2 mg/mL in 25 mM NaH₂PO₄/Na₂HPO₄ (pH 7.0), 50 mM NaCl, 1 mM EDTA, 1 mM DTT, 10 % (w/v) Glycerol, 0.12% (v/v) LDAO.

5.9. Summary of molecular envelopes dimensions for AtVDAC proteins

Overall, measurements for AtVDAC proteins in 25 mM NaH₂PO₄/Na₂HPO₄ (pH 7.0), 50 mM NaCl, 1 mM EDTA, 1 mM DTT, 10 % (w/v) Glycerol, 0.12% (v/v) LDAO are summarized in Table 5.10. Distances and diameters of the molecular envelopes were calculated using the Pymol distance measurement tool. AtVDAC1 molecular envelopes, generated through SAXS experiments, showed similar features to those of the D177N and D258N AtVDAC1 mutants for all parameters listed, with some minor differences in the lengths and diameters. Most noticeably, the measured diameters of the predicted 3D-models were consistently larger than those of their SAXS envelopes.

Table 5. 10. Summary of parameters for the SAXS envelopes and predicted 3D models of AtVDAC proteins.

Parameter (Å)	AtVDAC1 4 mg/mL	AtVDAC1 2 mg/mL	D177N 2 mg/mL	D177N 1 mg/mL	D258N 2 mg/mL	D258N 1 mg/mL
Radius of gyration (real)	13.88	14.05	13.96	14.25	13.70	13.77
Dmax	40	40	39	39	40	40
Diameter of the molecular envelope	27.3-42.9	31.9-42.7	36.5-39.3	33.5-42.1	37.0-37.8	35.4-36.2
Diameter of the homology model	38.3-54.9	38.3-54.9	39.5-53.4	39.5-53.4	37.3-50.7	37.3-50.7
Height of the molecular envelope	21.2-23.0	19.9-23.3	16.4-19.2	16.2-19.0	14.4-19.5	11.2-20.9
Height of the homology model	27.0-35.0	27.0-35.0	25.4-41.7	25.4-41.7	27.4-37.9	27.4-37.9

5.10. Structural characterization of LDAO by Small Angle X-ray Scattering (SAXS)

5.10.1. Data collection for LDAO

All AtVDAC proteins were refolded with the aid of LDAO at a final concentration of 0.12 % (v/v), at about 5 times of its critical micellar concentration (CMC). Further investigation was undertaken to properly distinguish between a free empty micelle and an AtVDAC1 generated envelope, possibly embedded within a micelle. Hence, four different LDAO samples were prepared at 0.01, 0.0575, 0.115 and 0.23 % (v/v) concentration in 25 mM NaH₂PO₄/Na₂HPO₄ (pH 7.0), 50 mM NaCl, 1 mM EDTA, 1 mM DTT, 10 % (w/v) Glycerol. These samples were prepared to monitor the Scattering pattern of LDAO below, at 2.5, 5 and 10 times its CMC respectively. SAXS data were collected for LDAO at the four different concentrations with series of triplicates that were averaged to produce a final scattering profiles for each concentration (Figure 5.24). The buffer blank (25 mM NaH₂PO₄/Na₂HPO₄ (pH 7.0), 50 mM NaCl, 1 mM EDTA, 1 mM DTT, 10 % (w/v) Glycerol) was subjected to SAXS and its scattering profile was subtracted from the scattering data of the LDAO samples. No high upturn of the scattering intensity at low q values could be observed for each sample above the CMC (Figure 5.24, red, grey and yellow curve), indicating a great degree of monodispersity in the samples. In contrast, the LDAO sample below the CMC showed a high degree of noise in the low q regions, due to a potential lack of structure as there are no micelles in the solution (Herrmann 1962).

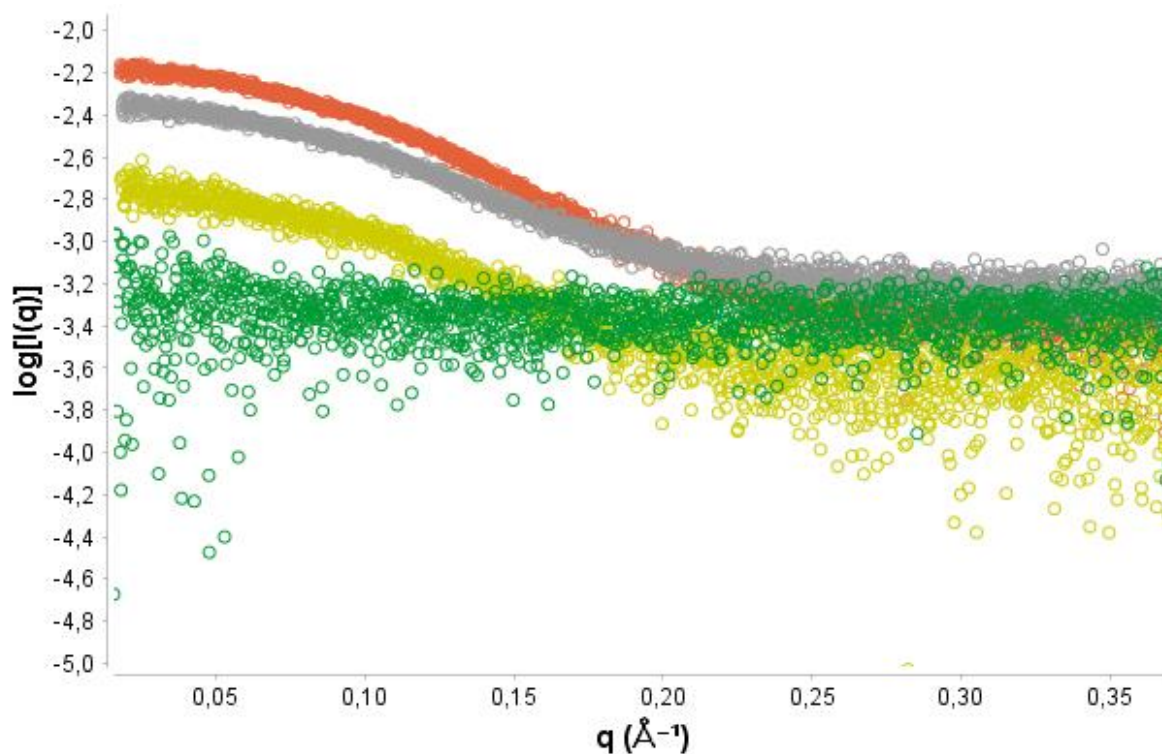


Figure 5.24 Scattering Intensity plots of LDAO at 0.01, 0.0575, 0.115 and 0.23 % (v/v). Scattering intensity data recorded and displayed as log of intensity over the scattering vector q (\AA^{-1}) and created using ScAtter® Software (Förster, Apostol et al. 2010). The scattering intensity curves for the LDAO at 0.23, 0.115, 0.0575 and 0.01 % (v/v) (in 25 mM $\text{NaH}_2\text{PO}_4/\text{Na}_2\text{HPO}_4$ (pH 7.0), 50 mM NaCl, 1 mM EDTA, 1 mM DTT, 10 % (w/v) Glycerol) are represented by an orange, grey, yellow and green line respectively.

5.10.2. Calculation of the radius of gyration for LDAO

Data analysis for LDAO at 0.01, 0.0575, 0.115 and 0.23 % (v/v) was carried out as previously described for the control protein BSA (sections 5.4). The R_g was calculated using the Guinier approximation (Figure 5.25) and GNOM for all concentrations except for the lowest (below the detergent's CMC). This last sample proved difficult as there was no apparent R_g due to the lack of micelles and noisy profile at low q values. Results are reported in Table 5.11.

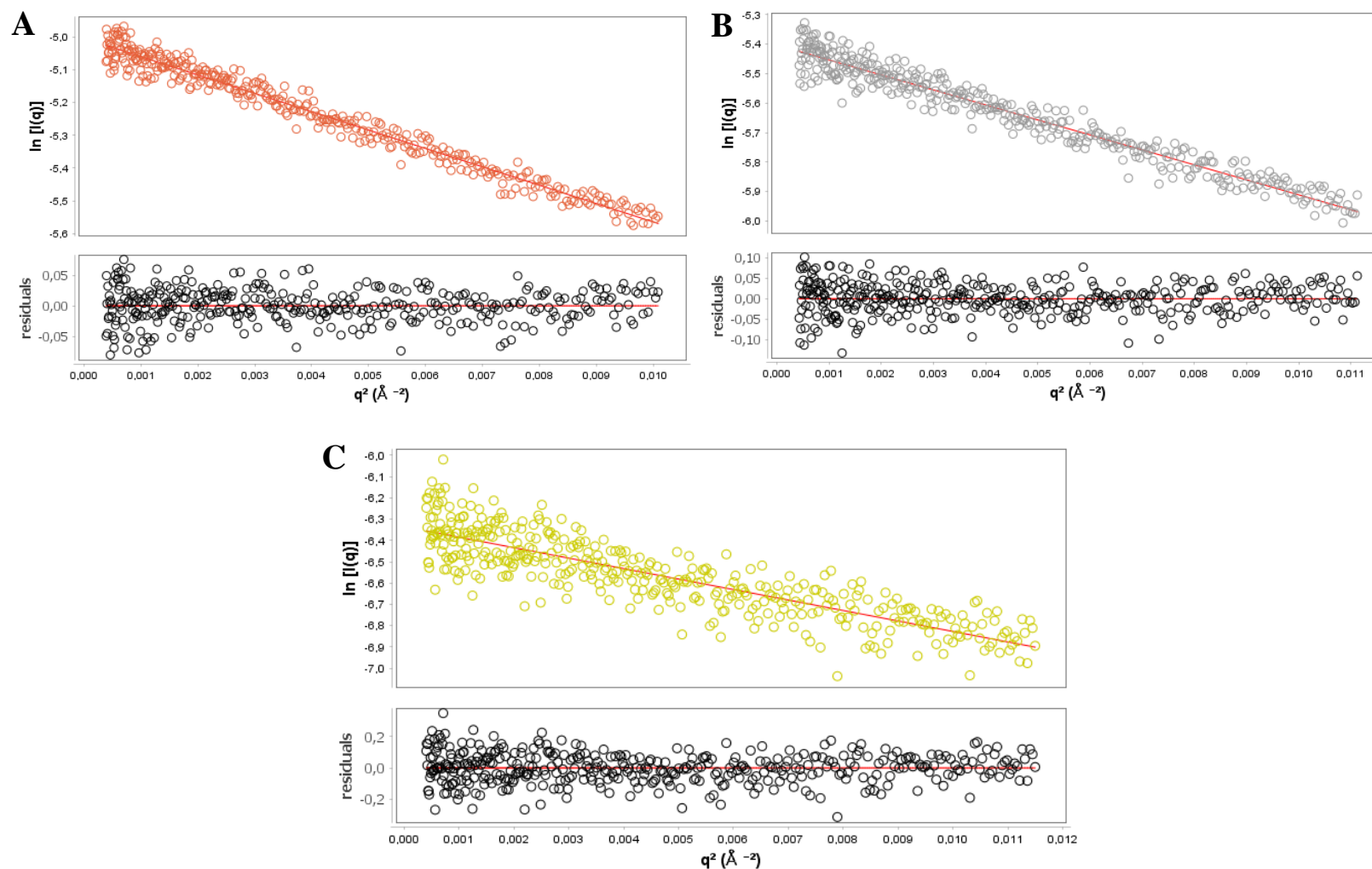


Figure 5.25 Initial Guinier analysis of LDAO at 0.0575, 0.115 and 0.23 % (v/v). First data points of the recorded scattering data displayed as log of intensity over the scattering vector q (\AA) and created using ScAtter Software® (Förster, Apostol et al. 2010). The first 200 points were used to fit a linear curve (red) that would be used to calculate the hypothetical R_g . Guinier plots of LDAO at 0.23 (A), 0.115 (B) and 0.0575 % (v/v) (C) are represented by orange, grey and yellow dots respectively. Residual analysis of the scattering data (black dots) from the tendency curve (red) is indicated at the bottom for each concentration.

Table 5.11 Summary Table of Rg values for LDAO.

Sample	Rg (Reciprocal Space)	Rg (Real space)
LDAO at 0.23 % (v/v)	12.90	13.28
LDAO at 0.115 % (v/v)	12.27	12.92
LDAO at 0.0575 % (v/v)	12.07	12.85

Parameters Rg calculated by Scatter® Software using approximation (reciprocal space) and GNOM (Real Space).

Reciprocal Space Rg values increased with LDAO concentration and were slightly higher than their corresponding real values (overall less than 0.8 units difference). A similar trend can be observed for the Real Rg values, calculated by GNOM, indicating an effect of the LDAO concentration on the real Rg and the micelles' size.

5.10.3. Kratky and Porod analysis of LDAO at 0.01, 0.0575, 0.115 and 0.23 % (v/v)

Initial assessment of the data quality was performed on LDAO at 0.01, 0.0575, 0.115 and 0.23 % (v/v) (Figure 5.26). Kratky plots confirmed the correlation between degree of “unfoldness” and LDAO concentration; as the concentration increased the profile resembled more and more a bell-shaped curve (Figure 5.26A), indicating an increasing level of compaction. This is to be expected as the micelle size increases and stabilizes with the detergent concentration. Porod plots showed a similar trend, with the flexibility increasing with decreasing detergent concentration, although a great degree of flexibility was evident in all samples (Figure 5.26B). The absence of an actual compact core was noticeable, as opposed to the analysis of AtVDAC proteins (sections 5.5.3, 5.6.3 and 5.7.3).

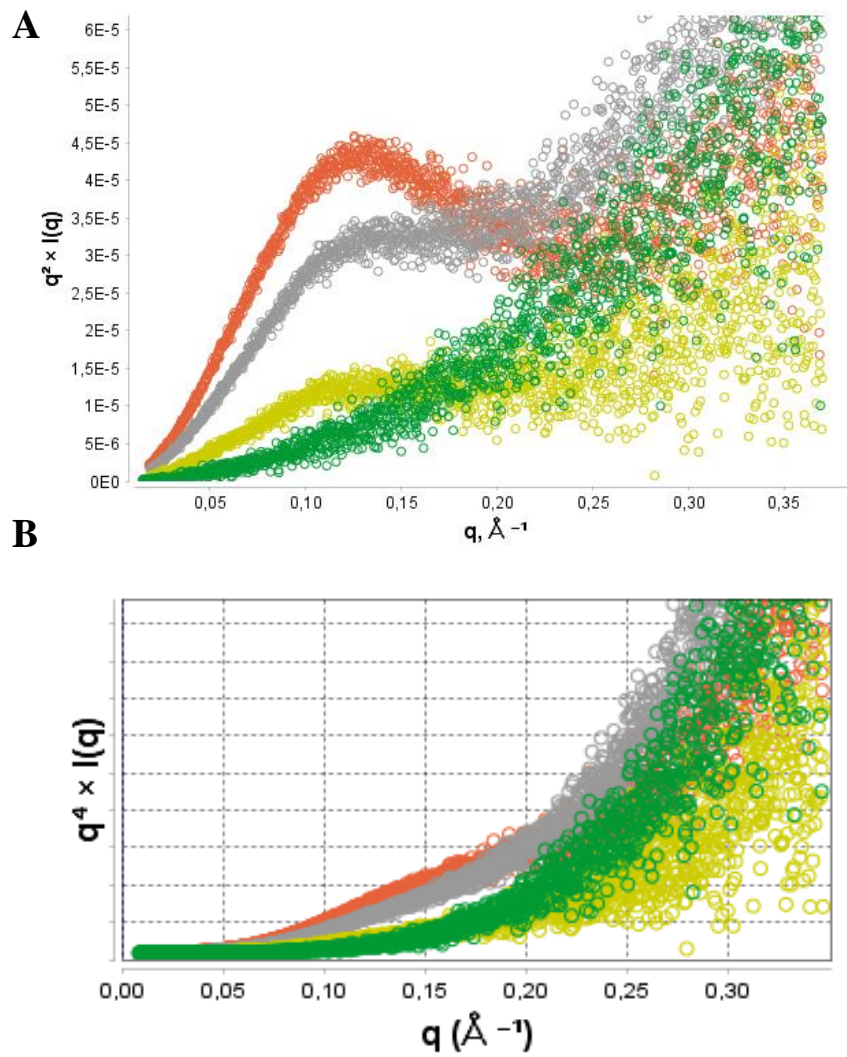


Figure 5.26 Quality assessment of LDAO scattering curves at different protein concentrations. (A) Kratky plot LDAO at 0.23, 0.115 and 0.0575 % (v/v) are represented by a red, grey, yellow and green line respectively. (B) Corresponding Porod plots for LDAO samples. Colours are as above.

5.10.4. Evaluation of the P(r) distribution for LDAO at 0.23 and 0.115 % (v/v)

Following the initial analysis of the scattering data from LDAO at various concentrations, GNOM was used as an indirect transform program for the establishment of the P(r) function for further *ab initio* modelling (Figure 5.27). For convenience, the fit between the scattering data and the tendency curve representing the P(r) distribution is indicated (Figure 5.27B, red line). Considering the concentration of LDAO in AtVDAC samples (0.12 % (v/v)), two datasets (LDAO 0.115 and 0.23 % (v/v)) were used for the *ab initio* analysis, as their concentrations were the most representative of those of AtVDAC samples ($0.115 < 0.12 < 0.23$). Both analyses revealed a similar bell-shaped curve with a small extension, indicating a relatively globular shape, as for the AtVDAC1 proteins (see 5.5.4).

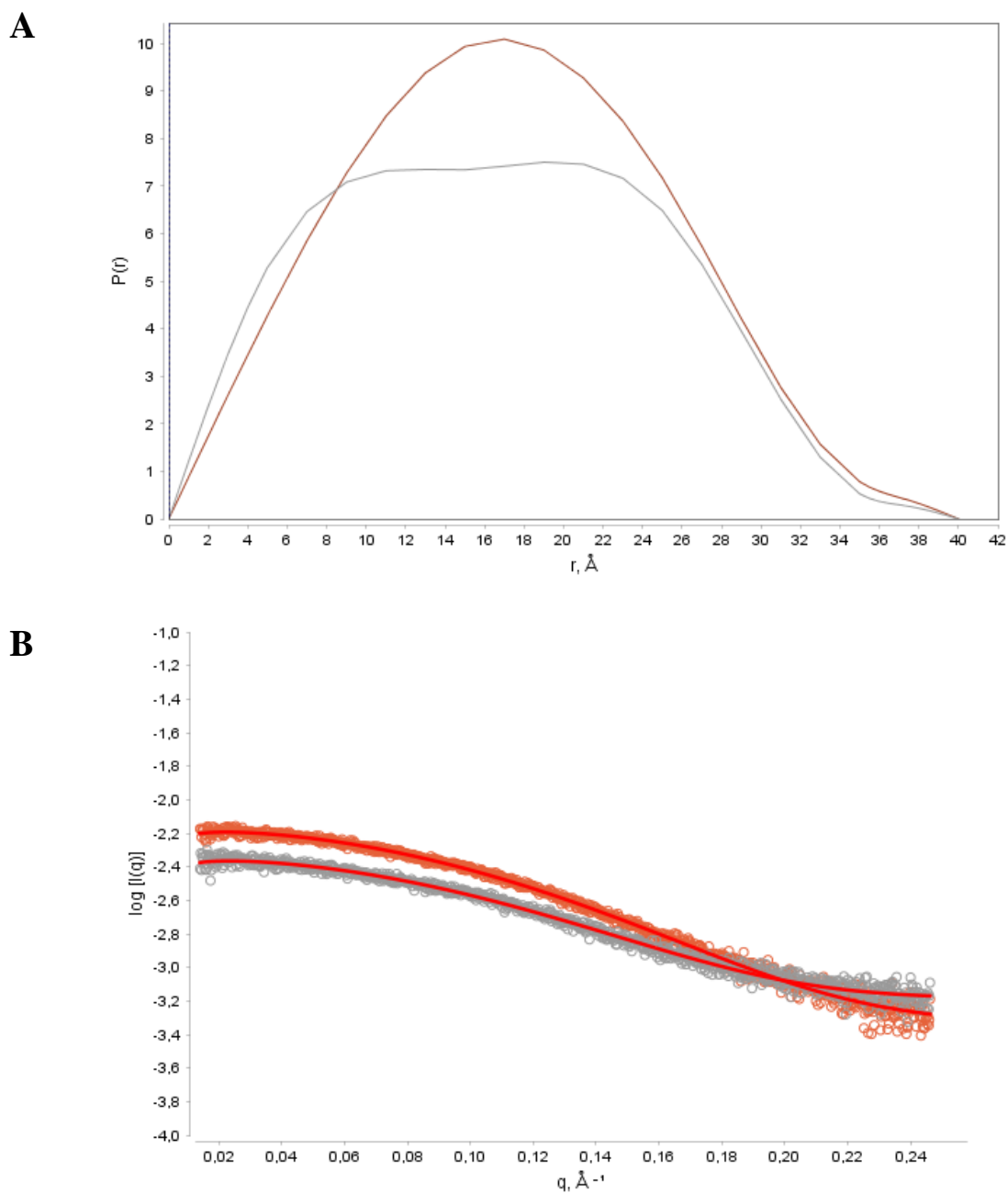


Figure 5.27 P(r) distribution plots of LDAO scattering data. (A) P(r) distribution function of the LDAO collected from the 0.23 % (v/v) (red) and 0.115 % (v/v) (grey) samples in 25 mM $\text{NaH}_2\text{PO}_4/\text{Na}_2\text{HPO}_4$ (pH 7.0), 50 mM NaCl, 1 mM EDTA, 1 mM DTT, 10 % (w/v) Glycerol. (B) Scattering intensity of LDAO at 0.115 and 0.23 % (v/v). For each concentration, the tendency curve representing the P(r) distribution is indicated in red.

5.10.5. Generation and refinement of calculated molecular envelopes for LDAO

Assessment of the generated envelopes (Table 5.12) was carried out by DAMSEL and DAMSUP as previously described for the BSA control protein and AtVDACs (sections 5.4.5, 5.5.5, 5.6.5 and 5.7.5). Outliers were identified (model 4 and 2 for the 2 mg/mL and 1 mg/mL sample respectively) as two standard deviation units away from the calculated mean NSD and removed from the superposition step. Envelopes 19 and 21 were used by DAMSEL as the reference envelopes for LDAO at 0.23 % (v/v) and 0.115 % (v/v) respectively.

Table 5.12 Summary of DAMSEL and DAMSUP results for LDAO at 0.23 and 0.115 % (v/v).

Model	DAMSEL NSD	FATE	DAMSUP NSD
LDAO at 0.23 % (v/v)			
19	0.515	Reference	0.000
3	0.518	Include	0.481
20	0.518	Include	0.488
21	0.522	Include	0.494
12	0.522	Include	0.495
15	0.525	Include	0.500
18	0.526	Include	0.509
5	0.528	Include	0.502
9	0.528	Include	0.482
6	0.532	Include	0.465
1	0.532	Include	0.497
16	0.533	Include	0.514
14	0.537	Include	0.496
17	0.538	Include	0.522
8	0.540	Include	0.516
23	0.550	Include	0.486
4	0.552	Include	0.506
10	0.564	Include	0.516
11	0.572	Include	0.550
13	0.572	Include	0.560
2	0.606	Include	0.608
22	0.607	Include	0.557
7	0.625	Discard	N/A
LDAO at 0.115 % (v/v)			
21	0.484	Reference	0.000
17	0.486	Include	0.470
10	0.487	Include	0.494
1	0.489	Include	0.471

4	0.490	Include	0.458
8	0.490	Include	0.471
15	0.490	Include	0.372
20	0.491	Include	0.471
16	0.493	Include	0.475
19	0.497	Include	0.469
9	0.498	Include	0.509
2	0.502	Include	0.493
6	0.505	Include	0.429
18	0.506	Include	0.499
3	0.509	Include	0.498
7	0.511	Include	0.503
12	0.512	Include	0.472
22	0.513	Include	0.489
11	0.516	Include	0.542
14	0.516	Include	0.510
5	0.516	Include	0.510
13	0.517	Include	0.498
23	0.529	Discard	N/A

The mean NSD value was calculated to be 0.546 with a standard deviation of 0.031 (0.23 % (v/v)), and 0.502 with a standard deviation of 0.013 (0.115 % (v/v)). Models are sorted from the lowest to the highest NSD value. Models 19 and 21 had the best NSD at 0.515 and 0.484 (for 0.23 and 0.115 % (v/v) respectively) and were taken as reference for the superposition with DAMSUP. On the opposite model 7 had an NSD value of 0.625 (LDAO at 0.23 % (v/v)) and was subsequently discarded. In a similar manner, model 23 (NSD of 0.529) was discarded for LDAO at 0.115 % (v/v). DAMSUP superposed the models and calculated a deviation from the reference NSD.

Following models' refinement by DAMAVER, the averaged probability map was created, then filtered by DAMFILT which removed regions of low occupancy to give a final molecular envelope for LDAO at both 0.23 and 0.115 % (v/v) concentrations (Figure 5.28).

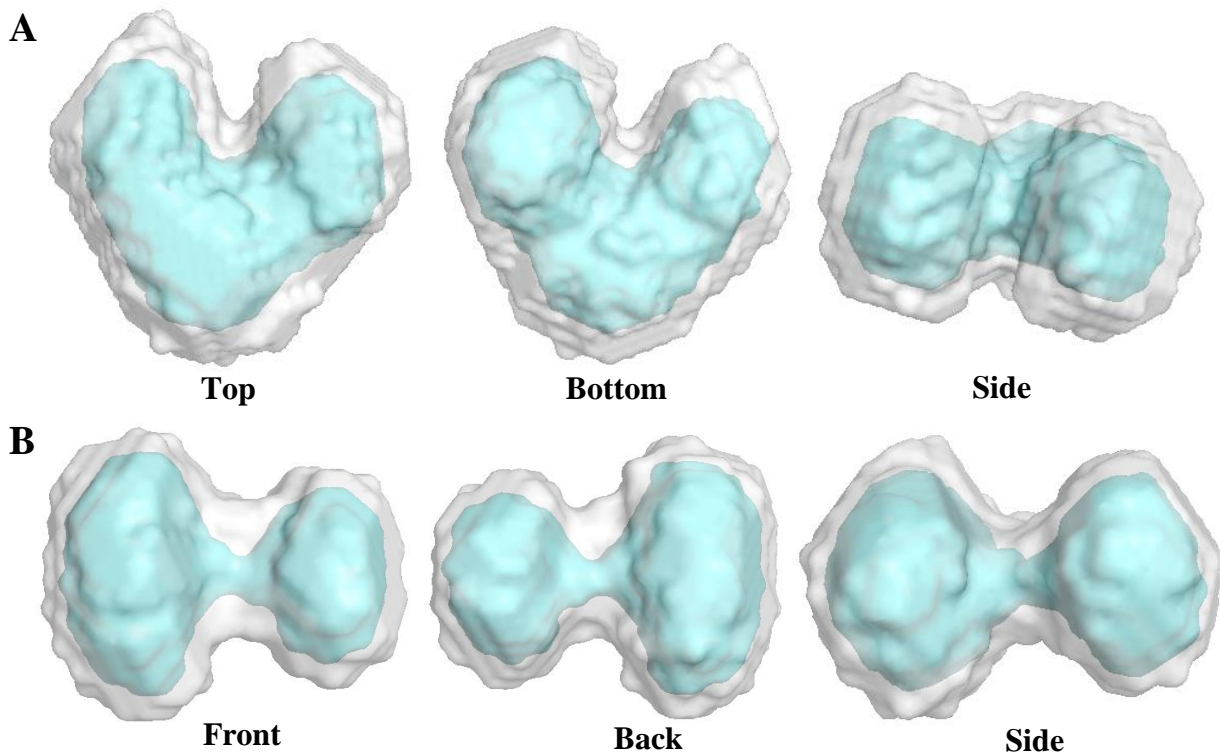


Figure 5.28 Generated molecular envelopes for LDAO at 0.23 and 0.115 % (v/v). Probability map (grey) and filtered (blue) molecular envelope generated by DAMAVER on LDAO samples at 0.23 % (v/v) (**A**) and 0.115 % (v/v) (**B**) in 25 mM NaH₂PO₄/Na₂HPO₄ (pH 7.0), 50 mM NaCl, 1 mM EDTA, 1 mM DTT, 10 % (w/v) Glycerol.

5.11. Discussion

SAXS experiments conducted at the Diamond Light Source at the Beamline B21 under the supervision of Dr Rambo proved very successful in capturing relatively good quality data for all AtVDAC samples. Aggregation of membrane protein is a common phenomenon, often affecting the quality of the collected scattering curves which is generally assessed through examination of the scattering profile at low q values (Trehwella, Duff et al. 2017). In this instance, AtVDAC1 and its D177N and D258N mutants all exhibited a small upturn of the scattering intensity at low q values (section 5.5.1, 5.6.1 and 5.7.1, Figure 5.8, 5.13 and 5.18). Despite the scattering intensities indicating a certain level of aggregation within the samples, data were deemed acceptable as they did not affect the overall quality of the scattering curves in a critical manner. Specific care was taken when centrifuging samples prior to the experiment, but this did not seem to drastically improve the quality of the SAXS scattering profiles. Feedback provided by Dr Rambo from the Diamond Light Source (Oxford) supported the hypothesis that small upturn might not always be a sign of aggregation but rather a sign of higher oligomer formation (often disordered).

Primary analysis of all the AtVDAC SAXS data revealed a compact, well folded envelope with relatively small flexibility, consistent with previous studies on β -barrel porins (Dyer, Brown et al. 2015). This compactness was accompanied with a relatively low R_g for a ~30 kDa protein as opposed to the reference protein BSA (~66 kDa) (section 5.4.2). The R_g was fairly consistent across individual experiments for all AtVDACs, albeit increasing very slightly upon dilution (section 5.5.1, 5.6.1 and 5.7.1, Figure 5.8, 5.13 and 5.18). This might be due to the dilution, potentially stabilizing the micelles in which the proteins are embedded (Yu, Raschle et al. 2012) by increasing the ratio between detergent and protein, and putatively reducing the natural aggregation propensity of membrane proteins.

The $P(r)$ distribution function of all the examined AtVDACs revealed bell-shaped curves with a small tail, suggesting a globular-type envelope with a relatively spherical shape. No significant differences could be observed between the native-like AtVDAC envelope and those of its mutants, (consistent D_{max} of 39 to 40 Å, Figure 5.29).

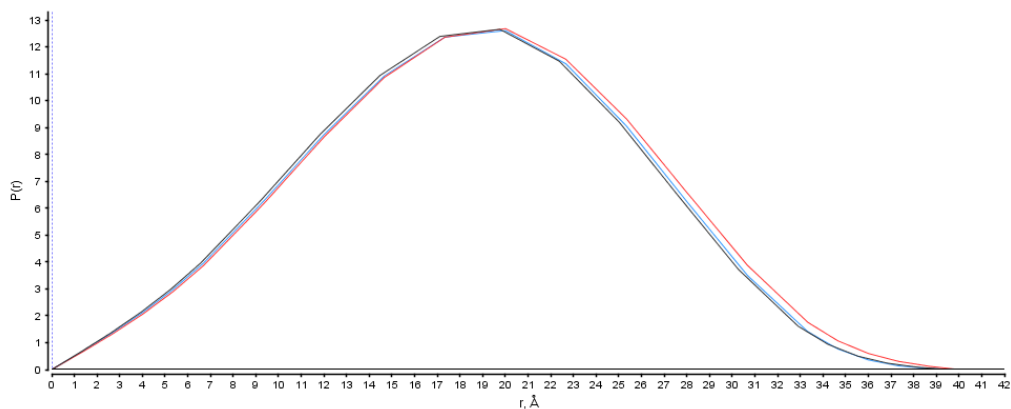


Figure 5.29 P(r) distribution plots of AtVDACs scattering data. P(r) distribution function of the AtVDACs samples in 25 mM NaH₂PO₄/Na₂HPO₄ (pH 7.0), 50 mM NaCl, 1 mM EDTA, 1 mM DTT, 10 % (w/v) Glycerol. The Native AtVDAC1 is shown in red, mutant D258N and D177N are shown in black and blue respectively.

Processing of data through GNOM lead to the generation of multiple envelopes that were averaged and filtered by DAMSUP to produce final molecular envelopes for each protein. All AtVDAC proteins exhibited thick disk shapes with similar dimensions. AtVDAC1 appeared slightly more elongated than its mutants, which shares a more homogenous disk shape.

When comparing the generated AtVDAC1 SAXS envelopes to the computed AtVDAC1 structures (generated by homology modelling; section 5.5.5), the filtered SAXS envelopes were smaller than expected and most of the amino acids forming the loops between each beta sheet were excluded from them. The relative flexibility of these secondary structures compared to beta sheets might explain why they were not included in the “core” density. Moreover, slight over-subtraction of the buffer might as well contribute to this smaller volume. As VDAC are likely embedded in micelles (Yu, Raschle et al. 2012), part of the micelle could be subtracted from the scattering intensity, leading to a reduction in the size of the molecular envelope.

Surprisingly, the computed SAXS profile generated via the Fox webserver (Schneidman-Duhovny, Hammel et al. 2010) revealed a completely different hypothetical scattering pattern. This pattern was strongly influenced by the crystal nature of the inputted PDB, thus producing a scattering profile indicative for the presence of an elongated tube (Svergun and Volkov, 2003). Even more surprising was the fact that in-house experiments often displayed a scattering profile closer to those of the simulated

experiments. Unfortunately, an incredibly high upturn of the scattering intensity at low q value prevented further analysis of these data. In conclusion, it is likely that the instrument and measurements made with a weaker X-ray beam (less sensitive) only revealed the internal core of the protein. This could be due to additional parameters such the lack of scattering of the sample due to possible X-ray absorption.

The general consensus around protein refolding in detergent relies around the membrane protein being “embedded” into micelles. Therefore, LDAO SAXS profiles were recorded at various concentrations matching the concentration of the blank/dialysis buffer. In summary, the radius of gyration of LDAO was consistent with a micelle size of 17 to 20 kDa (Herrmann 1962) and fairly close, although slightly lower, than the R_g values obtained for AtVDACs. The quality analysis of LDAO emphasized a partially folded, but definitely not compact envelope. This lack of proper compactness and folding in comparison to the AtVDAC envelopes was a key determinant in characterizing the main difference between a free empty micelle and a VDAC embedded in a micelle.

Finally, final molecular envelopes for LDAO at five times and ten times the CMC revealed a bi- and trilobate shape respectively, nowhere close to those of AtVDAC1 or its mutant. Although the LDAO micelle was found to be best fitted as an ellipsoid in SANS experiments (Thiyagarajan and Tiede 1994), the analysis of the size distribution of the particles in the different LDAO by BSc Student Thomas Goodfellow at the University of Huddersfield using a zeta sizer Nano Z from Malvern ® revealed a slow kinetic of micelle formation. Fresh LDAO samples would exhibit a large majority of monomer LDAO (around 4 nm in size) and would shift toward a bigger micelle after a few days. Considering the different LDAO samples subjected to SAXS were prepared in the same conditions, it is likely the micelles could stabilize and grow bigger in size after a few more days of incubation. Thus, the odd shapes observed here are likely the result of the slow kinetic of micelle in the process of stabilization. An interesting experiment could be designed to further characterize the kinetic of micelle formation using SAXS and samples mixed and incubated at various time-points.

6. Chapter 6: The Kinesin-like mKlp2C-Ter

In parallel to the structural and functional characterization of AtVDAC1 and its mutant D177N, D258N and T156C, several potential AtVDAC partner proteins such as *A.thaliana* Hexokinase 1, Bcl-Xs and mKlp2 were investigated for their ability to bind AtVDACs (see section 1.10.1). Only one protein was brought to the purification stage, namely mKlp2C-Ter, a truncated version of mKlp2 protein.

This Kinesin-like protein, called KIN-7D, MKRP2 or mKlp2 (accession number; Q8W5R5), contains an extended region in its N-Terminal motor domain that has been proven to act as an MTS (mitochondrial targeting signal) in plants (Itoh, Fujiwara et al. 2001). Moreover, it has already been demonstrated to harbour a microtubule-enhanced ATPase activity, an ability to bind ATP and ADP *in vitro*, as well as retaining its total enzymatic activity even after the removal of the ADP bound in the active site (Kondo, Umeki et al. 2006, Umeki, Maruta et al. 2006).

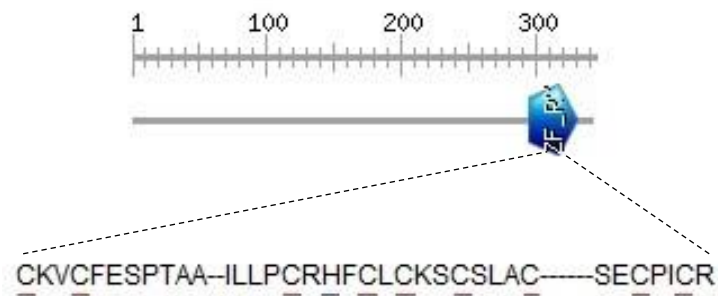


Figure 6.1 Identification of a zinc finger in the C-Terminal domain of mKlp2. Domain prediction was performed using Prosite webserver (Sigrist, de Castro et al. 2013) on the last 345 amino acids of mKlp2 (accession number; Q8W5R5). The typical cysteine and histidine residues forming the ring finger domain are indicated by a red and blue line respectively.

Interestingly, its record in UniProt Database (The UniProt 2018) revealed a potential zinc finger in the last 40 amino acids of its C-Terminal domain (Figure 6.1). Considering ring fingers are known mediator of ubiquitin ligase activity (Lorick, Jensen et al. 1999, Joazeiro and Weissman 2000), its presence on mKlp2 protein might suggest this kinesin might play a role in the mediation of mitochondrial protein degradation via the ubiquitination pathway.

To further characterize this specific region of the mKlp2 protein, a truncated version containing only the last 345 amino acids of the Native protein was designed. This truncated protein contained an His-tag on its N-Terminal domain for subsequent purification, and a thrombin cleavage site for the removal of the tag (post-purification). Tagged and untagged truncated mKlp2C-Ter would then be assessed by Iso-thermal calorimetry (ITC, section 6.7) for their ability to bind zinc ions via the ring finger domain. Additionally, their structure in solution would be probed by Small Angle X-Ray Scattering (SAXS, section 6.8).

6.1. Cloning of *mKlp2C-Ter*

Expression plasmid pET-20b(+) constructs harbouring the *mKlp2C-Ter* were constructed by Muktar Farah (MSc thesis 2014) under the supervision of Dr Georgios Psakis at the University of Huddersfield. Plasmid stocks were replenished by frequent mini-preps of transformed with the desired plasmid DH5 α to ensure constant supply of fresh DNA (section 2.3.3).

6.2. Heterologous expression of *mKlp2C-Ter* in *E.coli*

BL21 DE3 cells (Table 2.4) were first chemically transformed with the plasmid harbouring the *mKlp2C-Ter* gene (Kin-7D, locus At4g39050) and grown on selective medium. Typical expression conditions were screened (concentration of IPTG and time of incubation) and the optimal set of conditions was chosen (results not shown). This screen was conducted by Muktar Farah (MSc thesis 2014; results not shown) and would prove to work consistently. As a result, *MKLP2* gene expression in BL21D(DE3) cells was induced with 1 mM IPTG at 37 °C for 4h (see section 2.3.4.1).

6.3. Purification of *mKlp2-Ter* by affinity chromatography using a Protino Ni-Nta solid support

Following overexpression, IPTG-induced cells were harvested and resuspended in lysis buffer (see Table 2.1). Cells were then sonicated (Figure 6.2A lane 2) and harvested again, and the supernatant (Figure 6.2A lane 3) was applied onto a Protino 5 mL HisTrap Ni-NTA column from Merck Millipore® (see 2.5.4.2) and eluted using a high concentration of imidazole (see Table 2.1) using an Akta Start ®. Most of the protein bound to the matrix, as evidenced by the SDS-PAGE purification profile of the protein (Figure 6.2A; lane 4). To further investigate the ideal concentration of imidazole to use for the elution step, a gradient (up to 500 mM imidazole) was used (Figure 6.2B). Protein kept eluting during the experiment, to finally peak once 500 mM imidazole concentration was reached. Overall, all samples exhibited a high purity (above 90 %), with minor amounts of contaminants. As a result, a step gradient of 500 mM imidazole was chosen (see Table 2.1).

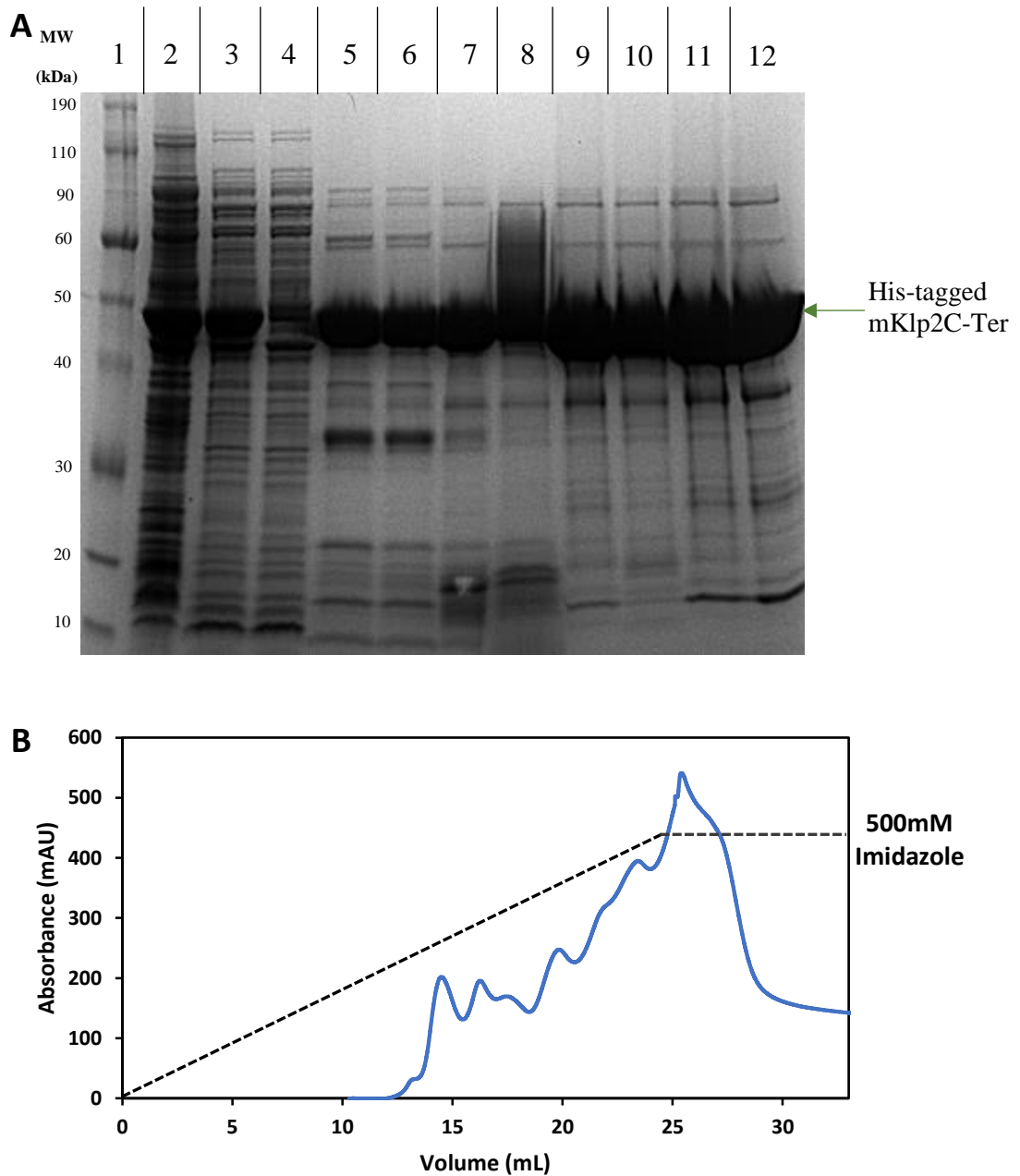


Figure 6.2 Ni-NTA affinity chromatography for mKlp2-Cter with an increasing gradient of [Imidazole] using a Protino 5 mL HisTrap. (A) Different samples taken during mKlp2C-Ter purification were analysed on 10 % (v/v) SDS-PAGE in 1x Laemmli buffer. First lane; ladder from Novex®. Lane 2; sonicated cell extract of BL21 DE3 cells expressing mKlp2; Lane 3; supernatant after sonication; Lane 4; flow-through after binding to the Ni-NTA column; Lanes 5 to 10; after 15, 16, 17, 18, 20 and 22 mL respectively. Lanes 11 and 12; samples collected after reaching the maximum concentration of imidazole (500 mM), at 24 and 26 mL, respectively. Position of mKlp2C-Ter on the gel is indicated (green arrow). (B) Elution profile (UV absorbance in blue) of the Ni-NTA affinity chromatography performed on mKlp2-Cter using a linear gradient of 20 mM to 500 mM imidazole (dark grey).

Protein eluted as a relatively broad single peak (see Figure 6.3B) of around 4 column volumes (CV) and tailing at the end. No further improvement on the maximum collection volume was made by using higher concentrations of imidazole (results not shown). No clear difference could be observed in terms of impurity on the main peak (Figure 6.3A, lane 4 to 8), thus final collection criteria were chosen (around 2 CV, Figure 6.3B green line) for subsequent purifications. Routinely, mKlp2C-Ter was purified to a volume of around 10 mL, with a concentration ranging from 6 to 8 mg/mL, from a 100 mg cell lysate.

Collected fractions were concentrated using a 30K cut-off AMICON Ultra-15 Centrifugal Filter Units® according to section 2.5.5. When attempting to concentrate the protein to higher than 10 mg/mL, the protein started exhibiting mild to severe aggregation. The presence of glycerol in the buffer did not prevent this phenomenon, and decision was made to concentrate the protein to a maximum of 8 mg/mL.

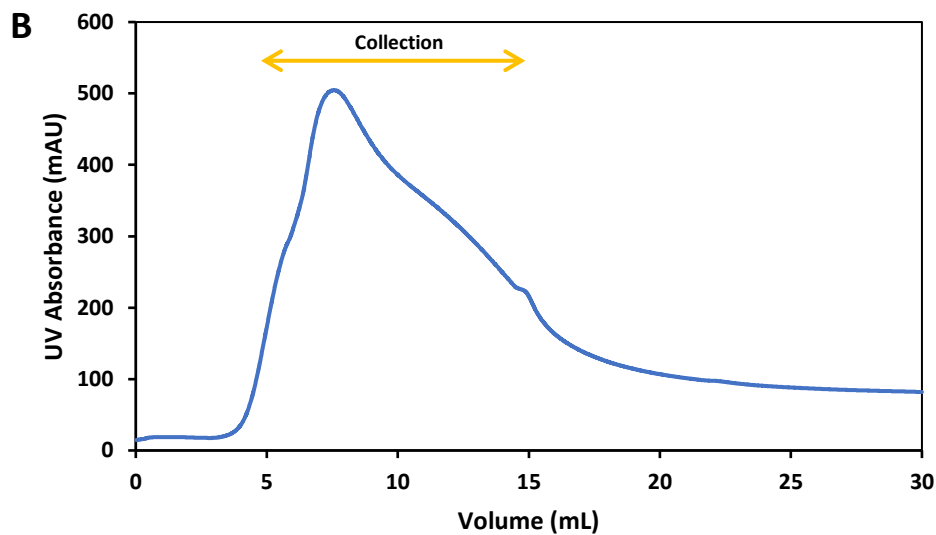
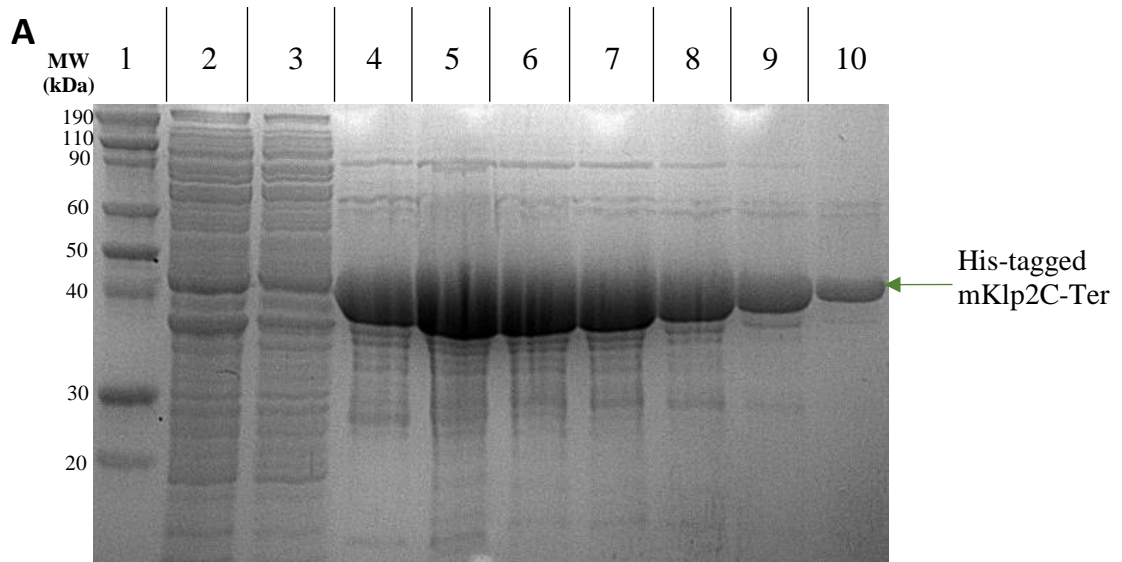


Figure 6.3 Ni-NTA affinity chromatography of mKlp2-Cter with a step-gradient of [Imidazole] using a Protino 5 mL HisTrap. (A) Different samples taken during mKlp2C-Ter purification were analysed on 10 % (v/v) SDS-PAGE in 1x Laemmli buffer. First lane; ladder from Novex®. Lane 2; samples from the flow-through after binding to the Ni-Nta column. Lanes 4 to 9; samples collected after 5, 7.5, 10, 12.5, 15 and 17.5 mL respectively. Lane 10; sample collected from the tail, around 24 mL. Position of mKlp2C-Ter on the gel is indicated (green arrow). (B). Elution profile (UV absorbance in blue) of the affinity chromatography performed on mKlp2-Cter using a single-step gradient of 500 mM imidazole. Pooling criteria is shown in yellow.

6.3.1. Resin reuse analysis of the Protino Ni-Nta solid support for the purification of mKlp2-Ter by affinity chromatography

Resin re-use was monitored throughout the PhD, and profiles were examined for reproducibility. After three years and above fifty purification runs, the binding capacity decreased over time. As a result, last runs yielded much lower amount of protein per cycle, which was confirmed by a lower maximum absorbance (170 mAU against 500 mAU previously) on the elution profile (Figure 6.4). Although sharper than previous experiments, the purity/impurity ratio was left unaffected. If needed, the supernatant would be reapplied to the matrix after a first run of affinity chromatography, and re-eluted using the same criteria.

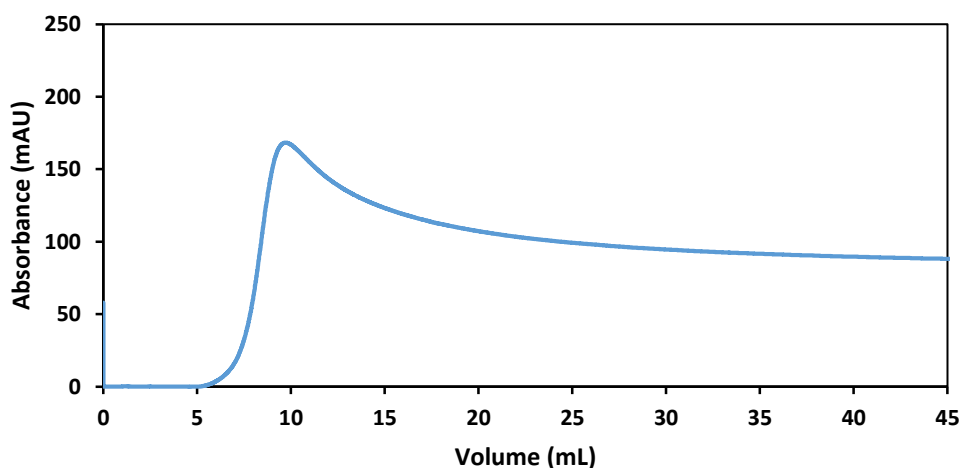


Figure 6.4 Ni-NTA affinity chromatography of mKlp2-Cter with a step-gradient of [Imidazole] using a Protino 5 mL HisTrap after 20 cycles. Elution profile (Absorbance in blue) of the affinity chromatography performed on mKlp2C-Ter at the end of the PhD using a single-step gradient of 500 mM imidazole.

6.4. Size exclusion chromatography of purified mKlp2C-Ter using a Superose6 Increase®

Size exclusion chromatography (SEC) was first performed using a Superdex 75 10/300 GL (Life Sciences®) column. Unfortunately, due to its aggregation-prone behaviour (section 6.3), the sample was not resolved on the column. In consequence, SEC was attempted using a Superose6 10/300 GL (Life Sciences®) column. A sample (500 µL of a 10 mg/mL eluate from affinity chromatography) was injected onto the column in SEC buffer (25 mM Tris-HCl (pH 7.0), 100 mM NaCl, 3 % (w/v) Glycerol) using an Akta Prime ® and the elution profile was recorded (Figure 6.5B). Collected fractions were analysed by 10 % (v/v) SDS PAGE in 1x Laemmli buffer (Figure 6.5A). mKlp2C-Ter eluted as a single peak, and the chromatography overall offered some impurity clearance. Indeed, two small peaks eluted at the end of the purification (Figure 6.5B, after 20 mL), and contained mostly lower molecular weight contaminants (Figure 6.5A lane 10).

However, this single peak maximum was observed around 15 mL after injection of the protein in the column, corresponding to an approximate size of 120 kDa, contrary to the expected 40 to 42 kDa size observed on SDS PAGE gels. To further understand whether the aforementioned SEC behaviour stemmed from protein aggregation resulting from sample over-concentrating, a second mKlp2C-Ter sample was two-fold diluted prior to injection onto the column. The two-fold diluted protein exhibited a complex profile (Figure 6.6A); most of the protein eluted with early peak maxima at 17.1 mL, corresponding to an approximate size of 45kDa. The maxima of later peaks correlated with the elution of impurities of smaller sizes (below 30 kDa).

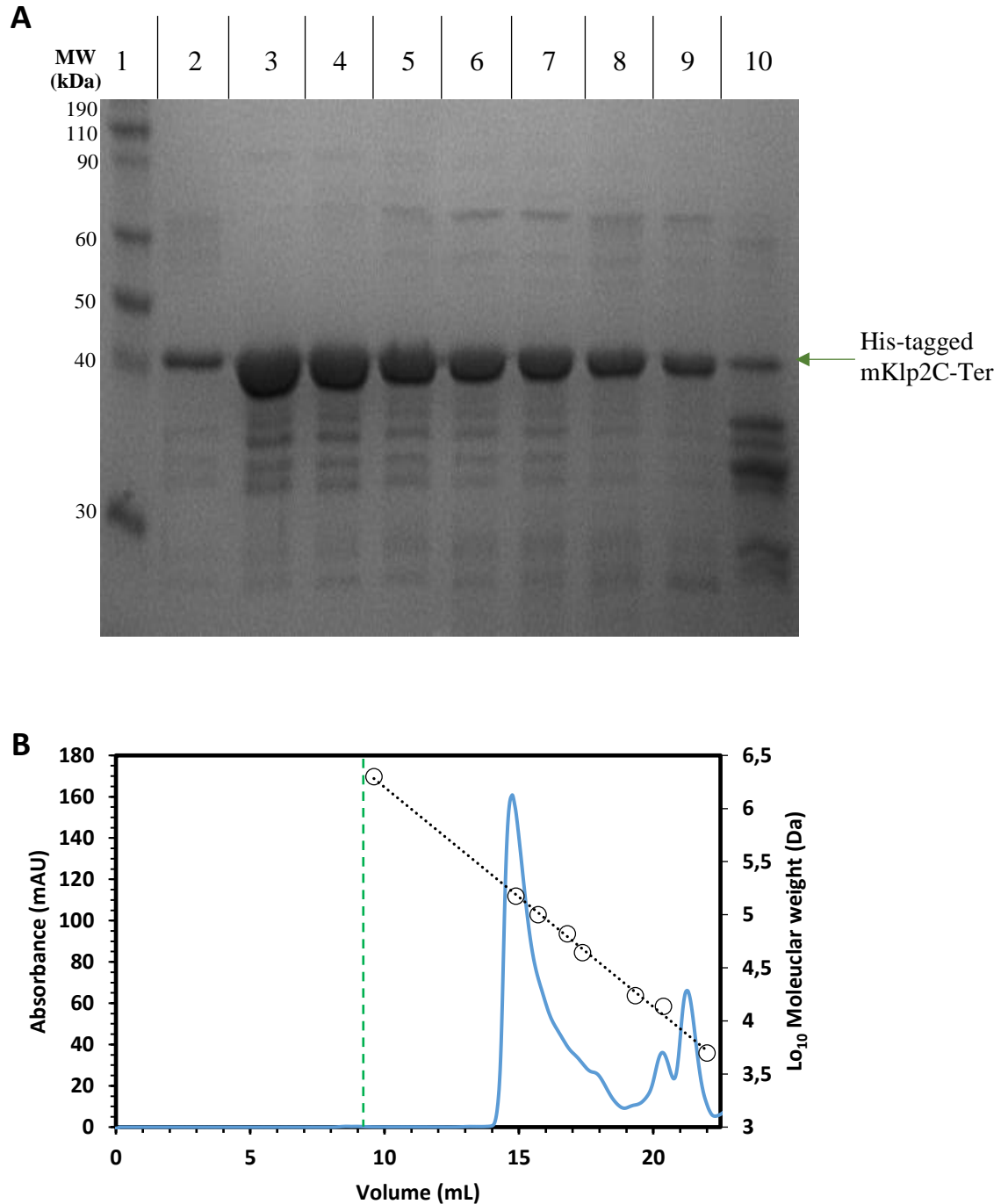


Figure 6.5 Size exclusion chromatography of 8 mg/mL (undiluted) mKlp2-Cter using a Superose6 Increase®. SEC was carried out in an Akta Prime ® device in SEC buffer (25 mM Tris-HCl (pH 7.0), 100 mM NaCl, 3 % (w/v) Glycerol). **(A)** 10 μL of each purified sample taken during mKlp2C-Ter SEC were analysed on 10 % (v/v) SDS-PAGE in 1x Laemmli buffer. First lane; ladder from Novex®. Lane 2 to 10; samples collected at 14, 15, 16, 17, 18 19, 20, 21 and 22 mL from 8 mg/mL mKlp2C-Ter loaded onto Superose6. Position of mKlp2C-Ter on the gel is indicated (green arrow). **(B)** Elution profile (UV absorbance in blue) of the size exclusion chromatography performed on mKlp2-Cter after injection of a purified sample (500 μL of an 8 mg/mL solution). The minimum working range (void volume) is indicated by a green dashed line.

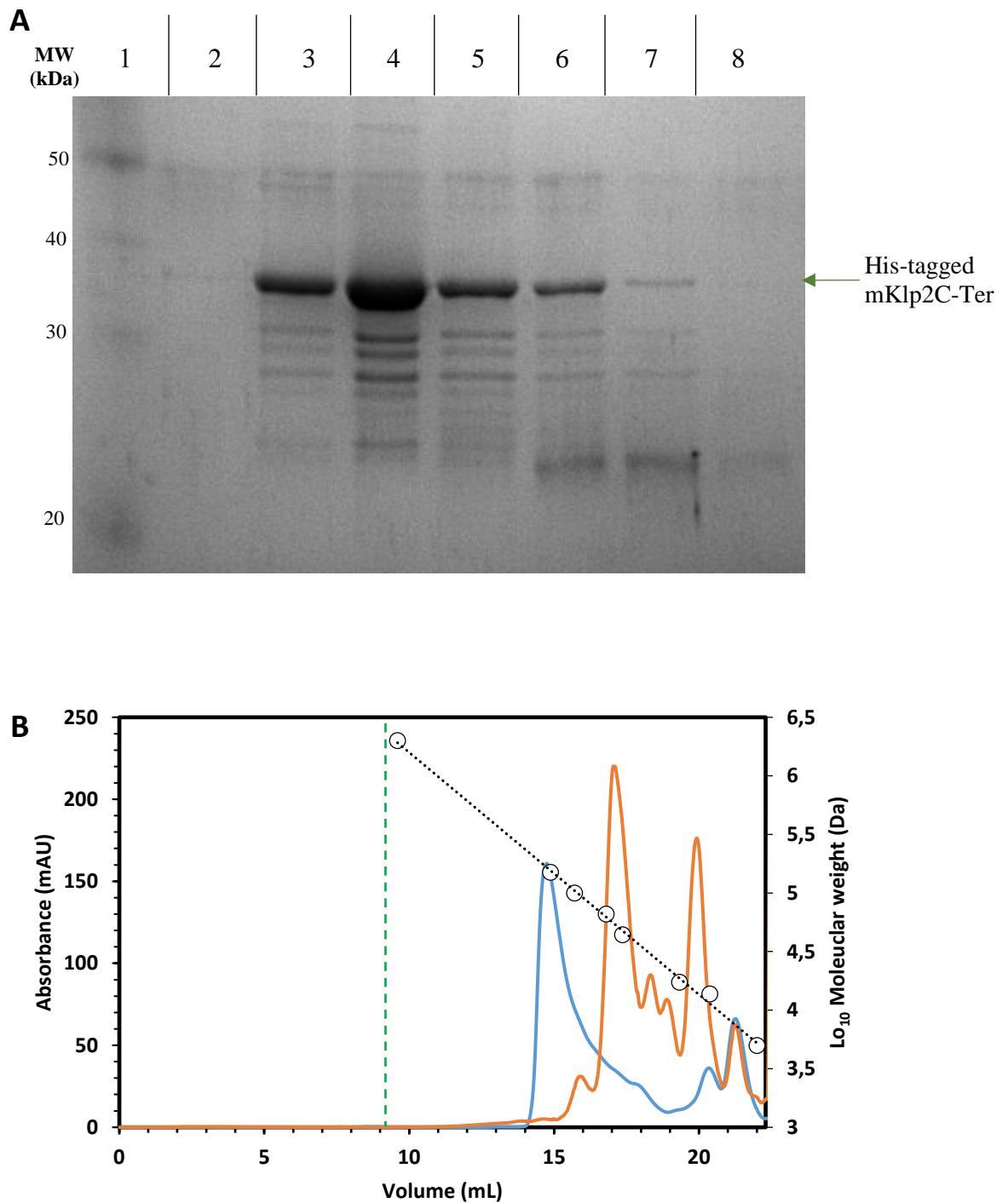


Figure 6.6 Size exclusion chromatography of 4 mg/mL (diluted) mKlp2-Cter using a Superose6 Increase®. SEC was carried out in an Akta Prime ® device in SEC buffer (25 mM Tris-HCl (pH 7.0), 100 mM NaCl, 3 % (w/v) Glycerol). (A) 10 µL of each purified sample taken during mKlp2C-Ter SEC were analysed on 10 % (v/v) SDS-PAGE in 1x Laemmli buffer. First lane; ladder from Novex®. Lane 2 to 8; samples collected 15, 16, 17, 18 19, 20, and 21 mL from 4 mg/mL mKlp2C-Ter loaded onto Superose6. Position of mKlp2C-Ter on the gel is indicated (green arrow). (B) Elution profile (UV absorbance in blue and orange) of the size exclusion chromatography performed on mKlp2-Cter after injection of a diluted sample (4 mg/mL, orange line) and undiluted sample (8 mg/mL, blue line). The minimum working range (void volume) is indicated by a green dashed line.

6.5. Stability studies on mKlp2C-Ter

The main two techniques used for the study of mKlp2C-Ter were SAXS (Small Angle X-Ray Scattering, see 2.6.1) and ITC (iso-thermal calorimetry, see 2.3.3), aimed at characterizing its structure in solution and testing its ability to bind zinc ions via its ring finger domain, respectively. Hence, dialysis had to be performed prior to SAXS studies and samples had to be titrated with Zinc, for ITC studies. The stability of mKlp2C-Ter was then assessed to define the experimental limitations of the different assays mentioned above.

6.5.1. Dialysis

A sample of mKlp2C-Ter (500 μ L of a 10mg/mL solution, Figure 6.7 lane 2) was dialyzed for up to four days in SEC buffer (25 mM Tris-HCl (pH 7.0), 100 mM NaCl, 3 % (w/v) Glycerol), and samples were collected on each day, centrifugated and loaded (10 μ L per lane) onto 10 % (v/v) SDS-PAGE in 1x Laemmli buffer (Figure 6.7, lane 3 to 5).

A significant loss of protein was observed after only few hours (Figure 6.7, lane 3), and most of the protein would aggregate after two days, leading to a near complete loss of the signal intensity (Figure 6.7, lane 4 and 5). Similar analysis was performed on mKlp2C-Ter samples pre- and post SAXS (X-ray exposure of around 10 hours) treatments (Figure 6.7, lane 6). Noticeably, the sample survived the exposure to X-Rays, as the band intensity observed post X-ray treatment (Figure 6.7 lane 6) remained similar to that of the pre-SAXS studied sample, and no apparent degradation was observed.

To further investigate the effect of imidazole, from the affinity chromatography elution step (using 25 mM Tris-HCl (pH 7.0), 100 mM NaCl, 3 % (w/v) Glycerol, 500 mM Imidazole), on the stability of mKlp2C-Ter during dialysis and X-Ray exposure, affinity chromatography eluted protein samples were buffer exchanged in SEC buffer and further dialyzed extensively in SEC buffer, before analysis of samples by SDS-PAGE (Figure 6.7, lane 7 to 10) . This time, the loss of protein was even faster, leading to a barely detectable signal of the mKlp2C-Ter monomer on 10 % (v/v) SDS-PAGE, even after one day (Figure 6.7 lane 8). Sample dialyzed for one day was subjected to SAXS, and subsequently loaded post SAXS exposure on a 10 % (v/v) SDS-PAGE in 1x Laemmli buffer (20 μ L, Figure 6.7 lane 10). In

the latter case, sample volume had to be doubled (20 μ L instead of 10 μ L), to allow detection on Coomassie Blue stained SDS PAGE.

Decision was made to buffer exchange samples (in SEC buffer) for future SAXS studies, rather than extensively dialyzing them due to the dramatic effect the dialysis had on the concentration of the mKlp2C-Ter protein.

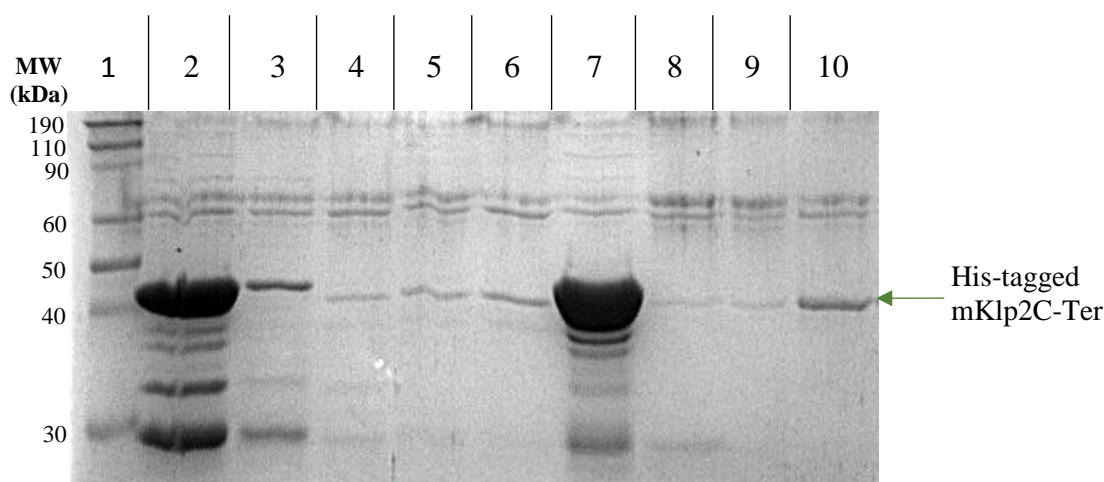


Figure 6.7 Stability study of dialyzed mKlp2C-Ter. Concentrated, and dialyzed samples of purified mKlp2C-Ter protein were analysed on 10 % (v/v) SDS-PAGE in 1x Laemmli buffer. First lane; ladder from Novex®. lane 2; concentrated mKlp2C-Ter protein (8 mg/mL); Lane 3 to 5; mKlp2C-Ter, dialyzed after 1, 3 or 4 days, respectively; lane 6; mKlp2C-Ter (after a 4-day dialysis), post SAXS exposure. Lane 7; buffer exchanged (in SEC buffer (25 mM Tris-HCl (pH 7.0), 100 mM NaCl, 3 % (w/v) Glycerol) and concentrated mKlp2C-Ter (8 mg/mL). Lane 8 to 9; mKlp2C-Ter dialyzed in SEC buffer after 1 or 4 days, respectively; lane 10 mKlp2C-Ter (after a 1day dialysis) post SAXS exposure.

6.5.2. Stability of mKlp2C-Ter in 10 mM Zinc

The second stability assay probed the utilization of zinc as a potential co-factor via ITC experiments. As a result, it was necessary to understand the effect of zinc on mKlp2C-Ter over time. A freshly purified and buffer exchanged 8 mg/mL mKlp2C-Ter sample (in 50 mM Tris-HCl (pH 7.5), 0.1 mM TCEP, 100 mM NaCl, 3 % (v/v) glycerol, Figure 6.8, lane 2), was mixed with zinc chloride to a final concentration of 10 mM (same as titrant solution in ITC assays) and left mixing for up to a week. Samples and controls (left mixing in absence of zinc) were collected daily and loaded onto 10 % (v/v) SDS-PAGE in 1x

Laemmli buffer (Figure 6.8A). Protein concentrations were determined daily by the BCA assay and reported for both the control and zinc-mixed samples (Figure 6.8B, blue and orange lines respectively).

Over the first 24 to 30 hours, both control and sample would remain relatively stable (Figure 6.8A, lane 2 and 3). However, both SDS-PAGE analysis and concentration determinations confirmed a negative effect of the zinc on the stability of the protein after more than 30 hours exposure (Figure 6.8A, lane 4 and 5). A 1.3-fold difference could be observed after only two days (1.5 versus 2 mg/mL for the control, Figure 6.8B). Following that time period, the protein reached a lower threshold (4 days) at which it remained stable over the next 3 days. However, the control sample exhibited a more linear precipitation pattern, with a similar reduction in gel staining intensity and concentration values (Figure 6.8B, after 5 days).

Altogether, these results highlighted a negative effect of zinc on the stability of mKlp2C-Ter over extended periods of time. Consequently, samples of mKlp2C-Ter would have to be exposed to zinc for no more than 24 to 30 hours during a single run of ITC titration experiment.

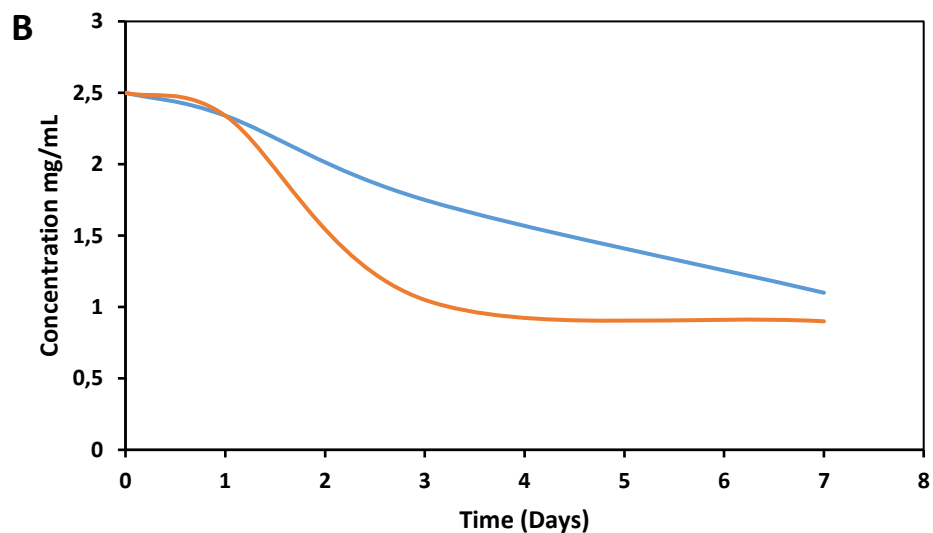
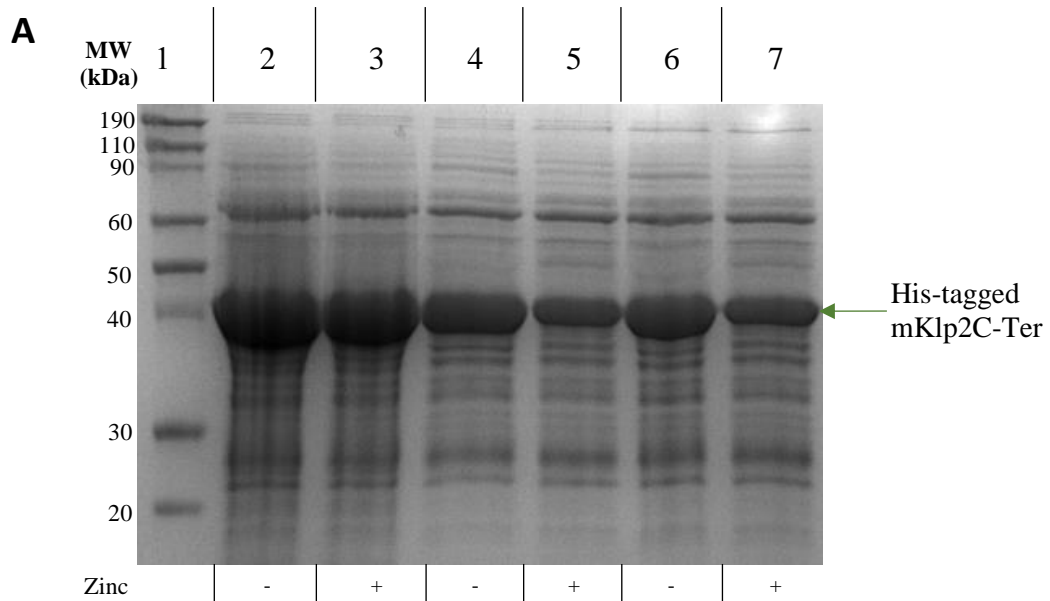


Figure 6.8 Stability study on mKlp2C-Ter in the presence of 10 mM zinc. (A) mKlp2C-Ter samples (8 mg/mL) mixed with Zinc Chloride at a final concentration of 10 mM were analysed on 10 % (v/v) SDS-PAGE in 1x Laemmli buffer. First lane; ladder from Novex®. Lanes 2, 4 and 6; control mKlp2C-Ter sample (10 μ L of a 10mg/mL solution) left mixing at room temperature for 1, 2 and 3 days, respectively, in the absence of zinc. Lanes 3, 5 and 7; mKlp2C-Ter mixed with zinc chloride (final concentration of 10 mM) and left mixing at room temperature for 1, 2 and 3 days, respectively. (B) Investigation of sample stability, as a function of protein concentration changes with time, in the presence (orange line) and absence (blue line) of 10 Mm ZnCl₂.

6.6. Removal of the N-Terminal 6xHis-Tag domain of mKlp2C-Ter

Although the use of a tag can greatly help in rapidly purifying great amounts of recombinant protein, its potential interference in various assays such as ITC or SAXS needs to be assessed. In the case of mKlp2C-Ter, a 6xHis-Tag was used to purify the protein using a Ni-Nta solid support for affinity chromatography (Figure 6.9, grey rectangle). Following its purification, the removal of the histidine tag could be achieved using a thrombin cleavage site introduced near the tag, downstream its location (Figure 6.9, blue rectangle).



Figure 6.9 N-Terminal domain of mKlp2C-Ter. First 35 amino acids of the N-terminal domain of mKlp2C-Ter. The 6xHis-Tag introduced for its purification by Ni-Nta affinity chromatography is highlighted in red, whereas the thrombin cleavage site used for the removal of the tag is highlighted in yellow.

6.6.1. Small scale optimization of His-Tag removal with thrombin cleavage

A first screen of the optimal conditions for the digestion of the Histidine-tag from mKlp2C-Ter was carried out using two parameters, a) time of incubation and b) thrombin concentration. amounts of thrombin used were decided according to the supplier's recommendations (1U thrombin/4mg of protein, according to Sigma-Aldrich®). 20 µg of freshly Ni-NTA-affinity purified mKlp2C-Ter were incubated with different thrombin dilutions for either 1, 2, 4, 6 or 18 hours. Reactions were stopped by the addition of 10 mM PMSF (phenylmethylsulfonyl fluoride), an inhibitor of serine (and cysteine) proteases. Samples were loaded on an 10% (v/v) SDS PAGE in 1x Laemmli buffer (Figure 6.10, panel A and B, "+" imidazole). In parallel, 20 µg of freshly Ni-NTA-affinity purified and without imidazole (removed by buffer exchange in SEC buffer through a PD-10 desalting column from GE Healthcare Life Sciences®) were treated and analysed in the same manner (Figure 6.10, panel A and B, "-" imidazole). Following a one- or two-hour digestion, most of mKlp2C-Ter-His6 was digested by thrombin in the absence of imidazole (Figure 6.10, A and B, "-" imidazole; 1H digest and 2H digest). A fragment of

approximately 39 kDa (black arrow), resulting from the shift due to the His-Tag (1.6 kDa) removal, is clearly produced and none of the original 41 kDa protein (green arrow) is present anymore. However, an additional fragment (black arrow) is produced when samples were subjected to thrombin digest longer than two hours, suggesting an over-digestion of mKlp2C-Ter by the protease. This is evident by the increasing band intensity (just below 30 kDa) with incubation time (Figure 6.10, all samples after 18 hours, lane 8 of each gel).

In the presence of imidazole (Figure 6.10, A and B, “+” imidazole), the full digestion of His-tagged mKlp2C-Ter required 4 to 6 hours depending on the dilution factor (1/50 and 1/100 respectively). Again, over time additional protein fragmentation occurred (Figure 6.10, black arrow).

In conclusion, a clear difference can be observed in the digestion patterns of the samples when imidazole was present. Although the complete removal of the tag was achieved faster without imidazole, the presence of imidazole allowed more control on the over-digestion of mKlp2C-Ter at lab-scale. The 1/50 dilution in the presence of imidazole was chosen for the large-scale digest of His-tagged mKlp2C-Ter. For large-scale works, digests were not allowed to proceed longer than two hours.

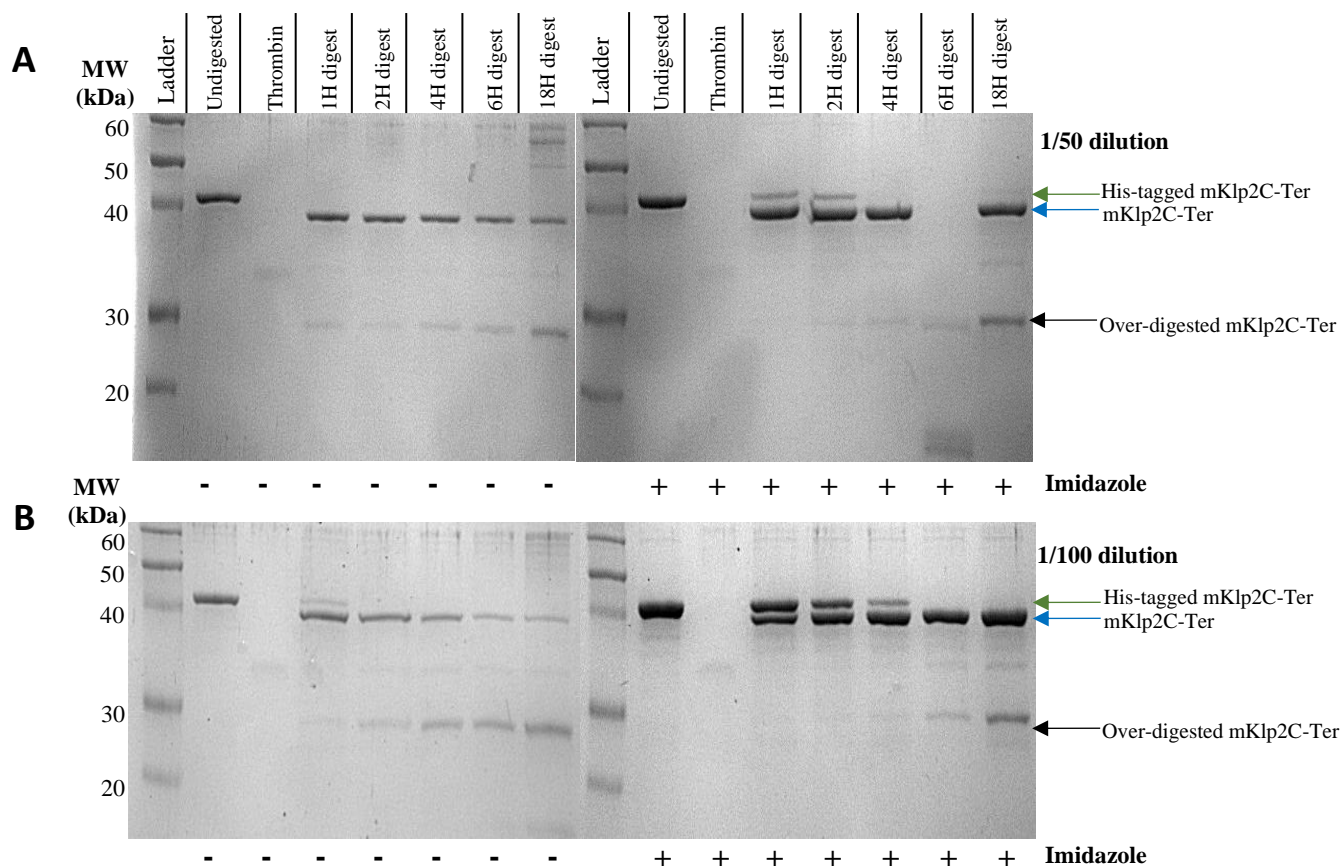


Figure 6.10 Optimisation of His-tag digestion from mKlp2C-Ter with thrombin cleavage. (A) 20 μ g of freshly purified mKlp2C-Ter were incubated with a 1/50 (panel A) or 1/100 (panel B) dilution of the thrombin (0.0002 or 0.0001 UE per sample) and incubated for either 1, 2, 4, 6 or 18 hours at room temperature. PMSF was added as an inhibitor (to stop the thrombin cleavage) and samples were loaded on an 10% (v/v) SDS PAGE in 1x Laemmli buffer. (B) 20 μ g of freshly purified and buffer exchanged mKlp2C-Ter (in 25 mM Tris-HCl (pH 7.0), 100 mM NaCl, 3 % (w/v) Glycerol 25 mM) to remove the excess imidazole, were treated as above.

6.6.2. Large scale of mKlp2C-Ter with thrombin cleavage

Having identified the best conditions for the cleavage of the purification tag from mKlp2C-Ter (section 6.6.1), a large-scale His-Tag removal experiment was performed on freshly purified mKlp2C-Ter (see section 6.3). A volume (8 mL) of a solution containing Ni-Nta purified mKlp2C-Ter-His6 (4 mg/mL, Figure 6.11 lane 2) was digested with 0.16 UE of thrombin (1/50 dilution of 8 Units). The mixture was incubated for 2 hours at room temperature and the correct removal of the tag was assessed via SDS PAGE (Figure 6.11). Samples were taken every fifteen minutes and loaded on 10 % (v/v) SDS PAGE in 1x Laemmli buffer for control.

After a 2 hour-incubation of mKlp2C-Ter with the thrombin, a complete digest of the His-tagged mKlp2C-Ter was achieved (Figure 6.11, lane 8). Only traces of undigested His-tagged mKlp2C-Ter-His6 can be found in the samples. After applying the solution through a Ni-NTA affinity column, the flow-through (Figure 6.11, lane 9) is completely free of undigested His-Tagged mKlp2C-Ter. The experiment yielded a high amount of digested mKlp2C-Ter (9 mL at 3.5 mg/mL), suitable for downstream applications.

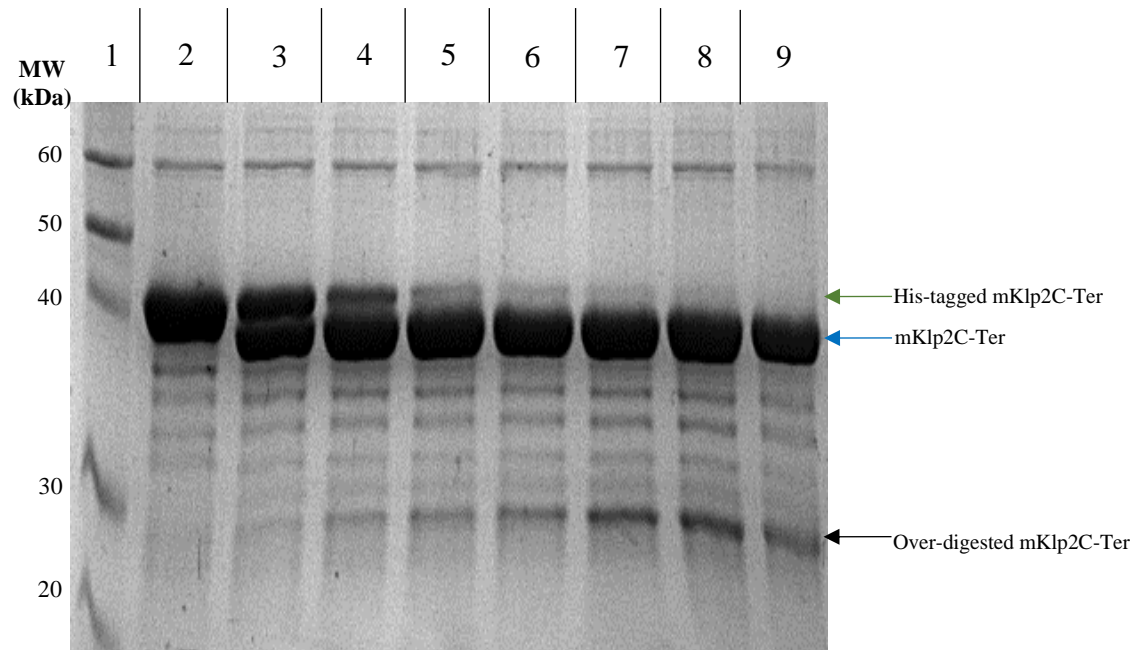


Figure 6.11 Large scale digestion of mKlp2C-Ter-His6 with thrombin. 8 mL of a solution containing purified mKlp2C-Ter-His6 (4 mg/mL, lane 2) was digested with 0.16 UE of thrombin (1/50 dilution of 8 Units), following the results obtained from the small-scale screen digest (section 6.6.1). The mixture was incubated for 2 hours at room temperature, and samples were taken every 15 minutes (lane 3 to 8) and analysed on 10% (v/v) SDS PAGE in 1x Laemmli buffer. After incubation and addition of PMSF to stop the reaction, the mixture was re-applied on a Ni-NTA matrix. A sample from the flow-through (lane 9) was taken and loaded on 10% (v/v) SDS PAGE to assess completeness in the removal of undigested His-tagged mKlp2C-Ter (green arrow). Digested mKlp2C-Ter (blue arrow) and over-digested mKlp2C-Ter (black arrow) are indicated.

6.7. Functional characterization of mKlp2C-Ter by Isothermal Titration Calorimetry (ITC)

6.7.1. Introduction to Isothermal Titration Calorimetry (ITC)

Isothermal Titration Calorimetry (ITC) is a powerful technique for the study of molecular interactions. ITC instrument such as the Malvern MicroCal VP-ITC® can perform quantitative measurements of the molecular interaction between a ligand and its receptor. One of the most important features of this methodology is the ability to determine every binding parameter (stoichiometry of the interaction (n), the association constant (K(a)), the free energy (ΔG), enthalpy (ΔH), entropy (ΔS) associated with the binding event (Pierce, Raman et al. 1999). Additionally, the experiments are normally conducted at room temperature in a closed chamber with the molecule being in solution, providing a more accurate probing of potential interactions in their native state.

Typically, sample (receptor) is titrated by a solution of ligand at specific concentrations. Multiple injections of a pre-defined volume of ligand into the solution will lead to a variation in the overall enthalpy of the chamber (Pierce, Raman et al. 1999). In fact, the binding event will lead to an absorption (endothermic reaction) or release of heat. As the chamber is set to a constant temperature (25 degrees Celcius conventionally, although it is possible to perform experiments under different conditions), any variation of heat will be compensated by the calorimeter (Pierce, Raman et al. 1999). As a result, the energy needed to keep the chamber at a set temperature can be quantified (in $\mu\text{Cal/s}$) and an overall titration profile can be generated over time.

According to the second and third laws of thermodynamics, calculation of the Gibbs free energy of the system can be obtained from the equation 6.1, where T is the temperature, ΔG is the variation of free energy, ΔH is the variation of enthalpy and ΔS is the variation of entropy within the system.

$$\Delta G^\circ = \Delta H^\circ - T\Delta S^\circ$$

Equation 6.1 Gibbs free energy main formula. T is the temperature, ΔG is the variation of free energy, ΔH is the variation of enthalpy and ΔS is the variation of entropy within the system.

In parallel, the binding constant of a ligand to its binding site can be defined as in equation 6.2, where ∂ is the number of sites occupied by the ligand and $[L]$ is the concentration of free ligand.

$$K = \left(\frac{\partial}{1 - \partial}\right) \times [L]$$

Equation 6.2 Definition of the binding affinity constant K for a single independent site. ∂ is the number of sites occupied by the ligand and $[L]$ is the concentration of free ligand.

Using mass conservation and chemical equilibrium equations it is possible to express the heat recorded as a function of the concentration of reactants, the association constant a ligand to its binding site and the enthalpy of binding (see equation 2.2). The affinity, enthalpy and stoichiometry for the binding reaction can be derived mathematically using software such as the OriginLab® or AFFINImeter®. A description of the analysis process is provided below.

6.7.2. Titration of mKlp2C-Ter with ZnCl₂

Original *in silico* analysis of mKlp2C-Ter protein secondary structure revealed a potential zinc finger motif, likely capable of mediating the binding of divalent cations to the kinesin (REF). Hence, the potential binding of zinc ions to the protein was probed by ITC using a Malvern MicroCal VP-ITC at the University of Huddersfield.

ITC experiment was performed on freshly purified mKlp2C-Ter protein at a concentration of 1.2 mg/mL or 31 μ M. The protein was buffer exchanged prior to the experiment in ITC buffer (50 mM Tris-HCl (pH 7.5), 0.1 mM TCEP, 100 mM NaCl, 3 % (v/v) glycerol). Protein sample was left mixing in the main chamber at a constant temperature of 25 degrees Celsius. Titration of mKlp2C-Ter was achieved via series of 5 microliters injections using a solution of ZnCl₂ at 40 mM in ITC buffer.

Additional control experiments such as the titration of the buffer with buffer, the titration of the buffer with ZnCl₂ and the titration of mKlp2C-Ter with the buffer alone were also conducted. Curve isotherms were subsequently subtracted from the protein-ligand data curves (Figure 6.12).

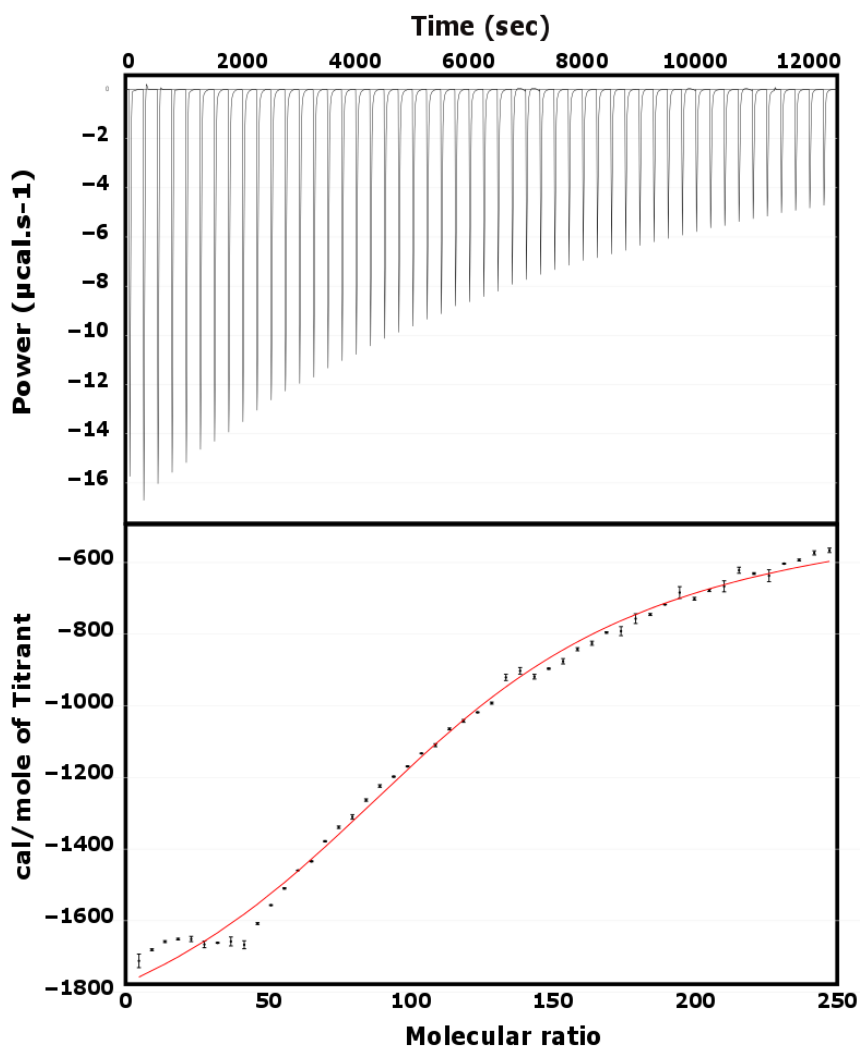


Figure 6.12 Single titration of 31 μM mKlp2C-Ter with 40 mM ZnCl_2 . (Top) Thermogram of ITC measurements. (Bottom) Peak-by peak integrated thermogram (with their error bars) with its mathematical fit, in red. One round of 50 injections (5 μL each) of 40 mM ZnCl_2 in 50 mM Tris-HCl (pH 7.5), 0.1 mM TCEP, 100 mM NaCl, 3 % (v/v) glycerol, was performed and analysed using AFFINImeter®.

Analysis of the data was performed with AFFINImeter® as well as OriginLab®. Unfortunately, no conventional models could fit the recorded data and provide binding parameters. Usually, one or two binding sites titration functions are used to analyse the data. This scenario involves independent binding sites, where the binding of the ligand on one site is independent from the second, although competition and inhibition can be involved (Pierce, Raman et al. 1999). In this instance, a combined approach had to be used, with a conventional binding analysis for the first event and an alternative but more permissive function called sequential binding (with n binding sites) for the second event (Duff, Grubbs et al. 2011).

This function relates to more than two ligand binding sites that might be identical or non-identical, regardless of cooperativity. The affinity constant is then defined as in equation 6.3.

$$K_i = \frac{n - i + 1}{i} K_i^0$$

Equation 6.3 Definition of the binding affinity constant K_i in sequential binding. More than two ligand binding sites (i) might be identical or non-identical regardless of cooperativity.

In essence, all possible states co-exist in equilibrium, but there is no specific order in which the binding sites are saturated (Duff, Grubbs et al. 2011). The data were analysed using this combined binding model in AFFINImeter® software, a user-friendly ITC analysis package for studying a particular binding hypothesis (Piñeiro, Muñoz et al. 2019). The binding parameters for the titration of mKlp2C-Ter with ZnCl₂ are presented in Table 6.1

Table 6.1 Binding parameters of zinc (40 mM) to mKlp2C-Ter (31 μM).

Parameter	First binding event		Second binding event	
	Value	Error	Value	Error
ΔH (cal/mol)	-22.36	1.761	-1460	7.836
K_A (mM ⁻¹)	0.437	1.640	1.378x10 ⁶	0.017
K_D (nM)	2.286	0.86	725	9.25

Values were calculated by AFFINIMETER® using a combined model of unique and sequential binding event. Errors are given and can be used to assess the statistical relevance of the data. An order of magnitude above 2 is preferable.

Unfortunately, the error in the calculation of the first binding site parameters was significant. It is recommended to have at least 2 orders of magnitude difference between the actual values of the binding parameters and their errors (Muñoz and Sabín 2019, Piñeiro, Muñoz et al. 2019). The lack of statistical relevance was attributed to the low number of points recorded during the first binding event, as only 8

injections covered the area of binding. A minimum of 10 to 15 was recommended by Malvern® and AFFINImeter® to produce statistically strong data.

The second binding event exhibited a sequential binding type of site (as mentioned above), thus any constants or parameter is to be taken with caution, as they represent not one binding site but a multitude of them (equation 6.3) (Duff, Grubbs et al. 2011). However, the absence of saturation at the end of the titration profile suggested some additional binding was possible, affecting the stoichiometry measurements (Pierce, Raman et al. 1999).

Reaching the saturation point is paramount in getting accurate and representative data for the different binding parameters. Additional injections were performed on the same sample, by simply refilling the syringe and restarting the titration. As usual, controls had to be performed again in parallel, mimicking the parameters used for the main experiment (injection volume, number of injections etc). They were subtracted from the main signal, and both runs were compiled in EXCEL®. The resulting curve is presented in Figure 6.13.

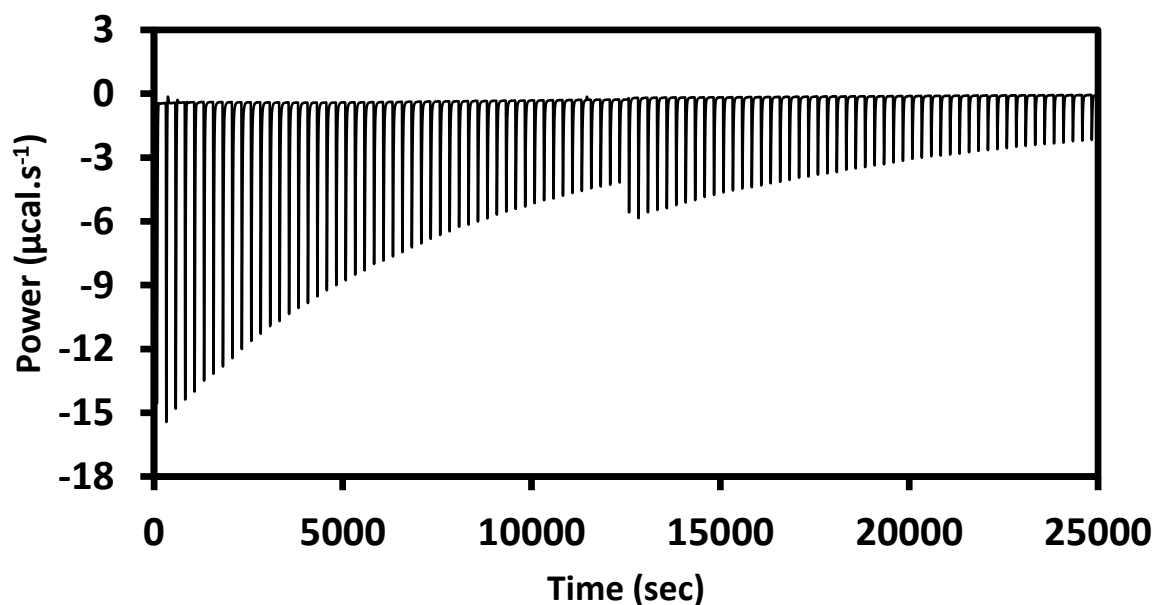


Figure 6.13 Prolonged titration of 31 µM mKlp2C-Ter with 40 mM ZnCl₂. Raw thermogram of ITC measurements. Two rounds of 50 injections (5 µL each) of 40 mM ZnCl₂ in 50 mM Tris-HCl (pH 7.5), 0.1 mM TCEP, 100 mM NaCl, 3 % (v/v) glycerol,) were performed and merged using EXCEL®.

Noticeably, the titration procedure led to a discrepancy between the first injection profile and the additional injections. One of the main issues encountered was the recalibration of the instrument, which had to be overcome by exporting the data to EXCEL®, removing the first injection of the second round and adjust the signal to the last point of the first round. Nevertheless, the corrected profile lacked smoothness and another hypothesis had to be formulated.

Looking at the original signal (Figure 6.13), the variation observed between first and second round of injection could stem from a readjustment of the baseline during the beginning of the second round (hypothesis explored so far). However, this variation could also be accounted by dissociation events happening between the end of the last injection of the first round and the beginning of the first injection of the second round. In this scenario, the data could be adjusted following the hypothesis that the second point (second injection since the first one is always considered an outlier) of the second round should coincide with one of the previous points in the first round. Once the correct point is identified, data are truncated to include only those after the dissociation event. The resulting profile is shown in Figure 6.14.

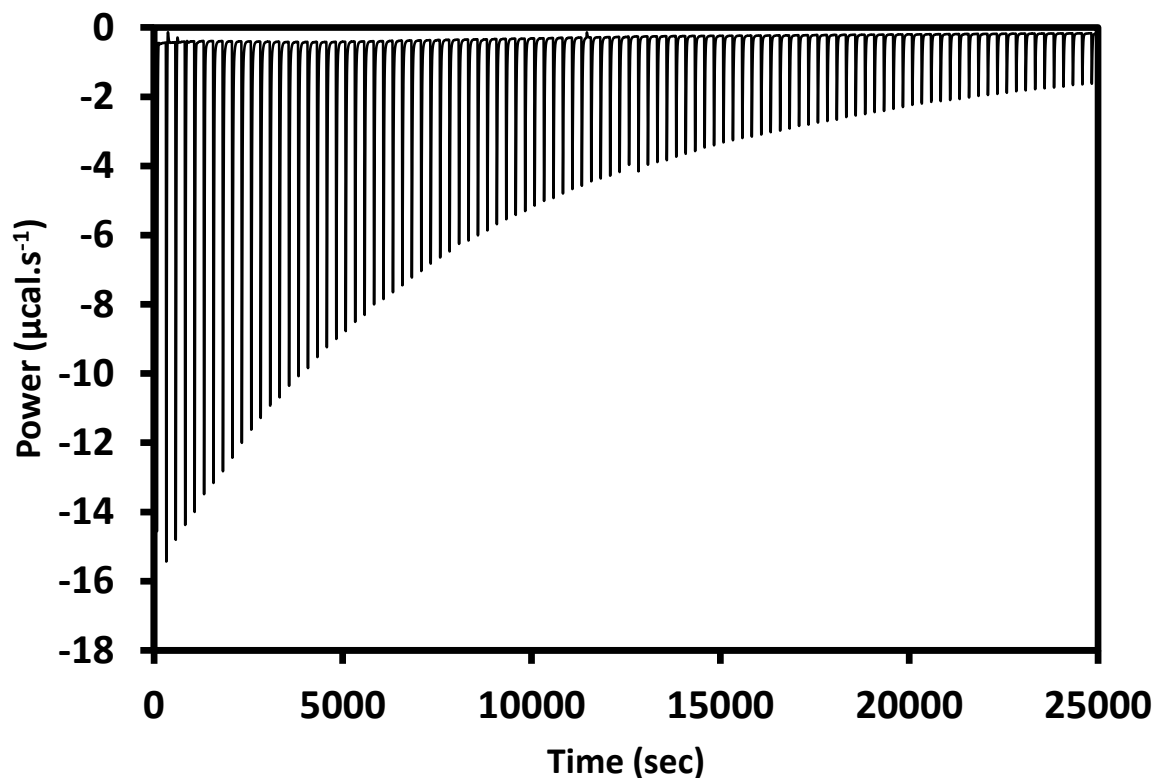


Figure 6.14 Corrected prolonged titration of 31 µM mKlp2C-Ter with 40 mM ZnCl₂. Raw thermogram of ITC measurements. Two rounds of 50 injections (5 µL each) of 40 mM ZnCl₂ in 50 mM Tris-HCl (pH 7.5), 0.1 mM TCEP, 100 mM NaCl, 3 % (v/v) glycerol,) were performed merged and re-adjusted using EXCEL® depending on a dissociation hypothesis.

A greater smoothness of the data was obtained using the newest methodology. This indicates the dissociation of zinc ions from mKlp2C-Ter is likely to be the cause of the variation between first and second rounds of injection. Although this new graph is probably more representative of the actual binding events occurring between mKlp2C-Ter and zinc ions, the data cannot be used. Indeed, since data are adjusted to a previous point from the first round of injection, a decent number of injections from the second round (first 5 to 8) were discarded. Hence, the final molar ratio was affected and was not accurate.

Different conditions had to be screened to further optimize the experiment. Therefore, various concentrations of ZnCl_2 and mKlp2C-Ter protein were tested in subsequent experiments. Surprisingly, the dilution of the protein by a factor of 5 in ITC buffer improved greatly the quality of the data compared to the concentration of zinc. Conversely, the concentration of titrant (zinc ions) was slightly increased to 50 mM. Results of the titration are compiled in Figure 6.15.

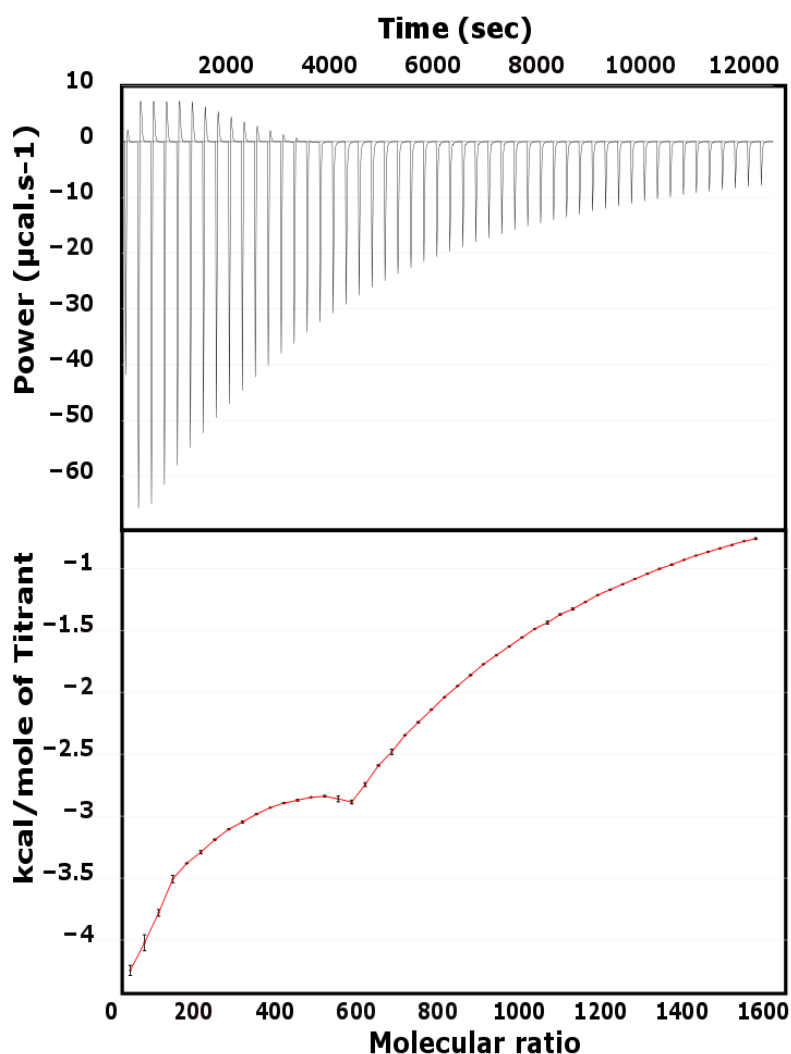


Figure 6.15 Single titration of 6 μM mKlp2C-Ter with 50 mM ZnCl_2 . **(Top)** Thermogram of ITC measurements. **(Bottom)** Peak-by peak integrated thermogram (with their error bars) with its mathematical fit, in red. One round of 50 injections (5 μL each) of 50 mM ZnCl_2 in 50 mM Tris-HCl (pH 7.5), 0.1 mM TCEP, 100 mM NaCl, 3 % (v/v) glycerol, was performed and analysed using AFFINImeter®.

The dilution of the protein offered more binding opportunities for the zinc onto mKlp2C-Ter, as the total number of injections covering the first binding event increased above 15. This was reflected in the accuracy of the parameters as the errors decreased significantly for all of them (Table 6.2). Both reactions were exothermic with variations of enthalpy (ΔH) of -1.913 and -2.899). Noticeably, the first binding event affinity is twice higher for zinc ions compared to the second, confirming the observations made on the raw data. Nevertheless, despite relatively good accuracy in most of the constants, the profile was still limiting for a precise calculation of the stoichiometry parameter. The lack of smoothness and high upturn at the start of the titration could be greatly improved to include the first inflexion point of the titration curve and further characterize this binding site.

Table 6.2 Binding parameters of zinc (40 mM) to mKlp2C-Ter (6 μ M).

Parameter	First binding event		Second binding event	
	Value	Error	Value	Error
ΔH (kcal/mol)	-1.913	0.0356	-2.899	0.0054
K_A (mM ⁻¹)	3.482	0.0098	1.540	0.0056
K_D (mM)	0.2872	0.0081	0.649	0.0023

Values were calculated by AFFINIMETER® using a combined model of unique and sequential binding event. Errors are given and can be used to assess the statistical relevance of the data. An order of magnitude above 2 is preferable.

Finally, despite dilution of the protein and the increase in concentration of its ligand, the saturation point was still not reached, thus the stoichiometry for the second set of sites was still inaccurate. A second round of injection was attempted, but the protein started aggregating dramatically. This was likely due to its lack of stability in the presence of zinc, highlighted during the stability study of mKlp2C-Ter after two days in 10 mM zinc (see section 6.5.2). Higher concentration of zinc was explored but did not fit within the instrument measurement capabilities.

Additional series of experiments were performed to reach the saturation point earlier. This was limited by the minimum and maximum signal the instrument can measure. Indeed, the signal recorded needs to be high enough to be distinguished from the noise, and low enough to be recorded. For the latter, the Malvern MicroCal VP-ITC has total coverage of 40 $\mu\text{Cal/s}$, which can be used to its fullest by adjusting the reference baseline. Besides, a limitation in the injection volume (no more than 5 microliters) is another parameter that must be taken into consideration. In the end, the experiment was stopped until further optimization of the protein stability could be achieved.

6.8. Structural characterization of mKlp2C-Ter by Small Angle X-ray Scattering (SAXS)

6.8.1. Data collection for mKlp2C-Ter

SAXS data were collected for mKlp2C-Ter at the Beamline B21 at three different concentrations. Sample (4 mg/mL) was diluted in a 96-well plate three times, each time by a factor of 2. The resulting samples (4, 2 and 1 mg/mL) were all subjected to SAXS for 2 seconds, and triplicated. Series of triplicates were then averaged to produce a final scattering profile for each of the different concentrations (Figure 6.16A). The buffer blank (25 mM Tris-HCl (pH 7.0), 100 mM NaCl, 3 % (w/v) Glycerol) was subjected to SAXS and its scattering profile (Figure 6.16A blue line) was removed from the samples data sets (Figure 6.16B). As for most previous proteins (section 5.5, 5.6 and 5.7), a high upturn of the scattering intensity at low q values could be observed for each mKlp2C-Ter sample. Consequently, sample dilution did not reduce this effect. This indicates a degree of polydispersity in the samples, generally associated with potential aggregation or oligomerization.

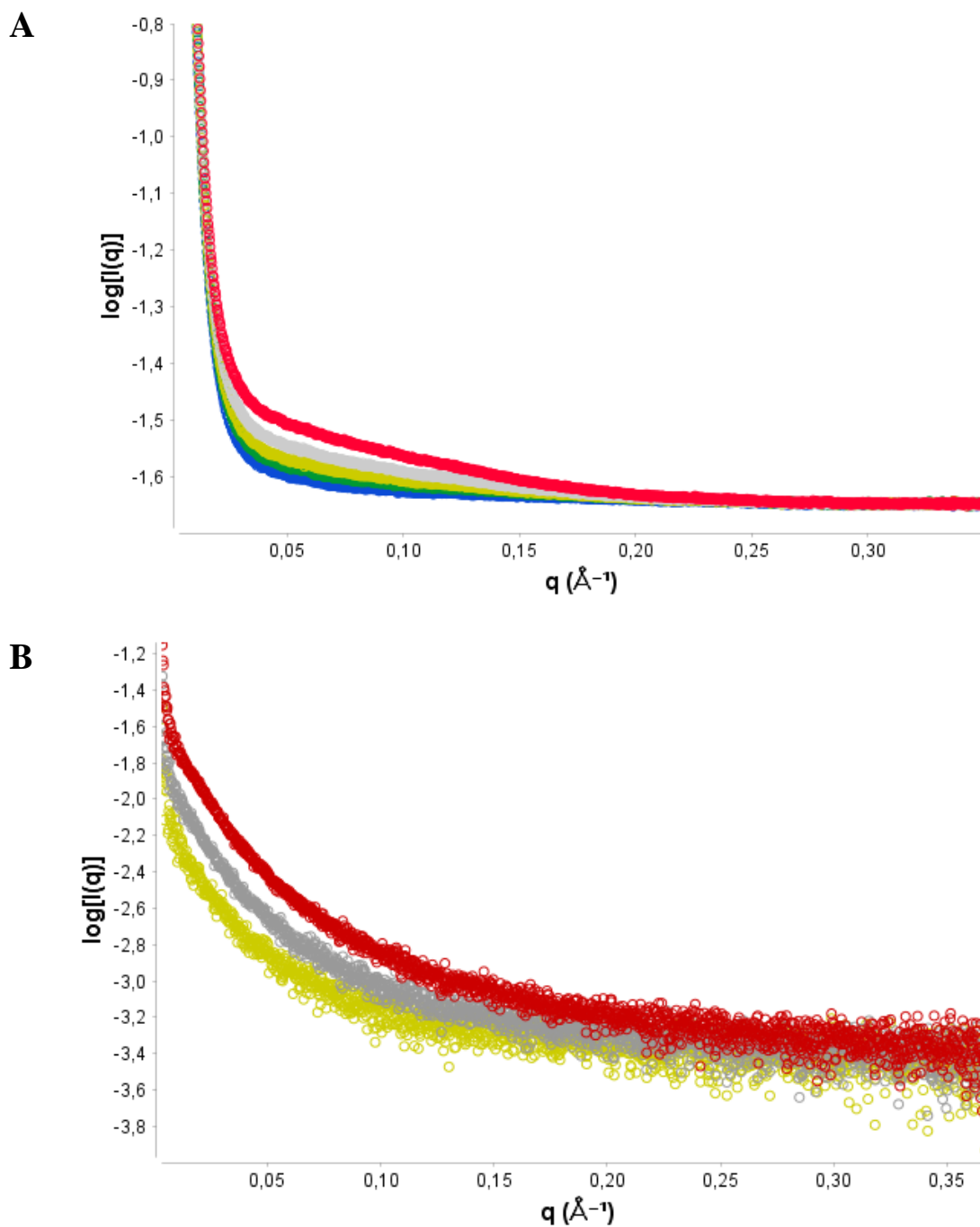


Figure 6.16 Raw Scattering Intensity plots of mKlp2C-Ter at 4, 2 and 1 mg/mL. Scattering data recorded at the Beamline B21 and displayed as log of intensity over the scattering vector q (\AA) and created using ScAtter Software® (Förster, Apostol et al. 2010). Samples were dialyzed for 1 hour in 25 mM Tris-HCl (pH 7.0), 100 mM NaCl, 3 % (w/v) Glycerol. **(A)** Raw Scattering data of mKlp2C-Ter. The buffer blank (as above) is represented by blue line. The scattering intensity curves for the mKlp2C-Ter sample at 4, 2 and 1 mg/mL are represented by a red, grey and yellow line respectively. **(B)** Subtracted scattering data for mKlp2C-Ter samples (colours are as above).

6.8.2. Calculation of the radius of gyration for mKlp2C-Ter

Data analysis for mKlp2C-Ter at 2, 1, 0.5 and 0.25 mg/mL was carried out as previously described (sections 5.4 to 5.7). The R_g was calculated using the Guinier approximation (Figure 6.17) and GNOM for all concentrations. Results are reported in Table 6.3.

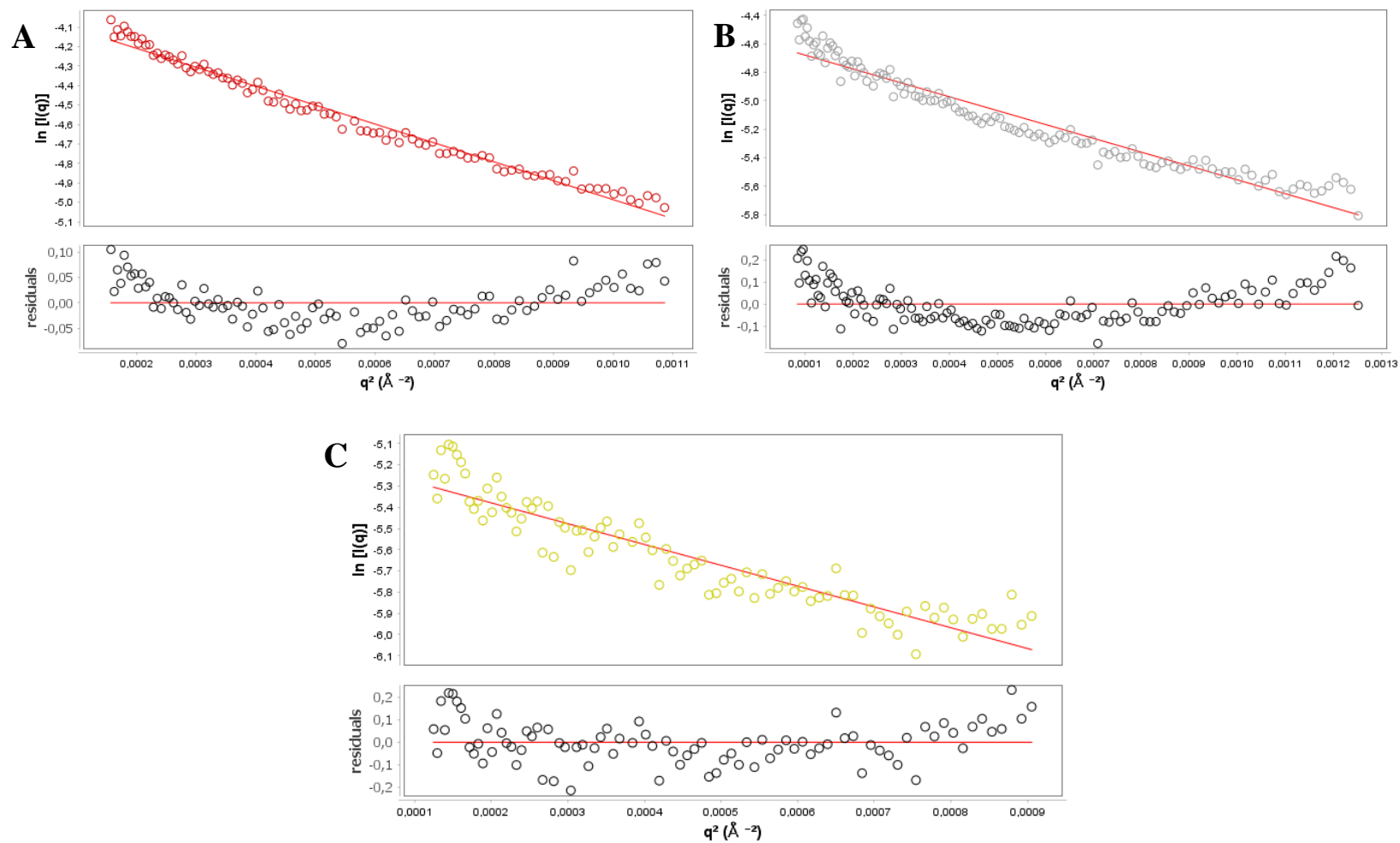


Figure 6.17 Guinier analysis of mKlp2C-Ter at 4, 2 and 1 mg/mL. First data points of the recorded scattering data displayed as log of intensity over the scattering vector q (\AA) and created using ScAtter Software® (Förster, Apostol et al. 2010). The first 200 points were used to fit a linear curve (red) that would be used to calculate the hypothetical R_g . Guinier plots of mKlp2C-Ter at 4 mg/mL (A), 2 mg/mL (B) and 1 mg/mL (C) are represented by red, grey and yellow dots respectively. Residual analysis of the scattering data (black dots) from the tendency curve (red) is indicated at the bottom for each concentration.

Table 6.3 Summary Table of Rg values for mKlp2C-Ter.

Sample	Rg (Reciprocal Space)	Rg (Real space)
mKlp2C-Ter at 4 mg/mL	53.94	53.18
mKlp2C-Ter at 2 mg/mL	53.68	53.55
mKlp2C-Ter at 1 mg/mL	53.89	53.22

Parameters Rg calculated by Scatter Software ® using approximation (reciprocal space) and GNOM (Real Space).

Reciprocal Space and real Rg values were relatively constant across the different samples. Moreover, reciprocal space Rg values were highly similar to their real (actual) value calculated by GNOM using Scatter® software (overall less than 0.5 units difference).

6.8.3. Kratky and Porod analysis of mKlp2C-Ter at at 4, 2 and 1 mg/mL

Initial assessment of the data quality was performed on mKlp2C-Ter at at 4, 2 and 1 mg/mL (Figure 6.18). Kratky plots for mKlp2C-Ter showed a low degree of folding, particularly for the two dilutions (2 and 1 mg/mL, Figure 6.18 A, grey and yellow lines). In addition, Porod plots suggested a high degree of flexibility for all mKlp2C-Ter samples. As a result, only the first concentration of mKlp2C-Ter (4 mg/mL) was used for further *ab initio* modelling. The other two dilutions (0.5 and 0.25 mg/mL) did not produce final models of good quality to guarantee statistically relevant molecular envelopes, as their concentrations were too low, and their quality analysis suggested a dramatic loss in compaction upon dilution.

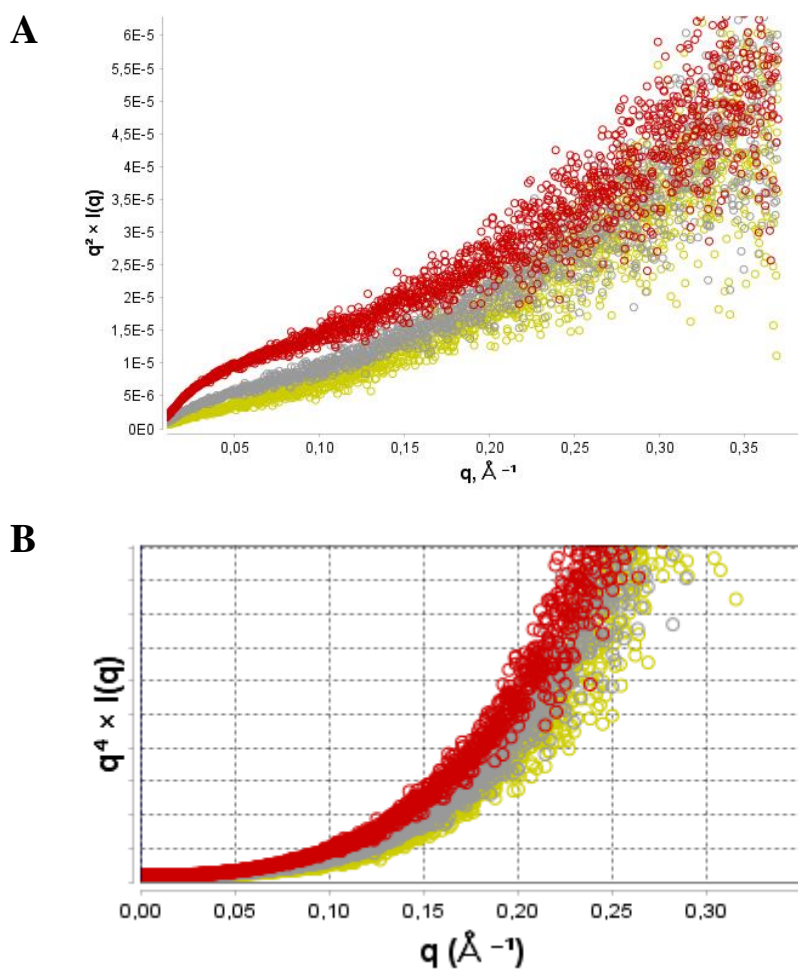


Figure 6.18 Quality assessment of mKlp2C-Ter. (A) Kratky plot of mKlp2C-Ter at 4, 2 and 1 mg/mL are represented by a red, grey and yellow line respectively. (B) Corresponding Porod plots for mKlp2C-Ter samples. Colours are as above.

6.8.4. Evaluation of the $P(r)$ distribution for mKlp2C-Ter scattering curve at 4 mg/mL

Following the initial analysis of the scattering data from mKlp2C-Ter at various concentrations (section 6.8.2 and 6.8.3), GNOM was used as an indirect transform program for the establishment of the $P(r)$ function for further *ab initio* modelling (Figure 6.19) and only the sample of highest concentration (4 mg/mL) was processed. The $P(r)$ distribution function for this sample revealed a multi-domain type of curve, with four potential sub-units.

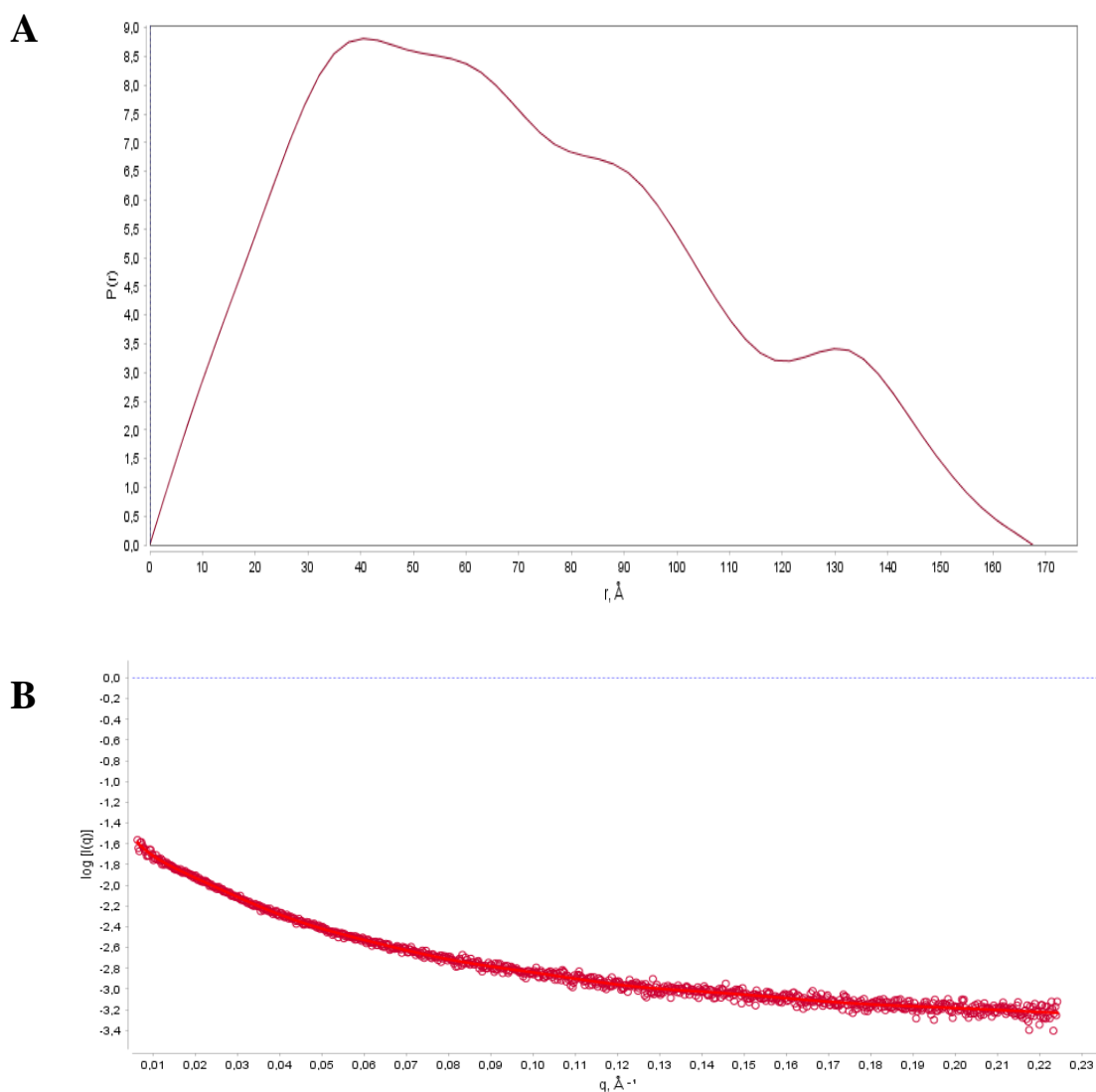


Figure 6.19 P(r) distribution plot of mKlp2C-Ter scattering data at 4 mg/mL. (A) P(r) distribution function of the mKlp2C-Ter at 4 mg/mL (red) in 25 mM Tris-HCl (pH 7.0), 100 mM NaCl, 3 % (w/v) Glycerol. (B) Scattering intensity of mKlp2C-Ter with the tendency curve representing the P(r) distribution indicated in red.

6.8.5. Generation and refinement of molecular envelopes for mKlp2C-Ter at 4 mg/mL

Assessment of the generated envelopes (Table 6.4) for mKlp2C-Ter was carried out by DAMSEL and DAMSUP as previously described for the previous proteins (sections 5.4.5, 5.5.5, 5.6.5 and 5.7.5). On one hand, envelope 1 was identified as having the best NSD value (0.634) and was used as a reference for DAMSUP superposition. On the other hand, no model was considered an outlier and discarded since their associated NSD values were all within two standard deviation units (one standard deviation = 0.033) from the mean NSD value (0.681).

Table 6.4 Summary of DAMSEL and DAMSUP results for mKlp2C-Ter at 4 mg/mL.

Model	DAMSEL NSD	FATE	DAMSUP NSD
mKlp2C-Ter at 4 mg/mL			
7	0.634	Reference	0.000
9	0.635	Include	0.554
17	0.636	Include	0.603
13	0.640	Include	0.550
21	0.642	Include	0.531
12	0.650	Include	0.596
16	0.656	Include	0.624
3	0.665	Include	0.622
18	0.668	Include	0.567
14	0.669	Include	0.622
5	0.677	Include	0.576
2	0.680	Include	0.601
1	0.684	Include	0.658
4	0.690	Include	0.606
23	0.695	Include	0.721
11	0.699	Include	0.592
22	0.701	Include	0.615
15	0.702	Include	0.679
19	0.717	Include	0.703
20	0.723	Include	0.735
8	0.726	Include	0.722
10	0.735	Include	0.734
6	0.740	Include	0.532

The mean NSD value was calculated to be 0.681 with a standard deviation of 0.033. Models are sorted from the lowest to the highest NSD value, and all are within two standard deviations from the mean NSD. As a consequence, no outlier was identified using this criterion. Model 1 showed the best NSD at 0.634 and was taken as the reference for the superposition with DAMSUP. DAMSUP superposed the models and calculated a deviation from the reference NSD.

Following all twenty-three models' refinement by DAMAVER, the averaged probability map was created, then filtered by DAMFILT removing regions of low occupancy, leading to the generation of a final molecular envelope for mKlp2C-Ter at 4 mg/mL (Figure 6.20).

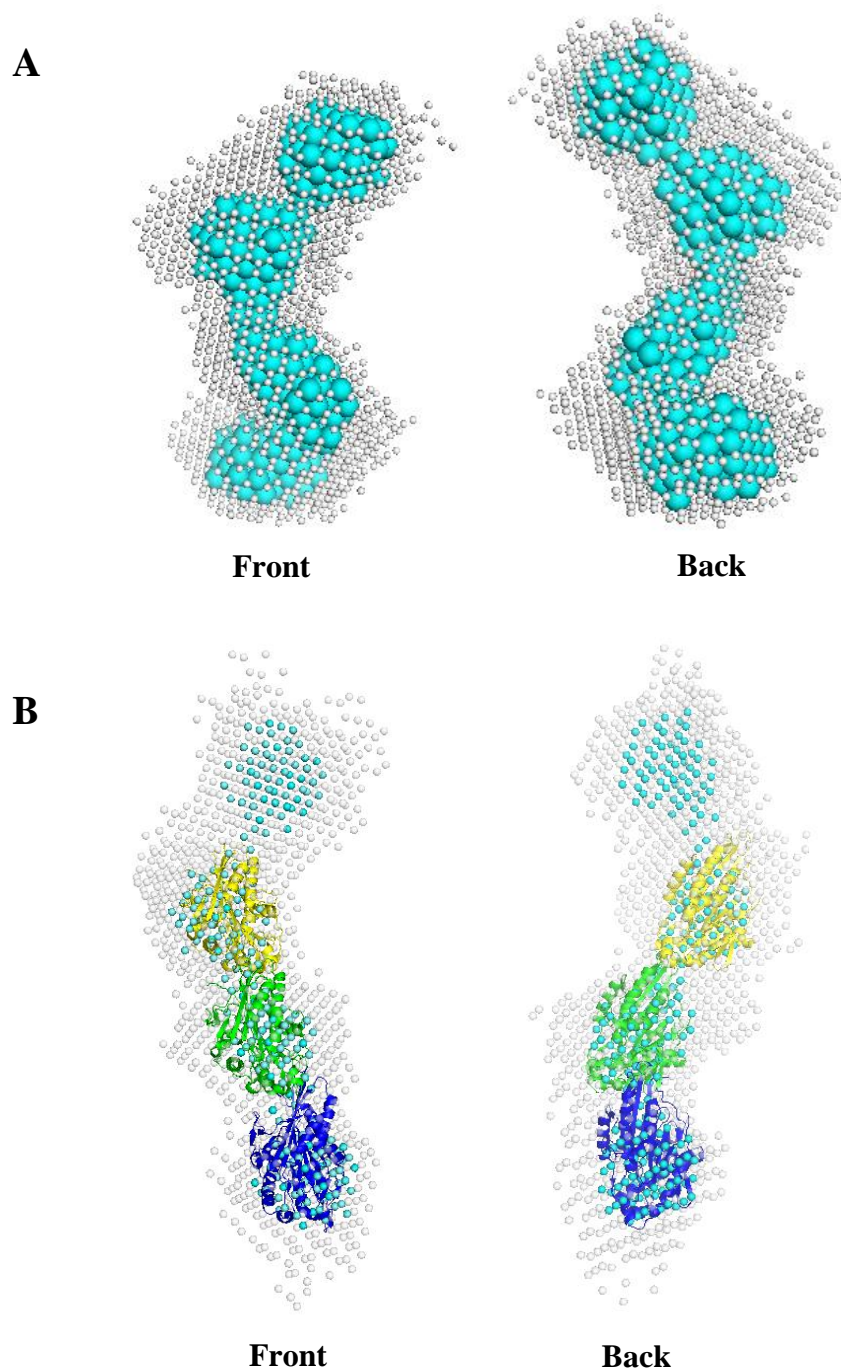


Figure 6.20 Final molecular envelopes for mKlp2C-Ter at 4 mg/mL. (A) Probability map (grey) and filtered (blue) molecular envelope generated by DAMAVER on mKlp2C-Ter at 4 mg/mL in 25 mM Tris-HCl (pH 7.0), 100 mM NaCl, 3 % (w/v) Glycerol. (B) Superposition of the crystal structure of Kinesin-1 heavy chain from human (4HNA) was added (in dark blue, green and yellow) and retrieved from the Protein Data Bank (Gigant, Wang et al. 2013).

6.9. Discussion

6.9.1. Heterologous production of mKlp2C-Ter in *E.coli* and purification by affinity chromatography

The successful cloning of mKlp2 gene into the pET-20b(+) was performed by Muktar Farah at the University of Huddersfield under the supervision of Dr Georgios Psakis. The expression of mKlp2C-Ter protein in BL21(DE3) *E. coli* cells using 1 mM IPTG proved very successful in yielding great amount of protein (up to 80 mg per 100 mg of cell lysate) that would be subsequently purified using a Protino HisTrap NiNta solid support from Merck®.

The protein eluted as a single peak using a single step gradient of 500 mM imidazole (25 mM Tris-HCl (pH 7.0), 100 mM NaCl, 3 % (w/v) Glycerol, 500 mM Imidazole), and its purity was estimated to be above 99 % on denaturing 10 % (v/v) SDS PAGE in 1x Laemmli buffer (section 6.3, Figure 6.3). This is mainly due to the presence of the 6xHis-Tag on the N-terminal extension of the mKlp2C-Ter protein.

The assessment of the monodispersity by Size exclusion chromatography using the Superose6 Increase® revealed a single peak with a maximal absorbance recorded at 15 mL (section 6.4, Figure 6.5), corresponding to an approximate size of 120 kDa, which was around 3 times the expected calculated size of mKlp2C-Ter (42 kDa from ExPasy webserver (Artimo, Jonnalagedda et al. 2012)). This suggested the protein could form aggregates or oligomers and would rarely exist as a monomer.

Interestingly, the dilution of the protein sample by a factor of 2 in SEC buffer 25 mM Tris-HCl (pH 7.0), 100 mM NaCl, 3 % (w/v) Glycerol) resulted in a shift of the profile, with a new maximum for the first peak culminating at 17 mL after injection (section 6.4, Figure 6.6). This elution volume corresponded to an approximate size of 40-45 kDa, in agreement with the expected size of the mKlp2C-Ter protein. This result highlighted a possible concentration dependence of the aggregate/oligomer formation. This hypothesis was reinforced by the high aggregation patterns exhibited when concentrating the protein above 10 mg/mL. The presence of glycerol in the buffer (10 % v/v) did not minimize the aggregation propensity of the molecule, thus further stabilizing agents must be screened to control the aggregation propensity of mKlp2C-Ter more effectively.

The relative dynamicity of the molecule and its response to the dilution likely arises from its native structure. Indeed, kinesins are usually composed of random coils and alpha helix (see chapter 1). In the case of mKlp2C-Ter, the truncated protein lacks most of the N-terminal sequence and only contains the last 345 amino acids of the native protein. Although the remaining domain is supposed to include a potential zinc finger motif, the rest of the protein is largely composed of helix, according to Jpred (Drozdetskiy, Cole et al. 2015) secondary structure predictions (see Appendix 9.6 for the simplified model). For this reason, homology modelling on mKlp2C-Ter was very difficult and often resulted in significant portion of sequence missing.

Finally, the concentrations, amounts and purity of the protein after its purification by affinity chromatography were all deemed suitable for downstream applications such as SAXS or Isothermal Titration Calorimetry.

6.9.2. Removal of the 6xHis-Tag from mKlp2C-Ter

The removal of the 6xHis-Tag From mKlp2C-Ter was needed to assess the effect of the tag on the structure and function of the truncated protein. For example, early ITC data (Section 6.7.2) suggested the presence of at least two binding sites for zinc ions on mKlp2C-Ter. The removal of the tag would then allow distinguish if one of the binding event is due to the interaction between zinc ions and histidines (Kluska, Adamczyk et al. 2018).

The screen for the identification of the best thrombin digestion conditions helped greatly in identifying optimal parameters for the complete removal of the purification tag (containing the 6xHis-Tag see figure 6.1). Optimal conditions were chosen based on the ability to control the over digestion of mKlp2C-Ter. Hence, a 2-hour incubation with 0.005 units/mg of protein were used for large scale experiments.

Large scale experiments proved highly successful in removing the tag as almost no undigested mKlp2C-Ter could be identified on 10 % (v/v) SDS PAGE. The mixture was then applied to the NiNta solid support to ensure the removal of the free 6xHis-Tag as well as the traces of undigested mKlp2C-Ter.

Finally, the removal of the thrombin from the protein mixture is the last stage in producing His-Tag-less mKlp2C-Ter. The use of a specific IEX solid support, HiTrap Benzamidine FF (Sepharose High Sub) was recommended, as Sepharose resin can efficiently remove proteases from a protein preparation (Rajalingam, Kathir et al. 2008). Unfortunately, both mKlp2C-Ter and the thrombin would bind the resin and could not be separated using a salt gradient (results not shown). Further improvements are required to optimize the removal of the thrombin from the digested mixture.

Noticeably, on occasion the addition of thrombin to the mixture often reduced the opaqueness of concentrated mKlp2C-Ter solutions, strongly suggesting the Tag might enhance the aggregation propensity of mKlp2C-Ter. The removal of the Tag along with stabilizing agents could greatly help in decreasing the instability of the kinesin-like protein.

6.9.3. SAXS experiments on mKlp2C-Ter protein

The protein mKlp2C-Ter proved very difficult to handle and showed high levels of aggregation in all of the profiles obtained from SAXS experiments. The presence of glycerol in the buffer did not seem to help stabilizing the protein to a great extent and only the highest concentration yielded decent scattering data that could be processed. The high flexibility and lack of completely folded structure lead to an elongated envelope with multiple domains (section 6.8.5, Figure 6.20). These four domains had an apparent shape of a chain, with repetitive motifs. Kinesins have the ability to form oligomers (Lawrence, Dawe et al. 2004, Li, Xu et al. 2012, Gigant, Wang et al. 2013) and the apparent aggregation observed at low q values might be the probable cause for this atypical shape (Petoukhov and Svergun 2013, Kikhney and Svergun 2015). Further experiments were undertaken at the Beamline with the buffer used for the elution of mKlp2-Cter protein but did not improve the scattering profile. The apparent instability of this protein has to be overcome before robust data can be collected in future SAXS studies.

As mentioned in 7.6.1 and 7.6.2, the aggregation prone-behaviour of the protein and its profile on SEC suggested the protein would mostly be oligomerized (or soluble aggregates) in solution. Although dilution was shown to modulate the equilibrium between oligomer and monomer, the diluted samples neither produce statistically relevant molecular envelopes nor displayed compaction.

In fact, mKlp2C-Ter is mainly composed of alpha helix and extended regions (see appendix 9.6), as well as zinc finger motif, containing 9 cysteine residues (Figure 6.1). The aggregation propensity of mKlp2C-Ter might be explained by a combination of these two factors. Indeed, Alpha helix are known to be able to promote aggregation (Ding, LaRocque et al. 2005, Kunjithapatham, Oliva et al. 2005, Ghosh, Singh et al. 2015) and cysteines can form disulphide bonds between each other. The addition of a reducing agent in the SEC buffer might help in enhancing the release of monomer from the oligomeric form.

The apparent dynamicity of kinesins is due to their role as cargo transporter in the cell and is the main cause for the lack of full crystal structures. For instance, the motor domain of kinesins has been mostly probed using crystallography experiments (Wang, Cao et al. 2015). In the case of the mKlp2C-Ter, the native mKlp2 protein was largely truncated, thus no motor domain is present in the protein. Therefore,

the design of hypothetical three-dimensional structure proved very difficult, often leading to largely truncated models. In an effort to illustrate the secondary structure predictions, hypothetical structures from segments of mKlp2C-Ter were created by homology modelling using SWISS MODELLER (Waterhouse, Rempfer et al. 2018) and reunited manually in Pymol (L DeLano 2002) (Figure 7.4).

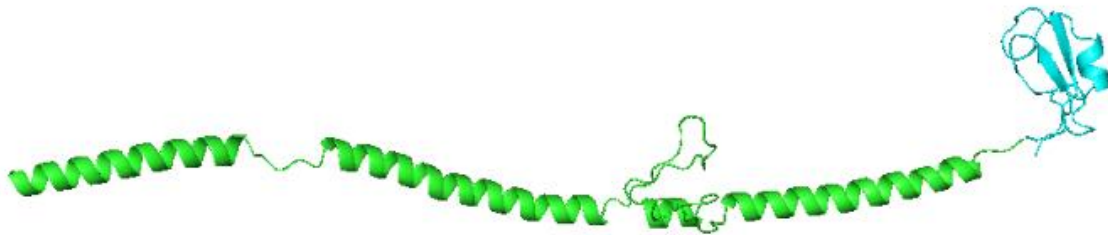


Figure 6.21 Hypothetical structure of mKlp2C-Ter by segmented homology modelling. A hypothetical structure of mKlp2C-Ter was created by homology modelling using SWISS MODELLER (Waterhouse, Rempfer et al. 2018), C-Terminal domain is thought to form a long alpha helix (in green), with a relatively well-defined tail domain (in blue), which include the hypothetical zinc finger motif.

As expected from the secondary structure predictions on mKlp2C-Ter, the reunited segments formed a long alpha helical segment (Figure 7.4, blue) with tail domain (containing the ring finger) composed of β -sheets, alpha helix and extended segments.

Even though this approach cannot generate a “valid” homology model, it offers an illustration of the three-dimensional structure of mKlp2C-Ter. In future studies, the use of RosettaCM (Song, DiMaio et al. 2013) could prove powerful to build a more accurate model using the different segments.

6.9.4. Titration of mKlp2C-Ter with zinc ions (ITC)

In summary, the mKlp2C-Ter protein displayed two separate binding events when titrated with zinc ions (section 6.7.2, Figure 6.15). Both reactions were exothermic ($\Delta H < 0$) at room temperature in 50 mM Tris-HCl (pH 7.5), 0.1 mM TCEP, 100 mM NaCl, 3 % (v/v) glycerol.

The first binding event (Figure 6.15) can be defined as a unique site displaying an affinity constant K_A for zinc ions of 3.482 mM^{-1} , relatively lower (one order of magnitude at best) than other proteins reported in previous publications, it is far weaker than some study reported (3 orders of magnitude) on zinc binding to zinc finger motifs (Lorick, Jensen et al. 1999, Kluska, Adamczyk et al. 2018).

The second binding event (with an affinity constant K_A equal to 1.540 mM^{-1}) is defined as sequential, implying more than one site involved. Although similar sequential binding mechanism has been identified for the binding of zinc by metalloregulator BsZur (Ma, Gabriel et al. 2011), the affinity parameters such as the K_A are still far from previous findings (3 orders of magnitude on average).

Since the binding of zinc to Histidine is possible (Kluska, Adamczyk et al. 2018), it is likely that the His-Tag used for the purification might interfere in the assay. The multitude of Histidine (6 repeats, see chapter 6 for the deduced amino acid sequence of mKlp2C-Ter N-Terminal tail) amino acids might as well explain the sequential type of scenario. As there is likely no preference for the binding of zinc to each histidine in the tag, the resulting binding kinetic should reflect this scenario. In conclusion, the removal of the 6xHis-tag would greatly help in confirming the identity of each binding site by potentially suppressing one of the two binding events.

Even though this experiment could not yet fully unveil the mechanism of zinc binding to mKlp2C-Ter, their interaction has been confirmed with this assay. The presence of at least two clear binding events indicate the zinc finger is likely capable of binding zinc ions. Considering other kinesins have demonstrated an ability to recruit ubiquitin ligase (Sako-Kubota, Tanaka et al. 2014), whereas zinc finger are known interactor of ubiquitin ligase, it is possible these feature was conserved in mKlp2. In parallel, the ability of mKlp2 to bind the mitochondria (Itoh, Fujiwara et al. 2001) might confer the kinesin a regulatory role in the degradation of the organelle. Finally, the established interaction between

VDAC3 and mKlp1 (Itoh, Fujiwara et al. 2001), the second kinesin-like isoform from *A.thaliana*, indicate the kinesin regulation of mitochondrial fate could be achieved through its interaction with the VDAC channel in plant.

Primarily, further optimization is needed to fully characterize the binding of zinc ions to mKlp2C-Ter. Different concentrations of protein in combination with various concentrations of zinc must be screened to determine the best parameters and clearly define the binding at low Zn²⁺ concentrations. Indeed, the lack of a clear sigmoidal curve suggests that the early binding of low Zn²⁺ ions to the protein, is perhaps masked by the presence of low traces of divalent ions in solution, leading to a rapid saturation of the first mKlp2C-Ter binding site. Although lower concentrations of zinc were tested (from 5 to 50 mM) they did not improve the quality of the generated titration curve. Instead, the dilution of the protein by a factor of five proved to be the main factor in generating a reasonable amount of data for the first binding site. Therefore, a two-dimensional screen must be performed, using different zinc concentration and various protein dilutions before attempting further ITC experiments. Finally, the beginning of the linear slope of the first binding event was very close to 0, indicating a possible low molar ratio. Considering, ring finger domains have the ability to bind one or two zinc ions (Kluska, Adamczyk et al. 2018), the expected molar ratio would likely be 1:1 or 2:1.

Another parameter that was not properly assessed in the ITC work, was the saturation point. Incidentally, the apparent dissociation of the protein from the zinc ions at the end of the run seems to prevent further rounds of injection to be performed. Although dissociation events can be mitigated by restarting the titration straight after the end of the first round, results still were affected and not representative of the actual stoichiometry. In the end, the ideal scenario would include reaching the saturation point during the first round of injection.

The second issue highlighted here is the propensity of the protein to aggregate, preventing additional rounds of injections. Further development is essential to find potential stabilizing agents for mKlp2C-Ter. Interestingly, the dilution of the protein seemed to greatly help in capturing good data for the first binding event. Observations during its production and purification led to the conclusion that high

concentrations (above 8 mg/mL) induced significant aggregation of the kinesin-like protein. Consequently, a small percentage of aggregates must coexist in equilibrium with the soluble protein, even at lower concentration. The great number of cysteines that can be found typically in a zinc finger motif could explain this propensity (Lorick, Jensen et al. 1999, Kluska, Adamczyk et al. 2018), since the reducing agent TCEP (tris(2-carboxyethylphosphine) is present in the ITC buffer. As the concentration of protein decreases during its dilution with the buffer, the ratio between TCEP and mKlp2C-Ter increases, thus enabling more cysteines to be reduced and exposed for the zinc ions to interact with.

The removal of the 6xHis-tag might contribute to enhance the overall stability of the protein. Experiments conducted during its purification revealed a clarification of the protein solution upon digestion of the tag by Thrombin (section 6.6), indicating an aggregation-prone effect of the 6xHis-tag for this protein.

7. Conclusion and Future directions

The main aim of this research was to primarily characterize the Voltage-dependent Anion channel AtVDAC1 from *Arabidopsis thaliana*. Being the most abundant protein in the mitochondrial outer membrane as well as playing a key role in the regulation and transport of metabolites and ions across the mitochondrial membrane (see Chapter 1), it was important to further understand the basic properties of such an indispensable protein. Its direct or indirect involvement in numerous cell processes such as the regulation of mitochondrial osmosis or the Krebs cycle, as well as its impact on plant resistance (Greenberg 1996), reinforced this need. Furthermore, this work helped to initiate the groundwork for future binding studies focusing on AtVDAC1 interaction with cytosolic partners.

First and foremost, a reproducible and consistent purification pipeline was successfully designed and tested on the native AtVDAC1 channel, generating suitable amount of pure protein for downstream applications such as SAXS, CD, and BLM.

The AtVDAC1 channel secondary structure content was then examined using CD and confirmed the successful refolding of the Native channel in 0.1 % (v/v) LDAO. The AtVDAC1 channel was mainly composed of beta sheet with a small helicity, in accordance with its secondary structure predictions, previously published VDAC crystal structures and CD studies on VDAC in detergent.

Furthermore, AtVDAC1 function as an ion channel was tested in BLM assays. The channel exhibited activity in 10 mM Tris-HCl (pH 7.4), 150 mM KCl, 50 mM CaCl₂, displaying an open state (S₀) conductance of 0.54 nS and at least two closed states, named S₁ and S₂, with respective conductance of 0.43 nS and 0.31 nS. These conductance values were in accordance with other VDACS at similar salt concentration.

Altogether, these data confirmed the successful purification and primary characterization of in vitro refolded AtVDAC1. The close proximity of the structural content and the conductance values to other VDACS confirmed the potential of AtVDACS as models for the study of VDAC properties in vitro.

Besides, the number of isoforms (4) and their apparent functional differences could broaden our understanding of the channel using the aforementioned assays on these isoforms.

In addition, a fast and relatively efficient mutagenesis method was successfully applied and allowed the generation of single point mutant of AtVDAC1. Three mutants, namely D177N, D258N and T156C were all purified using the approved methodology tested on the Native AtVDAC1, confirming the efficiency of the mutagenesis using the PCR-site directed mutagenesis and of the purification pipeline using the HiTrap SP XL ® and the Superose6 Increase®. This methodology will be re-used for the generation of additional AtVDAC mutants.

Following their purification, the Native and mutant AtVDAC1 proteins were all subjected to SAXS, revealing a compact and micelle-embedded structure for all proteins. Thus, this experiment successfully provided primary three-dimensional structural data on AtVDAC proteins in detergent solutions.

In parallel, a truncated version of the kinesin-like protein mKlp2, a potential AtVDAC partner, was also successfully purified, this time using an 6xHisTag and Ni-Nta affinity chromatography.

This protein, named mKlp2C-Ter, displayed an ability to bind zinc ions in ITC experiments, and a remarkable flexibility in SAXS. The SEC, ITC, and SAXS experiments all suggested this protein is in constant equilibrium between its monomeric and oligomeric form. The effect of dilution was also monitored, improving greatly the solubilization of the mKlp2C-Ter monomer.

These data indicate a potential function of mKlp2C-Ter in the ubiquitination pathway through its ring finger domain. Considering the restriction of the Native mKlp2 protein to the mitochondria, a hypothetical role as mitochondrial (or VDAC) regulator could be unveiled.

In conclusion, the objectives of this research were mostly achieved, and helped building knowledge and a consistent model for future studies on AtVDAC proteins and their interactions with multiple partners. Further work has already been undertaken, such as the cloning of the other AtVDAC isoform 2 and 4 (in progress) as well as additional cytosolic partners such as the *N. benthamiana* Hexokinase 1. Finally, various binding assays such as Far Western Blotting and Dot blotting are already in development and

will help greatly in defining the molecular interactions that drives the binding of AtVDAC to their cytosolic partners.

8. References

- Abu-Hamad, S., N. Arbel, D. Calo, L. Arzoine, A. Israelson, N. Keinan, R. Ben-Romano, O. Friedman and V. Shoshan-Barmatz (2009). "The VDAC1 N-terminus is essential both for apoptosis and the protective effect of anti-apoptotic proteins." Journal of Cell Science **122**(11): 1906.
- Abu-Hamad, S., S. Sivan and V. Shoshan-Barmatz (2006). "The expression level of the voltage-dependent anion channel controls life and death of the cell." Proceedings of the National Academy of Sciences **103**(15): 5787.
- Abu-Hamad, S., H. Zaid, A. Israelson, E. Nahon and V. Shoshan-Barmatz (2008). "Hexokinase-I Protection against Apoptotic Cell Death Is Mediated via Interaction with the Voltage-dependent Anion Channel-1: MAPPING THE SITE OF BINDING." Journal of Biological Chemistry **283**(19): 13482-13490.
- Aghazadeh, Y., M. B. Rone, J. Blonder, X. Ye, T. D. Veenstra, D. B. Hales, M. Culty and V. Papadopoulos (2012). "Hormone-induced 14-3-3 γ Adaptor Protein Regulates Steroidogenic Acute Regulatory Protein Activity and Steroid Biosynthesis in MA-10 Leydig Cells." Journal of Biological Chemistry **287**(19): 15380-15394.
- Ahmad, A., S. Ahmad, B. K. Schneider, C. B. Allen, L.-Y. Chang and C. W. White (2002). "Elevated expression of hexokinase II protects human lung epithelial-like A549 cells against oxidative injury." American Journal of Physiology-Lung Cellular and Molecular Physiology **283**(3): L573-L584.
- Akanda, N., R. Tofighi, J. Brask, C. Tamm, F. Elinder and S. Ceccatelli (2008). "Voltage-dependent anion channels (VDAC) in the plasma membrane play a critical role in apoptosis in differentiated hippocampal neurons but not in neural stem cells." Cell Cycle **7**(20): 3225-3234.
- Alibolandi, M. and H. Mirzahoseini (2011). "Chemical assistance in refolding of bacterial inclusion bodies." Biochemistry research international **2011**: 631607-631607.
- Altieri, D. C. (2010). "Survivin and IAP proteins in cell-death mechanisms." The Biochemical journal **430**(2): 199-205.
- Antonsson, B., S. Montessuit, S. Lauper, R. Eskes and J.-C. Martinou (2000). "Bax oligomerization is required for channel-forming activity in liposomes and to trigger cytochrome c release from mitochondria." Biochemical Journal **345**(2): 271.
- Antonsson, B., S. Montessuit, B. Sanchez and J.-C. Martinou (2001). "Bax Is Present as a High Molecular Weight Oligomer/Complex in the Mitochondrial Membrane of Apoptotic Cells." Journal of Biological Chemistry **276**(15): 11615-11623.
- Aram, L., S. Geula, N. Arbel and V. Shoshan-Barmatz (2010). "VDAC1 cysteine residues: topology and function in channel activity and apoptosis." Biochemical Journal **427**(3): 445.
- Artimo, P., M. Jonnalagedda, K. Arnold, D. Baratin, G. Csardi, E. de Castro, S. Duvaud, V. Flegel, A. Fortier, E. Gasteiger, A. Grosdidier, C. Hernandez, V. Ioannidis, D. Kuznetsov, R. Liechti, S. Moretti, K. Mostaguir, N. Redaschi, G. Rossier, I. Xenarios and H. Stockinger (2012). "ExPASy: SIB bioinformatics resource portal." Nucleic acids research **40**(Web Server issue): W597-W603.
- Arzoine, L., N. Zilberberg, R. Ben-Romano and V. Shoshan-Barmatz (2009). "Voltage-dependent Anion Channel 1-based Peptides Interact with Hexokinase to Prevent Its Anti-apoptotic Activity." Journal of Biological Chemistry **284**(6): 3946-3955.
- Asbury, C. L., A. N. Fehr and S. M. Block (2003). "Kinesin moves by an asymmetric hand-over-hand mechanism." Science (New York, N.Y.) **302**(5653): 2130-2134.
- Asenjo, A. B., N. Krohn and H. Sosa (2003). "Configuration of the two kinesin motor domains during ATP hydrolysis." Nature Structural Biology **10**: 836.
- Baggetto, L. G., E. Clottes and C. Vial (1992). "Low Mitochondrial Proton Leak Due to High Membrane Cholesterol Content and Cytosolic Creatine Kinase as Two Features of the Deviant Bioenergetics of Ehrlich and AS30-D Tumor Cells." Cancer Research **52**(18): 4935.
- Banerjee, J. and S. Ghosh (2004). "Bax increases the pore size of rat brain mitochondrial voltage-dependent anion channel in the presence of tBid." Biochemical and Biophysical Research Communications **323**(1): 310-314.

Bauer, A. J., S. Gieschler, K. M. Lemberg, A. E. McDermott and B. R. Stockwell (2011). "Functional model of metabolite gating by human voltage-dependent anion channel 2." Biochemistry **50**(17): 3408-3410.

Baumgartner, H. K., J. V. Gerasimenko, C. Thorne, P. Ferdek, T. Pozzan, A. V. Tepikin, O. H. Petersen, R. Sutton, A. J. M. Watson and O. V. Gerasimenko (2009). "Calcium Elevation in Mitochondria Is the Main Ca²⁺ Requirement for Mitochondrial Permeability Transition Pore (mPTP) Opening." Journal of Biological Chemistry **284**(31): 20796-20803.

Bayrhuber, M., T. Meins, M. Habeck, S. Becker, K. Giller, S. Villinger, C. Vonrhein, C. Griesinger, M. Zweckstetter and K. Zeth (2008). "Structure of the human voltage-dependent anion channel." Proceedings of the National Academy of Sciences **105**(40): 15370.

Benz, R., M. Kottke and D. Brdiczka (1990). "The cationically selective state of the mitochondrial outer membrane pore: a study with intact mitochondria and reconstituted mitochondrial porin." Biochimica et Biophysica Acta (BBA) - Biomembranes **1022**(3): 311-318.

Berrier, C., R. Peyronnet, J. M. Betton, G. Ephritikhine, H. Barbier-Brygoo, J. M. Frachisse and A. Ghazi (2015). "Channel characteristics of VDAC-3 from *Arabidopsis thaliana*." Biochemical and Biophysical Research Communications **459**(1): 24-28.

Betaneli, V., E. P. Petrov and P. Schwille (2012). "The role of lipids in VDAC oligomerization." Biophysical journal **102**(3): 523-531.

Blachly-Dyson, E. and M. Forte "VDAC channels." (1521-6543 (Print)).

Blachly-Dyson, E. and M. Forte (2001). "VDAC Channels." IUBMB Life **52**(3-5): 113-118.

Blachly-Dyson, E., S. Peng, M. Colombini and M. Forte (1990). "Selectivity changes in site-directed mutants of the VDAC ion channel: structural implications." Science **247**(4947): 1233.

Blachly-Dyson, E., J. Song, W. J. Wolfgang, M. Colombini and M. Forte (1997). "Multicopy suppressors of phenotypes resulting from the absence of yeast VDAC encode a VDAC-like protein." Molecular and cellular biology **17**(10): 5727-5738.

Bleicken, S., M. Classen, P. V. L. Padmavathi, T. Ishikawa, K. Zeth, H.-J. Steinhoff and E. Bordignon (2010). "Molecular Details of Bax Activation, Oligomerization, and Membrane Insertion." Journal of Biological Chemistry **285**(9): 6636-6647.

Blumenthal, A., K. Kahn, O. Beja, E. Galun, M. Colombini and A. Breiman (1993). "Purification and Characterization of the Voltage-Dependent Anion-Selective Channel Protein from Wheat Mitochondrial Membranes." Plant physiology **101**(2): 579-587.

Boffoli, D., S. C. Scacco, R. Vergari, G. Solarino, G. Santacrose and S. Papa (1994). "Decline with age of the respiratory chain activity in human skeletal muscle." Biochimica et Biophysica Acta (BBA) - Molecular Basis of Disease **1226**(1): 73-82.

Bondos, S. E. and A. Bicknell (2003). "Detection and prevention of protein aggregation before, during, and after purification." Analytical Biochemistry **316**(2): 223-231.

Bonora, M., S. Patergnani, A. Rimessi, E. De Marchi, J. M. Suski, A. Bononi, C. Giorgi, S. Marchi, S. Missiroli, F. Poletti, M. R. Wieckowski and P. Pinton (2012). "ATP synthesis and storage." Purinergic signalling **8**(3): 343-357.

Bortner, C. D., N. B. E. Oldenburg and J. A. Cidlowski (1995). "The role of DNA fragmentation in apoptosis." Trends in Cell Biology **5**(1): 21-26.

Brown, G. (2016). Characterisation and structural studies of a superoxide dismutase and OmpA-like proteins from *Borrelia burgdorferi sensu lato*. PhD award, University of Huddersfield.

Bryson, J. M., P. E. Coy, K. Gottlob, N. Hay and R. B. Robey (2002). "Increased Hexokinase Activity, of Either Ectopic or Endogenous Origin, Protects Renal Epithelial Cells against Acute Oxidant-induced Cell Death." Journal of Biological Chemistry **277**(13): 11392-11400.

Buettner, R., G. Papoutsoglou, E. Scemes, D. C. Spray and R. Dermietzel (2000). "Evidence for secretory pathway localization of a voltage-dependent anion channel isoform." Proceedings of the National Academy of Sciences **97**(7): 3201.

Bugger, H. and E. D. Abel (2010). "Mitochondria in the diabetic heart." Cardiovascular research **88**(2): 229-240.

Burdman, S., J. De Mot R Fau - Vanderleyden, Y. Vanderleyden J Fau - Okon, E. Okon Y Fau - Jurkevitch and E. Jurkevitch "Identification and characterization of the omaA gene encoding the major outer membrane protein of *Azospirillum brasilense*." (1042-5179 (Print)).

Buttke, T. M. and P. A. Sandstrom (1994). "Oxidative stress as a mediator of apoptosis." Immunology Today **15**(1): 7-10.

Báthori, G., G. Csordás, C. Garcia-Perez, E. Davies and G. Hajnóczky (2006). "Ca²⁺-dependent Control of the Permeability Properties of the Mitochondrial Outer Membrane and Voltage-dependent Anion-selective Channel (VDAC)." Journal of Biological Chemistry **281**(25): 17347-17358.

Böckmann, R. A., A. Hac, T. Heimburg and H. Grubmüller (2003). "Effect of sodium chloride on a lipid bilayer." Biophysical journal **85**(3): 1647-1655.

Campbell, A. M. and S. H. P. Chan (2008). "Mitochondrial membrane cholesterol, the voltage dependent anion channel (VDAC), and the Warburg effect." Journal of Bioenergetics and Biomembranes **40**(3): 193-197.

Carson, M., D. Johnson, H. McDonald, C. Brouillette and L. Delucas (2007). His-tag impact on structure.

Cascio, M. and B. A. Wallace (1995). "Effects of Local Environment on the Circular Dichroism Spectra of Polypeptides." Analytical Biochemistry **227**(1): 90-100.

Cervera, J., A. G. Komarov and V. M. Aguilera (2008). "Rectification properties and pH-dependent selectivity of meningococcal class 1 porin." Biophysical journal **94**(4): 1194-1202.

Checchetto, V., S. Reina, A. Magrì, I. Szabo and V. De Pinto (2014). "Recombinant Human Voltage Dependent Anion Selective Channel Isoform 3 (hVDAC3) Forms Pores with a Very Small Conductance." Cellular Physiology and Biochemistry **34**(3): 842-853.

Chen, Y. and B. A. Wallace (1997). "Secondary solvent effects on the circular dichroism spectra of polypeptides in non-aqueous environments: influence of polarisation effects on the far ultraviolet spectra of alamethicin." Biophysical Chemistry **65**(1): 65-74.

Cherry, J. M., E. L. Hong, C. Amundsen, R. Balakrishnan, G. Binkley, E. T. Chan, K. R. Christie, M. C. Costanzo, S. S. Dwight, S. R. Engel, D. G. Fisk, J. E. Hirschman, B. C. Hitz, K. Karra, C. J. Krieger, S. R. Miyasato, R. S. Nash, J. Park, M. S. Skrzypek, M. Simison, S. Weng and E. D. Wong (2012). "Saccharomyces Genome Database: the genomics resource of budding yeast." Nucleic acids research **40**(Database issue): D700-D705.

Cheung, H. O.-L., X. Zhang, A. Ribeiro, R. Mo, S. Makino, V. Puvindran, K. K. L. Law, J. Briscoe and C.-c. Hui (2009). "The Kinesin Protein Kif7 Is a Critical Regulator of Gli Transcription Factors in Mammalian Hedgehog Signaling." Science Signaling **2**(76): ra29.

Chinnery, P. F. and E. A. Schon (2003). "Mitochondria." Journal of neurology, neurosurgery, and psychiatry **74**(9): 1188-1199.

Claude, A. and E. F. Fullam (1945). "AN ELECTRON MICROSCOPE STUDY OF ISOLATED MITOCHONDRIA : METHOD AND PRELIMINARY RESULTS." The Journal of experimental medicine **81**(1): 51-62.

Colombini, M. (1989). "Voltage gating in the mitochondrial channel, VDAC." The Journal of Membrane Biology **111**(2): 103-111.

Colombini, M. (2004). "VDAC: The channel at the interface between mitochondria and the cytosol." Molecular and Cellular Biochemistry **256**(1): 107-115.

Colombini, M. (2016). "The VDAC channel: Molecular basis for selectivity." Biochimica et Biophysica Acta (BBA) - Molecular Cell Research **1863**(10): 2498-2502.

Colombini, M., E. Blachly-Dyson and M. Forte (1996). VDAC, a Channel in the Outer Mitochondrial Membrane. Ion Channels. T. Narahashi. Boston, MA, Springer US: 169-202.

Colombini, M. and C. A. Mannella (2012). "VDAC, The early days." Biochimica et Biophysica Acta (BBA) - Biomembranes **1818**(6): 1438-1443.

Comeau, S. R., D. W. Gatchell, S. Vajda and C. J. Camacho (2004). "ClusPro: a fully automated algorithm for protein-protein docking." Nucleic acids research **32**(Web Server issue): W96-W99.

Cory, S. and J. M. Adams (2002). "The Bcl2 family: regulators of the cellular life-or-death switch." Nature Reviews Cancer **2**: 647.

Cox, D. A. and M. A. Matlib (1993). "A role for the mitochondrial Na⁽⁺⁾-Ca²⁺ exchanger in the regulation of oxidative phosphorylation in isolated heart mitochondria." Journal of Biological Chemistry **268**(2): 938-947.

Crompton, M. (1999). "The mitochondrial permeability transition pore and its role in cell death." Biochemical Journal **341**(2): 233.

Cross, R. A. (2004). "The kinetic mechanism of kinesin." Trends in Biochemical Sciences **29**(6): 301-309.

D'Andrea, L. D. and L. Regan (2003). "TPR proteins: the versatile helix." Trends in Biochemical Sciences **28**(12): 655-662.

da-Silva, W. S., A. Gómez-Puyou, M. T. de Gómez-Puyou, R. Moreno-Sanchez, F. G. De Felice, L. de Meis, M. F. Oliveira and A. Galina (2004). "Mitochondrial Bound Hexokinase Activity as a Preventive Antioxidant Defense: STEADY-STATE ADP FORMATION AS A REGULATORY MECHANISM OF MEMBRANE POTENTIAL AND REACTIVE OXYGEN SPECIES GENERATION IN MITOCHONDRIA." Journal of Biological Chemistry **279**(38): 39846-39855.

De Bernardes Clark, E. (1998). Refolding of Recombinant Proteins.

De Grey, A. D. N. J. (2004). "Mitochondrial Mutations in Mammalian Aging: An Over-Hasty About-Turn?" Rejuvenation Research **7**(3): 171-174.

De Pinto, V., F. Guarino, A. Guarnera, A. Messina, S. Reina, F. M. Tomasello, V. Palermo and C. Mazzoni (2010). "Characterization of human VDAC isoforms: A peculiar function for VDAC3?" Biochimica et Biophysica Acta (BBA) - Bioenergetics **1797**(6): 1268-1275.

De Pinto, V., A. Messina, R. Accardi, R. Aiello, F. Guarino, F. Tomasello, M. Tommasino, G. Tasco, R. Casadio, R. Benz, F. De Giorgi, F. Ichas, M. Baker and A. Lawen (2003). New functions of an old protein: the eukaryotic porin or voltage dependent anion selective channel (VDAC).

De Pinto, V., A. Messina, D. J. R. Lane and A. Lawen (2010). "Voltage-dependent anion-selective channel (VDAC) in the plasma membrane." FEBS Letters **584**(9): 1793-1799.

De Pinto, V., S. Reina, F. Guarino and A. Messina (2008). "Structure of the voltage dependent anion channel: state of the art." Journal of Bioenergetics and Biomembranes **40**(3): 139.

Deniaud, A., L. Liguori, I. Blesneac, J. L. Lenormand and E. Pebay-Peyroula (2010). "Crystallization of the membrane protein hVDAC1 produced in cell-free system." Biochimica et Biophysica Acta (BBA) - Biomembranes **1798**(8): 1540-1546.

Dermietzel, R., T. K. Hwang, R. Buettner, A. Hofer, E. Dotzler, M. Kremer, R. Deutzmann, F. P. Thinnel, G. I. Fishman and D. C. Spray (1994). "Cloning and in situ localization of a brain-derived porin that constitutes a large-conductance anion channel in astrocytic plasma membranes." Proceedings of the National Academy of Sciences **91**(2): 499.

Ding, F., J. J. LaRocque and N. V. Dokholyan (2005). "Direct Observation of Protein Folding, Aggregation, and a Prion-like Conformational Conversion." Journal of Biological Chemistry **280**(48): 40235-40240.

Dolder, M., S. Wendt and T. Wallimann (2001). "Mitochondrial Creatine Kinase in Contact Sites: Interaction with Porin and Adenine Nucleotide Translocase, Role in Permeability Transition and Sensitivity to Oxidative Damage." Neurosignals **10**(1-2): 93-111.

Drozdetskiy, A., C. Cole, J. Procter and G. J. Barton (2015). "JPred4: a protein secondary structure prediction server." Nucleic acids research **43**(W1): W389-W394.

Duff, M. R., Jr., J. Grubbs and E. E. Howell (2011). "Isothermal titration calorimetry for measuring macromolecule-ligand affinity." Journal of visualized experiments : JoVE(55): 2796.

Dyer, A., G. Brown, L. Stejskal, P. R. Laity and R. J. Bingham (2015). "The *Borrelia afzelii* outer membrane protein BAPKO_0422 binds human factor-H and is predicted to form a membrane-spanning β -barrel." Bioscience reports **35**(4): e00240.

Echard, A., F. Jollivet, O. Martinez, J.-J. Lacapère, A. Rousselet, I. Janoueix-Lerosey and B. Goud (1998). "Interaction of a Golgi-Associated Kinesin-Like Protein with Rab6." Science **279**(5350): 580.

Elmore, S. (2007). "Apoptosis: a review of programmed cell death." Toxicologic pathology **35**(4): 495-516.

Engelhardt, H., T. Meins, M. Poyner, V. Adams, S. Nussberger, W. Welte and K. Zeth (2007). "High-Level Expression, Refolding and Probing the Natural Fold of the Human Voltage-Dependent Anion Channel Isoforms I and II." Journal of Membrane Biology **216**(2): 93-105.

Eriks, L. R., J. A. Mayor and R. S. Kaplan (2003). "A strategy for identification and quantification of detergents frequently used in the purification of membrane proteins." Analytical Biochemistry **323**(2): 234-241.

Ernster, L. and G. Schatz (1981). "Mitochondria: a historical review." The Journal of cell biology **91**(3 Pt 2): 227s-255s.

Eskes, R., S. Desagher, B. Antonsson and J.-C. Martinou (2000). "Bid Induces the Oligomerization and Insertion of Bax into the Outer Mitochondrial Membrane." Molecular and Cellular Biology **20**(3): 929.

Fiskum, G. (2000). "Mitochondrial Participation in Ischemic and Traumatic Neural Cell Death." Journal of Neurotrauma **17**(10): 843-855.

Franke, D., M. V. Petoukhov, P. V. Konarev, A. Panjkovich, A. Tuukkanen, H. D. T. Mertens, A. G. Kikhney, N. R. Hajizadeh, J. M. Franklin, C. M. Jeffries and D. I. Svergun (2017). "ATSAS 2.8: a comprehensive data analysis suite for small-angle scattering from macromolecular solutions." Journal of applied crystallography **50**(Pt 4): 1212-1225.

Franke, D. and D. I. Svergun (2009). "DAMMIF, a program for rapid ab-initio shape determination in small-angle scattering." Journal of applied crystallography **42**(Pt 2): 342-346.

Förster, S., L. Apostol and W. Bras (2010). "Scatter: software for the analysis of nano- and mesoscale small-angle scattering." Journal of Applied Crystallography **43**(3): 639-646.

Galluzzi, L. and G. Kroemer (2007). "Mitochondrial apoptosis without VDAC." Nature Cell Biology **9**: 487.

Garavito, R. M. and S. Ferguson-Miller (2001). "Detergents as Tools in Membrane Biochemistry." Journal of Biological Chemistry **276**(35): 32403-32406.

Geula, S., D. Ben-Hail and V. Shoshan-Barmatz (2012). "Structure-based analysis of VDAC1: N-terminus location, translocation, channel gating and association with anti-apoptotic proteins." Biochemical Journal **444**(3): 475.

Ghosh, D., P. K. Singh, S. Sahay, N. N. Jha, R. S. Jacob, S. Sen, A. Kumar, R. Riek and S. K. Maji (2015). "Structure based aggregation studies reveal the presence of helix-rich intermediate during α -Synuclein aggregation." Scientific Reports **5**: 9228.

Ghosh, T., N. Pandey, A. Maitra, S. K. Brahmachari and B. Pillai (2007). "A Role for Voltage-Dependent Anion Channel Vdac1 in Polyglutamine-Mediated Neuronal Cell Death." PLOS ONE **2**(11): e1170.

Giacomello, M., I. Drago, P. Pizzo and T. Pozzan (2007). "Mitochondrial Ca²⁺ as a key regulator of cell life and death." Cell Death And Differentiation **14**: 1267.

Gigant, B., W. Wang, B. Dreier, Q. Jiang, L. Pecqueur, A. Plückthun, C. Wang and M. Knossow (2013). "Structure of a kinesin-tubulin complex and implications for kinesin motility." Nature Structural & Molecular Biology **20**: 1001.

Gincel, D., V. Silberberg Sd Fau - Shoshan-Barmatz and V. Shoshan-Barmatz "Modulation of the voltage-dependent anion channel (VDAC) by glutamate." (1573-6881 (Electronic)).

Gincel, D., S. D. Silberberg and V. Shoshan-Barmatz (2000). "Modulation of the Voltage-Dependent Anion Channel (VDAC) by Glutamate1." Journal of Bioenergetics and Biomembranes **32**(6): 571-583.

Gincel, D., N. Vardi and V. Shoshan-Barmatz (2002). "Retinal Voltage-Dependent Anion Channel: Characterization and Cellular Localization." Investigative Ophthalmology & Visual Science **43**(7): 2097-2104.

Gincel, D., H. Zaid and V. Shoshan-Barmatz (2001). "Calcium binding and translocation by the voltage-dependent anion channel: a possible regulatory mechanism in mitochondrial function." Biochemical Journal **358**(1): 147.

Godbole, A., J. Varghese, A. Sarin and M. K. Mathew (2003). "VDAC is a conserved element of death pathways in plant and animal systems." Biochimica et Biophysica Acta (BBA) - Molecular Cell Research **1642**(1): 87-96.

Gogvadze, V., S. Orrenius and B. Zhivotovsky (2006). "Multiple pathways of cytochrome c release from mitochondria in apoptosis." Biochimica et Biophysica Acta (BBA) - Bioenergetics **1757**(5): 639-647.

Golan, V. S.-B. a. M. (2012). "Mitochondrial VDAC1: Function in Cell Life and Death and a Target for Cancer Therapy." Current Medicinal Chemistry **19**(5): 714-735.

Gonçalves, R. P., N. Buzhynskyy, V. Prima, J. N. Sturgis and S. Scheuring (2007). "Supramolecular Assembly of VDAC in Native Mitochondrial Outer Membranes." Journal of Molecular Biology **369**(2): 413-418.

Greenberg, J. T. (1996). "Programmed cell death: a way of life for plants." Proceedings of the National Academy of Sciences of the United States of America **93**(22): 12094-12097.

Greenfield, N. J. and G. D. Fasman (1969). "Computed circular dichroism spectra for the evaluation of protein conformation." Biochemistry **8**(10): 4108-4116.

Griffiths, K. K. and R. J. Levy (2017). "Evidence of Mitochondrial Dysfunction in Autism: Biochemical Links, Genetic-Based Associations, and Non-Energy-Related Mechanisms." Oxidative medicine and cellular longevity **2017**: 4314025-4314025.

Grigorian, A. L., J. J. Bustamante, P. Hernandez, A. O. Martinez and L. S. Haro (2005). "Extraordinarily stable disulfide-linked homodimer of human growth hormone." Protein science : a publication of the Protein Society **14**(4): 902-913.

Gunter, T. E., L. Buntinas, G. Sparagna, R. Eliseev and K. Gunter (2000). "Mitochondrial calcium transport: mechanisms and functions." Cell Calcium **28**(5): 285-296.

Guo, X. W., P. R. Smith, B. Cognon, D. D'Arcangelis, E. Dolginova and C. A. Mannella (1995). "Molecular Design of the Voltage-Dependent, Anion-Selective Channel in the Mitochondrial Outer Membrane." Journal of Structural Biology **114**(1): 41-59.

Gurnev, P. A., T. K. Rostovtseva and S. M. Bezrukov (2011). "Tubulin-blocked state of VDAC studied by polymer and ATP partitioning." FEBS Letters **585**(14): 2363-2366.

Halestrap, A. P., E. Doran, J. P. Gillespie and A. Toole (2000). "Mitochondria and cell death." Biochemical Society Transactions **28**(2): 170.

Hall, D. and L. Huang (2012). "On the use of size exclusion chromatography for the resolution of mixed amyloid aggregate distributions: I. Equilibrium partition models." Analytical Biochemistry **426**(1): 69-85.

Hammond, J. W., K. Griffin, G. T. Jih, J. Stuckey and K. J. Verhey (2008). "Co-operative Versus Independent Transport of Different Cargoes by Kinesin-1." Traffic **9**(5): 725-741.

Han, D., F. Antunes, R. Canali, D. Rettori and E. Cadenas (2002). "Voltage-dependent anion channels control the release of superoxide anion from mitochondria to cytosol." Journal of Biological Chemistry.

Hanke, W. and C. Miller (2008). Reconstitution of Ion Channel.

Harman, D. (1956). "Aging: A Theory Based on Free Radical and Radiation Chemistry." Journal of Gerontology **11**(3): 298-300.

Harman, D. (1972). "The Biologic Clock: The Mitochondria?" Journal of the American Geriatrics Society **20**(4): 145-147.

Hayashi, S. and S. Ikeda (1980). "Micelle size and shape of sodium dodecyl sulfate in concentrated sodium chloride solutions." The Journal of Physical Chemistry **84**(7): 744-751.

He, F. (2011). "Laemmli-SDS-PAGE." Bio-protocol **1**(11): e80.

Hedrich, R., O. Moran, F. Conti, H. Busch, D. Becker, F. Gambale, I. Dreyer, A. Kűch, K. Neuwinger and K. Palme (1995). "Inward rectifier potassium channels in plants differ from their animal counterparts in response to voltage and channel modulators." European Biophysics Journal **24**(2): 107-115.

Henry-Mowatt, J., C. Dive, J.-C. Martinou and D. James (2004). "Role of mitochondrial membrane permeabilization in apoptosis and cancer." Oncogene **23**: 2850.

Herrmann, J. M. and W. Neupert (2000). "Protein transport into mitochondria." (1369-5274 (Print)).

Herrmann, K. W. (1962). "NON-IONIC—CATIONIC MICELLAR PROPERTIES OF DIMETHYLDODECYLAMINE OXIDE1." The Journal of Physical Chemistry **66**(2): 295-300.

Hiller, S., J. Abramson, C. Mannella, G. Wagner and K. Zeth (2010). "The 3D structures of VDAC represent a native conformation." Trends in Biochemical Sciences **35**(9): 514-521.

Hiller, S., R. G. Garces, T. J. Malia, V. Y. Orekhov, M. Colombini and G. Wagner (2008). "Solution structure of the integral human membrane protein VDAC-1 in detergent micelles." Science (New York, N.Y.) **321**(5893): 1206-1210.

Hiller, S. and G. Wagner (2009). "The role of solution NMR in the structure determinations of VDAC-1 and other membrane proteins." Current opinion in structural biology **19**(4): 396-401.

Hirokawa, N., Y. Noda, Y. Tanaka and S. Niwa (2009). "Kinesin superfamily motor proteins and intracellular transport." Nature Reviews Molecular Cell Biology **10**: 682.

Hodge, T. and M. Colombini (1997). "Regulation of Metabolite Flux through Voltage-Gating of VDAC Channels." The Journal of Membrane Biology **157**(3): 271-279.

Holmuhamedov, E. and J. J. Lemasters (2009). "Ethanol exposure decreases mitochondrial outer membrane permeability in cultured rat hepatocytes." Archives of Biochemistry and Biophysics **481**(2): 226-233.

Homblé, F., E.-M. Krammer and M. Prévost (2012). "Plant VDAC: Facts and speculations." Biochimica et Biophysica Acta (BBA) - Biomembranes **1818**(6): 1486-1501.

Hong, P., S. Koza and E. S. P. Bouvier (2012). "Size-Exclusion Chromatography for the Analysis of Protein Biotherapeutics and their Aggregates." Journal of liquid chromatography & related technologies **35**(20): 2923-2950.

Hoogenboom, B. W., K. Suda, A. Engel and D. Fotiadis (2007). "The Supramolecular Assemblies of Voltage-dependent Anion Channels in the Native Membrane." Journal of Molecular Biology **370**(2): 246-255.

Huang, C. C., E. C. Meng, J. H. Morris, E. F. Pettersen and T. E. Ferrin (2014). "Enhancing UCSF Chimera through web services." Nucleic acids research **42**(Web Server issue): W478-W484.

Huang, H., X. Hu, C. O. Eno, G. Zhao, C. Li and C. White (2013). "An Interaction between Bcl-xL and the Voltage-dependent Anion Channel (VDAC) Promotes Mitochondrial Ca²⁺ Uptake." Journal of Biological Chemistry **288**(27): 19870-19881.

Imamura, T., J. Huang, I. Usui, H. Satoh, J. Bever and J. M. Olefsky (2003). "Insulin-induced GLUT4 translocation involves protein kinase C-lambda-mediated functional coupling between Rab4 and the motor protein kinesin." Molecular and cellular biology **23**(14): 4892-4900.

Inoue, H., H. Nojima and H. Okayama (1990). "High efficiency transformation of Escherichia coli with plasmids." Gene **96**(1): 23-28.

Iqbal, Z., M. Aatur Rahman, M. Sultan and M. Islam (2015). Apoptosis and cancer: Insights molecular mechanisms and treatments.

Itoh, R., M. Fujiwara and S. Yoshida (2001). "Kinesin-related proteins with a mitochondrial targeting signal." Plant physiology **127**(3): 724-726.

Joazeiro, C. A. P. and A. M. Weissman (2000). "RING Finger Proteins: Mediators of Ubiquitin Ligase Activity." Cell **102**(5): 549-552.

John, G. P. a. J. B. H. (2003). "Hexokinase II: The Integration of Energy Metabolism and Control of Apoptosis." Current Medicinal Chemistry **10**(16): 1535-1551.

Josse, D., C. Ebel, D. Stroebel, A. Fontaine, F. Borges, A. Echalié, D. Baud, F. Renault, M. le Maire, E. Chabrières and P. Masson (2002). "Oligomeric States of the Detergent-solubilized Human Serum Paraoxonase (PON1)." Journal of Biological Chemistry **277**(36): 33386-33397.

Junankar, P. R., A. F. Dulhunty, S. M. Curtis, S. M. Pace and F. P. Thinnés (1995). "Porin-type 1 proteins in sarcoplasmic reticulum and plasmalemma of striated muscle fibres." Journal of Muscle Research & Cell Motility **16**(6): 595-610.

Kanai, Y., N. Dohmae and N. Hirokawa (2004). "Kinesin Transports RNA: Isolation and Characterization of an RNA-Transporting Granule." Neuron **43**(4): 513-525.

Kantari, C. and H. Walczak (2011). "Caspase-8 and Bid: Caught in the act between death receptors and mitochondria." Biochimica et Biophysica Acta (BBA) - Molecular Cell Research **1813**(4): 558-563.

Keinan, N., H. Pahima, D. Ben-Hail and V. Shoshan-Barmatz (2013). "The role of calcium in VDAC1 oligomerization and mitochondria-mediated apoptosis." Biochimica et Biophysica Acta (BBA) - Molecular Cell Research **1833**(7): 1745-1754.

Keinan, N., D. Tyomkin and V. Shoshan-Barmatz (2010). "Oligomerization of the mitochondrial protein voltage-dependent anion channel is coupled to the induction of apoptosis." Molecular and cellular biology **30**(24): 5698-5709.

Kelly, S. M., T. J. Jess and N. C. Price (2005). "How to study proteins by circular dichroism." Biochimica et Biophysica Acta (BBA) - Proteins and Proteomics **1751**(2): 119-139.

Kikhney, A. G. and D. I. Svergun (2015). "A practical guide to small angle X-ray scattering (SAXS) of flexible and intrinsically disordered proteins." FEBS Letters **589**(19, Part A): 2570-2577.

Kim, M., J.-H. Lim, C. S. Ahn, K. Park, G. T. Kim, W. T. Kim and H.-S. Pai (2006). "Mitochondria-associated hexokinases play a role in the control of programmed cell death in *Nicotiana benthamiana*." The Plant cell **18**(9): 2341-2355.

Kluska, K., J. Adamczyk and A. Krężel (2018). "Metal binding properties, stability and reactivity of zinc fingers." Coordination Chemistry Reviews **367**: 18-64.

Kondo, K., N. Umeki, N. Umezu, S. Maruta and T. Mitsui (2006). "Preparation and Characterization of a Novel Rice Plant-Specific Kinesin." The Journal of Biochemistry **139**(4): 645-654.

Koppel, D. A., K. W. Kinnally, P. Masters, M. Forte, E. Blachly-Dyson and C. A. Mannella (1998). "Bacterial Expression and Characterization of the Mitochondrial Outer Membrane Channel: EFFECTS OF N-TERMINAL MODIFICATIONS." Journal of Biological Chemistry **273**(22): 13794-13800.

Kozakov, D., D. Beglov, T. Bohnuud, S. E. Mottarella, B. Xia, D. R. Hall and S. Vajda (2013). "How good is automated protein docking?" Proteins **81**(12): 2159-2166.

Kroemer, G., L. Galluzzi and C. Brenner (2007). "Mitochondrial Membrane Permeabilization in Cell Death." Physiological Reviews **87**(1): 99-163.

Kull, F. J., E. P. Sablin, R. Lau, R. J. Fletterick and R. D. Vale (1996). "Crystal structure of the kinesin motor domain reveals a structural similarity to myosin." Nature **380**(6574): 550-555.

Kumar, T. K. S., K. Gopalakrishna, V. V. H. Prasad and M. W. Pandit (1993). "Multiple Bands on the Sodium Dodecyl Sulfate-Polyacrylamide Gel Electrophoresis Gels of Proteins Due to Intermolecular Disulfide Cross-Linking." Analytical Biochemistry **213**(2): 226-228.

Kunjithapatham, R., F. Y. Oliva, U. Doshi, M. Pérez, J. Ávila and V. Muñoz (2005). "Role for the α -Helix in Aberrant Protein Aggregation." Biochemistry **44**(1): 149-156.

L DeLano, W. (2002). The PyMOL Molecular Graphics System (2002) DeLano Scientific, Palo Alto, CA, USA. <http://www.pymol.org>.

Lawrence, C. J., R. K. Dawe, K. R. Christie, D. W. Cleveland, S. C. Dawson, S. A. Endow, L. S. B. Goldstein, H. V. Goodson, N. Hirokawa, J. Howard, R. L. Malmberg, J. R. McIntosh, H. Miki, T. J. Mitchison, Y. Okada, A. S. N. Reddy, W. M. Saxton, M. Schliwa, J. M. Scholey, R. D. Vale, C. E. Walczak and L. Wordeman (2004). "A standardized kinesin nomenclature." The Journal of cell biology **167**(1): 19-22.

Lee, B., P. D. Miles, L. Vargas, P. Luan, S. Glasco, Y. Kushnareva, E. S. Kornbrust, K. A. Grako, C. B. Wollheim, P. Maechler, J. M. Olefsky and C. M. Anderson (2003). "Inhibition of Mitochondrial Na⁺-Ca²⁺ Exchanger Increases Mitochondrial Metabolism and Potentiates Glucose-Stimulated Insulin Secretion in Rat Pancreatic Islets." Diabetes **52**(4): 965.

Lee, K., J. Kerner and C. L. Hoppel (2011). "Mitochondrial Carnitine Palmitoyltransferase 1a (CPT1a) Is Part of an Outer Membrane Fatty Acid Transfer Complex." Journal of Biological Chemistry **286**(29): 25655-25662.

Li, J., Y. Xu and K. Chong (2012). "The novel functions of kinesin motor proteins in plants." Protoplasma **249 Suppl 2**(Suppl 2): S95-S100.

Li, P., D. Nijhawan, I. Budihardjo, S. M. Srinivasula, M. Ahmad, E. S. Alnemri and X. Wang (1997). "Cytochrome c and dATP-Dependent Formation of Apaf-1/Caspase-9 Complex Initiates an Apoptotic Protease Cascade." Cell **91**(4): 479-489.

Li, W., S. M. Srinivasula, J. Chai, P. Li, J.-W. Wu, Z. Zhang, E. S. Alnemri and Y. Shi (2002). "Structural insights into the pro-apoptotic function of mitochondrial serine protease HtrA2/Omi." Nature Structural Biology **9**: 436.

Lilie, H., E. Schwarz and R. Rudolph (1998). "Advances in refolding of proteins produced in E. coli." Current Opinion in Biotechnology **9**(5): 497-501.

Lim, Y.-A., V. Rhein, G. Baysang, F. Meier, A. Poljak, M. J. Raftery, M. Guilhaus, L. M. Ittner, A. Eckert and J. Götz (2010). "A β and human amylin share a common toxicity pathway via mitochondrial dysfunction." PROTEOMICS **10**(8): 1621-1633.

Lipmann, F. (1941). "Metabolic Generation and Utilization of Phosphate Bond Energy." Advances in Enzymology and Related Areas of Molecular Biology.

Lobley, A., B. A. Wallace and L. Whitmore (2002). "DICHROWEB: an interactive website for the analysis of protein secondary structure from circular dichroism spectra." Bioinformatics **18**(1): 211-212.

Lorick, K. L., J. P. Jensen, S. Fang, A. M. Ong, S. Hatakeyama and A. M. Weissman (1999). "RING fingers mediate ubiquitin-conjugating enzyme (E2)-dependent ubiquitination." Proceedings of the National Academy of Sciences of the United States of America **96**(20): 11364-11369.

Lovell, J. F., L. P. Billen, S. Bindner, A. Shamas-Din, C. Fradin, B. Leber and D. W. Andrews (2008). "Membrane Binding by tBid Initiates an Ordered Series of Events Culminating in Membrane Permeabilization by Bax." Cell **135**(6): 1074-1084.

Lu, S., W. Huang, Q. Wang, Q. Shen, S. Li, R. Nussinov and J. Zhang (2014). "The Structural Basis of ATP as an Allosteric Modulator." *PLOS Computational Biology* **10**(9): e1003831.

Lü, A.-J., C.-W. Dong, C.-S. Du and Q.-Y. Zhang (2007). "Characterization and expression analysis of *Paralichthys olivaceus* voltage-dependent anion channel (VDAC) gene in response to virus infection." *Fish & Shellfish Immunology* **23**(3): 601-613.

Ma, Z., S. E. Gabriel and J. D. Helmann (2011). "Sequential binding and sensing of Zn(II) by *Bacillus subtilis* Zur." *Nucleic Acids Research* **39**(21): 9130-9138.

Maack, C., S. Cortassa, A. Aon Miguel, N. Ganesan Anand, T. Liu and B. O'Rourke (2006). "Elevated Cytosolic Na⁺ Decreases Mitochondrial Ca²⁺ Uptake During Excitation-Contraction Coupling and Impairs Energetic Adaptation in Cardiac Myocytes." *Circulation Research* **99**(2): 172-182.

Madesh, M. and G. Hajnóczky (2001). "VDAC-dependent permeabilization of the outer mitochondrial membrane by superoxide induces rapid and massive cytochrome c release." *The Journal of cell biology* **155**(6): 1003-1015.

Maechler, P., E. D. Kennedy, T. Pozzan and C. B. Wollheim (1997). "Mitochondrial activation directly triggers the exocytosis of insulin in permeabilized pancreatic β -cells." *The EMBO Journal* **16**(13): 3833.

Maher, J. and M. Allen (2018). *Planar lipid bilayers in recombinant ion channel research*.

Mailloux, R. J., S. L. McBride and M.-E. Harper (2013). "Unearthing the secrets of mitochondrial ROS and glutathione in bioenergetics." *Trends in Biochemical Sciences* **38**(12): 592-602.

Malia, T. J. and G. Wagner (2007). "NMR Structural Investigation of the Mitochondrial Outer Membrane Protein VDAC and Its Interaction with Antiapoptotic Bcl-xL." *Biochemistry* **46**(2): 514-525.

Mannella, C. A. (1997). "On the Structure and Gating Mechanism of the Mitochondrial Channel, VDAC." *Journal of Bioenergetics and Biomembranes* **29**(6): 525-531.

Mares-Perlman, J. A. and E. Shrago (1988). "Energy Substrate Utilization in Freshly Isolated Morris Hepatoma 7777 Cells." *Cancer Research* **48**(3): 602.

Martel, C., M. Allouche, D. D. Esposti, E. Fanelli, C. Boursier, C. Henry, J. Chopineau, G. Calamita, G. Kroemer, A. Lemoine and C. Brenner (2013). "Glycogen synthase kinase 3-mediated voltage-dependent anion channel phosphorylation controls outer mitochondrial membrane permeability during lipid accumulation." *Hepatology* **57**(1): 93-102.

Martinovich, G. G., E. N. Golubeva, I. V. Martinovich and S. N. Cherenkevich (2012). "Redox regulation of calcium signaling in cancer cells by ascorbic Acid involving the mitochondrial electron transport chain." *Journal of biophysics (Hindawi Publishing Corporation : Online)* **2012**: 921653-921653.

Marx, A., M. Thormählen, J. Müller, S. Sack, E. M. Mandelkow and E. Mandelkow (1998). "Conformations of kinesin: solution vs. crystal structures and interactions with microtubules." *European Biophysics Journal* **27**(5): 455-465.

Maurya, S. R. and R. Mahalakshmi (2013). "Modulation of Human Mitochondrial Voltage-dependent Anion Channel 2 (hVDAC-2) Structural Stability by Cysteine-assisted Barrel-lipid Interactions." *Journal of Biological Chemistry* **288**(35): 25584-25592.

Maurya, S. R. and R. Mahalakshmi (2016). "VDAC-2: Mitochondrial outer membrane regulator masquerading as a channel?" *The FEBS Journal* **283**(10): 1831-1836.

Mavridis, L. and R. W. Janes (2016). "PDB2CD: a web-based application for the generation of circular dichroism spectra from protein atomic coordinates." *Bioinformatics* **33**(1): 56-63.

McCormack, M. L., R. P. Guttman, M. Schumann, J. M. Farmer, C. A. Stolle, V. Campuzano, M. Koenig and D. R. Lynch (2000). "Fratxin point mutations in two patients with Friedreich's ataxia and unusual clinical features." *Journal of Neurology, Neurosurgery & Psychiatry* **68**(5): 661.

McGinnis, S. and T. L. Madden (2004). "BLAST: at the core of a powerful and diverse set of sequence analysis tools." *Nucleic acids research* **32**(Web Server issue): W20-W25.

Mertins, B., G. Psakis, W. Grosse, K. C. Back, A. Salisowski, P. Reiss, U. Koert and L. O. Essen (2012). "Flexibility of the N-terminal mVDAC1 segment controls the channel's gating behavior." *PLoS One* **7**(10): e47938.

Miles, A. J. and B. A. Wallace (2016). "Circular dichroism spectroscopy of membrane proteins." *Chemical Society Reviews* **45**(18): 4859-4872.

Molleman, A., L. Thuneberg and J. D. Huizinga (1993). "Characterization of the outward rectifying potassium channel in a novel mouse intestinal smooth muscle cell preparation." The Journal of physiology **470**: 211-229.

Mruk, D. D. and C. Y. Cheng (2011). "Enhanced chemiluminescence (ECL) for routine immunoblotting: An inexpensive alternative to commercially available kits." Spermatogenesis **1**(2): 121-122.

Murphy, Michael P. (2009). "How mitochondria produce reactive oxygen species." Biochemical Journal **417**(1): 1.

Muñoz, E. and J. Sabín (2019). The Use of ITC and the Software AFFINImeter for the Quantification of the Anticoagulant Pentasaccharide in Low Molecular Weight Heparin. Microcalorimetry of Biological Molecules: Methods and Protocols. E. Ennifar. New York, NY, Springer New York: 215-223.

Mylonas, E. and D. I. Svergun (2007). "Accuracy of molecular mass determination of proteins in solution by small-angle X-ray scattering." Journal of Applied Crystallography **40**(s1): s245-s249.

Nangaku, M., R. Sato-Yoshitake, Y. Okada, Y. Noda, R. Takemura, H. Yamazaki and N. Hirokawa (1994). "KIF1B, a novel microtubule plus end-directed monomeric motor protein for transport of mitochondria." Cell **79**(7): 1209-1220.

Nichols, B. J. and R. M. Denton (1995). Towards the molecular basis for the regulation of mitochondrial dehydrogenases by calcium ions. Signal Transduction Mechanisms. J. A. Barnes, H. G. Coore, A. H. Mohammed and R. K. Sharma. Boston, MA, Springer US: 203-212.

Okada, S. F., W. K. Neal, P. Huang, R. A. Nicholas, L. E. Ostrowski, W. J. Craigen, E. R. Lazarowski and R. C. Boucher (2004). "Voltage-dependent Anion Channel-1 (VDAC-1) Contributes to ATP Release and Cell Volume Regulation in Murine Cells." The Journal of General Physiology **124**(5): 513.

Ott, M., V. Gogvadze, S. Orrenius and B. Zhivotovsky (2007). "Mitochondria, oxidative stress and cell death." Apoptosis **12**(5): 913-922.

Papadopoulos, V., J. Liu and M. Culty (2007). "Is there a mitochondrial signaling complex facilitating cholesterol import?" Molecular and Cellular Endocrinology **265-266**: 59-64.

Pastorino, J. G. and J. B. Hoek (2008). "Regulation of hexokinase binding to VDAC." Journal of bioenergetics and biomembranes **40**(3): 171-182.

Patel, M., B. J. Day, J. D. Crapo, I. Fridovich and J. O. McNamara (1996). "Requirement for Superoxide in Excitotoxic Cell Death." Neuron **16**(2): 345-355.

Pavlov, E., S. M. Grigoriev, L. M. Dejean, C. L. Zweihorn, C. A. Mannella and K. W. Kinnally (2005). "The mitochondrial channel VDAC has a cation-selective open state." Biochimica et Biophysica Acta (BBA) - Bioenergetics **1710**(2): 96-102.

Pecina, P., G. G. Borisenko, N. A. Belikova, Y. Y. Tyurina, A. Pecinova, I. Lee, A. K. Samhan-Arias, K. Przyklenk, V. E. Kagan and M. Hüttemann (2010). "Phosphomimetic Substitution of Cytochrome c Tyrosine 48 Decreases Respiration and Binding to Cardiolipin and Abolishes Ability to Trigger Downstream Caspase Activation." Biochemistry **49**(31): 6705-6714.

Pedersen, P. L. (1978). "Tumor Mitochondria and the Bioenergetics of Cancer Cells." Progress in Tumor Research: 190-274.

Peng, S., E. Blachly-Dyson, M. Forte and M. Colombini (1992). "Large scale rearrangement of protein domains is associated with voltage gating of the VDAC channel." Biophysical journal **62**(1): 123-135.

Petoukhov, M. V., D. Franke, A. V. Shkumatov, G. Tria, A. G. Kikhney, M. Gajda, C. Gorba, H. D. T. Mertens, P. V. Konarev and D. I. Svergun (2012). "New developments in the ATSAS program package for small-angle scattering data analysis." Journal of applied crystallography **45**(Pt 2): 342-350.

Petoukhov, M. V. and D. I. Svergun (2013). "Applications of small-angle X-ray scattering to biomacromolecular solutions." The International Journal of Biochemistry & Cell Biology **45**(2): 429-437.

Petrosillo, G., F. M. Ruggiero and G. Paradies (2003). "Role of reactive oxygen species and cardiolipin in the release of cytochrome c from mitochondria." The FASEB Journal **17**(15): 2202-2208.

Petrosillo, G., F. M. Ruggiero, M. Pistolese and G. Paradies (2001). "Reactive oxygen species generated from the mitochondrial electron transport chain induce cytochrome c dissociation from beef-

heart submitochondrial particles via cardiolipin peroxidation. Possible role in the apoptosis." *FEBS Letters* **509**(3): 435-438.

Pettersen, E. F., C. C. Goddard Td Fau - Huang, G. S. Huang Cc Fau - Couch, D. M. Couch Gs Fau - Greenblatt, E. C. Greenblatt Dm Fau - Meng, T. E. Meng Ec Fau - Ferrin and T. E. Ferrin "UCSF Chimera--a visualization system for exploratory research and analysis." (0192-8651 (Print)).

Pieczenik, S. R. and J. Neustadt (2007). "Mitochondrial dysfunction and molecular pathways of disease." *Experimental and Molecular Pathology* **83**(1): 84-92.

Pierce, M. M., C. S. Raman and B. T. Nall (1999). "Isothermal Titration Calorimetry of Protein-Protein Interactions." *Methods* **19**(2): 213-221.

Piñeiro, Á., E. Muñoz, J. Sabín, M. Costas, M. Bastos, A. Velázquez-Campoy, P. F. Garrido, P. Dumas, E. Ennifar, L. García-Río, J. Rial, D. Pérez, P. Fraga, A. Rodríguez and C. Coteló (2019). "AFFINImeter: A software to analyze molecular recognition processes from experimental data." *Analytical Biochemistry*.

Popp, B., D. A. Court, R. Benz, W. Neupert and R. Lill (1996). "The Role of the N and C Termini of Recombinant Neurospora Mitochondrial Porin in Channel Formation and Voltage-dependent Gating." *Journal of Biological Chemistry* **271**(23): 13593-13599.

Provencher, S. W. and J. Gloeckner (1981). "Estimation of globular protein secondary structure from circular dichroism." *Biochemistry* **20**(1): 33-37.

Puljung, M. C. and W. N. Zagotta (2012). "Fluorescent labeling of specific cysteine residues using CyMPL." *Current protocols in protein science Chapter 14*: Unit14.14-Unit14.14.

Purdie, N. (1996). "Circular Dichroism and the Conformational Analysis of Biomolecules Edited by Gerald D. Fasman (Brandeis University). Plenum Press: New York. 1996. x + 738 pp. \$125.00. ISBN 0-306-45142-5." *Journal of the American Chemical Society* **118**(50): 12871-12871.

Rajalingam, D., K. M. Kathir, K. Ananthamurthy, P. D. Adams and T. K. S. Kumar (2008). "A method for the prevention of thrombin-induced degradation of recombinant proteins." *Analytical biochemistry* **375**(2): 361-363.

Rambo, R. P. and J. A. Tainer (2013). "Accurate assessment of mass, models and resolution by small-angle scattering." *Nature* **496**(7446): 477-481.

Rapizzi, E., P. Pinton, G. Szabadkai, M. R. Wieckowski, G. Vandecasteele, G. Baird, R. A. Tuft, K. E. Fogarty and R. Rizzuto (2002). "Recombinant expression of the voltage-dependent anion channel enhances the transfer of Ca²⁺ microdomains to mitochondria." *The Journal of Cell Biology* **159**(4): 613.

Raschle, T., S. Hiller, T.-Y. Yu, A. J. Rice, T. Walz and G. Wagner (2009). "Structural and functional characterization of the integral membrane protein VDAC-1 in lipid bilayer nanodiscs." *Journal of the American Chemical Society* **131**(49): 17777-17779.

Rasola, A. and P. Bernardi (2011). "Mitochondrial permeability transition in Ca²⁺-dependent apoptosis and necrosis." *Cell Calcium* **50**(3): 222-233.

Reddy, P. H. (2013). "Is the mitochondrial outer membrane protein VDAC1 therapeutic target for Alzheimer's disease?" *Biochimica et Biophysica Acta (BBA) - Molecular Basis of Disease* **1832**(1): 67-75.

Reed, J. C. (2006). "Proapoptotic multidomain Bcl-2/Bax-family proteins: mechanisms, physiological roles, and therapeutic opportunities." *Cell Death And Differentiation* **13**: 1378.

Reina, S., V. Palermo, A. Guarnera, F. Guarino, A. Messina, C. Mazzoni and V. De Pinto (2010). "Swapping of the N-terminus of VDAC1 with VDAC3 restores full activity of the channel and confers anti-aging features to the cell." *FEBS Letters* **584**(13): 2837-2844.

Renne, M. F. and A. I. P. M. de Kroon (2018). "The role of phospholipid molecular species in determining the physical properties of yeast membranes." *FEBS Letters* **592**(8): 1330-1345.

Reymann, S., H. Florke, M. Heiden, C. Jakob, U. Stadtmuller, P. Steinacker, V. E. Lalk, I. Pardowitz and F. P. Thinner (1995). "Further Evidence for Multitopological Localization of Mammalian Porin (VDAC) in the Plasmalemma Forming Part of a Chloride Channel Complex Affected in Cystic Fibrosis and Encephalomyopathy." *Biochemical and Molecular Medicine* **54**(2): 75-87.

Rice, S., A. W. Lin, D. Safer, C. L. Hart, N. Naber, B. O. Carragher, S. M. Cain, E. Pechatnikova, E. M. Wilson-Kubalek, M. Whittaker, E. Pate, R. Cooke, E. W. Taylor, R. A. Milligan and R. D. Vale (1999). "A structural change in the kinesin motor protein that drives motility." *Nature* **402**(6763): 778-784.

Rice, S. A. (1956). "Small angle scattering of X-rays. A. Guinier and G. Fournet. Translated by C. B. Wilson and with a bibliographical appendix by K. L. Yudowitch. Wiley, New York, 1955. 268 pp. \$7.50." Journal of Polymer Science **19**(93): 594-594.

Rone, M. B., J. Fan and V. Papadopoulos (2009). "Cholesterol transport in steroid biosynthesis: Role of protein-protein interactions and implications in disease states." Biochimica et Biophysica Acta (BBA) - Molecular and Cell Biology of Lipids **1791**(7): 646-658.

Rone, M. B., A. S. Midzak, L. Issop, G. Rammouz, S. Jagannathan, J. Fan, X. Ye, J. Blonder, T. Veenstra and V. Papadopoulos (2012). "Identification of a dynamic mitochondrial protein complex driving cholesterol import, trafficking, and metabolism to steroid hormones." Molecular endocrinology (Baltimore, Md.) **26**(11): 1868-1882.

Rostovtseva, T. and M. Colombini (1997). "VDAC channels mediate and gate the flow of ATP: implications for the regulation of mitochondrial function." Biophysical Journal **72**(5): 1954-1962.

Rostovtseva, T. K. and S. M. Bezrukov (2012). "VDAC inhibition by tubulin and its physiological implications." Biochimica et biophysica acta **1818**(6): 1526-1535.

Sabirov, R., Dutta, A., K. and Okada, Y. (2001). "Volume-Dependent Atp-Conductive Large-Conductance Anion Channel as a Pathway for Swelling-Induced Atp Release." The Journal of General Physiology **118**(3): 251-66.

Saidani, H., D. Grobys, M. Léonetti, H. Kmita and F. Homblé (2016). "Towards understanding of plant mitochondrial VDAC proteins: An overview of bean (*Phaseolus*) VDAC proteins".

Sako-Kubota, K., N. Tanaka, S. Nagae, W. Meng and M. Takeichi (2014). "Minus end-directed motor KIFC3 suppresses E-cadherin degradation by recruiting USP47 to adherens junctions." Molecular biology of the cell **25**(24): 3851-3860.

Sampson, M. J., R. S. Lovell and W. J. Craigen (1997). "The Murine Voltage-dependent Anion Channel Gene Family: CONSERVED STRUCTURE AND FUNCTION." Journal of Biological Chemistry **272**(30): 18966-18973.

Santos, S. F., D. Zanette, H. Fischer and R. Itri (2003). "A systematic study of bovine serum albumin (BSA) and sodium dodecyl sulfate (SDS) interactions by surface tension and small angle X-ray scattering." Journal of Colloid and Interface Science **262**(2): 400-408.

Sayers, E. W., T. Barrett, D. A. Benson, S. H. Bryant, K. Canese, V. Chetvernin, D. M. Church, M. DiCuccio, R. Edgar, S. Federhen, M. Feolo, L. Y. Geer, W. Helmberg, Y. Kapustin, D. Landsman, D. J. Lipman, T. L. Madden, D. R. Maglott, V. Miller, I. Mizrachi, J. Ostell, K. D. Pruitt, G. D. Schuler, E. Sequeira, S. T. Sherry, M. Shumway, K. Sirotkin, A. Souvorov, G. Starchenko, T. A. Tatusova, L. Wagner, E. Yaschenko and J. Ye (2009). "Database resources of the National Center for Biotechnology Information." Nucleic acids research **37**(Database issue): D5-D15.

Schindelin, J., C. T. Rueden, M. C. Hiner and K. W. Eliceiri (2015). "The ImageJ ecosystem: An open platform for biomedical image analysis." Molecular reproduction and development **82**(7-8): 518-529.

Schneider, C. A., W. S. Rasband and K. W. Eliceiri (2012). "NIH Image to ImageJ: 25 years of image analysis." Nature methods **9**(7): 671-675.

Schneidman-Duhovny, D., M. Hammel and A. Sali (2010). "FoXS: a web server for rapid computation and fitting of SAXS profiles." Nucleic acids research **38**(Web Server issue): W540-W544.

Schredelseker, J., A. Paz, C. J. López, C. Altenbach, C. S. Leung, M. K. Drexler, J.-N. Chen, W. L. Hubbell and J. Abramson (2014). "High Resolution Structure and Double Electron-Electron Resonance of the Zebrafish Voltage-dependent Anion Channel 2 Reveal an Oligomeric Population." Journal of Biological Chemistry **289**(18): 12566-12577.

Scotto, A. W., D. Goodwyn and D. Zakim (1987). "Reconstitution of membrane proteins: sequential incorporation of integral membrane proteins into preformed lipid bilayers." Biochemistry **26**(3): 833-839.

Seeger, M. A. and S. E. Rice (2012). "Intrinsic Disorder in the Kinesin Superfamily." Biophysical reviews **5**(3): 233-247.

Sewell, A. P. (2010). Advances in Chromatography, Volume 47.

Shanmugavadivu, B., H.-J. Apell, T. Meins, K. Zeth and J. H. Kleinschmidt (2007). "Correct Folding of the β -Barrel of the Human Membrane Protein VDAC Requires a Lipid Bilayer." Journal of Molecular Biology **368**(1): 66-78.

Shao, L., K. W. Kinnally and C. A. Mannella (1996). "Circular dichroism studies of the mitochondrial channel, VDAC, from *Neurospora crassa*." *Biophysical journal* **71**(2): 778-786.

Shi, Y., J. Chen, C. Weng, R. Chen, Y. Zheng, Q. Chen and H. Tang (2003). "Identification of the protein-protein contact site and interaction mode of human VDAC1 with Bcl-2 family proteins." *Biochemical and Biophysical Research Communications* **305**(4): 989-996.

Shimizu, S., Y. Matsuoka, Y. Shinohara, Y. Yoneda and Y. Tsujimoto (2001). "Essential Role of Voltage-Dependent Anion Channel in Various Forms of Apoptosis in Mammalian Cells." *The Journal of Cell Biology* **152**(2): 237.

Shimizu, S., M. Narita and Y. Tsujimoto (1999). "Bcl-2 family proteins regulate the release of apoptogenic cytochrome c by the mitochondrial channel VDAC." *Nature* **399**(6735): 483-487.

Shimizu, S., Y. Shinohara and Y. Tsujimoto (2000). "Bax and Bcl-xL independently regulate apoptotic changes of yeast mitochondria that require VDAC but not adenine nucleotide translocator." *Oncogene* **19**: 4309.

Shoshan-Barmatz, V. and D. Ben-Hail (2012). "VDAC, a multi-functional mitochondrial protein as a pharmacological target." *Mitochondrion* **12**(1): 24-34.

Shoshan-Barmatz, V., V. De Pinto, M. Zweckstetter, Z. Raviv, N. Keinan and N. Arbel (2010). "VDAC, a multi-functional mitochondrial protein regulating cell life and death." *Molecular Aspects of Medicine* **31**(3): 227-285.

Shoshan-Barmatz, V. and D. Gincel (2003). "The voltage-dependent anion channel." *Cell Biochemistry and Biophysics* **39**(3): 279-292.

Shoshan-Barmatz, V., N. Hadad, W. Feng, I. Shafir, I. Orr, M. Varsanyi and L. M. G. Heilmeyer (1996). "VDAC/porin is present in sarcoplasmic reticulum from skeletal muscle." *FEBS Letters* **386**(2): 205-210.

Shoshan-Barmatz, V., A. Israelson and D. B. a. S. S. Sheu (2006). "The Voltage-Dependent Anion Channel (VDAC): Function in Intracellular Signalling, Cell Life and Cell Death." *Current Pharmaceutical Design* **12**(18): 2249-2270.

Shoshan-Barmatz, V. and D. Mizrahi (2012). "VDAC1: from structure to cancer therapy." *Frontiers in oncology* **2**: 164-164.

Shoshan-Barmatz, V., D. Mizrahi and N. Keinan (2013). Chapter Eleven - Oligomerization of the Mitochondrial Protein VDAC1: From Structure to Function and Cancer Therapy. *Progress in Molecular Biology and Translational Science*. J. Giraldo and F. Ciruela, Academic Press. **117**: 303-334.

Shoshan-Barmatz, V., R. Zalk, D. Gincel and N. Vardi (2004). "Subcellular localization of VDAC in mitochondria and ER in the cerebellum." *Biochimica et Biophysica Acta (BBA) - Bioenergetics* **1657**(2): 105-114.

Sigrist, C. J. A., E. de Castro, L. Cerutti, B. A. Cucho, N. Hulo, A. Bridge, L. Bougueleret and I. Xenarios (2013). "New and continuing developments at PROSITE." *Nucleic acids research* **41**(Database issue): D344-D347.

Simamura, E., K.-I. Hirai, H. Shimada, J. Koyama, Y. Niwa and S. Shimizu (2006). "Furanonaphthoquinones cause apoptosis of cancer cells by inducing the production of reactive oxygen species by the mitochondrial voltage-dependent anion channel." *Cancer Biology & Therapy* **5**(11): 1523-1529.

Slee, E. A., C. Adrain and S. J. Martin (2001). "Executioner Caspase-3, -6, and -7 Perform Distinct, Non-redundant Roles during the Demolition Phase of Apoptosis." *Journal of Biological Chemistry* **276**(10): 7320-7326.

Snyder, J. K. (1996). "Circular Dichroism: Principles and Applications K. Nakanishi and N. Berova (Columbia University) and R. W. Woody (Colorado State University). VCH Publishers, Inc., New York, NY. 1994. xvii + 576 pp. 15.5 × 23.5 cm. \$125.00. ISBN 1-56081-618-X." *Journal of Natural Products* **59**(12): 1219-1219.

Solary, E., B. Eymin, N. Droin and M. Haugg (1998). "Proteases, proteolysis, and apoptosis." *Cell Biology and Toxicology* **14**(2): 121-132.

Song, Y., F. DiMaio, R. Y.-R. Wang, D. Kim, C. Miles, T. Brunette, J. Thompson and D. Baker (2013). "High-resolution comparative modeling with RosettaCM." *Structure (London, England : 1993)* **21**(10): 1735-1742.

Sreerama, N. and R. W. Woody (2000). "Estimation of Protein Secondary Structure from Circular Dichroism Spectra: Comparison of CONTIN, SELCON, and CDSSTR Methods with an Expanded Reference Set." Analytical Biochemistry **287**(2): 252-260.

Stauber, T., J. C. Simpson, R. Pepperkok and I. Vernos (2006). "A Role for Kinesin-2 in COPI-Dependent Recycling between the ER and the Golgi Complex." Current Biology **16**(22): 2245-2251.

Strop, P. and A. T. Brunger (2005). "Refractive index-based determination of detergent concentration and its application to the study of membrane proteins." Protein science : a publication of the Protein Society **14**(8): 2207-2211.

Suen, D.-F., K. L. Norris and R. J. Youle (2008). "Mitochondrial dynamics and apoptosis." Genes & Development **22**(12): 1577-1590.

Summers, W. A. T. and D. A. Court (2010). "Origami in outer membrane mimetics: correlating the first detailed images of refolded VDAC with over 20 years of biochemical data." Biochemistry and Cell Biology **88**(3): 425-438.

Sun, L., S. Shukair, T. J. Naik, F. Moazed and H. Ardehali (2008). "Glucose Phosphorylation and Mitochondrial Binding Are Required for the Protective Effects of Hexokinases I and II." Molecular and Cellular Biology **28**(3): 1007.

Susin, S. A., H. K. Lorenzo, N. Zamzami, I. Marzo, B. E. Snow, G. M. Brothers, J. Mangion, E. Jacotot, P. Costantini, M. Loeffler, N. Larochette, D. R. Goodlett, R. Aebersold, D. P. Siderovski, J. M. Penninger and G. Kroemer (1999). "Molecular characterization of mitochondrial apoptosis-inducing factor." Nature **397**(6718): 441-446.

Svoboda, K., C. F. Schmidt, B. J. Schnapp and S. M. Block (1993). "Direct observation of kinesin stepping by optical trapping interferometry." Nature **365**(6448): 721-727.

Tan, W. and M. Colombini (2007). "VDAC closure increases calcium ion flux." Biochimica et biophysica acta **1768**(10): 2510-2515.

Tateda, C., K. Watanabe, T. Kusano and Y. Takahashi (2011). "Molecular and genetic characterization of the gene family encoding the voltage-dependent anion channel in Arabidopsis." Journal of experimental botany **62**(14): 4773-4785.

Taylor, R. W. and D. M. Turnbull (2005). "Mitochondrial DNA mutations in human disease." Nature reviews. Genetics **6**(5): 389-402.

Teixeira, F. K., C. G. Sanchez, T. R. Hurd, J. R. K. Seifert, B. Czech, J. B. Preall, G. J. Hannon and R. Lehmann (2015). "ATP synthase promotes germ cell differentiation independent of oxidative phosphorylation." Nature cell biology **17**(5): 689-696.

The UniProt, C. (2018). "UniProt: a worldwide hub of protein knowledge." Nucleic Acids Research **47**(D1): D506-D515.

Thinnes, F. P. and G. Burckhardt (2012). "On a fully closed state of native human type-1 VDAC enriched in Nonidet P40." Molecular Genetics and Metabolism **107**(3): 632-633.

Thiyagarajan, P. and D. M. Tiede (1994). "Detergent micelle structure and micelle-micelle interactions determined by small-angle neutron scattering under solution conditions used for membrane protein crystallization." The Journal of Physical Chemistry **98**(40): 10343-10351.

Thomas, L., E. Blachly-Dyson, M. Colombini and M. Forte (1993). "Mapping of residues forming the voltage sensor of the voltage-dependent anion-selective channel." Proceedings of the National Academy of Sciences **90**(12): 5446.

Thrash, J. C., A. Boyd, M. J. Huggett, J. Grote, P. Carini, R. J. Yoder, B. Robbertse, J. W. Spatafora, M. S. Rappé and S. J. Giovannoni (2011). "Phylogenomic evidence for a common ancestor of mitochondria and the SAR11 clade." Sci Rep **1**: 13.

Tikunov, A., C. B. Johnson, P. Padiaditakis, N. Markevich, J. M. Macdonald, J. J. Lemasters and E. Holmuhamedov (2010). "Closure of VDAC causes oxidative stress and accelerates the Ca²⁺-induced mitochondrial permeability transition in rat liver mitochondria." Archives of Biochemistry and Biophysics **495**(2): 174-181.

Tomii, K. and Y. Akiyama (2004). "FORTE: a profile-profile comparison tool for protein fold recognition." Bioinformatics **20**(4): 594-595.

Trewhella, J., A. P. Duff, D. Durand, F. Gabel, J. M. Guss, W. A. Hendrickson, G. L. Hura, D. A. Jacques, N. M. Kirby, A. H. Kwan, J. Pérez, L. Pollack, T. M. Ryan, A. Sali, D. Schneidman-Duhovny, T. Schwede, D. I. Svergun, M. Sugiyama, J. A. Tainer, P. Vachette, J. Westbrook and A. E. Whitten (2017). "2017 publication guidelines for structural modelling of small-angle scattering data

from biomolecules in solution: an update." Acta crystallographica. Section D, Structural biology **73**(Pt 9): 710-728.

Tsujimoto, Y. and S. Shimizu (2002). "The voltage-dependent anion channel: an essential player in apoptosis." Biochimie **84**(2): 187-193.

Tsujimoto, Y. and S. Shimizu (2007). "Role of the mitochondrial membrane permeability transition in cell death." Apoptosis **12**(5): 835-840.

Tucker, S. J. and T. Baukowitz (2008). "How highly charged anionic lipids bind and regulate ion channels." The Journal of general physiology **131**(5): 431-438.

Tuukkanen, A. T., A. Spilotros and D. I. Svergun (2017). "Progress in small-angle scattering from biological solutions at high-brilliance synchrotrons." IUCrJ **4**(Pt 5): 518-528.

Ujwal, R., D. Cascio, J.-P. Colletier, S. Faham, J. Zhang, L. Toro, P. Ping and J. Abramson (2008). "The crystal structure of mouse VDAC1 at 2.3 Å resolution reveals mechanistic insights into metabolite gating." Proceedings of the National Academy of Sciences of the United States of America **105**(46): 17742-17747.

Umeki, N., S. Maruta, T. Mitsui and Y. Koike (2006). "Intermolecular Cross-Linking of a Novel Rice Kinesin K16 Motor Domain with a Photoreactive ATP Derivative." The Journal of Biochemistry **139**(5): 831-836.

Valko, M., C. J. Rhodes, J. Moncol, M. Izakovic and M. Mazur (2006). "Free radicals, metals and antioxidants in oxidative stress-induced cancer." Chemico-Biological Interactions **160**(1): 1-40.

van Stokkum, I. H. M., H. J. W. Spoelder, M. Bloemendal, R. van Grondelle and F. C. A. Groen (1990). "Estimation of protein secondary structure and error analysis from circular dichroism spectra." Analytical Biochemistry **191**(1): 110-118.

Vander Heiden, M. G., N. S. Chandel, X. X. Li, P. T. Schumacker, M. Colombini and C. B. Thompson (2000). "Outer mitochondrial membrane permeability can regulate coupled respiration and cell survival." Proceedings of the National Academy of Sciences **97**(9): 4666.

Vander Heiden, M. G., X. X. Li, E. Gottleib, R. B. Hill, C. B. Thompson and M. Colombini (2001). "Bcl-x1 Promotes the Open Configuration of the Voltage-dependent Anion Channel and Metabolite Passage through the Outer Mitochondrial Membrane." Journal of Biological Chemistry **276**(22): 19414-19419.

Vanyushin, B. F., L. E. Bakeeva, V. A. Zamyatnina and N. I. Aleksandrushkina (2004). Apoptosis in Plants: Specific Features of Plant Apoptotic Cells and Effect of Various Factors and Agents. International Review of Cytology, Academic Press. **233**: 135-179.

Verhagen, A. M., P. G. Ekert, M. Pakusch, J. Silke, L. M. Connolly, G. E. Reid, R. L. Moritz, R. J. Simpson and D. L. Vaux (2000). "Identification of DIABLO, a Mammalian Protein that Promotes Apoptosis by Binding to and Antagonizing IAP Proteins." Cell **102**(1): 43-53.

Vijayakumar, S., S. Vishveshwara, G. Ravishanker and D. L. Beveridge (1993). "Differential stability of beta-sheets and alpha-helices in beta-lactamase: a high temperature molecular dynamics study of unfolding intermediates." Biophysical Journal **65**(6): 2304-2312.

Walker, J. E., M. Saraste, M. J. Runswick and N. J. Gay (1982). "Distantly related sequences in the alpha- and beta-subunits of ATP synthase, myosin, kinases and other ATP-requiring enzymes and a common nucleotide binding fold." The EMBO journal **1**(8): 945-951.

Wang, W., L. Cao, C. Wang, B. Gigant and M. Knossow (2015). "Kinesin, 30 years later: Recent insights from structural studies." Protein science : a publication of the Protein Society **24**(7): 1047-1056.

Wang, X. (2001). "The expanding role of mitochondria in apoptosis." Genes & Development **15**(22): 2922-2933.

Waterhouse, A., C. Rempfer, F. T. Heer, G. Studer, G. Tauriello, L. Bordoli, M. Bertoni, R. Gumienny, R. Lepore, S. Bienert, T. A P. de Beer and T. Schwede (2018). "SWISS-MODEL: homology modelling of protein structures and complexes." Nucleic Acids Research **46**(W1): W296-W303.

Wei, M. C., T. Lindsten, V. K. Mootha, S. Weiler, A. Gross, M. Ashiya, C. B. Thompson and S. J. Korsmeyer (2000). "tBID, a membrane-targeted death ligand, oligomerizes BAK to release cytochrome c." Genes & Development **14**(16): 2060-2071.

White, P. J. and M. R. Broadley (2003). "Calcium in plants." Annals of botany **92**(4): 487-511.

White, S. H. and T. E. Thompson (1973). "Capacitance, area, and thickness variations in thin lipid films." *Biochimica et Biophysica Acta (BBA) - Biomembranes* **323**(1): 7-22.

Whitmore, L. and B. A. Wallace (2004). "DICHROWEB, an online server for protein secondary structure analyses from circular dichroism spectroscopic data." *Nucleic acids research* **32**(Web Server issue): W668-W673.

Winterstein, L.-M., K. Kukovetz, O. Rauh, D. L. Turman, C. Braun, A. Moroni, I. Schroeder and G. Thiel (2018). "Reconstitution and functional characterization of ion channels from nanodiscs in lipid bilayers." *The Journal of General Physiology* **150**(4): 637.

Wozniak, M. J., M. Melzer, C. Dorner, H.-U. Haring and R. Lammers (2005). "The novel protein KBP regulates mitochondria localization by interaction with a kinesin-like protein." *BMC cell biology* **6**: 35-35.

Xia, C.-H., E. A. Roberts, L.-S. Her, X. Liu, D. S. Williams, D. W. Cleveland and L. S. B. Goldstein (2003). "Abnormal neurofilament transport caused by targeted disruption of neuronal kinesin heavy chain KIF5A." *The Journal of cell biology* **161**(1): 55-66.

Xu, X., W. Decker, M. J. Sampson, W. J. Craigen and M. Colombini (1999). "Mouse VDAC Isoforms Expressed in Yeast: Channel Properties and Their Roles in Mitochondrial Outer Membrane Permeability." *The Journal of Membrane Biology* **170**(2): 89-102.

Yamaguchi, H. and M. Miyazaki (2014). "Refolding techniques for recovering biologically active recombinant proteins from inclusion bodies." *Biomolecules* **4**(1): 235-251.

Yang, X.-Y., Z.-W. Chen, T. Xu, Z. Qu, X.-D. Pan, X.-H. Qin, D.-T. Ren and G.-Q. Liu (2011). "Arabidopsis kinesin KP1 specifically interacts with VDAC3, a mitochondrial protein, and regulates respiration during seed germination at low temperature." *The Plant cell* **23**(3): 1093-1106.

Young, M. J., D. C. Bay, G. Hausner and D. A. Court (2007). "The evolutionary history of mitochondrial porins." *BMC evolutionary biology* **7**: 31-31.

Yu, H., I. Lee, A. R. Salomon, K. Yu and M. Hüttemann (2008). "Mammalian liver cytochrome c is tyrosine-48 phosphorylated in vivo, inhibiting mitochondrial respiration." *Biochimica et Biophysica Acta (BBA) - Bioenergetics* **1777**(7): 1066-1071.

Yu, T.-Y., T. Raschle, S. Hiller and G. Wagner (2012). "Solution NMR spectroscopic characterization of human VDAC-2 in detergent micelles and lipid bilayer nanodiscs." *Biochimica et Biophysica Acta (BBA) - Biomembranes* **1818**(6): 1562-1569.

Yu, W., J.-S. Gong, M. Ko, W. S. Garver, K. Yanagisawa and M. Michikawa (2005). "Altered Cholesterol Metabolism in Niemann-Pick Type C1 Mouse Brains Affects Mitochondrial Function." *Journal of Biological Chemistry* **280**(12): 11731-11739.

Yuan, J. and B. A. Yankner (2000). "Apoptosis in the nervous system." *Nature* **407**(6805): 802-809.

Yuan, S., Y. Fu, X. Wang, H. Shi, Y. Huang, X. Song, L. Li, N. Song and Y. Luo (2008). "Voltage-dependent anion channel 1 is involved in endostatin-induced endothelial cell apoptosis." *The FASEB Journal* **22**(8): 2809-2820.

Yuste, V. J., R. S. Moubarak, C. Delettre, M. Bras, P. Sancho, N. Robert, J. d'Alayer and S. A. Susin (2005). "Cysteine protease inhibition prevents mitochondrial apoptosis-inducing factor (AIF) release." *Cell Death And Differentiation* **12**: 1445.

Zaid, H., S. Abu-Hamad, A. Israelson, I. Nathan and V. Shoshan-Barmatz (2005). "The voltage-dependent anion channel-1 modulates apoptotic cell death." *Cell Death And Differentiation* **12**: 751.

Zalk, R., A. Israelson, E. S. Garty, H. Azoulay-Zohar and V. Shoshan-Barmatz (2005). "Oligomeric states of the voltage-dependent anion channel and cytochrome c release from mitochondria." *The Biochemical journal* **386**(Pt 1): 73-83.

Zeth, K (2010). "Structure and evolution of mitochondrial outer membrane proteins of beta-barrel topology." (0006-3002 (Print)).

Zeviani, M. and S. Di Donato (2004). "Mitochondrial disorders." *Brain* **127**(10): 2153-2172.

Zhang, Z., W. Zhu, S. M. Lapolla, Y. Miao, Y. Shao, M. Falcone, D. Boreham, N. McFarlane, J. Ding, A. E. Johnson, X. C. Zhang, D. W. Andrews and J. Lin (2010). "Bax Forms an Oligomer via Separate, Yet Interdependent, Surfaces." *Journal of Biological Chemistry* **285**(23): 17614-17627.

Zheng, Y., Y. Shi, C. Tian, C. Jiang, H. Jin, J. Chen, A. Almasan, H. Tang and Q. Chen (2003). "Essential role of the voltage-dependent anion channel (VDAC) in mitochondrial permeability transition pore opening and cytochrome c release induced by arsenic trioxide." *Oncogene* **23**: 1239.

Zhi, W., S. J. Landry, L. M. Gierasch and P. A. Srere (1992). "Renaturation of citrate synthase: influence of denaturant and folding assistants." Protein science : a publication of the Protein Society **1**(4): 522-529.

9. Chapter 8 Appendixes

9.1. Sanger DNA sequencing of AtVDAC constructs

Table 9.1 Sanger sequencing of AtVDAC proteins. DNA sequences (in FASTA format) obtained by Sanger sequencing using the T7 forward and reverse primers (see Figure 2.1). Primers used for the mutagenesis of AtVDAC1 are highlighted by a red line (forward) and black line (reverse).

Gene	Forward/ Reverse	Sequence
AtVDAC1	Forward	CAACAAGAAAATATCCCTCCTAGTATTTTGTTTAACTTTAAGAAGGAGATATACATATG GTGAAAGGTCCCAGTCTACACCGAAATCGGCAAAAAGGCCAGAGATCTTCTGTACA AAGACCACAACAGTGACCAGAAATTCAGTATCACCACTTTCTCTCCTGCCGGTGTTC ATCACCTCAACCGAACTAAGAAAGGTGACTTATTGTTGGGAGATGTCGCTTTTCAGTC GAGGCGAAAGAACATTACTACTGATTTGAAAGTTTGCAGTATTCTACTTTTCTGATCA CCGCTACCGTTGATGAGGCTGCACCCGACTGAGGTCAATCTTCAGCTTCAAGTTCTCT GACCAAAATTCTGGCAAGGTTGAGCTGCAATACTTGCATGAGTACGCCGGTATCAGCA CAAGCATGGGATTGACTCAGAACCAACTGTCAACTTCTCTGGTGTGATTGGCTCCAAT GTCTTGGCTGTTGGTACTGATGTTTCATTTGACACCAAGTCTGGAAATTCACCAAGAT CAATGCTGGTTAAGCTTACCAAGGAGGACTTAATTGCCTCCCTTACTGTGAACGACA AGGGCGATCTATTGAATGCATCTTACTATCACATTGTGAACCCGCTGTTCACACTGCG GTTGGAGCCGAAGTGAGCCACAAGTTATCTAGCAAGGACAGCACCATAACTGTTGGAA CACAGCACTCGCTTGACCCCTTGACCTCTGTGAAGGCTCGTGTCAATAGTCCGGGTTT GCAAGTGCTCTCATTCAACACGAGTGGAACCAAGTCACTTTCACAATCTCTGGAGA AGTCGACACAAAAGTCAATTGACAAGAGTGCTAAAGTTGGATTGGCTCTCGCACTCAAG CCTTAAGAATTCGAGCTCCGTCGACAAGCTTGCGGCCGCACTCGAGCACCACCACCAC CACCCTGAAATCCGGCTGCTAACAAAGCCCGAAAGGAAGCTGAATTGGCTGCTGCCA CCGCTGAACAATAACTAGCATAACCCCTTGGGGCCTCTAAACGGGTCTTGAAGGGTTTT TTGCTGAAAGGAGGAACTATATCCGGATTGGCAATGGGAACCGCCCTGAACCGCCCAT TAACCCGGCGGGTGGGGGTTACCCACCTG
	Reverse	TAAAACACCCCTCCCTCTTCGGGCTTTGTTAGCAGCCGGATCTCAGTGGTGGTGGTGG TGGTGCTCGAGTGCGGCCGCAAGCTTGTGACGGAGCTCGAATTTTAAGGCTTGAGT GCGAGAGCCAATCCAACCTTAGCACTCTTGCAATTGACTTTGTGTCGACTTCTCCAGA GATTGTGAAGAATGACTTGGGTTTCCACTCGTGTGAATGAGAGCACTTGAATACCCG CACTATTGACACGAGCCTTACAGAGGTCAAGGGTCAAGCGAGTGTGTGTTCCAAC AGTTATGGTGTGCTGCTTGTAGATAACTTGTGGCTCACTTCGGCTCCAACCGCAGTGT TGAACAGCGGTTTACAATGTGATAGTAAGATGCATTCAATAGATCGCCCTTGTCTGTC

ACAGTAAGGGAGGCAATTAAGTCCTCCTTGGTGAAGCTTAAACCAGCATTGATCTTGG
TGAAATTTCCAGACTTGGTGTCAAATGAAACATCAGTACCAACAGCCAAGACATTGGA
GCCAATCACACCAGAGAAGTTGACAGTTGGGTCTGAGTCAATCCCATGCTTGTGCTGA
TACCGGCGTACTCATGCAAGTATTGCAGCTCAACCTTGCCAGAATTTTGGTCAGGAACC
TTGAAGCTGAAGATTGACCTCAGTCCGGGTGCAGCCTCATCAACGGTAGCGGTGATCA
GAAAAGTAGAATCAGTGCAAACCTTCAAATCAGTAGTAATGTTCTTTCGCCTCGACTGA
AAAGCGACATCTCCAACAATAAGTCACCTTCTTAGTCCGGTTGAGGTGATGGCAAC
ACCGGCAGGAGAGAAAAGTGGTGATACTGAATTTCTGGTCACTGTTGTGGTCTTTGTACA
GAAGATCTCTGGCCTTTTTGCGGATTTCCGGTGTAGAGACCGGGACCTTTCACCATATGT
ATATCTCCTTCTAAAGTTAAACAAAATTAATTTCTAGAGGGAAACCGTTGTGGTCTCCC
TATAGTGAGTGAATAATTTCCGGGATCGAGATCTCGGGCAGCGTTGGGTCTGGCC
ACGGGTGCCCAAATGAGAGGCCTTGCAATACCCGACTATTGACCCAGCCTTCCAAAAG
TCAAGGGGTCAACCAAGGGCTGGTTCCACAGTTATGGGCCTGCCTTGCAAAAAATTGG
GGCTCATTCGTTCA

Forward

CCCCGAGAAAATTTCCCTTAGTATTTGTTTACTTTAAGAAGGAGATATACATATGGT
GAAAGGTCCCGGTCTCTACACCGAAATCGGCAAAAAGGCCAGAGATCTTCTGTACAAA
GCCACAACAGTGACCAGAAATCAGTATCACCACCTTCTCTCTGCGGGTGTGGCCATC
ACCTCAACCGGAACTAAGAAAGGTGACTTATTGTTGGGAGATGTCGCTTTTCAGTCGA
GGCGAAAGAACATTACTACTGATTTGAAAGTTGCACTGATTCTACTTTTCTGATCACC
GCTACCGTTGATGAGGCTGCACCCGGACTGAGGTCAATCTTCAGCTTCAAGGTCTCTGA
CCAAAATTCTGGCAAGGTTGAGCTGCAATACTTGCATGAGTACGCCGGTATCAGCACA
AGCATGGGATTGACTCAGAACCAACTGTCAACTTCTCTGGTGTGATTGGCTCCAATGT
CTTGGCTGTTGGTACTGATGTTTCATTTGACACCAAGTCTGGAAAATTCACCAAGATCA
ATGCTGGTTTAAGCTTCAACAAGGAGGACTTAATTGCCTCCCTTACTGTCAACAACAAG
GGCGATCTATTGAATGCATCTTACTATCACATTGTGAACCCGCTGTCAACACTGCGGT
TGGAGCCGAAGTGAGCCACAAGTTATCTAGCAAGGACAGCACCATAACTGTTGGAACA
CAGCACTCGCTTGACCCCTTGACCTCTGTGAAGGCTCGTGTCAATAGTGGGGTATTGC
AAGTGCTCTCATTCAACACGAGTGGAACCCAAGTCATTCTTACAATCTCTGGAGAA
GTCGACACAAAAGTCAATTGACAAGAGTGCTAAAGTTGGATTGGCTCTCGCACTCAAGC
CTTAAGAATTCGAGCTCCGTCGACAAGCTTGCGGCCGCACTCGAGCACCACCACCACC
ACCACTGAAATCCGGCTGCTAACAAAGCCCGAAAGGAAGCTGAATTGGCTGCTGCCAC
CGCTGAACAATAACTAGCATAACCCCTTGGGGCCTCTAAACGGGTCTTGAGGGGTTTTT
TGCTGAAAGGAGGAACTAATTCCGGATTGGCGAATGGGACCGCCCTGGTACCGCCAT
TAACCGGGGCGGGTTGGGGGGTACCGGCACCTGGCCCTAACCTTTCAGGCCTACGC
GCCGTCCTTCGGTTTTCTCTTTTTCCGCCAGTTG

D177N

Reverse AGAGAACCAATTCCTCTTCGGGCTTTGTTAGCAGCCGGATCTCAGTGGTGGTGGTGGTG
GTGCTCGAGTGC GGCCGAAGCTTGTGACGGAGCTCGAATTCCTAAGGCTTGAGTGC
GAGAGCCAATCCAACCTTAGCACTCTTGTCAATTGACTTTGTGTCGACTTCTCCAGAGA
TTGTGAAGAATGACTTGGGTTTCCACTCGTGTGAATGAGAGCACTTGAATACCCGCA
CTATTGACACGAGCCTTCACAGAGGTCAAGGGTCAAGCGAGTGTGTGTTCCAACAG
TTATGGTGTGCTCCTTGCTAGATAACTTGTGGCTCACTTCGGCTCCAACCGCAGTGTG
AACAGCGGGTTCACAATGTGATAGTAAGATGCATTCAATAGATCGCCCTTGTGTTGAC
AGTAAGGGAGGCAATTAAGTCCTCCTTGGTGAAGCTTAAACCAGCATTGATCTTGGTG
AAATTTCCAGACTTGGTGTCAAATGAAACATCAGTACCAACAGCCAAGACATTGGAGC
CAATCACACCAGAGAAGTTGACAGTTGGGTTCTGAGTCAATCCCATGCTTGTGCTGATA
CCGGCGTACTCATGCAAGTATTGCAGCTCAACCTTGCCAGAATTTTGGTCAGGAACCTT
GAAGCTGAAGATTGACCTCAGTCCGGGTGCAGCCTCATCAACGGTAGCGGTGATCAGA
AAAGTAGAATCAGTGCAAACCTTCAAATCAGTAGTAATGTTCTTTTCGCTCGACTGAAA
AGCGACATCTCCAACAATAAGTCACCTTCTTAGTTCGGTTGAGGTGATGGCAACAC
CGGCAGGAGAGAAAGTGGTGATACTGAATTTCTGGTCACTGTTGTGGTCTTTGTACAGA
AGATCTCTGGCCTTTTGGCGATTTCGGTGTAGAGACCGGGACCTTTCACCATATGTAT
ATCTCCTTCTTAAAGTTAAACAAAATTATTTCTAGAGGGAAACCGTTGTGGTCTCCCTA
TAGTGAGTCGTATTAATTTGCGGGGATCGAGATCTCGGGCAGCGTTGGGTCTGGCCAC
GGGTGCCCATGATCTTGCTCCTGTCTTGAGGACCCGGCTAGGCTGGCGGGTTGCTTA
CTGGTTAACAAAATGATCCCCGAACCCGAGCGAACTTGAACGACTGGTGGTGGCAAAC
GTTGGCACCTGGACAACATCTGAAGGGTTCCCGTT

Forward CAAAAGAAAAATTCCTCCTTAGATATTTGTTTACTTTAAGAAGGAGATATACATATG
GTGAAAGGTCCCGGTCTCTACACCGAAATCGGCAAAAAGGCCAGAGATCTTCTGTACA
AAGACCACAACAGTGACCAGAAATTCAGTATCACCACTTCTCTCCTGCCGGTGTGCC
ATCACCTCAACCGAACTAAGAAAGGTGACTTATTGTTGGGAGATGTCGCTTTTCAGTC
GAGGCGAAAGAACATTACTACTGATTTGAAAGTTTGCAGTACTTACTTTTCTGATCA
CCGCTACCGTTGATGAGGCTGCACCCGGACTGAGGTCAATCTTCAGCTTCAAGGTTCTT
GACCAAAATTCGGCAAGGTTGAGCTGCAATACTTGCATGAGTACCGGTATCAGCA
CAAGCATGGGATTGACTCAGAACCCAACTGTCAACTTCTCTGGTGTGATTGGCTCCAAT
GTCTTGGCTGTTGGTACTGATGTTTCATTTGACACCAAGTCTGGAAATTTACCAAGAT
CAATGCTGGTTAAGCTTACCAAGGAGGACTTAATTGCCTCCCTTACTGTGAACGACA
AGGGCGATCTATTGAATGCATCTTACTATCACATTGTGAACCCGCTGTCAACACTGCG
GTTGGAGCCGAAGTGAGCCACAAGTTATCTAGCAAGGACAGCACCATAACTGTTGGAA
CACAGCACTCGCTTGACCCCTTGACCTCTGTGAAGGCTCGTGTCAATAGTGCGGGATT
GCAAGTGCTCTCATTCAACACGAGTGGAACCCAAAGTCATTCTCACAATCTCTGGAGA
AGTTAACACAAAAGTCAATTGACAAGAGTGCTAAAGTTGGATTGGCTCTCGCACTCAAG
CCTAAGAATTCGAGCTCCGTCGACAAGCTTGC GGCCGCACTCGAGCACCACCACCAC

D258N

CACCACTGAAATCCGGCTGCTAACAAAGCCCGAAAGGAAGCTGAATTGGCTGCTGCCA
CCGCTGAACAATAACTAGCATAACCCCTTGGGGCCTCTAAACGGGTCTTGAGGGGTTTT
TGCTGAAAGGAGGACTATATCCGGATTGGCAATGGGACCGCCCTGTACCGCCATTAAC
CCGGCGGGTGGGGGTACCGCAACGTGACCGTAACTTGCCAGGCCTAAGGCCGTCT
TTGGTTCTCCCTTCTTTTCGCAAGTCGCGGGTTT

Reverse

AACCCAGCAAAAACTTCTTCGGGCTTTGTTAGCAGCCGGATCTCAGTGGTGGTGGTG
GTGGTGTCTCGAGTGCGGCCGAAGCTTGTGACGAGGACTCGAATCTTAAGGCTTGAG
TGCGAGAGCCAATCCAACCTTAGCACTCTGTCAATTGACTTTGTGTTAACTTCTCCAG
AGATTGTGAAGAATGACTTGGGTTTCCACTCGTGTGAATGAGAGCACTGCAATACCC
GCACTATTGACACGAGCCTTCACAGAGGTCAAGGGGTCAAGCGAGTGTGTGTTCCAA
CAGTTATGGTGTCTCCTTGCTAGATAACTTGTGGCTCACTTCGGTCCAACCGCAGTG
TTGAACAGCGGGTTCACAATGTGATAGTAAGATGCATTCAATAGATCGCCCTTGTGCTT
CACAGTAAGGGAGGCAATTAAGTCTCCTTGGTGAAGCTTAAACCAGCATTGATCTTG
GTGAAATTTCCAGACTTGGTGTCAAATGAAACATCAGTACCAACAGCCAAGACATTGG
AGCCAATCACACCAGAGAAGTTGACAGTTGGGTTCTGAGTCAATCCCATGCTTGTGCTG
ATACCGGCGTACTCATGCAAGTATTGCAGCTCAACCTTGCCAGAATTTTGGTCAGGAAC
CTTGAAGCTGAAGATTGACCTCAGTCCGGGTGCAGCCTCATCAACGGTAGCGGTGATC
AGAAAAGTAGAATCAGTGCAAACCTTCAAATCAGTAGTAATGTTCTTTCGCCTCGACTG
AAAAGCGACATCTCCAACAATAAGTCACCTTCTTAGTTCCGGTTGAGGTGATGGCAA
CACCGGCAGGAGAGAAAAGTGGTGAATGACTGAATTTCTGGTCACTGTGTGGTCTTTGTAC
AGAAGATCTCTGGCCTTTTTCGGATTTCGGTGTAGAGACCGGGACCTTTCACCATATG
TATATCTCCTTCTTAAAGTTAAACAAAATTATTCTAGAAGGGAAACCGTTGTGGTCTC
CCTATAATTGAGTCGTATTAATTTCCCCGGGATCGAGATCTCGGGCAGCGTTGGGTCTT
GGCCACGGGTGCCCATGATCGTCTCTGCTTAAGGACCGGCTAGGCTGGCGGGT
TTGCCTTACTGGTTACCAAAATGAATCCCCGATCCCGGAGCGAACTTGAACCGACTGCT
GGTGGAAAACCTTGGACTGAGACACAATTCA

Forward

CCAAAGAAAATATCCCTTAGTATTTTGTACTTTAAGAAGGAGATATACATATGGT
GAAAGGTCCCGTCTCTACACCGAAATCGGCAAAAAGGCCAGAGATCTTCTGTACAAA
GACCACAACAGTGACCAGAAATTCAGTATCACCACTTCTCTCCTGCCGGTGTGCCAT
CACCTCAACCGGAACTAAGAAAGGTGACTTATTGTTGGGAGATGTCGCTTTTTCAGTCGA
GGCGAAAGAACATTACTACTGATTTGAAAGTTTGCAGTATTCTACTTTTCTGATCACC
GCTACCGTTGATGAGGCTGCACCCGGACTGAGGTCAATCTTCAGTTC AAGGTTCTGA
CCAAAATTCTGGCAAGGTTGAGCTGCAATACTTGCATGAGTACGCCGGTATCAGCACA
AGCATGGGATTGACTCAGAACCCAACTGTCAACTTCTCTGGTGTGATTGGCTCCAATGT
CTTGGCTGTTGGTACTGATGTTTCATTTGACACCAAGTCTGGAAATTTCTGCAAGATCA
ATGCTGGTTTAAGCTTCACCAAGGAGGACTTAATTGCCTCCCTTACTGTGAACGACAAG

T156C

GGCGATCTATTGAATGCATCTTACTATCACATTGTGAACCCGCTGTCAACACTGCGGT
TGGAGCCGAAGTGAGCCACAAGTTATCTAGCAAGGACAGCACCATAACTGTTGGAACA
CAGCACTCGCTTGACCCCTTGACCTCTGTGAAGGCTCGTGTCAATAGTGCGGGTATTGC
AAGTGCTCTCATTCAACACGAGTGGAACCCAAGTCATTCTCACAATCTCTGGAGAA
GTCGACACAAAAGTCAATTGACAAGAGTGCTAAAGTTGGATTGGCTCTCGCACTCAAGC
CTTAAGAATTCGAGCTCCGTCGACAAGCTTGCGGCCGCACTCGAGCACCACCACCACC
ACCACTGAAATCCGGCTGCTAACAAAGCCCGAAAGGAAGTGAATTGGCTGCTGCCAC
CGCTGAACAATAACTAGCATAACCCCTTGGGGCCTCTAACGGGTCTTGAGGGGTTTTT
TGCTGAAAGGAGGAATAATTCCGGATTGGCGAAAGGAACGCGCCTGGACCGCCATT
AACCCCGCGGGTTGGGGTTACCGAACGTGACCCTAACTTTGCAAGGCTAAGGCC
CGTCTTTCGTTTTTCTTCTTTCCCGCAAGTTCCCGGGTTTCCCGGAAAAG

Reverse

ACCCGAACAAAAACCTCTTCGGGCTTTGTTAGCAGCCGGATCTCAGTGGTGGTGGT
GGTGGTGCCTCGAGTGCGGCCGCAAGCTTGTGACGGAGCTCGAATTCTTAAGGCTTGA
GTGCGAGAGCCAATCCAACCTTAGCACTCTTGTCAATTGACTTTGTGTCGACTTCTCCA
GAGATTGTGAAGAATGACTTGGGTTTCCACTCGTGTGAATGAGAGCACTTGAATACC
CGCACTATTGACACGAGCCTTACAGAGGTCAAGGGTCAAGCGAGTGTGTGTTCCA
ACAGTTATGGTGCTGTCTTGTAGATAACTTGTGGCTCACTTCGGCTCCAACCGCAGT
GTTGAACAGCGGGTTCACAATGTGATAGTAAGATGCATTCAATAGATCGCCCTGTGCT
TCACAGTAAGGGAGGCAATTAAGTCCTCTTGGTGAAGCTTAAACCAGCATTGATCTTG
CAGAAATTTCCAGACTTGGTGTCAAATGAAACATCAGTACCAACAGCCAAGACATTGG
AGCCAATCACACCAGAGAAGTTGACAGTTGGGTTCTGAGTCAATCCCATGCTTGTGCTG
ATACCGCGTACTCATGCAAGTATTGCAGCTCAACCTTGCCAGAATTTTGGTCAGGAAC
CTTGAAGCTGAAGATTGACCTCAGTCCGGGTGCAGCCTCATCAACGGTAGCGGTGATC
AGAAAAGTAGAATCAGTGCAAACCTTCAAATCAGTAGTAATGTTCTTTCGCCTGACTG
AAAAGCGACATCTCCCAACAATAAGTCACCTTTCTTAGTCCGGTTGAGGTGATGGCAA
CACCGGCAGGAGAGAAAGTGGTGATACTGAATTTCTGGTCACTGTTGTGGTCTTTGTAC
AGAAGATCTCTGGCCTTTTGGCGATTTCCGGTGTAGAGACCGGGACCTTTCACCATATG
TATATCTCCTTCTAAAGTTAAACAAAATTATTTCTAGAGGGAAACCGTTGTGGTCTCC
CTATAGTGAGTCGTATTAATTTCCCGGATCGAGATCTCGGGCAGCGTTGGGTCCTGGC
CACGGGTGGCCATGATCTTGCTCCTGTGCTTGGAGACCCGGTAGGCTGGCGGGGTTGCT
TACTGGTAGCAAAATGATCACCGATCCCGAGCGAACGTGAACGATGGTGCTGAAAACG
TCTGGACTGGAACACAATGAATGGCTTTCGTTCTGTTCTAAATTC

9.2. Example of calculations for the lipid reconstitution of AtVDAC1 protein in DMPC

STEP A:

600 μL of DMPC (50 mg/mL or 73 mM in 0.1% (v/v) LDAO and 0.1% w/v Octyl glucoside)

=43.8 μmoles

To mix with $1/2000 \times 43.8 = 21.9$ nmole of AtVDAC1

[SECA_{AtVDAC1}Hitrap5mL oligo] = 2.35 mg/mL = 7.885×10^{-5} M

So $V_{\text{AtVDAC1}} = 21.9 \times 10^{-9} / 7.885 \times 10^{-5} = 2.77 \times 10^{-4} \text{L} = 277 \mu\text{L}$

STEP B:

-1 mL of washed biobeads = 75 mg

-DMPC (50 mg/mL or 73 mM in 0.1% (v/v) LDAO and 0.1% w/v OG)

So 100 μL corresponds to $1 \text{ mg/mL} \times 100 \mu\text{L} = 100 \mu\text{g}$ of OG and $100 \mu\text{L} \times 0.996 \mu\text{g/L} = 99.6 \mu\text{g}$

So Total amount of detergent = 200 μg

So $w_{\text{beads}}/w_{\text{detergent}} = 75/0.2 = 375 (>100)$

End: 877 μL of DMPC+protein+detergent

$W_{\text{OG}} = 600 \mu\text{L} \times 1 \text{ mg/mL} = 600 \mu\text{g}$ of OG

$W_{\text{LDAO}} = 600 \mu\text{L} \times 1 \text{ mg/mL (lipids)} + 200 \mu\text{L} \times 1.15 \text{ mg/mL (protein in SEC buffer)}$

$W_{\text{LDAO}} = 600 + 230 = 830 \mu\text{g}$

$W_{\text{Detergent}} = 830 + 600 = 1.43 \text{ mg}$

STEP C: Mix 877 μL lipids+refolded protein solution with 20 mL of lipid-presaturated biobeads:

-20 mL of lipid-presaturated biobeads = 150 mg

- $W_{\text{Detergent}} = 1.43 \text{ mg (lipids+protein solution)} + 200 \mu\text{g} \times 2 \text{ (biobeads)} = 1.83 \text{ mg of detergent}$

So $W_{\text{beads}}/W_{\text{detergent}} = 150/1.83 = 82$

Or $W_{\text{beads}}/W_{\text{detergent protein+lipid only}} = 150/1.43$

9.3. Identification of amino acids involved the docking of Hexokinase 1 to AtVDACs

Isoform	AtVDAC1		AtVDAC2				AtVDAC4	
Docking model	1	2	1	2	3	4	1	2
Amino acids involved	50D	48K	48K	48K	48K	24Q	48K	16K
	74D	50D	50G	50G	254E	27Q	49D	48K
	76T	74D	208E	74D	256E	47N	50D	49D
	97K	97K	254E	97K	258D	48K	72D	50D
	100D	99P	256E	99P	259A	154N	76S	180E
	101Q	100D	258D	101H	260I	156K	102K	203R
	103S	101Q	261D	156K	261D	177D	105K	205S
	105K	103S	262K	254E	262K	180E	124N	206N
	124T	105K	263S	256E	263S	181K	156T	207Y
	156T	124T	265K	258D	265K	205T	177D	208N
	177D	125Q		265K		208E	180E	228R
	180D	149D				228R	203R	230S
	205K	205K				254E	206N	231N
	210D	207S				256E	208N	232S
	230R	210D				258D	234K	256E
	232N	233S				261D	265K	258D
	256E	234A				262K		265K
	258D	256E				263S		
	267K	258D				265K		
		259T						
	260K							

9.4. Protein sequence alignment of VDACs

AtVDAC1
 -----¹MVKGPGLYTEIGKKARDLLYKDHNSDQ-KFSITTF³⁴
hVDAC3a
 -----MCNTPTYCDLGKAAKDVFNKGYGFGMVKIDLKTK
hVDAC3b
 -----MCNTPTYCDLGKAAKDVFNKGYGFGMVKIDLKTK
mVDAC1
 -----MAVPPTYADLGKSARDVFTKGYGFLIKLIDLKTK
XmVDAC1
 -----MRGSHHHHHHGSMAVPPTYADLGKSARDVFTKGYGFLIKLIDLKTK
hVDAC1
 -----MAVPPTYADLGKSARDVFTKGYGFLIKLIDLKTK
hVDAC1micelles
 -----MAVPPTYADLGKSARDVFTKGYGFLIKLIDLKTK
zfVDAC2
 -----MAVPPAYADLGKSAKDI FNKGYGFGMVKLDVKT
MmVDAC2
 MAECC-----VPVCPRPCMIPPPYADLGKAARDI FNKGFGLVKLDVKT
hVDAC2a
 MSWCNELRLPALQHSIGRGLSHITMCIPPSYADLGKAARDI FNKGFGLVKLDVKT
hVDAC2b
 -----MATHGQTCARPMCI PPSYADLGKAARDI FNKGFGLVKLDVKT
hVDAC2c
 -----MLVIPA
AtVDAC4
 -----MGSSPAPFADIGKKAKDLLNKDYIFDH-KFTLTML
AtVDAC2
 -----MSKGPGLFTDIGKKAKDLLTRDYNSDQ-KFSISTY
 : :
AtVDAC1
³⁵SPAGV-AITSTGTTKGD--LLLGDVAFQSRKN--ITDLKVCTDSTFLITATVDEAA-P⁸⁸
hVDAC3a
 SCSGV-EFSTSGHAYTDTGKASGNLETKYKVCNYGLTFTQKWNTDNTLGTEISWENKLAE
hVDAC3b
 SCSGVMEFSTSGHAYTDTGKASGNLETKYKVCNYGLTFTQKWNTDNTLGTEISWENKLAE
mVDAC1
 SENGL-EFTSSGSANTETTKVNGSLETKYRWTEYGLTFTEKWNTDNTLGTEITVEDQLAR
XmVDAC1
 SENGL-EFTSSGSANTETTKVNGSLETKYRWTEYGLTFTEKWNTDNTLGTEITVEDQLAR
hVDAC1
 SENGL-EFTSSGSANTETTKVNGSLETKYRWTEYGLTFTEKWNTDNTLGTEITVEDQLAR
hVDAC1micelles
 SENGL-EFTSSGSANTETTKVNGSLETKYRWTEYGLTFTEKWNTDNTLGTEITVEDQLAR
zfVDAC2
 SASGV-EFKTSGSSNTDTGKVVGSLETKYKRSEYGLTFTEKWNTDNTLGTEINIEDQIAK
MmVDAC2
 SCSGV-EFSTSGSSNTDTGKVSGLTETKYKWCEYGLTFTEKWNTDNTLGTEIAIEDQICQ
hVDAC2a
 SCSGV-EFSTSGSSNTDTGKVTGTLETKYKWCEYGLTFTEKWNTDNTLGTEIAIEDQICQ
hVDAC2b
 SCSGV-EFSTSGSSNTDTGKVTGTLETKYKWCEYGLTFTEKWNTDNTLGTEIAIEDQICQ
hVDAC2c
 TQAE-EFSTSGSSNTDTGKVTGTLETKYKWCEYGLTFTEKWNTDNTLGTEIAIEDQICQ
AtVDAC4
 SATGT-EFVATGLKKDD--FFFGDISTLYKQN--TIVDLKIDSHSSVSTKVTLKNLL-P
AtVDAC2
 SASGV-ALTSTALKKGG--VHAADVATQYKYKN--ALFDVKIDTDSSVLTTVTLTEIL-P

: . : : . . : : * : . . . :
AtVDAC1
 89 GLRSIFSF---KVPDQNSGKVELQYLHEYAGISTSMGLT-QNPTVNFSGVIGSNVLAVGT¹⁴⁴
hVDAC3a
 GLKLTLDITIFVPNTGKKSGKLGKASYKRDCFSVGSNVDIDFSGPTIYGWAVLAFEGWLAGY
hVDAC3b
 GLKLTLDITIFVPNTGKKSGKLGKASYKRDCFSVGSNVDIDFSGPTIYGWAVLAFEGWLAGY
mVDAC1
 GLKLTFDSSSFSPNTGKKNAKIKTGYKREHINLGCVDVDFDIAGPSIRGALVVLGYEGWLAGY
XmVDAC1
 GLKLTFDSSSFSPNTGKKNAKIKTGYKREHINLGCVDVDFDIAGPSIRGALVVLGYEGWLAGY
hVDAC1
 GLKLTFDSSSFSPNTGKKNAKIKTGYKREHINLGCMDVDFDIAGPSIRGALVVLGYEGWLAGY
hVDAC1micelles
 GLKLTFDSSSFSPNTGKKNAKIKTGYKREHINLGCMDVDFDIAGPSIRGALVVLGYEGWLAGY
zfVDAC2
 GLKLTFDTTTFSPNTGKKSGKVKTAYKREFVNLGCDVDFDFAGPTIHGAAVVGYEGWLAGY
MmVDAC2
 GLKLTFDTTTFSPNTGKKSGKIKSAYKRECINLGCVDVDFDFAGPAIHGSAVFGYEGWLAGY
hVDAC2a
 GLKLTFDTTTFSPNTGKKSGKIKSAYKRECINLGCVDVDFDFAGPAIHGSAVFGYEGWLAGY
hVDAC2b
 GLKLTFDTTTFSPNTGKKSGKIKSAYKRECINLGCVDVDFDFAGPAIHGSAVFGYEGWLAGY
hVDAC2c
 GLKLTFDTTTFSPNTGKKSGKIKSAYKRECINLGCVDVDFDFAGPAIHGSAVFGYEGWLAGY
AtVDAC4
 SAKAVISF---KIPDHKSGKLDVQYVHPHATLNSSIGLN-PTPLLDLSATIGSQNVCLGG
AtVDAC2
 STKAIASF---KVPDYNSAKLEVQYFHDHATVTAALALK-QNPLIDITATLGSPVISFGA
 . : . : . . . * : * : : * : . . *
AtVDAC1
 145 DVSFDTKSGNFTKINAGLSFTKEDLIASLTVNDKGDLLNASYYHIVNPLFNTAVGAEVSH²⁰⁴
hVDAC3a
 QMSFDTAKSKLSQNNFALGYKAADFQLHTHVNDGTE-FGGSYQKVNEKIETSIN--LAW
hVDAC3b
 QMSFDTAKSKLSQNNFALGYKAADFQLHTHVNDGTE-FGGSYQKVNEKIETSIN--LAW
mVDAC1
 QMNFETSKSRVTQSNFAVGKYKTDEFQLHTNVNDGTE-FGGSYQKVNKKLETAVN--LAW
XmVDAC1
 QMNFETSKSRVTQSNFAVGKYKTDEFQLHTNVNDGTE-FGGSYQKVNKKLETAVN--LAW
hVDAC1
 QMNFETAKSRVTQSNFAVGKYKTDEFQLHTNVNDGTE-FGGSYQKVNKKLETAVN--LAW
hVDAC1micelles
 QMNFETAKSRVTQSNFAVGKYKTDEFQLHTNVNDGTE-FGGSYQKVNKKLETAVN--LAW
zfVDAC2
 QMSFDTAKSKMTQNNFAVGKYKTGDFQLHTNVNDGSE-FGGSYQKVSDKLETAVN--LAW
MmVDAC2
 QMTFDSAKSKLTRSNFAVGKYRTGDFQLHTNVNDGTE-FGGSYQKVCEDFDTSVN--LAW
hVDAC2a
 QMTFDSAKSKLTRNNFAVGKYRTGDFQLHTNVNDGTE-FGGSYQKVCEDLDTSVN--LAW
hVDAC2b
 QMTFDSAKSKLTRNNFAVGKYRTGDFQLHTNVNDGTE-FGGSYQKVCEDLDTSVN--LAW
hVDAC2c
 QMTFDSAKSKLTRNNFAVGKYRTGDFQLHTNVNDGTE-FGGSYQKVCEDLDTSVN--LAW
AtVDAC4
 EVSFDTASSSLTKYNAGIGFNNQGVSAALILEDKGESLRATYVHTVNPT--TSFGAELIR
AtVDAC2
 EAGYDTTSKTFTKYNAGISVTKPDACLSIIIGDKGDSLKASYLHHFDEFKRTAAVGEVYR
 : : : . . : * . . : : : : : . * : :

AtVDAC1
205 KLSSKSDSTITVGTQHSLDPLTSVKARVNSAGIASALIQHEWKPKSFFTISGEV**D**TKSIDR²⁶⁴

hVDAC3a
TAGSNNTRFGIAAKYMLDCRTSLSAKVNNASLIGLGYTQTLRPGVKLTLSAL**I**DGKNFSA

hVDAC3b
TAGSNNTRFGIAAKYMLDCRTSLSAKVNNASLIGLGYTQTLRPGVKLTLSAL**I**DGKNFSA

mVDAC1
TAGSNNTRFGIAAKYQVDPDACFSAKVNNSSLIGLGYTQTLKPGIKLTLSALL**D**GKNVNA

XmVDAC1
TAGSNNTRFGIAAKYQVDPDACFSAKVNNSSLIGLGYTQTLKPGIKLTLSALL**D**GKNVNA

hVDAC1
TAGSNNTRFGIAAKYQIDPDACFSAKVNNSSLIGLGYTQTLKPGIKLTLSALL**D**GKNVNA

hVDAC1micelles
TAGSNNTRFGIAAKYQIDPDACFSAKVNNSSLIGLGYTQTLKPGIKLTLSALL**D**GKNVNA

zfVDAC2
TAGSNSTRFGIAAKYQLDKDASISAKVNNTSLVGVGYTQSLRPGIKLTLSAL**V**DGKSINS

MmVDAC2
TSGTNCTRFGIAAKYQLDPTASISAKVNNSSLIGVGYTQTLRPGVKLTLSAL**V**DGKSFNA

hVDAC2a
TSGTNCTRFGIAAKYQLDPTASISAKVNNSSLIGVGYTQTLRPGVKLTLSAL**V**DGKSINA

hVDAC2b
TSGTNCTRFGIAAKYQLDPTASISAKVNNSSLIGVGYTQTLRPGVKLTLSAL**V**DGKSINA

hVDAC2c
TSGTNCTRFGIAAKYQLDPTASISAKVNNSSLIGVGYTQTLRPGVKLTLSAL**V**DGKSINA

AtVDAC4
RFSNYNNSFTVGSSHSVDQFTVVKTRFSNSGKAGMVVQREWRPKSHITFSAEY**D**SKAVTS

AtVDAC2
KFSTNENTITVGGLYAIDHSTAVKAKLNNHGTGALLQHEVLPRLVTVSSE**I**DTKALEK
. . . : . . : :* : : * . * . * * .

AtVDAC1 265 SAKVGLALALKP²⁷⁶-----
hVDAC3a GGHKVGLGFELEA-----
hVDAC3b GGHKVGLGFELEA-----
mVDAC1 GGHKLGLGLEFQA-----
XmVDAC1 GGHKLGLGLEFQA-----
hVDAC1 GGHKLGLGLEFQA-----
hVDAC1micelles GGHKLGLGLEFQALEHHHHHH
zfVDAC2 GGHKLGLGLELEAHHHHHH--
MmVDAC2 GGHKLGLALELEA-----
hVDAC2a GGHKVGLALELEA-----
hVDAC2b GGHKVGLALELEA-----
hVDAC2c GGHKVGLALELEA-----
AtVDAC4 -SPKLGLALALKP-----
AtVDAC2 -HPRFGLSLALKP-----
: . * * . : . :

Figure 9.1 Multiple sequence alignment os VDAC orthologues. Sequence alignment of VDAC ORFs (open reading frames) from human (hVDAC1, 2 and 3), mouse (mVDAC1, MmVDAC2 and its crystallized form XmVDAC1) and zebrafish (zfVDAC2). Amino acids used for mutagenesis are indicated in bold colours: T156C in light blue, D177N in orange and D258N in red. The position of amino acids in AtVDAC1 protein is taken as a reference and indicated at beginning and end of the sequence.

9.5. TLC experiment on AtVDAC1 oligomer and monomer fractions

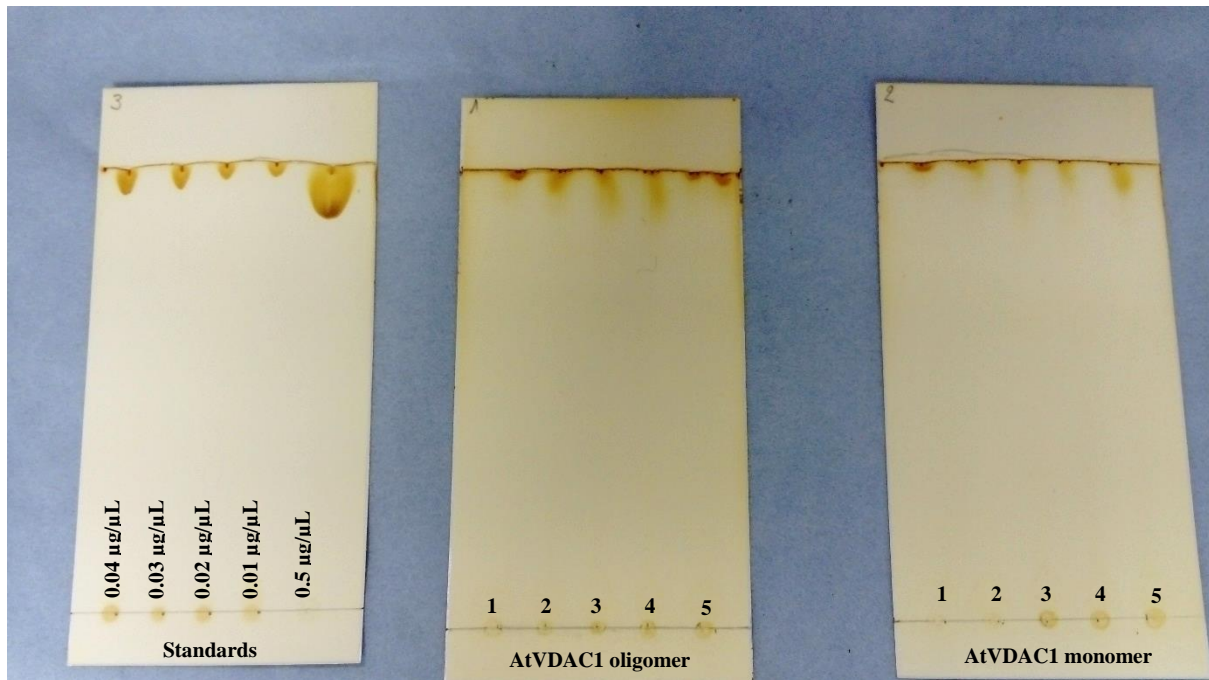


Figure 9.2 Thin layer Chromatography (TLC) experiments on AtVDAC1 samples. 1 to 5 μL of purified AtVDAC1 oligomer fractions (AtVDAC1 oligomer, 1 to 5) or monomer fractions (AtVDAC1 monomer), 1 to 5 were loaded and analysed by TLC using a TLC solvent (63: 35: 5, v/v/v chloroform: methanol: ammonium hydroxide). Standard concentrations of LDAO (Standards) were loaded for comparative analysis.

9.6. Secondary structure prediction of mKlp2C-Ter

```

HAVSGEYADELKKKIQSQEIENEELKLEHVQIVEENSGLRVQNQKLAEEASYAKELASAAAVELKNLASEVTKLS
----HHHHHHHHHHHHHHHHHHHHHHHHHHHEEEE-----HHHHHHHHHHHHHHHHHHHHHHHHHHHHHHHHHHHH
LQNTKLEKELAAARDLAQTRNPMNGVNRKYNDGARSGRKGRISRRSSGDEFDAWNLDPEDLKMELQVRKQREVA
HHHHHHHHHHHHHHHH-----HHHHHHHHHHHHHHHHHHHHHHHHHHHHHHHHHHHHHHHHHHHHHHHHHH
LESALAEKEFIEDEYRKKAEAKRREEALENDLANMWVLVAKLKKDNGALPEPNGTDPGRELEKSQSHAVLKERQ
HHHHHHHHHHHHHHHHHHHHHHHHHHHHHHHHHHHHHH-----HHHHHHHH-----HHHHHHHHHHHHHHHH
VSSAPRQPEVVVVAKTEETPKKEEPLVARLKARMQEMKEKEMKSQANGDANSHICKVCFESPTAAILLPCRHFCLC
-----HHHHHHHH-----EEEEEE-----EEEE-----EEH
KCSLACSECPICRTKISDRLFAFPS
HHHHHH-----EEEEEE--

```

Figure 9.3 Secondary structure prediction of mKlp2C-Ter. Simplified secondary structure prediction of the His-Tag-less mKlp2C-Ter using Jpred webserver [57]. The amino acids involved in the formation of a hypothetical alpha helix are highlighted by red “H”. Extended regions are highlighted by a yellow “E”.

9.7. High Tension (HT) Voltage of AtVDAC1 monomer and oligomer

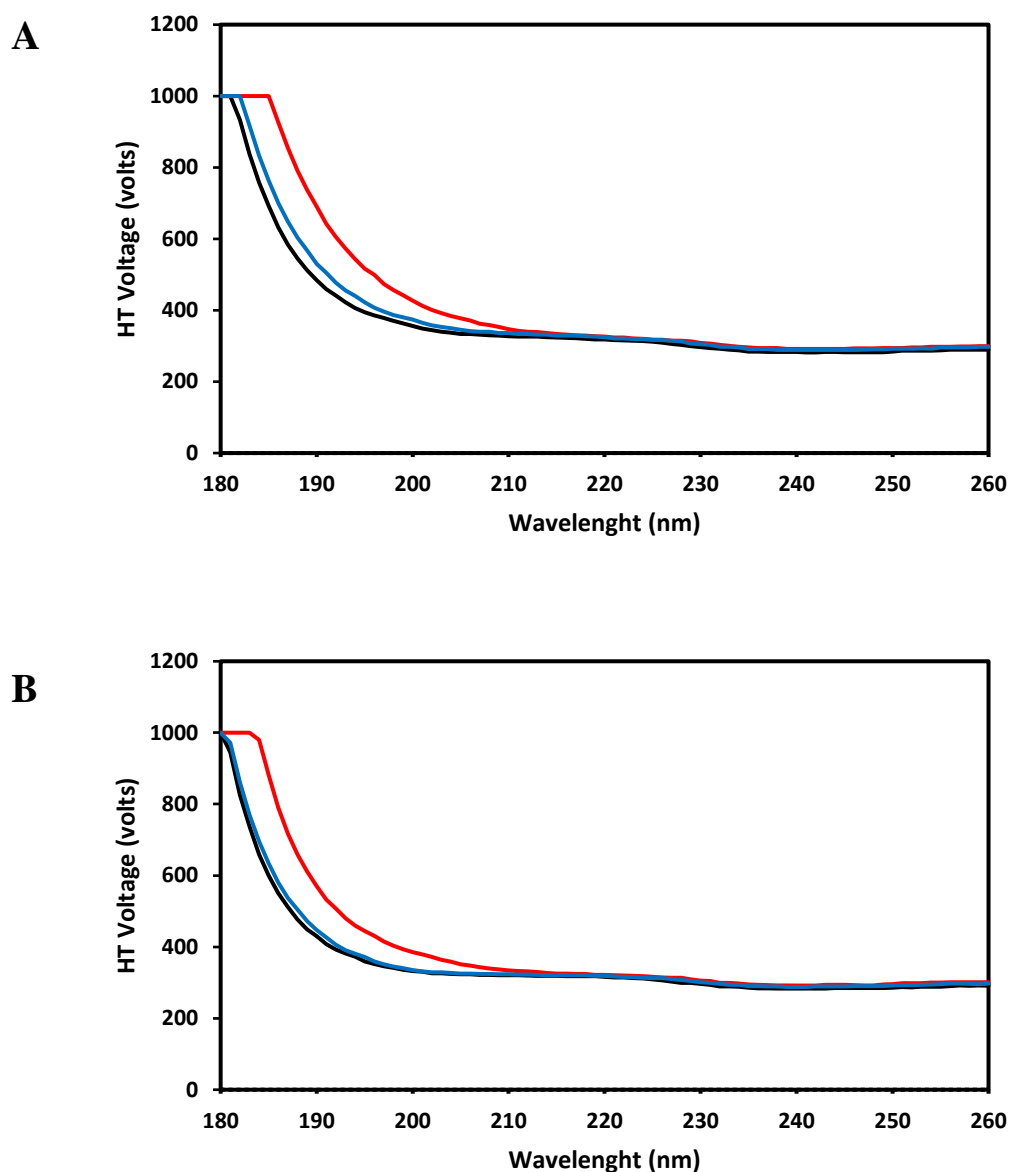


Figure 9.4 HT Voltage of AtVDAC1 oligomer and monomer fraction at various temperature. HT (High tension) Voltage curves of AtVDAC1 monomer (**A**) and oligomer (**B**) fractions during CD experiments. Measurements we performed at 20 °C (black curve), after heating at 90 °C (red curve) and after cooling at 20 °C (Blue curve).

9.8. Conversion between Theta (mDeg) and delta epsilon (M⁻¹.cm⁻¹)

$$\Delta\epsilon = \frac{\theta \times \text{MRW}}{c \times l \times 32980}$$

Equation 9.1 Relationship between Theta (θ) et delta epsilon ($\Delta\epsilon$). MRW is the mean residual weight of the protein (molecular weight divided by the total number of amino acids), c is the concentration of the sample (in mg/mL) and l is the path length (in cm).

9.9. Calculation the mean residue molar ellipticity [θ]

$$[\theta] = \frac{\theta_{\text{obs}} \times 100 \times \text{MW}}{c \times l \times n}$$

Equation 9.2 Relationship between Theta (θ) et delta epsilon ($\Delta\epsilon$). θ_{obs} is the observed ellipticity in degrees, MW is the molecular weight of the protein, c is the concentration of the sample (in mg/mL), l is the path length (in cm) and n is the number of amino acids.

9.10. Circular Dichroism analysis (raw data)

Table 9.2 Dichroweb CD analysis. Raw data obtained during the analysis of different samples using Dichroweb webserver, using either CONTINLL and CDSSTR algorithms and SMP180 database (optimized for 190 nm to 240 nm). The analysis was not successful for mVDAC1 3EMN using CDSSTR and any database. The analysis was performed with the most recent version of the database (2019), thus can differ slightly from the original data for this study (performed in 2015).

Sample	Algorithm	Helix	Strand	Turns	Unordered	Total
AtVDAC1 oligo	CONTINLL	0.061	0.352	0.188	0.399	1
	CDSSTR	0.41	0.14	0.13	0.30	0.98
AtVDAC1 mono	CONTINLL	0.107	0.281	0.156	0.456	1
	CDSSTR	0.34	0.13	0.16	0.36	0.99
mVDAC1 3EMN	CONTINLL	0.048	0.441	0.110	0.400	0.999
	CDSSTR					
AtVDACs (predicted)	CONTINLL	0.048	0.441	0.111	0.400	1
	CDSSTR	0.01	0.45	0.07	0.46	0.99